

AD-A240 404



8

3

1



Completed 1991

Volume 1: The RAND Corporation  
Annual Configuration

RAND CORPORATION CENTER

DISPATCHED TO THE

STANDARD

Accession For	
NTIS ORASI	<input checked="" type="checkbox"/>
NTIS TAB	<input type="checkbox"/>
Unannounced	<input type="checkbox"/>
Justification	
By	
Distribution/	
Availability Codes	
Avail and/or	Special
A-1	



# Ocean Engineering Studies

Compiled 1991

## Volume V: Acrylic Windows— Spherical Shell Configurations

J. D. Stachiw

PUBLISHED BY

NAVAL OCEAN SYSTEMS CENTER

SAN DIEGO, CALIFORNIA

91-10325



01 9 77 017

## Foreword

For successful operation, all manned diving systems, submersibles, and hyperbaric chambers require pressure-resistant viewports. These viewports allow the personnel inside the diving bells and submersibles to observe the environment outside the pressure-resistant hulls. In addition, on land, operators of hyperbaric chambers can observe the behavior of patients or divers undergoing hyperbaric treatment inside the chambers.

Since the viewports form a part of the pressure-resistant envelope, they must meet or surpass the safety criteria used for designing either the metallic or plastic composite pressure envelope. The ASME Boiler and Pressure Vessel Code Section 8 provides such design criteria, and the chambers/pressure hulls designed on their basis have generated an unexcelled safety record.

The viewports, because of the unique structural properties of the acrylic plastic used in constructing the windows, could not be designed according to the same criteria as for the pressure envelopes fabricated of metallic or plastic composite materials. To preclude potential catastrophic failures of windows designed on the basis of inadequate data, in 1965, the U.S. Navy initiated a window testing program at the Naval Civil Engineering Laboratory and the Naval Ocean Systems Center. Under this program, window testing was conducted until 1975.

The objective of the window testing program was to generate test data concerning the structural performance of acrylic-plastic windows fabricated in different shapes, sizes, and thicknesses. Candidates for investigation included the effect of major design parameters, like the thickness to diameter ratio, bevel angle of bearing surfaces, and the ratio of window diameter to seat-opening diameter on the structural performance of the windows, and empirical relationships were to be formulated between these variables and the critical pressures at which windows fail. To make the test results realistic, the test conditions were varied to simulate the in-service environment that the windows were to be subjected. Thus, during testing, the windows were subjected not only to short-term pressurization at room temperature, but also to long-term sustained and repeated pressurization at different ambient temperatures.

On the basis of these data, empirical relationships were formulated between design parameters and test conditions. Committees in the Pressure Technology Codes of the American Society of Mechanical Engineers subsequently incorporated these relationships into the Safety Standard for Pressure Vessels for Human Occupancy (ASME PVHO-1 Safety Standard). Since that time, this ASME Safety Standard has formed the basis — worldwide — for designing acrylic windows in pressure chambers for human occupancy. Their performance record is excellent, since the publication of the Safety Standard in 1977, no catastrophic failures have been recorded that resulted in personal injury.

The data generated by the Navy's window testing program were originally disseminated in technical reports of the Naval Civil Engineering Laboratory and the Naval Ocean Systems Center, and were made available to the general public through the Defense Technical Information Center. To facilitate distribution of these data to users inside and outside of the Department of Defense, the technical reports have been collected and are being reissued as volumes of the U.S. Navy Ocean Engineering Studies.

These volumes, containing the collected technical reports on pressure-resistant plastic windows, will be deposited in technical libraries of Naval Laboratories and universities with ocean engineering programs. This dissemination of collected data should significantly reduce the effort currently being expended by students, engineers, and scientists in their search for data dispersed among the many reports published over a 10-year period by several Naval activities.

→ Volume V of the Ocean Engineering Series is a compilation of three technical reports that discuss the performance of spherical shell acrylic windows having different edge configurations. The coverage describes both spherical shell hemispheres with equatorial flanges and spherical shell sectors with square edges. In addition, their static and cyclic fatigue lives are compared to spherical shell sectors with beveled edges. The superior cyclic fatigue life and lower fabrication costs of spherical shell sectors with square edges make them a more cost-effective design for spherical bow windows on manned submersibles than (1) spherical shell windows with beveled edges and (2) hemispherical shell windows with equatorial flanges.

The pressure and duration of loading data summarized in the reports apply directly to spherical shell windows of any size with an identical  $t/D_1$  ratio, while the displacements shown must be multiplied by a scale factor based on the ratio of minor diameters on the test and operational windows. To date, these test data have been used successfully in designing spherical bow windows in sizes up to 96 inches for tourist submarines.

J. D. Stachiw  
Marine Materials Office  
Ocean Engineering Division

→ (25) \* Acrylic,  
\* Spheres, \* Windows, \* Hemispherical  
shells, \* Flanges.



## TABLE OF CONTENTS: VOLUME V

- NUC TP 508**      Spherical Sector Windows with Restrained Edges for Undersea Application
- NUC TP 355**      Flanged Acrylic Plastic Hemispherical Shells for Undersea Systems
- TN N-1468**      Flanged Acrylic Plastic Hemispherical Shells for Undersea Systems - Static and Cyclic Fatigue Life Under Hydrostatic Loading



---

# SPHERICAL SECTOR WINDOWS WITH RESTRAINED EDGES FOR UNDERSEA APPLICATIONS

by

J. D. Stachiw

OCEAN TECHNOLOGY DEPARTMENT

December 1975

---





NAVAL UNDERSEA CENTER, SAN DIEGO, CA. 92132

---

AN ACTIVITY OF THE NAVAL MATERIAL COMMAND

**R. B. GILCHRIST, CAPT, USN**

Commander

**HOWARD L. BLOOD, PhD**

Technical Director

#### ADMINISTRATIVE INFORMATION

This report describes research performed between June 1972 and June 1975 as part of the investigation into acrylic plastic spherical sector windows for man-rated submersibles. Program efforts were funded under a project order from the Naval Material Command through the Independent Research and Independent Exploratory Development Program at the Naval Undersea Center under subproject task area number ZF-61-412-001.

Released by  
H. R. TALKINGTON, Head  
Ocean Technology Department

#### ACKNOWLEDGMENTS

The acrylic plastic windows and steel mounting flanges were fabricated by Reynolds and Taylor, Santa Ana, California, and the finished assemblies were tested by the Southwest Research Institute, San Antonio, Texas. The study partially owes its successful completion to the administrative support and technical interest of H. R. Talkington, NUC, Head, Ocean Technology Department, and Dr. W. B. McLean, NUC, Technical Director (Retired).

## UNCLASSIFIED

SECURITY CLASSIFICATION OF THIS PAGE (When Data Entered)

REPORT DOCUMENTATION PAGE		READ INSTRUCTIONS BEFORE COMPLETING FORM
1 REPORT NUMBER NUC TP 508	2 GOVT ACCESSION NO.	3 RECIPIENT'S CATALOG NUMBER
4 TITLE (and Subtitle) SPHERICAL SECTOR WINDOWS WITH RESTRAINED EDGES FOR UNDERSEA APPLICATIONS		5 TYPE OF REPORT & PERIOD COVERED Research and Development June 1972 to June 1975
		6 PERFORMING ORG REPORT NUMBER
7 AUTHOR J. D. L. Schiw		8 CONTRACT OR GRANT NUMBER(s)
9 PERFORMING ORGANIZATION NAME AND ADDRESS Naval Undersea Center San Diego, CA 92104		10 PROGRAM ELEMENT, PROJECT, TASK AREA & WORK UNIT NUMBERS ZF-61-412-001
11 CONTROLLING OFFICE NAME AND ADDRESS Naval Undersea Center San Diego, CA 92104		12 REPORT DATE December 1975
		13 NUMBER OF PAGES 144
14 MONITORING AGENCY NAME & ADDRESS (if different from Controlling Office)		15 SECURITY CLASS (if this report)  UNCLASSIFIED
15a DECLASSIFICATION/DOWNGRADING SCHEDULE		
16 DISTRIBUTION STATEMENT (of this Report)  Approved for public release; distribution unlimited.		
17 DISTRIBUTION STATEMENT (of the abstract entered in B1 & 2) (if different from Report)		
18 SUPPLEMENTARY NOTES		
19 KEY WORDS (Continue on reverse side if necessary and identify by block number)		
20 ABSTRACT (Continue on reverse side if necessary and identify by block number)  A new concept for the mounting of spherical sector windows has been experimentally evaluated under short-term, long-term, and cyclic pressure loadings. The new mounting concept requires that the spherical sector windows be provided with square edges instead of conical edges. The horizontal bearing surface of the square edge carries the axial thrust of the window and the vertical bearing surface the radial thrust.		

UNCLASSIFIED

SECURITY CLASSIFICATION OF THIS PAGE(When Data Entered)

20. Continued

Experimental evaluation has shown that the spherical windows with square edges are subjected to larger flexure moments than similar windows with conical edges. However, the short-term critical pressures of spherical sector windows with square edges and included angles  $75^\circ < \alpha < 180^\circ$  were found to be only 10 percent less than similar windows with conical edges. For spherical sectors with  $\alpha < 75^\circ$ , square-edge mounting provides significantly higher short-term implosion pressures than conical edge mountings.

Based on the short-term critical pressures, strains, stresses, and cyclic fatigue data generated by this study, the spherical shell sector windows with square-edge mountings are considered acceptable for service in manned submersibles, habitats, or diving bells.

UNCLASSIFIED

SECURITY CLASSIFICATION OF THIS PAGE(When Data Entered)

## SUMMARY

### PROBLEM

Submersibles require for their operational effectiveness large panoramic bow windows. To withstand high hydrostatic pressure acting upon the submersible, the bow windows must be made in the shape of a spherical shell sector with a conical edge. Many windows of this shape have been built and are operating successfully in manned submersibles.

The conical edge of the spherical shell sector window and the matching conical seat in the mounting flange require costly machining to achieve the desired angular tolerances. If such windows could be modified by replacing the conical edge with a square edge, significant economies could be achieved during fabrication.

### RESULTS

Acrylic plastic spherical shell sector windows with square edges have been found to perform satisfactorily under hydrostatic pressure when mounted in steel flanges with square seats. The square edge performs particularly well on spherical sector windows with a spherical angle less than  $75^\circ$ . The sealing of spherical shell sector windows with square edges is also more reliable and easier to achieve than for similar windows with conical edges.

### RECOMMENDATIONS

Acrylic plastic spherical shell sector windows with square edges should be seriously considered by engineers designing large bow windows for submersibles. For spherical angles less than  $75^\circ$ , spherical shell sector windows with square edges should be preferred over similar windows with conical edges.

## CONTENTS

INTRODUCTION	3
DESCRIPTION OF NEW MOUNTING CONCEPT	4
EVALUATION OF NEW MOUNTING CONCEPT	4
Designs	4
Test Specimens	5
Fabrication	6
Instrumentation	7
Test Arrangement	7
Test Procedure	7
Test Observations	8
FINDINGS	12
CONCLUSION	13
RECOMMENDATIONS	13
REFERENCES	14
APPENDIX A. EXPERIMENTAL DATA	83
APPENDIX B. DEFINITIONS	141

## INTRODUCTION

Since the introduction in 1969 of acrylic plastic spherical sector windows in the field of ocean engineering, their use has consistently increased until they have practically replaced flat disc and conical frustum windows in the bows of submersibles with design depths less than 3000 feet (references 1 through 4). Glass and transparent ceramics will soon extend the use of spherical sector windows to depths in excess of 30,000 feet (reference 5).

There are many reasons for the rapid acceptance of spherical sector windows, but the primary ones include superior resistance to hydrostatic, hydrodynamic, and point impact loadings (reference 6). It is because of their spherical shape that panoramic windows with an outside diameter of 40 inches or more are considered common, while flat disc and conical frustum windows larger than 12 inches are considered rare.

For some applications, the idea of panoramic visibility, extended one step beyond the spherical sector window, has resulted in acrylic plastic spherical hulls. Their structural and optical attributes (references 7 through 22), like those of spherical sector windows, make them desirable replacements for spherical steel hulls with multiple view ports. Several submersibles with acrylic plastic hulls have been built and evaluated (references 7, 13, and 14). The performance of these hulls has been found to be not only equal, but in some cases superior, to metallic hulls. The long-term entrapment of the Johnson-Sea-Link submersible off the Florida Coast in 1972 with the accompanying death of two aquanauts inside the metallic lockout chamber and the survival of two crew members inside the acrylic pilot capsule is a good example of one advantage of acrylic material, that is, its excellent thermal insulation against low temperatures experienced at great depths even in subtropical and tropical areas (reference 23).

The mounting of spherical sector acrylic windows in metallic hulls must be carefully performed, or unacceptably high stresses can be generated in the bearing surface of the window (references 1 and 19). The classical design solution, the use of matched conical bearing surfaces on the window and the flange seat (figure 1), has proven itself in countless installations and will continue to be used. The primary advantages of this mounting are the abilities of conical surfaces to act as a secondary high pressure seal and to accommodate windows with slightly smaller or larger diameters than specified.

Unfortunately, spherical windows with conical bearing surfaces also possess some disadvantages. (1) the high cost of accurately machining the angle of conical surfaces and (2) the susceptibility to static and cyclic fatigue cracks in the conical bearing surface caused by sliding of the window on the seat in the flange. Since the conical mounting design is less than ideal, other designs have been considered as possible alternatives. One such design has shown sufficient promise to merit experimental evaluation. This report covers the design and experimental evaluation of spherical sector windows equipped with square vertical bearing and radial thrust surfaces (figure 2). Windows equipped with such bearing and thrust surfaces are totally restrained at the edge.



## DESCRIPTION OF NEW MOUNTING CONCEPT

The square edges on the spherical sector windows have as their objective total restraint of the window edge during application of hydrostatic loading to the convex surface of the window. Total restraint has been achieved by carrying all vertical bearing forces on a flat horizontal surface around the circumference of the window, while the radial thrust of the window is carried by a vertical cylindrical surface forming the outside diameter of the window (figure 3A). The seat in the window flange has a set of surfaces that matches that of the window (figure 3B). Since both the horizontal and vertical surfaces on the window as well as on the flange can be rapidly and precisely machined on a lathe, there is a good fit between the edge of the window and the seat in the flange. This fit assures even distribution of compressive stresses in the edge of the window. Furthermore, because of the small clearance between the cylindrical surface of the window's circumference and the outside diameter of the seat in the flange, very little sliding occurs between the horizontal bearing surface on the window and the seat in the flange. This fact alone should substantially increase the fatigue life of the window's bearing surface. This minimal effect of minute sliding can be totally eliminated through the use of hard neoprene or a cork bearing gasket which is placed between the horizontal bearing surfaces of the window and the flange. In effect, the new window mounting design eliminates to a large degree surface crazing and cracks initiated on the window's horizontal bearing surface by shear forces between the moving window and the stationary flange seat. However, because of the restraint imposed on the edge of the window, bending stresses of higher magnitude are imposed on the spherical sector window with a square edge than upon a similar window with a conical edge. The seriousness of these stresses was evaluated during this experimental study.

## EVALUATION OF NEW MOUNTING CONCEPT

The evaluation of the new mounting concept for spherical sector windows with square edges was experimental. It consisted of (1) designing a series of acrylic plastic spherical sectors with square edges; (2) fabricating the sectors; (3) instrumenting the sectors with electric resistance strain gages; (4) subjecting the instrumented sectors to external hydrostatic pressure; and (5) comparing the experimentally generated strains with those from past tests on spherical sectors with conical edges.

### DESIGNS

The design of the square edge on the window required that the available surface be proportioned between the horizontal bearing and vertical thrust surfaces. The relationship between the membrane force acting on the conical bearing surface and the vertical and horizontal force components acting on the horizontal and vertical surfaces in the flange seat can be expressed as

$$F_K = F_M \cos \frac{\alpha}{2} \quad (1)$$

$$F_V = F_M \sin \frac{\alpha}{2}, \quad (2)$$

where

$F_R$  is radial thrust, pounds/inch of circumference

$F_V$  is vertical bearing force, pounds/inch of circumference

$F_M$  is membrane force, pounds/inch of circumference.

From equations 1 and 2, one can readily see that as the total included angle of the spherical sector increases so does the vertical force component, while the horizontal force component decreases until for a hemisphere it is equal to zero. Only for an included angle of  $90^\circ$  are both components of equal magnitude.

Since it is desirable to maintain a uniform compressive bearing stress on the edge of the window, the areas of the horizontal and vertical edge surfaces must be proportional to the magnitude of the vertical and horizontal force components (figure 4). This can be readily accomplished by assigning the following dimensions to the vertical and horizontal surfaces of the window edge:

$$h = t \cos \frac{\alpha}{2} \quad (3)$$

$$w = t \sin \frac{\alpha}{2}, \quad (4)$$

where

$h$  is the height of the cylindrical surface

$w$  is the width of the horizontal surface

$t$  is the thickness of the shell.

The design of the edge can also be rapidly accomplished by (1) drawing to scale the cross section of the spherical sector window with the conical edge, (2) converting the conical edge into a square edge by placement of vertical and horizontal lines that originate at the outer and inner diameters of the sector, and (3) measuring the resultant dimensions of the window to the nearest 0.01 of an inch.

## TEST SPECIMENS

Model scale sectors with  $t/R_i = 0.159$  were selected as test specimens. This ratio was selected as representative of spherical sector windows either in service or soon to be in service aboard submersibles with design depths in the 1000- to 3000-foot range.

A total of eight window specimens was prepared (table 1). Seven were fabricated with the square edge, and one was made with a conical edge (figures 5 through 11). The

Table 1. Spherical Sector Window Test Specimens.

Spherical Angle, deg	$D_i$ , in	$R_i$ , in	$t$ , in	$t/D_i$	$t/R_i$	Type of Mounting
30	1.786	3.450	0.540	0.302	0.157	Square edge
60	3.445	3.452	0.550	0.160	0.159	Square edge
90	4.881	3.448	0.545	0.112	0.158	Square edge
120	5.965	3.452	0.548	0.092	0.158	Square edge
120	5.970	3.452	0.551	0.092	0.160	Square edge
120	5.975	3.453	0.550	0.092	0.159	Conical edge
150	6.655	3.451	0.550	0.083	0.159	Square edge
180	6.890	3.445	0.547	0.079	0.159	Square edge

- Notes: 1. Acrylic plastic serving as machining stock was 4-inch-thick Plexiglas G.  
2. All surfaces of the window test specimens were polished.

window with the conical edge had an included angle of  $120^\circ$ , typical of most spherical sector windows in modern submersibles (figure 9). The window with the conical edge was included to allow a direct comparison between strains in both window edge designs for a typical submersible window. Since both types of window were to be tested at the same time in a single pressure vessel, the effect of experimental variables, such as temperature and pressure variations on the strain readings, would be eliminated.

## FABRICATION

The spherical sector windows were fabricated (figure 12) by machining from 4-inch-thick Plexiglas G plate, the physical properties of which were in excess of Navy and ASME specifications for acrylic plastic in man-rated windows (references 19 and 20). The fabrication of the windows concluded with polishing of all surfaces and annealing at  $175^\circ\text{F}$  for 6 hours.

Flanges for the windows were fabricated (figure 12) from steel with a minimum yield point of 80,000 psi. All surfaces were machined to a 32 root-mean-square finish to insure smooth surfaces in the window seat. The flanges were substantial enough to withstand the radial thrust of the window without yielding at the hydrostatic loadings required to cause the window's failure.

The clearance between the vertical edge of the window and the seat in the flange was usually less than 0.005 inch and in no case more than 0.010 inch.

## INSTRUMENTATION

Each window test specimen was instrumented with 0.125-inch-long strain gage rosettes (figure 13). The gages were bonded to the interior surface of the spherical sectors along a single meridian at  $15^\circ$  intervals of elevation. In addition, one gage was bonded to the external surface opposite the internal gage at the edge of the window (figure 14). Because of this arrangement, some windows had as many as eight, or as few as three, rosettes. The gages were waterproofed. The wires from the external gages were conducted to the exterior of the pressure vessel via a pipe conduit, while those from the internal gage penetrated the vessel's end closure via a pressure-resistant wire feedthrough.

## TEST ARRANGEMENT

Testing was conducted in a 10-inch-diameter pressure vessel with a 20,000-psi pressure capability at Southwest Research Institute, San Antonio, Texas. Water ( $70^\circ$  to  $75^\circ\text{F}$ ) was used as the pressurizing medium. Each specimen was mounted in its respective flange which, in turn, was placed on a flat steel bulkhead with infinite rigidity. Joints between the window and the flange and the flange and the bulkhead were sealed with room-temperature-vulcanizing silicone rubber (figure 15). When mounted inside the pressure vessel, the interior of the window was always maintained at atmospheric pressure via the open instrumentation conduit between the bulkhead and the pressure vessel cover (figure 16).

When two  $120^\circ$  sectors were tested simultaneously, the bulkhead was replaced by a ring separating the two window flanges (figure 17). Sealing was also achieved with room-temperature-vulcanizing silicone rubber and ambient atmospheric pressure was maintained between the two windows by a pressure resistant conduit which connected the interior of the window assembly to the exterior of the pressure vessel.

## TEST PROCEDURE

Short-term implosion testing was conducted by individually pressurizing at a rate of 650 psi/minute to implosion each window that had been previously subjected to 24-hour sustained loading. Strains were recorded at 500-psi intervals, while the 650-psi/minute pressurization rate was maintained until implosion occurred.

Long-term testing was done by individually subjecting the  $30^\circ$ ,  $60^\circ$ ,  $90^\circ$ ,  $120^\circ$ ,  $150^\circ$ , and  $180^\circ$  spherical sectors with square edges to 1200 psi\* of sustained external hydrostatic pressure for 24 hours. Strain readings were recorded at 200-psi increments during the 650-psi/minute pressurization and at 6-hour intervals during sustained loading. Sustained loading was followed by depressurization at a 650-psi/minute rate and a 24-hour period of relaxation. Strain readings were recorded again at 200-psi increments during depressurization and at 6-hour intervals during the relaxation period.

Cyclic testing was conducted on a twin window assembly consisting of two  $120^\circ$  spherical sectors (figure 17). One sector had a square edge, and the other a conical edge.

---

\*Equal to approximately 25 percent of the short-term critical pressure for windows with  $t/R_1 = 0.159$  and included angles in the  $60^\circ$  to  $180^\circ$  range (reference 1).

The first pressure cycle consisted of (1) pressurizing the twin window assembly to 1200 psi at a 650-psi/minute rate, (2) maintaining the pressure for 24 hours, (3) depressurizing at a 650-psi/minute rate to 0 psi, and (4) relaxing at 0 psi for 24 hours. Strains were read at 200-psi increments during pressurization and at 6-hour intervals during sustained loading. During depressurization, the strains were read again at 200-psi increments and 6-hour relaxation intervals. The following 100 pressure cycles were shorter; sustained loading and relaxation periods were only 4 hours each. During the 100 short cycles, the strains were read only from gages located at 90° elevations on both windows. The readings were taken every third pressure cycle four times: (1) prior to pressurization, (2) immediately after pressurization, (3) after 4 hours of sustained loading at 1200 psi, and (4) immediately after depressurization.

Static fatigue testing was performed by pressurizing the twin window assembly (figure 17) to 2500 psi (approximately 50 percent of short-term critical pressure) and maintaining this pressure until implosion of one window in the assembly.

## TEST OBSERVATIONS

### Short-Term Testing

Implosions of spherical sector windows with square edges took place at critical pressures comparable to those of spherical sectors with conical edges that were tested in a previous study (table 2). Some critical pressures were above the minimum critical pressures of windows with conical edges (reference 1), while others were below (figure 18). It is interesting to note that spherical sector windows with square edges failed at higher pressures than ones with conical edges, if the spherical angle was less than 75°. However, if the spherical angle was larger than 75° but less than 180°, the spherical sectors with square edges failed at approximately 10 to 15 percent lower pressures than those with conical edges. Only if the spherical angle was 75° or 180° were the failure pressures the same, regardless of window edge shape. It would thus appear that spherical sector windows with square edges and spherical angles less than 75° are probably better suited to withstand short-term overpressurizations than identical windows with conical edges. However, in the 75° to 180° range of spherical angles, the windows with square edges are less suited to withstand short-term overpressurizations than identical windows with conical edges.

The failure mode of windows with square edges was plastic instability accompanied by large-scale flexure moments (figures 19 through 26). This postulate is supported by the presence of cone-shaped fractures located in the center of concave surfaces on some of the windows (figures 19, 20, and 21). This fracture pattern is typical of flexure fractures in flat disc and conical frustum windows with similar  $t/R_i$  ratios. In addition, a deep crack was observed on the convex surface of the 90° window around its periphery (figure 21). Both fractures are indicative of tensile stresses on the surface of the window at the moment of failure; the central interior fracture cone is the result of tensile stresses on the concave surface at the center of the window, while the external crack around the periphery was generated by tensile stresses on the exterior surface.

The presence of two fracture surfaces in the spherical sector windows with square edges is distinctly different from the fracture pattern observed during past studies in windows with conical edges (reference 1). In windows with conical edges, only the central fracture

Table 2. Implosion Pressures of Spherical Sector Windows with Square Edges Under Short-Term Hydrostatic Loading.

Spherical Angle, deg	$t/R_i$	$t$	$R_i$	Implosion Pressure, psi
30	0.157	0.540	3.450	11,700
60	0.159	0.550	3.452	5850
90	0.158	0.545	3.448	4700
120	0.158	0.548	3.452	4500
150	0.159	0.550	3.451	4550
180	0.159	0.547	3.445	5200

- Notes: 1. Rate of pressurization, 650 psi/minute.  
2. Ambient temperature during test, 65 to 75°F.  
3. Prior to implosion testing, each window was subjected to a 24-hour-long sustained loading of 1200-psi magnitude followed by a 24-hour-long relaxation period at 0 psi.

cone originating on the concave surface at the apex has been observed. This is evidence that in a spherical sector window with a conical edge tensile stresses that exceed the tensile strength of acrylic are present at the moment of failure only at the apex of the window on the concave surface. The absence of high tensile stresses on the convex surface around the periphery of the window with a conical edge is explained by the fact that only a very low flexure moment exists at the edge of the window. The presence of a low flexure moment at this location is in turn explained by the ability of the conical edge to slide on the steel seat and thus help relieve the window of the radial restraint imposed by the steel flanges. Since the spherical sector window with a square edge is restrained radially by the square window seat, high bending moments are generated in such windows not only at the center during the moment of failure but also around the periphery of the window prior to failure.

Strains in windows with square edges were fairly linear to approximately 2500 psi of hydrostatic loading (figures 27 through 33). Above that value, they became highly non-linear and in many cases reversed direction. The meridional strains in particular indicated large-scale bending occurring around the periphery and at the center of the window. Bending around the periphery was deduced from the observation that the meridional compressive strain on the convex surface of the window around its periphery (location 1-0)\* generally showed only a small increase with pressure (or even became positive), while the meridional compressive strain on the concave surface of the window around its periphery (location 1) showed a rapid increase with pressure. Flattening of the window's center was deduced from observation of the meridional strain at the center of the concave surface. This strain

\*Location numbers refer to figure 13.

generally increased linearly with pressure. It was only just before implosion that the plotted strain showed radical departure from the linearity that is typical of large-scale window deflection during elastic or plastic buckling failure.

It is interesting to note that there is a marked difference between the character of strains on  $30^\circ$  to  $60^\circ$  square-edged windows and the  $90^\circ$ ,  $120^\circ$ , and  $150^\circ$  square-edged windows: In the latter instance the strains on the concave surface at the apex are negative, while in the former they are positive and as the external pressure increases so does their magnitude. This substantiates the postulate that square-edged windows with spherical angles  $\leq 60^\circ$  fail in flexure at the apex while those with spherical angles  $\geq 60^\circ$  fail because of plastic instability characterized by high compressive strains on the concave surface at the apex which reverse their direction just prior to implosion.

### Long-Term Testing

Strains recorded during the pressurization of spherical sector windows with square edges to 1200 psi were quite linear and exhibited the same characteristics as strains recorded during short testing to implosion. These characteristics are (1) a very small rate of increase in compressive strain on the convex surface around the periphery of the window, along meridional and hoop directions, and (2) a very large increase in compressive strain on the concave surface around the periphery of the window in the meridional direction. It is interesting to note that the magnitude of compressive meridional strain on the concave surface around the periphery of the window is a function of spherical angle (figure 34). The meridional strain at this location reaches a maximum in square-edged windows with a  $150^\circ$  angle. For larger angles, the magnitude of strain decreases. Strains at the apex on the concave surface behave somewhat differently (figure 35). For included angles  $0^\circ < \alpha < 50^\circ$ , the magnitude of tensile strain is an inverse function of the angle, reaching zero at  $50^\circ$ . For  $\alpha > 50^\circ$  the strain becomes compressive, its magnitude increasing linearly with the angle reaching a maximum at  $135^\circ$ . At angles above  $135^\circ$ , the compressive strain decreases with an increase in angle.

This distribution of strains is quite different in spherical sector windows with conical edges. There the difference in strain rates between different locations on the window is much less, although the least compressive strain is found on the convex surface and the maximum compressive strain on the concave surface around the periphery of the window. In general, the salient characteristics of spherical sector windows with conical surfaces are (1) uniformity of strain distribution on the concave and convex surfaces and (2) linearity of strain rates.

Stresses in  $150^\circ$  and  $120^\circ$  spherical sector windows with square edges were found to be somewhat higher than in windows with conical edges, the highest stress being observed in the window with a  $150^\circ$  included angle (figures 36 through 42). This compressive stress, located on the concave surface around the periphery of the window, was oriented meridionally. Its magnitude was approximately 30 percent higher than in a window of the same dimensions with a conical edge. Square-edged windows with spherical angles  $\leq 90^\circ$  had maximum stresses that were less than those in comparable windows with conical edges.

Creep in spherical sector windows with square edges was found to be highest on the concave surface around the periphery of the window. Its magnitude after 24 hours of sustained pressurization at 1200 psi was approximately 20 to 30 percent of the short-term

strain at that location. By comparison, the creep on the concave surface at the apex of the window was only 10 to 15 percent of the short-term strain at that location.

### Cyclic Testing

The results from cyclic testing are very valuable because they permit a comparison between strains on 120° spherical sector windows equipped with either conical or square edge. Since this type of window is widely utilized in modern submarine experimental data generated by the 120° spherical angle test specimen in this study can be utilized immediately to both verify existing bow windows and design future ones.

At the conclusion of the first pressure cycle of 24 hours, strains measured on the 120° window with a conical edge were found (table A2) to be highest (-12,250 microinches/inch) on the concave surface around the interior periphery of the window oriented in the meridional direction. The highest strain (-15,875 microinches/inch) on the window with a square edge was also at the same location and oriented in the same direction (table A1). The lowest strain on the 120° window with a conical edge was found (table A2) to be (-600 microinches/inch) on the convex surface around the periphery of the window oriented in the circumferential direction. The lowest strain in the window with square edge was also (figure 30) at the same location and oriented in the same direction (+30 microinches/inch). On the concave surface at the apex, the strains for the 120° window with a conical edge were, after 24 hours of sustained loading at 1200 psi, -8200 microinches/inch in the hoop direction and -7750 microinches/inch in the meridional direction. For the window with the square edge, the strains at the same location were -8200 microinches/inch in the hoop direction and -8450 microinches/inch in the meridional direction.

During the following 99 pressure cycles of 4 hours, the strains on the concave and convex surfaces at the apex were found to change very little, except on the concave surface for the window with the square edge where the magnitude of strains both in the hoop and meridional directions decreased significantly (about 30 percent) between the first and the ninety-ninth cycle.

Visual inspection of the windows' square and conical bearing surfaces failed to detect any signs of incipient cracks or crazing. Visual observation, however, detected radial scratches (figure 43) on the conical bearing surface of the steel flanges; the scratches were generated by repeated sliding of the window in the conical flange during 100 cyclic pressurizations to 1200 psi. The length of the individual scratches was measured to be about 0.025 inch. Radial scratches were not observed (figure 44) on the square edge's bearing surfaces of the steel flange, which indicated that sliding did not take place between window with the square edge and its seat in the flange because of the tight fit between them.

### Static Fatigue Testing

After subjecting the twin window test assembly (figure 17) to 2500 psi of sustained hydrostatic loading for 800 hours at 70°F ambient temperature, one window imploded. Investigation revealed (figures 45 and 46) that the implosion was initiated by the 120° spherical sector window with a square edge. This was expected since previous short- and long-term tests had shown the maximum strain to be higher in the window with the square edge.



The 800-hour-long static fatigue life of the spherical sector window with a square edge at pressure loading equal to 56 percent short-term critical pressure compares favorably with the 900-hour-long static fatigue life previously established for acrylic plastic NEMO spheres with 0.153  $t/R_i$  ratio at 56 percent of their short-term critical pressure (reference 8). On the basis of these data, it can be postulated that the high compressive meridional strain on the concave surface around the periphery of the window does not significantly decrease the static fatigue life of a spherical sector window with a square edge.

## FINDINGS

1. Spherical shell sector windows with square edges and included angles  $75^\circ < \alpha < 180^\circ$  fail at approximately 10 percent lower short-term pressure loading than spherical shell sector windows with conical edges, if they have the same  $t/R_i$  ratio of 0.159 and included angle  $\alpha$ . Windows with square edges and included angles  $\alpha < 75^\circ$  fail under short-term loading at significantly higher pressures than similar windows with conical edges.

2. The magnitude of the maximum compressive strain on spherical shell sector windows with square edges is generally higher than in windows with conical edges and identical  $t/R_i$  ratios and included angles  $\alpha$ .

3. The maximum compressive strain on windows with square edges is located on the concave surface around the periphery of the window and is oriented in the meridional direction. Its magnitude is approximately 30 percent higher than the strain at the same location in  $120^\circ$  spherical shell windows with conical edges.

4. Spherical shell sector windows with square edges properly fitted into steel retaining flanges do not slide upon the flange seat when subjected to external hydrostatic loading of a cyclic nature. As a result, the fatigue life of the window's bearing surface is much longer for windows with square edges than for windows with conical edges.

5. Spherical shell sector windows with square edges and included angles  $\alpha \leq 60^\circ$  fail at the apex in simple flexure. The strains on the concave surface at the apex are tensile at all times, and their magnitude increases linearly with hydrostatic loading.

6. Spherical shell sector windows with square edges and included angles  $\alpha \geq 90^\circ$  generally fail because of plastic instability. The strains on the concave surface at the apex are compressive at all times and their magnitude increases linearly with hydrostatic loading until immediately prior to plastic instability.

7. Maximum creep in spherical shell sector windows with square edges was found to be equal to approximately 30 percent of the short-term strain value after 24 hours of sustained loading at 25 percent of the short-term critical pressure.

## CONCLUSION

Acrylic plastic spherical shell sector windows with square edges have been found to be acceptable for service in manned hyperbaric chambers, submersibles, diving bells, or habitats, if they are operated at lower pressures than similar spherical shell sector windows with conical edges.

## RECOMMENDATIONS

1. Acrylic plastic spherical shell sector windows with square edges can be used as pressure-resistant viewports in pressure vessels for human occupancy, if the hydrostatic loading to which they are subjected is less than their short-term critical pressure divided by a conversion factor of 7 (reference 19). For service at temperatures above 75°C, higher conversion factors must be used.
2. To maximize the cyclic fatigue life of such windows with square edges, it is required that (1) a thin neoprene gasket be bonded to the horizontal bearing surface of the window, (2) the radial clearance between the edge of the window and the inner surface of the seat be kept to a minimum during assembly at room temperature, and (3) O-ring grooves be absent from the bearing surfaces on the window or the flange.
3. Spherical shell sector windows should be sealed with an elastomeric gasket or O-ring compressed between the convex surface of the window and a retainer ring (figure 47).
4. When the design parameters of a submersible system call for a spherical sector window with an included spherical angle less than 75°, a square edge mounting is preferred over a conical edge mounting. The square edge provides not only a more secure mounting in the flange seat, but also gives thin windows a significantly higher short-term implosion pressure.

## CONCLUSION

Acrylic plastic spherical shell sector windows with square edges have been found to be acceptable for service in manned hyperbaric chambers, submersibles, diving bells, or habitats, if they are operated at lower pressures than similar spherical shell sector windows with conical edges.

## RECOMMENDATIONS

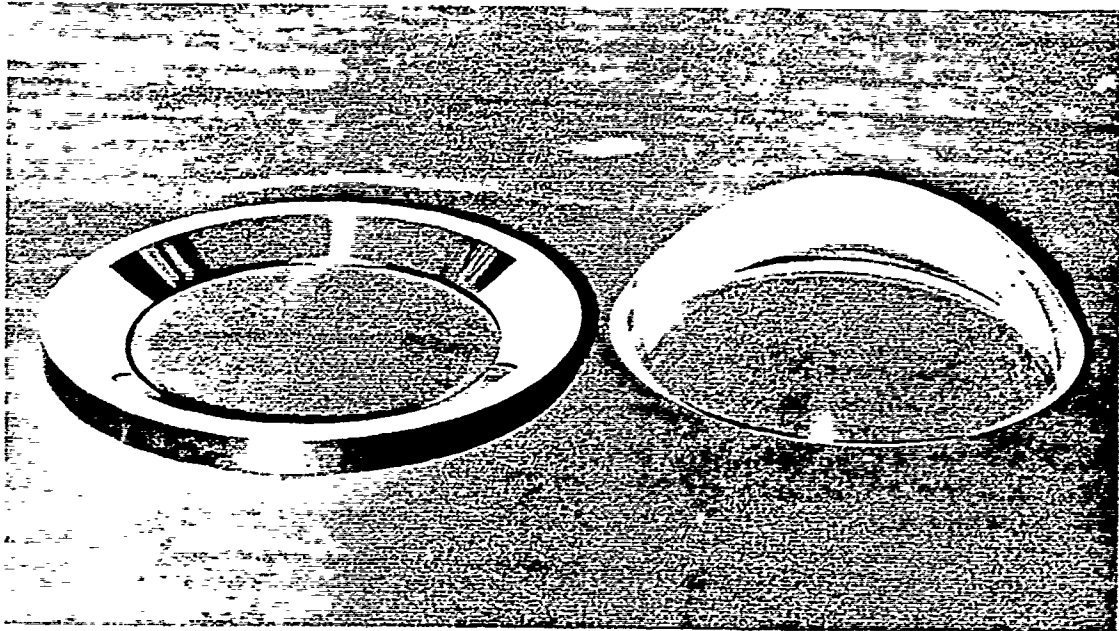
1. Acrylic plastic spherical shell sector windows with square edges can be used as pressure-resistant viewports in pressure vessels for human occupancy, if the hydrostatic loading to which they are subjected is less than their short-term critical pressure divided by a conversion factor of 7 (reference 19). For service at temperatures above 75°C, higher conversion factors must be used.

2. To maximize the cyclic fatigue life of such windows with square edges, it is required that (1) a thin neoprene gasket be bonded to the horizontal bearing surface of the window, (2) the radial clearance between the edge of the window and the inner surface of the seat be kept to a minimum during assembly at room temperature, and (3) O-ring grooves be absent from the bearing surfaces on the window or the flange.

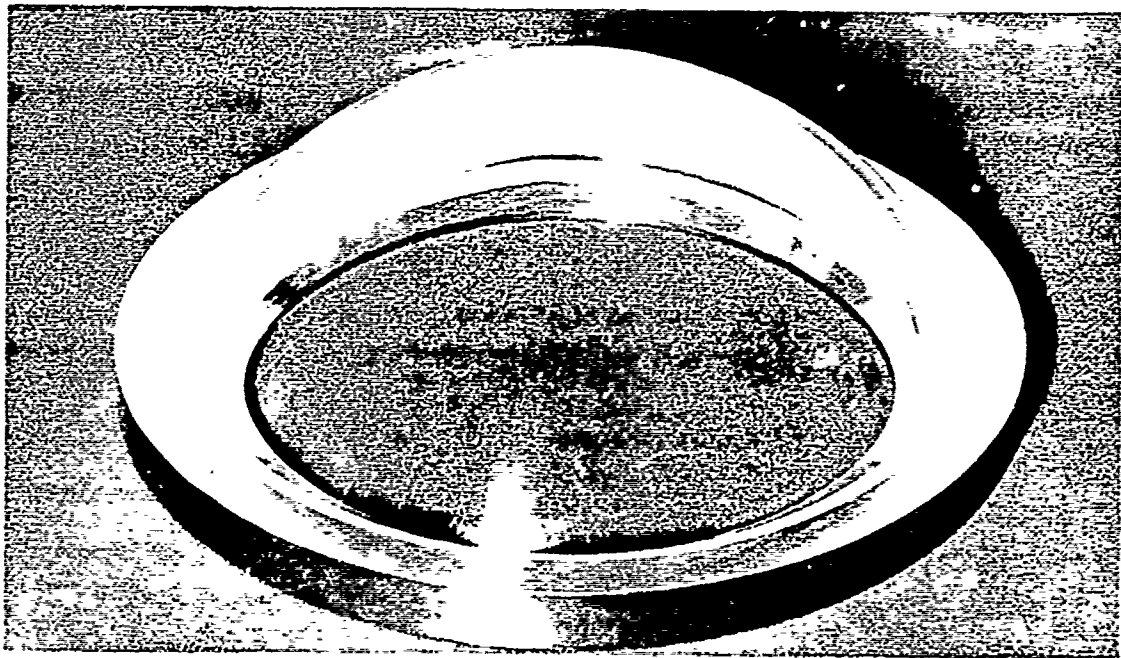
3. Spherical shell sector windows should be sealed with an elastomeric gasket or O-ring compressed between the convex surface of the window and a retainer ring (figure 47).

4. When the design parameters of a submersible system call for a spherical sector window with an included spherical angle less than 75°, a square edge mounting is preferred over a conical edge mounting. The square edge provides not only a more secure mounting in the flange seat, but also gives thin windows a significantly higher short-term implosion pressure.

12. American Society of Mechanical Engineers, Paper No. 70-WA/UnT-3. Spherical Acrylic Pressure Hulls for Undersea Exploration, by J. D. Stachiw. *Journal of Engineering for Industry*. May 1971.
13. American Society of Mechanical Engineers, Paper No. 72-WA/OCT-8. Transparent Hull Submersible MAKAKAI, by D. W. Murphy and W. F. Mazzone. December 1972.
14. American Society of Mechanical Engineers, Paper No. 70-WA/UnT-6. The JOHNSON SEA-LINK – The First Deep Diving Welded Aluminum Submersible, by R. A. Kelsey and R. B. Dolan. December 1970.
15. American Society of Mechanical Engineers, Paper No. 71-WA/UnT-6. Acrylic Pressure Hull for JOHNSON SEA-LINK Submersible, by J. R. Maison and J. D. Stachiw. December 1971.
16. Naval Undersea Center, NUC TP 451. NEMO Module 2000 Acrylic Plastic Spherical Hull for Manned Submersible Operation, by J. D. Stachiw. December 1974 (AD A012471).
17. Naval Undersea Center, NUC TP 410. Development of a Precision Casting Process for Acrylic Plastic Spherical Shell Windows Applicable to High Pressure Service, by J. D. Stachiw. May 1974 (AD 782337).
18. American Society of Mechanical Engineers, Paper No. 70-WA/UnT-4. Fabrication of NEMO-Type Spherical Acrylic Capsules for Underwater Vehicles, by K. Tsuji and R. Shelton. December 1970.
19. Naval Undersea Center, NUC TP 378. Recommended Practices for the Design, Fabrication, Prooftesting, and Inspection of Windows in Man-rated Hyperbaric Chambers, by J. D. Stachiw. December 1973 (AD 773737).
20. American Society of Mechanical Engineers, Paper No. 73-WA/OCT-18. Recommended Practices for the Design, Fabrication, and Prooftesting of Acrylic Plastic Windows in Man-Rated Hyperbaric Chambers, by J. D. Stachiw, et al. December 1973.
21. American Society of Mechanical Engineers, Paper No. 70-UnT-A. Optical Properties of a Spherical Plastic Underwater Observatory NEMO, by T. Trowbridge. December 1970.
22. American Society of Mechanical Engineers, Paper No. 72-WA/OCT-11. Modulated Light Beam Information Transmission System for Transparent Pressure Hulls, by J. E. Holzschuh and G. R. Beaman. December 1972.
23. Naval Undersea Center, NUC TP 493. Development of Economical Casting Process for NEMO Type Acrylic Pressure Hulls, by J. D. Stachiw. December 1975.
24. The Smithsonian Institution, Report of the Johnson-Sea-Link Expert Review Panel to the Secretary Smithsonian Institution, by R. A. Brooks, et al. December 1973.

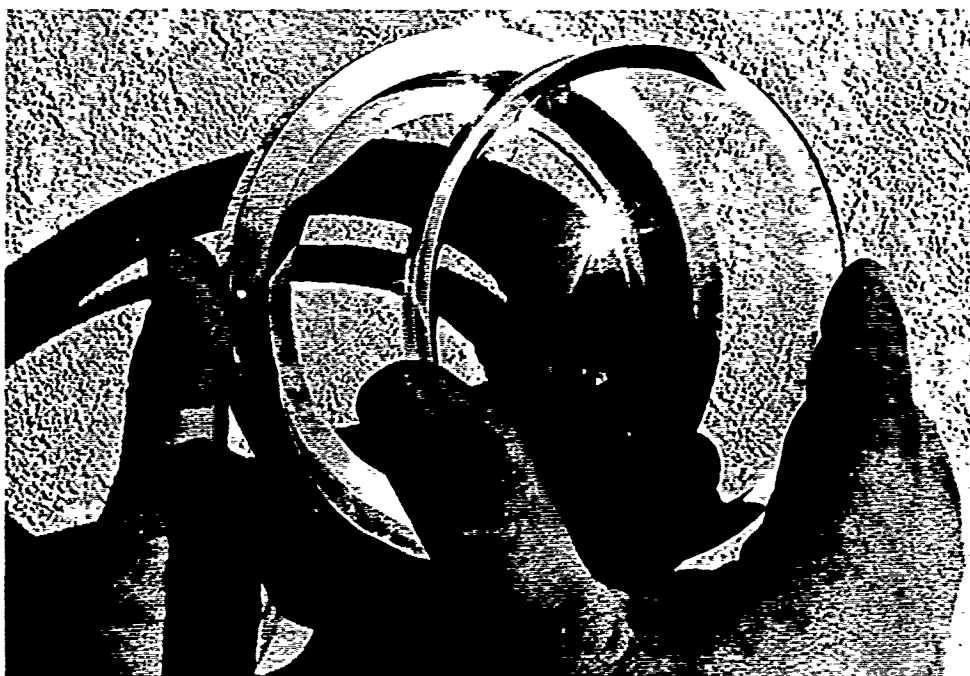


Part A. Disassembled.



Part B. Assembled.

Figure 1. Typical spherical sector window with conical edge and associated steel flange for mounting.



Part A. Disassembled.

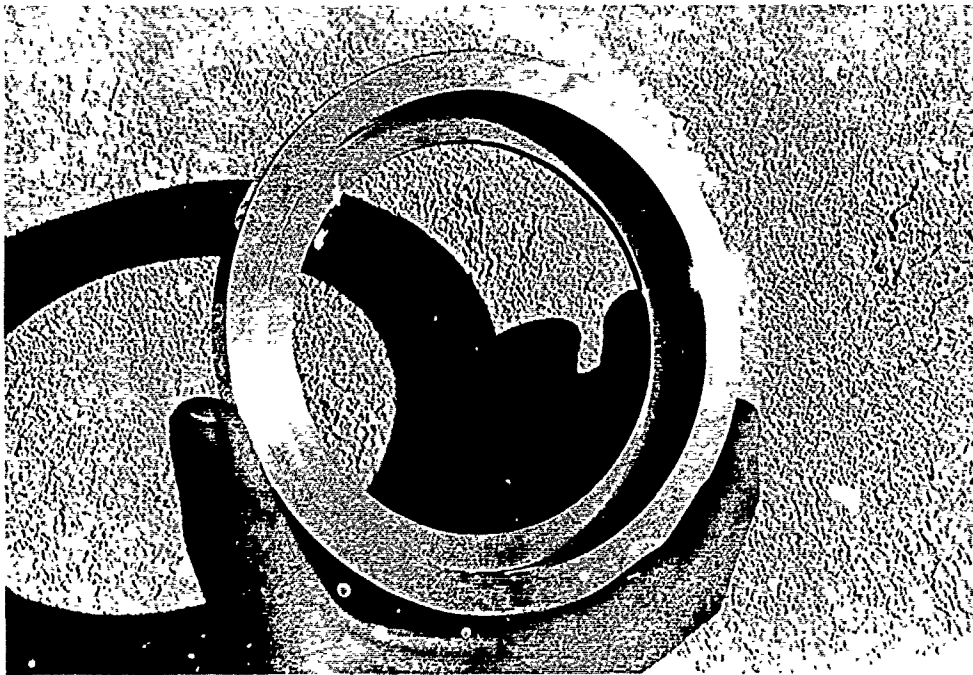


Part B. Assembled.

Figure 2. Typical spherical sector window with square edge and associated steel flange for mounting



Part A. Bearing surface of window.



Part B. Window seat in flange.

Figure 3. Salient features of spherical sector window with square edge and mounting.

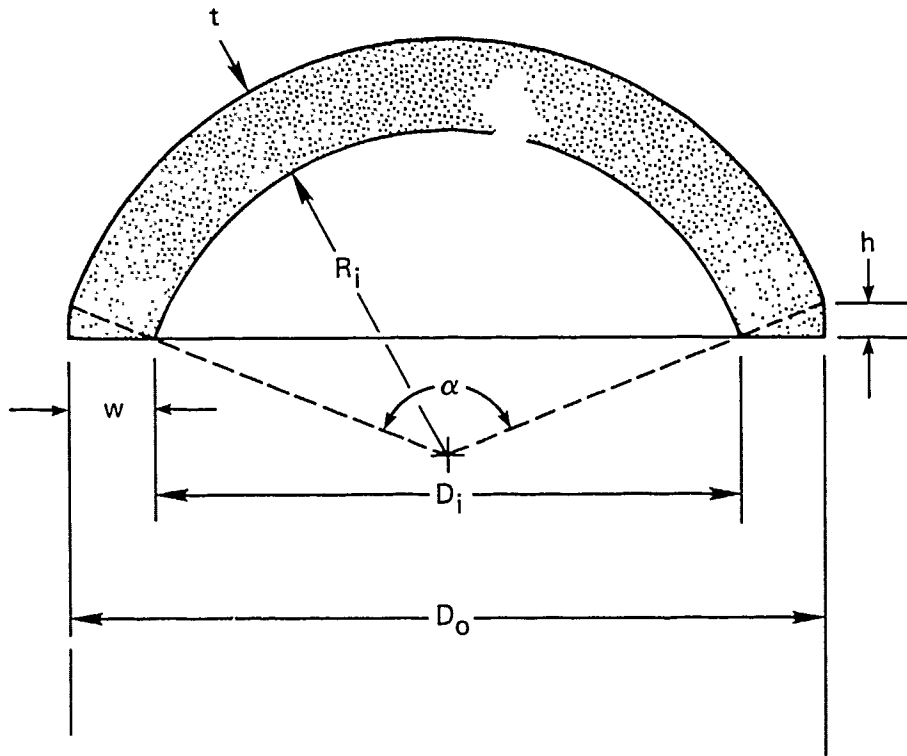


Figure 4. Critical design features of spherical sector window with square-edge concept.



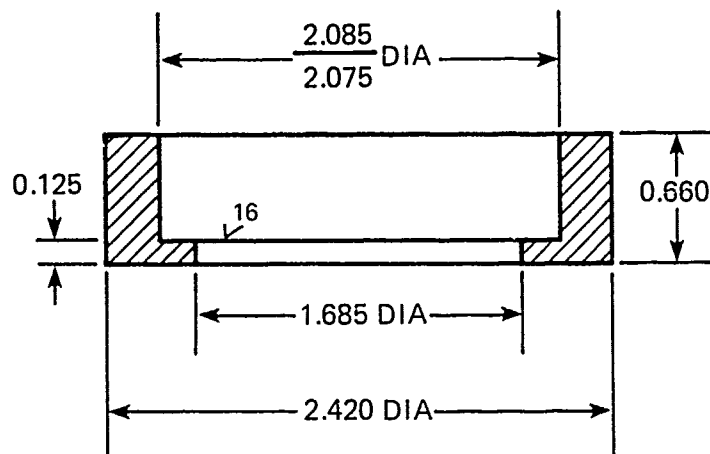
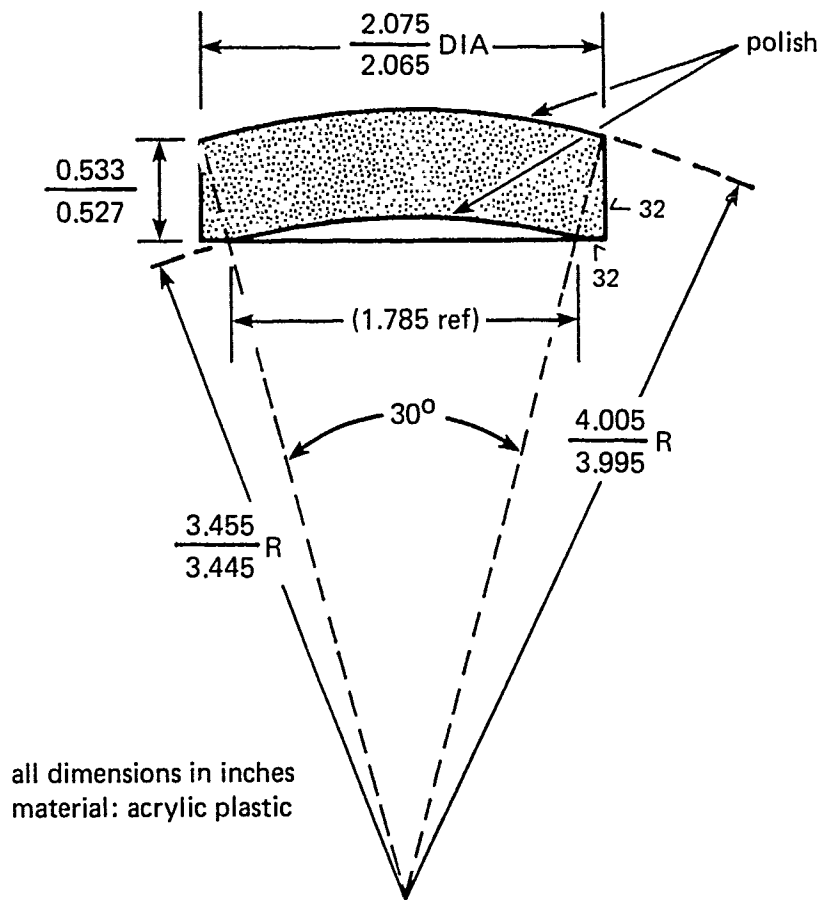


Figure 5. 30° spherical sector window with square edge and associated steel mounting flange.

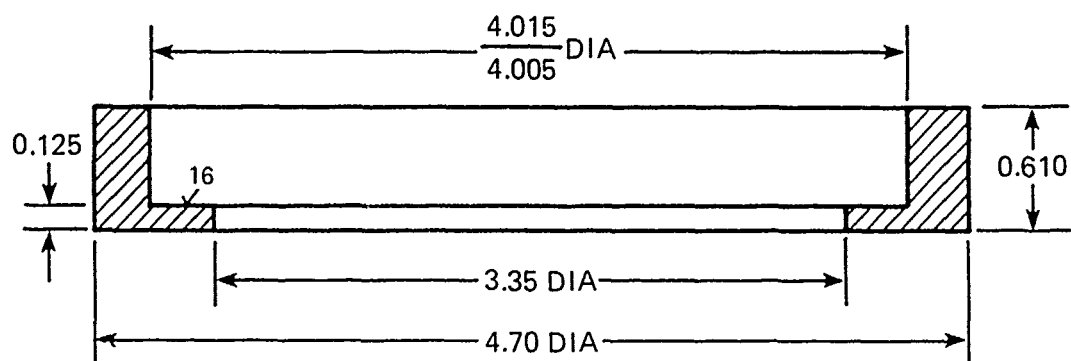
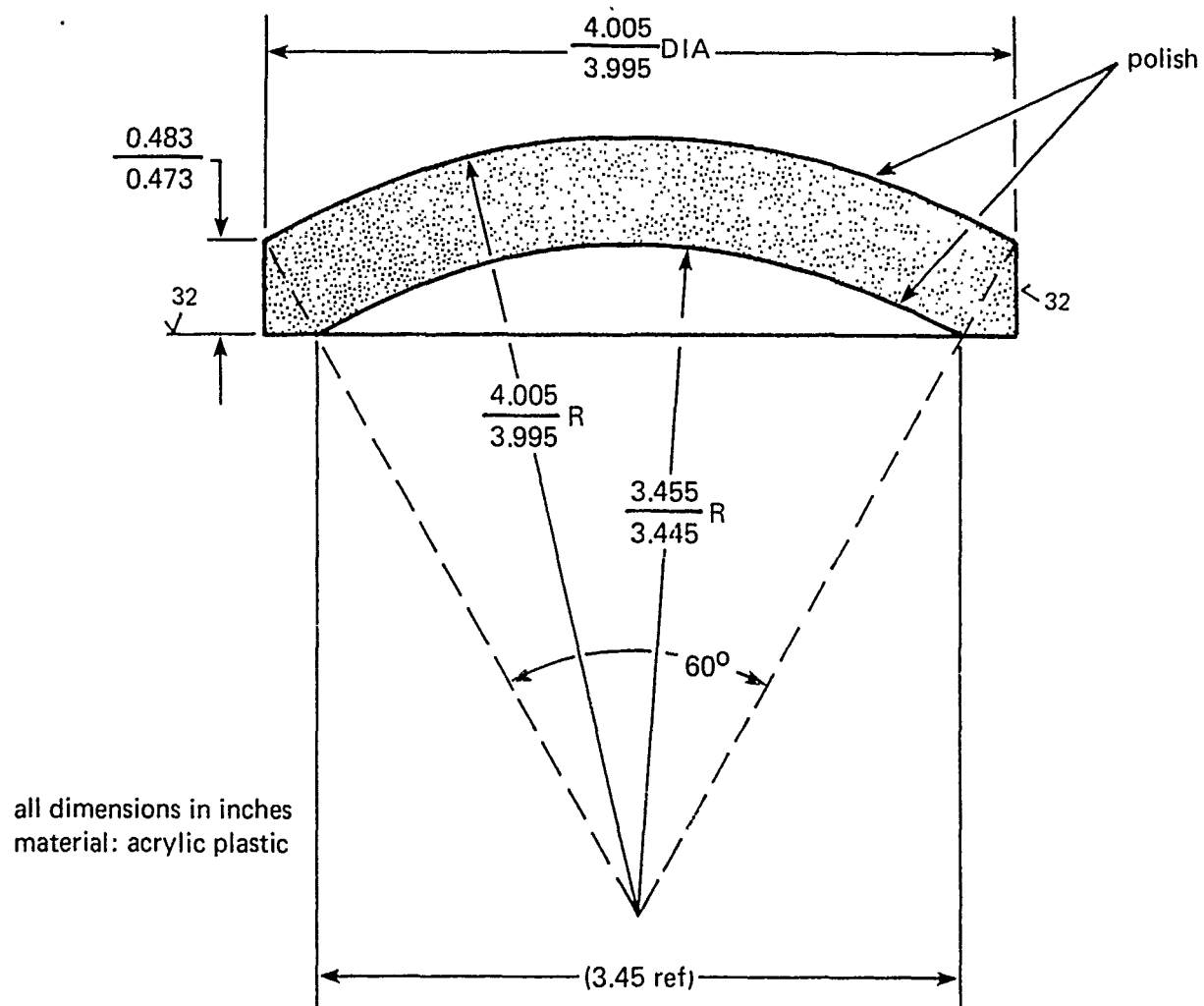
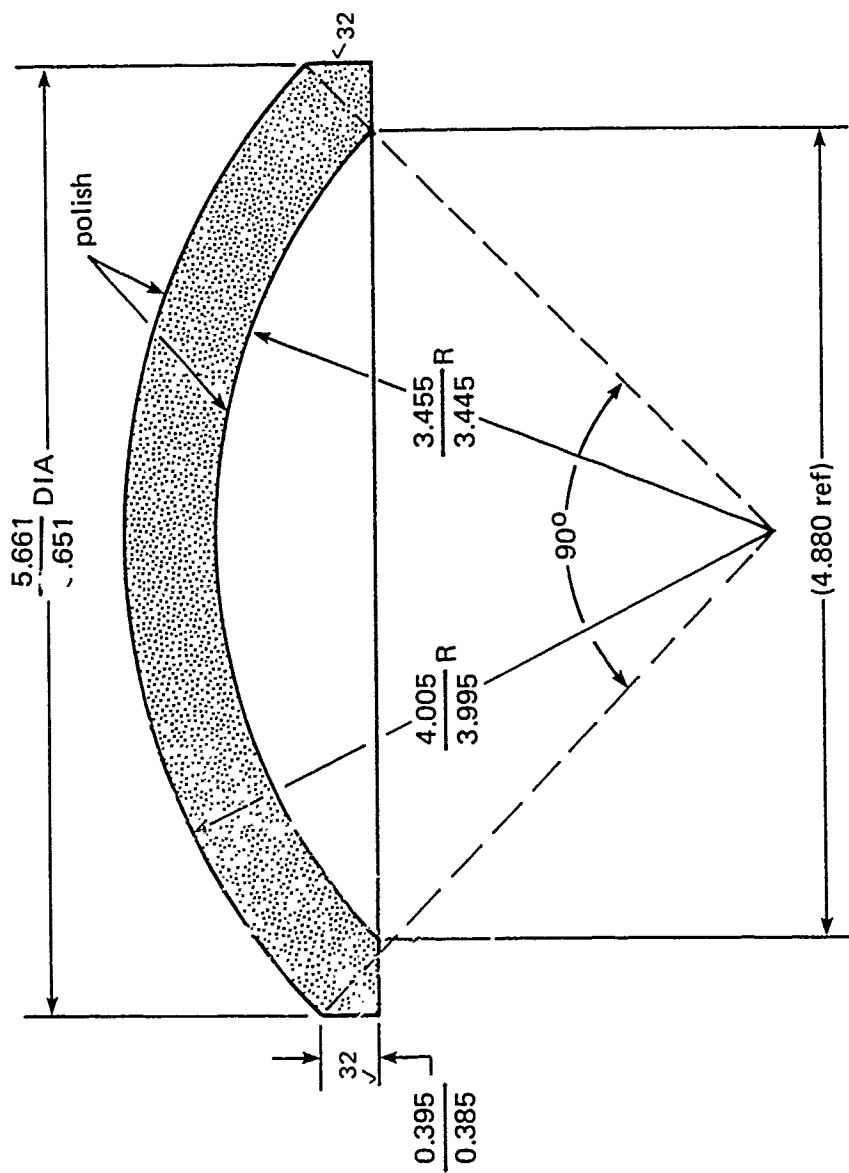
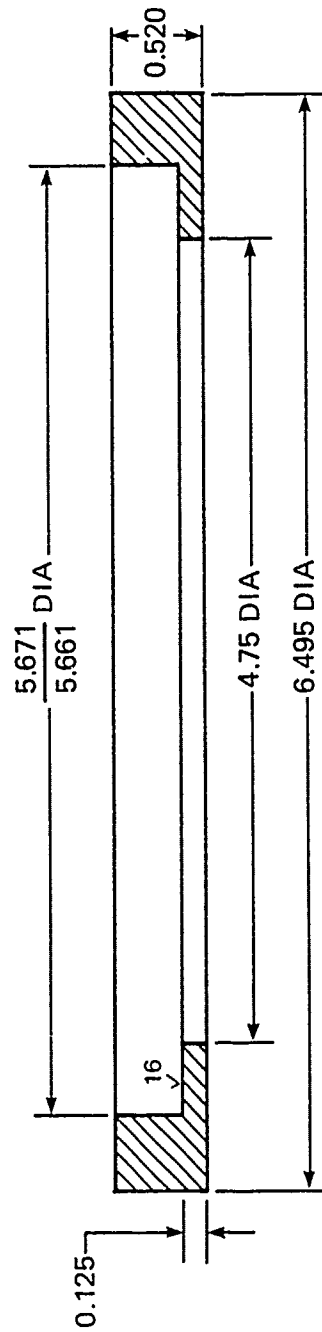


Figure 6. 60° spherical sector window with square edge and associated steel mounting flange



all dimensions in inches  
material: acrylic plastic

Figure 7. 90° spherical sector window with square edge and associated steel mounting flange.



all dimensions in inches  
material: steel, 80,000-psi yield

Figure 7. Continued.

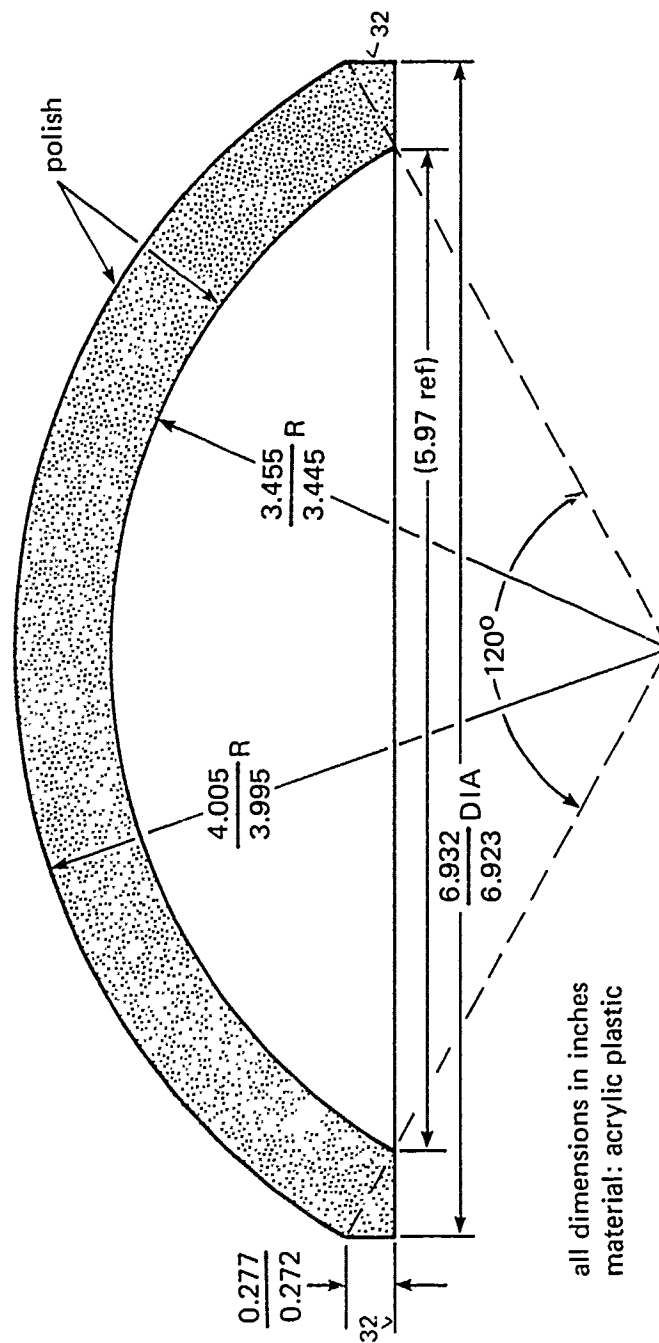
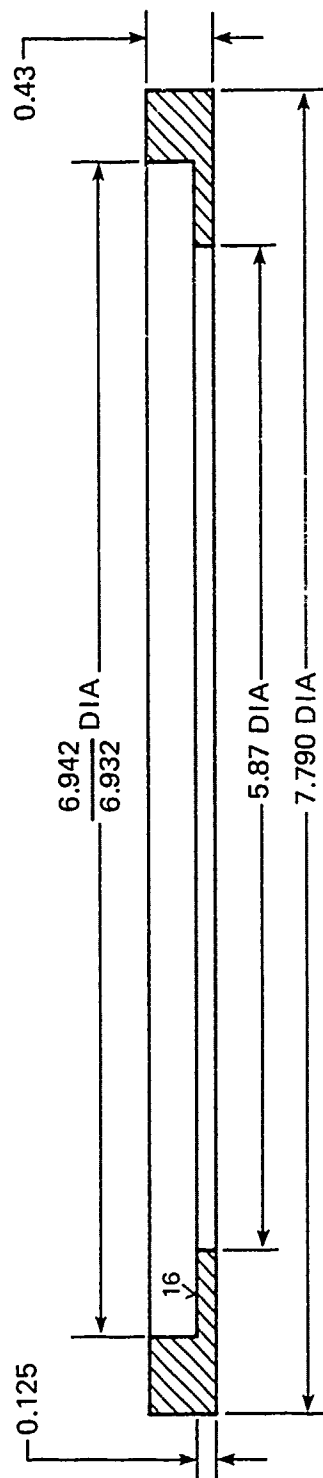
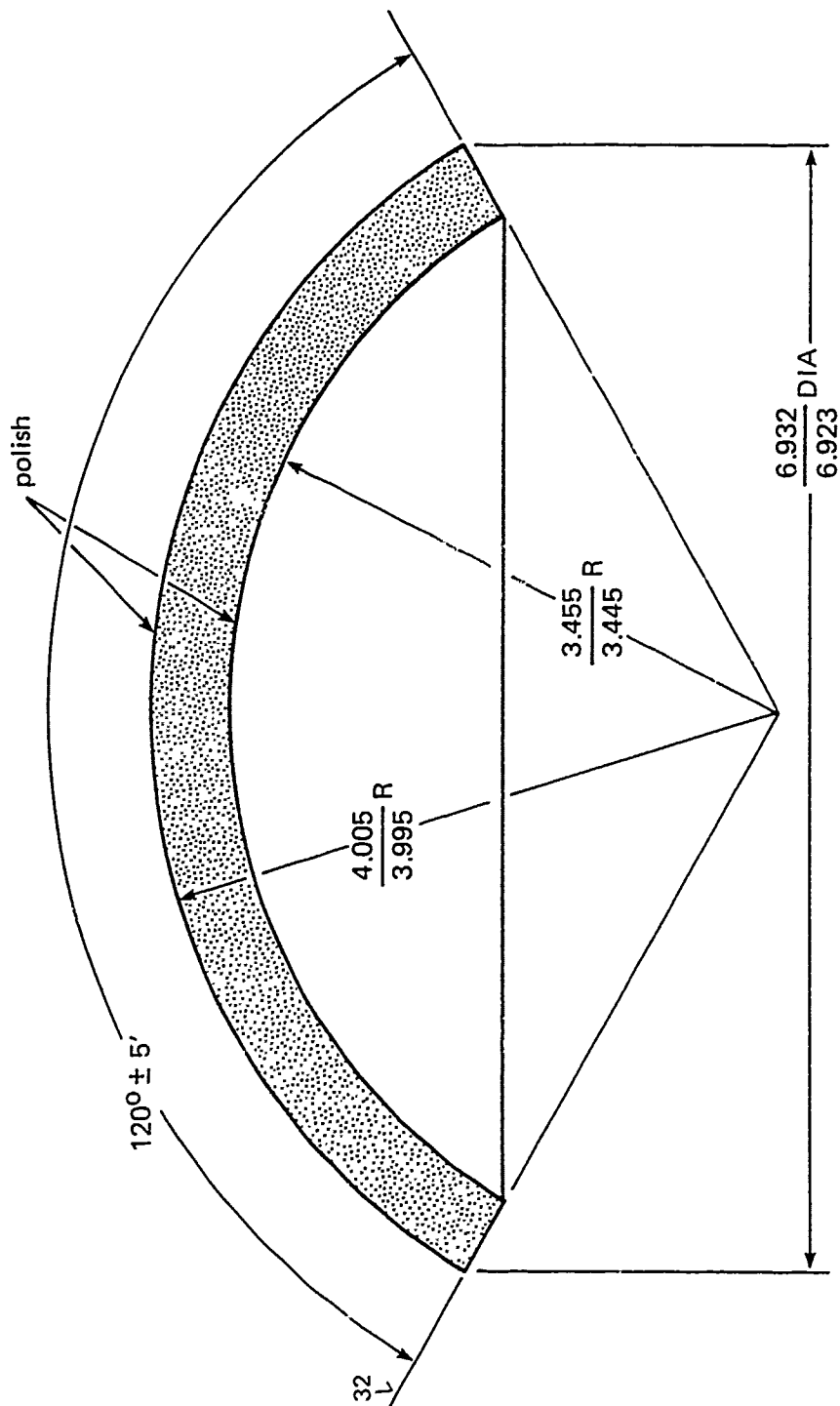


Figure 8. 120° spherical sector window with square edge and associated steel mounting flange.



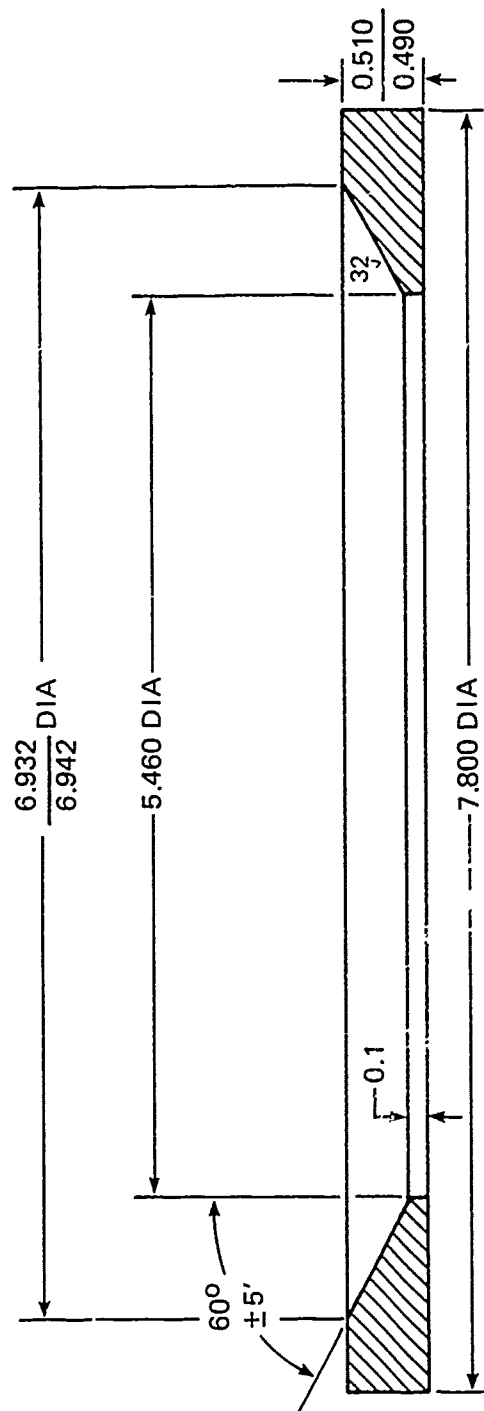
all dimensions in inches  
material: steel 80,000-psi yield

Figure 8. Continued.



all dimensions in inches  
material: acrylic plastic

Figure 9. 120° spherical sector window with conical edge and associated steel mounting flange.  
The thickness and spherical radii of this window are identical to those of figure 8, the only  
difference being in the shape of the bearing surface.



all dimensions in inches  
material: steel, 80,000-psi yield

Figure 9. Continued.



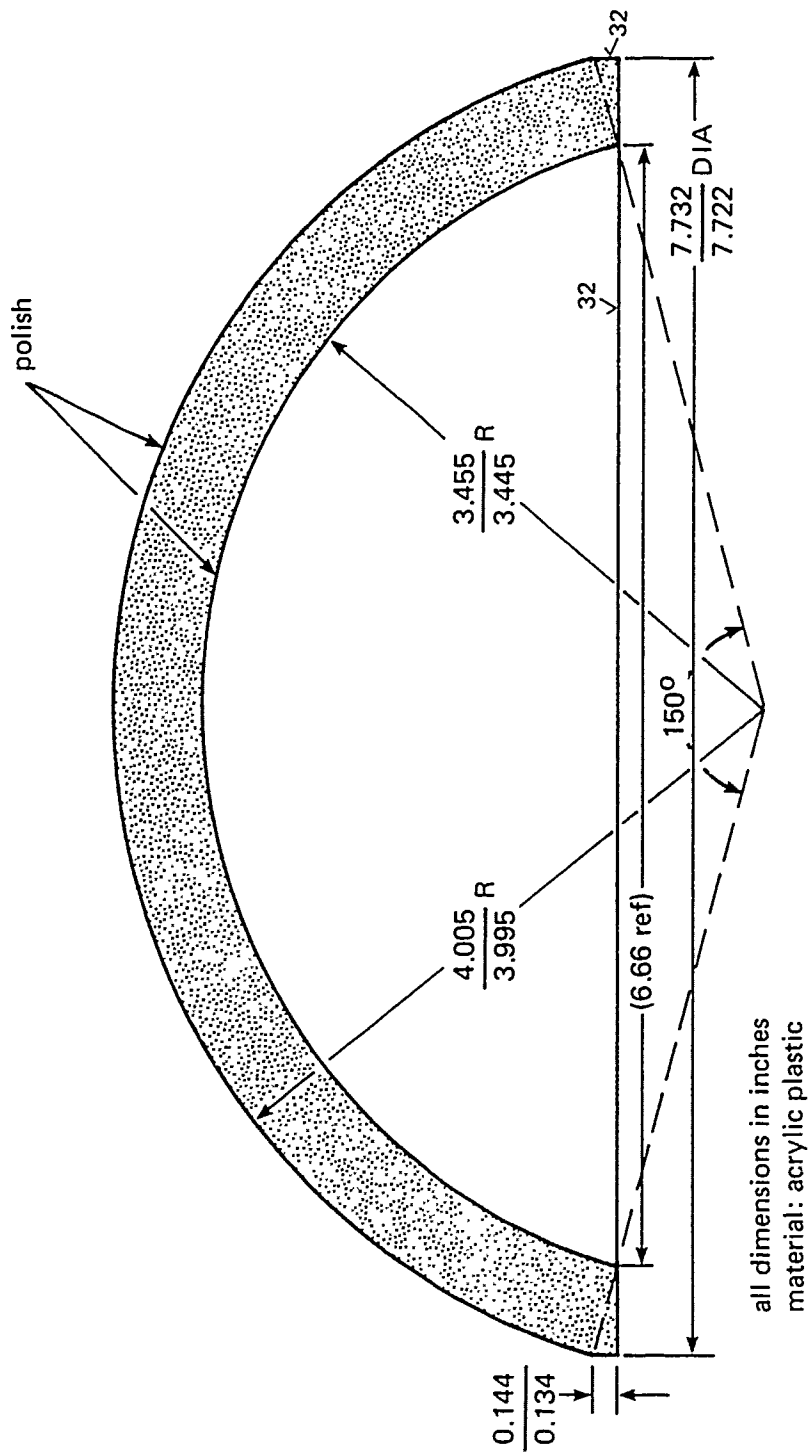
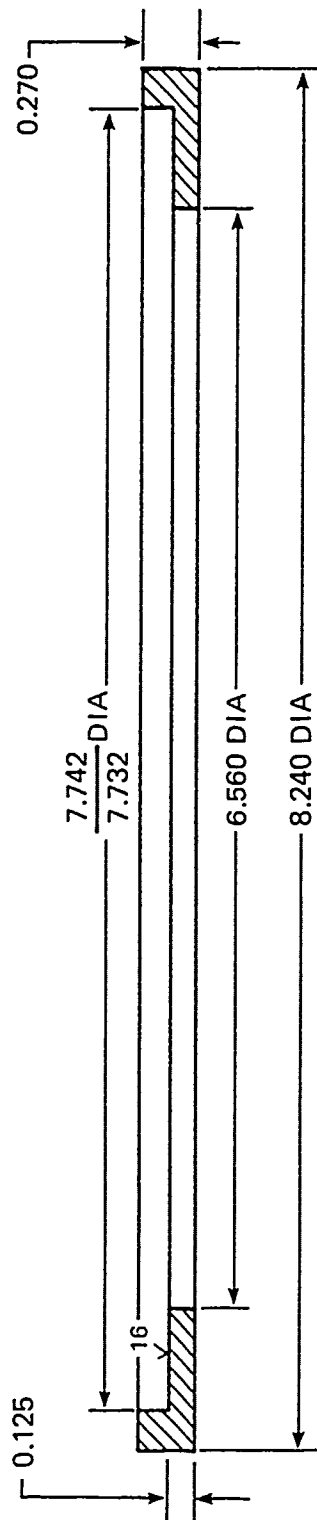


Figure 10. 150° spherical sector window with square edge and associated steel mounting flange.



all dimensions in inches  
material: steel, 80,000 psi yield

Figure 10. Continued.

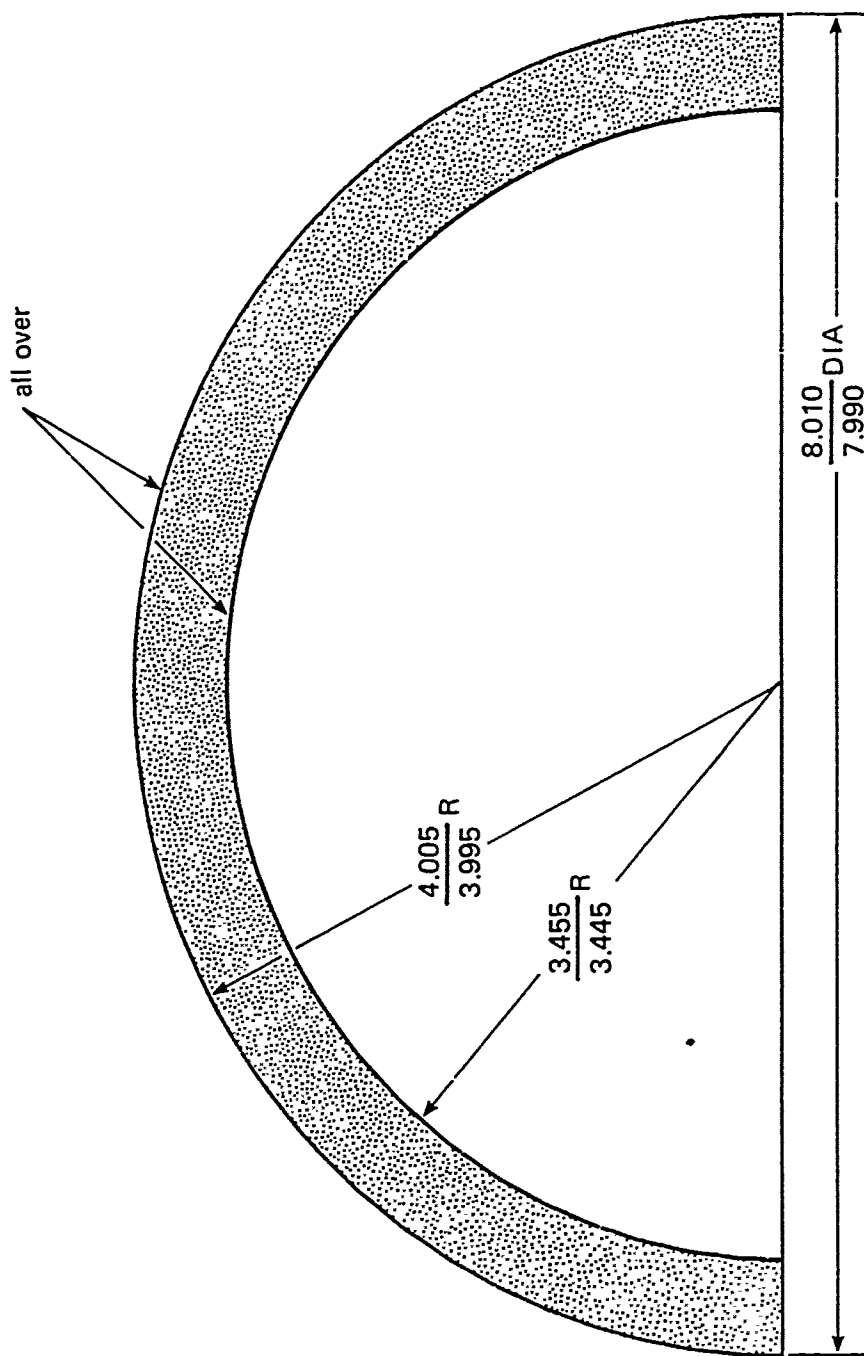
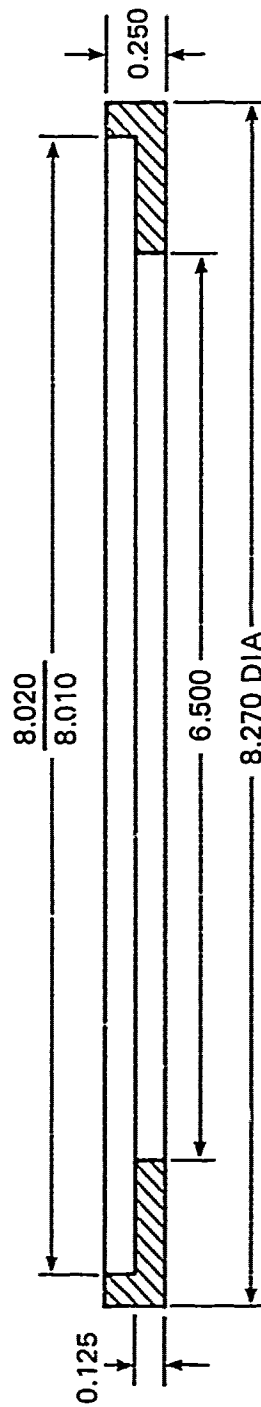


Figure 11. 180° spherical sector window with square edge and associated steel mounting flange.



all dimensions in inches  
material: steel, 80,000-psi yield

Figure 11. Continued.



Part A. Interior.



Part B. Exterior.

Figure 12. Window test specimens, dimensions are in figures 5 through 11.

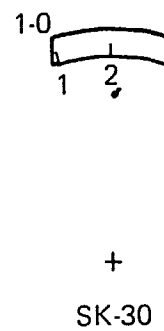
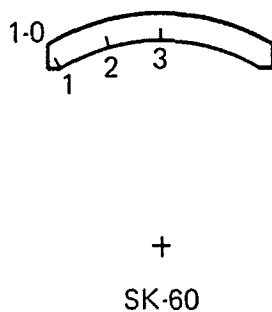
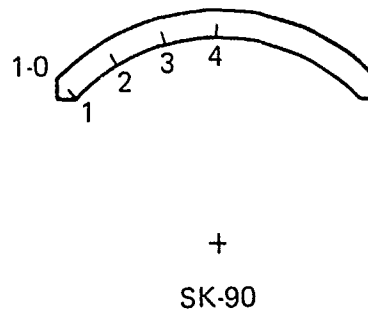
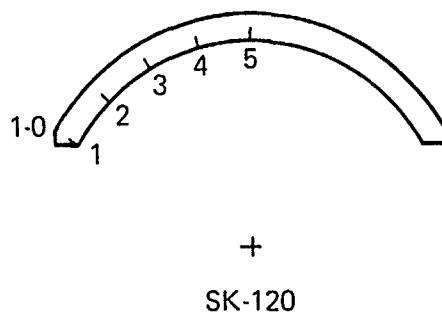
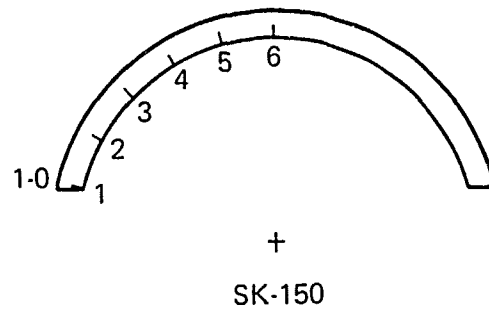
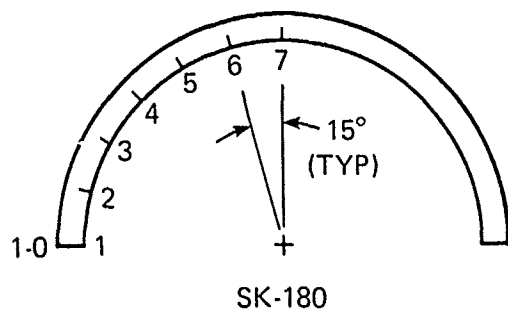


Figure 13. Locations of strain gages on windows subjected to long- and short-term hydrostatic tests.

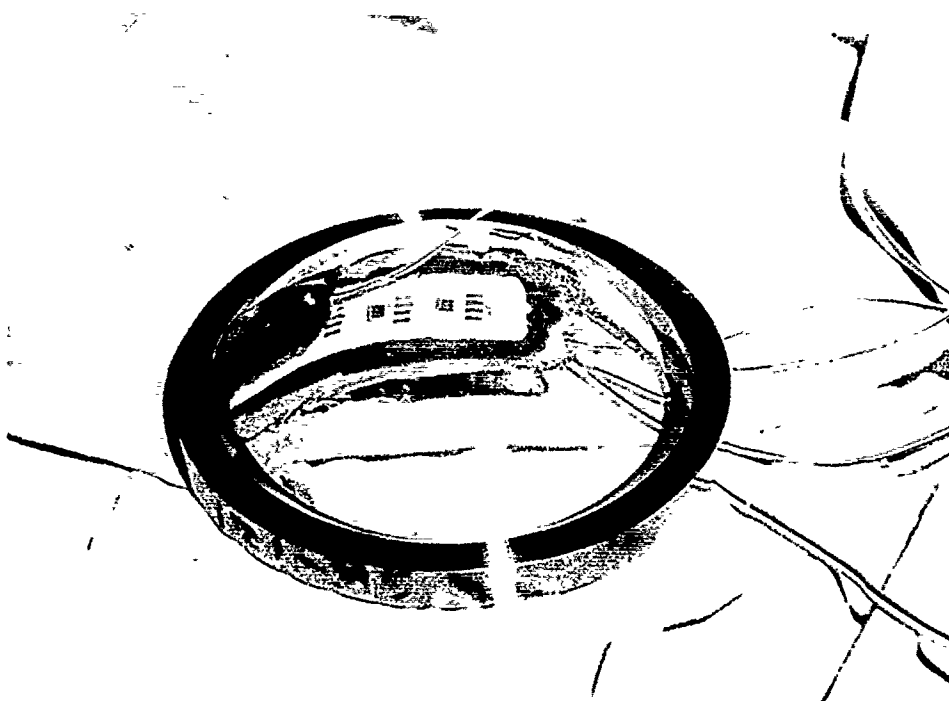


Figure 14. Typical window test specimen after instrumentation with strain gages.



Figure 15. Typical installation of window test assembly on steel bulkhead. Room-temperature-vulcanizing silicone rubber was used to seal the window test assembly.

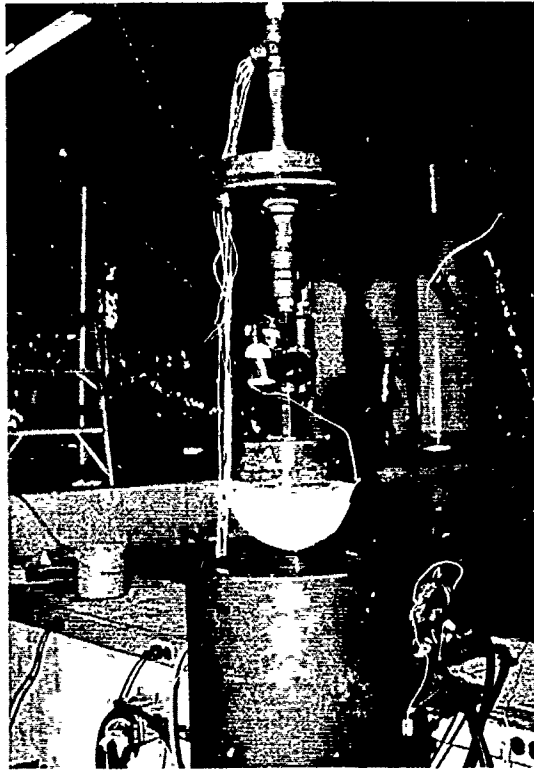


Figure 16. Test jig for testing individual window assemblies inside pressure vessels. The screen was used to catch window fragments.



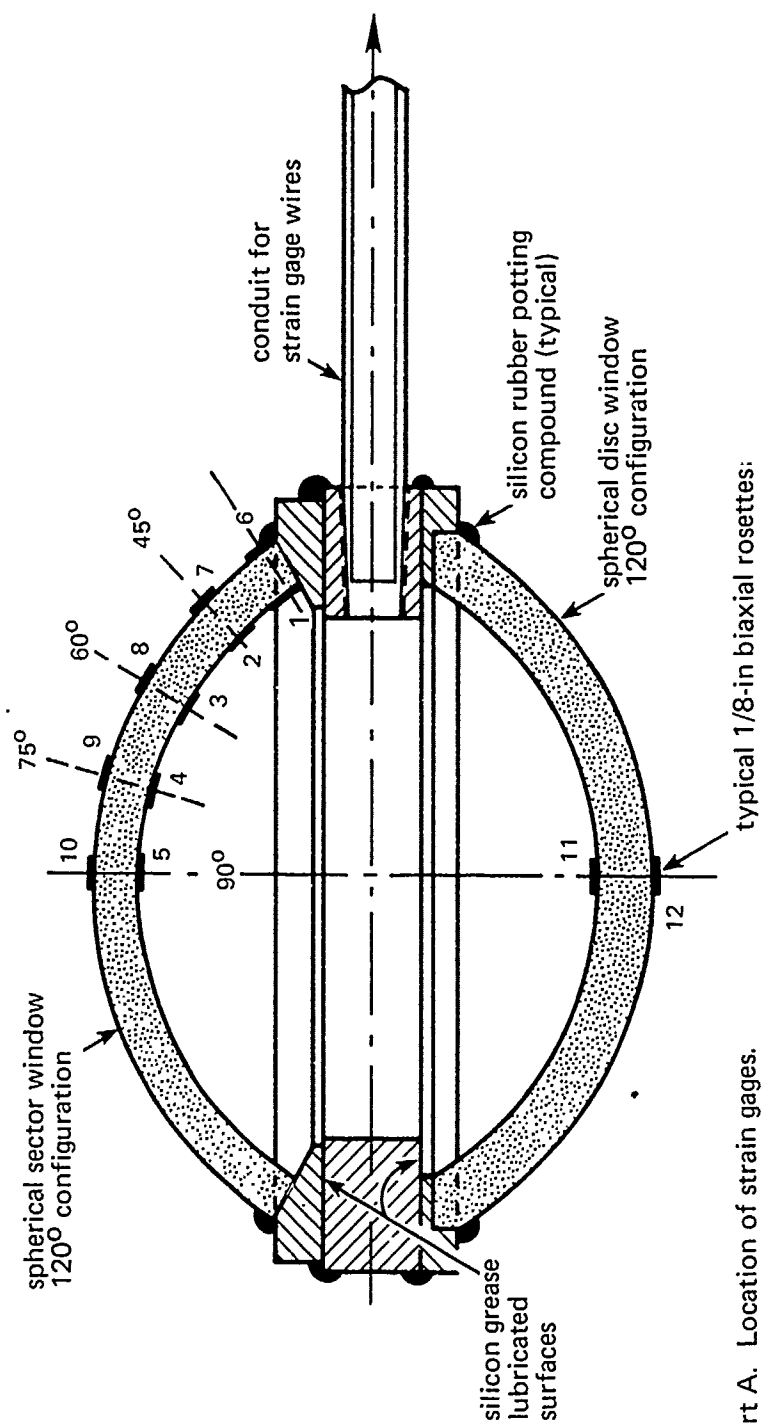
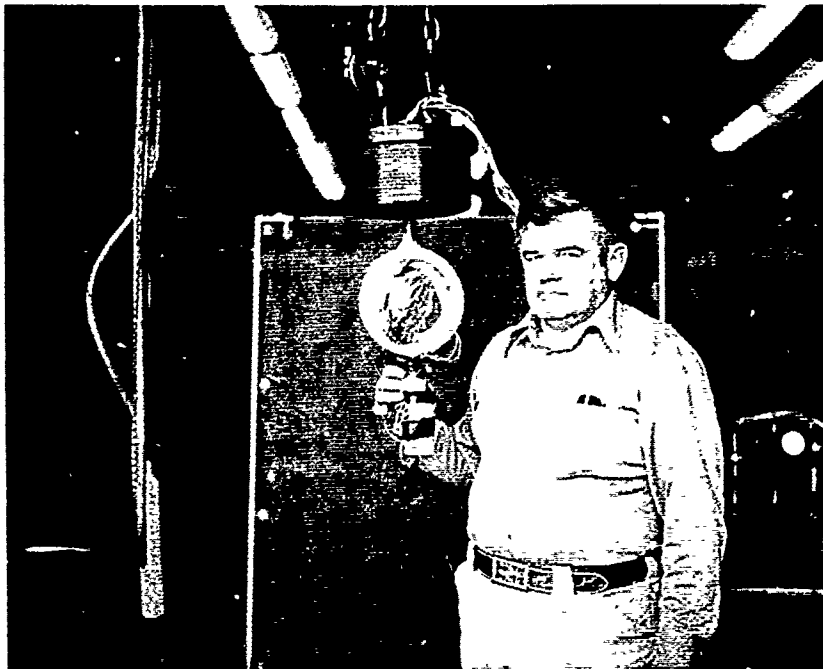
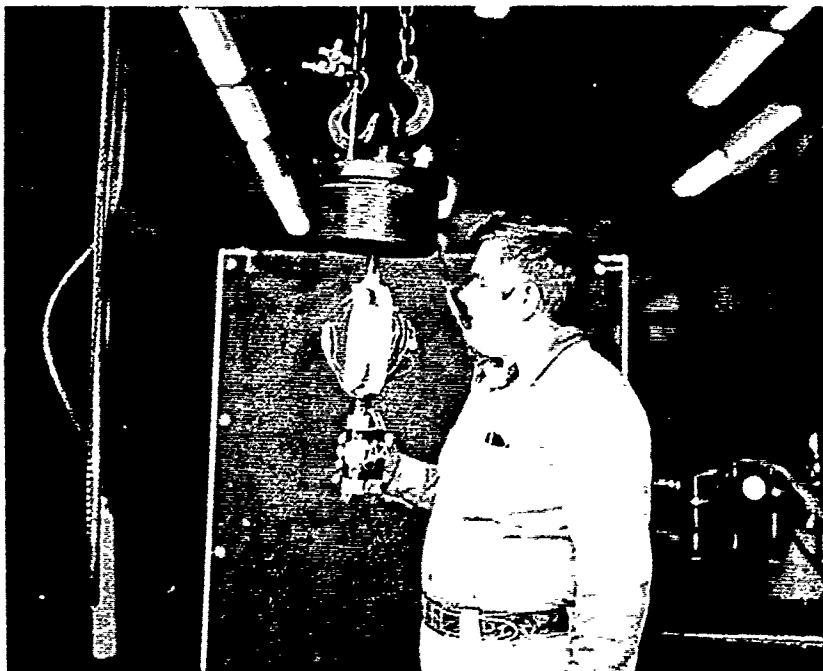


Figure 17. Twin window assembly.

Part A. Location of strain gages.



Part B. Twin window test jig prior to mounting inside a pressure vessel, front view.



Part C. Twin window test jig prior to mounting inside a pressure vessel, side view.

Figure 17. Continued

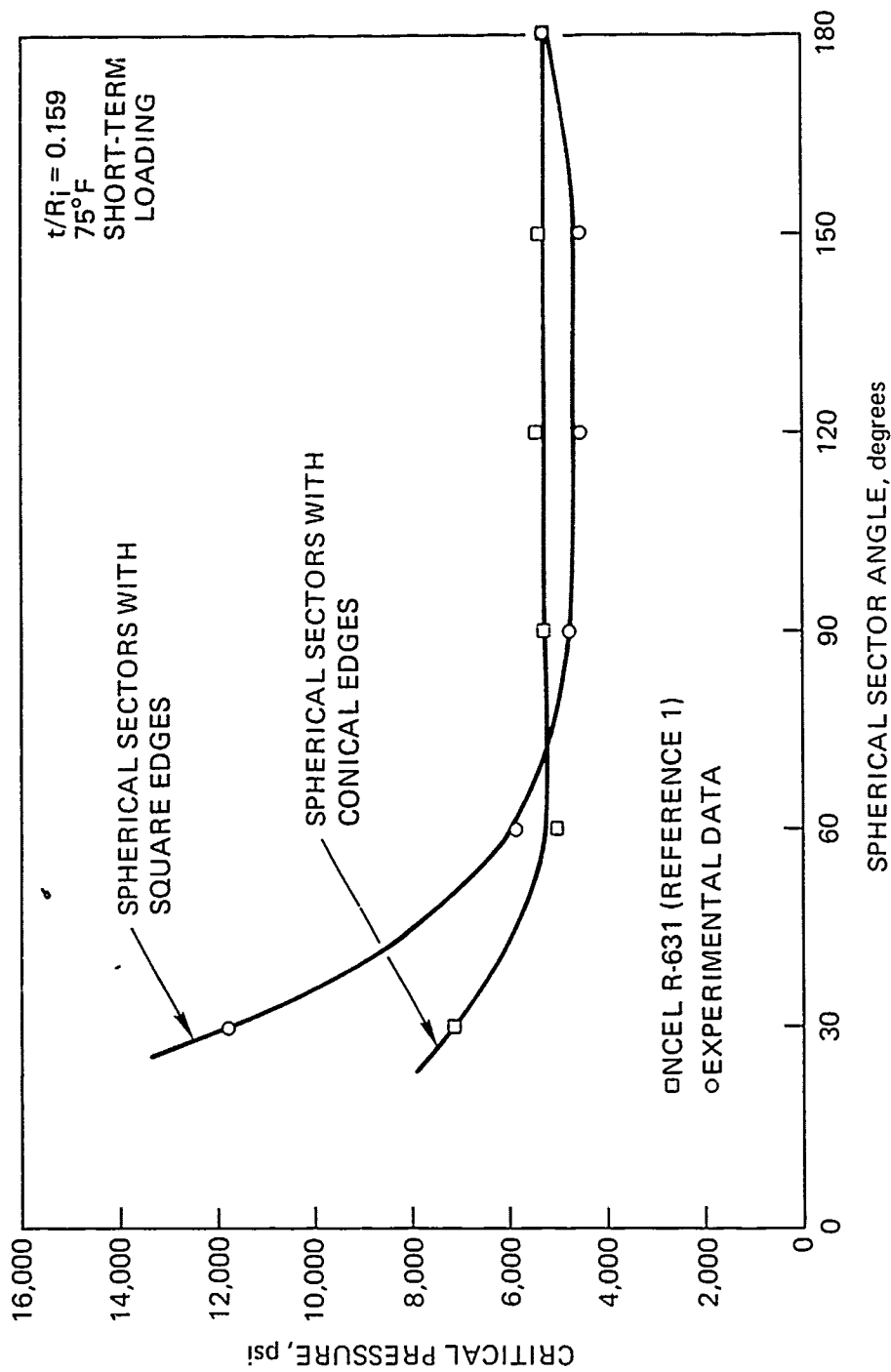
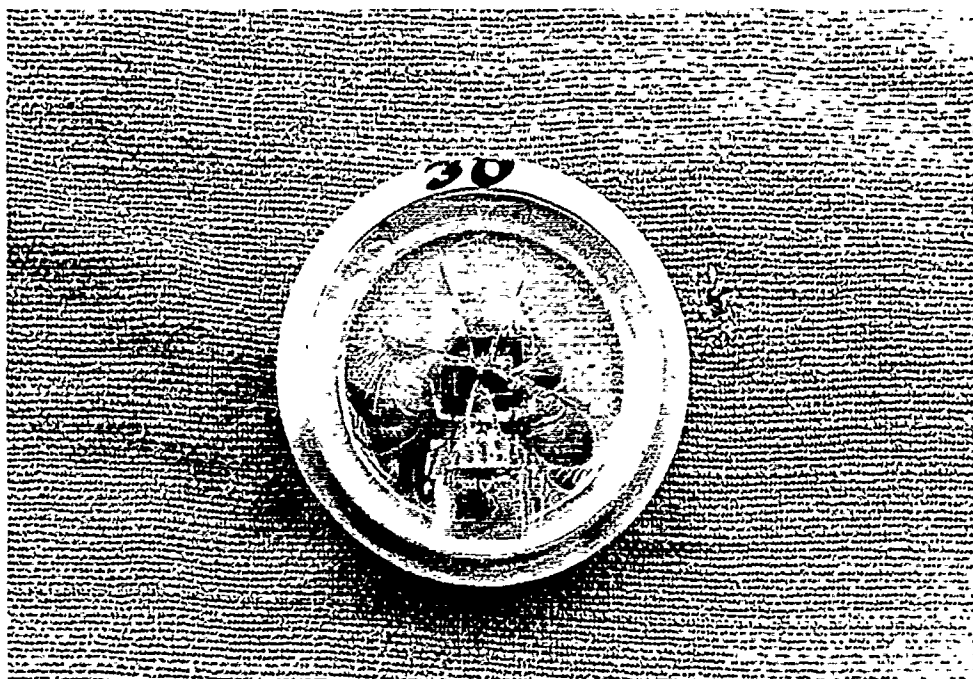
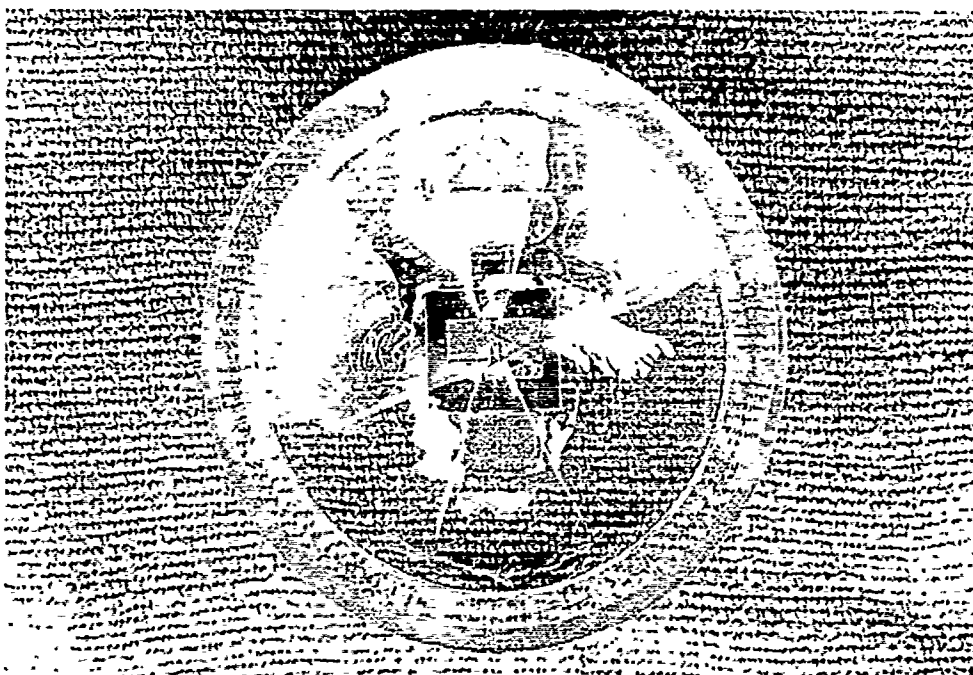


Figure 18. Comparison between short-term implosion pressures of spherical sector windows with square edges and spherical sector windows with conical edges. Both types have a  $t/R_i = 0.159$ .

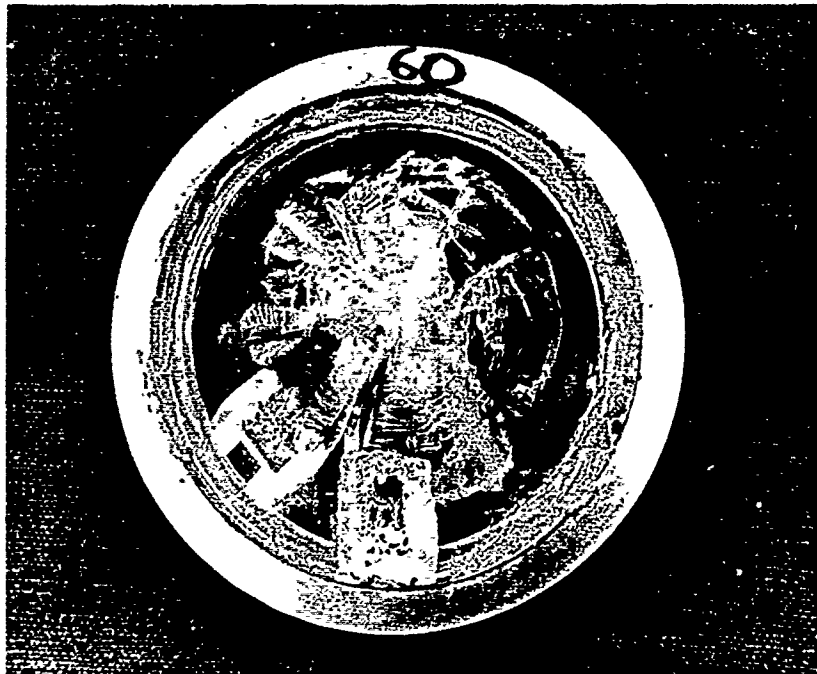


Part A. Convex surface.

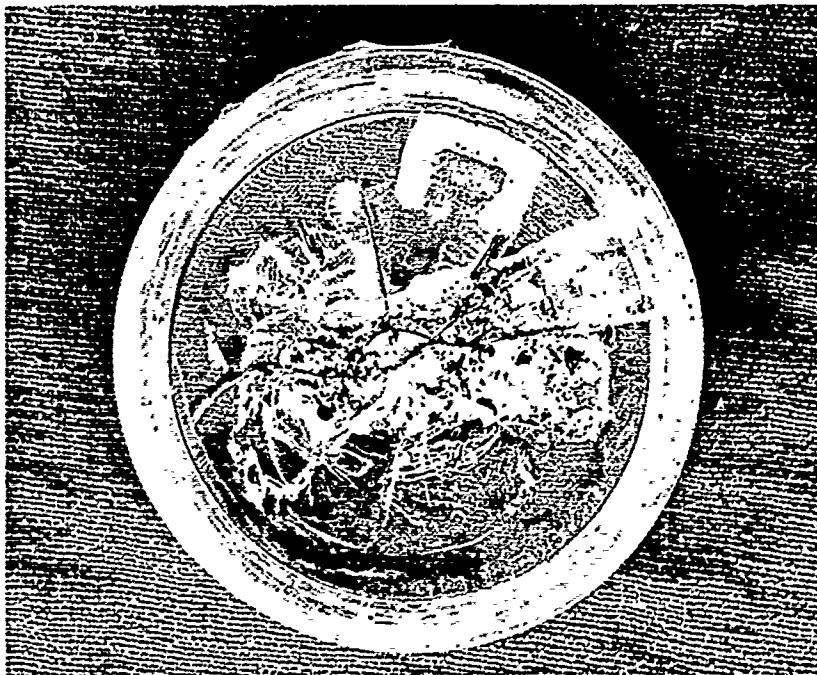


Part B. Concave surface.

Figure 19.  $30^\circ$  spherical sector window with square edge after being subjected to short-term hydrostatic pressure of sufficient magnitude to initiate crack formation without catastrophic implosion.



Part A. Convex surface.

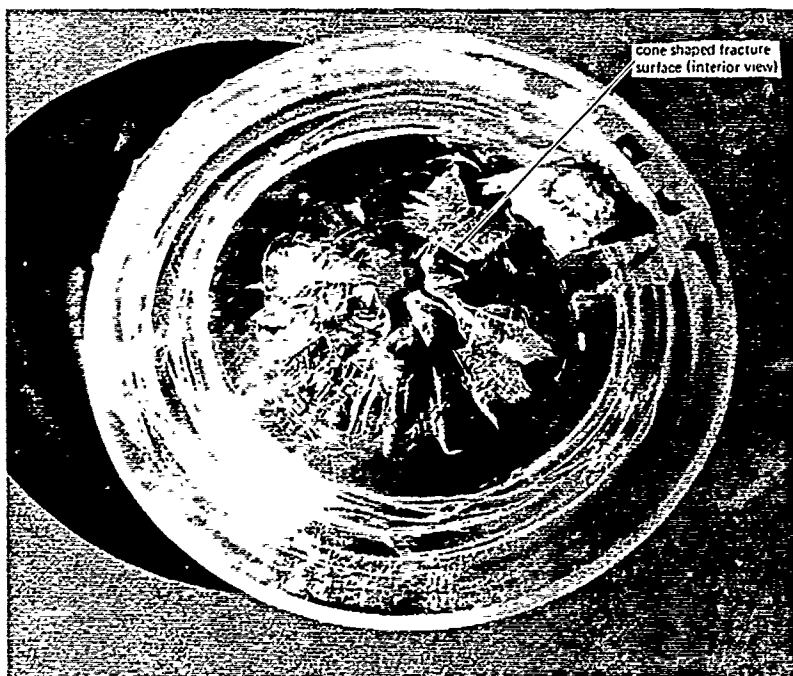


Part B. Concave surface.

Figure 20. 60° spherical sector window with square edge after being subjected to short-term hydrostatic pressure of sufficient magnitude to initiate crack formation without catastrophic implosion.



Part A. Convex surface.



Part B. Concave surface.

Figure 21. 90° spherical sector window with square edge after catastrophic implosion.

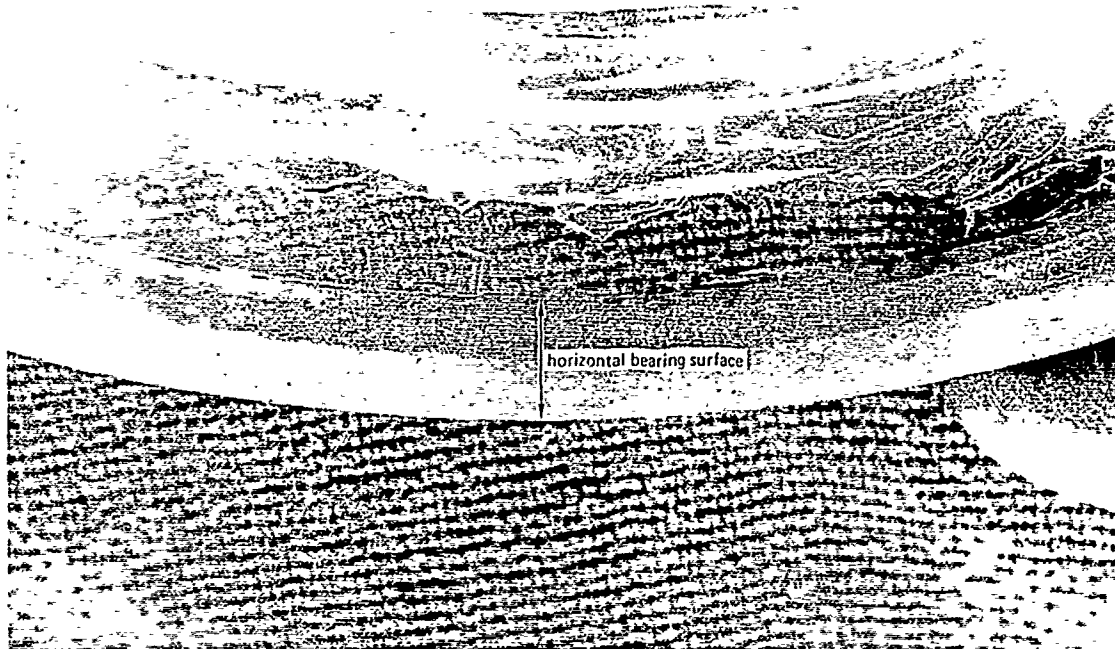


Figure 22. Horizontal bearing surface on 90° spherical sector window with square edge after catastrophic implosion. Note the absence of circumferential cracks in the bearing surface.

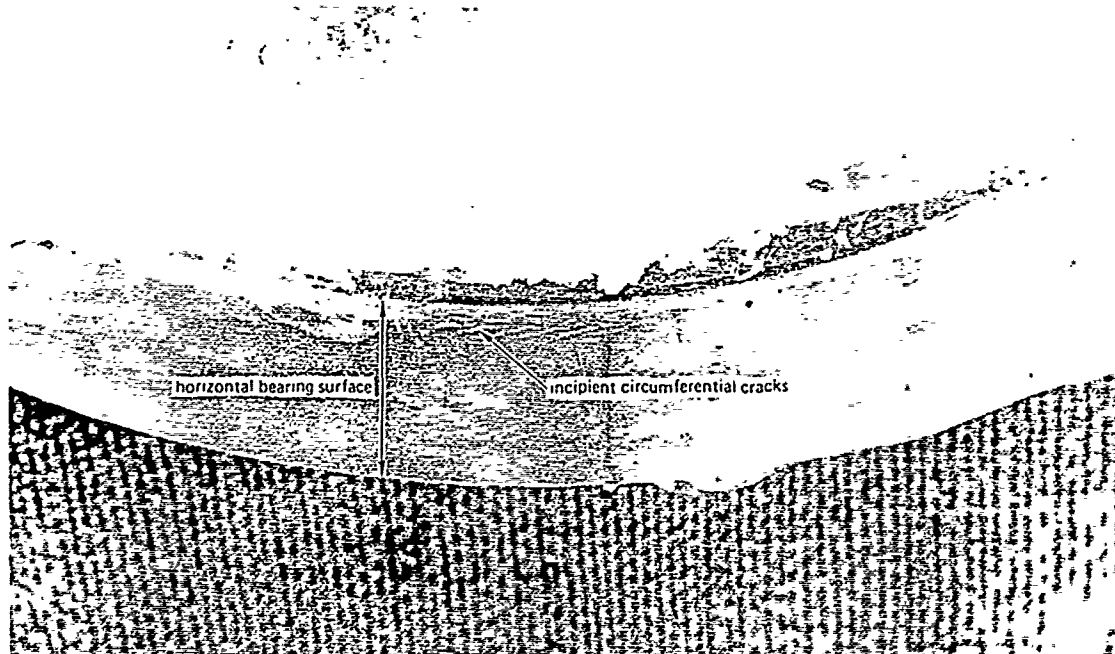


Figure 23. Horizontal bearing surface on 120° spherical sector window with square edge after catastrophic implosion. Note the presence of a few circumferential cracks in the bearing surface.

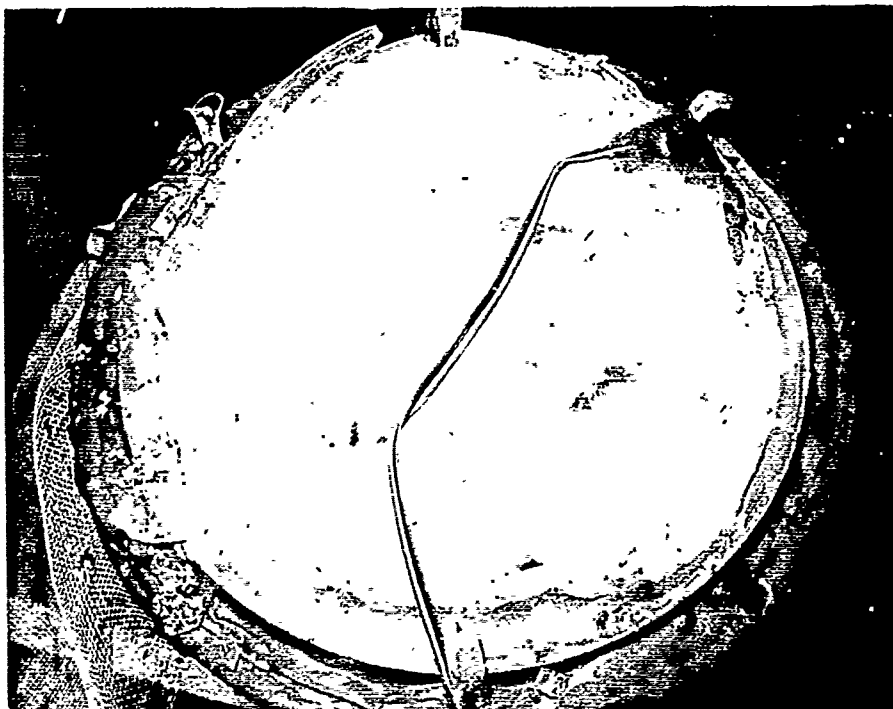


Figure 24. 120° spherical sector window with square edge after catastrophic implosion.

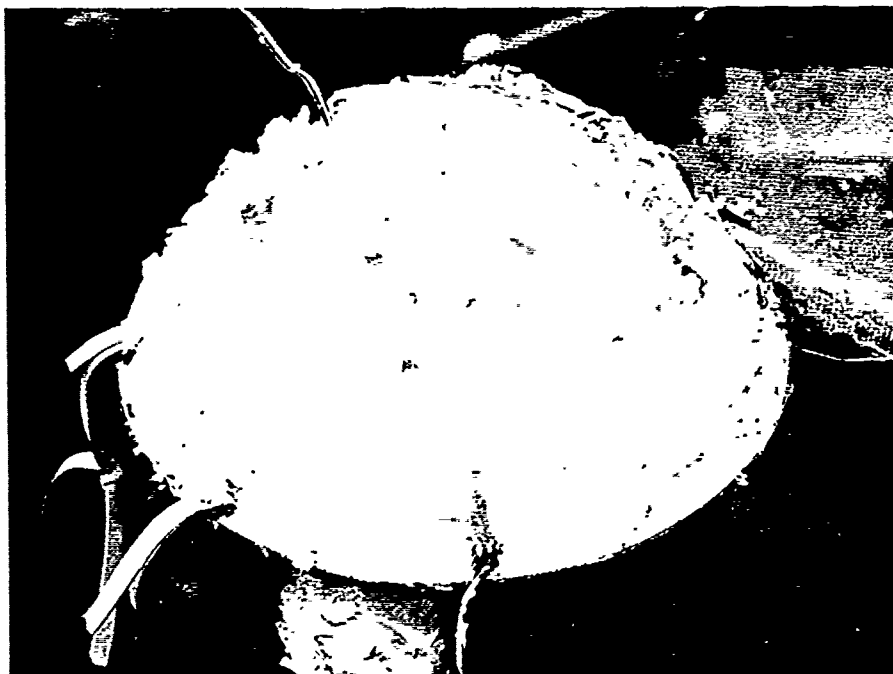


Figure 25. 150° spherical sector window with square edge after catastrophic implosion.



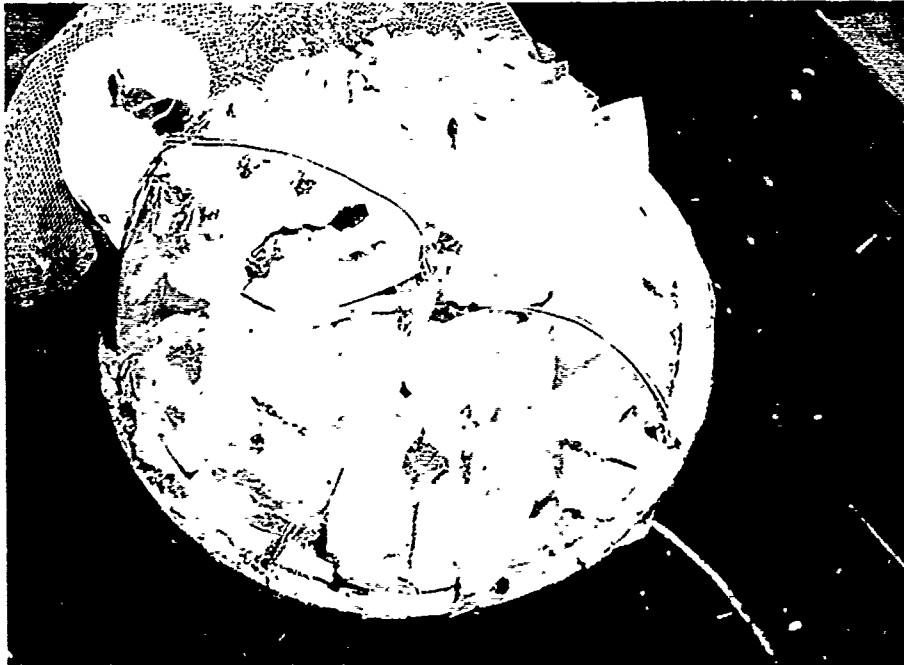


Figure 26. 180° spherical sector window with square edge after catastrophic implosion.

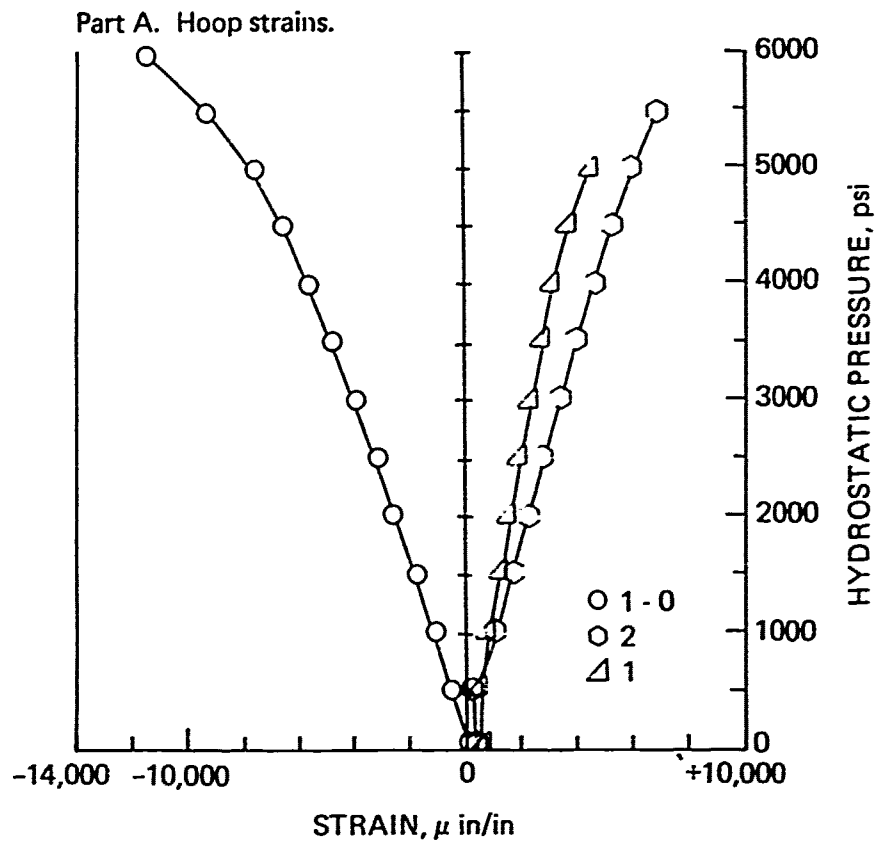


Figure 27. 30° spherical sector window with square edge and  $t/R_i = 0.159$  (figure 5) under short-term hydrostatic loading.

Part B. Meridional strains.

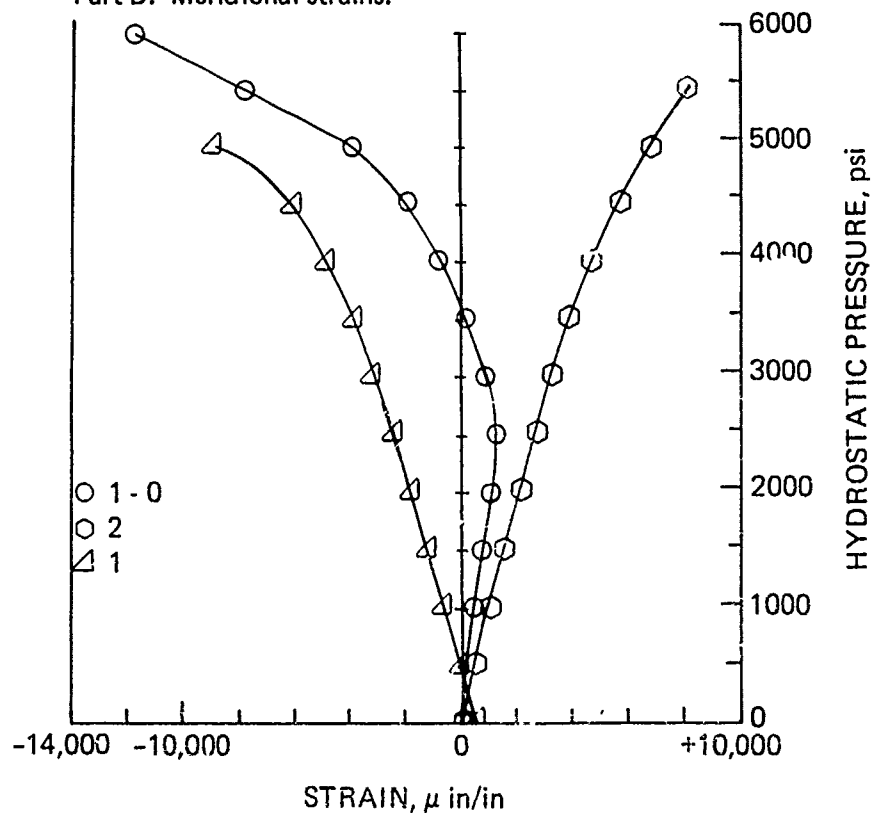


Figure 27. Continued.

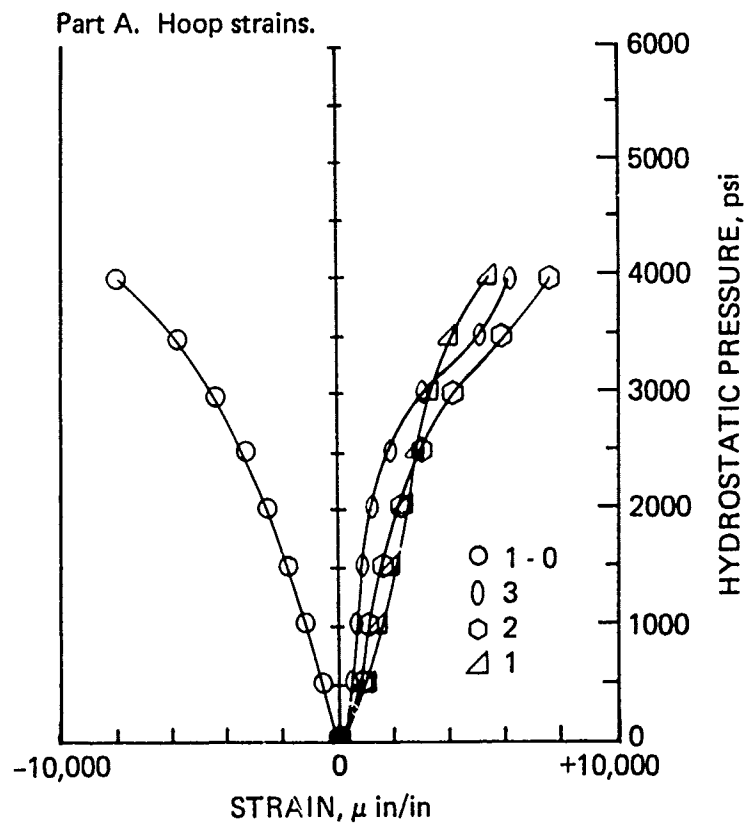


Figure 28. 60° spherical sector window with square edge and  $t/R_i = 0.159$  (figure 6) under short-term hydrostatic loading.

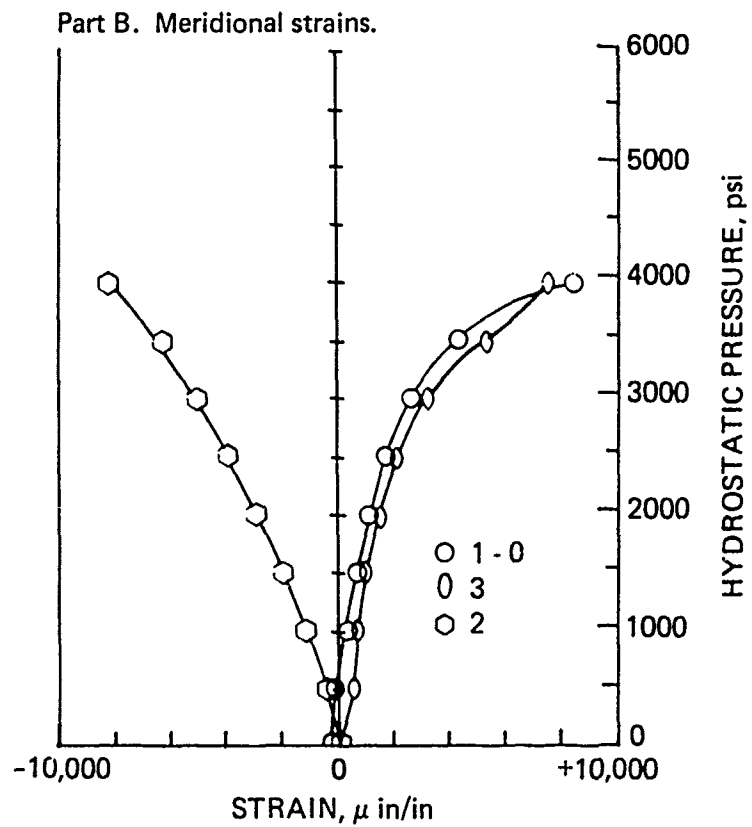


Figure 28. Continued.

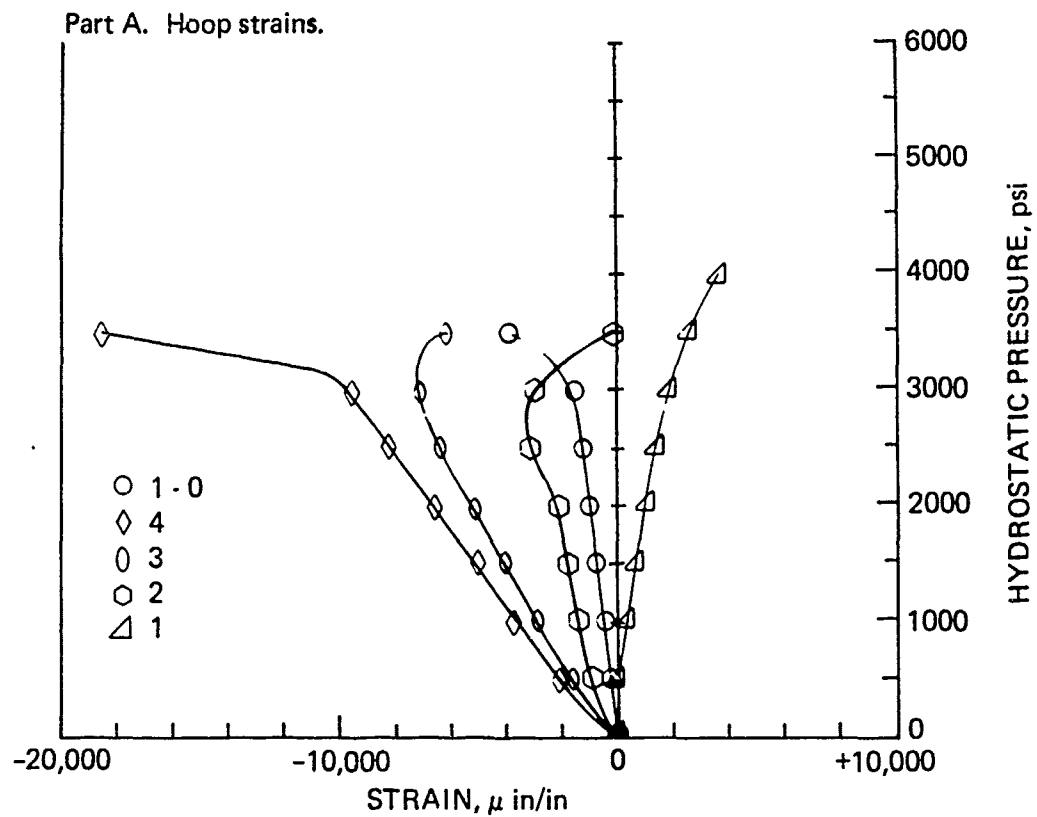


Figure 29. 90° spherical sector window with square edge and  $t/R_i = 0.159$  (figure 7) under short-term hydrostatic loading.

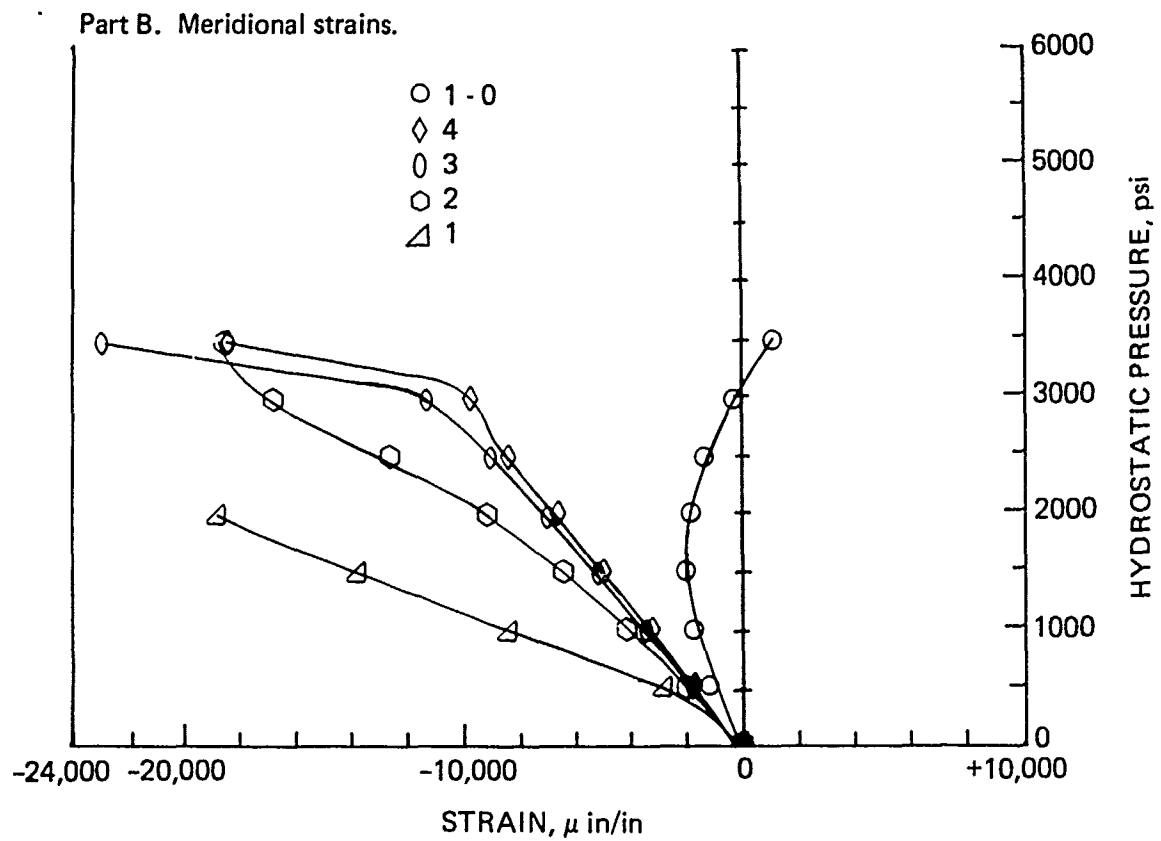


Figure 29. Continued.

Part A. Hoop strains.

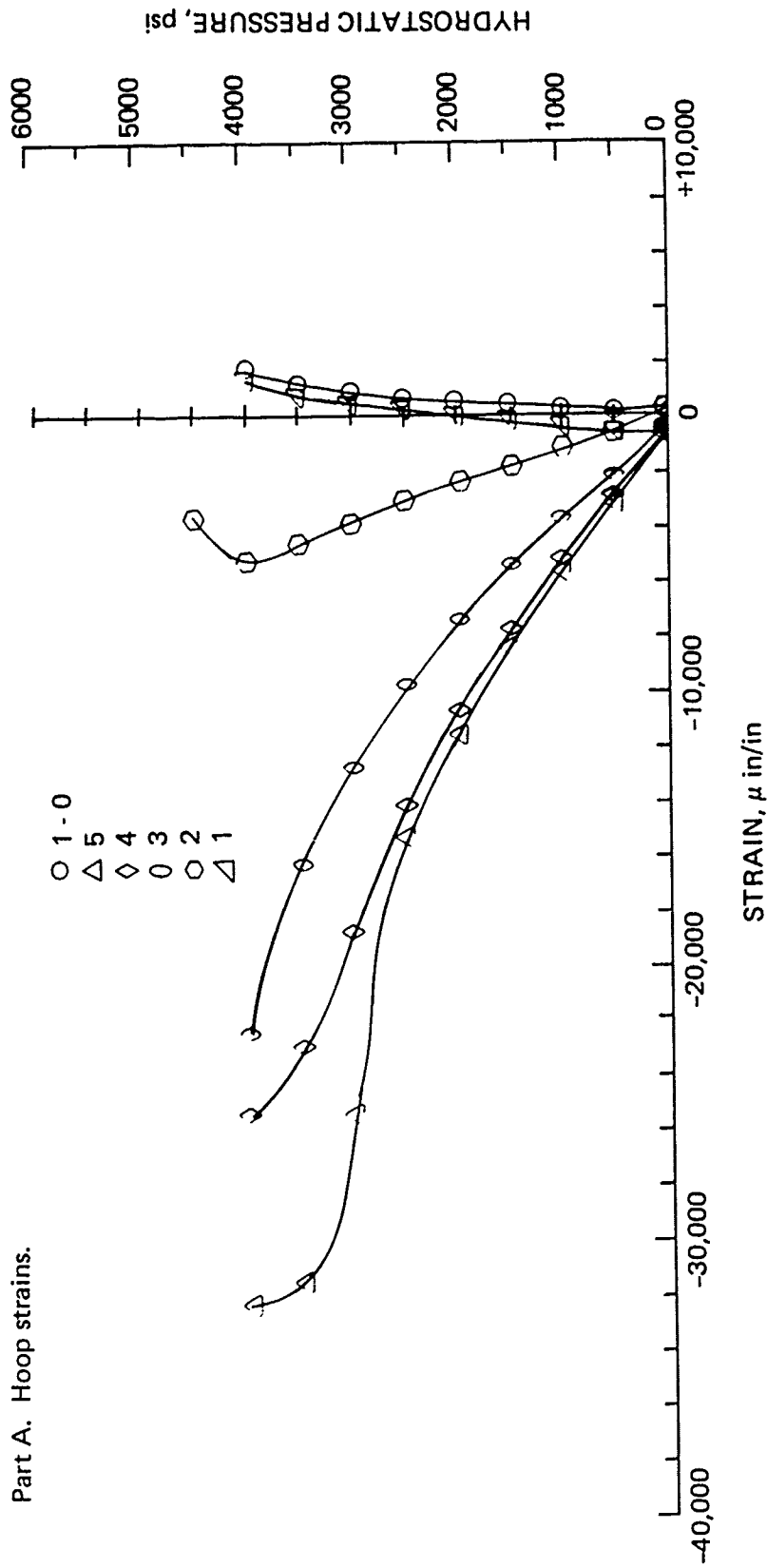


Figure 30. 120° spherical sector window with square edge and  $t/R_i = 0.159$  (figure 8) under short-term hydrostatic loading.



Part B. Meridional strains.

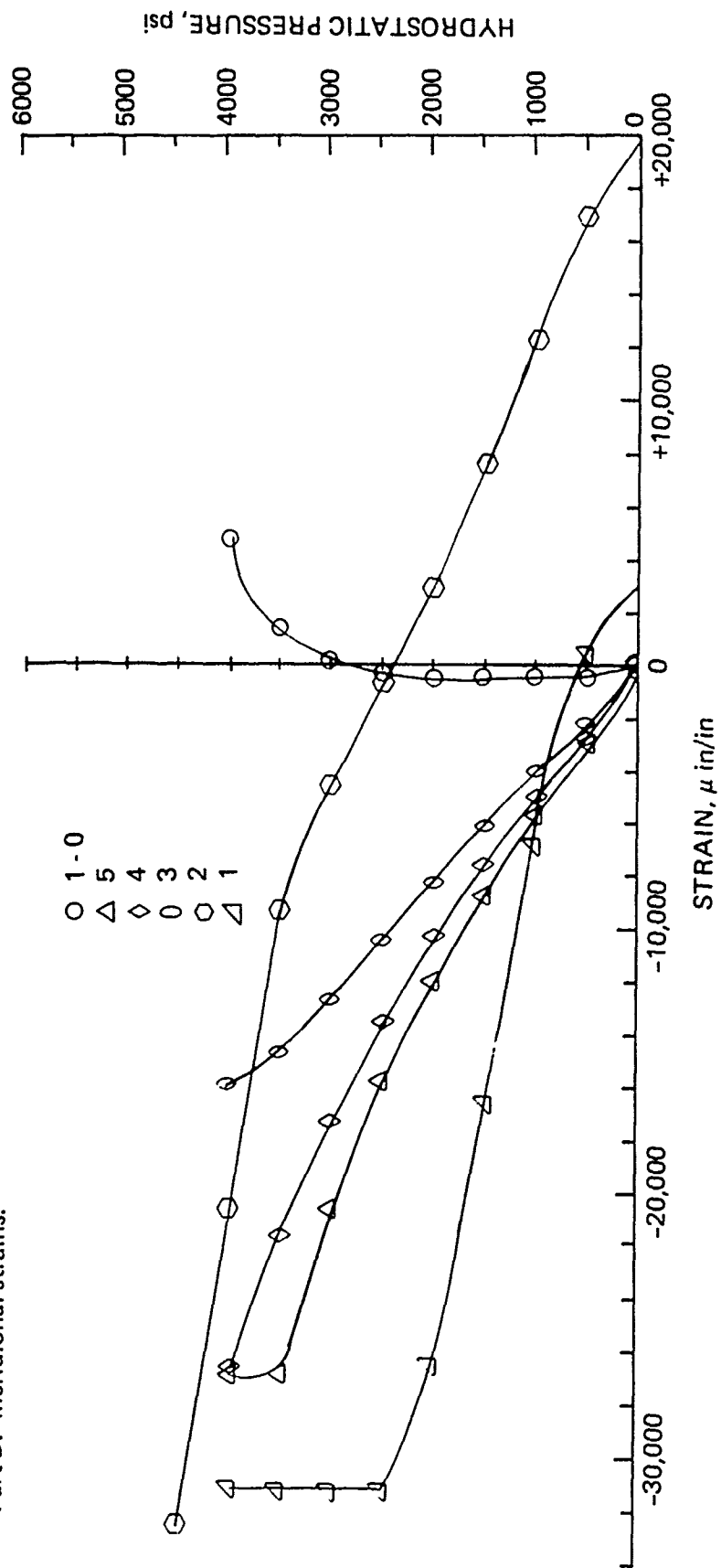


Figure 30. Continued.

Part A. Hoop strains on concave surface.

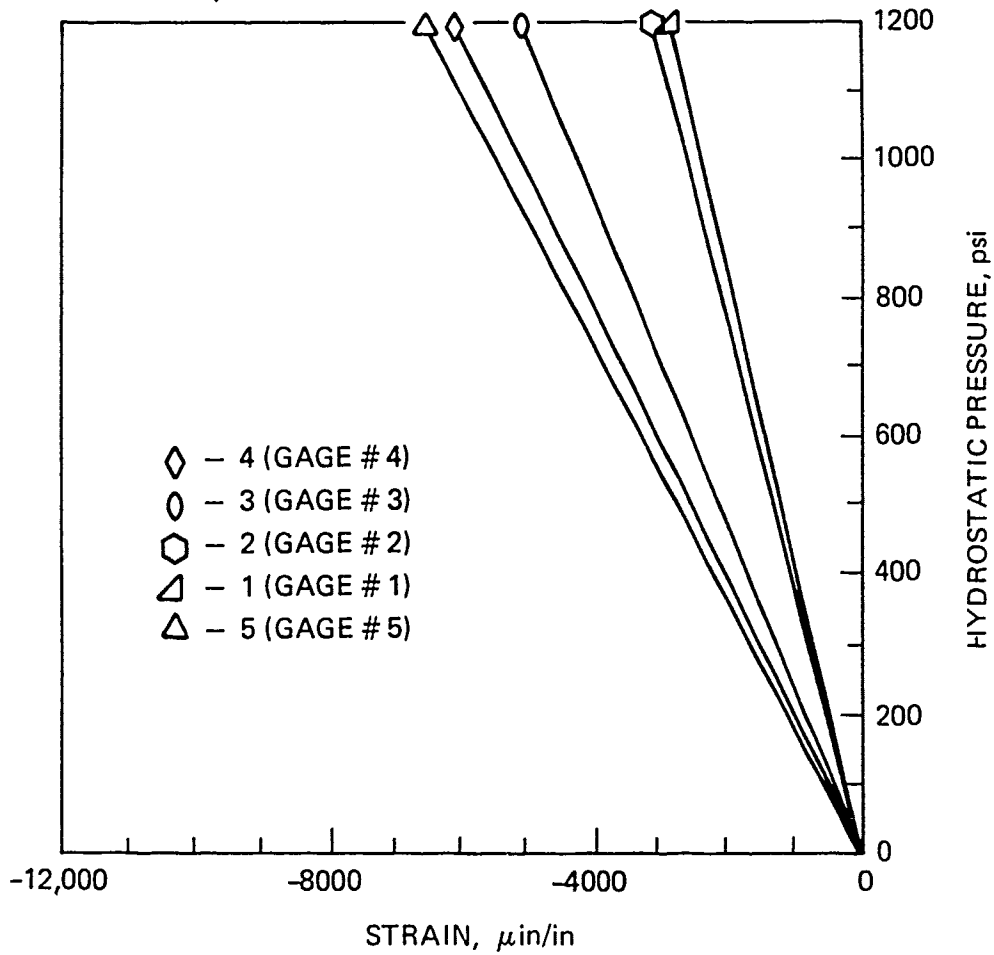


Figure 31. 120° spherical sector window with conical edge and  $t/R_i = 0.159$  (figure 9) under short-term hydrostatic loading. See figure 17 for location of gages.

Part B. Meridional strains on concave surface.

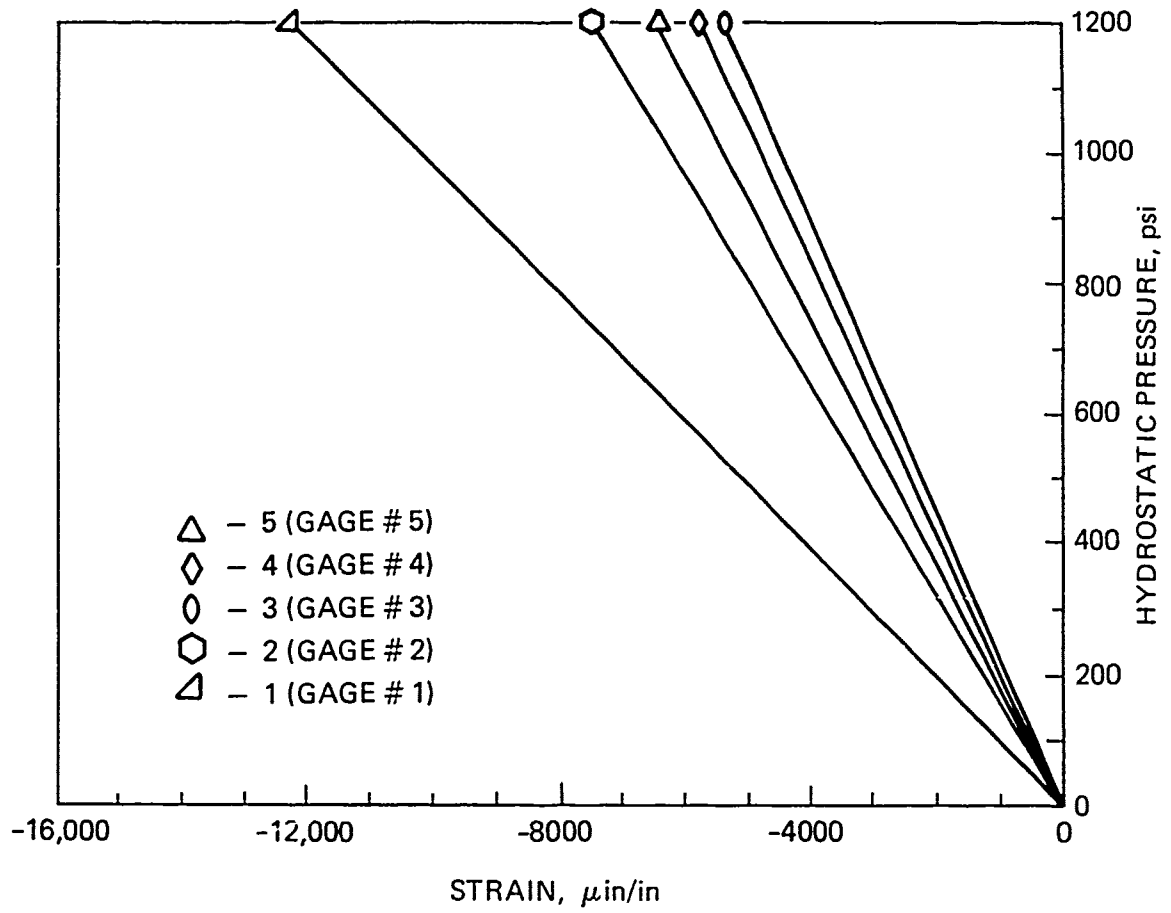


Figure 31. Continued.

Part C. Hoop strains on convex surface.

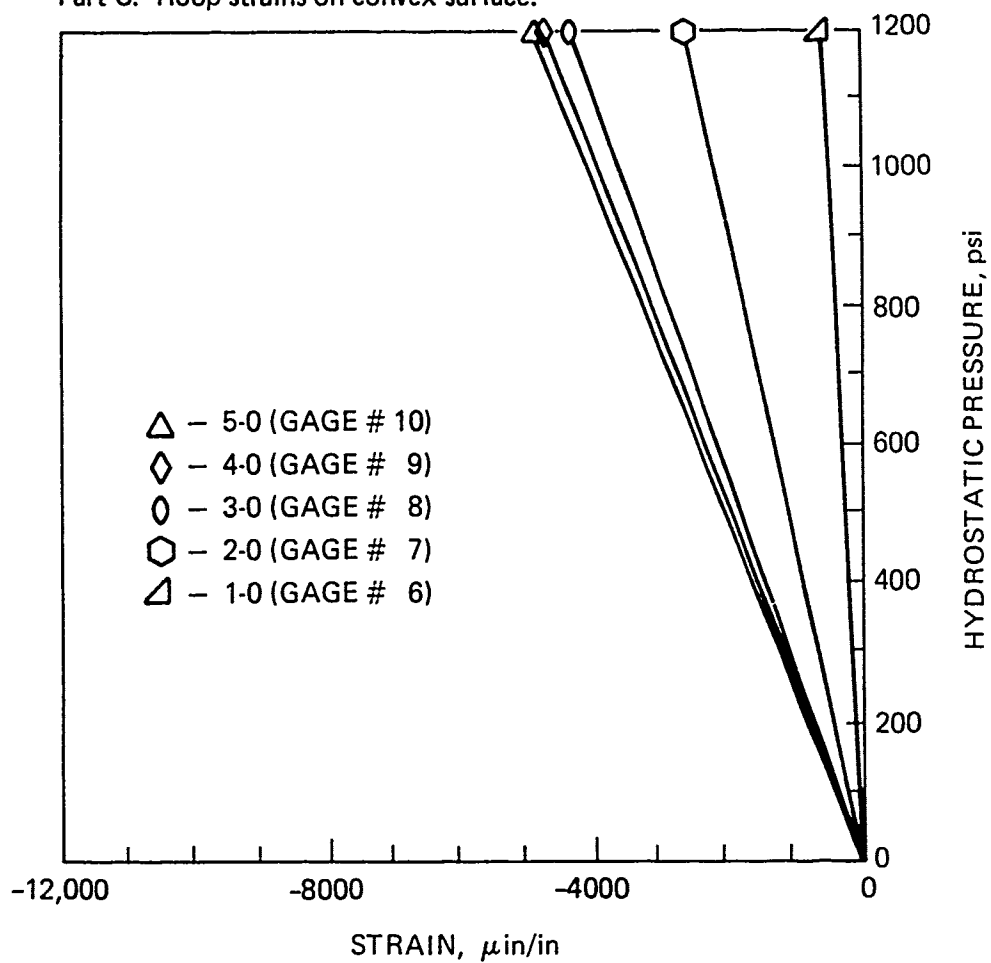


Figure 31. Continued.

Part D. Meridional strains on convex surface.

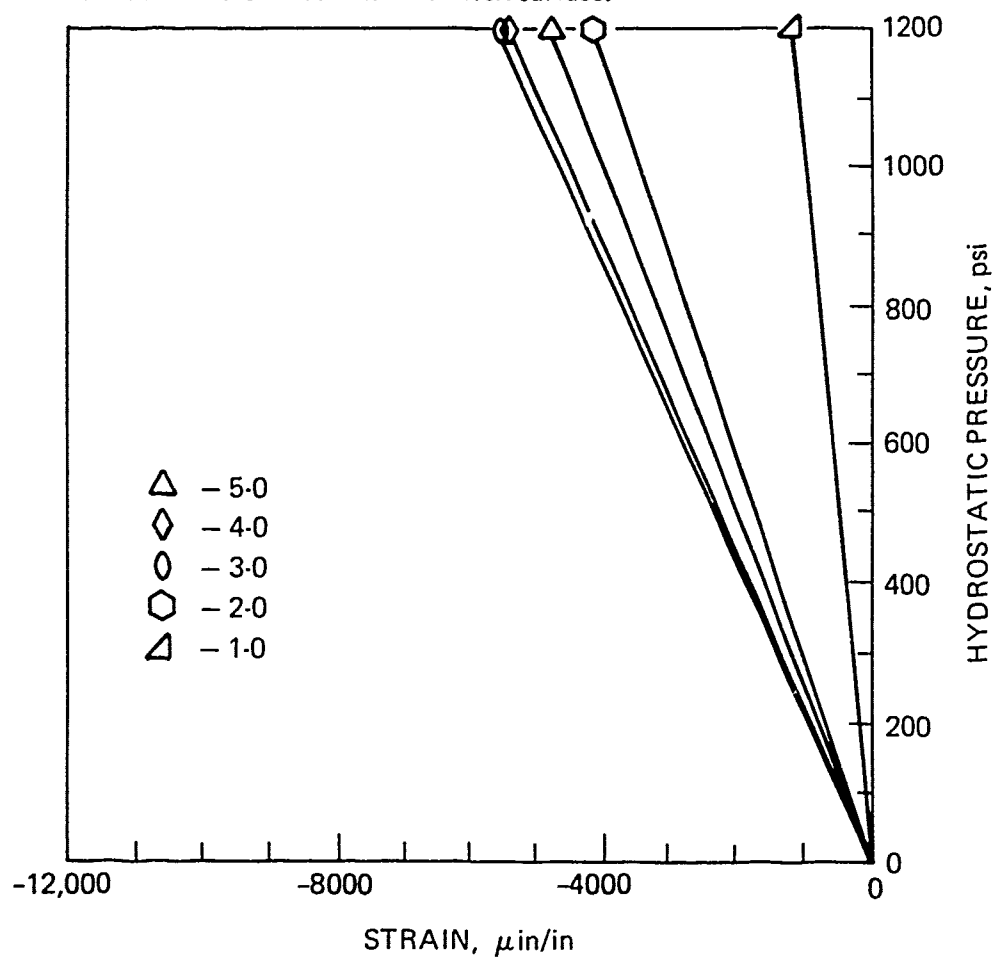


Figure 31. Continued.

Part A. Hoop strains.

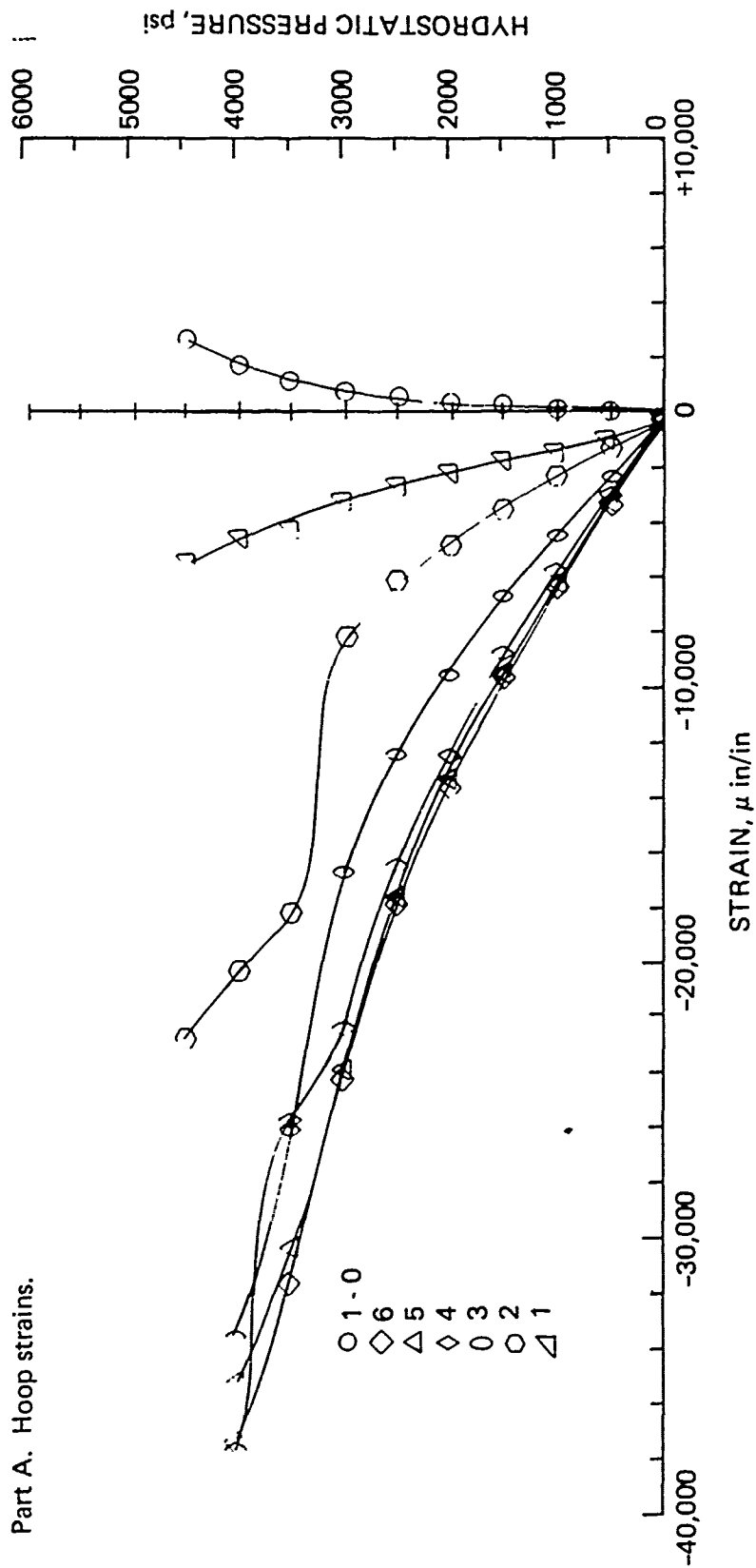


Figure 32. 150° spherical sector window with square edge and  $t/R_i = 0.159$  (figure 10) under short-term hydrostatic loading.

Part B. Meridional strains.

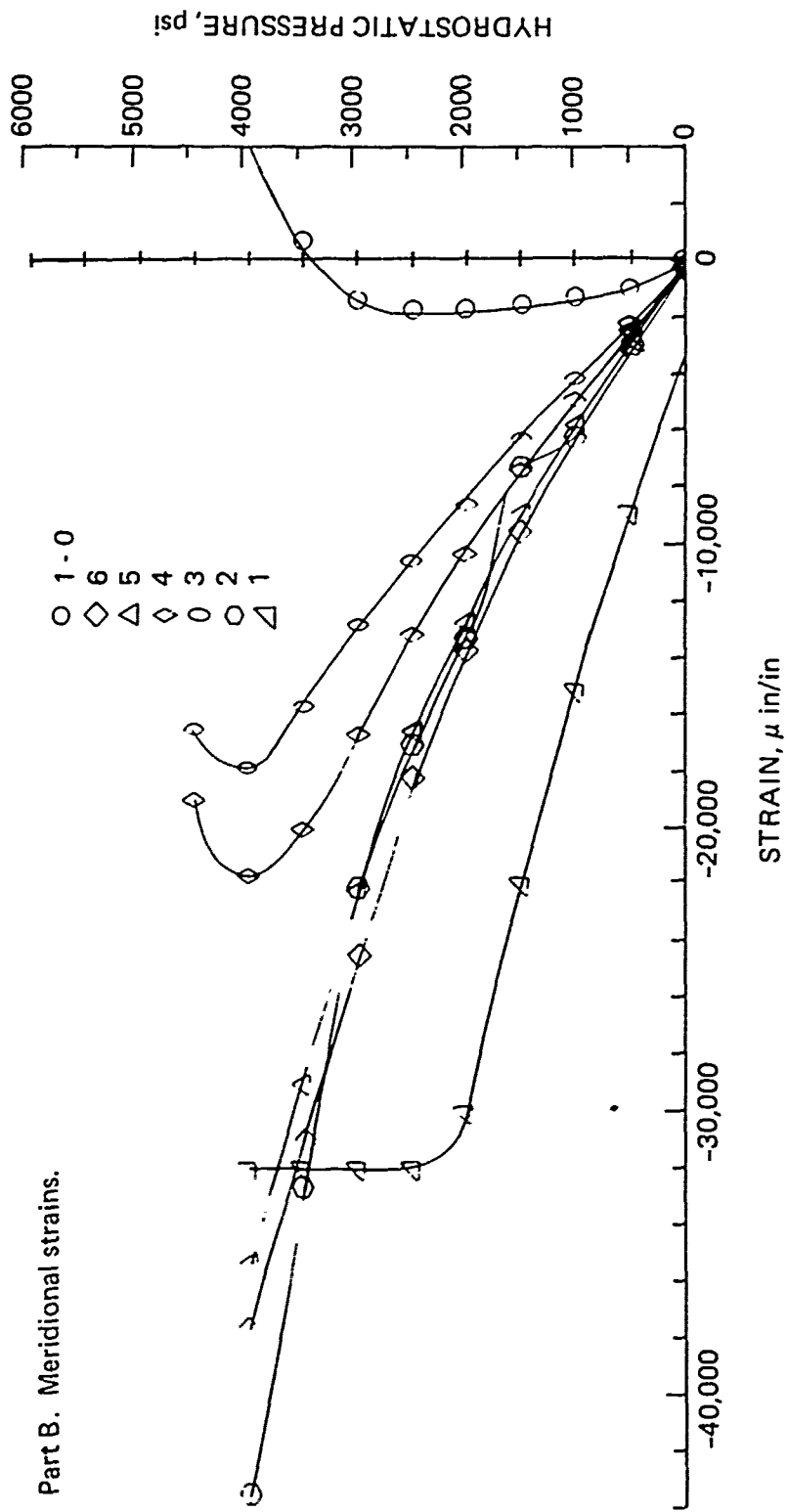


Figure 32. Continued.

Part A. Hoop strains.

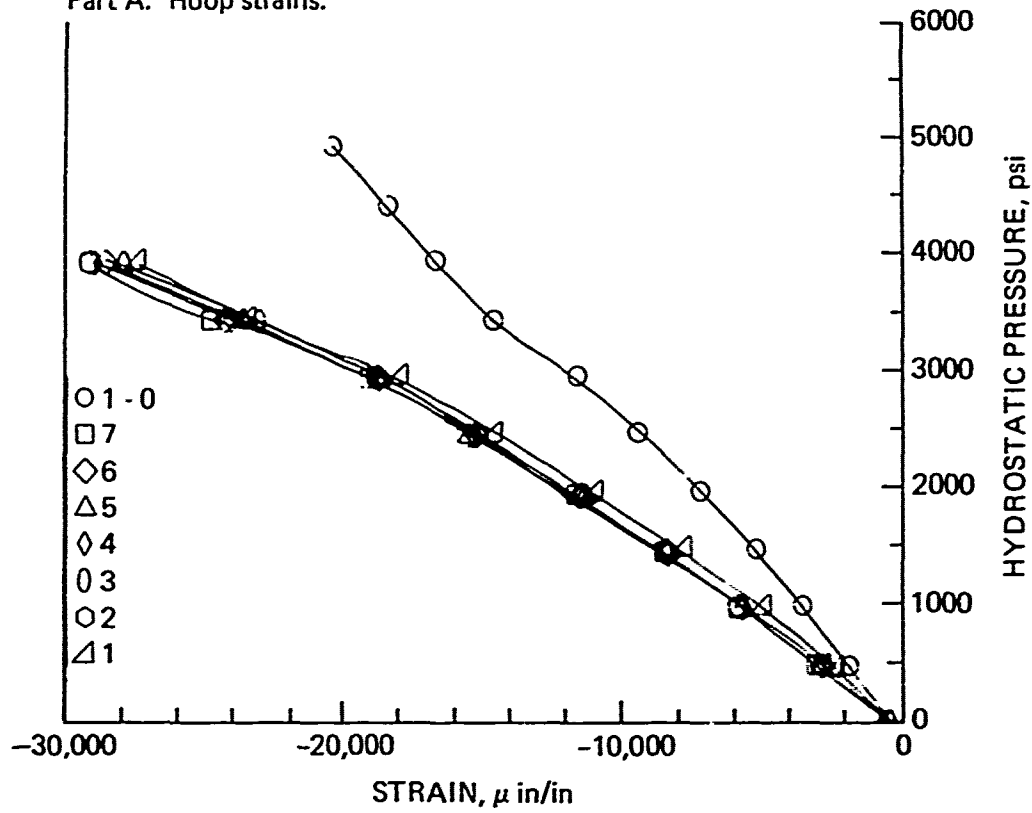


Figure 33. 180° spherical sector window with square edge and  $t/R_1 = 0.159$  (figure 11) under short-term hydrostatic loading.



Part B. Meridional strains.

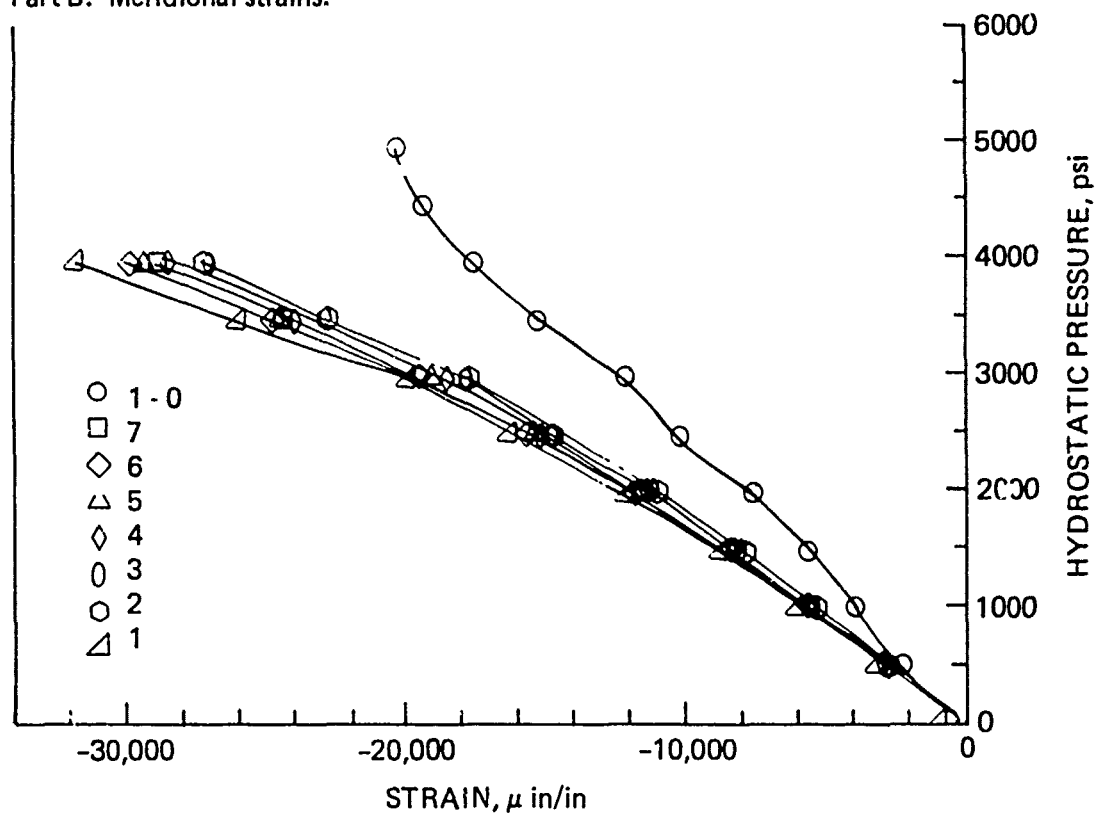


Figure 33. Continued.

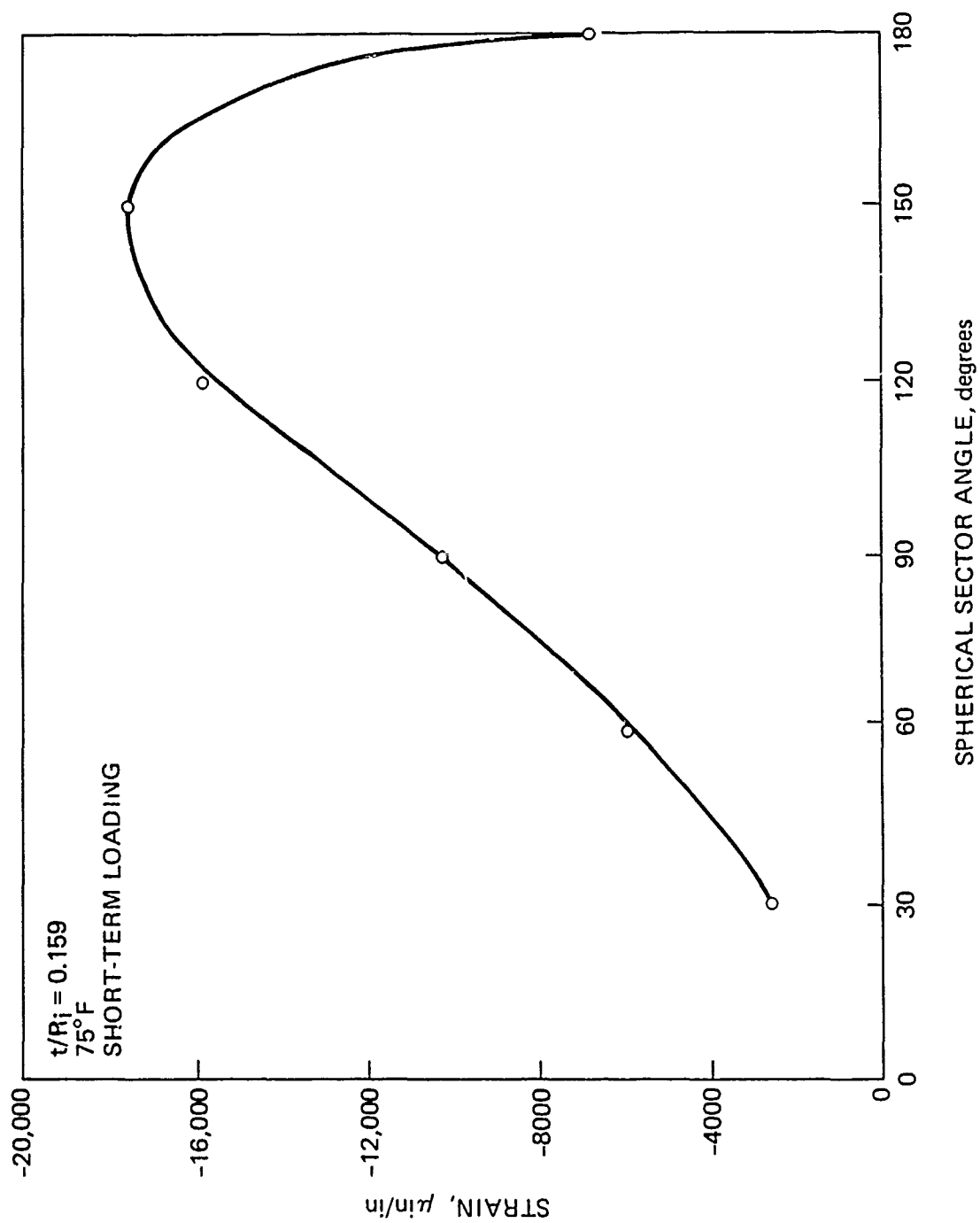


Figure 34. Relationship of spherical angle to meridional strain on concave surface around periphery of spherical sector windows with square edges and  $t/R_i = 0.159$  subjected to 1200-psi short-term hydrostatic loading.

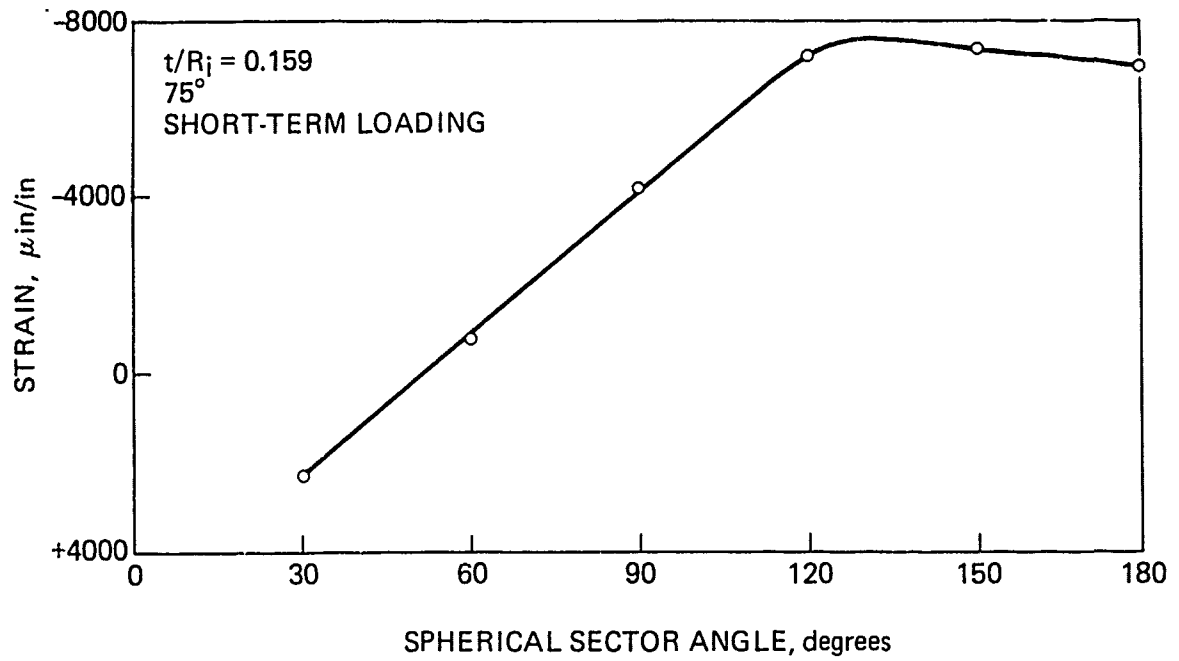


Figure 35. Relationship of spherical angle to strain on concave surface at apex of spherical sector windows with square edges and  $t/R_i = 0.159$  subjected to 1200-psi short-term hydrostatic loading.

Part A. Hoop stresses.

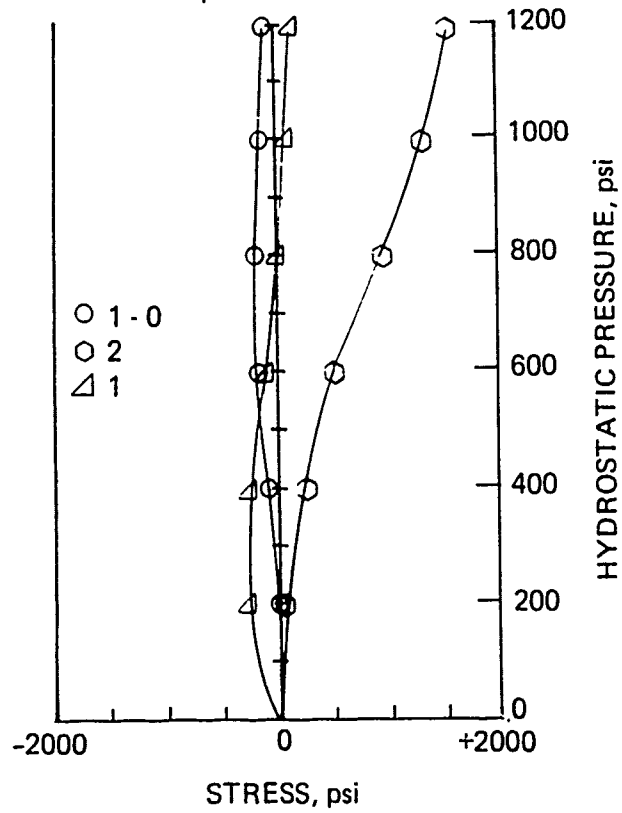


Figure 36. 30° spherical sector window with square edge and  $t/R_1 = 0.159$  during short-term hydrostatic loading to 1200 psi.

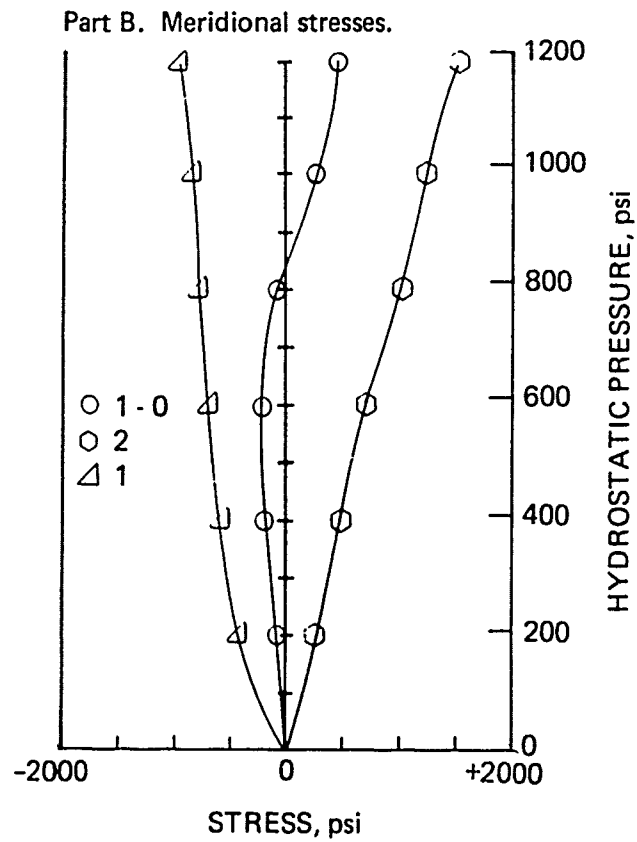


Figure 36. Continued.

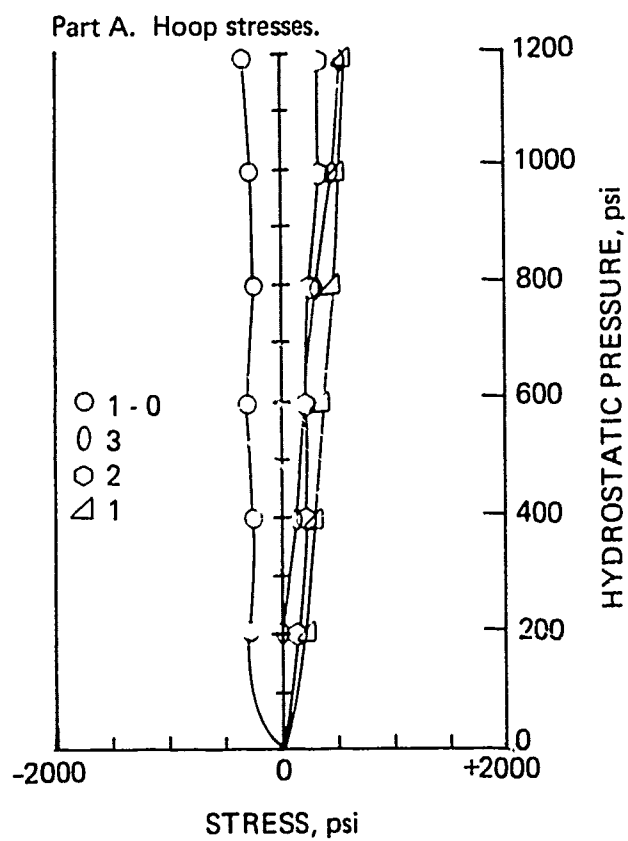


Figure 37. 60° spherical sector window with square edge and  $t/R_1 = 0.159$  during short-term hydrostatic loading to 1200 psi.

Part B. Meridional stresses.

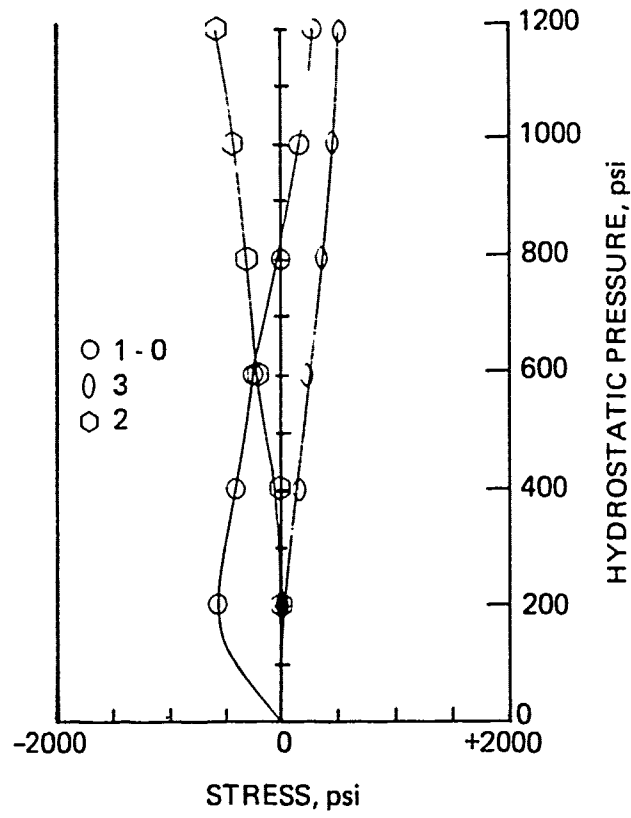


Figure 37. Continued.

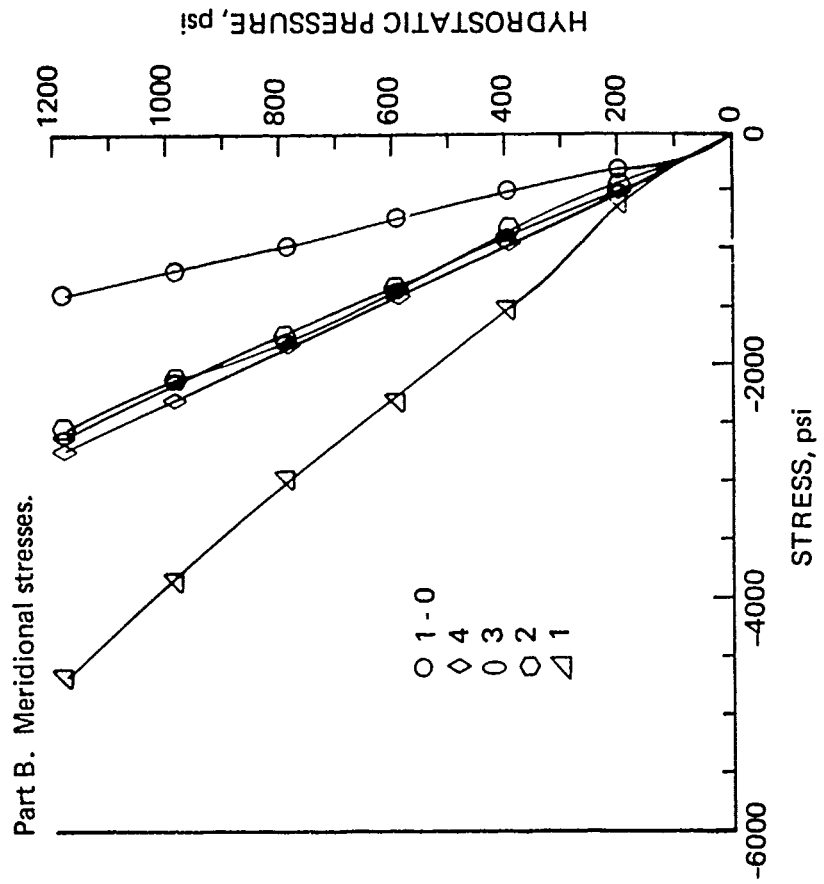
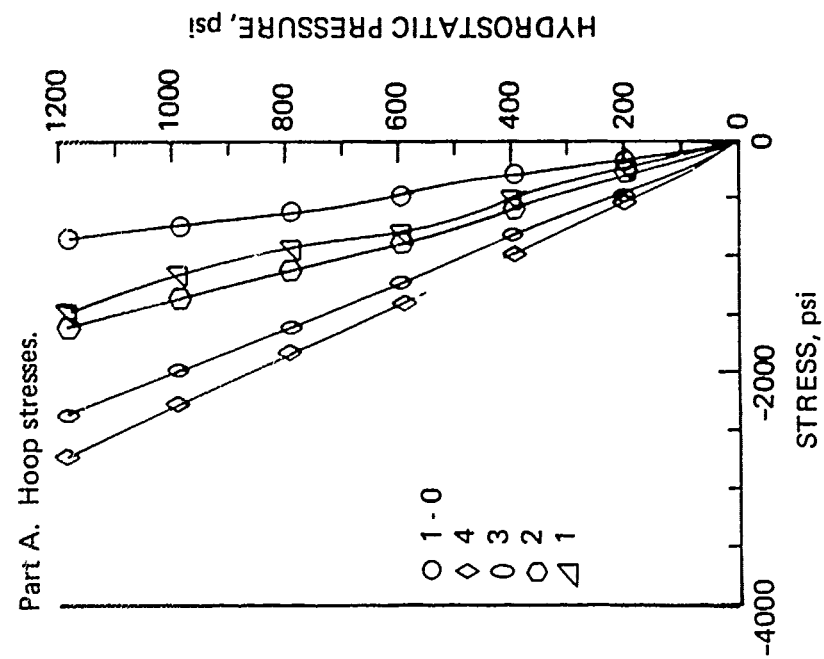


Figure 38. 90° spherical sector window with square edge and  $t/R_i = 0.159$  during short-term hydrostatic loading to 1200 psi.



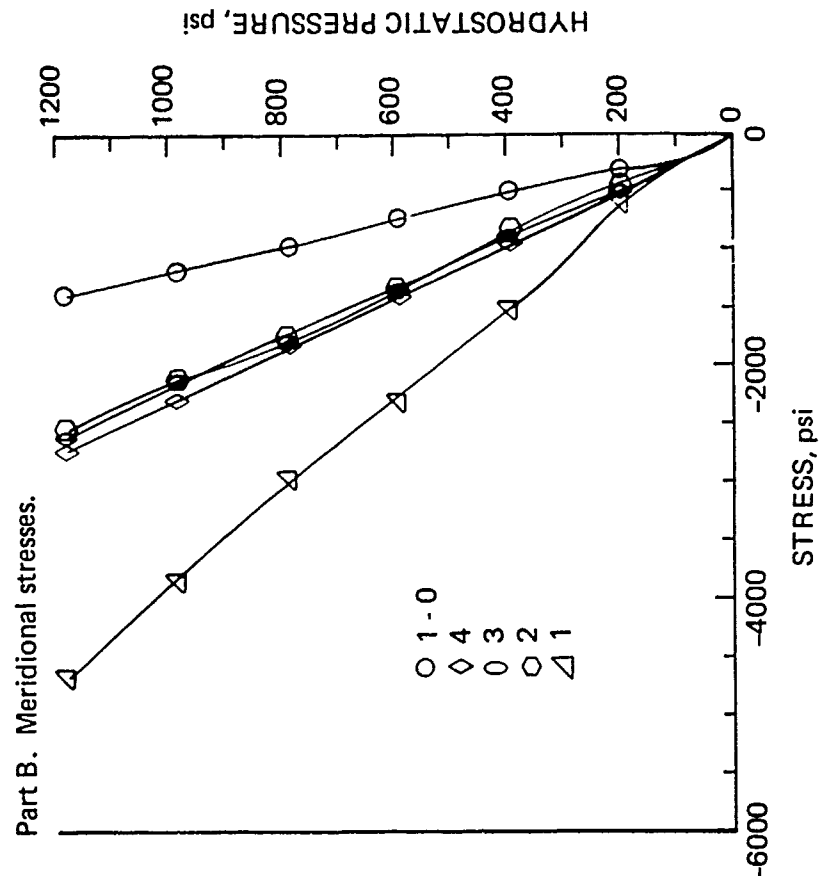
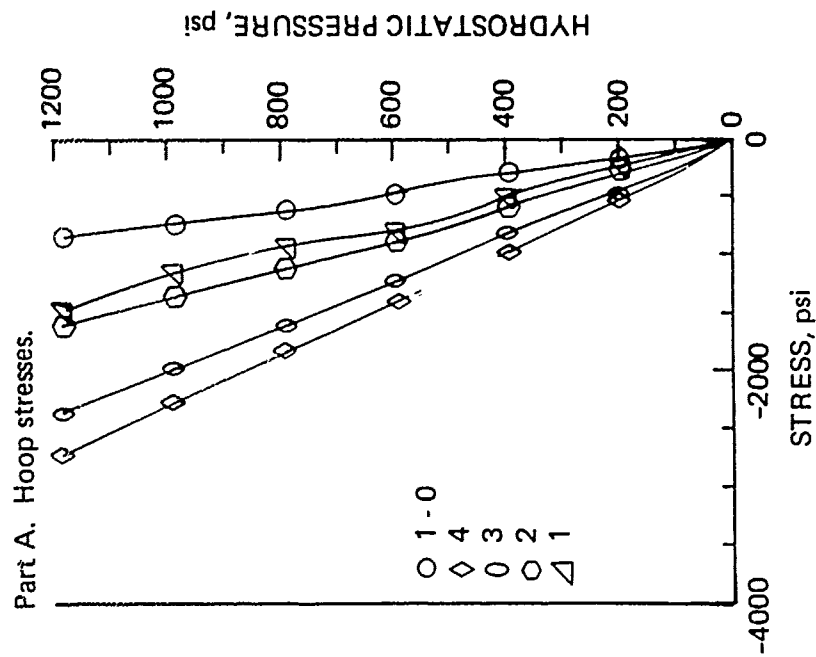


Figure 38. 90° spherical sector window with square edge and  $t/R_1 = 0.159$  during short-term hydrostatic loading to 1200 psi.

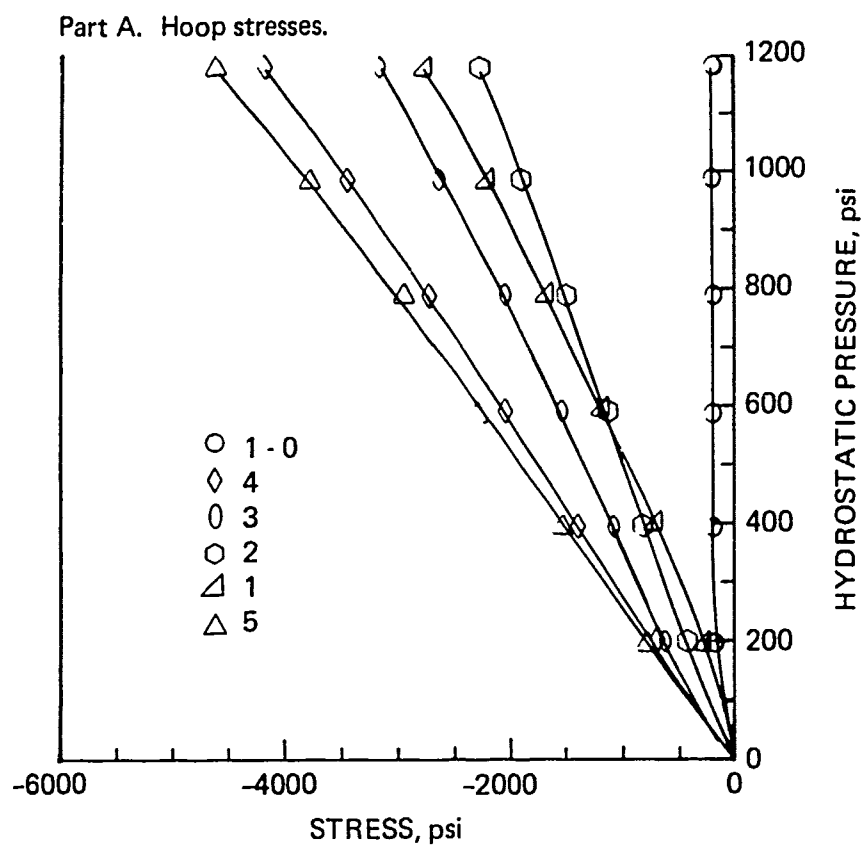


Figure 39. 120° spherical sector window with square edge and  $t/R_i = 0.159$  during short-term hydrostatic loading to 1200 psi.

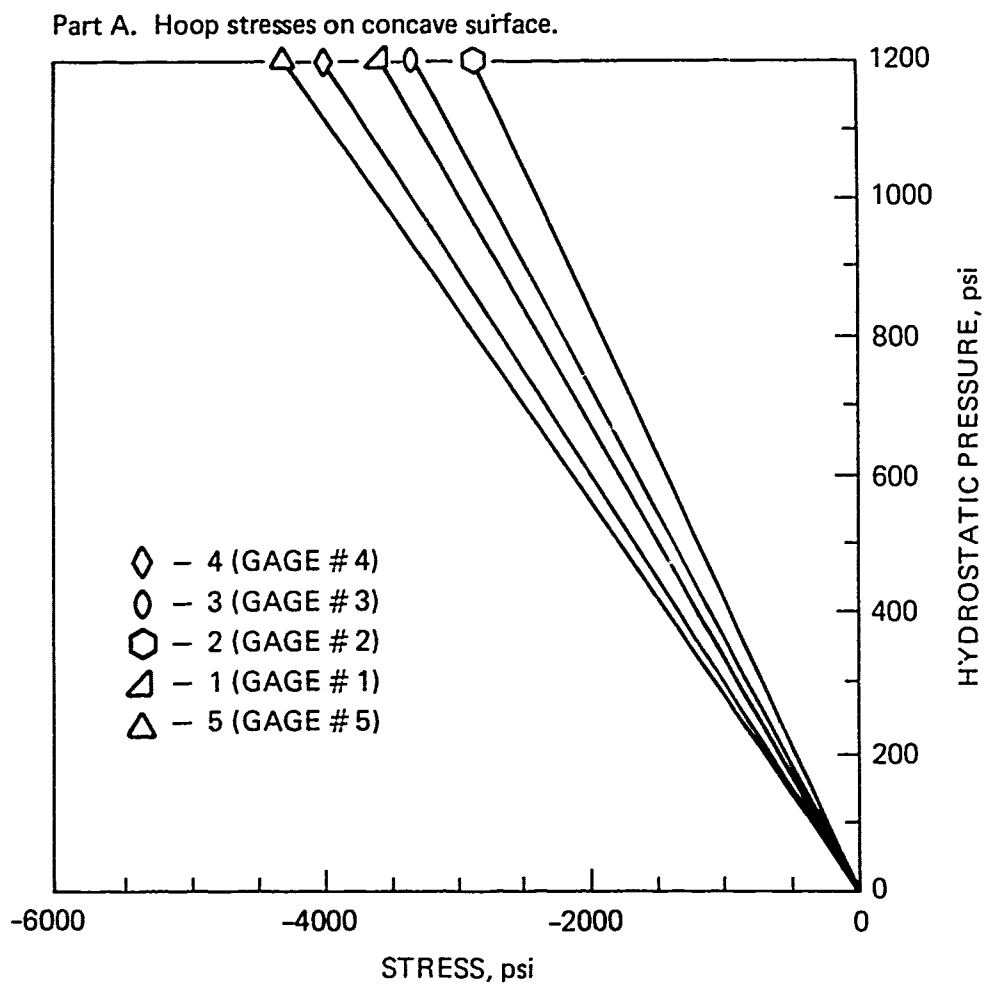


Figure 40. 120° spherical sector window with conical edge and  $t/R_i = 0.159$  during short-term hydrostatic loading to 1200 psi.

Part B. Meridional stresses on concave surface.

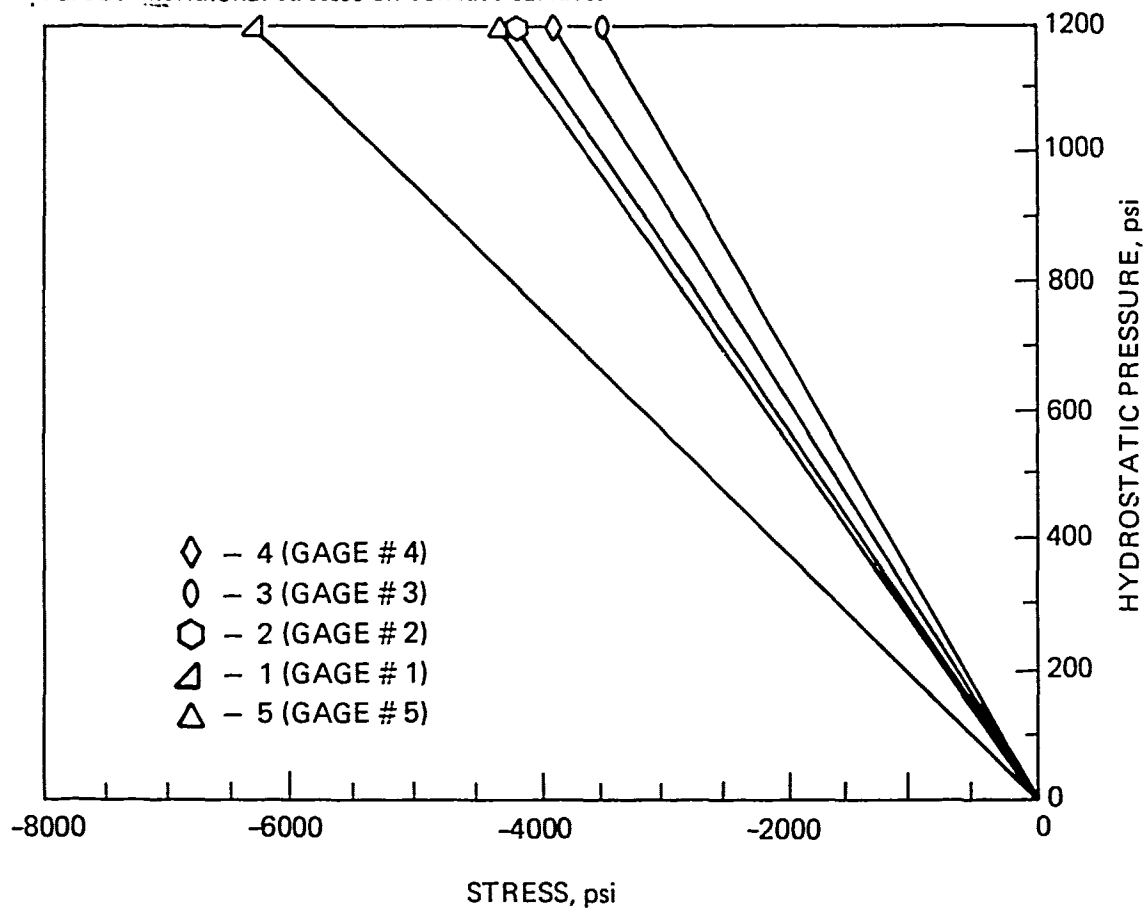


Figure 40. Continued.

Part D. Meridional stresses on convex surface.

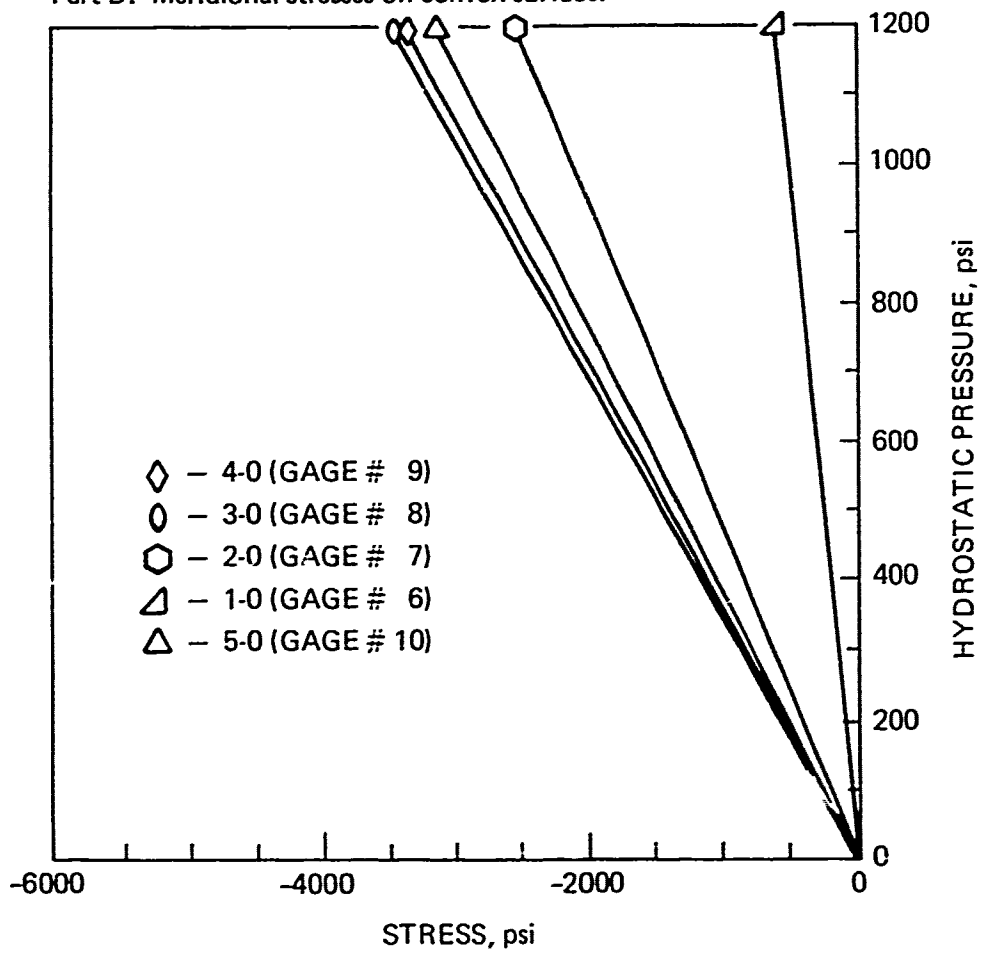


Figure 40. Continued.

Part A. Hoop stresses.

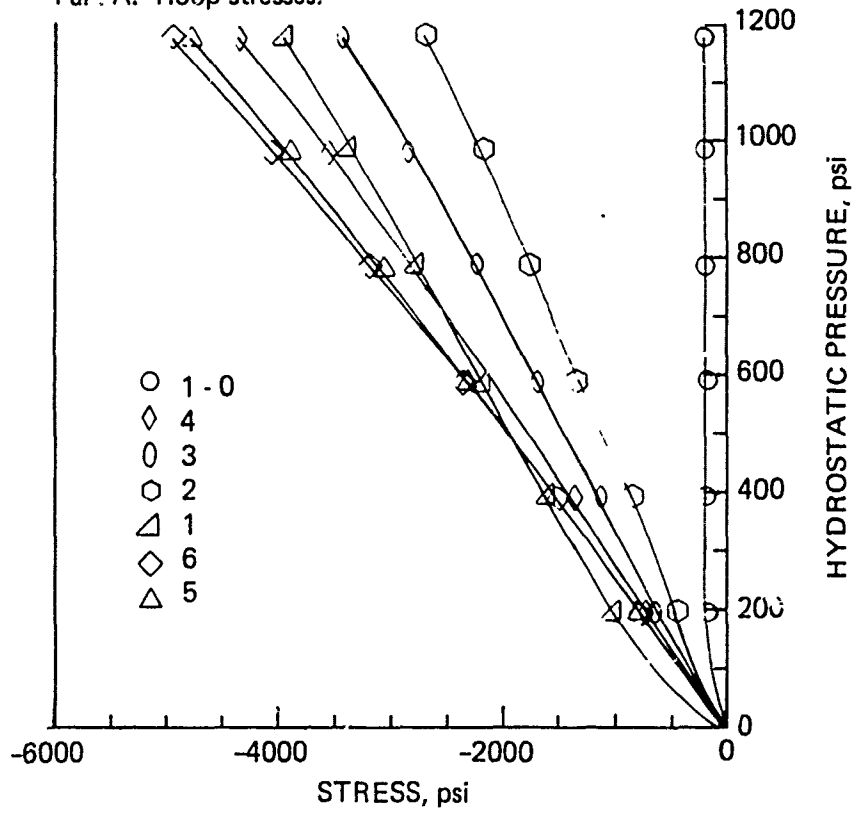


Figure 41. 150° spherical sector window with square edge and  $t/R_i = 0.159$  during short-term hydrostatic loading to 1200 psi.

Part B. Meridional stresses.

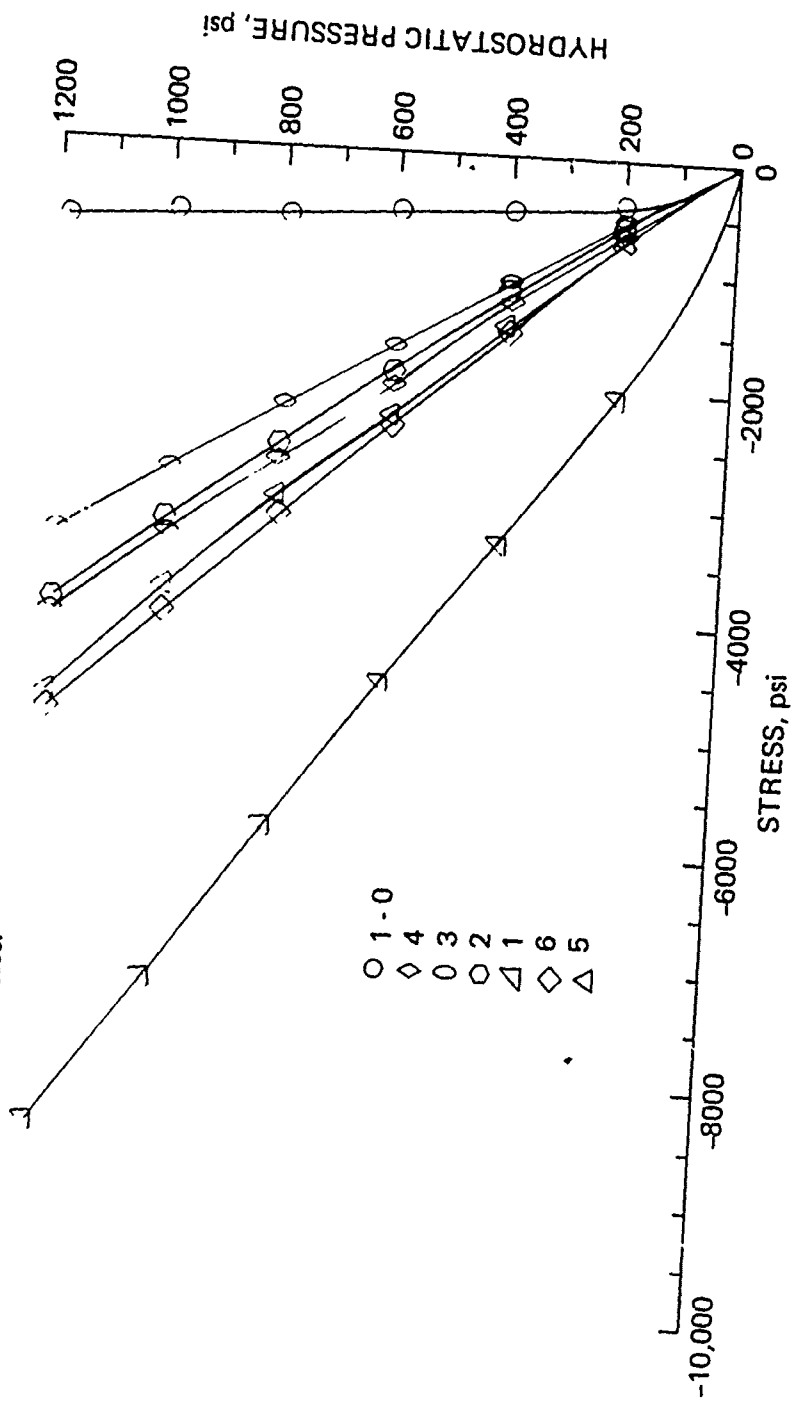


Figure 41. Continued

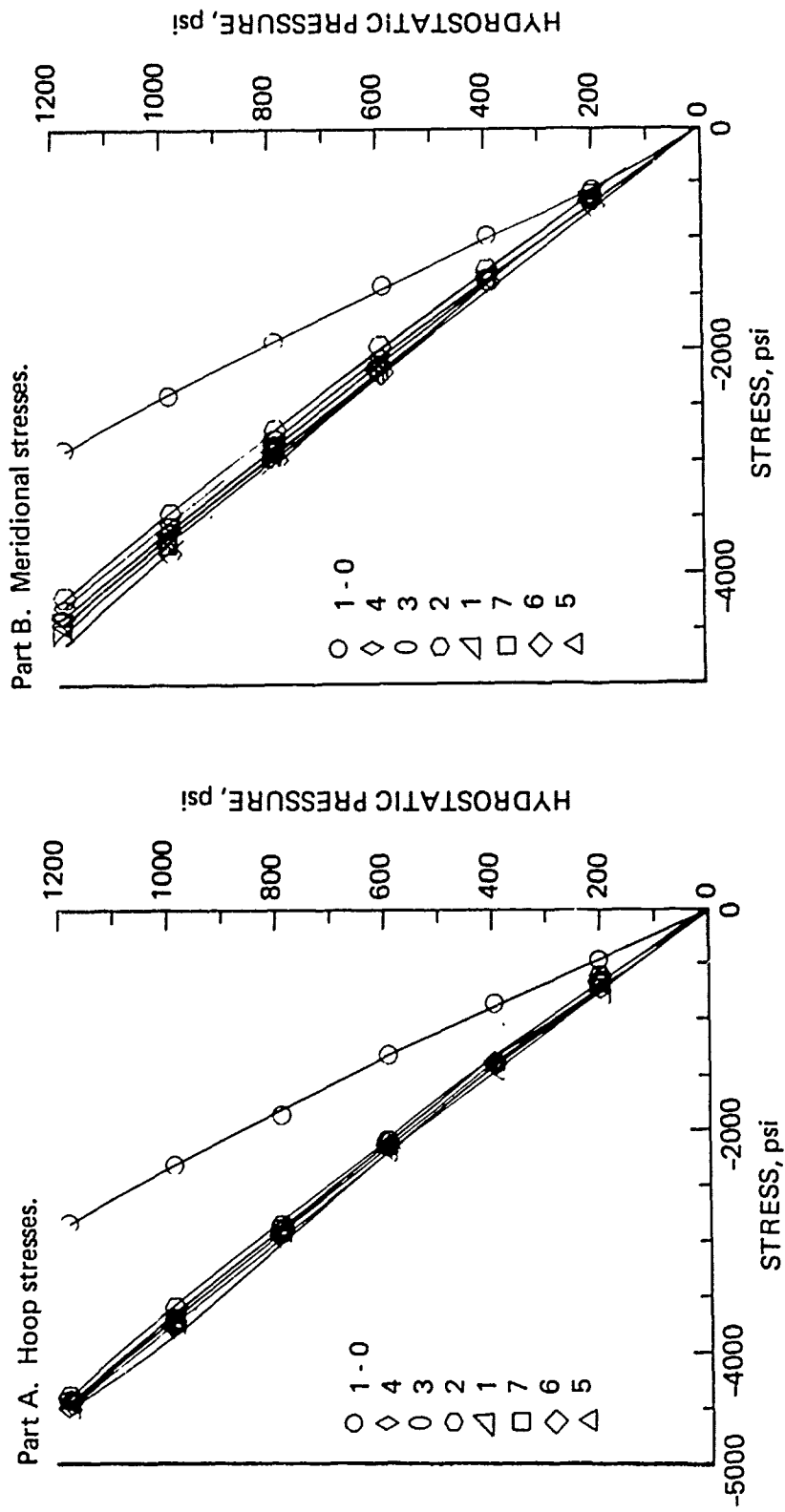


Figure 42. 180° spherical sector window with square edge and  $t/R_i = 0.159$  during short-term hydrostatic loading to 1200 psi.





Part A. Overall view.



Part B. Close up view.

Figure 43. Radial scratches on conical window seat of steel flange for 120° spherical sector window with conical edge after 100 pressure cycles. Each cycle consisted of 4 hours of sustained 1200-psi hydrostatic loading followed by 4 hours of relaxation at 0 psi.

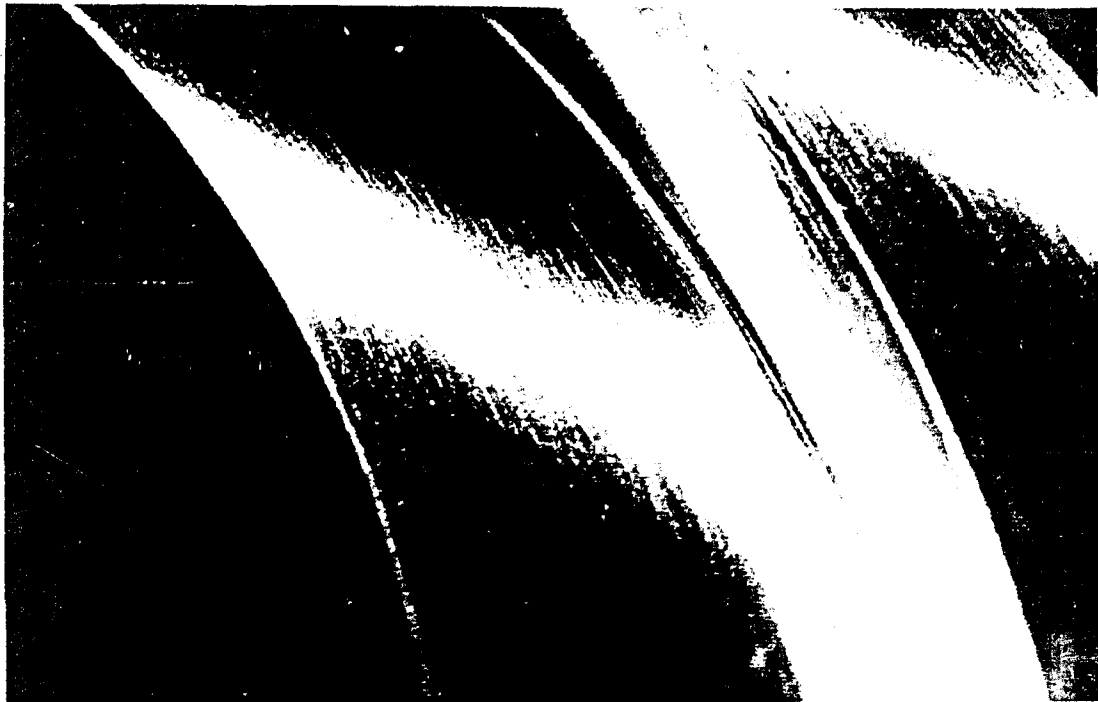
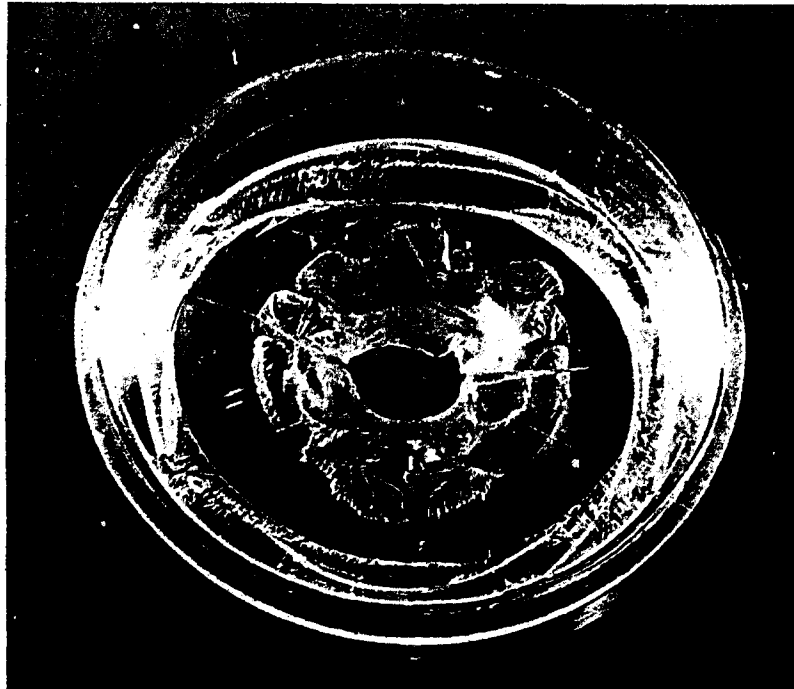


Figure 44. Absence of scratches on bearing surfaces of square window seat in flange for 120° spherical sector window with square edge.



Part A. Convex surface.

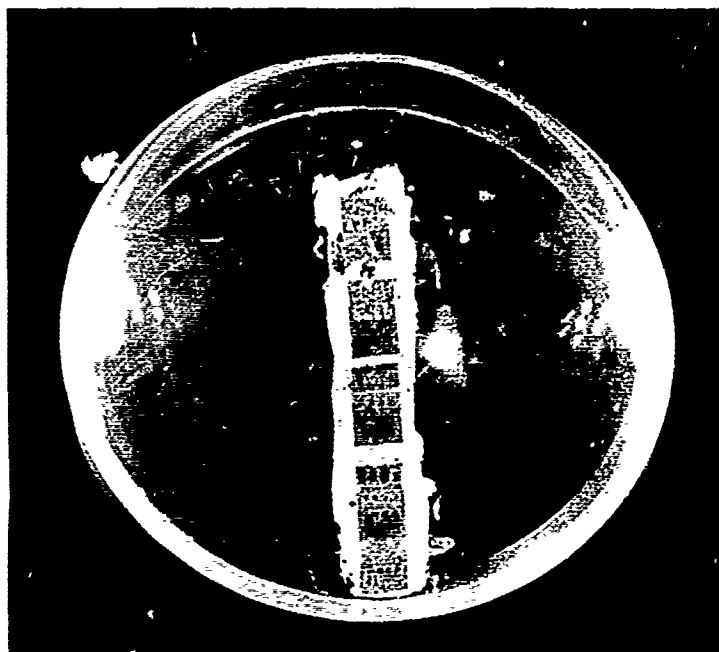


Part B. Concave surface.

Figure 45. 120° spherical sector window with square edge after implosion, which occurred after 800 hours of sustained hydrostatic loading at 2500 psi.



Part A. Concave surface.



Part B. Convex surface.

Figure 46. 120° spherical sector window with conical edge after 800 hours of sustained hydrostatic loading at 2500 psi. This window was tested with the one shown in figure 45. Note the total absence of cracks.

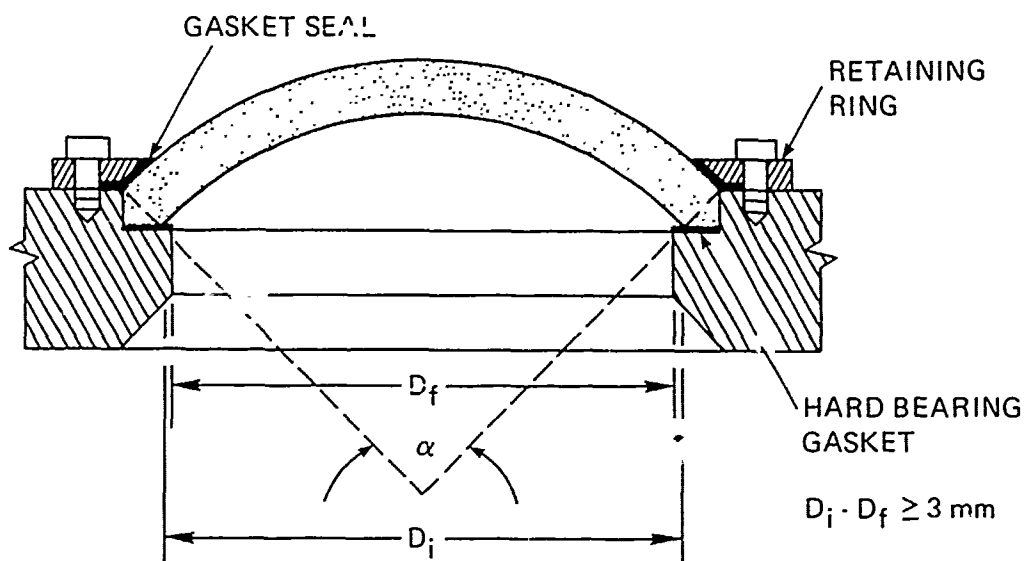
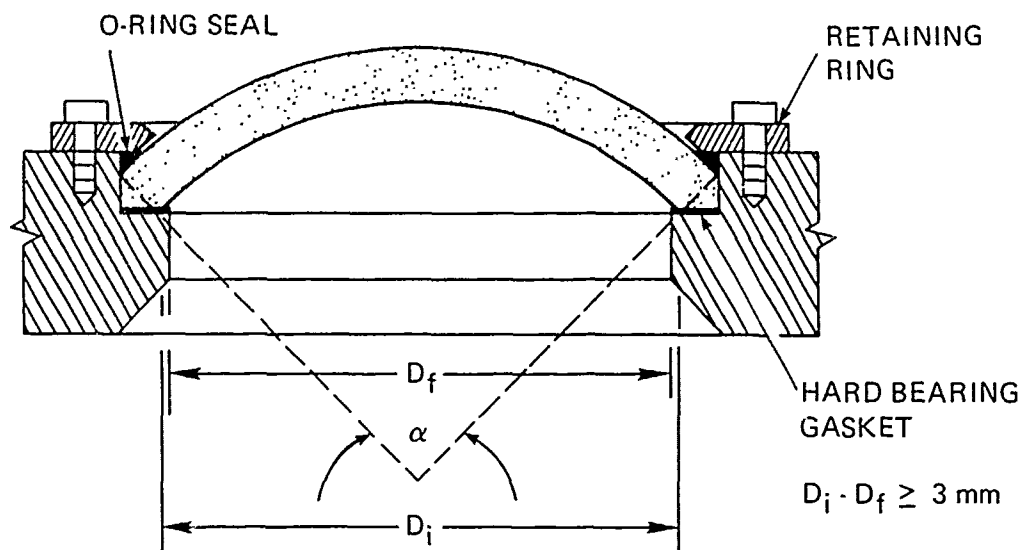


Figure 47. Recommended sealing arrangements for spherical sector windows with square edges.

## APPENDIX A. EXPERIMENTAL DATA

Experimental data generated by electric resistance strain gages during the testing of spherical sector test specimens are in figures 27 through 42. However, since these data are very basic for understanding the structural response of spherical windows to hydrostatic loading, they are presented here in numerical form (tables A1, A2, and A3). The EP1 column shows hoop strains. EP2 column, meridional strains, SIGMA MAX column, hoop stresses; SIGMA MIN column, meridional stresses; and TAU MAX column, maximum shear stress.

Data from long- and short-term implosion tests on 30°, 60°, 90°, 120°, 150°, and 180° spherical sectors with square edges are in table A1. The data from a 24-hour test at 1200 psi followed by a 24-hour relaxation period at 0 psi are at the top; the strains recorded during sustained loading at 1200 psi and a relaxation period at 0 psi were taken at 6-hour intervals. The short-term data recorded during pressurization to implosion are on the bottom portion. The strains were recorded at approximately 1-minute intervals. Since the windows were previously subjected to long-term pressurization, some of the strain gages did not return to their original zero prior to initiation of the short-term implosion tests.

Data from the 24-hour test at 1200 psi on the twin window assembly (figure 17) are in table A2. During sustained loading and relaxation periods, the data were recorded at 6-hour intervals. While the twin window assembly was being pressurized or depressurized, the readings were taken at 1-minute intervals.

Data from the 4-hour cyclic tests at 1200 psi on the twin window assembly are in table A3. The readings were taken only every third pressure cycle; these numbers are shown in the load column as 1201, 1203, 1206 etc. (the first two digits of the number should be disregarded). During a typical pressure cycle the readings were taken (1) immediately after pressurization, (2) after 4 hours of sustained loading at 1200 psi, (3) immediately after depressurization, and (4) after 4 hours of relaxation at 0 psi.

Table A1. Data from Long- and Short-Term Implosion Tests on 30°, 60°, 90°, 120°, 150°, and 180° Spherical Sectors with Square Edges.

STRAIR REDUCTION OF A 1-0 GAGE ROSETTE							GAGE NO. 23-OUTSIDE (30-1-0)	
E =	LOAD	EP1	EP2	POISSON'S RATIO = .40	SIGMA MAX	SIGMA MIN	TAU MAX	
	0	0	0	0	0	0	0	0
	200	200	-240	-65	50	-76	63	63
	400	40	-440	-145	-65	-202	69	69
	600	-160	-360	-173	-145	-202	29	29
	800	-380	40	-131	-173	-53	-60	-60
	1000	-600	810	-78	-131	271	-201	-201
	1200	-660	1240	-876	-78	465	-271	-271
	1200	-2000	400	-810	-876	-190	-349	-349
	1200	-1860	400	-810	-810	-164	-323	-323
	1200	-1860	390	-788	-810	-164	-323	-323
	1000	-1600	350	-693	-788	-159	-314	-314
	800	-1400	250	-614	-693	-133	-280	-280
	600	-1200	210	-531	-614	-148	-236	-236
	400	-920	-80	-453	-531	-129	-201	-201
	200	-590	-580	-391	-453	-213	-120	-120
	0	-200	0	-95	-391	-384	-1	-1
	0	-80	-100	-57	-95	-38	-29	-29
	0	-60	-100	-48	-57	-67	3	3
	0	-20	-30	-15	-48	-59	6	6
	0	-60	-10	-30	-15	-18	1	1
	500	-580	240	-230	-30	-16	-7	-7
	1000	-1180	470	-472	-230	4	-117	-117
	1500	-1800	770	-710	-472	-1	-236	-236
	2000	-2510	1060	-993	-710	24	-367	-367
	2500	-3220	1340	-1278	-993	27	-510	-510
	3000	-4030	820	-1763	-1278	25	-651	-651
	3500	-4860	210	-2274	-1763	-377	-693	-693
	4000	-5760	-820	-2899	-2274	-826	-724	-724
	4500	-6600	-1950	-3514	-2899	-1488	-706	-706
	5000	-7600	-3900	-4362	-3514	-2186	-664	-664
	5500	-9400	-7820	-5966	-4362	-3305	-529	-529
	6000	-11500	-11800	-7724	-5966	-5514	-226	-226
							43	43

Table A1. Continued.

STRAINS REDUCTION OF A T-0 GAGE ROSETTE

L = 0.40	LOAD	CPI	POISSON'S RATIO = 0.40		SIGMA MAX	SIGMA MIN	GAGE NO. = 22-INSIDE (30-1)	
			CP2	CP1			TAU MAX	TAU MIN
0	0	0	0	0	0	0	0	0
200	200	-200	-810	-250	-424	-424	87	87
400	400	-400	-1210	-250	-580	-580	170	170
600	600	-600	-1580	-250	-676	-676	283	283
800	800	-800	-1900	-250	-755	-755	383	383
1000	1000	-1000	-2200	-250	-825	-825	481	481
1200	1200	-1200	-2500	-250	-954	-954	564	564
1400	1400	-1400	-2810	-250	-810	-810	443	443
1600	1600	-1600	-3200	-250	-899	-899	466	466
1800	1800	-1800	-3380	-250	-962	-962	469	469
2000	2000	-2000	-3580	-250	-886	-886	446	446
2200	2200	-2200	-3700	-250	-636	-636	353	353
2400	2400	-2400	-3800	-250	-390	-390	273	273
2600	2600	-2600	-3900	-250	-255	-255	201	201
2800	2800	-2800	-4000	-250	-202	-202	149	149
3000	3000	-3000	-4100	-250	-111	-111	111	111
3200	3200	-3200	-4200	-250	93	93	60	60
3400	3400	-3400	-4300	-250	212	212	24	24
3600	3600	-3600	-4400	-250	346	346	-16	-16
3800	3800	-3800	-4500	-250	373	373	-10	-10
4000	4000	-4000	-4600	-250	383	383	-13	-13
4200	4200	-4200	-4700	-250	70	70	53	53
4400	4400	-4400	-4800	-250	-146	-146	196	196
4600	4600	-4600	-4900	-250	-349	-349	329	329
4800	4800	-4800	-5000	-250	-567	-567	470	470
5000	5000	-5000	-5100	-250	-789	-789	619	619
5200	5200	-5200	-5200	-250	-1059	-1059	776	776
5400	5400	-5400	-5300	-250	-1318	-1318	931	931
5600	5600	-5600	-5400	-250	-1720	-1720	1130	1130
5800	5800	-5800	-5500	-250	-2125	-2125	1379	1379
6000	6000	-6000	-5600	-250	-3439	-3439	1927	1927



Table A1. Continued.

L = .40	STRAIN REDUCTION OF A TWO GAGE ROSETTE				GAGE NO. = 21-INSIDE (30-2)	
	LOAD	CPI	POISSONS RATIO = .40	SIGMA MAX	SIGMA MIN	TAU MAX
			EP2			
0	0	0	0	0	0	0
200	-80	600	600	26	270	-97
400	240	450	450	295	498	-101
600	820	1220	1220	623	737	-57
800	1400	1640	1640	979	1048	-34
1000	2000	2060	2060	1345	1362	-9
1200	2380	2320	2320	1525	1558	1
1400	1540	1420	1420	1004	970	17
1600	1460	1500	1500	901	992	-6
1800	1420	1500	1500	462	985	-11
2000	1400	1440	1440	941	952	-6
2200	1200	1220	1220	804	810	-3
2400	1050	1020	1020	694	686	4
2600	850	820	820	551	552	4
2800	680	680	680	453	453	0
3000	440	370	370	280	260	10
3200	310	-10	-10	146	54	46
3400	250	-10	-10	117	43	37
3600	260	-10	-10	122	45	39
3800	250	0	0	119	48	36
4000	260	10	10	126	54	36
4200	200	460	460	103	257	-37
4400	960	990	990	646	654	-4
4600	1600	1520	1520	1051	1029	11
4800	2200	2100	2100	1448	1419	14
5000	2750	2700	2700	1824	1810	7
5200	3350	3250	3250	2214	2186	14
5400	3950	3850	3850	2614	2586	14
5600	4600	4700	4700	3006	3114	-14
5800	5200	5700	5700	3562	3705	-71
6000	5950	6800	6800	4139	4371	-121
6200	6850	8100	8100	4805	5162	-179

Table A1. Continued.

STRAIN REDUCTION OF A TAU GAGE ROSETTE					AGE 10, %		60-1-0	
E, %	LOAD	EPI	POISSON'S RATIO, %		SIGMA MAX	SIGMA MIN	TAU MAX	
			EP2	EP1				
0	0	0	0	0	0	0	0	
200	200	-170	-1130	-296	-570	137	137	
400	400	-250	-760	-264	-410	73	73	
600	600	-480	-340	-293	-253	-20	-20	
800	800	-600	230	-242	-5	-19	-19	
1000	1000	-830	660	-270	156	-213	-213	
1200	1200	-1130	1050	-338	285	-311	-311	
1200	1200	-1340	1350	-381	388	-384	-384	
1200	1200	-1370	1400	-386	406	-396	-396	
1200	1200	-1400	1500	-391	448	-414	-414	
1200	1200	-1280	1530	-355	466	-416	-416	
1000	1000	-1150	1060	-408	261	-334	-334	
800	800	-920	500	-452	19	-234	-234	
600	600	-750	0	-433	-175	-131	-131	
400	400	-500	-400	-392	-333	-56	-56	
200	200	-330	-810	-342	-481	44	44	
0	0	-100	-610	-273	-353	80	80	
0	0	-240	-480	-173	-333	63	63	
0	0	-170	-460	-244	-370	41	41	
0	0	-100	-303	-105	-251	29	29	
500	500	-450	-120	-237	-162	-47	-47	
1000	1000	-1120	350	-462	-143	-210	-210	
1500	1500	-1750	650	-710	-24	-343	-343	
2000	2000	-2500	1030	-994	14	-504	-504	
2500	2500	-3300	1700	-1248	181	-714	-714	
3000	3000	-4350	2580	-1580	400	-990	-990	
3500	3500	-5660	4200	-1895	922	-1469	-1469	
4000	4000	-7450	8450	-2176	2510	-2343	-2343	

Table A1.. Continued.

E = %	STRAIN REDUCTIONS OF A TRIAXIAL GAGE			GAGE NO. 2	E-0-1
	LOAD	POISSONS RATIO = EP	SIGMA		
	0	0	0		
	200	600	240		
	400	740	312		
	600	980	392		
	800	1160	444		
	1000	1280	512		
	1200	1460	584		
	1200	1420	569		
	1200	1440	574		
	1200	1450	580		
	1200	1440	576		
	1000	1300	520		
	800	1180	472		
	600	1020	409		
	400	860	344		
	200	680	272		
	0	100	40		
	0	-100	-40		
	0	-80	-32		
	0	0	0		
	0	120	48		
	500	1160	464		
	1000	1530	612		
	1500	1900	760		
	2000	2360	944		
	2500	2860	1144		
	3000	3370	1344		
	3500	4020	1608		
	4000	5420	2168		

Table A1. Continued.

E <sub>x</sub>	LOAD	EP1	EP2	POISSONS RATIO <sub>x</sub> , %D	SIGMA <sub>x</sub> MAX	SIGMA <sub>y</sub> MIN	GAGE NO., z	bD=2
	0	0	0	0	0	0		
	200	300	-150	114	-14	64		
	400	550	-300	205	-38	121		
	600	750	-750	214	-214	214		
	800	970	-1030	266	-304	286		
	1000	1280	-1370	344	-404	374		
	1200	1440	-1720	344	-564	454		
	1200	1630	-2080	380	-680	530		
	1200	1600	-2150	352	-714	536		
	1200	1650	-2200	367	-734	550		
	1200	1680	-2200	381	-728	554		
	1000	1580	-1870	346	-540	493		
	800	1200	-1520	282	-495	389		
	600	1000	-1180	251	-371	311		
	400	740	-780	244	-192	246		
	200	520	-440	164	-110	137		
	0	180	-300	24	-104	64		
	0	-20	0	-10	-4	-3		
	0	-20	-50	-14	-28	4		
	0	100	30	53	33	10		
	0	120	60	64	51	9		
	500	880	-380	347	-13	180		
	1000	1220	-1180	356	-330	343		
	1500	1600	-1940	383	-643	513		
	2000	2200	-2460	484	-940	737		
	2500	2450	-4030	637	-1357	997		
	3000	4100	-5100	481	-1648	1314		
	3500	5880	-6400	1581	-1928	1754		
	4000	7650	-8330	2056	-2510	2283		

Table A1. Continued.

STRAIN REDUCTION OF A TWO GAGE ROSETTE						
$E_s$	$\nu_0$	LOAD	EP1	POISSON'S RATIO $\nu_0$	SIGMA $\mu_0$	GAGE NO. =
				EP2	SIGMA $\mu_1$	TAU $\mu_2$
						MAX
						60-3
		0	0	0	0	0
		200	0	30	14	-4
		400	180	250	153	-19
		600	250	370	224	-17
		800	470	550	351	-11
		1000	660	720	469	-9
		1200	800	820	543	-3
		1200	900	970	633	-10
		1200	940	950	624	-7
		1200	1000	1040	646	-6
		1200	820	830	674	-6
		1000	630	650	551	-1
		800	460	424	430	-3
		600	330	318	335	-9
		400	200	224	230	-3
		200	40	149	171	-11
		0	40	30	22	1
		0	-100	-20	-29	-11
		0	-80	-30	-30	-7
		0	100	100	67	0
		0	200	180	124	3
		500	450	530	315	-11
		1000	620	690	447	-10
		1500	850	900	590	-7
		2000	1230	1500	871	-39
		2500	1950	2020	1313	-10
		3000	3100	3150	2076	-7
		3500	5160	5340	3574	-26
		4000	6220	7550	4780	-190

Table A1. Continued.

STRAIN REDUCTION OF A TWO GAGE ROSETTE		POISSONS RATIO $\nu$				GAGE NO. $\epsilon$		$\epsilon_0 = 1 = 0$	
$\epsilon$	$\nu$	LOAD	EP1	EP2	SIGMA MAX	SIGMA MIN	TAU MAX		
0	0	0	0	0	0	0	0	0	0
200	0	150	-150	-600	-186	-314	64	100	100
400	0	225	-225	-925	-283	-483	100	100	100
600	0	400	-400	-1400	-457	-743	179	179	179
800	0	550	-550	-1800	-605	-962	232	232	232
1000	0	625	-625	-2250	-726	-1190	271	271	271
1200	0	700	-700	-2600	-824	-1371	204	204	204
1200	0	500	-500	-1925	-605	-1012	189	189	189
1200	0	425	-425	-1750	-536	-895	179	179	179
1200	0	450	-450	-1700	-538	-895	179	179	179
1200	0	450	-450	-1700	-538	-895	179	179	179
1000	0	400	-400	-1700	-514	-862	186	186	186
800	0	275	-275	-1700	-455	-785	204	204	204
600	0	175	-175	-1600	-388	-785	204	204	204
400	0	100	-100	-1275	-248	-604	181	181	181
200	0	100	-100	-1025	-148	-464	161	161	161
0	0	175	175	-700	-50	-300	125	125	125
0	0	125	125	-150	31	-48	34	34	34
0	0	100	100	-250	0	-100	50	50	50
0	0	10	10	-225	-38	-105	34	34	34
0	0	10	10	-225	-38	-105	34	34	34
500	0	225	-225	-1300	-355	-662	154	154	154
1000	0	325	-325	-1825	-602	-931	214	214	214
1500	0	750	-750	-2125	-762	-1155	196	196	196
2000	0	450	-450	-1900	-814	-1086	136	136	136
2500	0	1225	-1225	-1375	-845	-888	21	21	21
3000	0	1450	-1450	-100	-748	-414	-164	-164	-164
3500	0	3050	-3050	1000	-1628	-214	-704	-704	-704

Table A1. Continued.

P #	LOAD #	STRAIN REDUCTION OF A TWO GAGE ROSETTE			POISSONS RATIOS .40		SIGMA MIN	SIGMA MAX	GAGE NO.s	
		EP1	EP2	EP3	EP1	EP2			TAU MAX	TAU MIN
0	0	0	0	0	0	0	0	0	0	0
200	200	150	1500	1500	0.214	0.214	0.686	0.686	236	236
400	400	280	3250	3250	0.500	0.500	0.1500	0.1500	500	500
600	600	360	5000	5000	0.781	0.781	0.2312	0.2312	766	766
800	800	720	6550	6550	0.903	0.903	0.2982	0.2982	1039	1039
1000	1000	980	8600	8600	0.1152	0.1152	0.3861	0.3861	1354	1354
1200	1200	1000	10250	10250	0.1476	0.1476	0.4690	0.4690	1607	1607
1200	1200	1100	12550	12550	0.1867	0.1867	0.5767	0.5767	1950	1950
1200	1200	1075	12450	12450	0.1935	0.1935	0.5462	0.5462	2004	2004
1200	1200	1050	13150	13150	0.2005	0.2005	0.6062	0.6062	2029	2029
1200	1200	1010	13350	13350	0.2062	0.2062	0.6165	0.6165	2051	2051
1000	1000	960	11050	11050	0.1648	0.1648	0.5079	0.5079	1716	1716
800	800	870	9000	9000	0.1300	0.1300	0.4120	0.4120	1410	1410
600	600	660	6800	6800	0.886	0.886	0.3074	0.3074	1094	1094
400	400	450	4600	4600	0.471	0.471	0.2029	0.2029	779	779
200	200	320	3450	3450	0.267	0.267	0.1487	0.1487	610	610
0	0	360	2800	2800	0.362	0.362	0.1265	0.1265	451	451
0	0	60	1000	1000	0.214	0.214	0.488	0.488	134	134
0	0	175	0	0	0.83	0.83	0.33	0.33	25	25
0	0	225	0	0	0.107	0.107	0.43	0.43	32	32
0	0	145	0	0	0.60	0.60	0.24	0.24	18	18
500	500	25	2875	2875	0.536	0.536	0.1364	0.1364	414	414
1000	1000	350	8350	8350	0.1424	0.1424	0.3910	0.3910	1243	1243
1500	1500	700	13750	13750	0.2286	0.2286	0.6414	0.6414	2064	2064
2000	2000	1075	18850	18850	0.3094	0.3094	0.8771	0.8771	2846	2846
2800	2800	1450	19850	19850	0.2900	0.2900	0.8700	0.8700	2900	2900
3000	3000	1900	18850	18850	0.266	0.266	0.8614	0.8614	2964	2964
3500	3500	2675	18850	18850	0.2317	0.2317	0.8467	0.8467	3075	3075
4000	4000	3700	18850	18850	0.1829	0.1829	0.8271	0.8271	3221	3221

Table A1. Continued.

P = LOAD	STRAIN REDUCTION OF A TWO GAGE ROSETTE				GAGE NO. =	
	POISSON'S RATIO = .40	EP1	EP2	SIGMA MAX	SIGMA MIN	TAU MAX
0	0	0	0	0	0	0
200	-250	-790	-1525	-270	-424	77
400	-600	-875	-2425	-576	-840	132
600	-875	-1100	-3190	-879	-1321	221
800	-1100	-1300	-3925	-1131	-1729	299
1000	-1300	-1500	-4750	-1367	-2117	375
1200	-1500	-1400	-5275	-1619	-2548	464
1200	-1400	-1300	-5335	-1671	-2779	554
1200	-1300	-1350	-5450	-1681	-2852	574
1200	-1350	-1125	-5500	-1690	-2876	586
1000	-1125	-1075	-4475	-1388	-2345	593
800	-775	-775	-3550	-1188	-1895	479
600	-500	-275	-2675	-879	-1421	354
400	-275	75	-1290	-577	-943	271
200	75	125	-925	-377	-667	183
0	125	25	-75	-212	-455	145
0	25	0	0	74	-107	121
0	0	0	0	12	5	57
0	0	0	0	0	0	7
500	-890	-2000	-4090	-1805	-1122	4
1000	-1400	-4090	-6400	-1446	-2214	0
1500	-1750	-4100	-6400	-2052	-3381	159
2000	-2050	-2180	-12600	-2710	-4724	384
2500	-2180	-1900	-16800	-3424	-6410	664
3000	-1900	-100	-18600	-4105	-8362	1007
3500	-100			-3590	-8876	1493
						2129
						2643



Table A1. Continued.

STRAIN REDUCTION OF A TWO GAGE ROSETTE					GAGE NO.s		
P	LOAD	POISSONS RATIOs		EP2	SIGMA MAX	SIGMA MIN	TAU MAX
		EP1	EP2				
0	0	0	0	0	0	0	0
200	200	-680	-800	-800	-476	-510	17
400	400	-1130	-1450	-1450	-814	-906	46
600	600	-1725	-2180	-2180	-1237	-1367	65
800	800	-2225	-2850	-2850	-1602	-1781	84
1000	1000	-2775	-3375	-3375	-1944	-2136	96
1200	1200	-3285	-4180	-4180	-2362	-2621	129
1200	1200	-3340	-4340	-4340	-2450	-2736	143
1200	1200	-3480	-4500	-4500	-2552	-2741	144
1200	1200	-3500	-4500	-4500	-2500	-2800	150
1000	1000	-3075	-3850	-3850	-2148	-2814	146
800	800	-2650	-3200	-3200	-1871	-2414	111
600	600	-2175	-2500	-2500	-1512	-2024	79
400	400	-1575	-1875	-1875	-1064	-1605	46
200	200	-1130	-1425	-1425	-752	-1098	14
0	0	-815	-850	-850	-550	-751	7
0	0	-200	-175	-175	-124	-560	5
0	0	80	75	75	52	-121	4
0	0	50	0	0	24	51	1
0	0	10	0	0	5	10	7
500	500	-1620	-1875	-1875	-1124	-1201	36
1000	1000	-2800	-3500	-3500	-2000	-2200	100
1500	1500	-4020	-5000	-5000	-2905	-3242	164
2000	2000	-5100	-7000	-7000	-3762	-4305	271
2500	2500	-6300	-9075	-9075	-4724	-5521	396
3000	3000	-7080	-11300	-11300	-5524	-6730	603
3500	3500	-8100	-23000	-23000	-7286	-12114	2414

Table A1. Continued.

LOAD	EP1	POISSONS RATIO= .40	SIGMA MAX	SIGMA MIN	GAGE NO.=	TAU MAX	90=4
0	0	0	0	0	0	0	0
200	-800	-775	-524	-521	-4	-4	
400	-1425	-1425	-950	-950	0	0	
600	-2100	-2150	-1410	-1424	7	7	
800	-2700	-2775	-1810	-1836	11	11	
1000	-3400	-3450	-2276	-2290	7	7	
1200	-4075	-4125	-2724	-2740	7	7	
1400	-4725	-4750	-3174	-3190	18	18	
1600	-5350	-5375	-3633	-3653	0	0	
1800	-5950	-5975	-4083	-4097	0	0	
2000	-6525	-6550	-4524	-4540	7	7	
2200	-7075	-7100	-4957	-4973	14	14	
2400	-7600	-7625	-5381	-5402	20	20	
2600	-8100	-8125	-5795	-5808	20	20	
2800	-8575	-8600	-6207	-6243	32	32	
3000	-9025	-9050	-6616	-6649	36	36	
3200	-9450	-9475	-7021	-7043	25	25	
3400	-9850	-9875	-7425	-7448	25	25	
3600	-10225	-10250	-7827	-7850	29	29	
3800	-10575	-10600	-8224	-8246	32	32	
4000	-10900	-10925	-8616	-8638	37	37	
4200	-11200	-11225	-9003	-9024	18	18	
4400	-11475	-11500	-9385	-9405	32	32	
4600	-11725	-11750	-9761	-9781	40	40	
4800	-11950	-11975	-10131	-10151	41	41	
5000	-12150	-12175	-10495	-10515	41	41	
5200	-12325	-12350	-10853	-10873	41	41	
5400	-12475	-12500	-11205	-11225	41	41	
5600	-12600	-12625	-11551	-11571	41	41	
5800	-12700	-12725	-11891	-11911	41	41	
6000	-12775	-12800	-12224	-12244	41	41	
6200	-12825	-12850	-12551	-12571	41	41	
6400	-12850	-12875	-12873	-12893	41	41	
6600	-12850	-12875	-13195	-13215	41	41	
6800	-12825	-12850	-13516	-13536	41	41	
7000	-12775	-12800	-13831	-13851	41	41	
7200	-12700	-12725	-14145	-14165	41	41	
7400	-12600	-12625	-14458	-14478	41	41	
7600	-12475	-12500	-14770	-14790	41	41	
7800	-12325	-12350	-15081	-15101	41	41	
8000	-12150	-12175	-15391	-15411	41	41	
8200	-11950	-11975	-15695	-15715	41	41	
8400	-11725	-11750	-16003	-16023	41	41	
8600	-11475	-11500	-16316	-16336	41	41	
8800	-11200	-11225	-16631	-16651	41	41	
9000	-10900	-10925	-16951	-16971	41	41	
9200	-10575	-10600	-17273	-17293	41	41	
9400	-10225	-10250	-17595	-17615	41	41	
9600	-9850	-9875	-17916	-17936	41	41	
9800	-9450	-9475	-18231	-18251	41	41	
3500	-10100	-10125	-18551	-18571	41	41	

Table A1. Continued.

STRAIN REDUCTION OF A TAO GAGE ROSETTE					GAGE NO. = 120-1-0	
PZ	LOAD	EP1	POISSONS RATIO = $\nu$	SIGMA MAX	SIGMA $\nu$ IN	TAU MAX
			EP2			
0	0	0	0	0	0	0
200	200	0	-800	-152	-381	114
400	400	0	-850	-162	-405	121
600	600	0	-900	-171	-429	129
800	800	20	-925	-167	-437	135
1000	1000	20	-950	-171	-449	139
1200	1200	30	-975	-171	-459	144
1200	1200	30	-900	-157	-423	131
1200	1200	30	-800	-138	-375	119
1200	1200	30	-750	-129	-351	111
1200	1200	30	-725	-124	-340	108
1000	1000	30	-700	-119	-328	104
800	800	30	-725	-124	-340	108
600	600	20	-675	-114	-318	99
400	400	0	-600	-114	-286	84
200	200	-10	-475	-95	-228	66
0	0	200	400	171	229	-29
0	0	200	250	143	157	-27
0	0	200	250	143	157	-27
0	0	200	150	124	110	7
0	0	300	175	176	140	18
500	500	200	-325	33	-117	75
1000	1000	300	-325	81	-98	89
1500	1500	500	-450	152	-119	136
2000	2000	600	-400	210	-76	143
2500	2500	650	-275	257	-27	132
3000	3000	400	225	471	279	96
3500	3500	1200	1500	857	493	-43
4000	4000	1750	4900	1767	2667	-450

Table A1. Continued.

STRAIN REDUCTION OF A TWO GAGE ROSETTE					GAGE NO. = 120-1	
$\epsilon_x$	$\epsilon_y$	LOAD	EP1	POISSONS RATIO = $\nu$	SIGMA MIN	TAU MAX
			EP2	SIGMA MAX		
0	0	0	0	0	0	0
200	225	200	-1900	-255	-862	304
400	400	400	-4675	-700	-2150	725
600	500	600	-7650	-1214	-3548	1164
800	575	800	-10150	-1660	-4724	1532
1000	600	1000	-13050	-2200	-6100	1950
1200	625	1200	-15875	-2726	-7440	2357
1200	100	1200	-14325	-2776	-6940	2032
1200	200	1200	-15200	-2990	-7276	2143
1200	200	1200	-15600	-3067	-7467	2200
1200	275	1200	-15875	-3155	-7612	2224
1000	200	1000	-13325	-2633	-6383	1875
800	140	800	-10800	-2148	-5174	1516
600	250	600	-8025	-1648	-3864	1111
400	300	400	-5675	-1224	-2760	768
200	325	200	-3150	-755	-1562	404
0	275	0	-1300	-374	-671	146
0	700	0	3050	248	1314	-536
0	725	0	3050	236	1314	-534
0	700	0	3050	248	1314	-536
0	650	0	3050	271	1324	-524
500	500	500	500	214	114	-164
1000	400	1000	6875	-1600	-3350	925
1500	150	1500	16775	-3286	-8024	2364
2000	75	2000	26675	-5045	-12608	3821
2500	250	2500	31475	-5876	-14440	4522
3000	475	3000	31475	-5764	-14008	4544
3500	700	3500	31475	-5662	-14855	4596
4000	1310	4000	31475	-5371	-14734	4684

STRAIN REDUCTION OF A TWO GAGE ROSETTE

98

Table A1. Continued.

STRAIN REDUCTION OF A TWO GAGE ROSETTE

F <sub>2</sub>	LOAD	EPI	EPI	POISSON'S RATIO	EPI	SIGMA MAX	SIGMA MIN	GAGE NO. 2 TAU MAX	120-3
0	0	0	0	0	0	0	0	0	0
200	200	-930	-930	-900	-900	-614	-606	-4	-4
400	400	-1500	-1500	-1800	-1800	-1057	-1143	43	43
600	600	-2140	-2140	-2600	-2600	-1538	-1655	59	59
800	800	-2840	-2840	-3400	-3400	-2024	-2170	73	73
1000	1000	-3700	-3700	-4420	-4420	-2604	-2810	103	103
1200	1200	-4440	-4440	-5200	-5200	-3129	-3331	101	101
1200	1200	-5240	-5240	-5490	-5490	-3565	-3622	29	29
1200	1200	-5400	-5400	-5500	-5500	-3619	-3648	14	14
1200	1200	-5450	-5450	-5550	-5550	-3652	-3681	14	14
1200	1200	-5525	-5525	-5575	-5575	-3693	-3707	7	7
1000	1000	-4900	-4900	-4750	-4750	-3238	-3195	-21	-21
800	800	-4240	-4240	-3900	-3900	-2786	-2674	-36	-36
600	600	-3600	-3600	-3100	-3100	-2305	-2152	-71	-71
400	400	-2880	-2880	-2290	-2290	-1808	-1639	-84	-84
200	200	-2100	-2100	-1400	-1400	-1267	-1067	-100	-100
0	0	-990	-990	-490	-490	-563	-422	-71	-71
0	0	-310	-310	0	0	-148	-59	-44	-44
0	0	-240	-240	0	0	-138	-55	-41	-41
0	0	-240	-240	50	50	-124	-31	-44	-44
0	0	-240	-240	100	100	-114	-8	-56	-56
500	500	-2180	-2180	-2200	-2200	-1457	-1463	3	3
1000	1000	-3740	-3740	-4000	-4000	-2567	-2627	30	30
1500	1500	-5500	-5500	-6150	-6150	-3790	-3976	43	43
2000	2000	-7500	-7500	-8300	-8300	-5152	-5381	114	114
2500	2500	-9900	-9900	-10500	-10500	-6714	-6884	84	84
3000	3000	-12900	-12900	-12800	-12800	-8581	-8552	-14	-14
3500	3500	-16400	-16400	-14990	-14990	-10646	-10214	-216	-216
4000	4000	-22675	-22675	-16100	-16100	-13864	-11984	-439	-439

Table A1. Continued.

P LOAD	STRAIN REDUCTION OF A TWO GAGE ROSETTE			GAGE NO. 2	SIGMA MIN	TAU MAX	120 100-4
	POISSON'S RATIO, $\nu$	POISSON'S RATIO, $\nu$					
	EP1	EP2	SIGMA MAX				
0	0	0	0	0	0	0	0
200	-1000	-1200	-705	-762	29	29	29
400	-2000	-2300	-1390	-1476	43	43	43
600	-3000	-3300	-2010	-2124	57	57	57
800	-4000	-4300	-2724	-2810	71	71	71
1000	-5050	-5350	-3424	-3510	85	85	85
1200	-6200	-6400	-4171	-4224	99	99	99
1400	-7300	-7500	-4910	-4924	113	113	113
1600	-8400	-8600	-5671	-5624	127	127	127
1800	-9500	-9700	-6467	-6424	141	141	141
2000	-10700	-10900	-7200	-7143	155	155	155
2200	-11900	-12100	-7907	-7824	169	169	169
2400	-13100	-13300	-8600	-8524	183	183	183
2600	-14300	-14500	-9281	-9190	197	197	197
2800	-15500	-15700	-9950	-9840	211	211	211
3000	-16700	-16900	-10600	-10480	225	225	225
3200	-17900	-18100	-11240	-11110	239	239	239
3400	-19100	-19300	-11871	-11730	253	253	253
3600	-20300	-20500	-12500	-12340	267	267	267
3800	-21500	-21700	-13110	-12940	281	281	281
4000	-22700	-22900	-13710	-13530	295	295	295
4200	-23900	-24100	-14300	-14110	309	309	309
4400	-25100	-25300	-14881	-14680	323	323	323
4600	-26300	-26500	-15460	-15250	337	337	337
4800	-27500	-27700	-16030	-15810	351	351	351
5000	-28700	-28900	-16600	-16380	365	365	365
500	-1000	-1200	-705	-762	29	29	29
1000	-2000	-2300	-1390	-1476	43	43	43
1500	-3000	-3300	-2010	-2124	57	57	57
2000	-4000	-4300	-2724	-2810	71	71	71
2500	-5050	-5350	-3424	-3510	85	85	85
3000	-6200	-6400	-4171	-4224	99	99	99
3500	-7300	-7500	-4910	-4924	113	113	113
4000	-8400	-8600	-5671	-5624	127	127	127
4500	-9500	-9700	-6467	-6424	141	141	141
5000	-10700	-10900	-7200	-7143	155	155	155
5500	-11900	-12100	-7907	-7824	169	169	169
6000	-13100	-13300	-8600	-8524	183	183	183
6500	-14300	-14500	-9281	-9190	197	197	197
7000	-15500	-15700	-9950	-9840	211	211	211
7500	-16700	-16900	-10600	-10480	225	225	225
8000	-17900	-18100	-11240	-11110	239	239	239
8500	-19100	-19300	-11871	-11730	253	253	253
9000	-20300	-20500	-12500	-12340	267	267	267
9500	-21500	-21700	-13110	-12940	281	281	281
10000	-22700	-22900	-13710	-13530	295	295	295

Table A1. Continued.

LOAD	EPI	STRAIN REDUCTION OF A TWO GAGE ROSETTE		GAGE NO. 3	120 -550-5
		POISSONS RATIO, $\nu$	SIGMA MAX	SIGMA MIN	TAU MAX
$\epsilon =$		$\epsilon P2$			
0	0	0	0	0	0
200	-1120	-1240	-779	-828	24
400	-2120	-2590	-1503	-1637	67
600	-3300	-3700	-2276	-2390	57
800	-4300	-4700	-2943	-3057	57
1000	-5500	-6000	-3762	-3905	71
1200	-6740	-7250	-4614	-4746	66
1200	-7800	-8000	-5238	-5295	29
1200	-8000	-8300	-5390	-5476	43
1200	-8100	-8320	-5442	-5505	31
1200	-8200	-8450	-5514	-5586	36
1000	-7300	-7250	-4857	-4843	7
800	-6300	-6100	-4162	-4105	-29
500	-5200	-5000	-3429	-3371	29
400	-4190	-3800	-2714	-2608	-56
200	-3800	-2600	-2305	-1962	-171
0	-1550	-1100	-948	-819	-64
0	-700	-300	-340	-276	-57
0	-500	-300	-367	-267	-50
0	-650	-300	-367	-267	-50
0	-650	-300	-367	-267	7
500	-3150	-3200	-2110	-2124	14
1000	-5700	-5800	-3819	-3848	56
1500	-8500	-8890	-5791	-5852	56
2000	-11700	-12100	-7876	-7990	57
2500	-15500	-16025	-10433	-10583	75
3000	-25700	-20900	-16219	-14848	-686
3500	-31800	-27050	-20295	-18938	-679
4000	-32600	-27125	-20690	-19126	-782



Table A1. Continued.

STRAIN REDUCTION OF A TWO GAGE ROSETTE					GAGE NO. 150-100	
E = LOAD	EPI	POISSONS RATIO = .40		SIGMA MAX	SIGMA MIN	TAU MAX
		EP2	EP1			
0	0	0	0	0	0	0
200	0	-850	0	-162	-405	121
400	0	-1000	0	-140	-476	143
600	75	-1100	75	-174	-510	168
800	100	-1250	100	-190	-576	193
1000	150	-1300	150	-176	-590	207
1200	200	-1425	200	-186	-664	239
1200	150	-1425	150	-200	-650	225
1200	125	-1425	125	-212	-655	221
1200	150	-1425	150	-210	-674	232
1200	125	-1475	125	-221	-674	229
1000	75	-1325	75	-226	-640	207
800	25	-1250	25	-226	-590	182
600	0	-1200	0	-229	-571	171
400	0	-1050	0	-200	-500	150
200	-25	-900	-25	-183	-433	125
0	0	100	0	14	48	-14
0	100	125	100	71	79	-4
0	125	150	125	88	95	-4
0	25	50	25	21	29	-4
0	0	-25	0	-5	-12	4
500	25	-1075	25	-193	-507	157
1000	125	-1325	125	-202	-631	214
1500	225	-1650	225	-207	-743	268
2000	350	-1825	350	-181	-802	311
2500	500	-1875	500	-119	-798	339
3000	700	-1475	700	52	-569	311
3500	1025	650	1025	612	505	54
4000	1650	4200	1650	1586	2314	-344
4500	2625	4200	2625	2050	2500	-225

Table A1. Continued.

E	LOAD	STRAIN REDUCTION OF A TWO GAGE ROSETTE				GAGE NO.=	150=1
		POISSONS RATIO= .40	SIGMA MAX	SIGMA MIN	TAU MAX		
E	LOAD	EP1	EP2	SIGMA MAX	SIGMA MIN	TAU MAX	
0	0	0	0	0	0	0	0
200	200	-475	-4125	-1012	-2055	521	521
400	400	-650	-6850	-1414	-3386	886	886
600	600	-875	-9325	-2193	-4607	1207	1207
800	800	-1000	-12000	-2762	-5905	1571	1571
1000	1000	-1200	-14800	-3340	-7276	1943	1943
1200	1200	-1300	-17500	-3952	-8581	2314	2314
1200	1200	-1350	-20550	-4557	-10043	2743	2743
1200	1200	-1400	-21325	-4729	-10421	2846	2846
1200	1200	-1400	-21900	-4838	-10695	2929	2929
1200	1200	-1400	-22000	-4857	-10743	2943	2943
1000	1000	-1350	-19650	-4386	-9614	2614	2614
800	800	-1350	-17250	-3929	-8471	2271	2271
600	600	-1140	-14750	-3352	-7241	1944	1944
400	400	-950	-11850	-2710	-5824	1557	1557
200	200	-1050	-8500	-2119	-4248	1064	1064
0	0	450	-7000	-1548	-3419	936	936
0	0	150	-3350	-710	-1624	457	457
0	0	250	-3450	-776	-1690	457	457
0	0	225	-3350	-745	-1638	446	446
0	0	245	-3300	-760	-1624	432	432
500	500	900	-4050	-2152	-4481	1164	1164
1000	1000	1300	-15400	-3552	-7581	2014	2014
1500	1500	1700	-22200	-5038	-10895	2929	2929
2000	2000	2200	-30350	-6824	-14871	4021	4021
2500	2500	2650	-32350	-7424	-15910	4243	4243
3000	3000	3250	-32350	-7710	-16024	4157	4157
3500	3500	4200	-32350	-8162	-16205	4021	4021
4000	4000	4425	-32350	-8364	-16286	3961	3961
4500	4500	5525	-32350	-8793	-16457	3832	3832

Table A1. Continued.

STRAIN REDUCTION OF A TWO GAGE ROSETTE						
$\epsilon = \mu\text{in}$	LOAD	EP1	POISSONS RATIO = $\mu\text{in}$	SIGMA MIN	SIGMA MAX	GAGE NO. = 150-2
			EP2		TAU MAX	
0	0	0	0	0	0	0
200	-550	-550	-900	-533	171	171
400	-900	-900	-2100	-1171	293	293
600	-1400	-1400	-3450	-1910	414	414
800	-1800	-1800	-4700	-2581	550	550
1000	-2150	-2150	-6000	-3267	664	664
1200	-2700	-2700	-7350	-4014	714	714
1200	-3150	-3150	-8150	-4481	744	744
1200	-3190	-3190	-8400	-4608	769	769
1200	-3220	-3220	-8600	-4709	773	773
1200	-3190	-3190	-8400	-4703	651	651
1000	-2890	-2890	-7450	-4098	507	507
800	-2450	-2450	-6000	-3324	393	393
600	-2000	-2000	-4750	-2643	257	257
400	-1500	-1500	-3300	-1857	146	146
200	-1100	-1100	-2120	-1219	129	129
0	-300	-300	-1200	-629	36	36
0	100	100	-150	52	36	36
0	100	100	-150	52	36	36
0	50	50	-200	86	32	32
0	25	25	-200	90	271	271
500	-1300	-1300	-3200	-1771	586	586
1000	-2300	-2300	-6400	-3486	571	571
1500	-3500	-3500	-7500	-4238	1229	1229
2000	-4900	-4900	-13500	-7362	1586	1586
2500	-6200	-6200	-17300	-9419	2029	2029
3000	-8200	-8200	-22400	-12229	2100	2100
3500	-18350	-18350	-33050	-19233	3357	3357
4000	-20500	-20500	-44000	-24857	3000	3000
4500	-23000	-23000	-47000	-25333		

Table A1. Continued.

STRAIN REDUCTION OF A 4-0 GAGE ROSETTE				GAGE NO. 2		150-3	
$\epsilon = .40$	LOAD	$\epsilon P1$	POISSONS RATIO = .40	SIGMA MAX	SIGMA MIN	TAU MAX	
0	0	0	0	0	0	0	
200	1000	-1000	-629	-571	-29	-29	
400	1700	-1600	-1114	-1086	-14	-14	
600	2400	-2450	-1705	-1642	-21	-21	
800	3400	-3300	-2248	-2219	-14	-14	
1000	4300	-4200	-2848	-2819	-14	-14	
1200	5200	-5050	-3438	-3395	-21	-21	
1200	6040	-5475	-3914	-3758	-81	-81	
1200	6300	-5650	-4076	-3890	-93	-93	
1200	6400	-5800	-4152	-3981	-86	-86	
1200	6450	-5800	-4176	-3990	-93	-93	
1000	5700	-4950	-3657	-3443	-107	-107	
800	4800	-4100	-3067	-2867	-100	-100	
600	3900	-3300	-2486	-2314	-86	-86	
400	2850	-2300	-1795	-1638	-79	-79	
200	2000	-1550	-1248	-1119	-64	-64	
0	800	-675	-510	-474	-18	-18	
0	0	0	0	0	0	0	
0	25	0	12	5	4	4	
0	50	-50	-43	-57	7	7	
0	50	-50	-43	-57	7	7	
500	-2300	-2275	-1529	-1521	-4	-4	
1000	-4450	-4325	-2943	-2907	-18	-18	
1500	-6650	-6400	-4386	-4314	-36	-36	
2000	-8725	-8550	-6210	-5974	-118	-118	
2500	-12500	-10700	-7990	-7476	-257	-257	
3000	-16800	-13000	-10476	-9390	-543	-543	
3500	-26300	-15850	-15543	-12557	-1493	-1493	
4000	-33450	-18050	-19605	-15062	-2271	-2271	
4500	-35450	-16750	-20071	-14729	-2671	-2671	

Table A1. Continued.

STRAIN REDUCTION OF A TWO GAGE ROSETTE					
E = .40	POISSONS RATIO = .40	GAGE NO. = 150 = 4			
LOAD	EP1	EP2	SIGMA MAX	SIGMA MIN	TAU MAX
0	0	0	0	0	0
200	-1100	-925	700	-650	-25
400	-2100	-1800	1343	-1257	-43
600	-3300	-2900	2124	-2010	-57
800	-4400	-3900	2838	-2695	-71
1000	-5525	-4900	3564	-3386	-84
1200	-6800	-5900	4362	-4105	-129
1200	-7800	-6825	4976	-4640	-158
1200	-8150	-6850	5186	-4814	-184
1200	-8350	-7000	5310	-4924	-193
1200	-8400	-6975	5324	-4921	-204
1000	-7300	-6075	4633	-4283	-175
800	-6150	-5100	3900	-3600	-150
600	-5050	-4125	3190	-2926	-132
400	-3700	-3000	2333	-2133	-100
200	-2600	-2000	1614	-1448	-86
0	-1200	-850	733	-633	-50
0	-200	-50	105	-62	-21
0	-150	0	71	-24	-21
0	-250	-75	133	-83	-25
0	-250	-75	133	-83	-25
500	-3100	-2600	1471	-1424	-71
1000	-5700	-5075	3681	-3502	-84
1500	-8800	-7550	5624	-5271	-174
2000	-12575	-10450	7924	-7371	-304
2500	-16550	-13300	10414	-9486	-464
3000	-22500	-18400	13933	-12333	-800
3500	-25950	-20350	16233	-14633	-800
4000	-38000	-21450	22276	-17690	-2243
4500	-38000	-19300	21771	-16424	-2671

Table A1. Continued.

Z = .40	STRAIN REDUCTION OF A TWO GAGE ROSETTE					GAGE NO. = 150-5
	LOAD	EP1	EP2	POISSONS RATIO = .40	SIGMA MIN	TAU MAX
0	0	0	0	0	0	0
200	-1125	-1100	-1100	-745	-738	-4
400	-2275	-2200	-2200	-1502	-1481	-11
600	-3350	-3400	-3400	-2314	-2286	-14
800	-4475	-4500	-4500	-3083	-3033	-25
1000	-5600	-5700	-5700	-3443	-3357	-43
1200	-6700	-7300	-7000	-4810	-4724	-43
1200	-8400	-8400	-7950	-5514	-5386	-64
1200	-8750	-8750	-8200	-5729	-5571	-79
1200	-8450	-8450	-8450	-5821	-5729	-71
1200	-9000	-9000	-8450	-5895	-5738	-79
1000	-7800	-7800	-7325	-5110	-4974	-58
800	-6550	-6550	-6150	-4250	-4176	-57
600	-5400	-5400	-5000	-3524	-3410	-57
400	-3950	-3950	-3675	-2581	-2502	-39
200	-2750	-2750	-2400	-1767	-1667	-50
0	-1300	-1300	-1100	-829	-771	-29
0	-250	-250	-150	-148	-119	-14
0	-200	-275	-125	-119	-98	-11
0	-300	-225	-225	-174	-160	-7
0	-3300	-3150	-3150	-186	-164	-11
1000	-6300	-6000	-6000	-2171	-2124	-21
1500	-9500	-9075	-9075	-4143	-4057	-43
2000	-13500	-12400	-12400	-6252	-6131	-61
2500	-17750	-16350	-16350	-8886	-8714	-86
3000	-24100	-22550	-22550	-11462	-11405	-129
3500	-30650	-29350	-29350	-15771	-15329	-221
4000	-35550	-35550	-35750	-20186	-19814	-186
				-23738	-23745	29

Table A1. Continued.

R = .40	STRAIN REDUCTION OF A TWO GAGE ROSETTE				GAGE NO. 150-6
	LOAD	EP1	POISSONS RATIO .40 EP2	SIGMA MAX	SIGMA MIN TAU MAX
0	0	0	0	0	0
200	-1150	-1100	-757	-743	-7
400	-2300	-2300	-1533	-1533	0
600	-3550	-3575	-2371	-2379	4
800	-4775	-4775	-3183	-3183	0
1000	-6075	-6100	-4055	-4062	4
1200	-7450	-7450	-4967	-4967	0
1200	-8550	-8500	-5690	-5675	-7
1200	-8875	-8750	-5893	-5857	-18
1200	-9100	-9000	-6048	-6019	-14
1200	-9150	-9050	-6081	-6052	-14
1000	-7900	-7825	-5252	-5231	-11
800	-6600	-6500	-4381	-4352	-14
600	-5450	-5300	-3605	-3562	-21
400	-4000	-3875	-2643	-2607	-18
200	-2750	-2600	-1805	-1762	-21
0	-1350	-1175	-867	-817	-25
0	-750	-75	-181	-102	-39
0	-250	-100	-138	-95	-21
0	-300	-200	-181	-121	-14
0	-300	-200	-181	-121	-14
500	-3400	-3350	-2257	-2143	-7
1000	-6400	-6350	-4257	-4243	-7
1500	-9550	-9475	-6438	-6445	4
2000	-13775	-13900	-9207	-9243	18
2500	-18075	-18200	-12074	-12110	18
3000	-24475	-24800	-16374	-16471	46
3500	-31875	-31400	-21160	-21024	-68
4000	-35875	-38000	-24321	-24929	304

Table A1. Continued.

E <sub>2</sub> , %	LOAD	STRAIN REDUCTION OF A TWO GAGE ROSETTE			GAGE NO., 180-1-0
		EP1	POISSONS RATIO, %	SIGMA	TAU
			EP2	MAX	MAX
0	0	0	0	0	0
200	-500	-1050	-438	-545	74
400	-1100	-1600	-824	-971	71
600	-1775	-2300	-1283	-1433	75
800	-2600	-3000	-1810	-1924	57
1000	-3300	-3700	-2276	-2340	57
1200	-4100	-4450	-2800	-2400	50
1200	-4400	-4850	-3014	-3148	64
1200	-4525	-4925	-3043	-3207	57
1200	-4600	-5100	-3162	-3305	71
1200	-4550	-5125	-3143	-3307	82
1000	-4500	-4650	-3024	-3071	21
800	-3900	-4000	-2614	-2648	14
600	-3100	-3175	-2081	-2132	11
400	-2350	-2400	-1595	-1638	21
200	-1550	-1675	-1057	-1093	18
0	-850	-125	-434	-221	104
0	-475	100	-207	-43	82
0	-400	150	-162	-5	74
0	-300	125	-162	-15	74
0	-350	150	-138	5	71
500	-1725	-2325	-1264	-1436	86
1000	-3450	-4050	-2414	-2584	86
1500	-5100	-5800	-3533	-3733	100
2000	-7075	-7800	-4855	-5062	104
2500	-9400	-10250	-6424	-6671	121
3000	-11500	-12350	-7824	-8071	121
3500	-14500	-15500	-9857	-10143	143
4000	-16500	-17875	-11262	-11655	146
4500	-18300	-19600	-12448	-12814	184
5000	-20350	-20525	-13600	-13650	25



Table A1. Continued.

LOAD %0	STRAIN REDUCTION OF A TWO GAGE ROSETTE				GAGE NO. = 190-1	
	EP1	POISSONS RATIO = %0	SIGMA MAX	SIGMA MIN	TAU MAX	
0	0	0	0	0	0	0
200	-1150	-800	-200	-600	-50	
400	-2100	-2000	-1381	-1352	-14	
600	-3300	-3050	-2152	-2081	-36	
800	-4600	-4175	-2986	-2864	-61	
1000	-5800	-5550	-3814	-3748	-36	
1200	-6550	-6675	-4390	-4426	18	
1400	-6700	-7700	-4657	-4943	143	
1600	-7050	-8025	-4886	-5164	139	
1800	-6750	-8400	-4814	-5286	236	
1000	-6575	-8600	-4734	-5348	289	
800	-5400	-6600	-4067	-4267	100	
600	-4650	-5450	-3267	-3481	114	
400	-3500	-4600	-2343	-2857	157	
200	-1900	-3300	-1539	-1933	200	
0	-800	-2075	-776	-1140	182	
0	425	-1750	-721	-752	311	
0	450	-425	133	-117	125	
0	425	-525	102	-169	136	
0	475	-600	112	-145	154	
0	475	-500	131	-148	139	
500	-2125	-3300	-1640	-1976	168	
1000	-4825	-6100	-3460	-3824	182	
1500	-7700	-8925	-5367	-5717	175	
2000	-10900	-12225	-7514	-7898	189	
2500	-14525	-16425	-10045	-10588	271	
3000	-17875	-20200	-12360	-13024	332	
3500	-23350	-26350	-16138	-16995	429	
4000	-27400	-32150	-19171	-20529	679	

Table A1. Continued.

E <sub>r</sub>	LOAD	STRAIN REDUCTION OF A TWO GAGE ROSETTE			GAGE NO. 2	TAU MAX
		POISSONS RATIO = .40	SIGMA MAX	SIGMA MIN		
		EP1	EP2			
0	0	0	0	0	0	0
200	200	400	800	881	552	14
400	400	2100	1875	1387	1293	32
600	600	3050	2925	2010	1974	18
800	800	4350	4025	2839	2745	46
1000	1000	5425	5175	3564	3448	26
1200	1200	6650	6250	4337	4243	87
1400	1400	7350	6975	4824	4721	84
1600	1600	7700	7125	4924	4821	54
1800	1800	7700	7300	5037	4943	87
2000	2000	7700	7375	5071	4974	46
2200	2200	6950	6300	4510	4324	93
2400	2400	6000	5275	3862	3655	104
2600	2600	4850	4150	3100	2900	100
2800	2800	3625	2925	2283	2083	100
3000	3000	2325	1700	1431	1252	84
3200	3200	1100	900	695	638	29
3400	3400	400	350	257	243	7
3600	3600	200	250	143	137	14
3800	3800	150	250	114	148	11
4000	4000	50	125	48	64	7
500	500	2750	2700	1824	1810	17
1000	1000	5475	5400	3636	3614	11
1500	1500	8200	8075	5443	5407	18
2000	2000	11325	11125	7512	7455	29
2500	2500	15100	14875	10024	9960	32
3000	3000	18600	18000	12286	12114	86
3500	3500	24200	23125	15924	15621	154
4000	4000	29900	27350	19200	18700	250

Table A1. Continued.

STRAIN REDUCTION OF A TWO GAGE ROSETTE					GAGE NO. = 180-3	
E = %	LOAD	EP1	POISSONS RATIO = %	SIGMA MAX	SIGMA MIN	TAU MAX
			EP2			
	0	0	0	0	0	0
200	-975	-900	-936	-614	-614	-11
400	-2050	-1950	-1348	-1319	-1319	-24
600	-3175	-3075	-2048	-2069	-2069	-14
800	-4300	-4125	-2833	-2783	-2783	-25
1000	-5500	-5275	-3624	-3560	-3560	-22
1200	-6650	-6400	-4395	-4338	-4338	-24
1200	-7350	-7000	-4833	-4733	-4733	-30
1200	-7550	-7150	-4957	-4843	-4843	-37
1200	-7775	-7350	-5102	-4981	-4981	-51
1200	-7825	-7400	-5136	-5014	-5014	-62
1000	-6800	-6425	-4462	-4355	-4355	-54
800	-5800	-5475	-3805	-3712	-3712	-46
600	-4700	-4300	-3057	-2943	-2943	-37
400	-3500	-3150	-2267	-2157	-2157	-30
200	-2275	-1900	-1445	-1338	-1338	-24
0	-1100	-900	-645	-538	-538	-24
0	-400	-400	-267	-267	-267	0
0	-300	-275	-195	-188	-188	-4
0	-350	-300	-224	-210	-210	-7
0	-300	-225	-186	-164	-164	-11
500	-3000	-2800	-1462	-1403	-1403	-24
1000	-5700	-5500	-3742	-3703	-3703	-24
1500	-8400	-8150	-5588	-5481	-5481	-36
2000	-11450	-11225	-7590	-7526	-7526	-32
2500	-15150	-14900	-10032	-9981	-9981	-36
3000	-18550	-18100	-12281	-12252	-12252	-64
3500	-23050	-23150	-15386	-15414	-15414	-14
4000	-27900	-27300	-18466	-18314	-18314	-86

Table A1. Continued.

E2	LOAD	STRAIN REDUCTION OF A TWO GAGE ROSETTE										GAGE NO. 180°	TAU MAX
		EP1	EP2	POISSONS RATIO = .40		SIGMA MAX	SIGMA MIN						
0	0	0	0	0	0	0	0	0	0	0	0	0	
200	200	0.0010	0.1075	0.681	0.4000	0.702	0.11	0	0	0	0	0	
400	400	0.0020	0.2150	0.8100	0.4000	0.8100	0.215	0	0	0	0	0	
600	600	0.0030	0.3225	0.9375	0.4000	0.9375	0.3225	0.215	0.215	0.215	0.215	0.215	
800	800	0.0040	0.4300	1.0650	0.4000	1.0650	0.4300	0.3225	0.3225	0.3225	0.3225	0.3225	
1000	1000	0.0050	0.5375	1.1925	0.4000	1.1925	0.5375	0.4300	0.4300	0.4300	0.4300	0.4300	
1200	1200	0.0060	0.6450	1.3200	0.4000	1.3200	0.6450	0.5375	0.5375	0.5375	0.5375	0.5375	
1400	1400	0.0070	0.7525	1.4475	0.4000	1.4475	0.7525	0.6450	0.6450	0.6450	0.6450	0.6450	
1600	1600	0.0080	0.8600	1.5750	0.4000	1.5750	0.8600	0.7525	0.7525	0.7525	0.7525	0.7525	
1800	1800	0.0090	0.9675	1.7025	0.4000	1.7025	0.9675	0.8600	0.8600	0.8600	0.8600	0.8600	
2000	2000	0.0100	1.0750	1.8300	0.4000	1.8300	1.0750	0.9675	0.9675	0.9675	0.9675	0.9675	
2200	2200	0.0110	1.1825	1.9575	0.4000	1.9575	1.1825	1.0750	1.0750	1.0750	1.0750	1.0750	
2400	2400	0.0120	1.2900	2.0850	0.4000	2.0850	1.2900	1.1825	1.1825	1.1825	1.1825	1.1825	
2600	2600	0.0130	1.3975	2.2125	0.4000	2.2125	1.3975	1.2900	1.2900	1.2900	1.2900	1.2900	
2800	2800	0.0140	1.5050	2.3400	0.4000	2.3400	1.5050	1.3975	1.3975	1.3975	1.3975	1.3975	
3000	3000	0.0150	1.6125	2.4675	0.4000	2.4675	1.6125	1.5050	1.5050	1.5050	1.5050	1.5050	
3200	3200	0.0160	1.7200	2.5950	0.4000	2.5950	1.7200	1.6125	1.6125	1.6125	1.6125	1.6125	
3400	3400	0.0170	1.8275	2.7225	0.4000	2.7225	1.8275	1.7200	1.7200	1.7200	1.7200	1.7200	
3600	3600	0.0180	1.9350	2.8500	0.4000	2.8500	1.9350	1.8275	1.8275	1.8275	1.8275	1.8275	
3800	3800	0.0190	2.0425	2.9775	0.4000	2.9775	2.0425	1.9350	1.9350	1.9350	1.9350	1.9350	
4000	4000	0.0200	2.1500	3.1050	0.4000	3.1050	2.1500	2.0425	2.0425	2.0425	2.0425	2.0425	

Table A1. Continued.

STRAIN REDUCTION OF A TWO GAGE ROSETTE					
$\nu$	LOAD	EP1	POISSONS RATIO = $\nu$	SIGMA MAX	GAGE NO. = 180 = 5
			EP2	SIGMA MIN	TAU MAX
0	0	0	0	0	0
200	1050	1050	-1125	-736	11
400	2050	2050	-2150	-1414	14
600	3175	3175	-3325	-2188	21
800	4300	4300	-4500	-2962	29
1000	5475	5475	-5650	-3733	35
1200	6500	6500	-6800	-4476	43
1400	7300	7300	-7350	-4890	7
1600	7900	7900	-7500	-5000	0
1800	7725	7725	-7750	-5162	4
2000	7600	7600	-7800	-5200	0
2200	6600	6600	-6600	-4400	0
2400	5600	5600	-5550	-3710	27
2600	4350	4350	-4150	-2805	29
2800	3350	3350	-3125	-2126	32
3000	2200	2200	-1900	-1324	43
0	-1100	-1100	-775	-574	46
0	-550	-550	-375	-283	25
0	-425	-425	-250	-200	28
0	-425	-425	-200	-176	32
0	-495	-495	-175	-164	36
500	-3000	-3000	-2450	-1976	47
1000	-5700	-5700	-5800	-3848	14
1500	-8350	-8350	-8600	-5614	36
2000	-11325	-11325	-11800	-7776	68
2500	-15000	-15000	-15650	-10310	93
3000	-18300	-18300	-18150	-12124	21
3500	-23600	-23600	-23000	-16400	200
4000	-28000	-28000	-27400	-19476	243

Table A1. Continued.

STRAIN REDUCTION OF A TWO GAGE ROSETTE				GAGE NO.s		TAU MAX
E = .40	LOAD	EP1	POISSONS RATIO = .40	SIGMA MAX	SIGMA MIN	
			EP2			
0	0	0	0	0	0	0
200	1050	1050	-1150	-719	-748	24
400	2000	2000	-2225	-1376	-1440	32
600	3000	3000	-3350	-2133	-2233	50
800	4200	4200	-4650	-3086	-3214	64
1000	5400	5400	-5900	-3695	-3838	71
1200	6525	6525	-7175	-4474	-4660	93
1200	7400	7400	-7600	-4971	-5029	29
1200	7600	7600	-7750	-5045	-5138	21
1200	7850	7850	-7800	-5224	-5210	27
1200	7900	7900	-8050	-5295	-5338	21
1000	8700	8700	-8750	-4476	-4490	7
800	8695	8695	-5600	-3764	-3748	11
600	9600	9600	-4400	-3029	-2971	29
400	2450	2450	-3150	-2243	-2157	43
200	2300	2300	-1900	-1457	-1343	87
0	1200	1200	-725	-910	-574	68
0	525	525	300	307	-243	22
0	425	425	200	240	-176	28
0	400	400	200	224	-171	29
0	372	372	100	198	-119	39
800	3000	3000	-3000	-2000	-2000	0
1000	3700	3700	-4000	-3867	-3943	43
1500	4325	4325	-5950	-5664	-5848	84
2000	11500	11500	-12000	-7762	-7903	71
2500	23300	23300	-18400	-10314	-10486	86
3000	28700	28700	-24500	-12619	-12848	124
3500	29100	29100	-25550	-13843	-14757	207
4000	28525	28525	-30200	-16336	-16824	239

Table A1. Continued.

STRAIN REDUCTION OF A TWO GAGE ROSETTE					
EP	LOAD	EP1	POISSONS RATIO, %	SIGMA MAX	GAGE NO., 100=7
			EP2	SIGMA MIN	TAU MAX
0	0	0	0	0	0
200	200	-1050	-1125	-714	11
400	400	-2000	-2200	-1371	29
600	600	-3125	-3375	-2131	36
800	800	-4250	-4375	-2893	18
1000	1000	-5400	-5800	-3676	57
1200	1200	-6600	-7000	-4476	57
1200	1200	-7300	-7650	-4914	36
1200	1200	-7475	-7750	-5036	39
1200	1200	-7800	-8000	-5238	29
1200	1200	-7850	-8075	-5276	
1000	1000	-6650	-6775	-4493	17
800	800	-5625	-5650	-3755	4
600	600	-4475	-4450	-2971	4
400	400	-3350	-3250	-2214	-14
200	200	-2200	-2000	-1424	-29
0	0	-1100	-850	-686	-29
0	0	-425	-350	-269	-11
0	0	-350	-250	-214	-14
0	0	-350	-200	-205	-21
0	0	-350	-125	-190	-22
500	500	-3000	-3000	-2000	0
1000	1000	-5750	-5925	-3917	25
1500	1500	-8400	-8725	-5662	46
2000	2000	-11600	-11900	-7790	49
2500	2500	-15500	-15950	-10419	64
3000	3000	-19000	-19675	-12795	96
3500	3500	-24700	-25825	-16681	161
4000	4000	-29150	-30525	-19695	196

Table A2. Data from 24-Hour Test at 1200 psi on Twin Window Assembly.

STRAIN REDUCTION OF A TWO GAGE ROSETTE				TWA	
F = 440	LOAD	POISSON'S RATIO = .40		GAGE NO. = 1-INSIDE	TAU MAX
		FPI	EP2	SIGMA MPA	
0	0	0	0	0	0
200	400	-400	-2450	-1243	293
400	850	-850	-4250	-2186	486
600	-1300	-1300	-6300	-3248	714
800	-1500	-1500	-8550	-4357	1007
1000	-2700	-2700	-9850	-5205	1021
1200	-2800	-2800	-12250	-6367	1250
1400	-3050	-3050	-9100	-4914	864
1600	-3100	-3100	-9350	-5043	893
1800	-3100	-3100	-9650	-5186	936
2000	-3150	-3150	-10000	-5342	979
2200	-3050	-3050	-7850	-4314	486
2400	-2950	-2950	-5550	-3205	371
2600	-2700	-2700	-3400	-2162	79
2800	-2500	-2500	-850	-919	-264
3000	-2500	-1450	-1450	-1405	-79
3200	-550	900	900	324	-207
3400	-150	950	950	424	-157
3600	-150	950	950	474	-157
3800	-150	1000	1000	448	-164
4000	-150	1050	1050	471	-171



33

118

Table A2. Continued.

STRAIN REDUCTION OF A TWO GAGE ROSETTE				TWA	
E = % LOAD	E <sub>P1</sub>	E <sub>P2</sub>	POISSONS RATIO = % SIGMA MAX	GAGE NO. = 3-INSIDE	
				SIGMA MIN	TAU MAX
200	0	0	0	0	0
400	-850	-1150	-624	-710	43
600	-1550	-1950	-1110	-1224	57
800	-2450	-2750	-1640	-1774	43
1000	-3150	-3600	-2186	-2314	64
1200	-4300	-4600	-2924	-3010	43
1400	-5000	-5450	-3419	-3548	64
1600	-5800	-6150	-3933	-4033	50
1800	-6850	-6200	-3467	-4067	50
2000	-8000	-6250	-4000	-4100	50
2200	-8900	-6550	-4000	-4100	50
2400	-9550	-4650	-3605	-3662	29
2600	-9900	-3900	-3052	-3081	14
2800	-3100	-3000	-2600	-2600	0
3000	-2250	-2100	-2048	-2019	-14
3200	-750	-800	-1471	-1429	-21
3400	-200	-200	-510	-524	7
3600	-200	-200	-133	-133	0
3800	-200	-200	-133	-133	0
4000	-200	-250	-143	-157	7
4200	-100	-150	-76	-90	7

Table A2. Continued.

STRAIN REDUCTION OF A TWO GAGE ROSETTE				TWA	
LOAD	EPI	POISSONS RATIO= .40	SIGMA MAX	SIGMA MIN	TAU MAX
0	0	0	0	0	0
200	-1100	-1100	-733	-733	0
400	-1950	-2000	-1310	-1324	0
600	-3000	-3000	-2000	-2000	0
800	-3950	-3900	-2624	-2610	-7
1000	-5100	-5000	-3381	-3352	-14
1200	-6100	-5900	-4024	-4029	-29
1200	-7150	-6700	-4681	-4552	-54
1200	-7300	-6800	-4771	-4629	-71
1200	-7400	-6900	-4838	-4695	-71
1200	-7400	-6900	-4838	-4695	-71
1000	-6600	-6050	-4295	-4138	-74
800	-5550	-5100	-3614	-3486	-64
600	-4450	-4150	-3005	-2862	-71
400	-3550	-3150	-2390	-2176	-57
200	-2500	-2100	-1590	-1476	-57
0	-1000	-750	-619	-548	-34
0	-300	-100	-142	-105	-29
0	-300	-100	-142	-105	-29
0	-300	-100	-142	-105	-29
0	-200	-50	-105	-62	-21

Table A2. Continued.

STRAIN REDUCTION OF A TAU GAGE ROSETTE			TWA	
f =	LOAD	POISSON'S RATIO = $\nu$	GAGE NO. = 5-IN-SIDE	TAU MAX
		EPP	SIGMA MIN	
	EPI	n	n	n
0	-1150	-1150	-767	0
200	-2150	-2150	-1433	0
400	-3250	-3250	-2167	0
600	-4350	-4250	-2881	-14
800	-5500	-5350	-3638	-21
1000	-6650	-6450	-4395	-24
1200	-7750	-7450	-5110	-43
1400	-8100	-7550	-5110	-57
1600	-8200	-7650	-5314	-64
1800	-7150	-7750	-5381	-64
2000	-6050	-6750	-4690	-57
2200	-5000	-5450	-3957	-57
2400	-3750	-4650	-3267	-50
2600	-2500	-3500	-2452	-36
2800	-1100	-2350	-1686	-36
3000	-350	-950	-705	-21
3200	-300	-200	-205	-21
3400	-200	-200	-181	-14
3600	-200	-200	-133	0
3800	-200	-100	-114	-14

Table A2. Continued.

E <sub>s</sub>	LOAD	STRAIN REDUCTION OF A TWO GAGE ROSETTE			TWA	
		POISSONS RATIO <sub>s</sub> .40	SIGMA MAX	SIGMA MIN	GAGE NO.= 5=OUTSIDE	TAU MAX
		EP1	EP2			
0	0	0	0	0	0	0
200	0	0	0	0	0	0
400	-200	-200	-250	-143	-157	7
600	-400	-400	-450	-276	-290	7
800	-500	-500	-500	-333	-333	0
1000	-550	-550	-1150	-481	-652	86
1200	-600	-600	-1150	-505	-662	79
1200	-600	-600	-1000	-476	-590	57
1200	-650	-650	-950	-430	-576	43
1200	-600	-600	-950	-467	-567	50
1200	-600	-600	-900	-457	-543	43
1000	-500	-500	-1000	-429	-571	71
800	-400	-400	-1050	-390	-576	93
600	-400	-400	-1100	-400	-600	100
400	-400	-400	-1100	-400	-600	100
200	-300	-300	-950	-324	-510	93
0	-50	-50	100	-5	38	-21
0	-50	0	100	-5	38	-21
0	0	0	50	10	24	-7
0	0	0	50	10	24	-7
0	0	0	150	29	71	-21

Table A2. Continued.

LOAD	EPI	POISSON'S RATIO= .49	SIG.A "AX	SIGMA MIT	TAU MAX	GAGE NO.= 7-OUTSIDE	TWA
0	0						
200	-450	-550	-319	-349	0		
400	-900	-1300	-626	-790	14		
600	-1300	-2050	-1010	-1224	52		
800	-1650	-2800	-1319	-1648	107		
1000	-2350	-3400	-1767	-2067	164		
1200	-2650	-4250	-2171	-2529	150		
1400	-2950	-4850	-2329	-2871	229		
1600	-3000	-4850	-2352	-2881	271		
1800	-3100	-5100	-2444	-2929	264		
2000	-2750	-4300	-2129	-2571	273		
2200	-2550	-3550	-1590	-2176	286		
2400	-2250	-2850	-1674	-1786	221		
2600	-1900	-1900	-1267	-1267	143		
2800	-1500	-1100	-924	-810	86		
3000	-550	-500	-352	-343	6		
3200	-400	-100	-210	-124	-57		
3400	-100	-100	-67	-67	-43		
3600	-100	-100	-67	-67	0		
3800	-100	-100	-67	-67	0		
4000	-100	-100	-67	-67	-14		

Table A2. Continued.

STRAIN REDUCTION OF A TWO GAGE ROSETTE				TWA	
$\epsilon =$	$\mu$	POISSON'S RATIO $\nu$	$\epsilon_{P1}$	SIGMA MAX	GAGE NO. $\epsilon$ 8-OUTSIDE
					TAU MAX
			$\mu$	$\mu$	$\mu$
	200	-750	-750	-548	0
	400	-1450	-1450	-1133	14
	600	-2200	-2200	-1729	50
	800	-2900	-2900	-2338	79
	1000	-3600	-3600	-2951	121
	1200	-4350	-4350	-3495	129
	1400	-5000	-5000	-4024	179
	1600	-5550	-5550	-4090	207
	1800	-6700	-6700	-4181	214
	2000	-8250	-8250	-4271	221
	2200	-9750	-9750	-3614	164
	2400	-10800	-10800	-2981	114
	2600	-11400	-11400	-2348	64
	2800	-12500	-12500	-1648	14
	3000	-1400	-1400	-1019	-64
	3200	-850	-850	-557	7
	3400	-250	-250	-143	-7
	3600	-150	-150	-119	-14
	3800	-150	-150	-119	-14
	4000	-200	-200	-133	0

Table A2. Continued.

E=	LOAD	STRAIN REDUCTION OF A TWO GAGE ROSETTE				GAGE NO. 3	9-OUTSIDE
		EP1	EP2	SIG-MA MAX	SIG-MA MIN		
0	0	0	0	0	0	0	0
200	-800	-850	-850	-543	-557	7	21
400	-1600	-1750	-1750	-1095	-1138	29	43
600	-2400	-2600	-2600	-1438	-1685	50	64
800	-3200	-3500	-3500	-2190	-2276	71	71
1000	-3900	-4250	-4250	-2667	-2767	64	57
1200	-4800	-5300	-5300	-3319	-3448	64	71
1200	-5500	-6000	-6000	-3786	-3914	64	71
1200	-5650	-6150	-6150	-3862	-4005	64	71
1200	-5850	-6250	-6250	-3974	-4090	64	71
1200	-5950	-6400	-6400	-4052	-4181	64	71
1000	-5000	-5500	-5500	-3429	-3571	64	71
800	-5250	-4400	-4400	-3338	-3095	-121	-121
600	-3400	-3400	-3400	-2267	-2267	0	0
400	-2500	-2400	-2400	-1648	-1619	-14	-14
200	-1850	-1300	-1300	-1129	-971	-79	-79
0	-850	-750	-750	-548	-519	-14	-14
0	-250	-200	-200	-157	-143	-7	-7
0	-250	-150	-150	-148	-119	-14	-14
0	-250	-150	-150	-148	-119	-14	-14
0	-200	-50	-50	-105	-62	-21	-21



Table A2. Continued.

E =	LOAD	STRAIN REDUCTION OF A TWO GAGE ROSETTE			TWA	
		POISSON'S RATIO = $\nu$	SIGMA MAX	SIGMA MIN	GAGE NO. = 10-OUTSIDE	TAU MAX
		EP1	EP2			
0	0	0	0	0	0	0
200	-750	-700	-700	-490	-476	-7
400	-1550	-1500	-1500	-1024	-1010	-7
600	-2350	-2350	-2350	-1567	-1567	0
800	-3200	-3150	-3150	-2124	-2110	-7
1000	-3900	-3850	-3850	-2590	-2576	-7
1200	-4800	-4800	-4800	-3200	-3200	0
1200	-5500	-5500	-5500	-3667	-3667	0
1200	-5600	-5600	-5600	-3733	-3733	0
1200	-5750	-5750	-5750	-3833	-3833	0
1200	-5850	-5850	-5850	-3900	-3900	0
1000	-4950	-4900	-4900	-3290	-3276	-7
800	-4150	-4100	-4100	-2757	-2743	-7
600	-3350	-3300	-3300	-2205	-2162	-21
400	-2400	-2300	-2300	-1581	-1552	-14
200	-1550	-1400	-1400	-1005	-962	-21
0	-850	-750	-750	-548	-519	-14
0	-250	-150	-150	-148	-119	-14
0	-250	-150	-150	-148	-119	-14
0	-250	-150	-150	-148	-119	-14
0	-150	-50	-50	-81	-52	-14

Table A2. Continued.

E =	LOAD	STRAIN REDUCTION OF A TAU GAGE HOSTTYPE				GAGE NO. = 11-10104	TWA
		EP1	EP2	SIGMA MAX	SIGMA MIN		
0	0	0	0	0	0	0	0
200	-950	-1000	-643	-1200	-657	7	7
400	-1800	-1800	-1200	-1800	-1200	0	0
600	-2750	-2700	-1824	-2429	-1810	-2	-2
800	-3700	-3500	-2429	-2976	-2371	-29	-29
1000	-4550	-4250	-2976	-3533	-2890	-43	-43
1200	-5400	-5050	-3533	-4340	-3433	-50	-50
1400	-6200	-5800	-4340	-5200	-4076	-157	-157
1600	-7050	-6600	-5200	-6019	-5019	-164	-164
1800	-7900	-7400	-6019	-6862	-5905	-179	-179
2000	-8750	-8200	-6862	-7710	-6700	-200	-200
2200	-9600	-9000	-7710	-8562	-7505	-179	-179
2400	-10450	-9800	-8562	-9419	-8448	-114	-114
2600	-11300	-10600	-9419	-10274	-9244	-136	-136
2800	-12150	-11400	-10274	-11124	-10110	-107	-107
3000	-13000	-12200	-11124	-11974	-10964	-93	-93
3200	-13850	-13000	-11974	-12824	-11811	-64	-64
3400	-14700	-13800	-12824	-13674	-12664	-43	-43
3600	-15550	-14600	-13674	-14524	-13514	-29	-29
3800	-16400	-15400	-14524	-15374	-14364	-14	-14
4000	-17250	-16200	-15374	-16224	-15214	-5	-5

Table A2. Continued.

STRAIN REDUCTION OF A TWO GAGE ROSETTE				TWA	
$\epsilon =$	LOAD	POISSON'S RATIO = .40	SIGMA MAX	SIGMA MIN	GAGE NO. = 12-OUTSIDE
		EP2			TAU MAX
0	0	0	0	0	0
200	-800	-900	-552	-581	14
400	-1750	-1900	-1195	-1238	21
600	-2650	-2750	-1786	-1814	14
800	-3500	-3700	-2371	-2429	29
1000	-4350	-4600	-2948	-3019	36
1200	-5350	-5550	-3605	-3662	29
1200	-5950	-6150	-4005	-4062	29
1200	-6050	-6200	-4062	-4105	21
1200	-6150	-6250	-4119	-4198	14
1200	-6300	-6350	-4210	-4224	7
1000	-5300	-5350	-3543	-3557	7
800	-4500	-4500	-3000	-3000	0
600	-3650	-3650	-2433	-2433	0
400	-2700	-2700	-1800	-1800	0
200	-1850	-1800	-1224	-1210	-7
0	-850	-650	-529	-471	-29
0	-300	-100	-162	-105	-29
0	-300	-150	-171	-129	-21
0	-300	-150	-171	-129	-21
0	-200	-150	-124	-110	-7

Table A3. Data from 4-Hour Cyclic Tests at 1200 psi on Twin Window Assembly.

STRAIN MEASUREMENT OF A TAC GAGE ROSETTE					POISSON'S RATIO		GAGE 'O.S. 5-1/2 SIDE	
FE	LOAD	EP1	EP2	SIGMA MAX	SIGMA MIN	TAU MAX		
1201	n	-6200	-5000	-3405	n	n		
1201	n	-6800	-5450	-4276	-3562	-171		
1201	n	-700	-750	-210	-224	-192		
1203	n	-250	-250	-167	-167	0		
1203	n	-6400	-5050	-4010	-3624	-193		
1203	n	-6850	-5400	-4310	-3824	-194		
1204	n	500	-300	181	-44	114		
1204	n	50	150	52	81	-14		
1204	n	-6350	-5000	-2071	1171	-1621		
1204	n	-6500	-5150	-4076	-3690	-193		
1204	n	-650	-150	-338	-195	-71		
1204	n	-100	-50	-57	-43	0		
1204	n	-6350	-5050	-3984	-3614	-184		
1204	n	-6400	-5450	-4324	-3810	-202		
1204	n	-400	-750	-257	-243	-7		
1204	n	-100	50	-34	5	-21		
1212	n	-6450	-5000	-3947	-3467	-250		
1212	n	-6400	-5400	-4314	-3886	-214		
1212	n	-600	-750	-524	-510	-7		
1215	n	-150	50	-42	-5	-28		
1215	n	-6400	-5050	-4248	-3718	-264		
1215	n	-6450	-5300	-4319	-3840	-234		
1215	n	-700	-500	-420	-371	-29		
1218	n	-150	50	-62	-5	-20		
1218	n	-7000	-5150	-4314	-3784	-264		
1218	n	-6400	-5300	-4245	-3838	-229		
1218	n	-600	-400	-362	-305	-29		
1221	n	-250	50	-110	-24	-43		
1221	n	-6400	-4950	-4229	-3671	-274		
1221	n	-6850	-5250	-4242	-3805	-224		
1224	n	-500	-200	-274	-190	-44		
1224	n	-150	-150	-106	-100	0		
1224	n	-7000	-5350	-4342	-3881	-234		
1224	n	-6450	-5550	-4372	-3967	-200		
1224	n	-550	-550	-367	-367	0		
1227	n	-150	0	-71	-24	-21		
1227	n	-7000	-5200	-4324	-3810	-252		
1227	n	-6450	-5350	-4090	-3776	-157		
1227	n	-400	-300	-248	-219	-14		
1230	n	0	0	0	0	0		
1230	n	-6000	-5700	-3943	-3857	-43		
1230	n	-6750	-6450	-4443	-4357	-43		
1233	n	-750	-750	-500	-500	0		
1233	n	0	-50	-10	-24	7		
1233	n	-6000	-5750	-3952	-3881	-36		
1233	n	-6850	-6500	-4500	-4400	-50		
1233	n	-600	-400	-400	-400	0		
1233	n	-400	-500	-284	-314	14		

Table A3. Continued.

STRAIN REDUCTION OF A TYPICAL GAGE POSITIVE (2)						
Fz	LOAD	EP1	EP2	PROPORTION RATIO= .50	SIGMA MAX	GAGE 'O.E.= 5-I-SIDE
						TAU MAX
1234	1234	-6000	-5750	-3452	-3881	-34
1236	1236	-6800	-6550	-4486	-4914	-34
0	0	-550	-550	-248	-314	35
0	0	-250	-300	-176	-190	7
1239	1239	-6050	-5850	-3945	-3938	-24
1239	1239	-6200	-6500	-4140	-4276	43
0	0	-340	-400	-243	-257	7
0	0	50	-50	-10	-24	7
1242	1242	-6150	-5900	-4052	-3981	-36
1242	1242	-6800	-6500	-4476	-4390	-43
0	0	-300	-350	-219	-248	14
0	0	200	100	114	86	14
1245	1245	-6350	-6100	-4186	-4114	-36
1245	1245	-6800	-6500	-4476	-4390	-43
0	0	-450	-350	-281	-252	-14
0	0	200	50	135	62	21
1248	1248	-6400	-6150	-4214	-4148	-34
1248	1248	-6800	-6500	-4457	-4383	-57
0	0	-200	-300	-152	-181	14
0	0	250	100	138	95	21
1251	1251	-6450	-6200	-4210	-4124	-43
1251	1251	-6800	-6500	-4476	-4390	-43
0	0	-150	-200	-110	-124	7
0	0	250	100	138	95	21
1254	1254	-6400	-6100	-4210	-4124	-43
1254	1254	-6800	-6500	-4476	-4390	-43
0	0	-150	-300	-128	-171	21
0	0	250	50	128	71	24
1257	1257	-6400	-6150	-4214	-4148	-36
1257	1257	-6800	-6550	-4484	-4414	-36
0	0	-250	-250	-167	-167	0
0	0	50	150	52	81	-14
1260	1260	-6550	-6300	-4176	-3990	-14
1260	1260	-6800	-6550	-4476	-4390	-43
0	0	-350	-450	-348	-314	86
0	0	100	100	14	-514	86
1263	1263	-6200	-5700	-4038	-3895	-14
1263	1263	-7000	-6500	-4552	-4381	-21
0	0	-1050	-650	-624	-510	-57
0	0	100	100	14	48	-14
1266	1266	-6200	-5750	-4148	-3914	-64
1266	1266	-7000	-6500	-4576	-4390	-64
0	0	-800	-450	-467	-367	-50
0	0	100	100	14	48	-14
1269	1269	-6250	-5750	-4171	-3929	-71
1269	1269	-7000	-6500	-4552	-4381	-84
0	0	-450	-800	-405	-362	-21
0	0	100	100	14	48	-14
1272	1272	-6200	-5750	-4148	-3914	-64
1272	1272	-7000	-6500	-4552	-4381	-86

Table A3. Continued.

t	LOAD	EPI	POISSON'S RATIO		SIGMA MAX	SIGMA MIN	GAGE NO. & LOCATION	
			EP1	EP2			TAU MAX	TAU MIN
1275	0	-61000	-800	-800	-424	-571	-29	-29
1275	0	-6100	100	100	19	48	-14	-14
1275	0	-6300	-5800	-5800	-4105	-3962	-71	-71
1275	0	-7000	-6400	-6400	-4542	-4381	-84	-84
1275	0	-850	-800	-800	-405	-462	-21	-21
1278	0	-6400	150	150	29	71	-86	-86
1278	0	-7050	-5800	-5800	-4152	-3981	-93	-93
1278	0	-1000	-800	-800	-4476	-4340	-29	-29
1281	0	-6300	150	150	29	71	-21	-21
1281	0	-7050	-5800	-5800	-4095	-3938	-79	-79
1284	0	-1000	-800	-800	-4576	-4390	-93	-93
1284	0	-6250	150	150	29	71	-21	-21
1284	0	-6950	-5800	-5800	-4471	-3929	-71	-71
1284	0	-800	-800	-800	-4529	-4371	-79	-79
1287	0	-6350	100	100	-571	-529	-21	-21
1287	0	-7150	-5800	-5800	-4139	-3971	-14	-14
1287	0	-850	-6450	-6450	-4433	-4233	-79	-79
1290	0	-6250	150	150	52	81	-34	-34
1290	0	-7000	-6250	-6250	-4071	-3929	-71	-71
1290	0	-800	-800	-800	-4552	-4381	-86	-86
1293	0	-6250	150	150	-571	-529	-21	-21
1293	0	-7000	-6250	-6250	-4062	-3905	-14	-14
1293	0	-800	-800	-800	-4543	-4357	-79	-79
1294	0	-6250	150	150	-371	-329	-21	-21
1294	0	-7000	-6250	-6250	-4062	-3905	-14	-14
1294	0	-800	-800	-800	-4552	-4381	-79	-79
1294	0	-6250	150	150	-562	-505	-29	-29
1294	0	-7000	-6250	-6250	-4129	-3971	-86	-86
1294	0	-800	-800	-800	-4552	-4381	-29	-29
1294	0	-6250	150	150	-562	-505	-14	-14
1294	0	-7000	-6250	-6250	-4129	-3971	-79	-79
1294	0	-800	-800	-800	-4552	-4381	-86	-86
1294	0	-6250	150	150	-562	-505	-29	-29
1294	0	-7000	-6250	-6250	-4129	-3971	-86	-86
1294	0	-800	-800	-800	-4552	-4381	-29	-29

Table A3. Continued.

LOAD	POISSON'S RATIO = .40	SIGMA MAX	EP2	EP1	SIGMA MAX	SIGMA MIN	GAGE JOINT IN-OUTSIDE	TAC MAX
E = .40								
1201	0	-5650	0	0	-3762	0	0	0
1201	0	-6050	-6100	-6050	-4053	-4053	0	0
0	0	-250	-250	-300	-190	-176	0	0
1203	0	-150	-200	-150	-110	-124	0	0
1203	0	-5700	-5800	-5700	-3819	-3898	14	14
1203	0	-6050	-6100	-6050	-4043	-4057	0	0
0	0	-250	-250	-250	-167	-167	0	0
1204	0	-5400	0	0	-3629	-3621	0	0
1204	0	-5800	-5850	-5800	-3876	-3890	21	21
0	0	-500	-500	-500	-333	-333	0	0
1209	0	-250	-250	-250	-167	-167	0	0
1209	0	-5650	-5700	-5650	-3726	-3790	0	0
1209	0	-6150	-6200	-6150	-4110	-4124	0	0
0	0	-350	-350	-350	-233	-233	0	0
0	0	-50	-50	-50	-33	-33	0	0
1212	0	-5750	-5800	-5750	-3862	-3905	0	0
1212	0	-5850	-5900	-5850	-4042	-4085	0	0
0	0	-700	-650	-700	-457	-443	0	0
0	0	-50	-50	-50	-33	-33	0	0
1215	0	-5400	-5400	-5400	-3655	-3638	0	0
1215	0	-5400	-5450	-5400	-3886	-3814	0	0
0	0	-600	-600	-600	-400	-400	0	0
0	0	-100	-100	-100	-67	-67	0	0
1214	0	-5500	-5750	-5500	-3619	-3548	0	0
1214	0	-5400	-5450	-5400	-3884	-3814	0	0
0	0	-600	-550	-600	-340	-376	0	0
0	0	-150	-200	-150	-110	-124	0	0
1221	0	-5550	-5350	-5550	-3662	-3665	0	0
1221	0	-5850	-5700	-5850	-3871	-3829	0	0
0	0	-550	-550	-550	-367	-367	0	0
0	0	-50	-100	-50	-43	-57	0	0
1224	0	-5400	-5400	-5400	-3495	-3638	0	0
1224	0	-5850	-5450	-5850	-3862	-3805	0	0
0	0	-500	-450	-500	-324	-310	0	0
0	0	-100	-50	-100	-57	-43	0	0
1227	0	-5600	-5400	-5600	-3645	-3638	0	0
1227	0	-5900	-5650	-5900	-3886	-3814	0	0
0	0	-500	-450	-500	-324	-310	0	0
0	0	0	-150	0	-28	-21	0	0
1230	0	-5100	-5750	-5100	-3390	-3376	0	0
1230	0	-5650	-5650	-5650	-3787	-3787	0	0
0	0	-550	-700	-550	-345	-438	0	0
0	0	-50	-200	-50	-62	-105	0	0
1233	0	-5150	-5050	-5150	-3414	-3386	0	0
1233	0	-5750	-5750	-5750	-3833	-3833	0	0
0	0	-750	-600	-750	-421	-429	0	0
0	0	-350	-450	-350	-252	-281	0	0

Table A3. Continued.

STRAIN REDUCTION OF A TAIL GAGE ROSETTE (2)				POISSON'S RATIO, $\nu_0$		GAGE $\nu_0$ IN UNITS OF	
$\epsilon$	$\nu_0$	EP1	FP2	SIGMA MAX	SIGMA MIN	TAU MAX	TAU MIN
1236	0	-5150	-5250	-3452	-3481	14	14
1236	0	-5750	-5750	-3833	-3833	0	0
1236	0	-450	-600	-329	-371	21	21
1239	0	-200	-250	-193	-157	7	7
1239	0	-5150	-5000	-3405	-3362	-21	-21
1239	0	-5750	-5700	-3824	-3810	-7	-7
1239	0	-450	-600	-329	-371	21	21
1242	0	-50	-200	-62	-105	21	21
1242	0	-5350	-5350	-3567	-3567	0	0
1242	0	-5700	-5750	-3810	-3824	7	7
1242	0	-350	-500	-262	-305	21	21
1245	0	50	-100	5	-38	21	21
1245	0	-5450	-5400	-3624	-3610	-7	-7
1245	0	-5700	-5750	-3810	-3824	7	7
1245	0	-250	-400	-145	-238	21	21
1248	0	0	-100	-19	-48	14	14
1248	0	-5450	-5400	-3624	-3610	-7	-7
1248	0	-5700	-5750	-3810	-3824	7	7
1251	0	50	-100	-19	-48	14	14
1251	0	-5450	-5400	-3624	-3610	-7	-7
1251	0	-5700	-5750	-3810	-3824	7	7
1254	0	50	-100	-19	-48	14	14
1254	0	-5450	-5400	-3624	-3610	-7	-7
1254	0	-5700	-5750	-3810	-3824	7	7
1257	0	50	-100	-19	-48	14	14
1257	0	-5450	-5400	-3624	-3610	-7	-7
1257	0	-5700	-5750	-3810	-3824	7	7
1260	0	50	-100	-19	-48	14	14
1260	0	-5450	-5400	-3624	-3610	-7	-7
1260	0	-5700	-5750	-3810	-3824	7	7
1263	0	50	-100	-19	-48	14	14
1263	0	-5450	-5400	-3624	-3610	-7	-7
1263	0	-5700	-5750	-3810	-3824	7	7
1266	0	50	-100	-19	-48	14	14
1266	0	-5450	-5400	-3624	-3610	-7	-7
1266	0	-5700	-5750	-3810	-3824	7	7
1269	0	50	-100	-19	-48	14	14
1269	0	-5450	-5400	-3624	-3610	-7	-7
1269	0	-5700	-5750	-3810	-3824	7	7
1272	0	50	-100	-19	-48	14	14
1272	0	-5450	-5400	-3624	-3610	-7	-7
1272	0	-5700	-5750	-3810	-3824	7	7
1272	0	50	-100	-19	-48	14	14
1272	0	-5450	-5400	-3624	-3610	-7	-7
1272	0	-5700	-5750	-3810	-3824	7	7





Table A3. Continued.

①

Ez	LOAD	EPI	FPZ	POISSON'S RATIO = .49		SIGMA %A	SIGMA %B	GAGE "C" = 11-1 SIDE	
				TAU MAX	TAU MAX			TAU MAX	TAU MAX
1201	n	-4150	-3350	-2414	-2386	-114	-114	n	n
1201	n	-3650	-2250	-2167	-1767	-206	-206	n	n
1203	n	-3700	200	85	138	-21	-21	n	n
1203	n	-3500	200	86	114	-14	-14	n	n
1204	n	-3500	300	152	181	-14	-14	n	n
1204	n	-4000	100	90	76	-114	-114	n	n
1206	n	-3150	-3200	-1014	-1648	-134	-134	n	n
1206	n	200	450	141	252	-34	-34	n	n
1209	n	-3400	-150	-152	-81	14	14	n	n
1209	n	-3400	-2450	-2414	-2148	-134	-134	n	n
1209	n	-3450	500	2040	-1776	-157	-157	n	n
1212	n	250	500	214	286	-34	-34	n	n
1212	n	-3450	-2350	-2090	-1726	-157	-157	n	n
1212	n	-2900	-1450	-1676	-1290	-193	-193	n	n
1215	n	300	450	305	462	-29	-29	n	n
1215	n	250	500	214	286	-34	-34	n	n
1215	n	-3100	-1850	-1844	-1519	-14	-14	n	n
1215	n	-2400	-1550	-1652	-1281	-184	-184	n	n
1215	n	400	900	362	505	-21	-21	n	n
1214	n	250	500	214	286	-34	-34	n	n
1214	n	-3350	-2300	-2043	-1233	-160	-160	n	n
1218	n	-2850	1000	-1652	-1281	-186	-186	n	n
1221	n	200	400	171	220	-29	-29	n	n
1221	n	-3200	-2050	-1914	-1586	-164	-164	n	n
1221	n	-2750	1500	-1595	-1238	-174	-174	n	n
1221	n	150	1000	242	504	-21	-21	n	n
1224	n	250	500	214	286	-34	-34	n	n
1224	n	-3300	-2100	-1471	-1624	-171	-171	n	n
1224	n	-2850	1500	-2457	-1257	-193	-193	n	n
1224	n	500	900	410	524	-57	-57	n	n
1227	n	250	450	205	262	-24	-24	n	n
1227	n	-3450	-2450	-1938	-1595	-171	-171	n	n
1227	n	-2800	1500	-1619	-1248	-184	-184	n	n
1230	n	500	450	443	552	-57	-57	n	n
1230	n	350	200	300	400	-50	-50	n	n
1230	n	-2900	1800	-1724	-1410	-157	-157	n	n
1230	n	-2900	1400	-1444	-1314	-186	-186	n	n
1230	n	350	900	332	495	-29	-29	n	n
1233	n	350	200	300	400	-50	-50	n	n
1233	n	-2850	1250	-1640	-1326	-157	-157	n	n
1233	n	-2850	900	-1643	-1257	-193	-193	n	n
1233	n	350	250	310	424	-57	-57	n	n

Table A3. Continued.

E-3	LOAD	STRAIN REDUCTION OF A T-U GAGE ROSETTE			POISSON'S RATIO, $\nu$	SIGMA MAX	SIGMA MIN	GAGE NO. 2 11-11-1504	
		EP1	EPP	SIGMA MAX				TAU MAX	TAU MIN
1234	1234	-2900	-1800	-1724	-1910	-157			
1236	1236	-2850	-1550	-1652	-1281	-186			
n	n	450	900	386	514	-44			
1239	1239	450	900	367	467	-50			
1239	1239	-2890	-1650	-1648	-1419	-164			
1239	1239	-2800	-1400	-1600	-1200	-200			
n	n	550	950	443	557	-57			
1242	1242	450	750	357	443	-43			
1242	1242	-2800	-1700	-1647	-1343	-157			
n	n	600	1000	476	590	-179			
1245	1245	250	500	214	286	-57			
1245	1245	-3000	-1850	-1781	-1452	-34			
1245	1245	-2800	-1600	-1638	-1295	-164			
n	n	500	1000	424	571	-171			
1248	1248	250	500	214	286	-36			
1248	1248	-3000	-1800	-1771	-1429	-171			
n	n	500	950	419	548	-44			
1251	1251	250	500	214	286	-34			
1251	1251	-3000	-1800	-1771	-1429	-171			
n	n	550	950	443	557	-57			
1254	1254	250	500	214	286	-34			
1254	1254	-3000	-1800	-1771	-1429	-171			
n	n	500	900	410	524	-57			
1257	1257	250	500	214	286	-36			
1257	1257	-3000	-1750	-1714	-1386	-164			
n	n	550	900	433	533	-51			
1260	1260	400	600	305	362	-29			
1260	1260	-2850	-600	-1471	-829	-321			
n	n	300	800	236	294	-284			
1263	1263	350	550	271	295	-29			
1263	1263	-2800	-200	-1447	-867	-106			
n	n	450	850	310	324	-279			
1266	1266	300	500	248	314	-34			
1266	1266	-2850	-700	-1490	-876	-307			
n	n	550	850	348	319	-14			
1269	1269	300	500	248	314	-34			
1269	1269	-2800	-650	-1495	-874	-307			
n	n	500	800	284	305	-274			
1272	1272	300	500	248	314	-34			
1272	1272	-2850	-700	-1490	-876	-307			
n	n	550	850	348	319	-14			
1275	1275	300	500	248	314	-34			
1275	1275	-2800	-650	-1495	-874	-307			
n	n	500	800	284	305	-274			



Table A3. Continued.

E = %	LOAD	EPI	STRAIN REDUCTION OF A T-O GAGE RESETTE		POISSON'S RATIO, $\nu$	SIGMA VAX	SIGMA VIA	GAGE #0.3 1P=OUTSIDE	
			FP2	FP1				TAU MAX	TAU MAX
n	1201	0	n	0	n	-1852	n	n	n
1201	1201	-5650	-6100	-6000	-6000	-4085	-4238	64	64
n	1201	-6000	-6000	-6000	-6000	-157	-143	71	71
n	1201	-250	-200	-250	-250	-124	-110	-7	-7
1201	1201	-5800	-6300	-5800	-5800	-3462	-4105	71	71
1201	1201	-6050	-6550	-6050	-6050	-4127	-4271	71	71
n	1201	-250	-200	-250	-250	-157	-143	-7	-7
n	1201	-50	n	-50	-50	-24	-10	-7	-7
1206	1206	-5400	-6150	-5400	-5400	-3838	-3895	79	79
1206	1206	-5750	-6250	-5750	-5750	-3979	-4071	71	71
n	1206	-450	-400	-450	-450	-290	-276	-7	-7
0	1209	-150	-400	-150	-150	-148	-219	36	36
1209	1209	-5700	-6250	-5700	-5700	-3905	-4042	79	79
1209	1209	-6100	-6600	-6100	-6100	-4162	-4305	71	71
n	1209	-300	-350	-300	-300	-210	-224	7	7
n	1210	-150	-50	-150	-150	-81	-52	-14	-14
1212	1212	-5650	-6200	-5650	-5650	-3821	-4029	79	79
1212	1212	-6150	-6550	-6150	-6150	-4176	-4290	57	57
n	1212	-750	-650	-750	-750	-481	-452	-14	-14
n	1212	-150	n	-150	-150	-71	-29	-21	-21
1215	1215	-5900	-6300	-5900	-5900	-4010	-4124	57	57
1215	1215	-6150	-6500	-6150	-6150	-4167	-4267	50	50
n	1215	-700	-500	-700	-700	-29	-371	-29	-29
n	1218	-100	-150	-100	-100	-76	-80	7	7
1218	1218	-5900	-6300	-5900	-5900	-4010	-4124	57	57
1218	1218	-6250	-6450	-6250	-6250	-4205	-4262	29	29
n	1218	-650	-500	-650	-650	-405	-362	-21	-21
n	1220	-200	-200	-200	-200	-133	-133	0	0
1221	1221	-5900	-6300	-5900	-5900	-4010	-4124	57	57
1221	1221	-6150	-6500	-6150	-6150	-4167	-4267	50	50
n	1221	-600	-450	-600	-600	-771	-329	-21	-21
n	1221	-150	n	-150	-150	-71	-29	-21	-21
1224	1224	-5950	-6350	-5950	-5950	-4043	-4157	57	57
1224	1224	-6100	-6500	-6100	-6100	-4143	-4257	57	57
n	1224	-550	-200	-550	-550	-300	-200	-50	-50
n	1227	-150	n	-150	-150	-71	-29	-50	-50
1227	1227	-5950	-6350	-5950	-5950	-4043	-4157	57	57
1227	1227	-6150	-6500	-6150	-6150	-4167	-4267	50	50
n	1227	-500	-350	-500	-500	-305	-262	-21	-21
n	1230	-300	-150	-300	-300	-121	-124	-21	-21
1230	1230	-5550	-5950	-5550	-5550	-3774	-3890	57	57
1230	1230	-6150	-6450	-6150	-6150	-4157	-4243	43	43
n	1230	-750	-650	-750	-750	-481	-452	-14	-14
n	1233	-300	-150	-300	-300	-121	-124	-21	-21
1233	1233	-5450	-6000	-5450	-5450	-3833	-3933	50	50
1233	1233	-6200	-6450	-6200	-6200	-4181	-4262	36	36
n	1233	-750	-600	-750	-750	-471	-424	-21	-21
n	1233	-550	-400	-550	-550	-338	-295	-21	-21

Table A3. Continued.

[illegible]

Table A3. Continued.

STATISTICAL REDUCTION OF A TAU GAGE AND SETTING				POISSONS RATIO, $\nu_0$		GAGE NO. 12-OUTSIDE	
$\tau$	$\nu_0$	$\epsilon_{PI}$	$\epsilon_{PP}$	SIGMA MAX	SIGMA MIN	TAU MAX	TAU MIN
1240	0	-700	-850	-495	-538	21	21
1240	0	-150	0	-71	-29	-21	-21
1240	0	-5700	-4900	-3834	-3895	29	29
1240	0	-6250	-6500	-4214	-4286	36	36
1240	0	-750	-900	-529	-571	21	21
1240	0	-150	0	-71	-29	-21	-21
1240	0	-5700	-4900	-3834	-3895	29	29
1240	0	-6250	-6500	-4214	-4286	36	36
1240	0	-700	-800	-484	-514	14	14
1240	0	-150	0	-71	-29	-21	-21
1240	0	-5700	-4900	-3834	-3895	29	29
1240	0	-6250	-6500	-4214	-4286	36	36
1240	0	-700	-800	-484	-505	21	21
1240	0	-150	50	-42	-5	-29	-29
1240	0	-5700	-4850	-3824	-3871	21	21
1240	0	-6250	-6450	-4205	-4262	29	29
1240	0	-650	-750	-452	-481	14	14
1240	0	-100	100	-29	29	-29	-29
1240	0	-5600	-5800	-3721	-3829	29	29
1240	0	-6000	-6300	-4157	-4143	43	43
1240	0	-550	100	-29	29	-29	-29
1240	0	-5550	-5800	-3748	-3819	36	36
1240	0	-6000	-6300	-4057	-4143	43	43
1240	0	-450	-350	-241	-252	14	14
1240	0	-100	100	-29	29	-29	-29
1240	0	-5500	-5750	-3714	-3786	36	36
1240	0	-6000	-6300	-4057	-4143	43	43
1240	0	-600	-550	-390	-376	29	29
1240	0	-100	100	-29	29	-29	-29
1240	0	-5500	-5750	-3714	-3786	36	36
1240	0	-6000	-6300	-4057	-4143	43	43
1240	0	-500	-500	-333	-333	0	0

## APPENDIX B. DEFINITIONS

Creep – Time-dependent deformation of material under sustained loading of constant magnitude.

Cyclic loading – Pressurizing the window repeatedly to specified pressure at a rate of 650 psi/minute, maintaining this pressure for a specified number of hours, depressurizing at 650 psi/minute to 0 psi, and allowing the window to relax for a specified number of hours before repeating the procedure.

Hoop orientation of strains or stresses – Direction parallel to the edge of the spherical sector window.

Long-term loading – Pressurizing the window to a specified pressure at a rate of 650 psi/minute and maintaining this pressure for a specified number of hours.

Meridional orientation of strains or stresses – Direction at right angle to hoop direction.

Relaxation – Time-dependent restoration of material to its original dimensions under absence of external loading.

Short-term critical pressure – Pressure at which catastrophic failure of the window occurs when subjected to short-term hydrostatic loading at 75°F ambient temperature.

Short-term loading – Increasing the hydrostatic pressure at a rate of 650 psi/minute.

Strain – Unit deformation, inch/inch of original length.





---

# FLANGED ACRYLIC PLASTIC HEMISPHERICAL SHELLS FOR UNDERSEA SYSTEMS

by

Jerry D. Stachiw, Naval Undersea Center

Jack R. Maison, Naval Civil Engineering Laboratory

September 1973

---



Approved for public release; distribution unlimited.



NAVAL UNDERSEA CENTER, SAN DIEGO, CA. 92132

---

AN ACTIVITY OF THE NAVAL MATERIAL COMMAND

ROBERT H. GAUTIER, CAPT, USN

Commander

Wm. B. McLEAN, Ph.D.

Technical Director

### ADMINISTRATIVE STATEMENT

The work described in this report was performed between January 1971 and December 1972 as part of the investigation of transparent structural materials for undersea application. The work was supported by the Director of Naval Laboratories through the Independent Exploratory Development Program.

Released by

H. R. Talkington, Head  
Ocean Technology Department

## SUMMARY

### PROBLEM

Acrylic plastic hemispherical shells have been found to be, from structural and optical viewpoints, ideally suited for incorporation into undersea systems as pressure-resistant windows. Free thermal forming of plastic hemispheres with compressed air is an economical fabrication technique, but it produces hemispheres that (1) terminate at the equator with an integral flange, and (2) have a thinner shell at the apex than do precision-made shells. Until the effect of these structural factors on the short-term critical pressure of hemispheres is determined, inexpensive hemispherical shells cannot be produced by this fabrication technique for man-rated undersea structures.

### RESULTS

Experimental data generated by this study show that the addition of an integral equatorial ring to a hemisphere of uniform thickness does not decrease its short-term critical pressure providing that the ratio of its thickness to its inner radius is less than 0.2. For thicker hemispheres there appears to be a significant decrease of short-term critical pressure when an integral equatorial ring is incorporated into the shell.

Reduced wall thickness at the apex of free-formed acrylic plastic hemispheres significantly lowers the actual short-term critical pressure of these hemispheres below the critical-pressure value calculated on the basis of maximum wall thickness. Their short-term critical pressure can be predicted accurately, however, if instead of maximum thickness their mean thickness is used in computation.

### RECOMMENDATIONS

Hemispheres with integral equatorial flanges and walls of nonuniform thickness can be utilized as pressure-resistant windows in undersea systems providing that the effects of the equatorial flange and the nonuniform wall thickness on the short-term critical pressure are taken into account. The results of this report can be applied without any major modification to hemispheres where (1) the thickness of the shell at the apex is no less than 65 percent of the thickness of the shell at the base, (2) the width of the flange is equal to its thickness, and (3) there is a reasonable radius at the instep and no radius at the heel of the flange.

## CONTENTS

INTRODUCTION	1
CONDUCT OF STUDY	1
Experimental Program	2
Analytical Program	3
EXPERIMENTAL RESULTS	15
Short-Term Implosions	15
Axial Displacement	16
Failure Modes	18
Strains and Stresses	18
ANALYTICAL RESULTS	27
Principal Stresses	27
Effective Stress	28
Effective Strain	28
CONCLUSIONS	38
RECOMMENDATIONS	38
REFERENCES	39
APPENDIX: RESULTS OF HYDROSTATIC TESTS	41

## INTRODUCTION

Acrylic plastic has been utilized almost from the very beginning of ocean exploration for viewports in submersibles, ocean bottom habitats, personnel transfer capsules, decompression chambers, and deep-ocean simulators. In some cases, acrylic plastic was even utilized as a pressure-resistant hull to achieve panoramic visibility in manned submersibles.

The shape of acrylic plastic viewports can vary depending on the operational pressure and visibility required of a particular submersible system. Typical shapes used are conical frustum (reference 1), flat circular disc (reference 2), and spherical shell sector. This latter shape is optimally suited to resist pressure loading because of its double curvature; additionally, it gives the largest field of vision for any given viewport diameter.

Spherical shell sectors provide optimal pressure resistance only when the wall thickness and sphericity of the shell are uniform and no restraints are imposed on the edge of the shell when it deforms under hydrostatic loading. Such spherical shell windows have been fabricated, tested, and described in the literature (reference 3). Because of their excellent performance, they have already found application as picture windows in the bows of work submersibles (reference 4).

Although spherical shell windows have been shown to offer optimal resistance to hydrostatic pressure, the fairly high cost of fabricating such windows within tight dimensional tolerances has deterred their wide application. For this reason, techniques have been investigated whereby such windows might be produced more cheaply, sacrificing some structural quality if necessary. One technique investigated, free thermal forming using compressed air, permits fabrication of inexpensive spherical shell windows having radii ranging from 10 to 100 times the shell's thickness. This technique has been used to produce several large, hemispherical shell windows for submersibles at some 20 percent the cost of precision-made shells. However, shells produced by this technique have walls of varying thickness and an equatorial flange, two characteristics known from theoretical considerations to decrease the ultimate pressure resistance of the shell. Until the effect of these structural factors is determined and made available to ocean engineers, low-cost acrylic plastic hemispherical shells cannot be reliably specified for ocean engineering systems.

An exploratory study into the effect of equatorial flanges and varying wall thickness has been initiated at NUC; the results of this study form the subject of this paper.

## CONDUCT OF STUDY

The study was conducted in two phases, experimental and analytical. The objective of the experimental phase was to (1) generate implosion pressure, axial displacement, and strain data for hemispherical acrylic shells with equatorial flanges and to (2) compare these experimental values with data for hemispherical shells without flanges. Some of the flanged

shells tested were of constant thickness, others were thinner at the apex as is typical of free-formed shells. Since a considerable store of data for flangeless shells was recorded in an earlier study (reference 3) only a few additional flangeless shells were tested to complement the existing data.

The analytical phase of the study utilized an elastic finite-element computer program that had been previously successfully applied to acrylic plastic structures (reference 6). The resultant stress contours were compared to the experimentally derived stresses to establish the proper boundary conditions for future investigations and to provide insight into the failure mechanism.

## EXPERIMENTAL PROGRAM

The experimental phase of the study was conducted using 40 hemispherical shells with identical internal diameters of 5.500 inches. Of these, 10 were of uniform wall thickness and had no equatorial flanges (figure 1)\*, 15 were of uniform wall thickness and had equatorial flanges (figure 2), and 15 were of varying thickness and had equatorial flanges; the thickness varied uniformly from a maximum at the flange to a minimum at the apex (figure 3). The minimum thickness was 65 percent of the shell thickness at the flange.

Test specimens were machined from cast Plexiglas G plate and annealed after machining (figure 4). Except for a few used in photography, they were left unpolished. The mechanical properties of the Plexiglas G plate met the minimum level of properties established previously (reference 5) by the authors as a requirement for man-rated acrylic structures (table 1).

Instrumentation for all of the acrylic hemispherical shells consisted of mechanical dial indicators with 0.001-inch reading increments that measured the axial displacement of the shell's apex. The displacement of the shell was transmitted to the dial indicator by a piano-wire linkage bonded to the apex of the shell with silicon RTV.

On one specimen of each thickness and type, electric resistance strain gages were installed on the interior of the shells (figure 5). The three-element rosette gages (Baldwin Lima Hamilton, FAER-12RB-12S6ET) were bonded to the inside shell surface with Eastman 910 cement at the apex, at a 20-degree elevation above the flange, and at the flange. Water proofing (BLH Gagecote 1) and silicone RTV completed the installation.

Test equipment consisted of internal pressure vessels with 20,000-psi pressure capability. The pressure vessel's end closure contained an opening through which the interior of the acrylic shell could be reached with strain gage wires and the mechanical linkage to the dial indicator.

Test procedure for the hydrostatic testing of acrylic hemispheres was identical to the one used in previous test programs for implosion of acrylic hemispheres under short-term loading conditions. The rigid steel bearing plate used to support the hemispheres (figure 6) was liberally coated with DC-4 silicone grease prior to placement of the test specimen. The grease coating not only decreased the friction between the acrylic and the steel plate but also acted as a water seal. Pressurization of the acrylic hemisphere was accomplished with tap water at 70°F whose pressure was raised at a rate of 650 psi/minute until the hemisphere imploded.

---

\*Figures are grouped at the end of each section

Table 1. Specified<sup>a</sup> Properties for Acrylic Plastic Viewports.

Property	Required Value	ASTM Test
Hardness, Rockwell	M90 minimum	D785-62
Specific gravity	1.19 ±0.01	D792-66
Refractive index	1.49 ±0.01	D542-50
Tensile, ultimate strength	9,000 psi, minimum	D638-68
elongation at break	2% minimum	
modulus	400,000 psi minimum	
Compressive, yield strength	15,000 psi, minimum	D695-69
modulus	400,000 psi, minimum	
Flexural, ultimate strength	14,000 psi, minimum	D790-70
Shear, ultimate strength	8,000 psi, minimum	D732-46
Compressive deformation	1.0% maximum at 4000 psi and 122°F for 24 hrs	D621-64
Water absorption	0.25% maximum in 24 hrs	D570-63
Izod, notched impact strength	0.3 ft. lbs/in./in.	D256-70
Ultraviolet light transmittance	5% maximum	D1003-61

<sup>a</sup>Originated by the authors (reference 5) at the U. S. Naval Civil Engineering Laboratory for Navy use and subsequently proposed for adoption by ASME.

Data reduction for the imploded acrylic shells consisted of averaging the implosion pressures and displacement for groups of shells with identical dimensions. Strains, which were measured only on a single specimen from each group of shells, were not averaged but were converted into principal stresses. A modulus of elasticity of 450,000 psi and a Poisson's ratio of 0.35 were used to convert strains into stresses.

## ANALYTICAL PROGRAM

The Wilson axisymmetric shell finite-element computer program (reference 7) was utilized to investigate the elastic stress patterns in a typical flanged hemispherical window of constant thickness. The purpose of the analysis was to locate areas of high stress which would be indicative of the failure location but might not have been detected by the strain gages and, secondly, to correlate the experimentally derived stresses with the computer-generated detailed stress patterns. Previous studies (reference 6) established the suitability of the Wilson code for elastic analysis of acrylic plastic structures.

Figure 7 shows the mesh used for the 0.500-inch-thick ( $t/R_1 = 0.182$ ) spherical window. The quadrilateral mesh elements were sized to match the anticipated stress gradients. High-stress gradients were expected at the flange-to-dome junction and, therefore, the mesh elements were reduced in size and increased in number in this region.

The actual boundary condition at the flange bearing surface was not modeled directly but rather bracketed by two extreme conditions. In one case, the boundary was rigidly fixed; in the other case, it was free to move in the radial direction. Although the actual restraint to radial movement due to friction lies somewhere between these extremes, this approach was judged to be adequate.



actual shell thickness of shell specimens (inches)

t	0.062	0.125	0.250	0.500	0.750
$t/D_i$	0.011	0.023	0.046	0.091	0.137

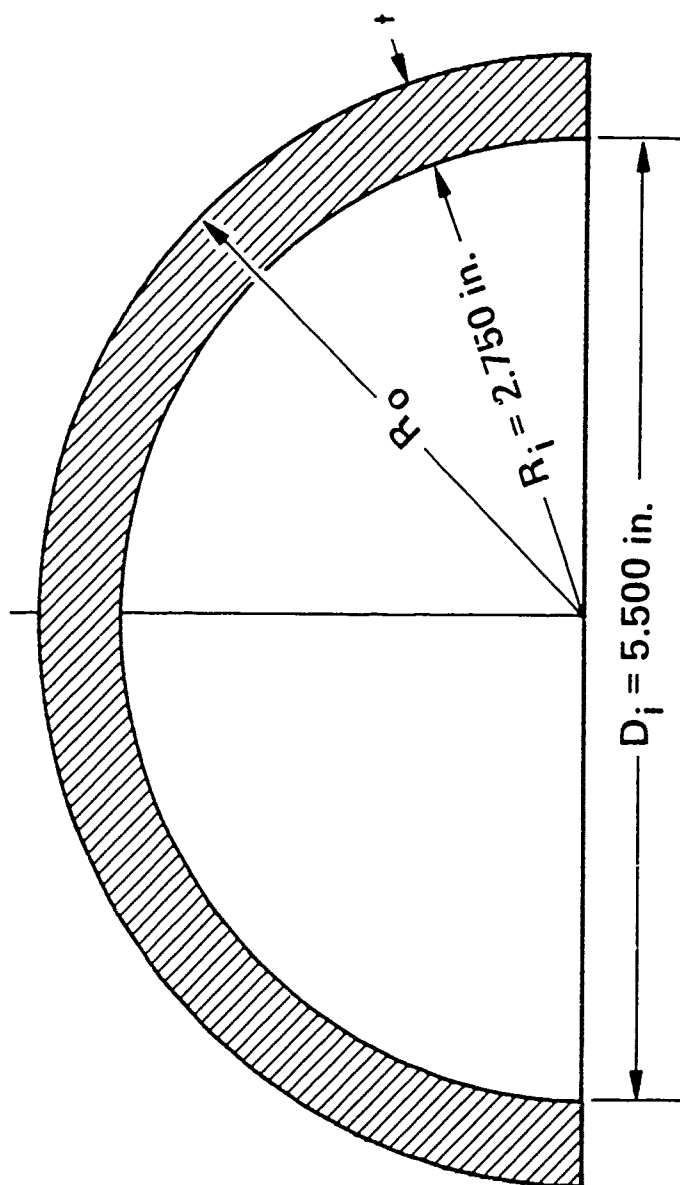


Figure 1. Dimensions of Shell Specimens of Constant Thickness Without Flanges.

actual shell thickness of shell specimens (inches)

$t$	0.062	0.125	0.250	0.500	0.750
$t/D_i$	0.011	0.023	0.046	0.091	0.137

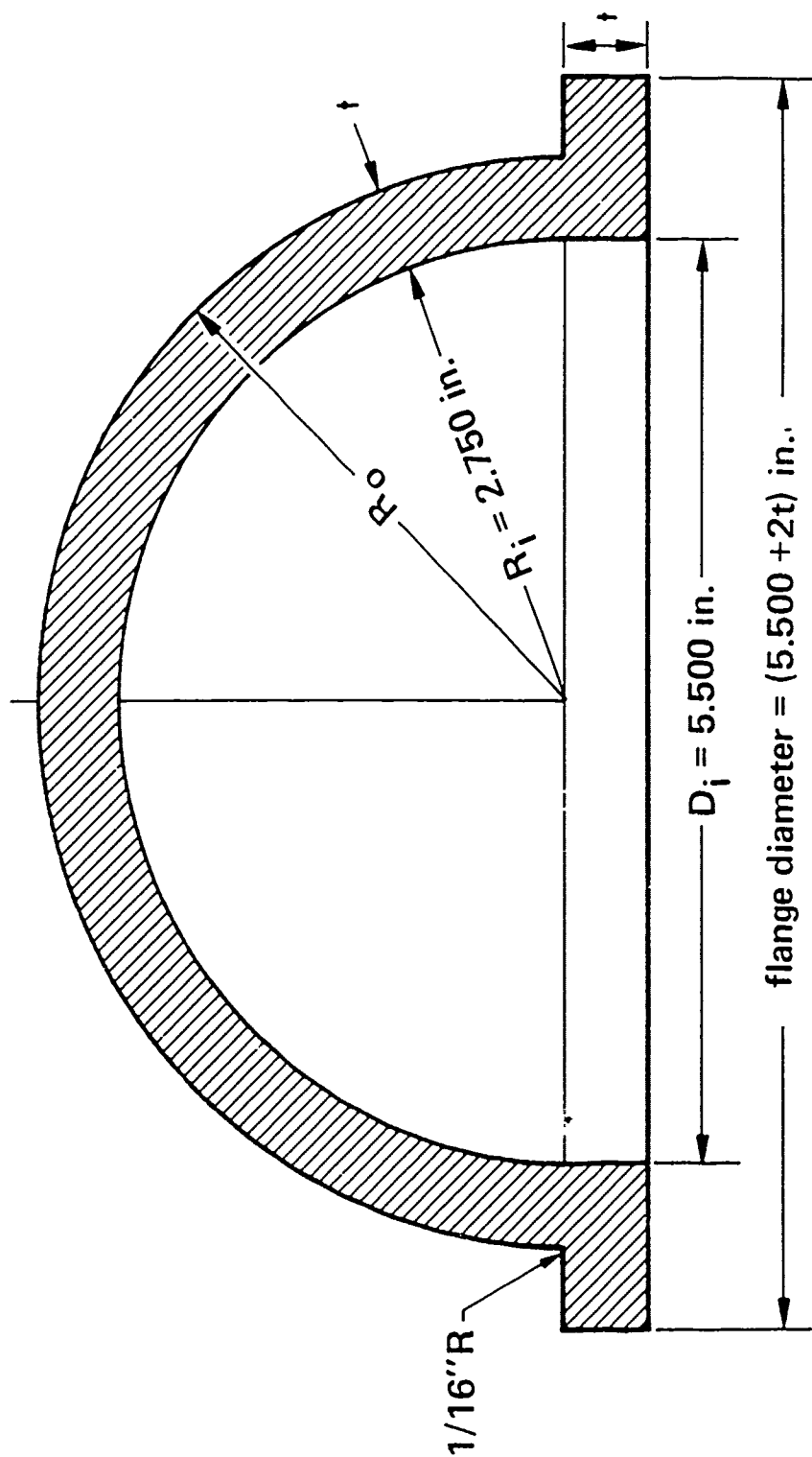


Figure 2. Dimensions of Shell Specimens of Constant Thickness with Equatorial Flanges.

nominal sheet thickness	location											
	$\theta = 0$		$\theta = 10$		$\theta = 20$		$\theta = 30$		$\theta = 40$		$\theta = 50$	
	$R_i$	$t$	$R_i$	$t$	$R_i$	$t$	$R_i$	$t$	$R_i$	$t$	$R_i$	$t$
0.062	2.812	0.062	2.752	0.060	2.754	0.058	2.756	0.056	2.758	0.054	2.760	0.052
0.125	2.875	0.125	2.754	0.121	2.759	0.116	2.764	0.111	2.769	0.106	2.774	0.101
0.250	3.000	0.250	2.759	0.241	2.768	0.232	2.776	0.222	2.788	0.212	2.798	0.202
0.500	3.250	0.500	2.769	0.481	2.788	0.462	2.807	0.443	2.826	0.424	2.845	0.405
0.750	3.500	0.750	2.779	0.721	2.808	0.692	2.837	0.663	2.866	0.634	2.895	0.605

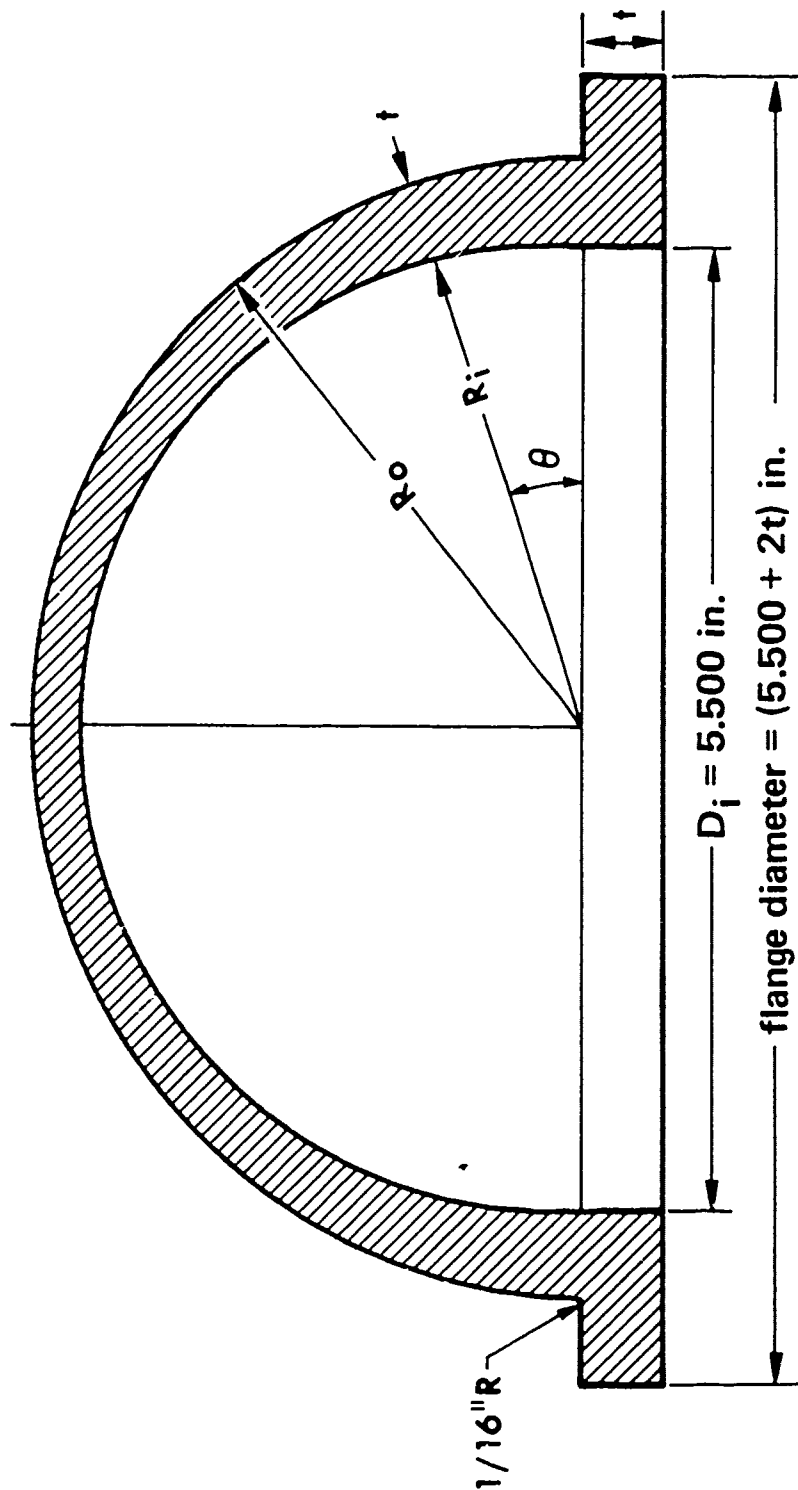


Figure 3. Dimensions of Shell Specimens of Variable Thickness with Equatorial Flanges.

A

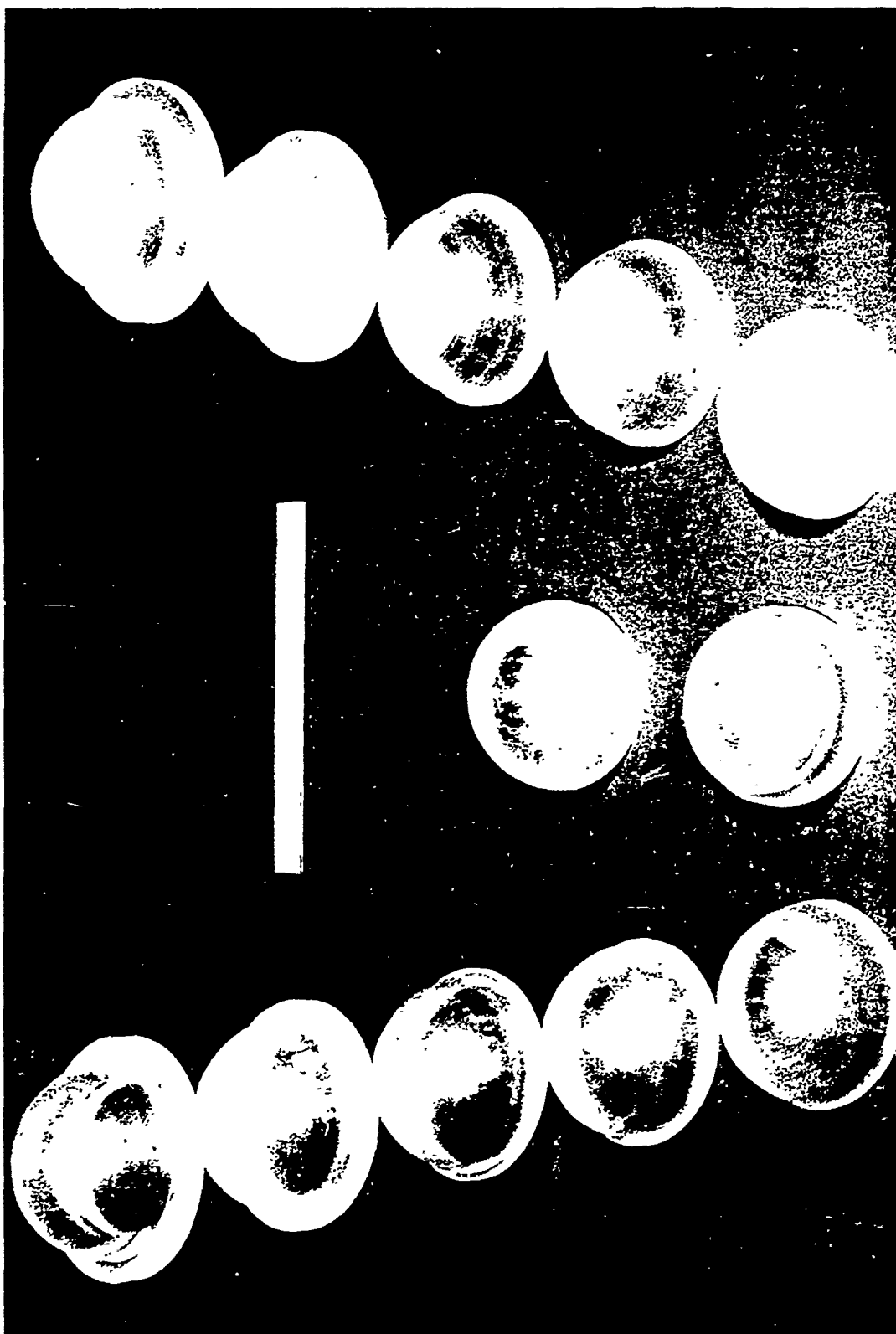


Figure 4. Typical Shell Specimens Machined from Acrylic Plastic Plate; (A) top view, (B) bottom view.

B

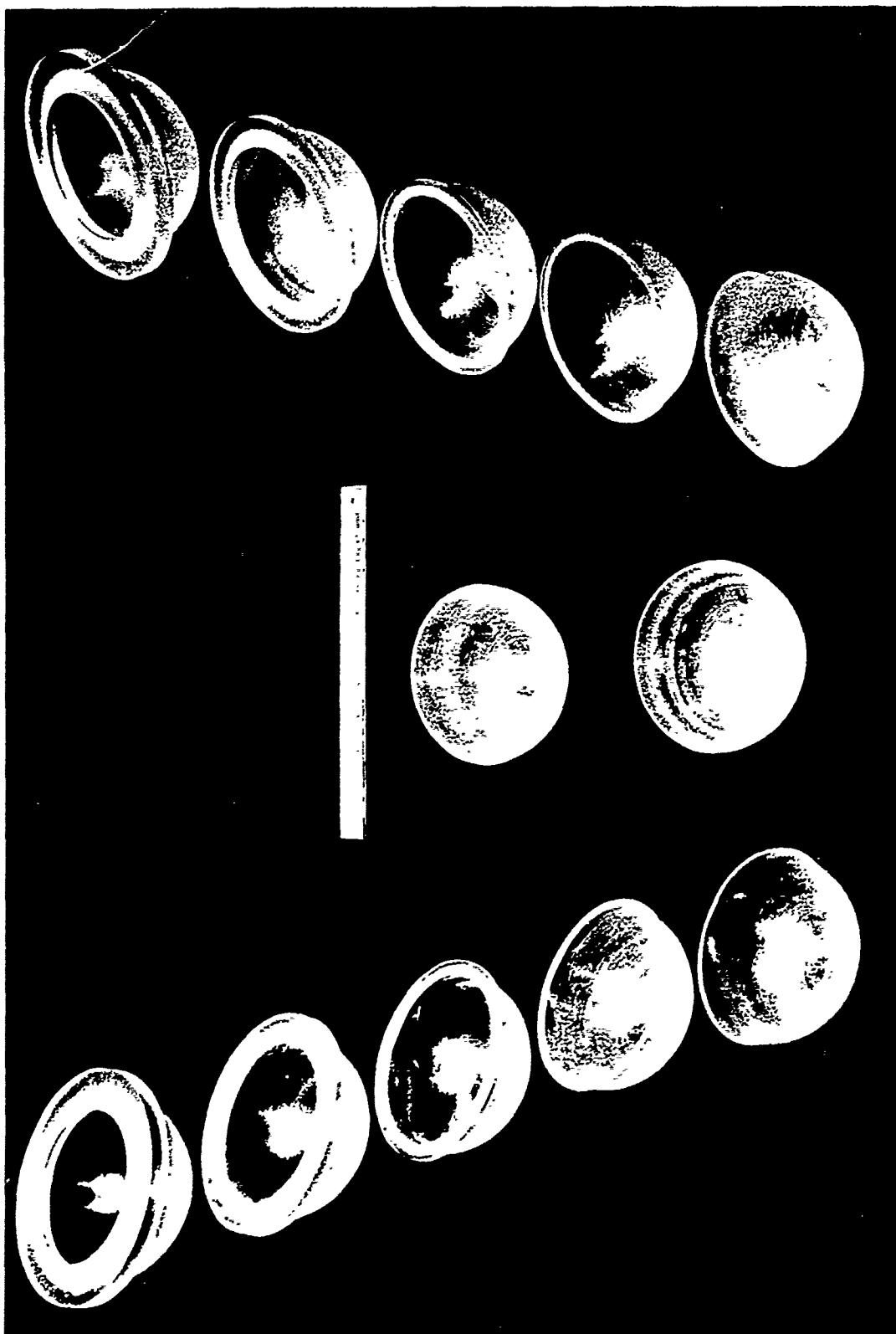


Figure 4. (Continued)

A

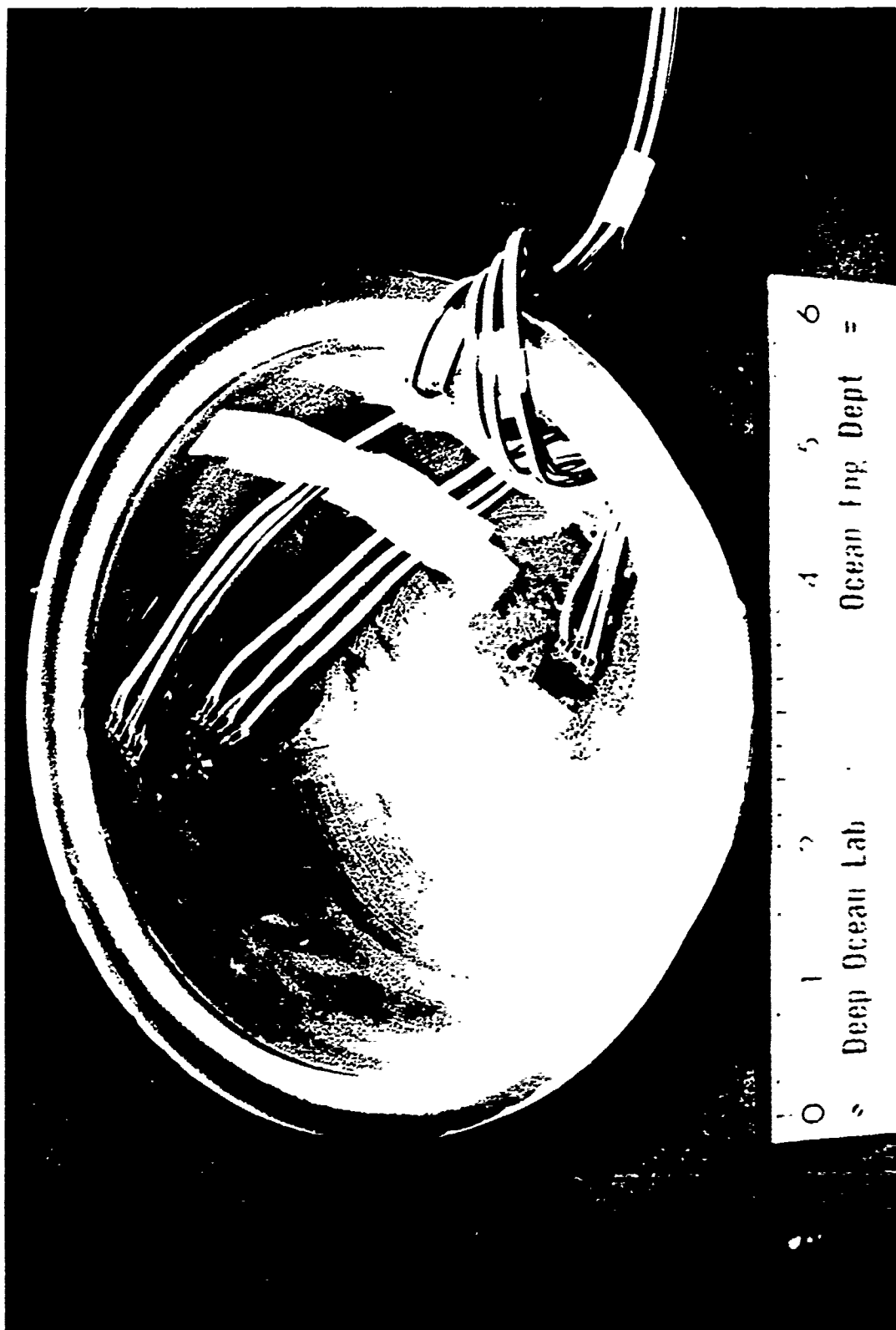


Figure 5. Installation of Strain Gages on the Interior Surface of the Shell Specimen;  
(A) overall view, (B) close up.

B

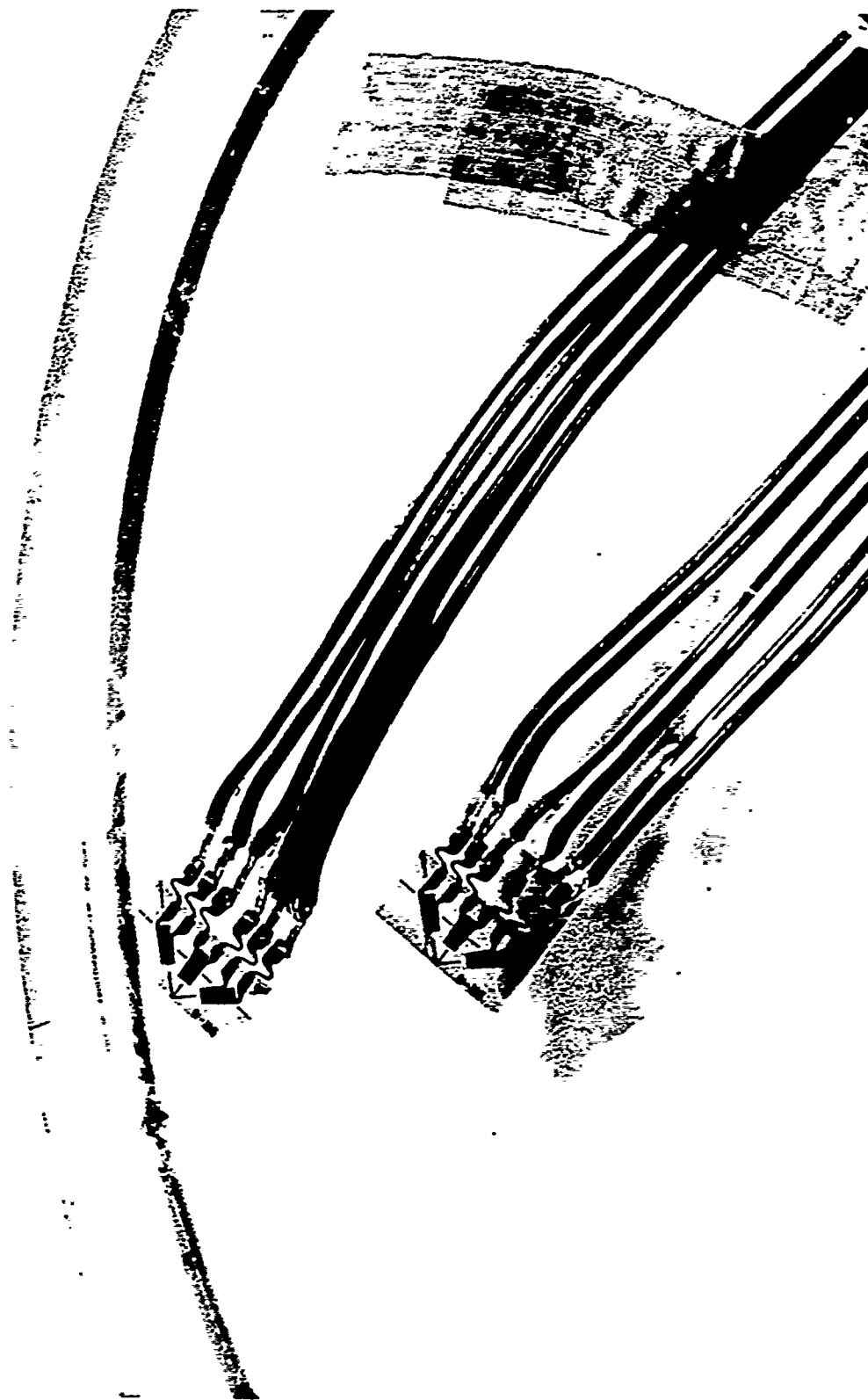


Figure 5. (Continued)

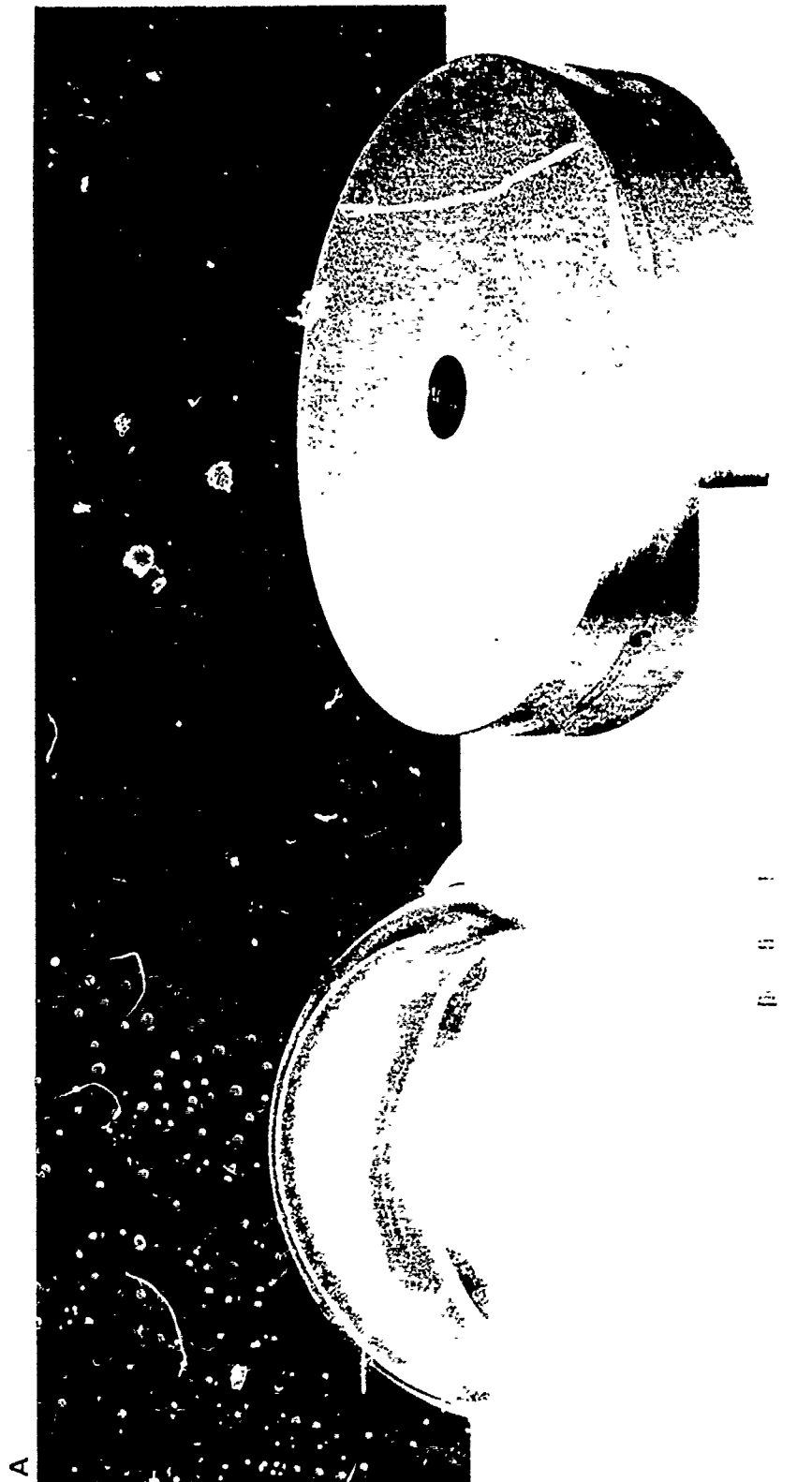


Figure 6. Mounting Arrangement of the Shell Specimen for External Hydrostatic Testing in a Deep Ocean Pressure Simulator;  
(A) Flat Disc Support Flange on which the Shell is to be Mounted, (B) Shell Mounted on the Flange.



B

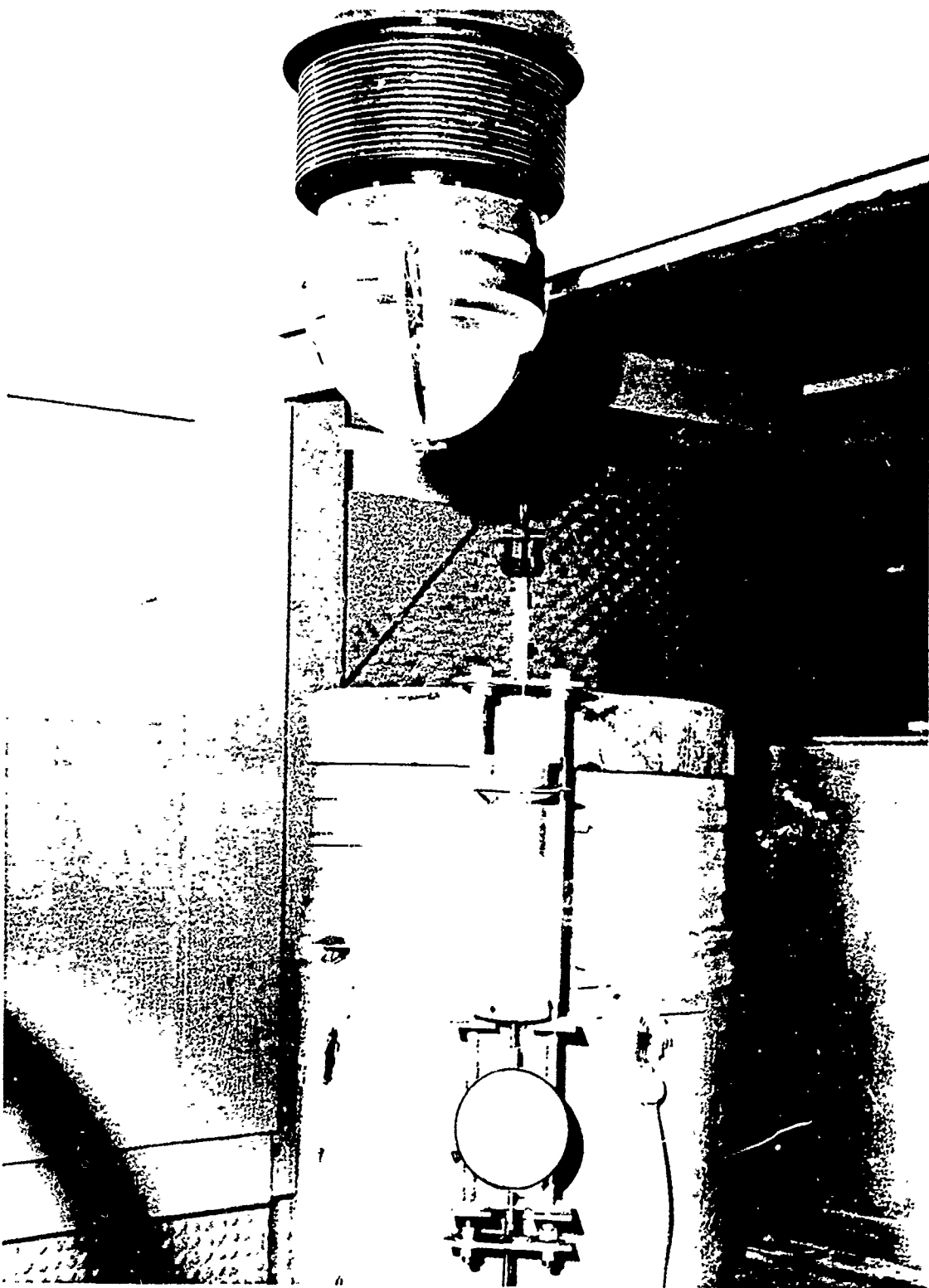


Figure 6. (Continued)

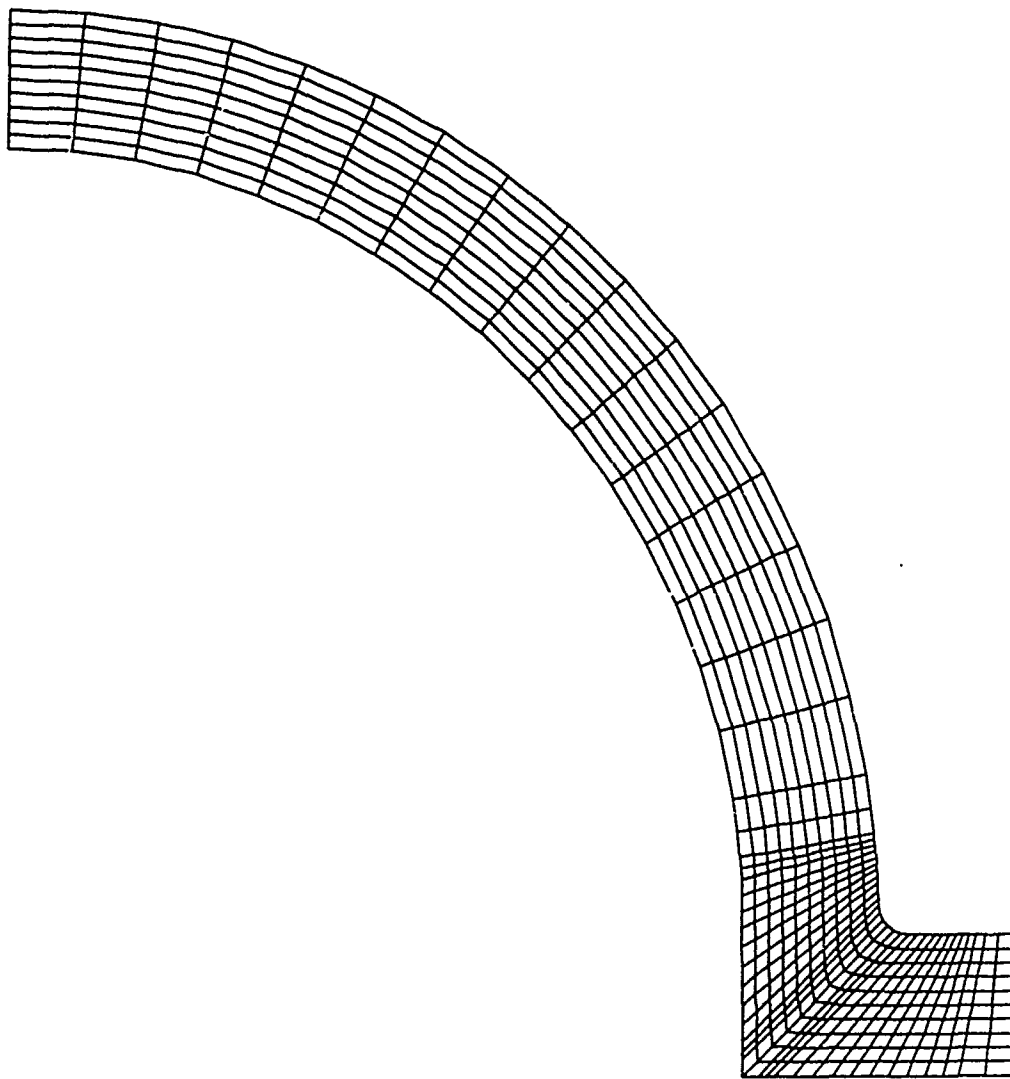


Figure 7. Finite-Element Mesh of Flanged Hemispherical Window of Constant Thickness;  $t/R_i = 0.182$ .

## EXPERIMENTAL RESULTS

### SHORT-TERM IMPLOSIONS

Implosion pressures recorded (table 2) during short-term pressurization of hemispherical shells were fairly reproducible for specimens of the same configuration and nominal  $t/R_i$  ratio. The spread of implosion pressures for any given configuration and  $t/R_i$  ratio was generally less than 10 percent of the average pressure. The average collapse pressures for the specimens are plotted against the actual  $t/R_i$  in figure 8.

For shells of constant thickness there appeared to be no significant difference between implosion pressures of shells with flanges and those without them providing that  $t/R_i < 0.200$ . For shells with  $t/R_i > 0.200$ , the implosion pressures of shells with flanges appeared to be lower than for shells without flanges.

For shells of variable thickness with flanges, the implosion pressures were always lower than that of flanged shells with constant thickness, providing that the comparison was made at the same nominal  $t/R_i$  ratio, where  $t$  = thickness at the flange. However, if the full range of  $t/R_i$ , which varied from a minimum at the shell apex to a maximum at the flange, was used in the comparison, the data for variable-thickness flanged shells intersects the curve for the constant-thickness windows. Two inferences can be drawn from this observation; namely, that implosion pressure for variable-thickness windows can be predicted using the mean  $t/R_i$  ratio for that shell and, secondly, that failure probably originates at about a 45-degree elevation from the flange for these shells (where the mean thickness of the shell is located).

Table 2. Implosion Pressures.

Window type	Nominal values			Mean values <sup>a</sup>		Implosion pressures		
	Thickness inches	$t/D_i$	$t/R_i$	Thickness inches	$t/R_i$	Min. psi	Ave. psi	Max. psi
No flange constant thickness	0.062	0.011	0.022	NA	NA	180	203	237
With flange constant thickness	0.062	0.011	0.022	NA	NA	200	227	250
With flange variable thickness	0.062	0.011	0.022	0.051	0.018	103	106	110
No flange constant thickness	0.125	0.023	0.046	NA	NA	920	995	1040
With flange constant thickness	0.125	0.023	0.046	NA	NA	946	992	1085

<sup>a</sup>Thickness at 45-degree elevation.

Table 2. (Continued)

Window type	Nominal values			Mean values <sup>a</sup>		Implosion pressures		
	Thickness inches	t/D <sub>i</sub>	t/R <sub>i</sub>	Thickness inches	t/R <sub>i</sub>	Min. psi	Ave. psi	Max. psi
With flange variable thickness	0.125	0.023	0.046	0.103	0.037	750	775	800
No flange constant thickness	0.250	0.046	0.091	NA	NA	2800 <sup>b</sup>	2996 <sup>b</sup>	3160 <sup>b</sup>
With flange constant thickness	0.250	0.046	0.091	NA	NA	3150	3280	3390
With flange variable thickness	0.250	0.046	0.091	0.206	0.075	2860	3007	3080
No flange constant thickness	0.500	0.091	0.182	NA	NA	7000 <sup>b</sup>	7322 <sup>b</sup>	7550 <sup>b</sup>
With flange constant thickness	0.500	0.091	0.182	NA	NA	7500	7713	7990
With flange variable thickness	0.500	0.091	0.182	0.412	0.149	5700	5900	6000
No flange constant thickness	0.750	0.137	0.273	NA	NA	11750 <sup>b</sup>	11970 <sup>b</sup>	12300 <sup>b</sup>
With flange constant thickness	0.750	0.137	0.273	NA	NA	9470	9735	10990
With flange variable thickness	0.750	0.137	0.273	0.618	0.225	9100	9400	9700

<sup>a</sup>Thickness at 45-degree elevation. <sup>b</sup>Experimental values taken from reference 3.

## AXIAL DISPLACEMENT

Axial displacements measured for shells of constant thickness were not significantly influenced by the presence of flanges (figure 9) providing that the comparison between flanged and flangeless shells was always made between shells of the same nominal t/R<sub>i</sub> ratio loaded to only approximately 50 percent of their short-term critical pressure.

Shells of variable thickness with flanges exhibited significantly higher axial displacements for a given nominal t/R<sub>i</sub> ratio than did flanged shells of constant thickness subjected to approximately 50 percent of their short-term critical pressure.

Table 3 summarizes the displacements measured for flanged and flangeless shells. Displacement measured for individual shell specimen are presented in the appendix.

Table 3. Axial Displacements.

Window type	Nominal thickness <sup>a</sup>			Displacement, inches <sup>b</sup>			Pressure, psi
	Inches	$t/D_i$	$t/R_i$	Min.	Ave.	Max.	
No flange constant thickness	0.062	0.011	0.022	0.001	0.002	0.003	100
With flange constant thickness	0.062	0.011	0.022	0.003	0.004	0.006	100
With flange varying thickness	0.062	0.011	0.022	0.004	0.006	0.009	100
No flange constant thickness	0.125	0.023	0.046	0.018	0.024	0.030	500
With flange constant thickness	0.125	0.023	0.046	0.014	0.018	0.022	500
With flange varying thickness	0.125	0.023	0.046	0.024	0.027	0.031	500
No flange constant thickness	0.250	0.046	0.091	0.022 <sup>c</sup>	0.036 <sup>c</sup>	0.051 <sup>c</sup>	1500
With flange constant thickness	0.250	0.046	0.091	0.031	0.033	0.034	1500
With flange varying thickness	0.250	0.046	0.091	0.040	0.043	0.050	1500
No flange constant thickness	0.500	0.091	0.182	0.041 <sup>c</sup>	0.061 <sup>c</sup>	0.080 <sup>c</sup>	3500
With flange constant thickness	0.500	0.091	0.182	0.046	0.056	0.066	3500
With flange varying thickness	0.500	0.091	0.182	0.066	0.074	0.084	3500
No flange constant thickness	0.750	0.137	0.273	0.055 <sup>c</sup>	0.074 <sup>c</sup>	0.080 <sup>c</sup>	5000
With flange constant thickness	0.750	0.137	0.273	0.065	0.074	0.091	5000
With flange varying thickness	0.750	0.137	0.273	0.079	0.085	0.091	5000

<sup>a</sup>Thickness of shell at the flange.<sup>b</sup>Radial displacement of the apex.<sup>c</sup>Experimental values taken from reference 3.

## FAILURE MODES

Modes of failure for flanged shells varied with the nominal  $t/R_i$  ratio. Very thin shells ( $t/R_i = 0.022$ ) failed by local elastic instability centered at approximately 15 to 20 degrees of elevation from the flange. The local instability failure was characterized (figure 10) by a nearly circular fracture that intersected the flange. No shear cracks were observed at the reentrant corner (instep) of the equatorial flange. This type of failure was very reproducible from one shell to another.

Thin shells ( $t/R_i = 0.046$ ) failed by local elastic instability centered at about 45 degrees of elevation. The failure pattern (figure 11) was somewhat irregular but reproduced well from one shell to another. No cracks were observed at the instep of the equatorial flange.

Medium thick ( $0.091 \leq t/R_i \leq 0.182$ ) shells failed by plastic instability originating near the apex of the shell. The fracture pattern (right hand side of figure 12) was characterized by "orange peel" fragments originating at the apex. Circumferential shear cracks were observed at the instep of the flange propagating toward the flange-bearing surface. In one case, the flange sheared completely from the hemisphere prior to implosion (left hand side of figure 12).

Thick ( $t/R_i \geq 0.273$ ) shells failed by total plastic instability. The fracture pattern was quite irregular due to the fragmentation of the shell into very minute shards (figure 13). The circumferential crack at the instep of the flange produced complete separation of the flange from the shell in each test specimen.

The debris from many of the medium-thick and from all of the thick windows contained large segments of the flange. In one test, the pressurization of the thick shell was terminated after the flange sheared off. Upon inspection of the shell, the fragmented flange was the only visible indication of failure. These large flange segments suggest that the flange breaks away prior to plastic instability of the thick dome. The loss of the flange may then trigger plastic collapse of the dome.

## STRAINS AND STRESSES

Experimentally measured strains and the derived stresses on shells varied from location to location on a single shell and from one shell to another depending on its nominal  $t/R_i$  ratio and whether it was of constant or varying thickness. A complete discussion of the experimental strains and stresses measured on shells of constant and varying thickness would make the main body of the report too long and therefore has been delegated to the appendix. However, since a finite-element analysis of a moderately thick flanged shell of constant thickness is used as an example in the main body of the report, the experimental data for that shell thickness has been included for comparison (figure 14).

Plotted data indicate that the stresses in a moderately thick flanged shell of constant thickness increased almost linearly with pressure and, with the exception of the meridional stress at the flange, were of about the same value. At approximately 50 percent of implosion pressure some of the strain gages failed because of the very high strains associated with these stresses, but gages which were on other flanged shells of similar thickness continued to function and recorded a nonlinear increase in strain as the specimen neared implosion. Figure 15

shows not only the nonlinear increase in strain, but also the nonlinear increase in radial apex displacement. The radial apex displacement becomes almost a step function just prior to plastico-elastic instability failure of the shell.

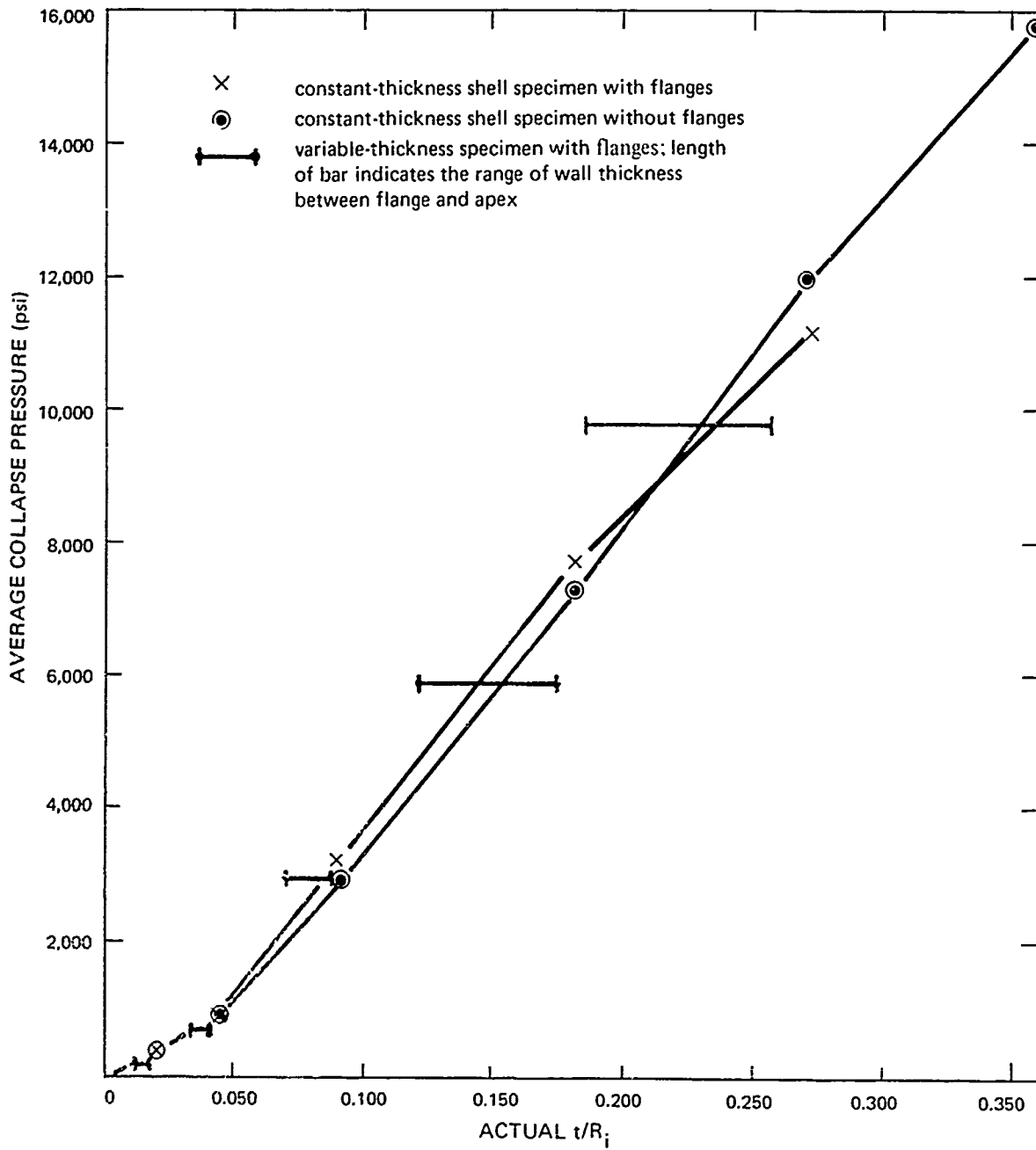


Figure 8. Collapse Pressure Versus  $t/R_i$  Ratio for Hemispherical Shells.

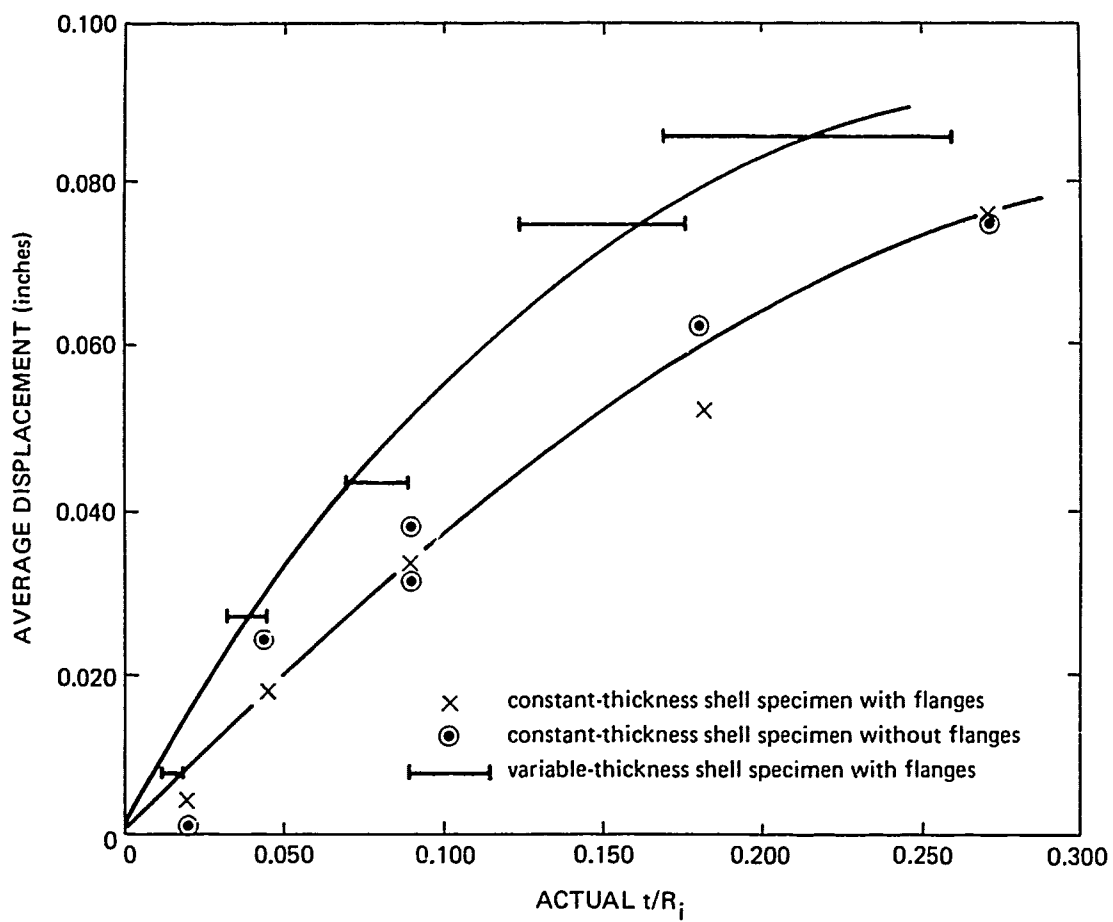


Figure 9. Average Displacement of Hemispherical Acrylic Shells at Approximately 50 Percent of Short-Term Failure Pressure.



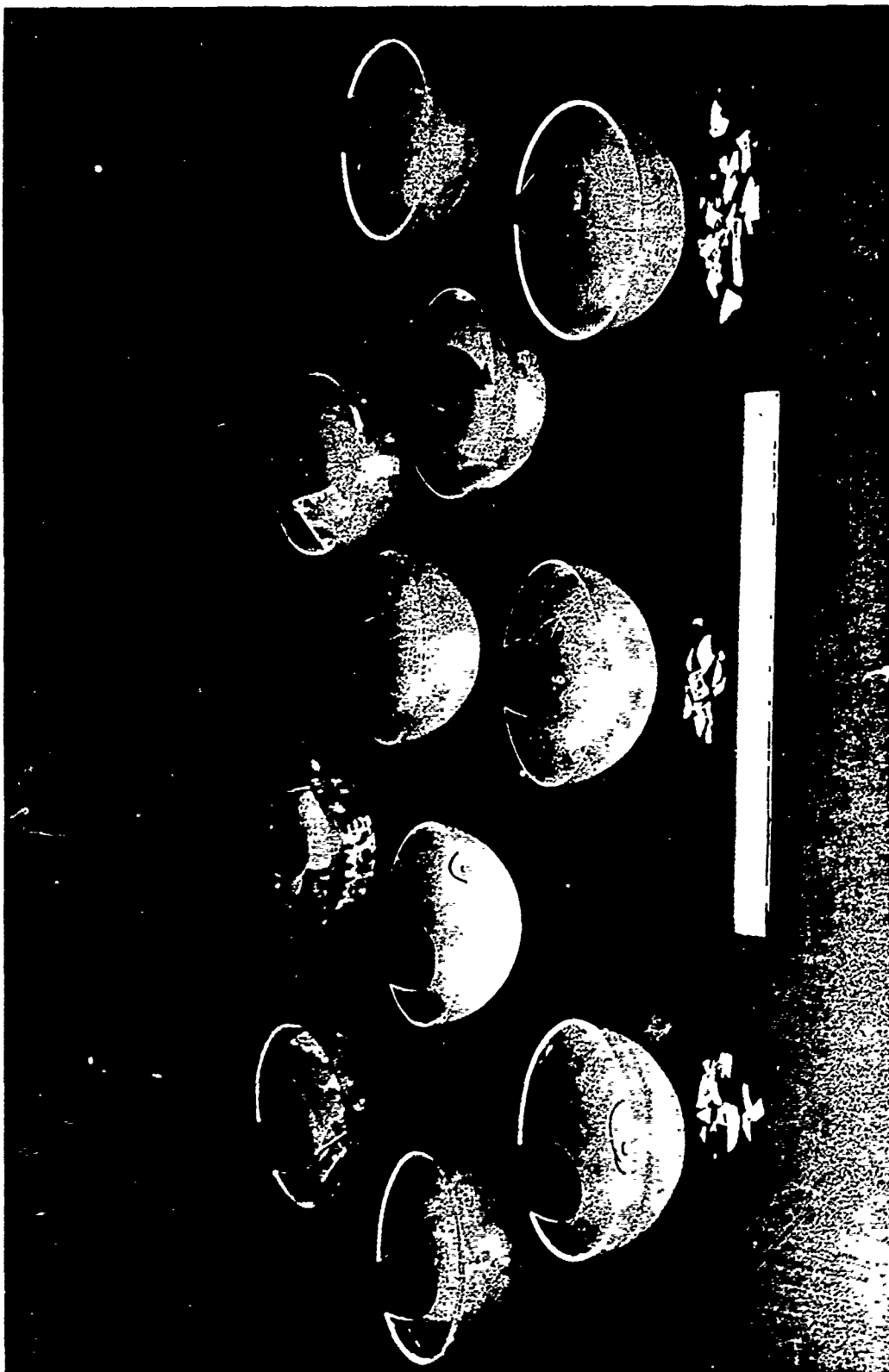


Figure 10. Imploded Flanged and Flangeless Shells of Constant Thickness;  $t/R_i = 0.022$ . Note the regularity of the local failure pattern and the location of its center at 20 degrees of elevation.

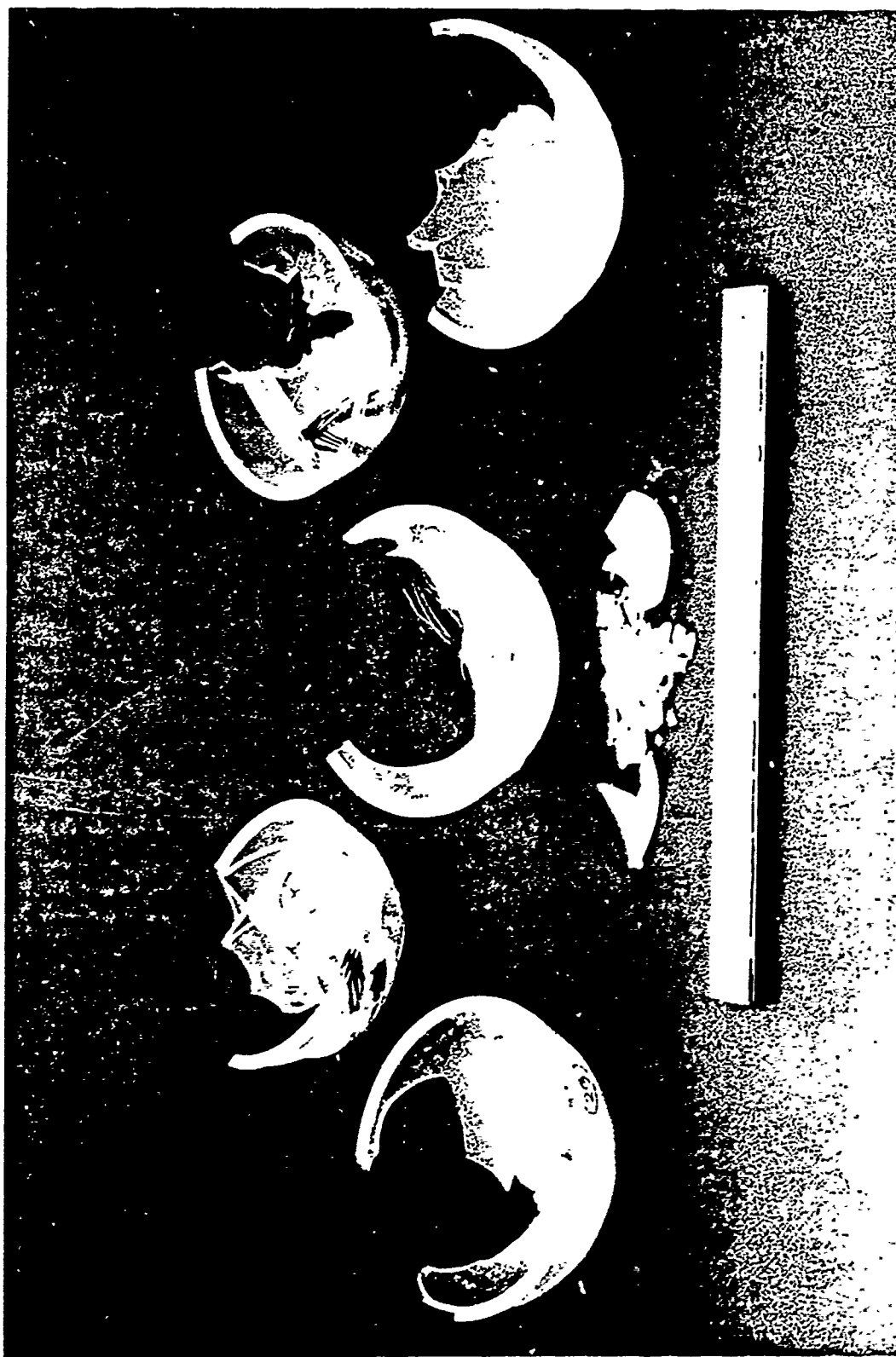


Figure 11. Imploded Flanged Shells of Constant Thickness:  $t/R_1 = 0.046$ . Note the regularity of the local failure pattern and the location of its center at 45 degrees of elevation.



Figure 12. Imploded Flanged Shell of Constant Thickness;  $t/R_1 = 0.182$ . Note that the failure is general rather than local and that the center of the failure pattern is at 90 degrees of elevation. Note that the flange appears to fracture prior to the general implosion. The testing of the shell on the left was terminated after fracturing of flange but prior to general implosion shown at right.



Figure 13. Imploded Flanged Shell of Constant Thickness;  $t/R_i = 0.273$ . Note that the failure is general rather than local. The fragments from this thick shell have been found to be smaller than fragments from thinner shells.

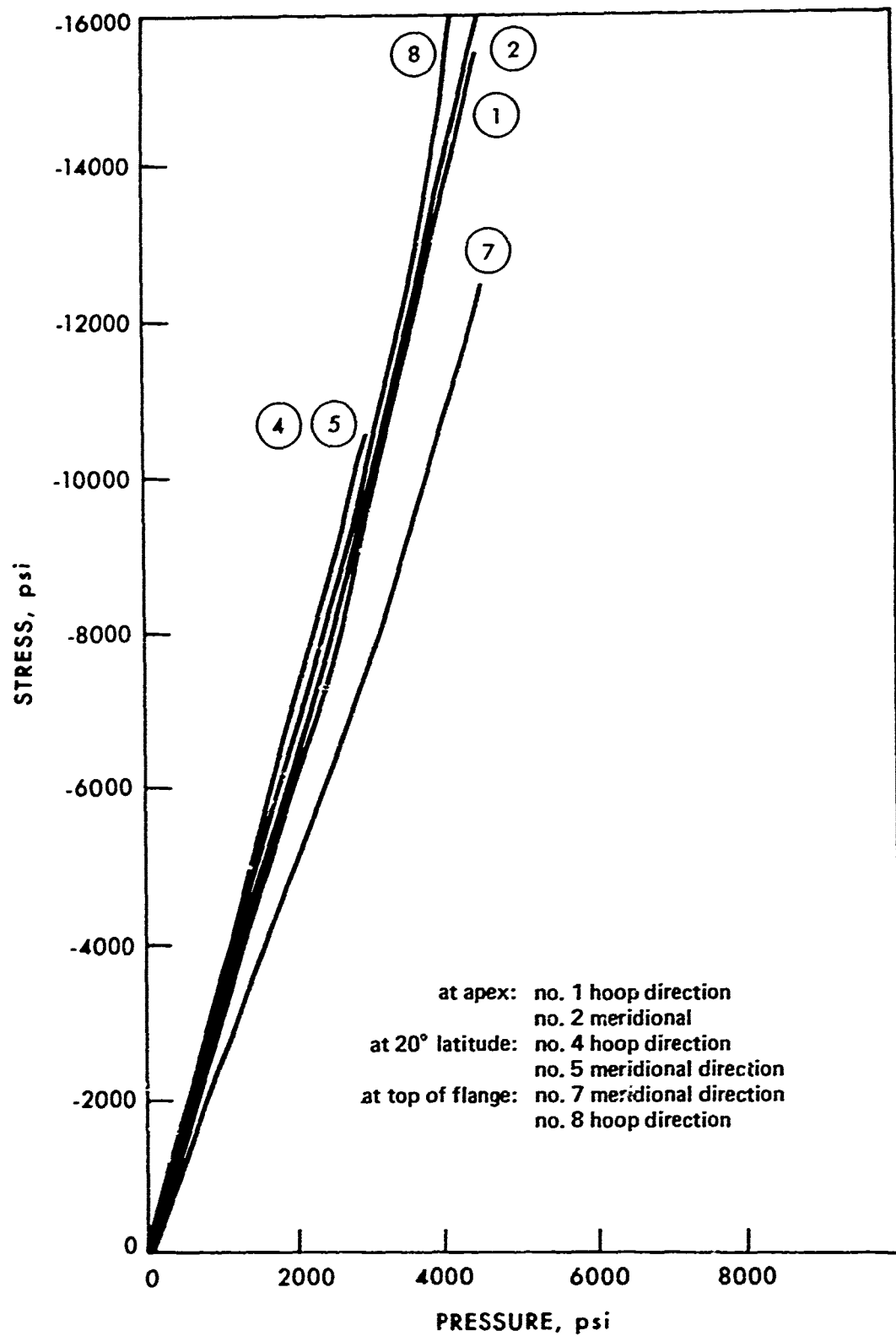


Figure 14. Stress Measured on the Interior of a Flanged Window of Constant Thickness;  $t/R_i = 0.182$ .

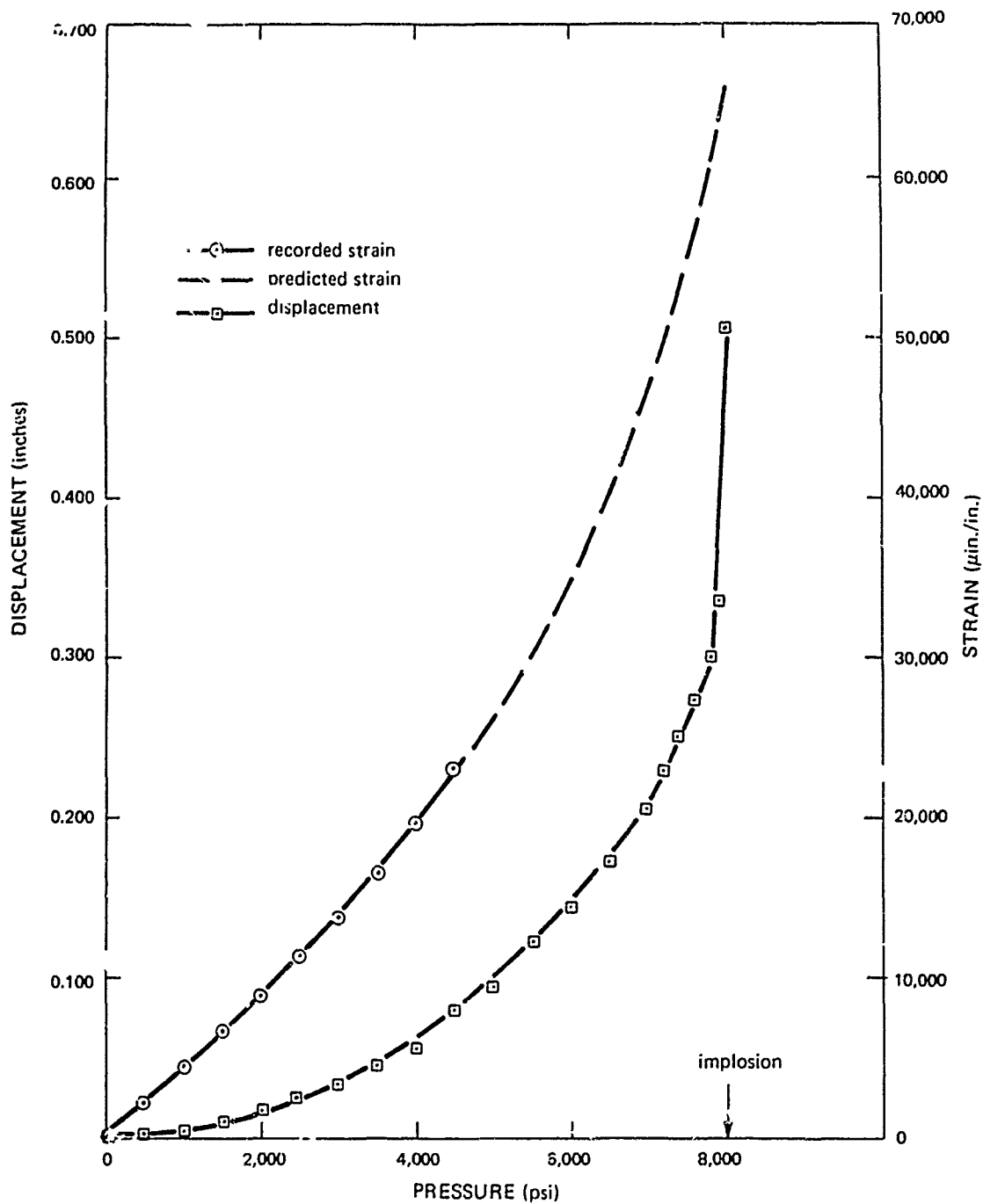


Figure 15. Measured Strain and Displacement at the Apex of Flanged, Constant-Thickness Window With  $t/R_1 = 0.182$ . Strain predictions were based upon data from other window tests.

## ANALYTICAL RESULTS

An elastic finite-element computer analysis of a moderately thick shell ( $t/R_1 = 0.182$ ) was conducted for two different flange boundary conditions. In one case, the flange-bearing surface was free to move in the radial direction; in the other, it was restrained. The computer produced contours of principal stresses, effective stress and effective strain.

The principal stresses were primarily utilized in the comparison of analytical and experimental data. The effective stress, which is an overall measure of stress at a point and is useful for the prediction of initial yielding, is defined as

$$\sigma_{\text{effective}} = \frac{\sqrt{2}}{2} \sqrt{(\sigma_c - \sigma_m)^2 + (\sigma_m - \sigma_r)^2 + (\sigma_r - \sigma_c)^2},$$

where  $\sigma_c, \sigma_m, \sigma_r$  are the circumferential, meridional, and radial principal stresses, respectively. Effective strain combines the principal strains according to the formula

$$\epsilon_{\text{effective}} = \frac{\sqrt{2}}{3} \sqrt{(\epsilon_c - \epsilon_m)^2 + (\epsilon_m - \epsilon_r)^2 + (\epsilon_r - \epsilon_c)^2}$$

and has been suggested as an indicator of plastic collapse in acrylic structures. Although no attempt was made to extend the elastic analyses to the inelastic regime and thereby predict the implosion pressure of the shell, the effective strain plots give an indication as to the probable origin of the failure.

## PRINCIPAL STRESSES

The meridional and circumferential stress contours (figures 16-19) indicate that the stresses at the shell apex are basically the same for both boundary conditions. However, as the shell is traversed from apex to flange, the boundary conditions have an effect on the principal stresses. Both the meridional and circumferential stresses in the unrestrained shell (figures 16 and 17) are fairly uniform and numerically equivalent, whereas the stresses in the restrained shell (figures 18 and 19) differ noticeably from each other and tend to diverge from the unrestrained case. The circumferential stresses decrease and the meridional stresses increase as the restrained flange is approached. Figure 20, which presents only the inside surface stresses, illustrates this divergence clearly.

One of the uses for stress contour plots is to locate stress concentrations. The stress concentration in the unrestrained shell is slight (15-20 percent greater than the nominal apex stress) and is located at the reentrant corner (inset) of the flange, whereas the restrained case produces a minor stress concentration of about a 70-percent increase at the inside corner (heel) of the flange. Neither concentration is judged serious enough to degrade shell performance.

The difference in the principal stresses for the two boundary conditions is readily explained by an examination of the physical processes involved. The freely moving shell acts much like a flangeless hemisphere and therefore the stresses are uniform and nearly equal. Only the meridional stress, which becomes the bearing stress at the flange, differs

from ideal; this is due to the large available bearing surface at the flange, which tends to lower the stress. Restraint of the flange changes the shell behavior markedly. The shell tends to act as two separate segments, the dome and the flange. The dome moves, but the flange is restrained and cannot. Therefore, the circumferential stress, which is generated by the radial movement of the shell, decreases as the restrained flange is approached. The relative movement between the dome and the flange tends to offset the dome and flange center lines, which introduces a bending effect and increases the meridional stress. A final observation is that the stresses for both cases are in agreement within 30 degrees of the apex and therefore the effect of the boundary condition restraint is limited to less than a 60-degree elevation from the flange.

The experimental data has been plotted in figure 20 to allow a visual comparison between the experimental and calculated interior surface stress values. The agreement of the experimental stresses with the free boundary condition stresses is generally quite good with the exception of the meridional stress 20 degrees from the flange. The agreement with the fixed boundary condition is poor except at the apex; therefore, it is concluded that a free boundary condition better describes the structural behavior of a flanged, hemispherical acrylic shell of medium thickness lubricated with silicone grease at the bearing surface than does the fixed boundary condition.

## EFFECTIVE STRESS

The plots of effective stress (figures 21 and 22) support the postulates that the unrestrained shell acts like a flangeless hemisphere and the restrained shell behaves as two separate structures, a hemispherical shell and a restrained ring. The effective stress, which is used to predict initial yielding, indicates that a large portion of the unrestrained shell yields at the same hydrostatic pressure, whereas the restrained shell yields first at the heel of the flange. The pressure at which initial yielding of the restrained shell occurs is about 25 percent lower than the pressure at which yielding begins in a moderately thick shell that is permitted to move freely in the radial direction.

## EFFECTIVE STRAIN

The differences between the two cases largely disappear when one plots only effective strains (figures 23 and 24). Not only do the strain contours agree in location but they also agree in value. These plots suggest that a strain-dependent failure is probable at 45 degrees of elevation in a moderately thick shell.



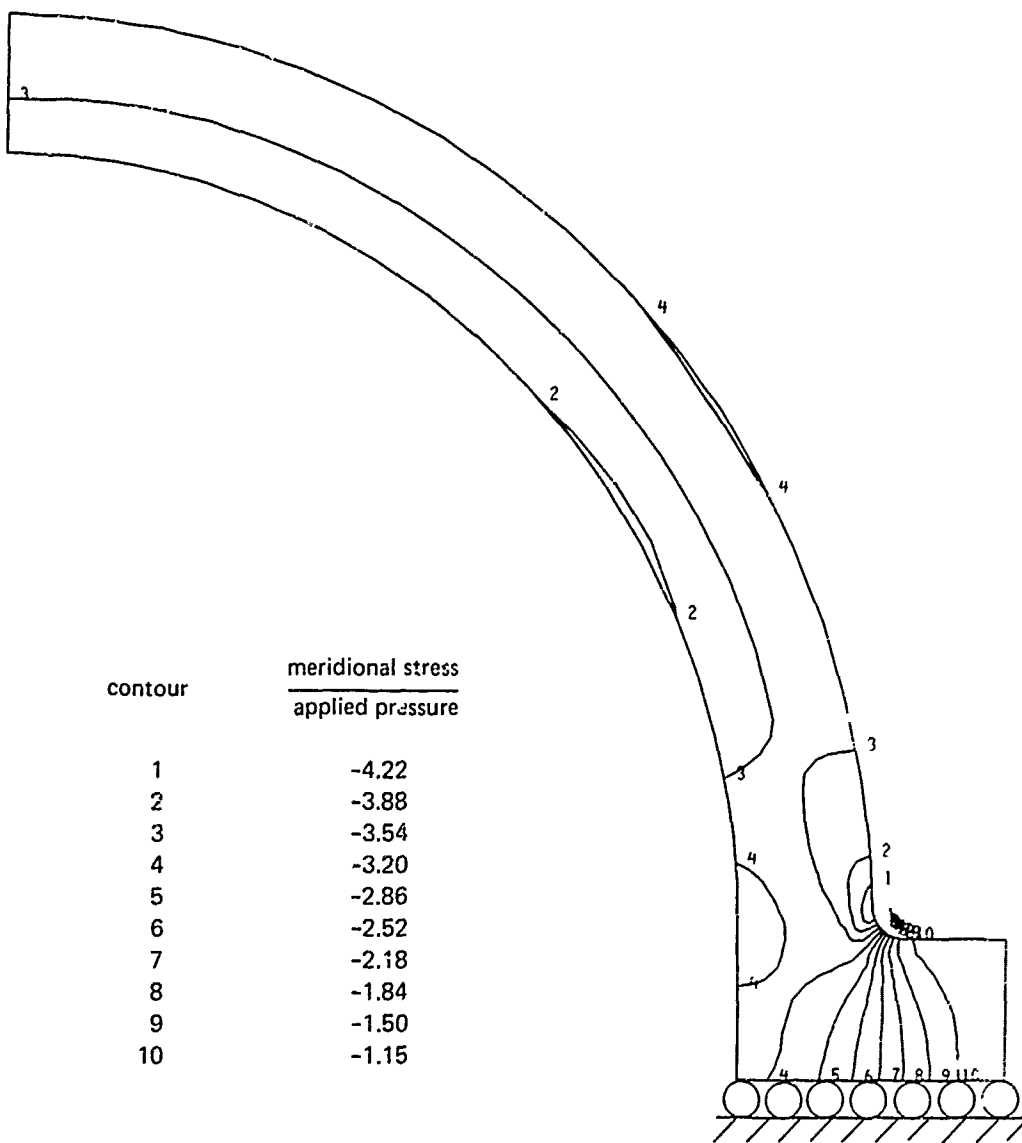


Figure 16. Meridional Stresses in a Flanged Shell of Constant Thickness With Free-Sliding Boundary Condition;  $t/R_i = 0.182$ .

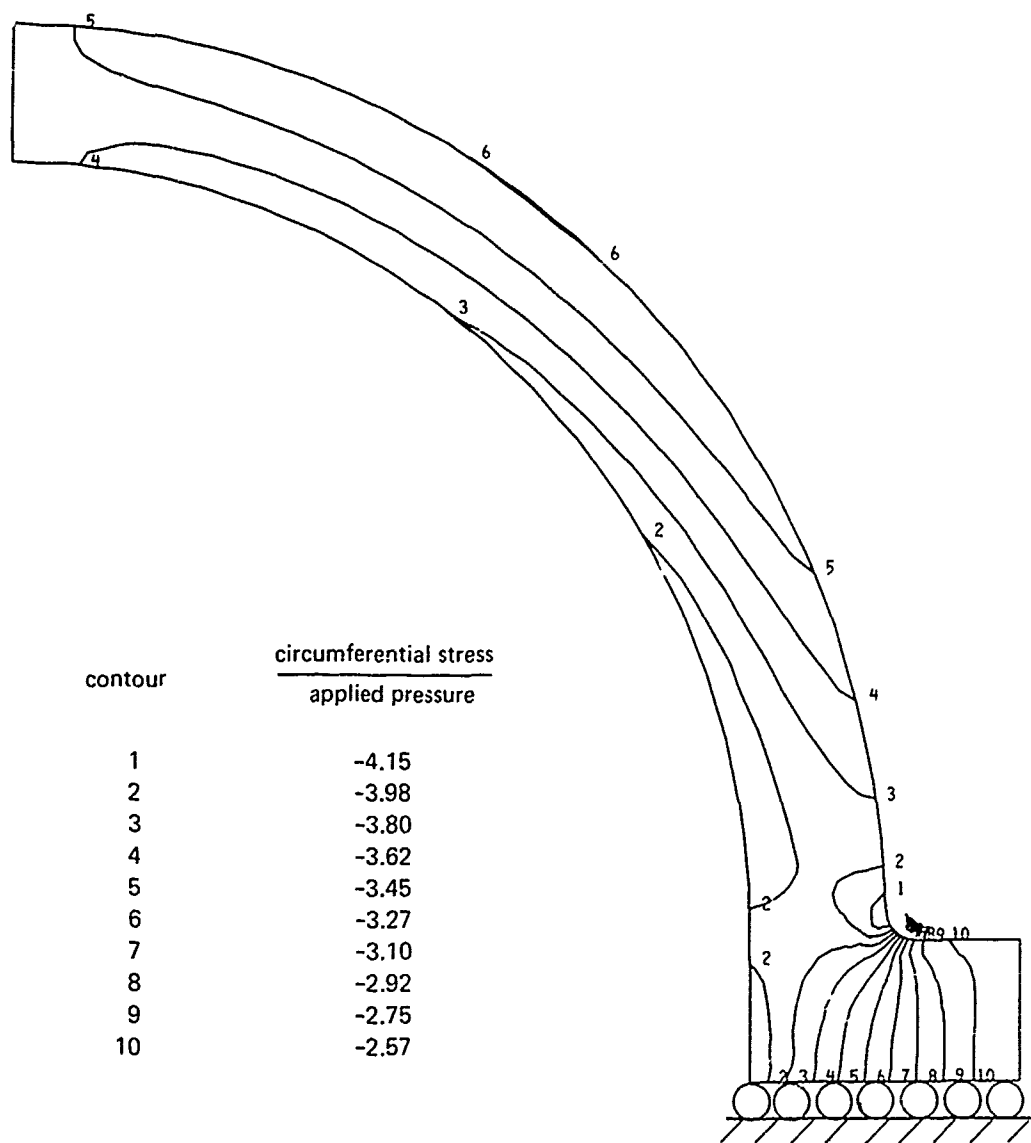


Figure 17. Circumferential Stresses in a Flanged Shell of Constant Thickness with Free-Sliding Boundary Condition;  $t/R_i = 0.182$ .

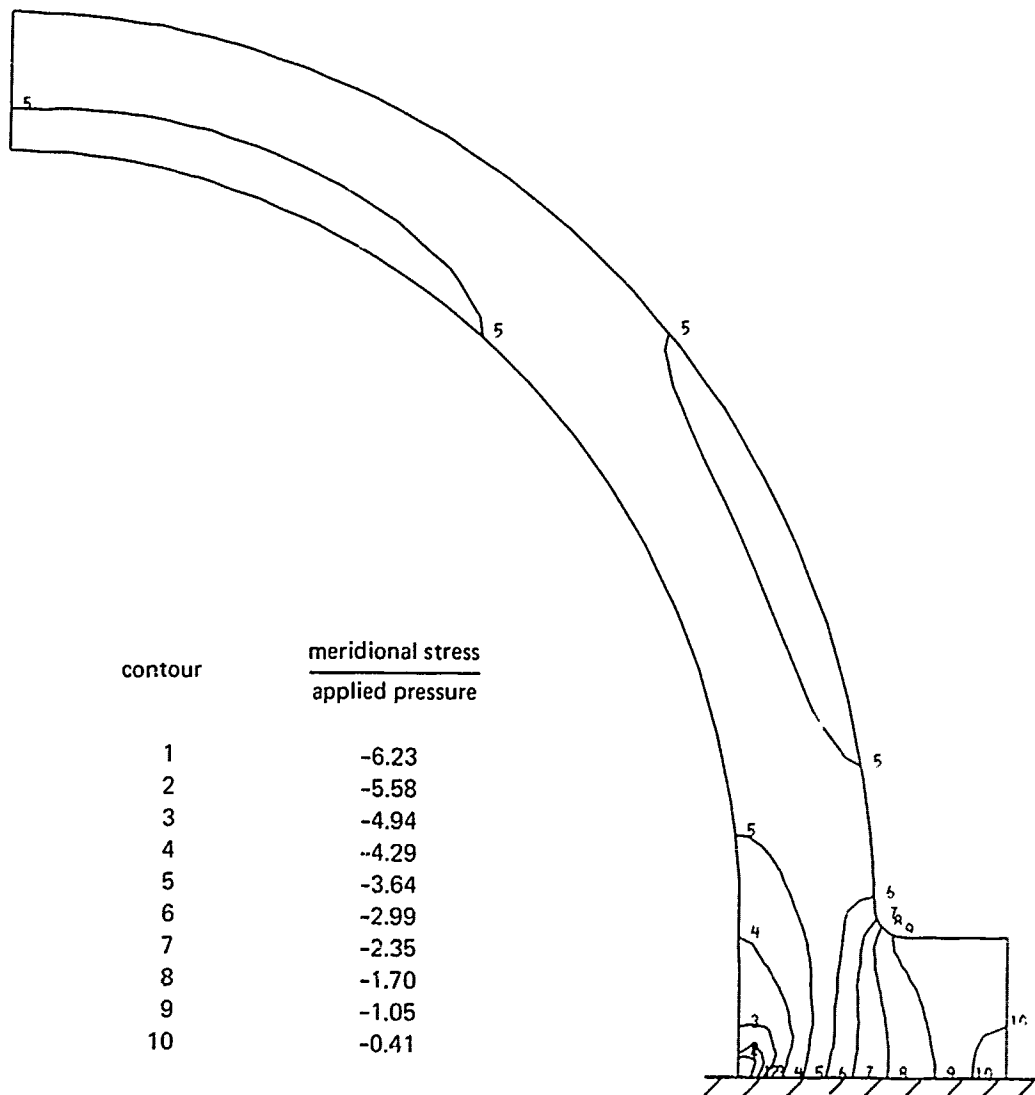


Figure 18. Meridional Stresses in a Flanged Shell of Constant Thickness with Restrained Boundary Condition;  $t/R_i = 0.182$ .

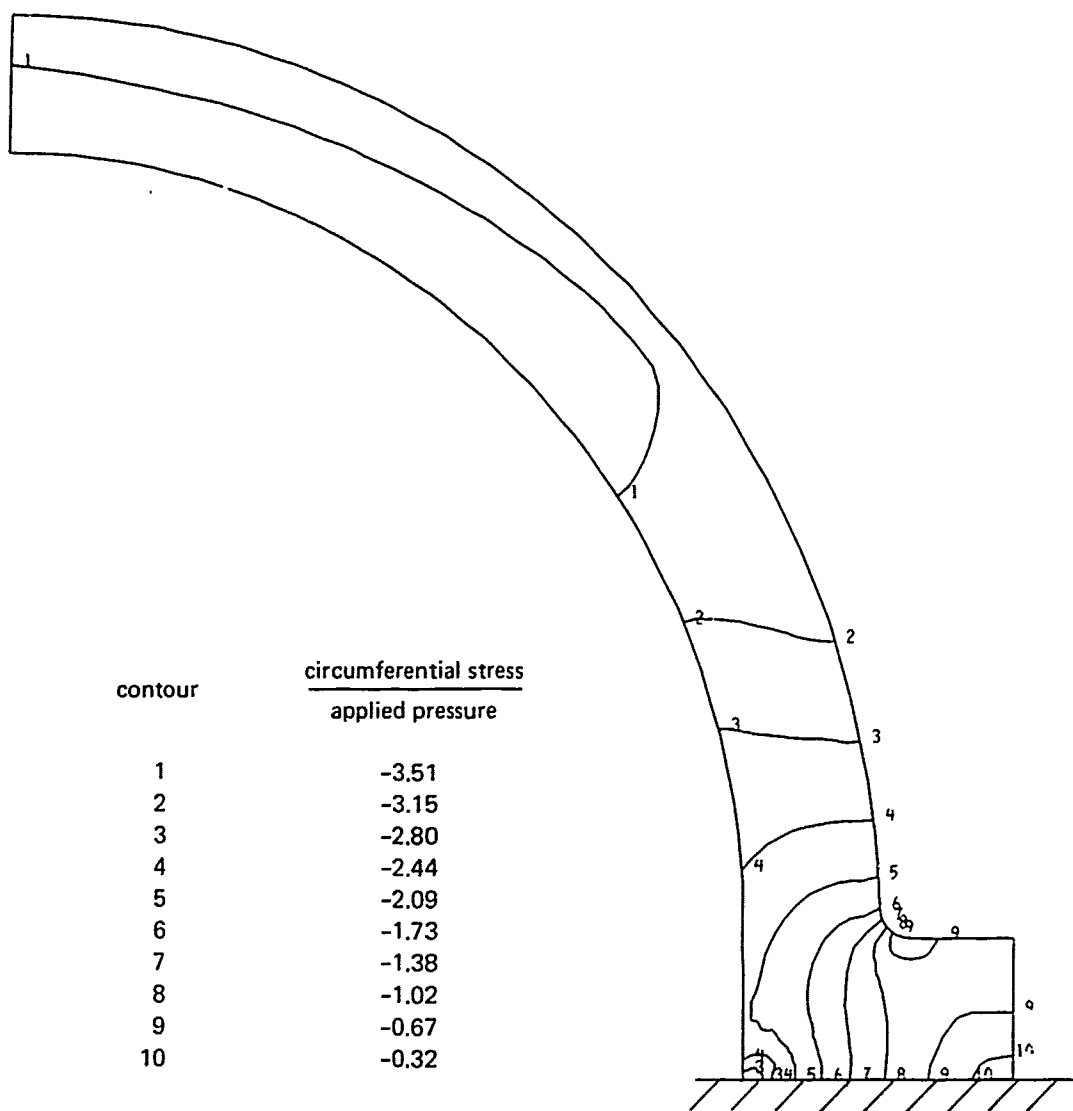


Figure 19. Circumferential Stresses in a Flanged Shell of Constant Thickness With Restrained Boundary Conditions;  $t/R_i = 0.182$ .

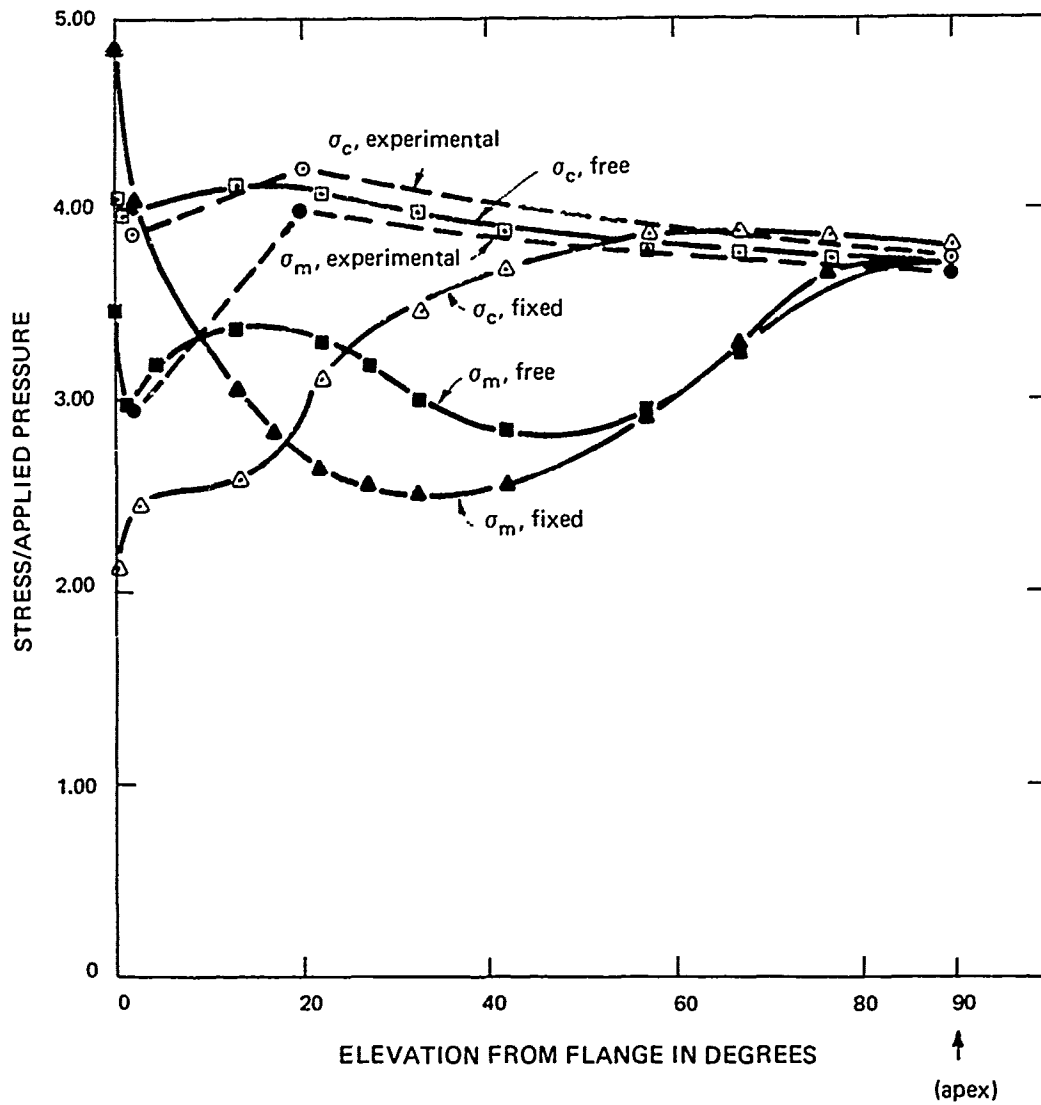


Figure 20. Comparison of Analytical and Experimental Circumferential and Meridional Stresses in a Flanged Acrylic Plastic Hemisphere of Constant Thickness,  $t/R_i = 0.182$ .

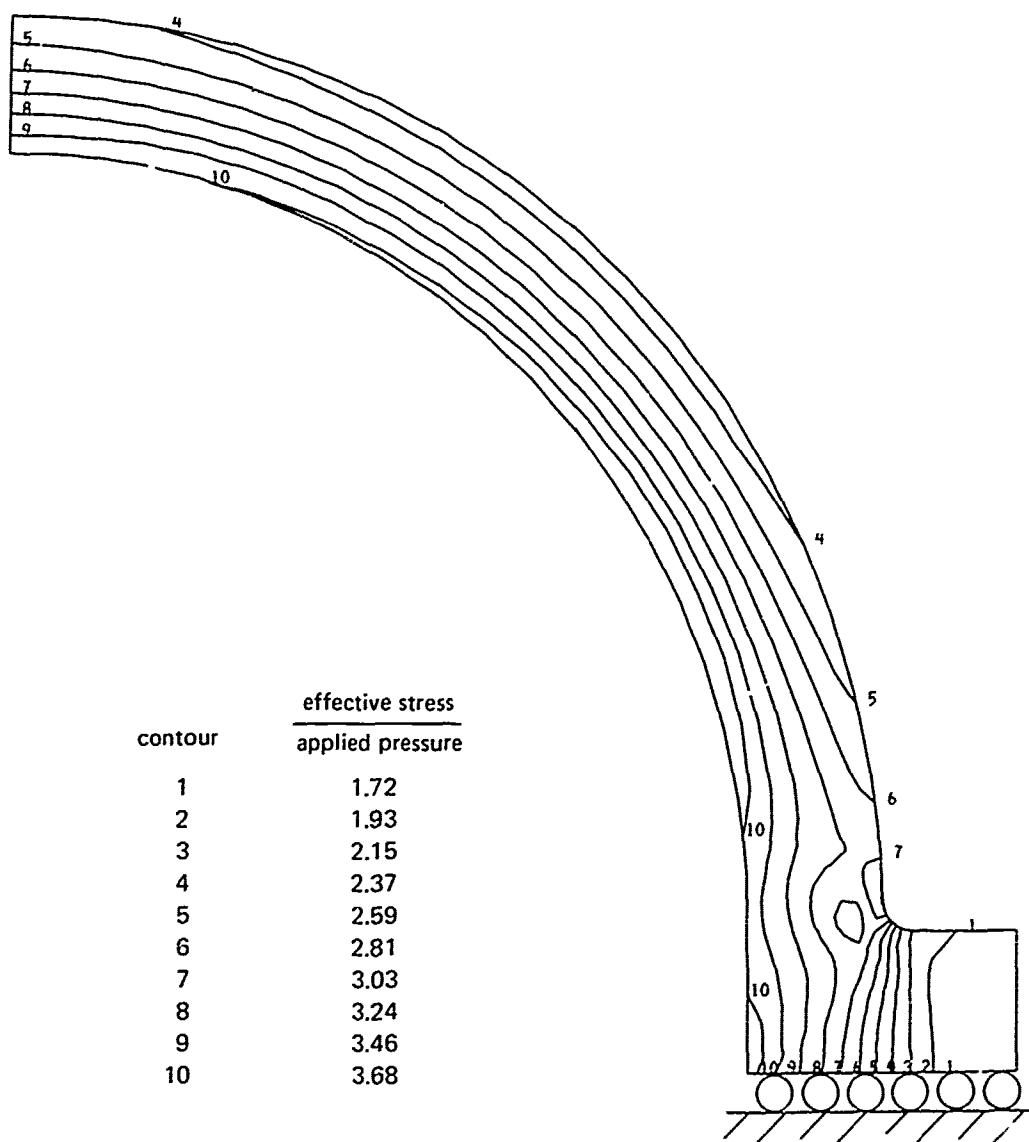


Figure 21. Effective Stresses in a Flanged Shell of Constant Thickness  
With Free-Sliding Boundary Condition:  $t/R_i = 0.182$ .

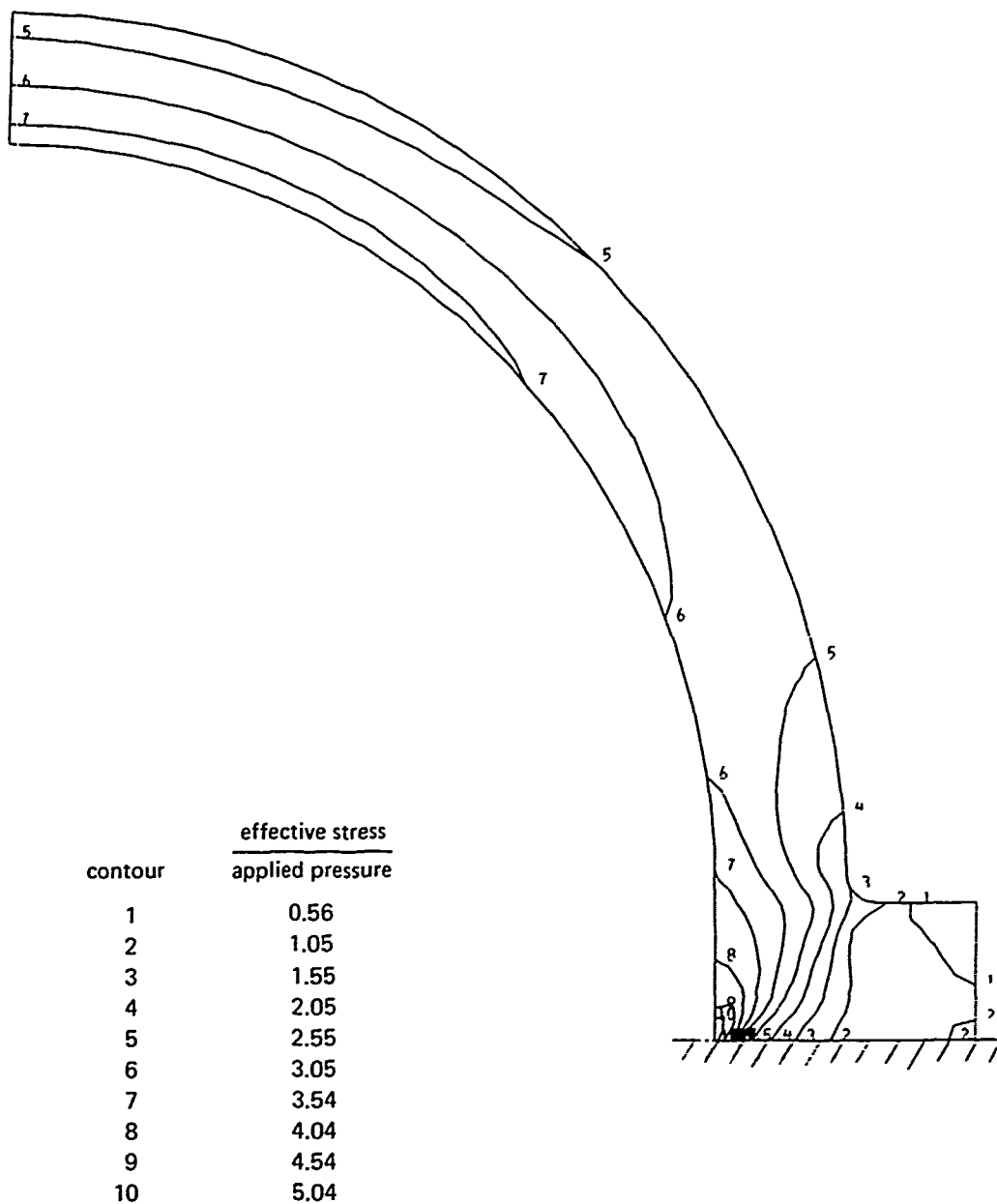


Figure 22. Effective Stresses in a Flanged Shell of Constant Thickness  
With Restrained Boundary Condition;  $t/R_i = 0.182$ .

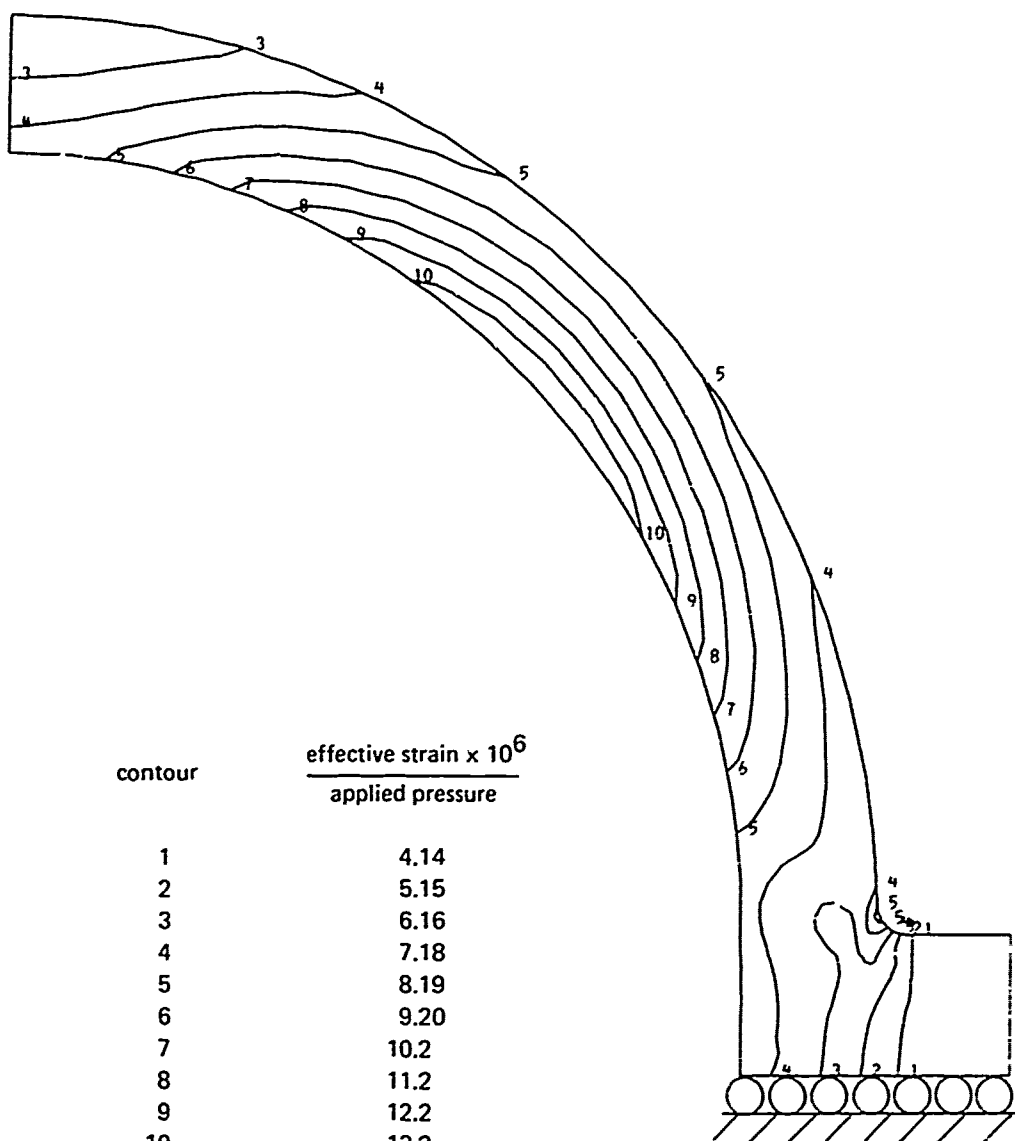


Figure 23. Effective Strains in a Flanged Shell of Constant Thickness  
With Free-Sliding Boundary Condition:  $t/R_i = 0.182$ .



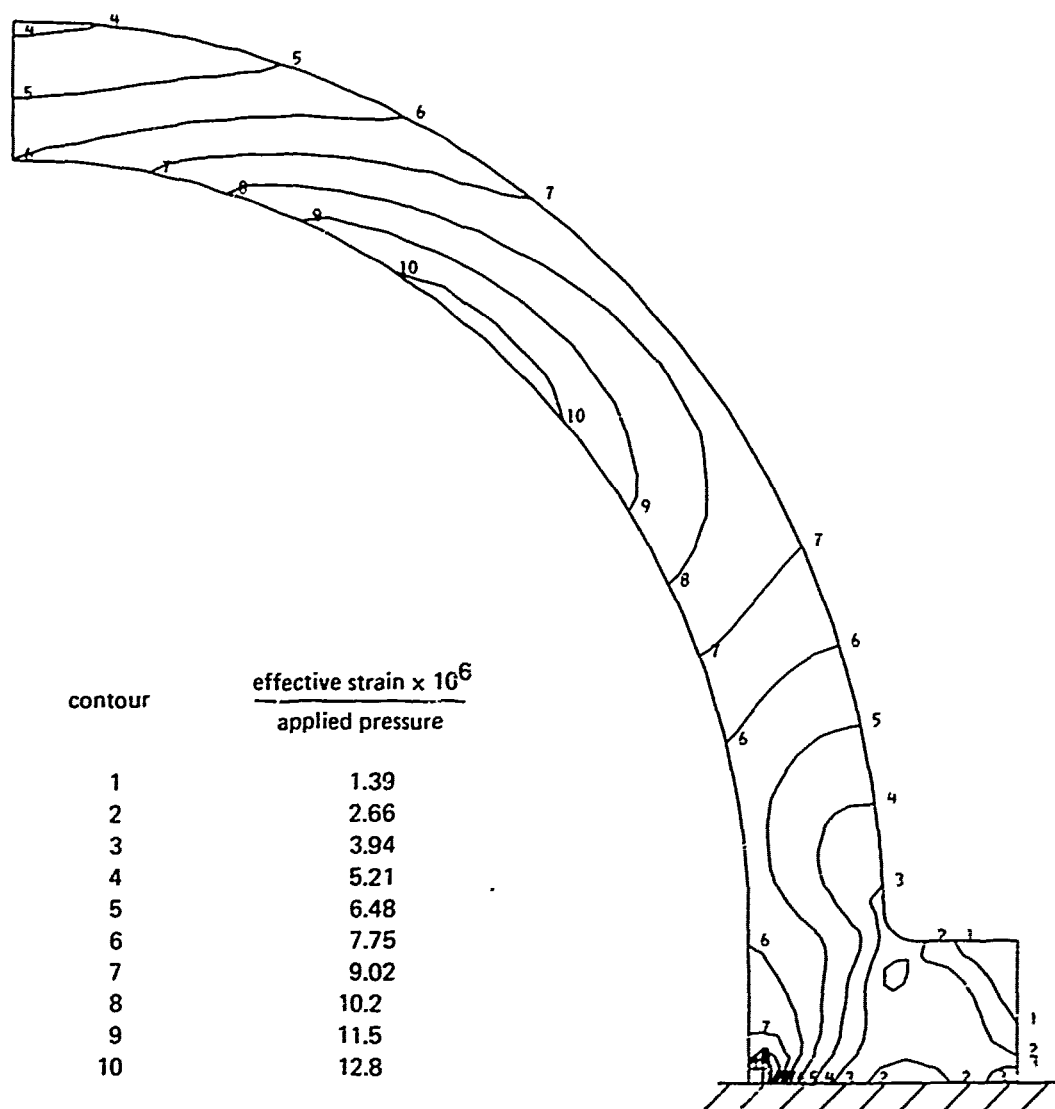


Figure 24. Effective Strains in a Flanged Shell of Constant Thickness  
With Restrained Boundary Condition:  $t/R_i = 0.182$ .

## CONCLUSIONS

1. Under short-term hydrostatic loading, the implosion pressure of hemispherical shells of uniform thickness with an equatorial flange (whose width and thickness are equal to shell thickness) did not differ significantly from that of similar hemispherical shells without an equatorial flange unless the  $t/R_i$  ratio was greater than 0.200. For shells with  $t/R_i > 0.200$ , the flange appears to reduce the collapse pressure by about 10 percent.
2. The short-term collapse pressure of hemispherical shells of variable thickness (maximum variation of 35 percent) can be fairly well predicted from data for windows of constant thickness if the mean thickness of the shell is used rather than the nominal  $t/R_i$  ratio at the flange.
3. Apex displacements for shells of constant thickness loaded to 50 percent of the collapse pressure are independent of the presence of an equatorial flange. The apex displacements of shells of variable thickness are approximately 35 to 45 percent greater than the apex displacement of constant thickness shells.
4. Stresses were linear to at least 50 percent of collapse pressure for all shells.
5. The finite-element computer model that allowed the flange to move freely in the radial direction produced stresses that agreed reasonably well with the experimentally derived stresses and also gave insight into the mode of shell failure.

## RECOMMENDATIONS

1. In the prediction of critical pressures for hemispherical shells of nonuniform thickness, it is conservative to use the minimum thickness found at the apex of the shell rather than its mean thickness because the variation in shell thickness may be more than the 35 percent typical for the experimental data described in this report.
2. Equatorial flanges can be incorporated (reference 9) into the hemispherical shell for ease of mounting providing that (a) the instep has a reasonable radius, (b) the heel is square, (c) the width and thickness of the flange are equal to the nominal shell thickness, (d) the top surface of the flange is the equatorial plane of the hemisphere, and (e) the  $t/R_i$  ratio of the hemisphere is less than 0.2.

## REFERENCES

1. J. D. Stachiw. Critical Pressure of Conical Acrylic Windows Under Short Term Hydrostatic Loading. ASME Transactions: Journal of Engineering for Industry. Volume 89, No. 3, 1967. Also published as Technical Report R-512 by the U. S. Naval Civil Engineering Laboratory, Port Hueneme, California, 1967.
2. J. D. Stachiw. Critical Pressure of Flat Acrylic Windows Under Short Term Hydrostatic Loading. ASME Paper No. 67-WA/Unt-1, 1967. Also published as Technical Report R-512 by the U. S. Naval Civil Engineering Laboratory, Port Hueneme, California, 1967.
3. J. D. Stachiw. Critical Pressure of Spherical Shell Acrylic Windows Under Short Term Pressure Loading. ASME Transactions: Journal of Engineering for Industry. Volume 91, No. 3, 1969. Also published as Technical Report R-631 by the U. S. Naval Civil Engineering Laboratory, Port Hueneme, California, 1967.
4. C. Wright. Development of a Large Spherical Acrylic Viewport For the PC8B Submarine. ASME Paper No. 71-WA/Unt-4, 1971.
5. J. D. Stachiw and K. O. Gray. Procurement of Safe Viewports for Hyperbaric Chambers. ASME Transactions: Journal of Engineering for Industry. Volume 93, No. 4, 1971.
6. J. R. Maison and J. D. Stachiw. Acrylic Pressure Hull for Johnson Sea-Link Submersible. ASME Paper No. 71-WA/Unt-6, 1971.
7. E. L. Wilson. Structural Analysis of Axisymmetric Solids. American Institute of Aeronautics and Astronautics, Journal. Vol. 3, No. 12, December 1965.
8. J. D. Stachiw. Spherical Acrylic Pressure Hulls for Undersea Exploration. ASME Transactions: Journal of Engineering for Industry. Vol. 93, No. 2, 1971.
9. J. D. Stachiw. Acrylic Hemispheres for NUC Undersea Elevator. ASME Paper No. 72-WA/Oct-4, 1972. Also published as NUC Technical Report 315, Acrylic Plastic Hemispherical Shells for NUC Undersea Elevator, by the Naval Undersea Center, San Diego, California, September 1972.

## **APPENDIX. RESULTS OF HYDROSTATIC TESTS**

This appendix presents axial displacements as well as strains and stresses recorded during hydrostatic testing of windows to implosion.

### **EXPERIMENTAL DISPLACEMENTS**

Displacements measured for flanged shells of constant and varying thickness are plotted versus pressure in figures A.1-A.4. Tables A.1-A.12 follow and present displacements measured for individual specimens of flanged shells of constant and varying thickness and for flangeless shells of constant thickness.

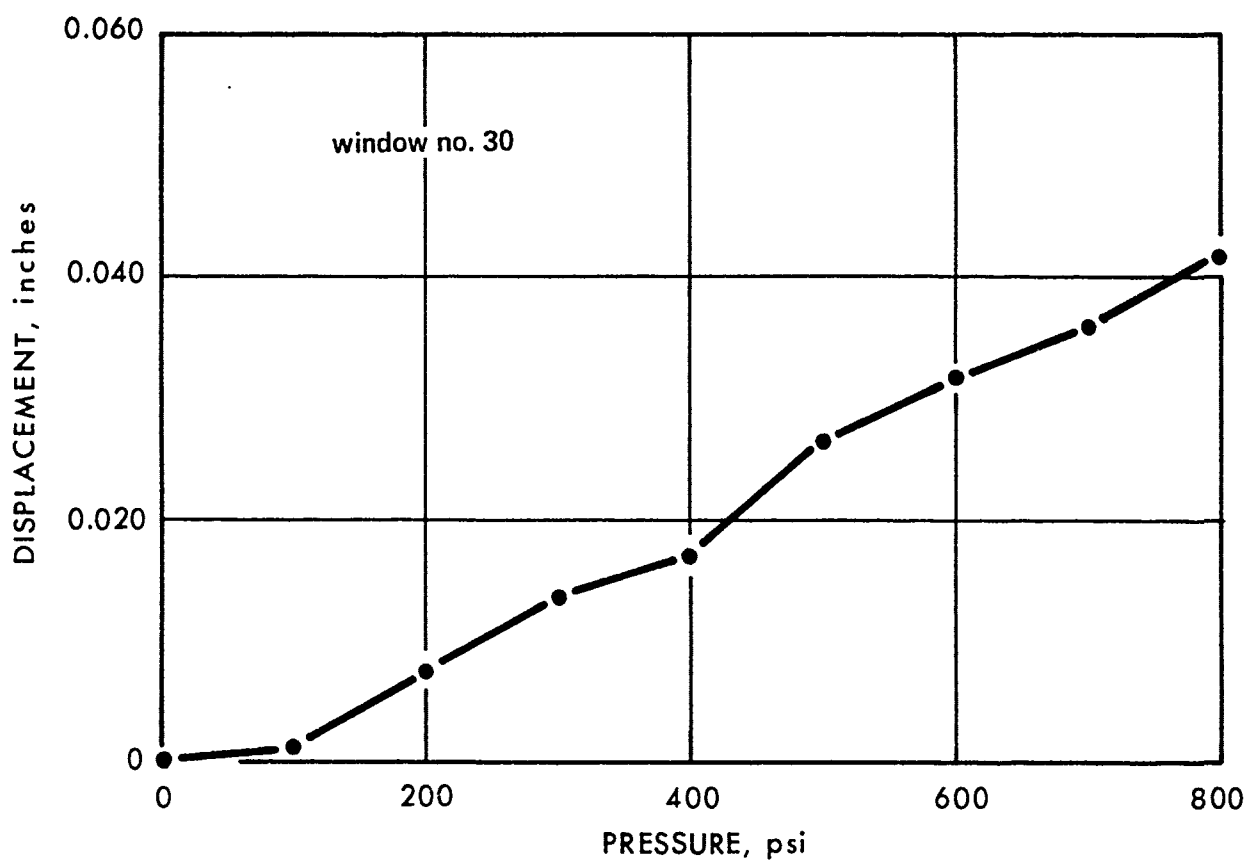


Figure A.1.A. Axial Displacement of a Flanged Shell of Variable Thickness ( $t/R_1 = 0.046$ ).

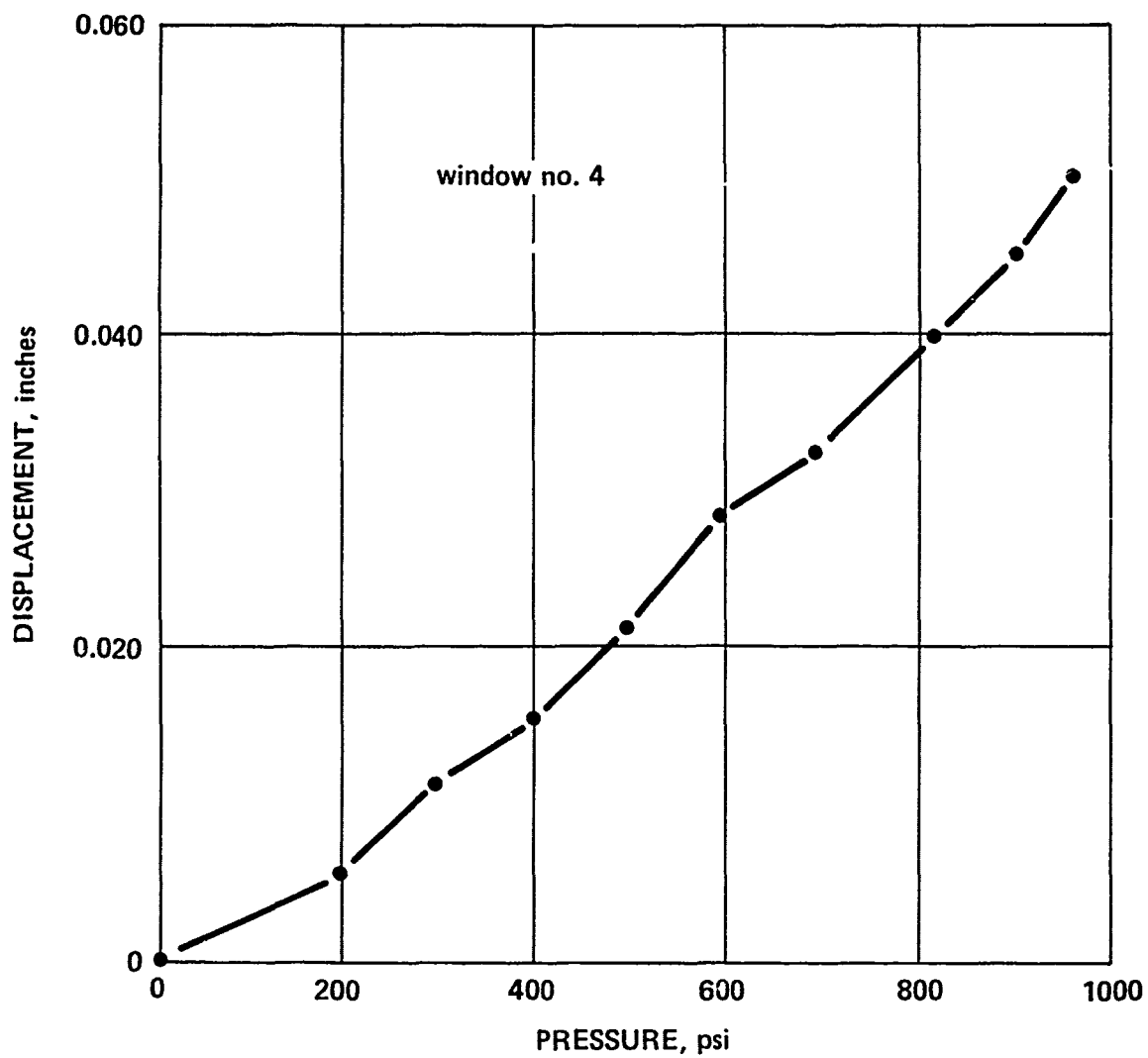


Figure A.1.B. Axial Displacement of a Flanged Shell of Constant Thickness ( $t/R_1 = 0.046$ ).

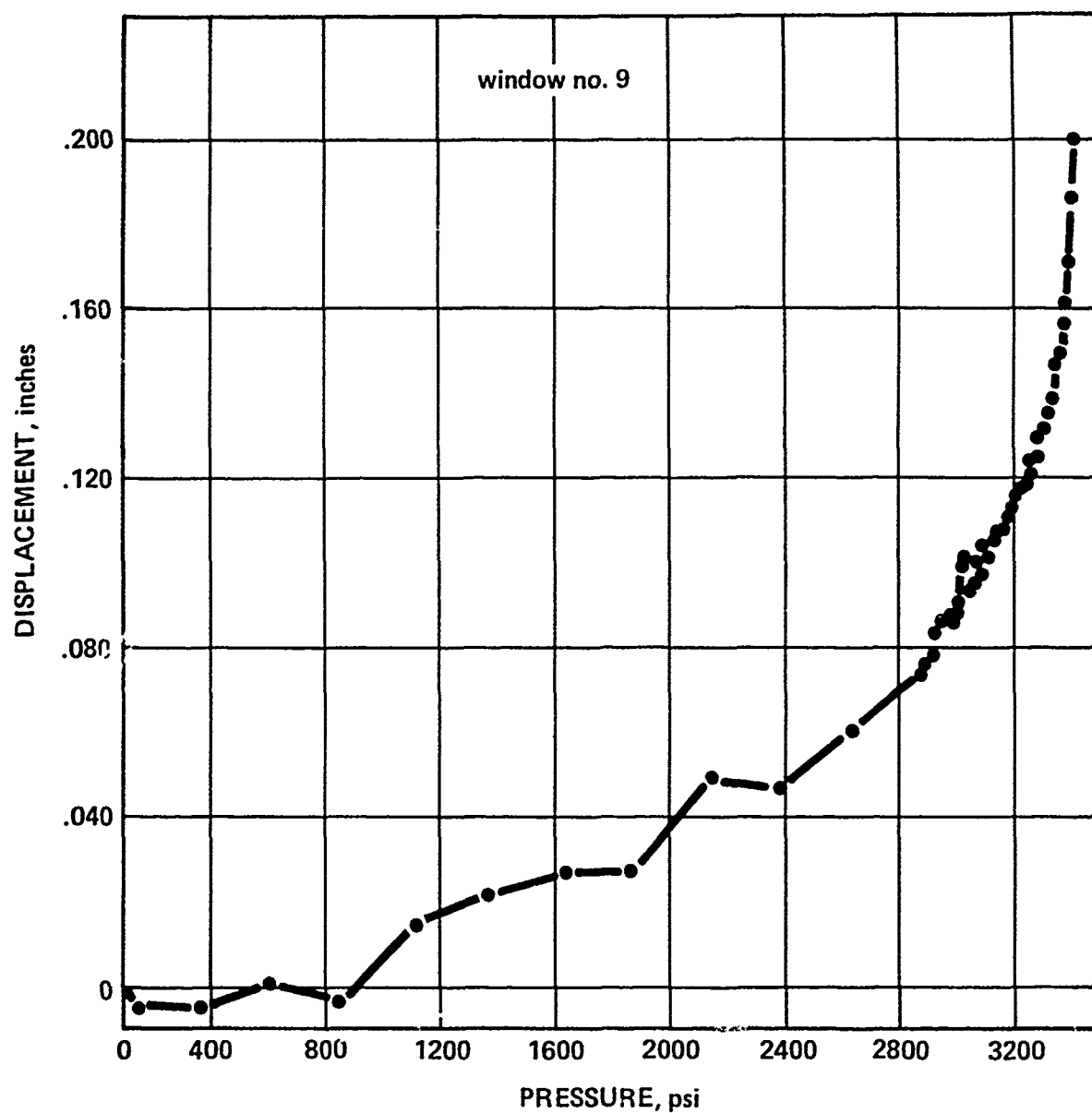


Figure A.2.A. Axial Displacement of a Flanged Shell of Constant Thickness ( $t/R_i = 0.091$ ).

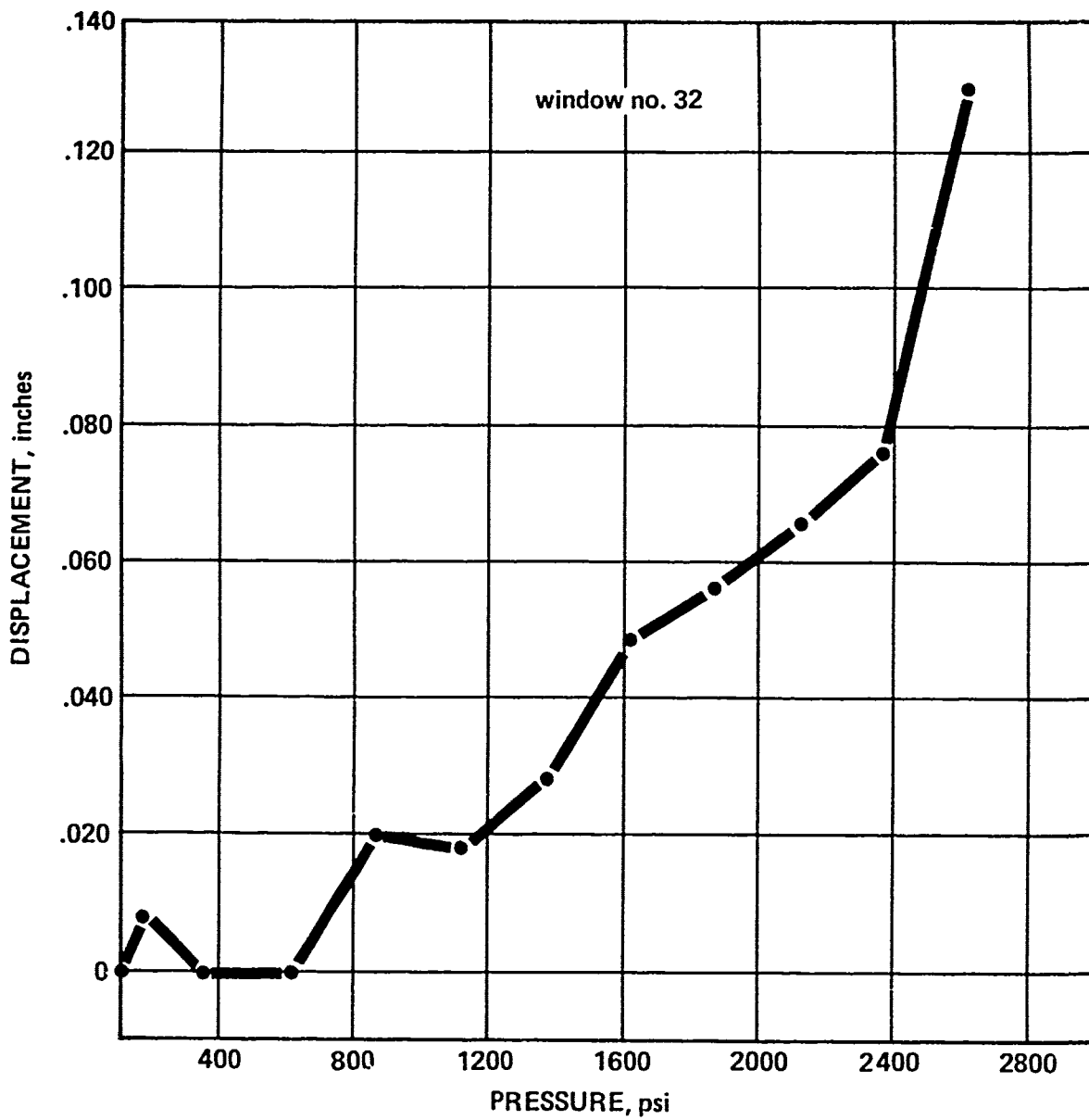


Figure A.2.B. Axis' Displacement of a Flanged Shell of Variable Thickness ( $t/R_1 = 0.091$ ).



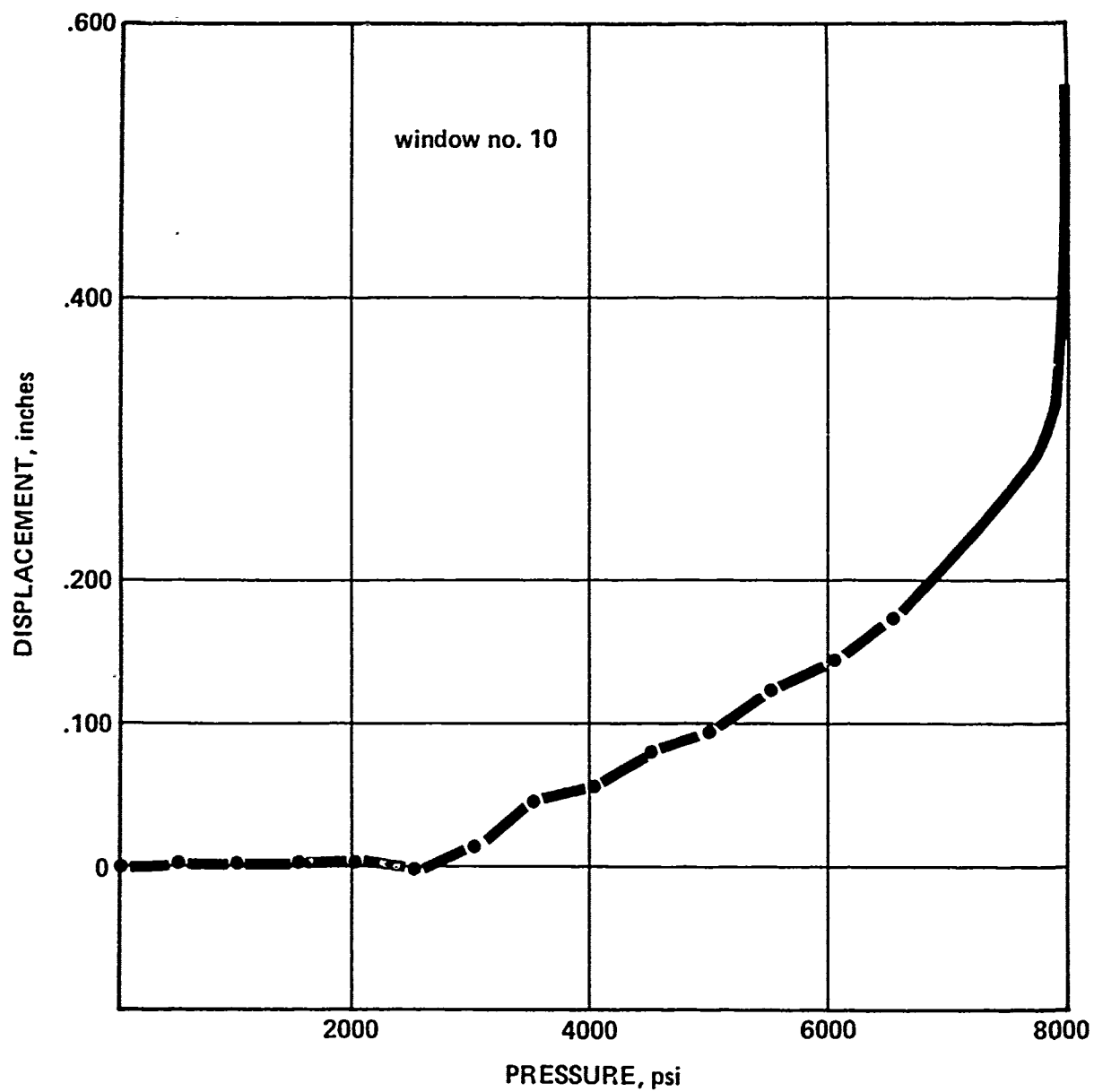


Figure A.3.A. Axial Displacement of a Flanged Shell of Constant Thickness ( $t/R_i = 0.182$ ).

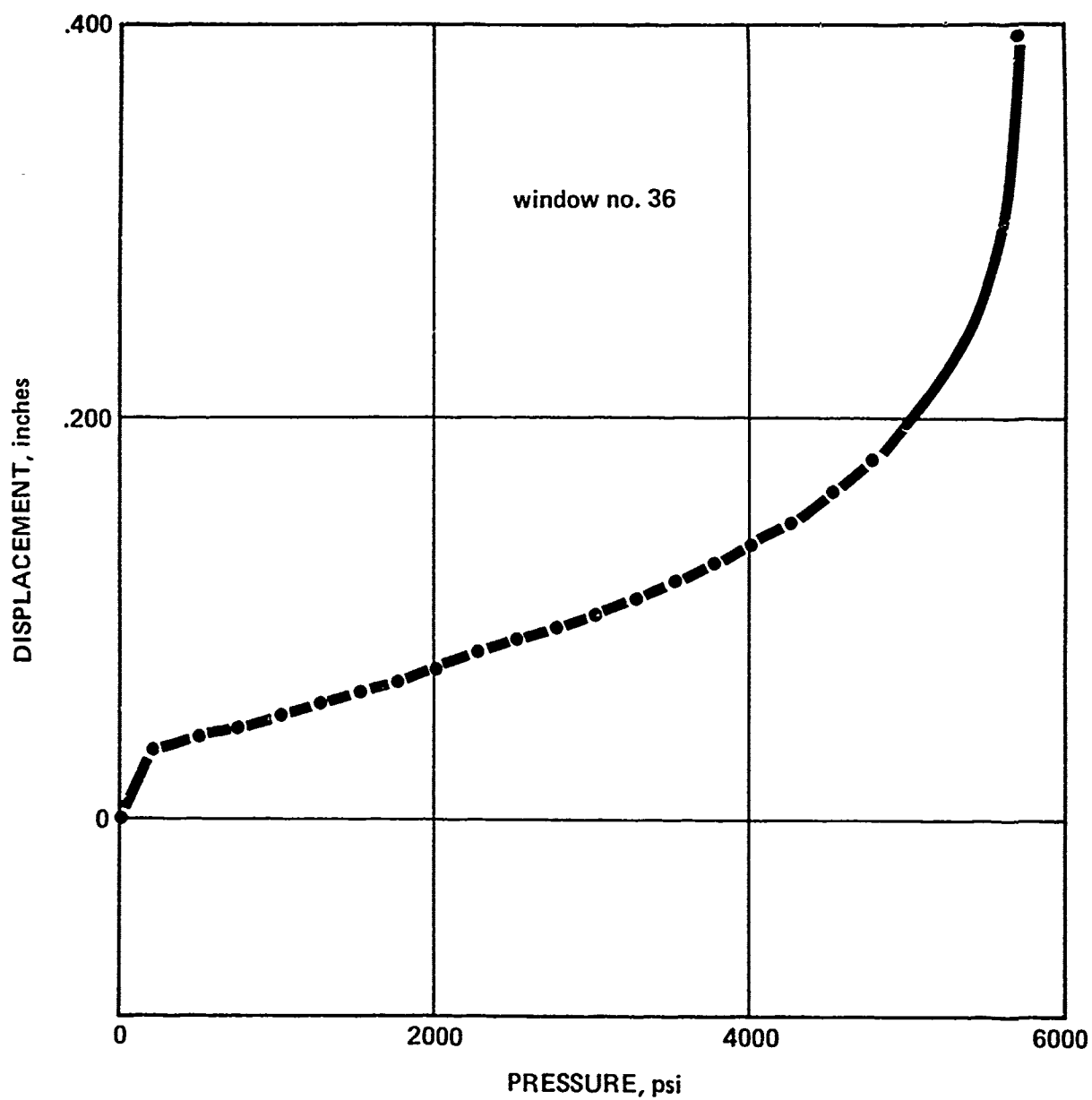


Figure A.3.B. Axial Displacement of a Flanged Shell of Variable Thickness ( $t/R_1 = 0.182$ ).

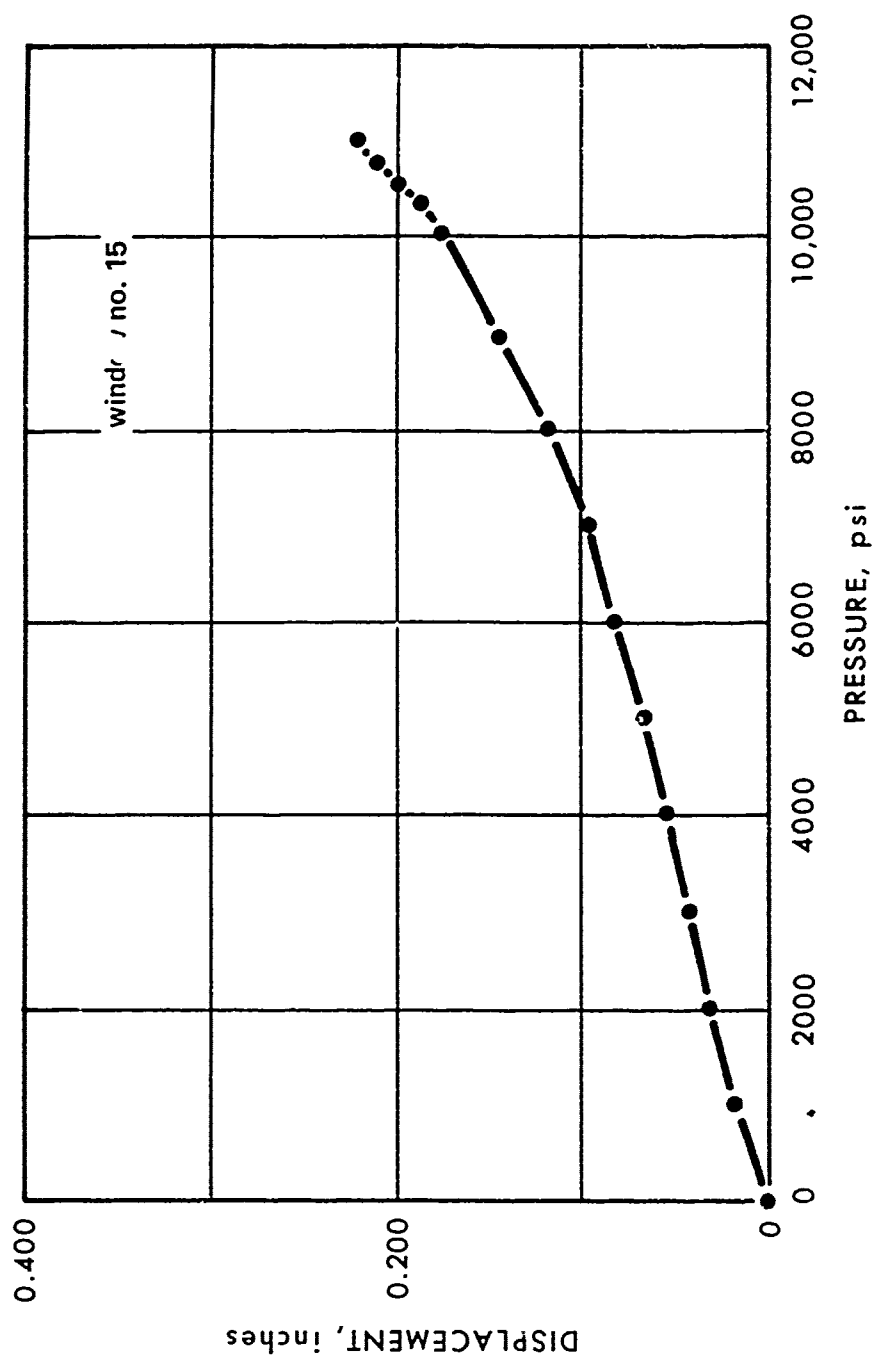


Figure A.4.A. Axial Displacement of a Flanged Shell of Constant Thickness ( $t/R_i = 0.273$ ).

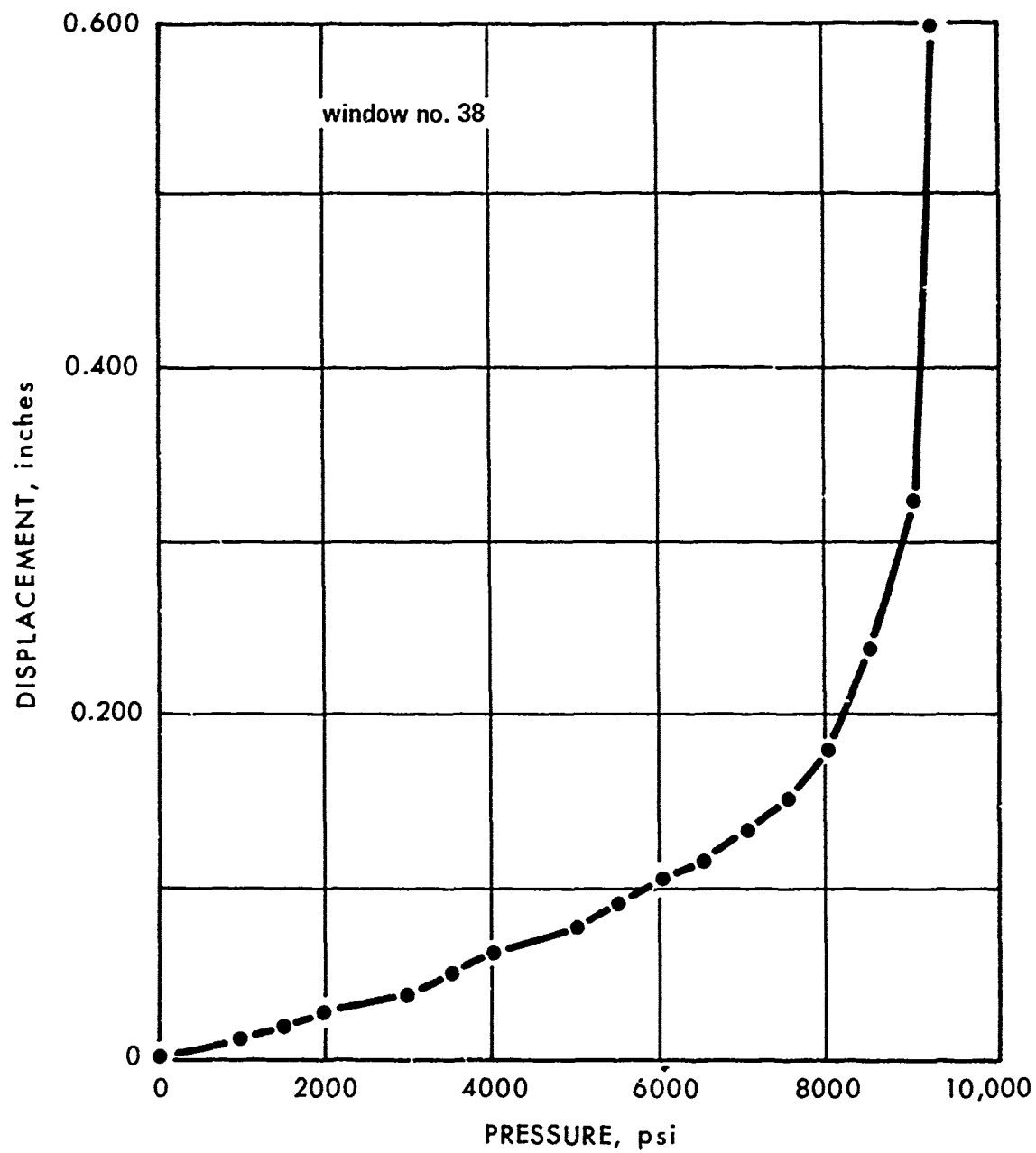


Figure A.4.B. Axial Displacement of a Flanged Shell of Variable Thickness ( $t/R_i = 0.273$ ).

Table A.1. Displacement of Apex Measured on a Flanged Hemisphere of Constant Thickness (# 3) Under Short-Term Hydrostatic Loading. Nominal  $t/R_i = 0.023$ ; Actual thickness of flange = 0.062 in., of apex = 0.069 in.; Temperature = 65°F; Pressurization rate = 82 psi/minute.

Pressure (psi)	0	10	20	30	40	50
Displacement (inches)	0.00	0.00	0.010	0.010	0.020	0.020
Pressure (psi)	60	70	80	90	100	110
Displacement (inches)	0.003	0.003	0.004	0.004	0.005	0.005
Pressure (psi)	120	130	140	150	160	170
Displacement (inches)	0.006	0.007	0.009	0.009	0.011	0.013
Pressure (psi)	200	220	250			
Displacement (inches)	0.014	0.017	0.021			

Table A.2. Displacement of Apex Measured on a Flanged Hemisphere of Constant Thickness (# 5) Under Short-Term Hydrostatic Loading. Nominal  $t/R_i = 0.046$ ; Actual Thickness of flange = 0.116 in., of apex = 0.113 in.; Temperature = 60°F; Pressurization rate = 100 psi/minute.

Pressure (psi)	0	50	100	150	200	250
Displacement (inches)	0.000	0.000	0.002	0.003	0.005	0.007
Pressure (psi)	300	350	400	450	500	550
Displacement (inches)	0.012	0.013	0.016	0.019	0.022	0.025
Pressure (psi)	600	650	700	750	800	850
Displacement (inches)	0.028	0.030	0.033	0.035	0.038	0.042
Pressure (psi)	900	950	955			
Displacement (inches)	0.045	0.049	0.052			

Table A.3. Displacement of Apex Measured on a Flanged Hemisphere of Constant Thickness (# 8) Under Short-Term Hydrostatic Loading. Nominal  $t/R_i = 0.091$ : Actual thickness of flange = 0.249 in., apex = 0.256 in.; Temperature = 62°F: Pressurization rate = 100 psi/minute.

Pressure (psi)	0	50	100	200	300	400
Displacement (inches)	0.000	0.000	0.000	0.002	0.006	0.008
Pressure (psi)	500	600	700	800	900	1000
Displacement (inches)	0.012	0.013	0.015	0.017	0.017	0.017
Pressure (psi)	1100	1200	1300	1400	1500	1600
Displacement (inches)	0.020	0.027	0.031	0.031	0.034	0.039
Pressure (psi)	1700	1800	1900	2000	2100	2200
Displacement (inches)	0.042	0.045	0.048	0.054	0.056	0.058
Pressure (psi)	2300	2400	2500	2600	2700	2800
Displacement (inches)	0.060	0.067	0.073	0.083	0.092	0.098
Pressure (psi)	2900	3000	3100			
Displacement (inches)	0.106	0.125	0.150			

Table A.4. Displacement of Apex Measured on a Flanged Hemisphere of Constant Thickness (# 11) Under Short-Term Hydrostatic Loading. Nominal  $t/R_i = 0.182$ : Actual thickness of flange = 0.503 in., of apex = 0.505 in.; Temperature = 56°F: Pressurization rate = 500 psi/minute.

Pressure (psi)	0	250	500	750	1000	1250
Displacement (inches)	0.000	0.008	0.012	0.014	0.022	0.025
Pressure (psi)	1500	1750	2000	2250	2500	2750
Displacement (inches)	0.029	0.037	0.041	0.045	0.048	0.052
Pressure (psi)	3000	3250	3500	3750	4000	4250
Displacement (inches)	0.058	0.063	0.066	0.072	0.075	0.083
Pressure (psi)	4500	4750	5000	5250	5500	5750
Displacement (inches)	0.087	0.091	0.098	0.102	0.109	0.113
Pressure (psi)	6000	6250	6500	6750	7000	7250
Displacement (inches)	0.118	0.125	0.135	0.145	0.158	0.178
Pressure (psi)	7500					
Displacement (inches)	0.186					

Table A.5. Displacement of Apex Measured on a Flanged Hemisphere of Constant Thickness (#15) Under Short-Term Hydrostatic Loading. Nominal  $t/R_i = 0.273$ : Actual thickness of flange = 0.752 in.. of apex = 0.750 in.: Temperature = 65° F: Pressurization rate = 500 psi/minute.

Pressure (psi)	0	500	1000	1500	2000	2500
Displacement (inches)	0.000	0.010	0.019	0.026	0.031	0.037
Pressure (psi)	3000	3500	4000	4500	5000	5500
Displacement (inches)	0.043	0.049	0.055	0.062	0.068	0.073
Pressure (psi)	6000	6500	7000	7500	8000	8500
Displacement (inches)	0.083	0.091	0.099	0.108	0.118	0.129
Pressure (psi)	9000	9500	10.000	10.400	10.600	10.800
Displacement (inches)	0.142	0.157	0.175	0.194	0.194	0.205
Pressure (psi)	10.990					
Displacement (inches)	0.221					

Table A.6. Displacement of Apex Measured on a Flangeless Hemisphere of Constant Thickness (#18) Under Short-Term Hydrostatic Loading. Nominal  $t/R_i = 0.023$ : Actual thickness of equator = 0.059 in.. of apex = 0.063 in.: Temperature = 64° F: Pressurization rate = 90 psi/minute.

Pressure	0	10	20	30	40	50
Displacement (inches)	0.000	0.00	0.00	0.00	0.00	0.00
Pressure (psi)	60	70	80	90	100	110
Displacement (inches)	0.00	0.001	0.002	0.003	0.003	0.003
Pressure (psi)	120	130	140	150	160	170
Displacement (inches)	0.004	0.005	0.006	0.007	0.009	0.010
Pressure (psi)	180	185	190	200	205	208
Displacement (inches)	0.011	0.014	0.016	0.018	0.020	0.021
Pressure (psi)	210	215	220	225	230	235
Displacement (inches)	0.023	0.024	0.025	0.026	0.027	0.028
Pressure (psi)	236	237				
Displacement (inches)	0.029	0.031				

Table A.7. Displacement on Apex Measured on a Flangeless Hemisphere of Constant Thickness (#22) Under Short-Term Hydrostatic Loading. Nominal  $t/R_i = 0.046$ ; Actual thickness of equator = 0.126 in., of apex = 0.129 in.; Temperature = 68°F; Pressurization rate = 100 psi/minute.

Pressure (psi)	0	50	100	150	200	250
Displacement (inches)	0.000	0.004	0.007	0.009	0.011	0.013
Pressure (psi)	300	350	400	450	500	550
Displacement (inches)	0.018	0.021	0.023	0.024	0.026	0.030
Pressure (psi)	600	700	800	900	950	1000
Displacement (inches)	0.032	0.038	0.043	0.048	0.053	0.059

Table A.8. Displacement of Apex Measured on a Flanged Hemisphere of Variable Thickness (#28) Under Short-Term Hydrostatic Loading. Nominal  $t/R_i = 0.023$ ; Actual thickness of flange = 0.063 in., of apex = 0.050 in.; Temperature = 68°F; Pressurization rate = 100 psi/minute.

Pressure (psi)	0	10	20	30	40	50
Displacement (inches)	0.000	0.000	0.000	0.002	0.003	0.004
Pressure (psi)	60	70	80	90	100	103
Displacement (inches)	0.005	0.006	0.008	0.008	0.009	0.010

Table A.9. Displacement of Apex Measured on a Flanged Hemisphere of Variable Thickness (#31) Under Short-Term Hydrostatic Loading. Nominal  $t/R_i = 0.046$ ; Actual thickness of flange = 0.125 in., of apex = 0.092 in.; Temperature = 68°F; Pressurization rate = 100 psi/minute.

Pressure (psi)	0	50	100	150	200	250
Displacement (inches)	0.000	0.001	0.001	0.003	0.007	0.012
Pressure (psi)	300	350	400	450	500	550
Displacement (inches)	0.014	0.017	0.017	0.023	0.027	0.030
Pressure (psi)	600	650	700	750	800	
Displacement (inches)	0.032	0.035	0.036	0.039	0.041	



Table A.10. Displacement of Apex Measured on a Flanged Hemisphere of Variable Thickness (#33) Under Short-Term Hydrostatic Loading. Nominal  $t/R_i = 0.091$ ; Actual thickness of flange = 0.253 in., of apex = 0.193 in.; Temperature = 62°F; Pressurization rate = 500 psi/minute.

Pressure (psi)	0	50	150	250	350	450
Displacement (inches)	0.00	0.001	0.003	0.005	0.007	0.009
Pressure (psi)	550	650	750	850	950	1050
Displacement (inches)	0.012	0.018	0.022	0.028	0.030	0.033
Pressure (psi)	1150	1250	1350	1450	1550	1650
Displacement (inches)	0.038	0.042	0.046	0.048	0.052	0.058
Pressure (psi)	1750	1850	1950	2050	2150	2250
Displacement (inches)	0.061	0.064	0.068	0.073	0.076	0.082
Pressure (psi)	2350	2450	2550	2650	2750	2850
Displacement (inches)	0.086	0.088	0.090	0.092	0.098	0.103
Pressure (psi)	2950	3000				
Displacement (inches)	0.108	0.115				

Table A.11. Displacement of Apex Measured on a Flanged Hemisphere of Variable Thickness (#37) Under Short-Term Hydrostatic Loading. Nominal  $t/R_i = 0.182$ , Actual thickness of flange = 0.508 in., of apex = 0.340 in.; Temperature = 62°F; Pressurization rate = 500 psi/minute.

Pressure (psi)	0	250	500	750	1000	1250
Displacement (inches)	0.000	0.008	0.012	0.017	0.021	0.027
Pressure (psi)	1500	1700	2000	2250	2500	2750
Displacement (inches)	0.031	0.034	0.039	0.043	0.048	0.057
Pressure (psi)	3000	3250	3500	3750	4000	4250
Displacement (inches)	0.060	0.066	0.072	0.076	0.086	0.093
Pressure (psi)	4500	4750	5000	5250	5500	5750
Displacement (inches)	0.103	0.112	0.118	0.136	0.162	0.222
Pressure (psi)	6000					
Displacement (inches)	0.382					

Table A.12. Displacement of Apex Measured on a Flanged Hemisphere of Variable Thickness (#38) Under Short-Term Hydrostatic Loading. Nominal  $t/R_i = 0.273$ , Actual thickness of flange = 0.752 in., of apex = 0.240 in.; Temperature = 60°F; Pressurization rate = 600 psi/minute.

Pressure (psi)	0	500	1000	1500	2000	2500
Displacement (inches)	0.000	0.010	0.013	0.020	0.028	0.036
Pressure (psi)	3000	3500	4000	4500	5000	5500
Displacement (inches)	0.046	0.052	0.062	0.068	0.079	0.092
Pressure (psi)	6000	6500	7000	7500	8000	8500
Displacement (inches)	0.101	0.114	0.135	0.156	0.183	0.238
Pressure (psi)	9000	9100				
Displacement (inches)	0.328	0.623				

## EXPERIMENTAL STRAINS AND STRESSES

Several interesting observations can be made on the basis of experimentally generated strain data. It is understood that these observations are tentative, as only a single window of each type was instrumented with three electrical-resistance strain rosettes.

Strains were fairly linear to the point of implosion for thin and very thin shells. In thick shells the strains were nonlinear just prior to failure, indicating some yielding. Since in many cases the magnitude of strains exceeded 20,000 microinches/inch, the readings of electric-resistance gauges mounted on thick shells became quite erratic just before the failure of the shells. On thin shells the strains were, as rule, less than 20,000 microinches/inch; thus, the gauges were able to function to the very moment of failure. For this reason, the strain records of thin shells (figures A.5, A.6, A.7) can show whether elastic instability was the cause of failure. It appears that this was the case (Note the reversal of strain curves on figures A.5.B, C, D and figures A.6.B, C, D).

Stresses at the apex of the flanged and flangeless shells of constant thickness fall between the maximum and minimum stresses values measured on these shells and therefore provide a representative stress value for a given  $t/R_i$  ratio. In flanged shells of constant thickness (figures A.8.A, B, C, D, E), the highest stresses were, as rule, found 20 degrees above the flange. In flanged shells of variable thickness, the highest stresses were, as rule, found at the apex (figures A.9.A, B, C, D).

An interesting shift occurs in the orientation of principal maximum stress at the flange as constant- and variable-thickness shells of different thicknesses are observed. In very thin and thin shells ( $t/R_i \leq 0.046$ ), the maximum principal stress at the flange is along the meridian; in medium thick and thick shells, the maximum principal stress at the flange is in the hoop direction.

WINDOW NO.21 GAGE NO.

FT4  
3

08/07/72 126

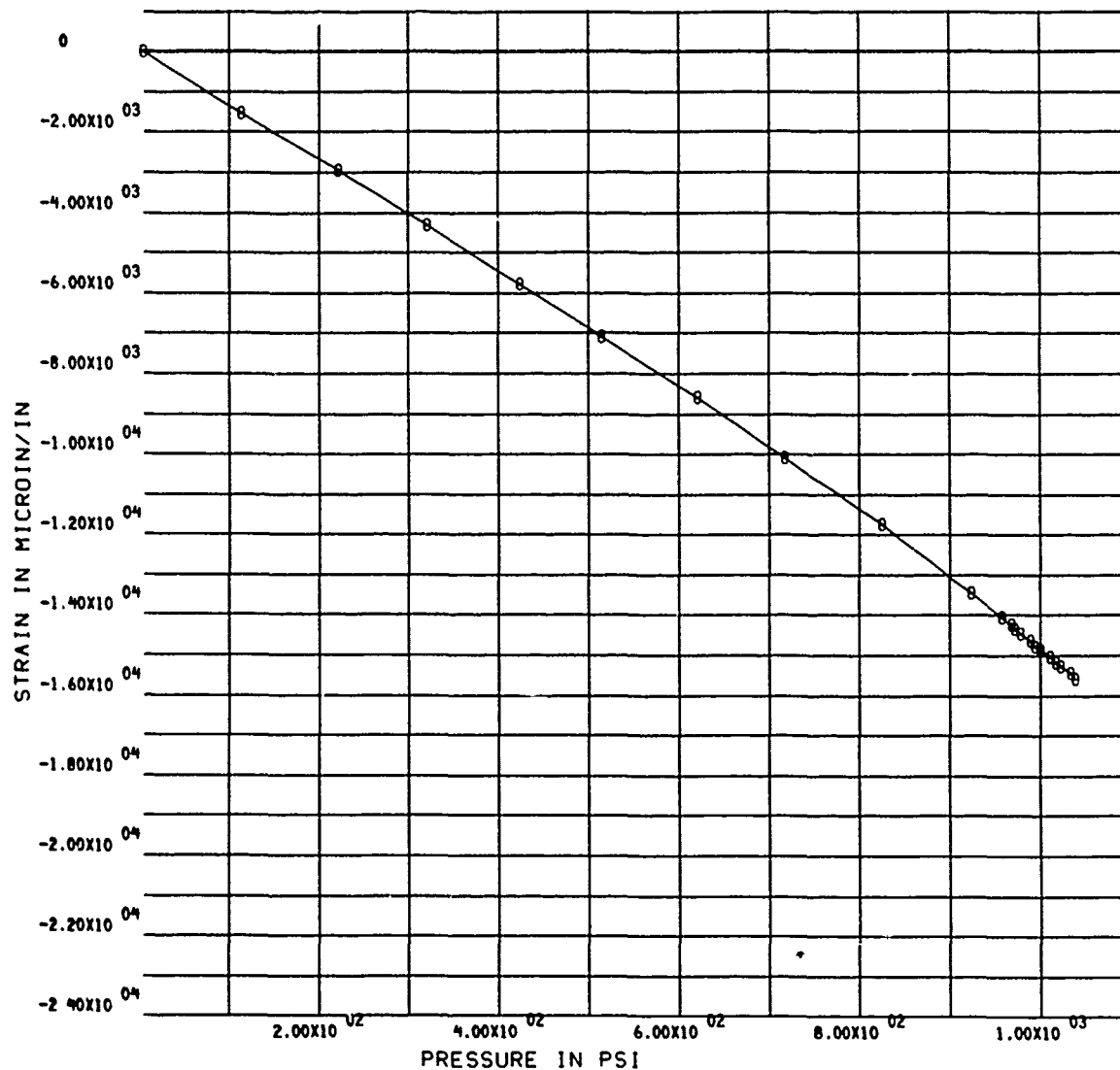


Figure A.5.A. Strain on the Interior Surface at the Apex of a Flangeless Shell of Constant Thickness ( $t/R_1 = 0.046$ ) Under Short-Term Hydrostatic Loading.

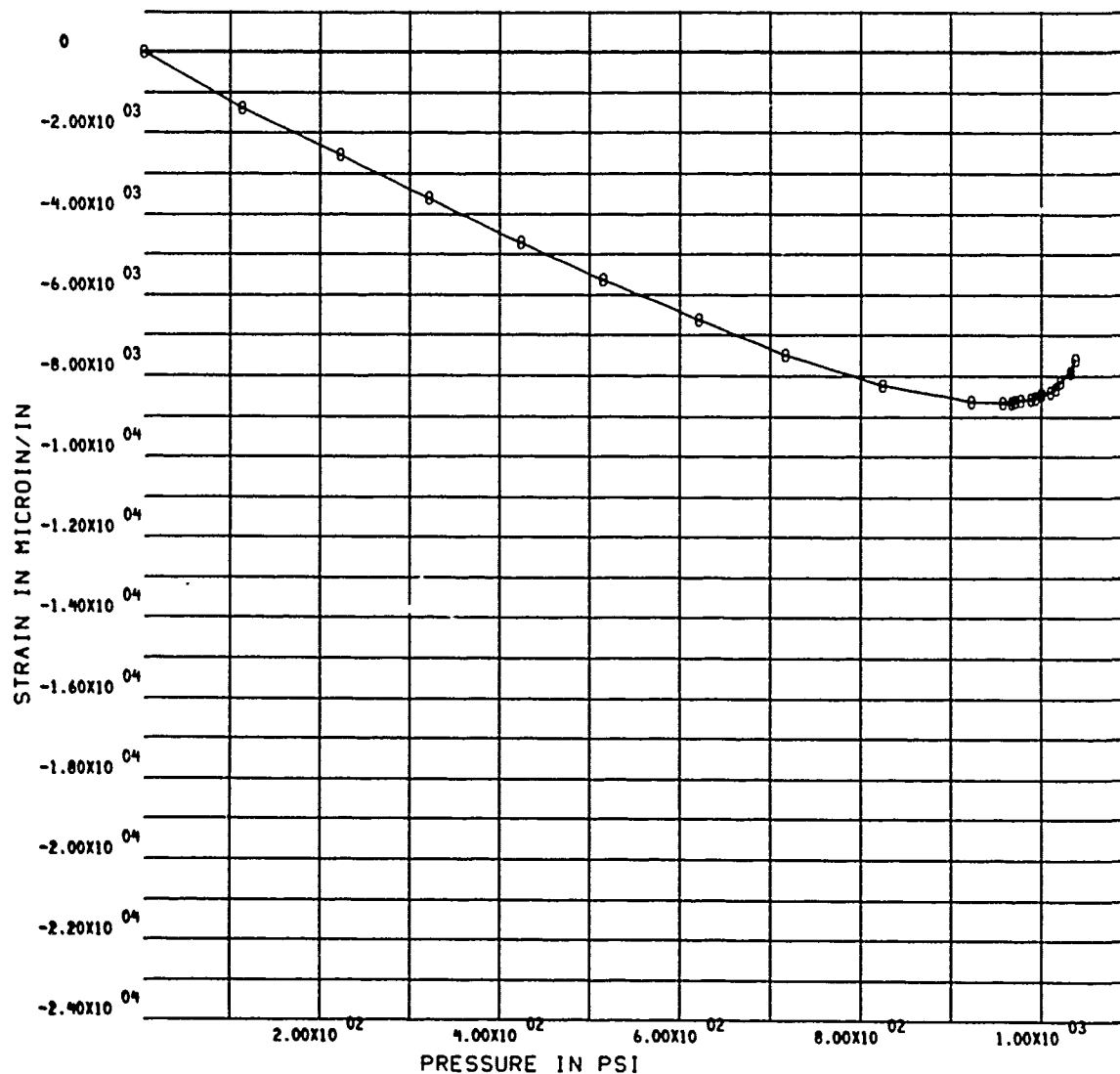


Figure A.5.B. Strain on the Interior Surface  $2^\circ$  Degrees Above the Equator of a Fringeless Shell of Constant Thickness ( $t/R_i = 0.046$ ) Under Short-Term Hydrostatic Loading. Orientation: meridional.

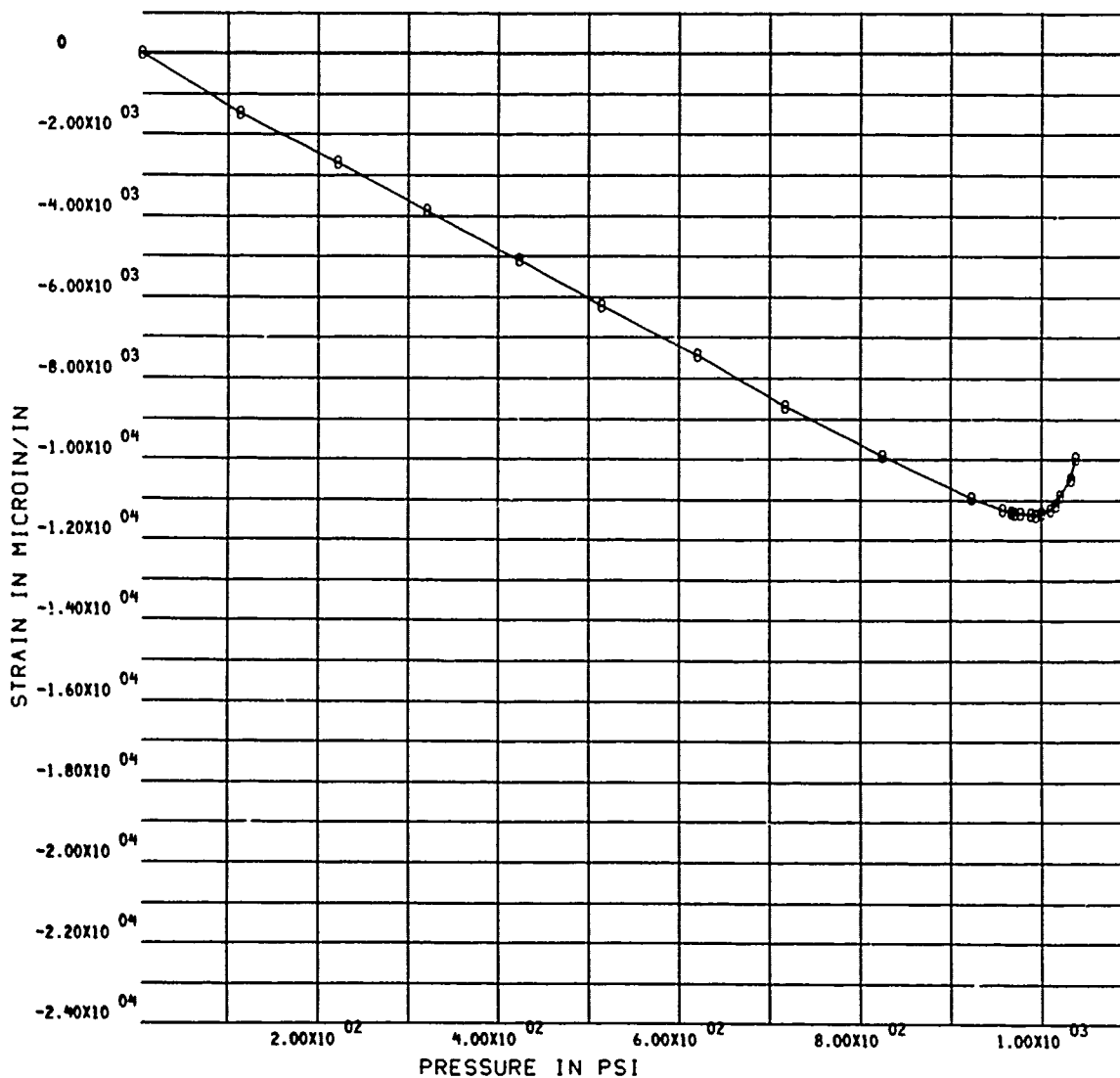
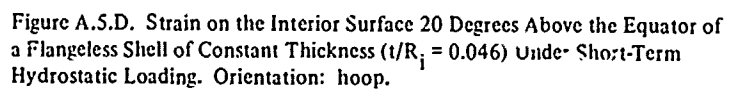


Figure A.5.C. Strain on the Interior Surface 20 Degrees Above the Equator of a Flangeless Shell of Constant Thickness ( $t/R_1 = 0.046$ ) Under Short-Term Hydrostatic Loading. Orientation: 45 degrees with meridian.



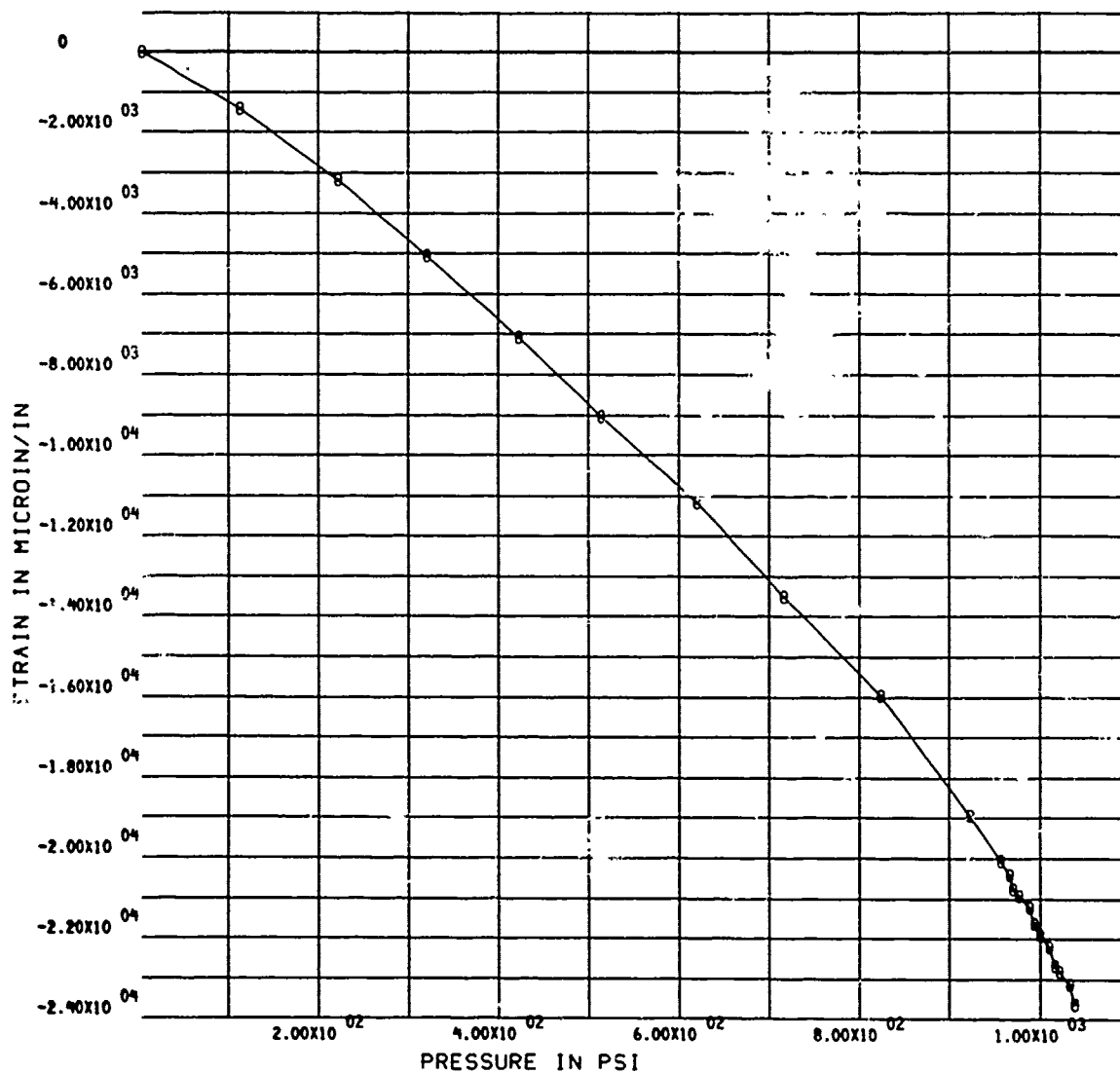


Figure A.5.E. Strain on the Interior Surface at the Equator of a Flangeless Shell of Constant Thickness ( $t/R_i = 0.046$ ) Under Short-Term Hydrostatic Loading. Orientation: meridional.

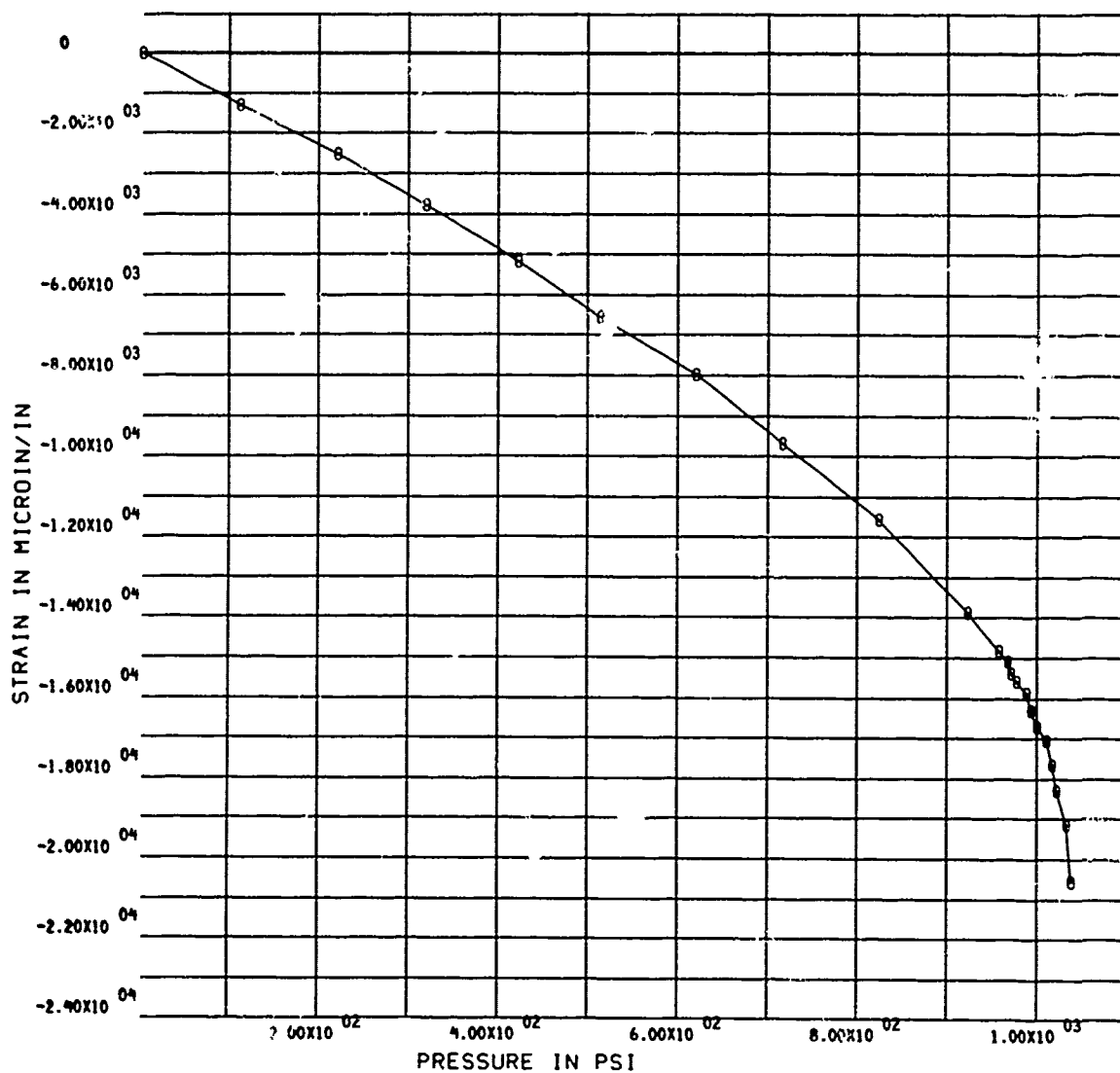


Figure A.5.F. Strain on the Interior Surface at the Equator of a Flangeless Shell of Constant Thickness ( $t/R_i = 0.046$ ) Under Short-Term Hydrostatic Loading. Orientation: 45 degrees with meridian.



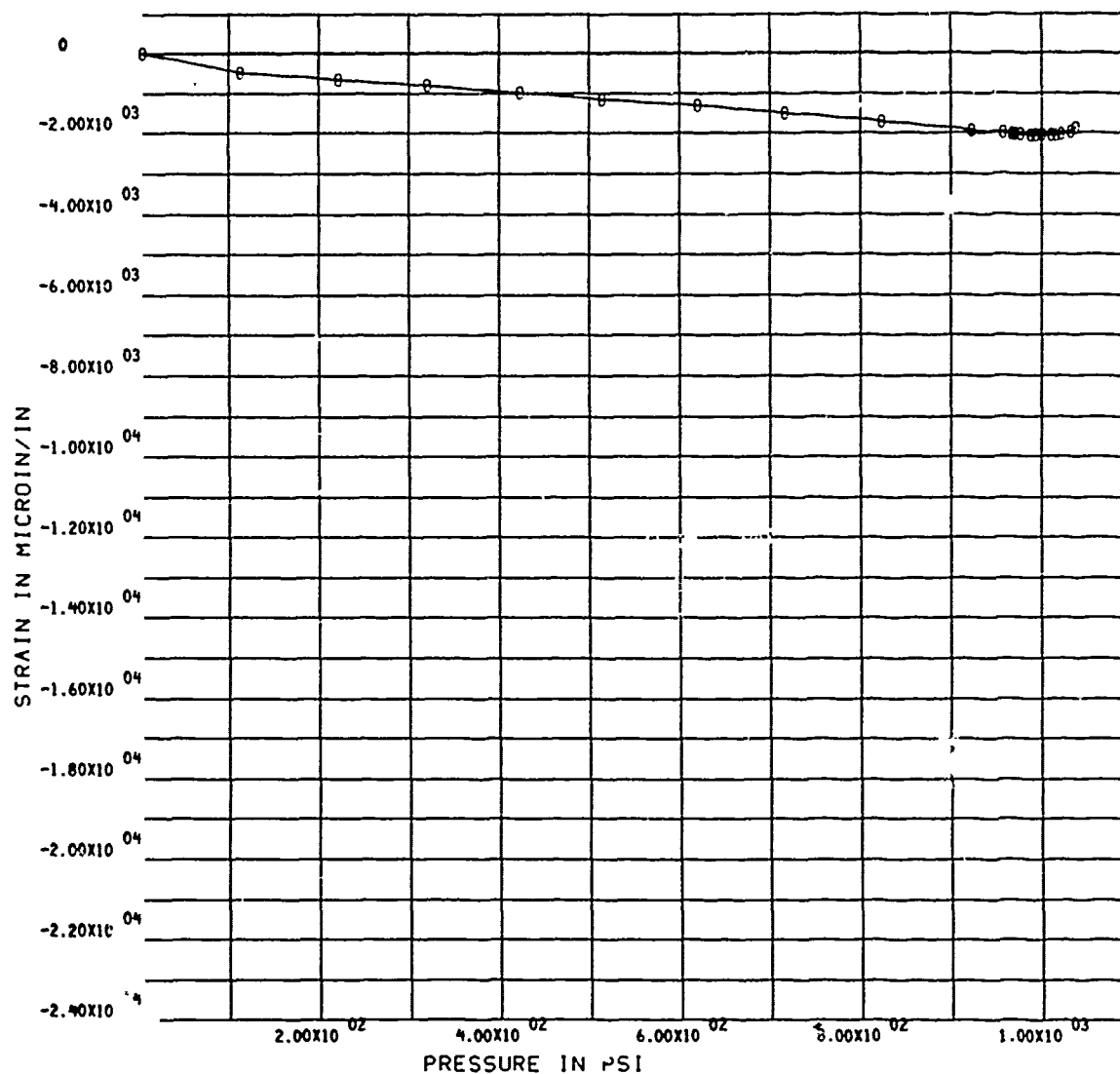


Figure A.5.G. Strain on the Interior Surface at the Equator of a Flangeless Shell of Constant Thickness ( $t/R_i = 0.046$ ) Under Short-Term Hydrostatic Loading. Orientation: hoop.

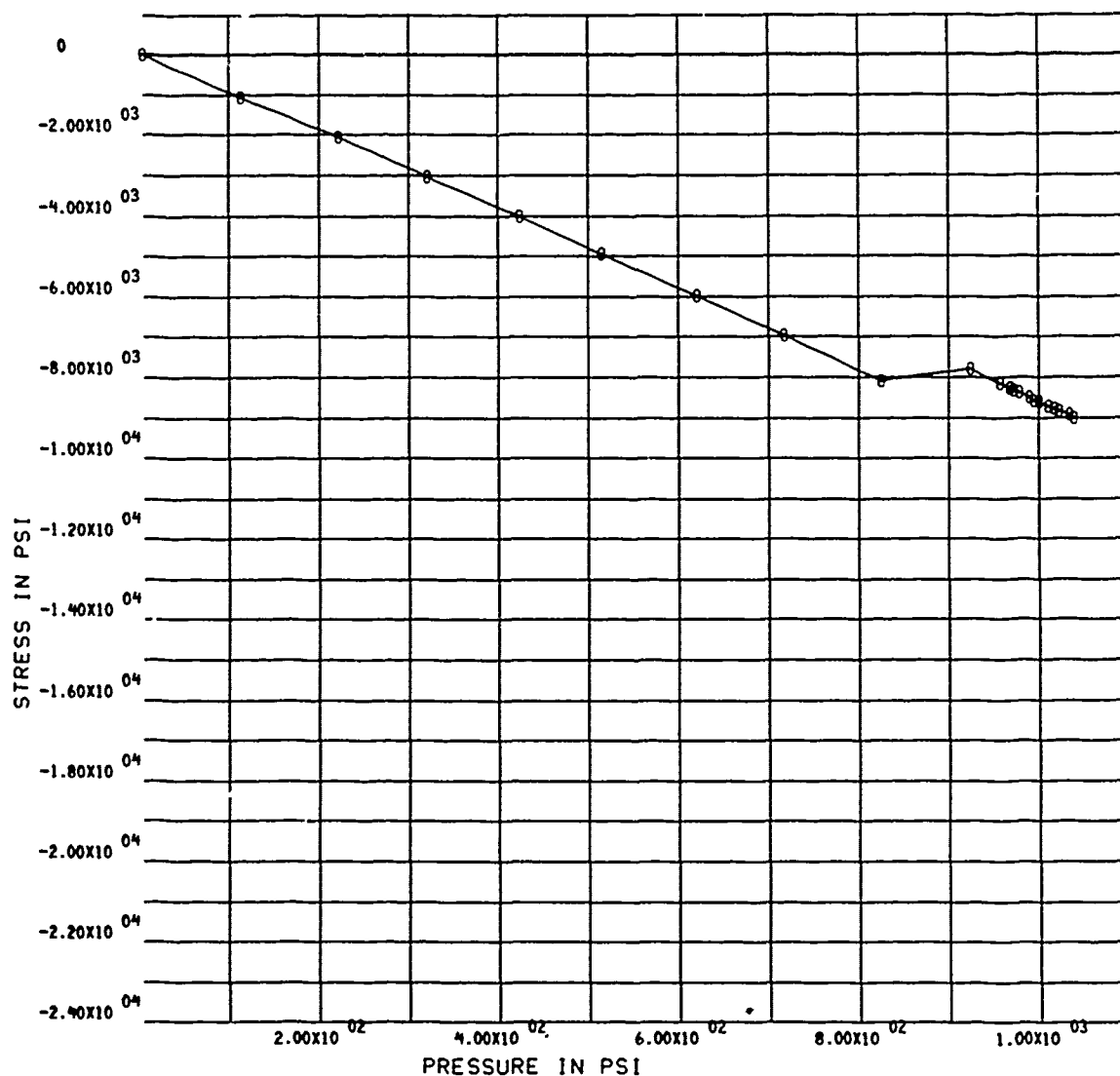


Figure A.5.H. Maximum Principal Stress on the Interior Surface at the Apex of a Flangeless Shell of Constant Thickness ( $t/R_i = 0.046$ ) Under Short-Term Hydrostatic Loading.

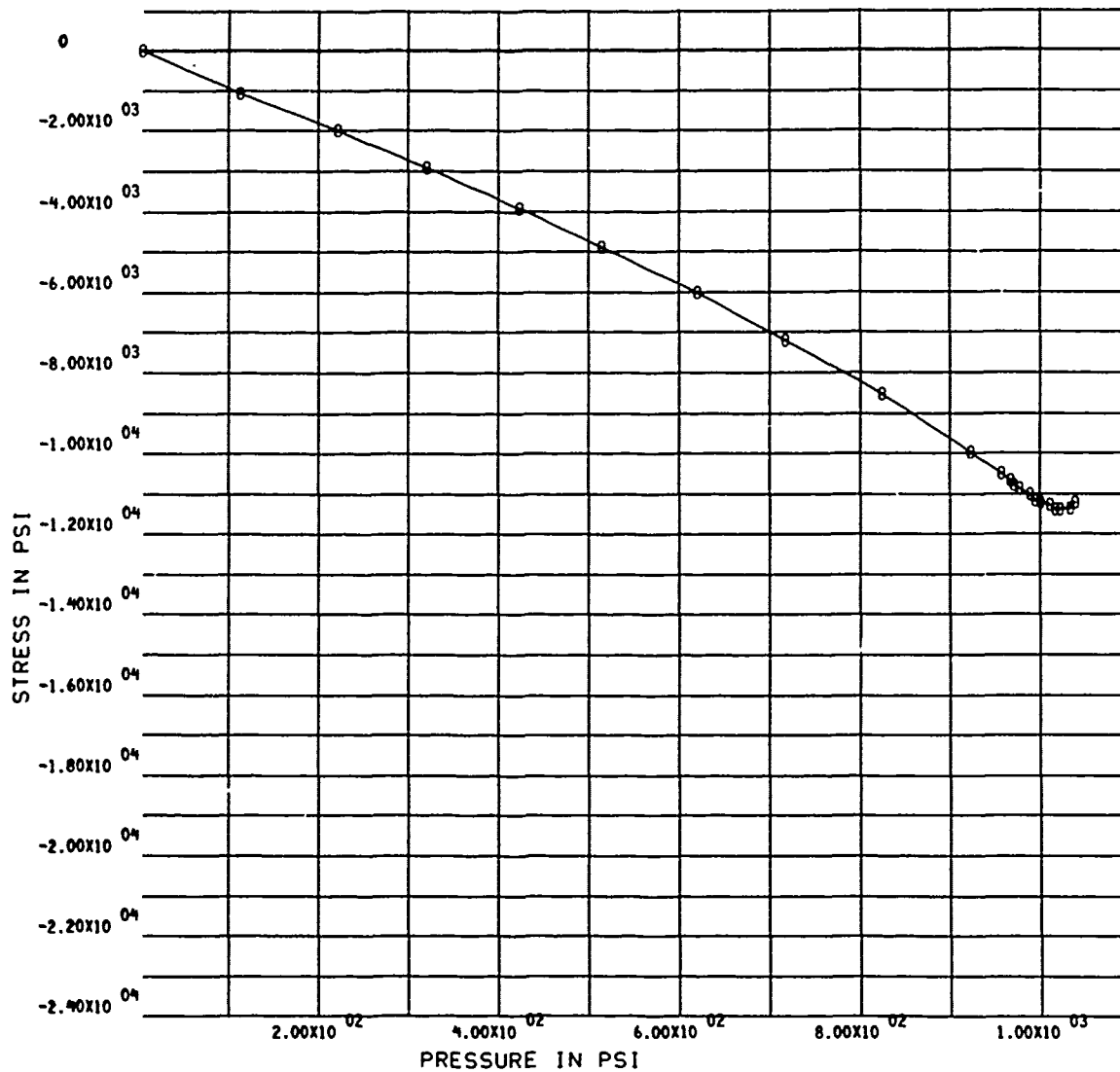


Figure A.5.I. Maximum Principal Stress on the Interior Surface 20 Degrees Above the Equator of a Flangeless Shell of Constant Thickness ( $t/R_i = 0.046$ ) Under Short-Term Hydrostatic Loading. Orientation: hoop.

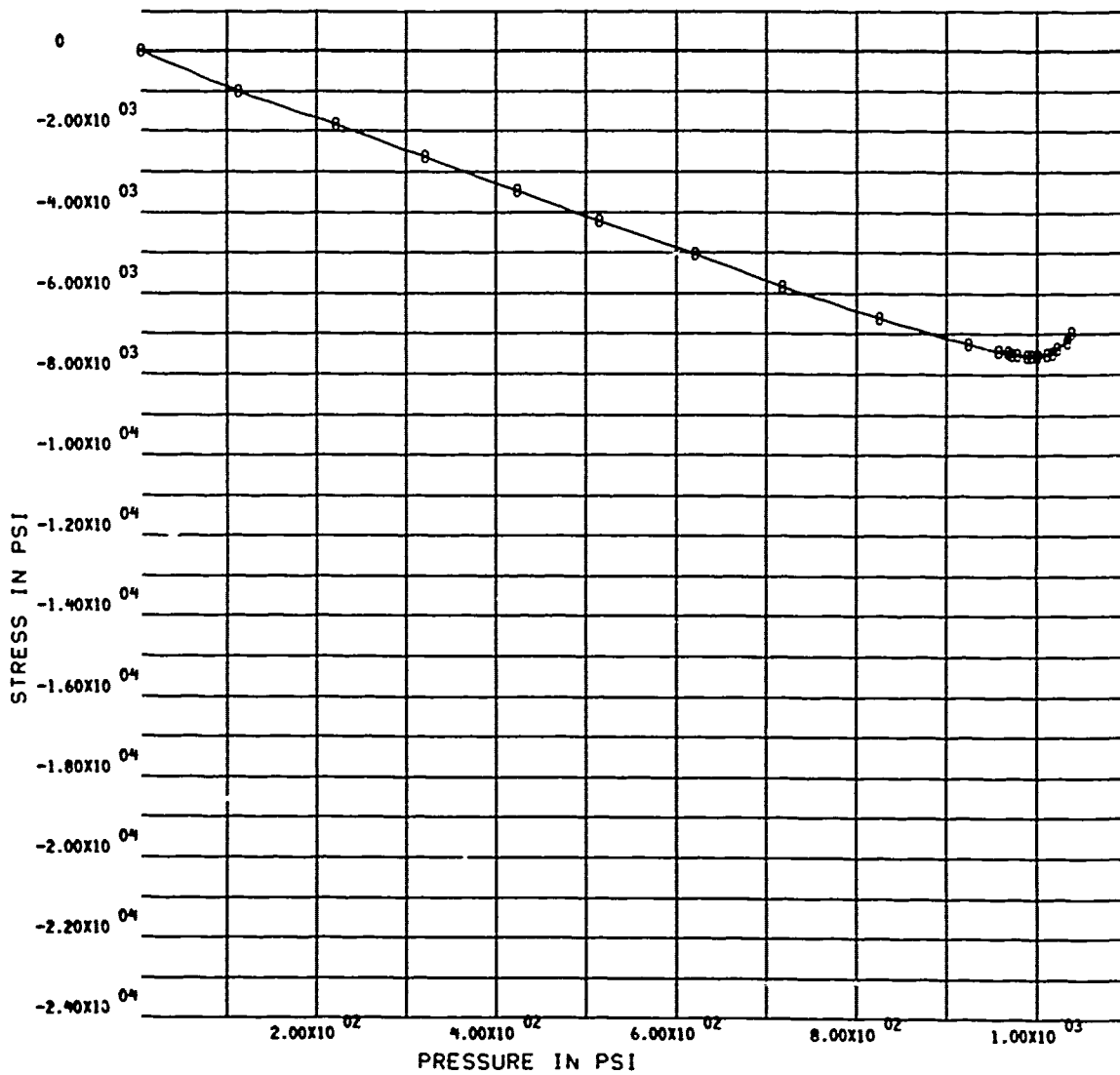


Figure A.5.J. Minimum Principal Stress on the Interior Surface 20 Degrees Above the Equator of a Flangeless Shell of Constant Thickness ( $t/R_i = 0.046$ ) Under Short-Term Hydrostatic Loading. Orientation: meridional.

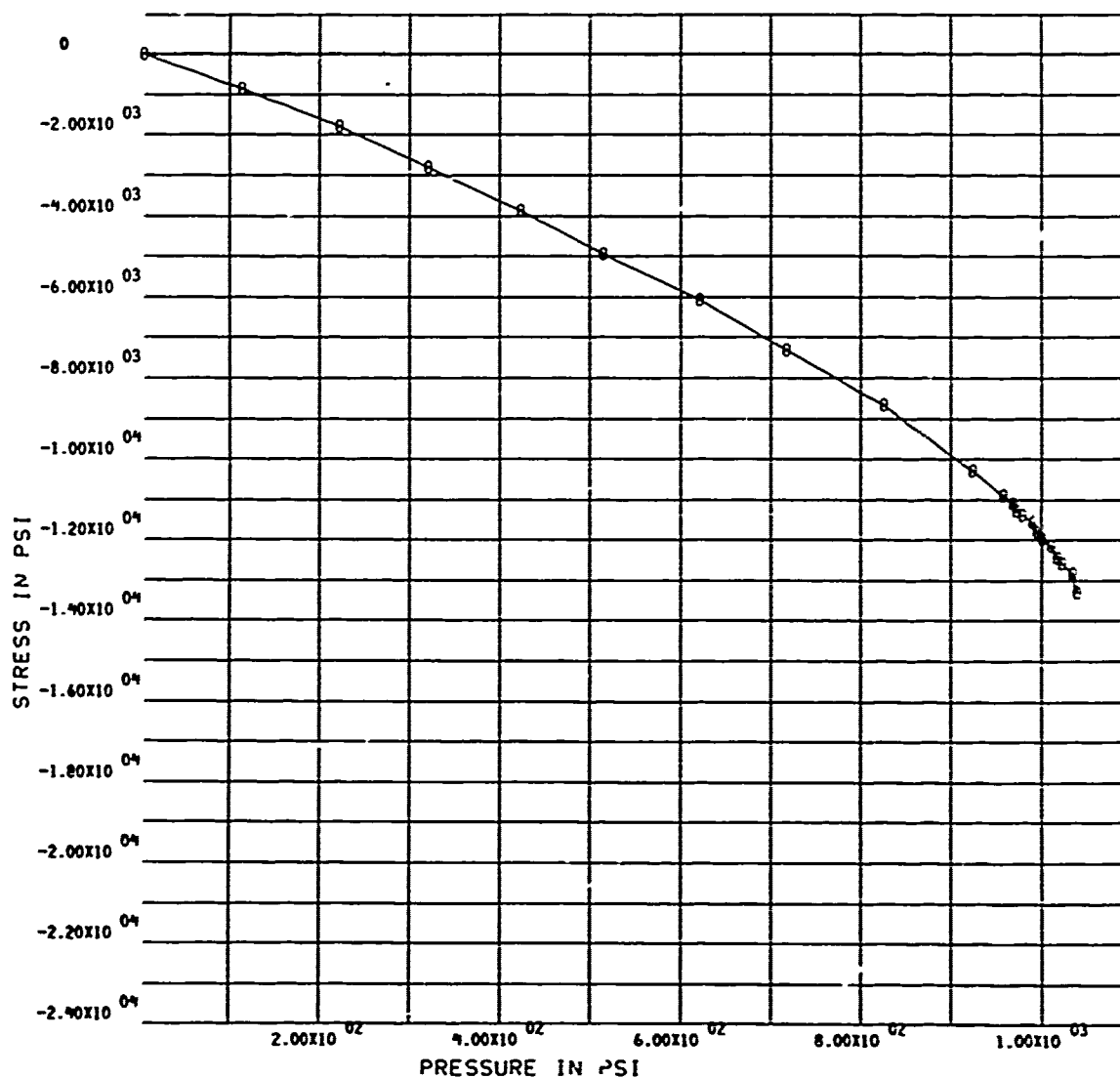


Figure A.5.K. Maximum Principal Stress on the Interior Surface at the Equator of a Flangeless Shell of Constant Thickness ( $t/R_1 = 0.046$ ) Under Short-Term Hydrostatic Loading. Orientation: meridional.

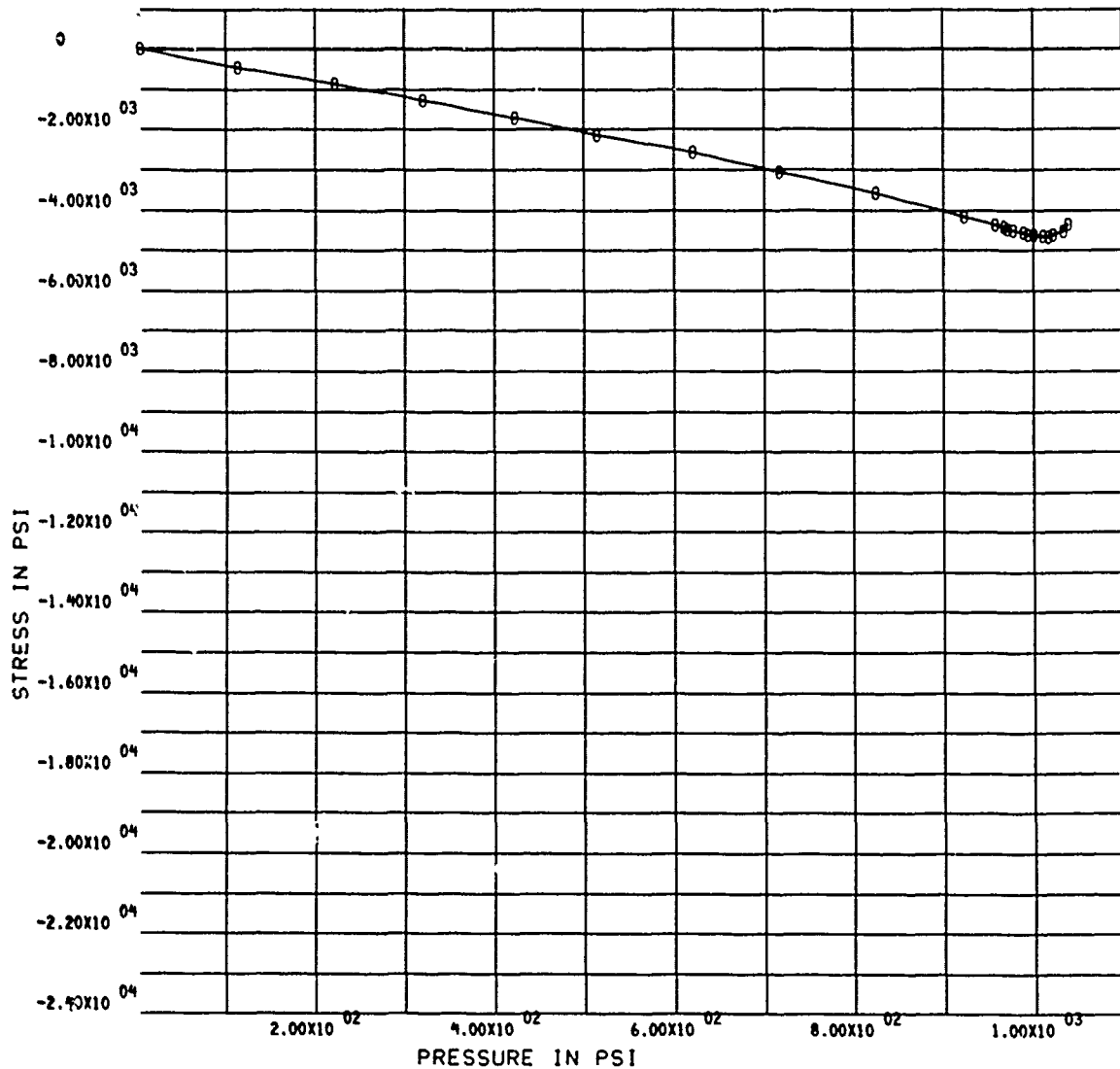


Figure A.5.L. Minimum Principal Stress on the Interior Surface at the Equator of a Flangeless Shell of Constant Thickness ( $t/R_i = 0.046$ ) Under Short-Term Hydrostatic Loading. Orientation: hoop.

WINDOW NO. 4 GAGE NO.

FT4  
3

08/07/72 110

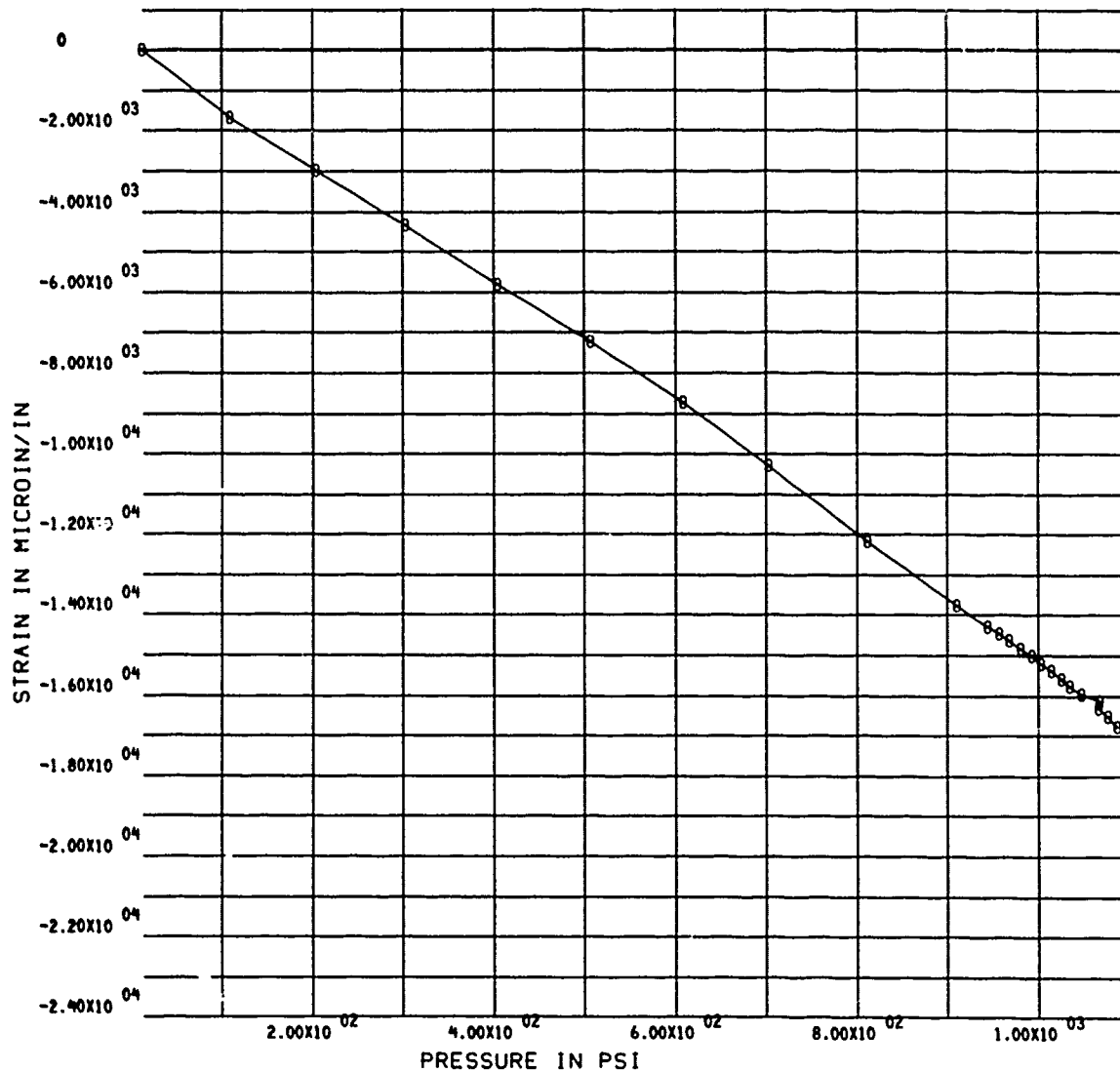


Figure A.6.A. Strain on the Interior Surface at the Apex of a Flanged Shell of Constant Thickness ( $t/R_i = 0.046$ ) Under Short-Term Hydrostatic Loading.

WINDOW NO. 4 GAGE NO.

FT4.  
4

08/07/72 1:1

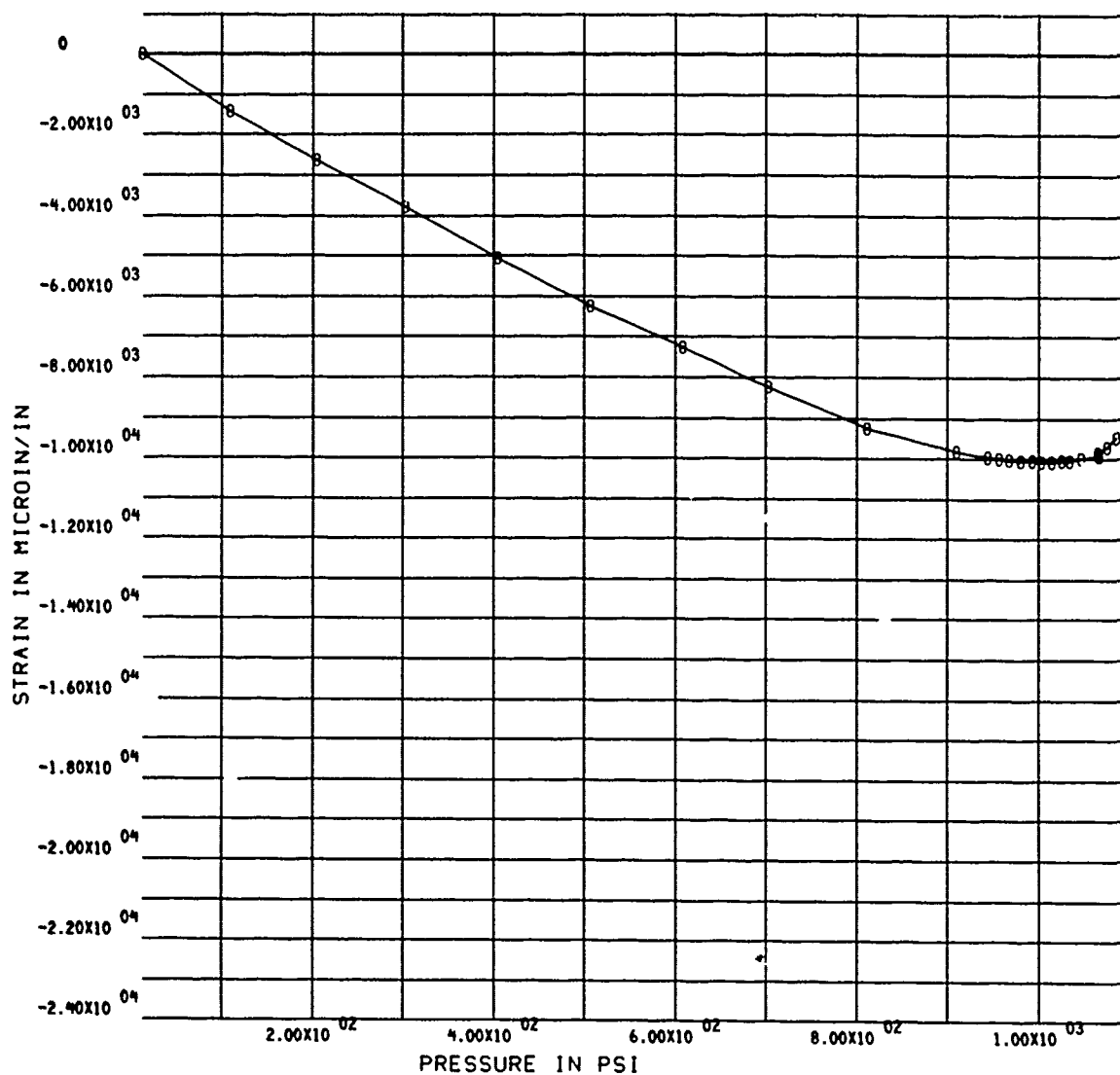


Figure A.6.B. Strain on the Interior Surface 20 Degrees Above the Flange of a Shell of Constant Thickness ( $t/R_i = 0.046$ ) Under Short-Term Hydrostatic Loading. Orientation: meridional.



WINDOW NO. 4 GAGE NO.

FT4.  
5

08/07/72 112

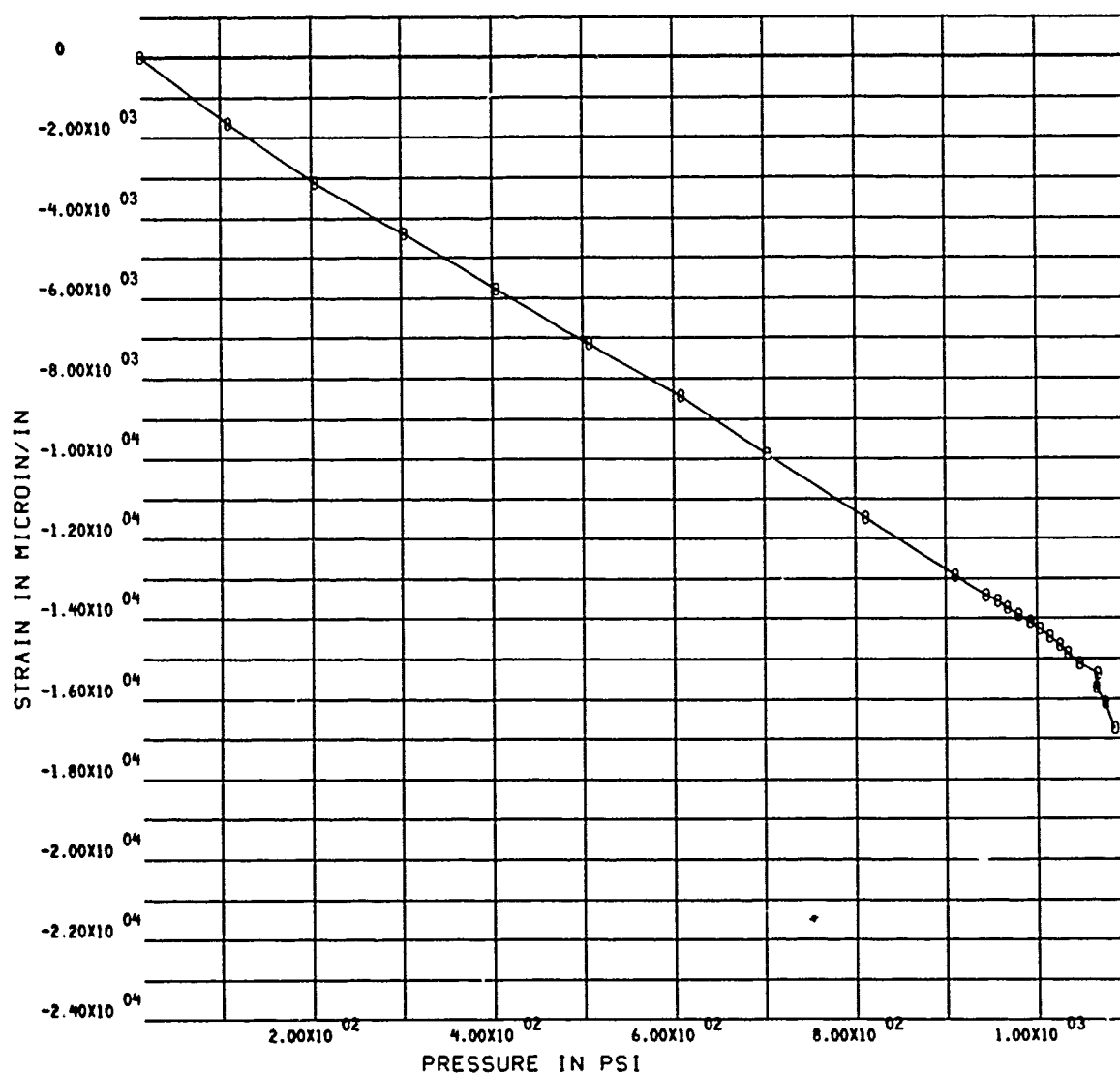


Figure A.6.C. Strain on the Interior Surface 20 Degrees Above the Flange of a Shell of Constant Thickness ( $t/R_i = 0.046$ ) Under Short-Term Hydrostatic Loading. Orientation: 45 degrees with meridian.

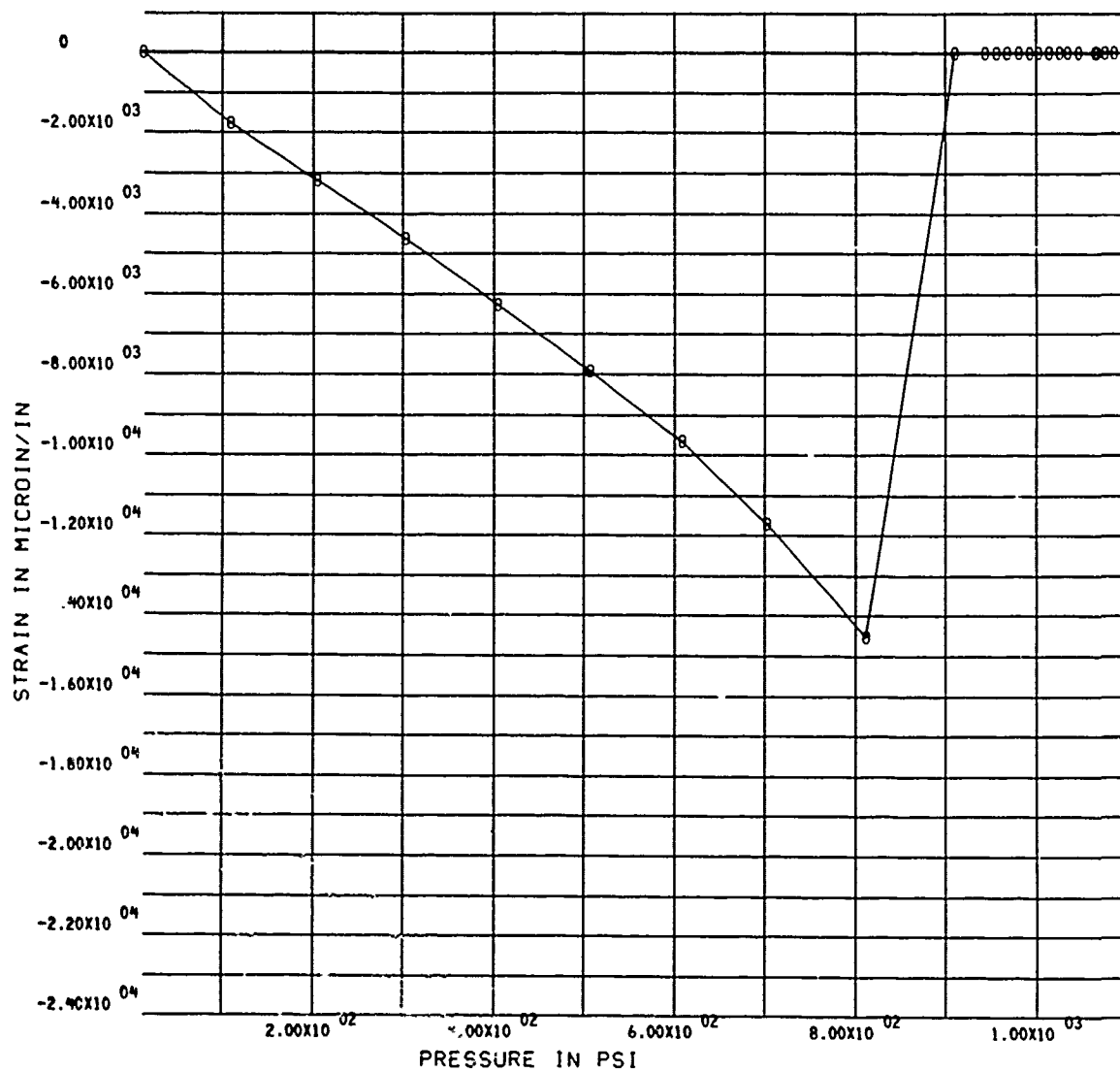


Figure A.6.D. Strain on the Interior Surface 20 Degrees Above the Flange of a Shell of Constant Thickness ( $t/R_i = 0.046$ ) Under Short-Term Hydrostatic Loading. Orientation: hoop.

WINDOW NO. 4 GAGE NO.

FT<sup>4</sup>  
7

08/07/72 11<sup>4</sup>

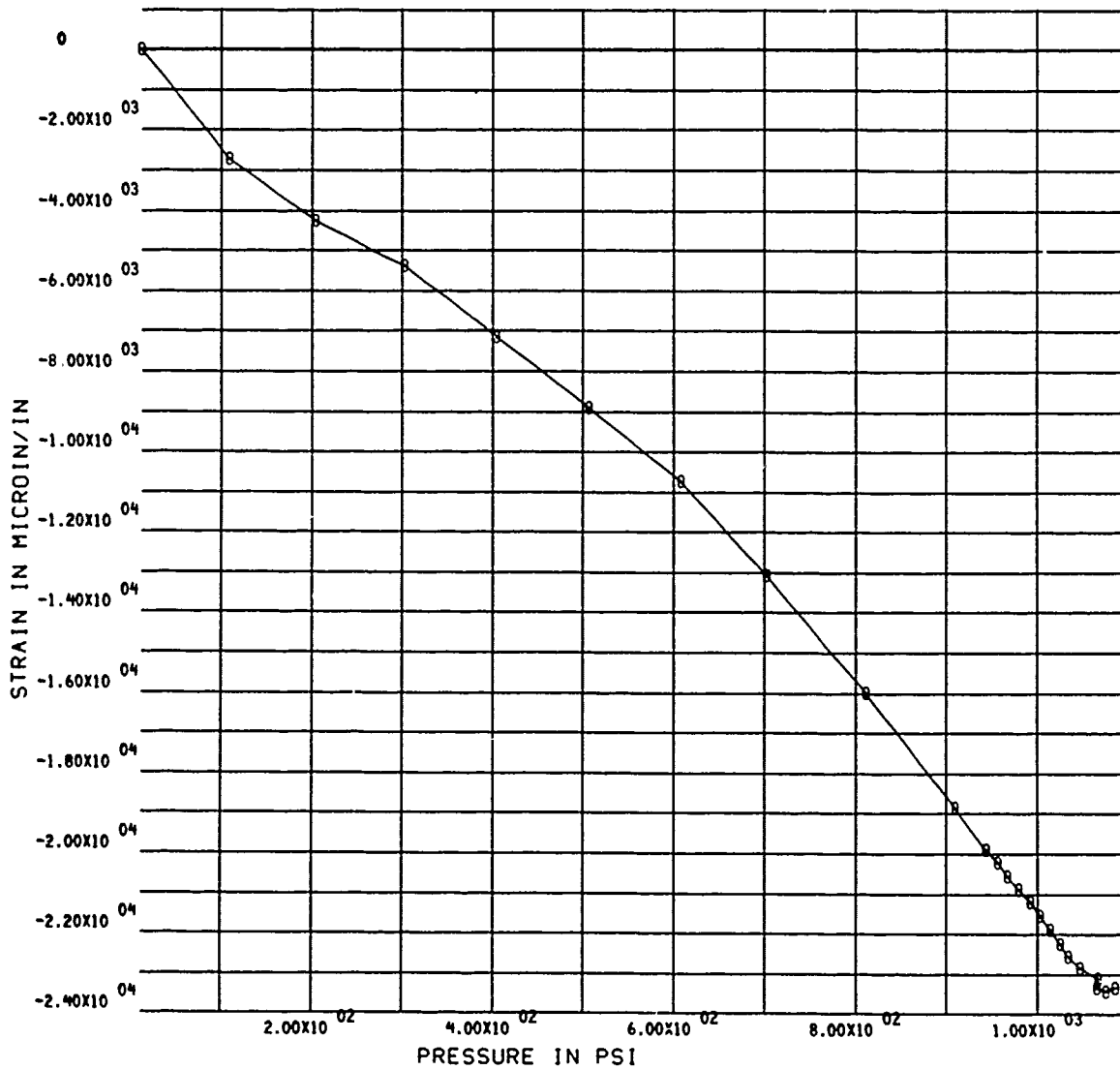


Figure A.6.E. Strain on the Interior Surface of the Flange of a Shell of Constant Thickness ( $t/R_i = 0.046$ ) Under Short-Term Hydrostatic Loading. Orientation: meridional.

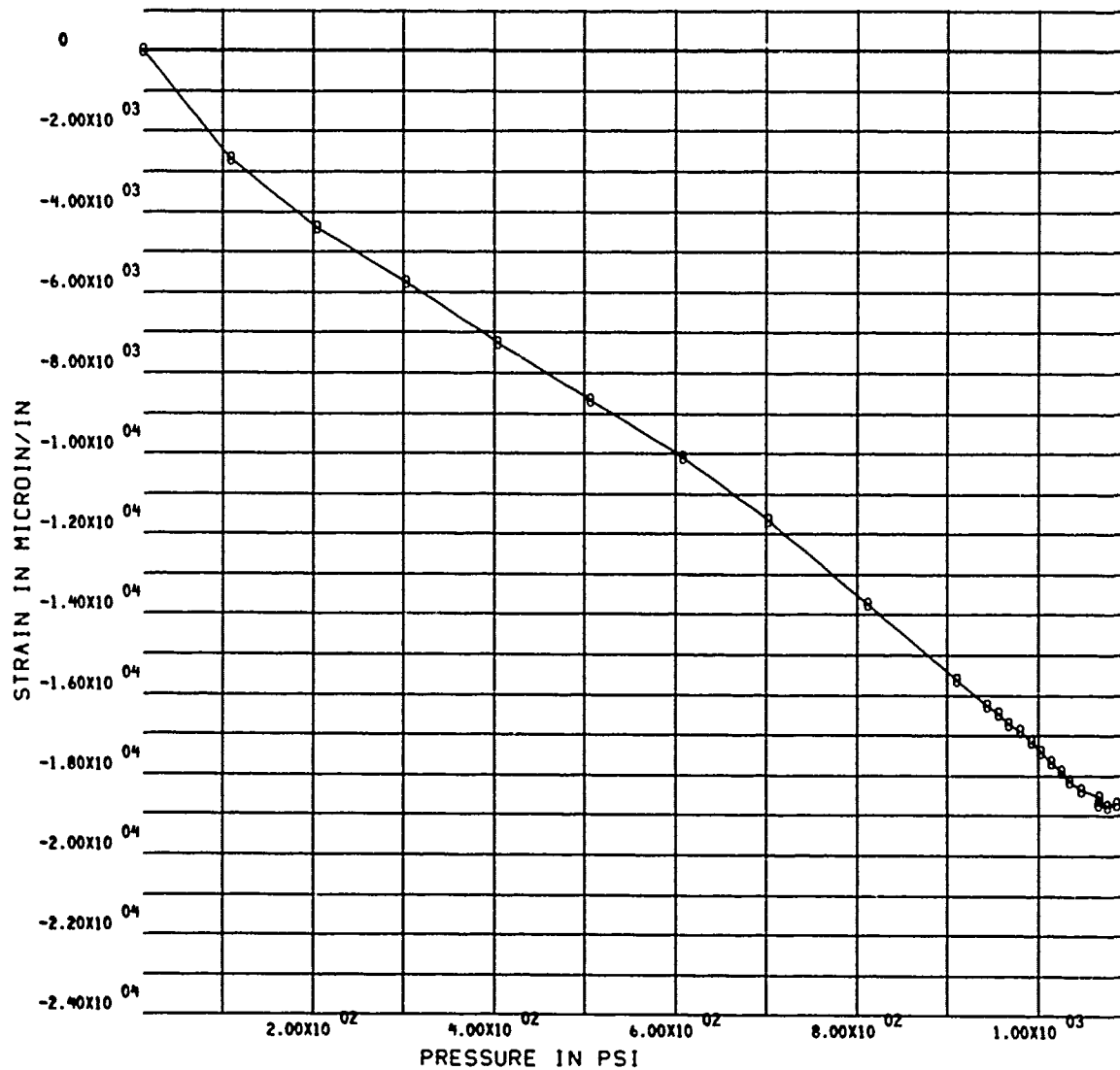


Figure A.6.F. Strain on the Interior Surface of the Flange of a Shell of Constant Thickness ( $t/R_i = 0.046$ ) Under Short-Term Hydrostatic Loading. Orientation: 45 degrees with meridian.

WINDOW NO. 4 GAGE NO.

FT4.  
9

08/07/72 116

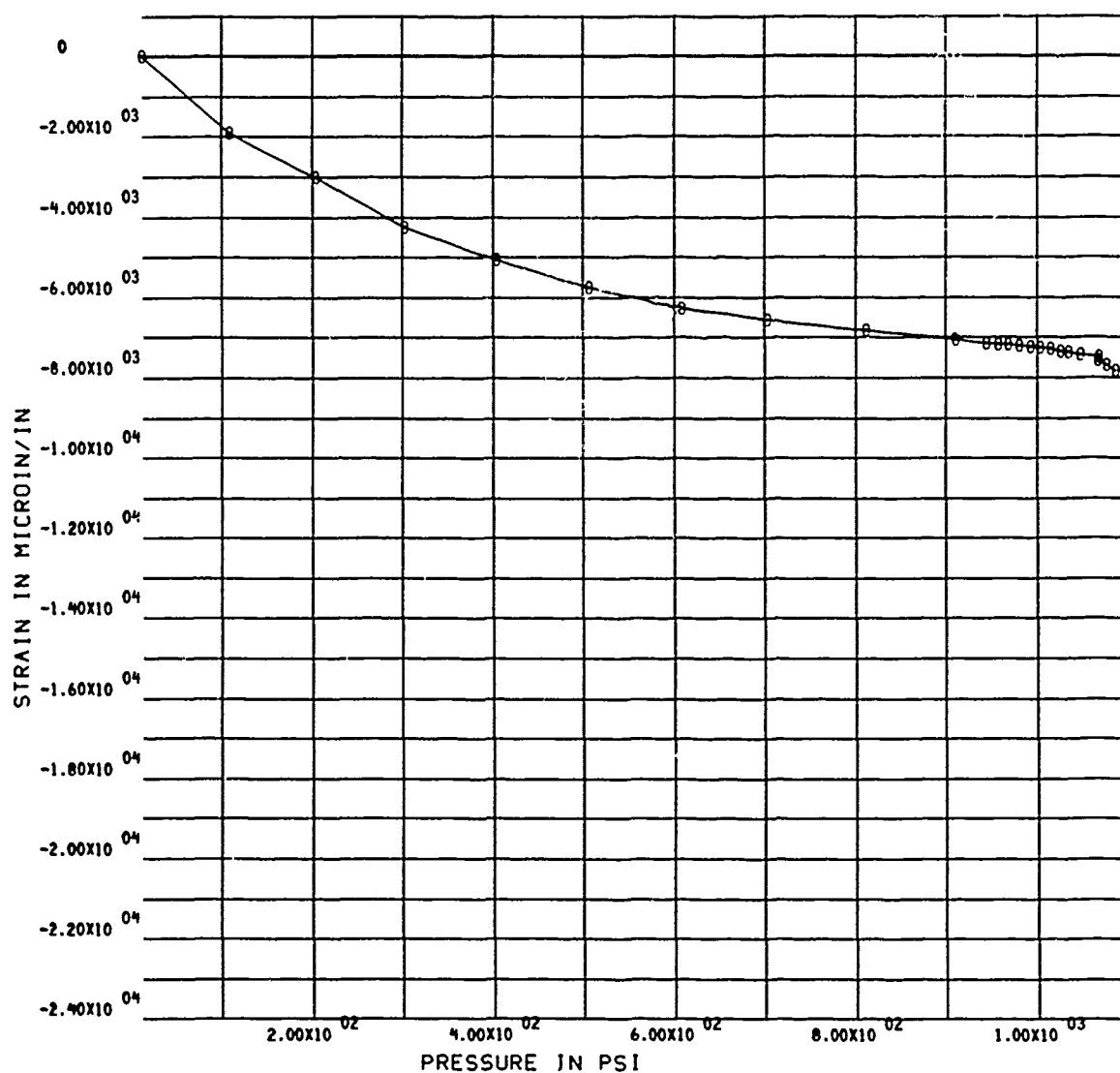


Figure A.6.G. Strain on the Interior Surface of the Flange of a Shell of Constant Thickness ( $t/R_i = 0.046$ ) Under Short-Term Hydrostatic Loading. Orientation: hoop.

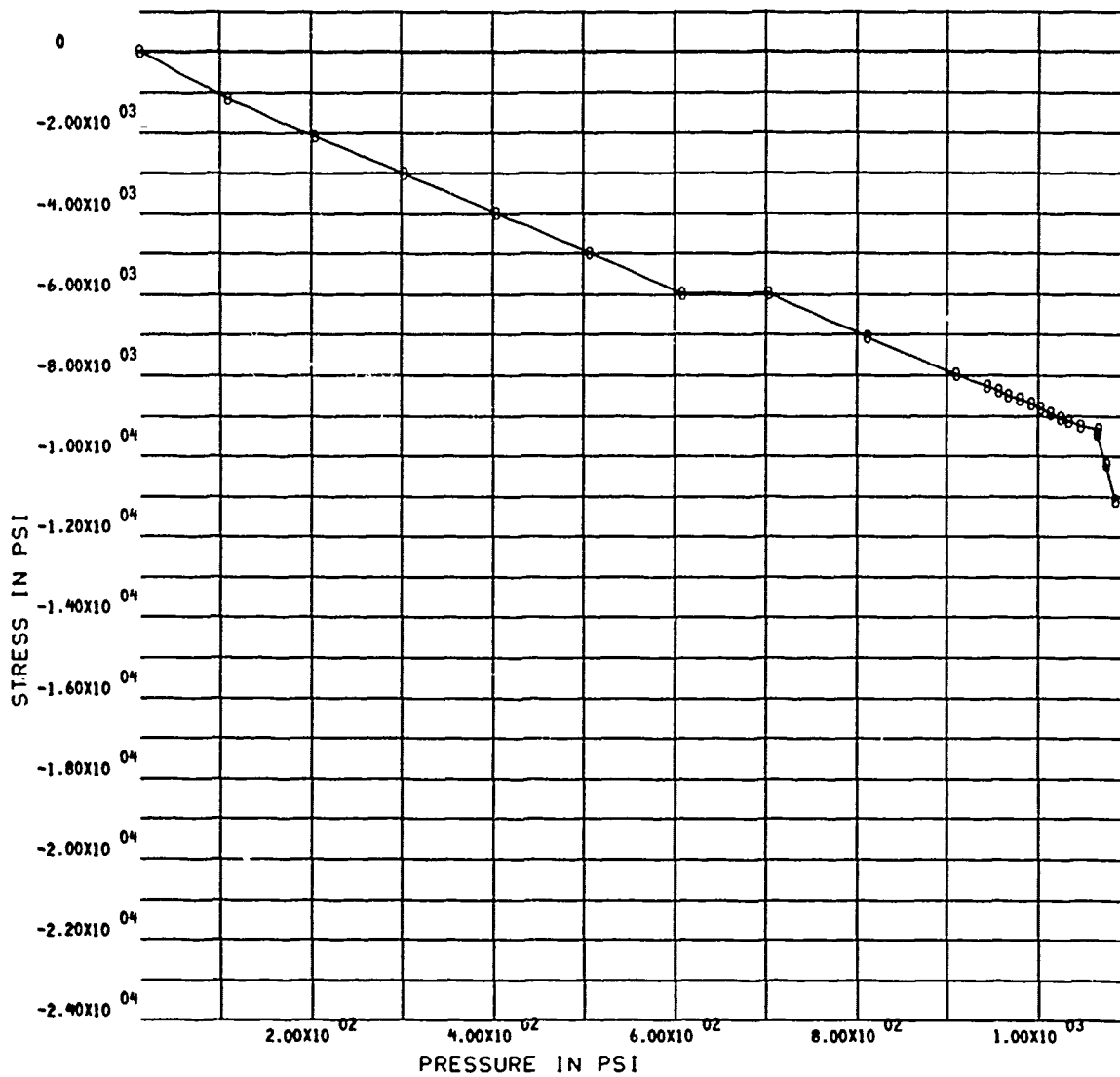


Figure A.6.H. Maximum Principal Stress on the Interior Surface at the Apex of a Flanged Shell of Constant Thickness ( $t/R_1 = 0.046$ ) Under Short-Term Hydrostatic Loading.

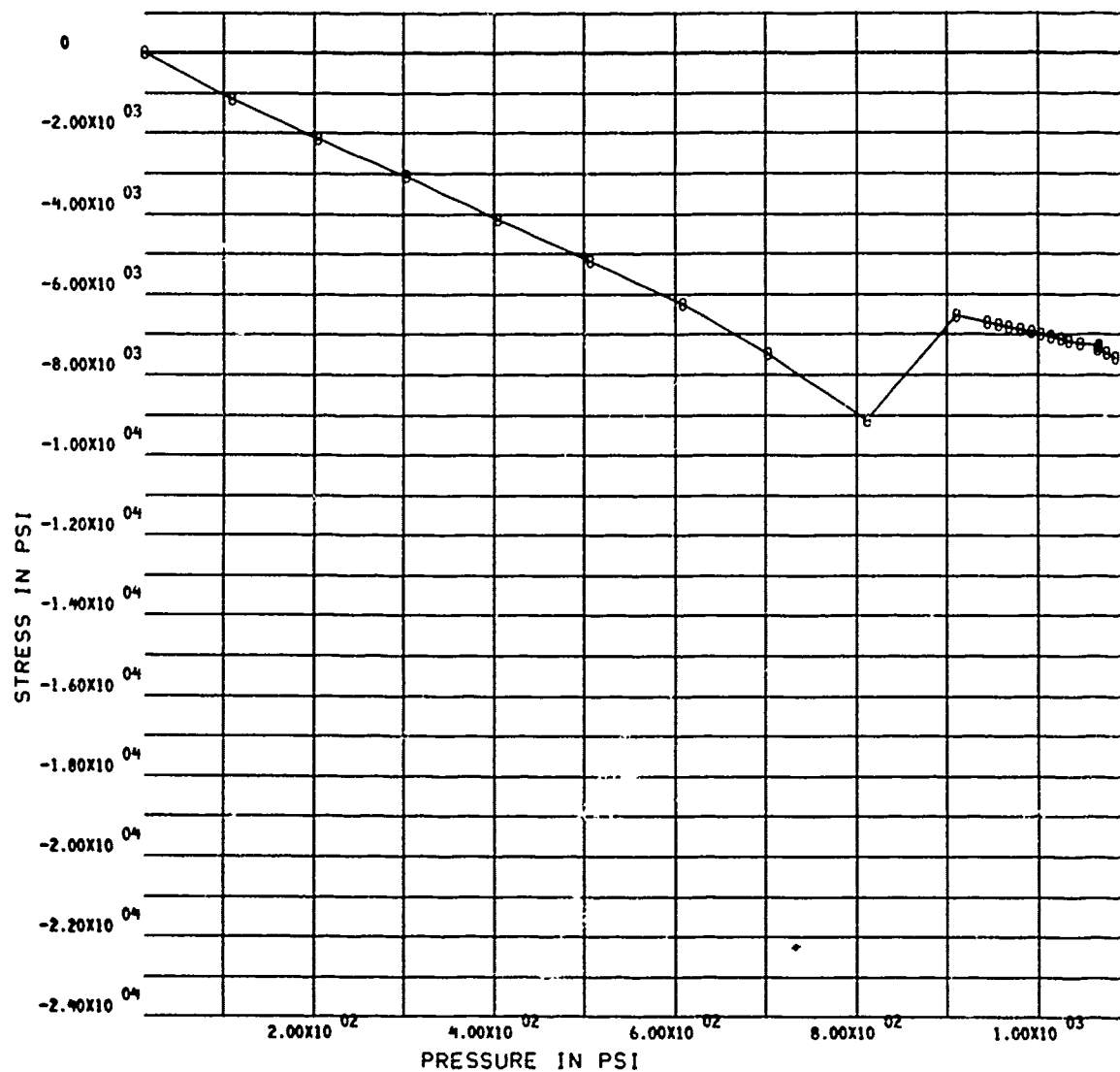


Figure A.6.1. Maximum Principal Stress on the Interior Surface 20 Degrees Above the Flange of a Shell of Constant Thickness ( $t/R_i = 0.046$ ) Under Short-Term Hydrostatic Loading. Orientation: hoop.

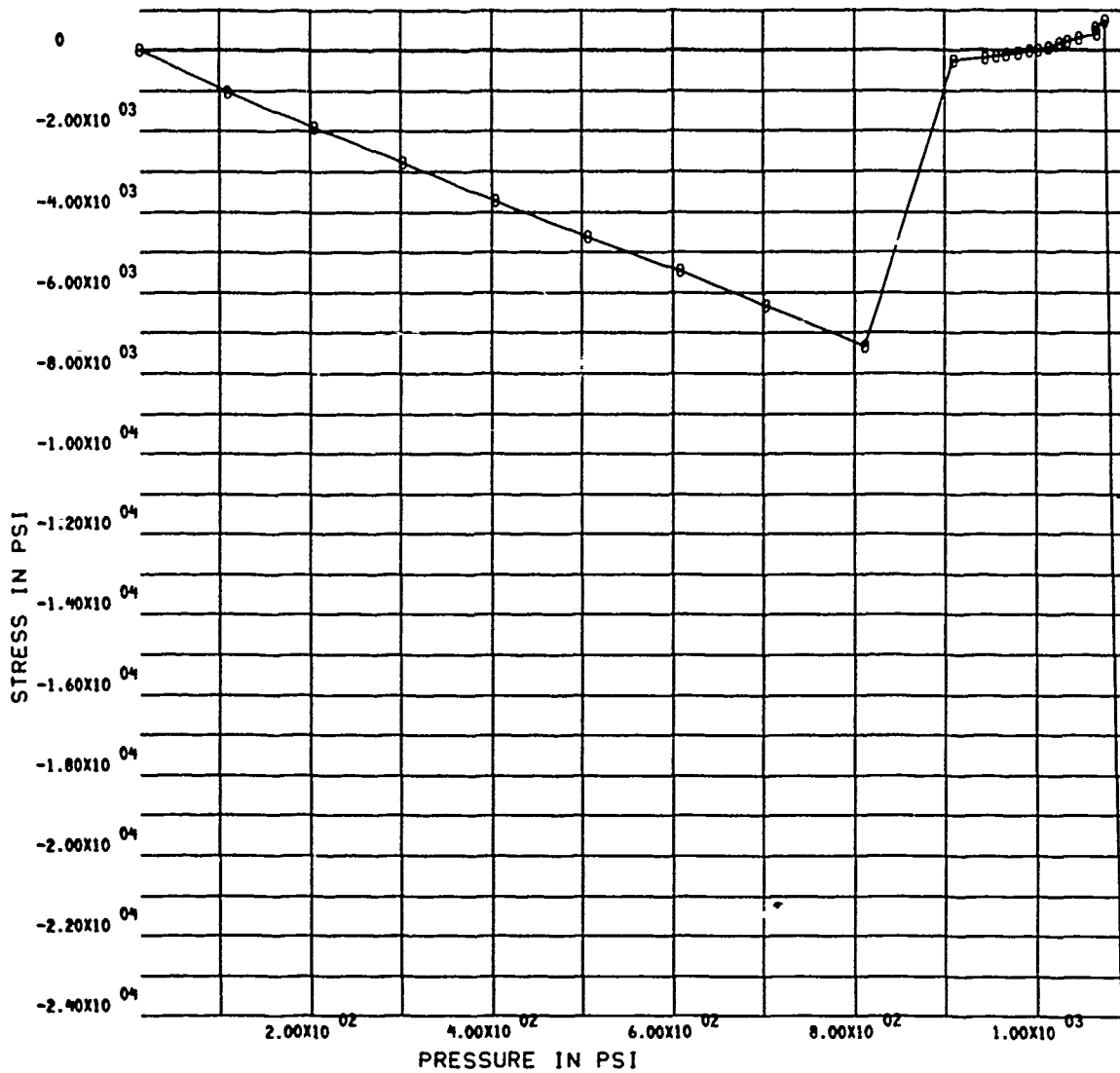


Figure A.6.J. Minimum Principal Stress on the Interior Surface 20 Degrees Above the Flange of a Shell of Constant Thickness ( $t/R_i = 0.046$ ) Under Short-Term Hydrostatic Loading. Orientation: meridional.



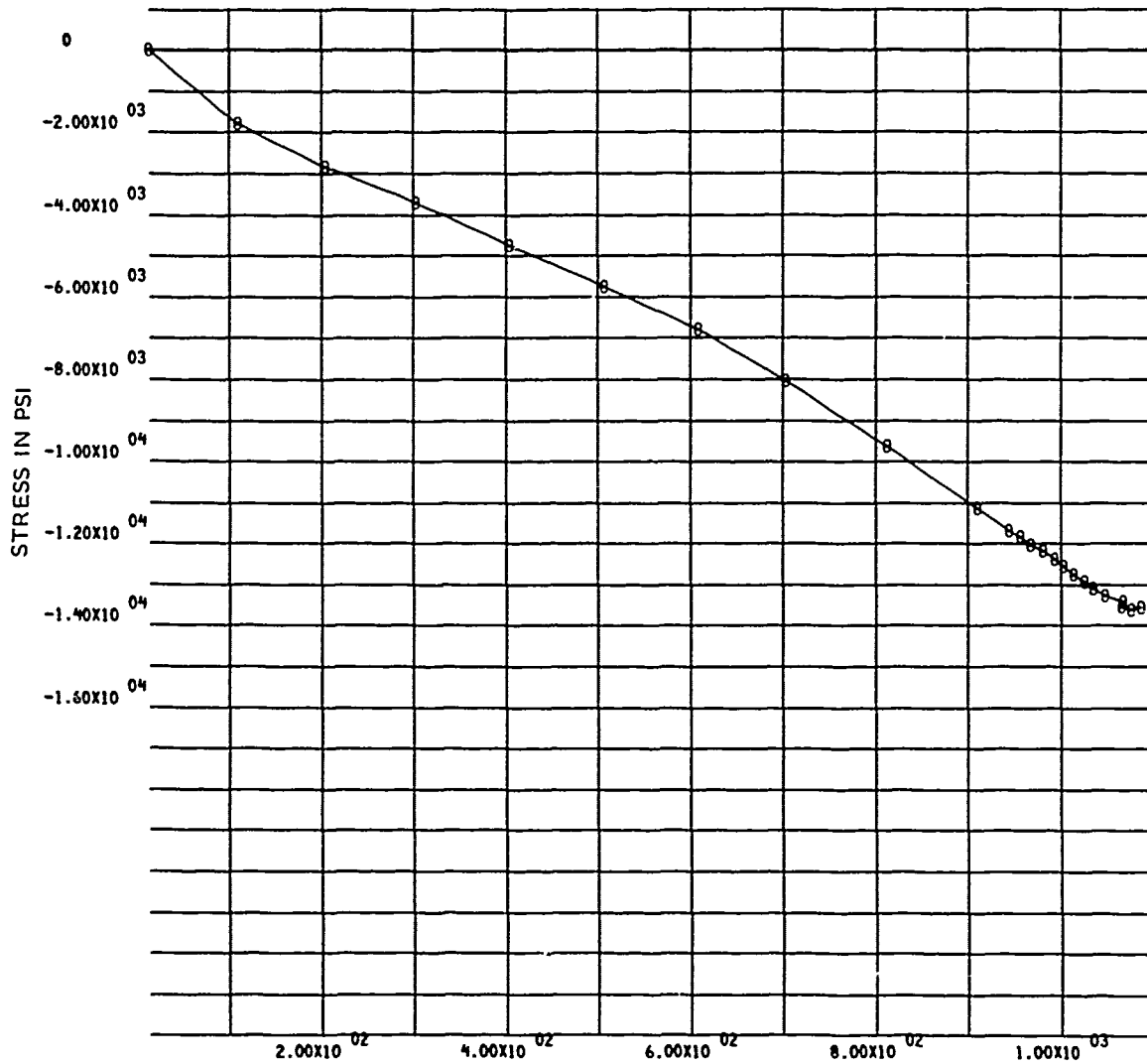


Figure A.6.K. Maximum Principal Stress on the Interior Surface of the Flange of a Shell of Constant Thickness ( $t/R_i = 0.046$ ) Under Short-Term Hydrostatic Loading. Orientation: meridional.

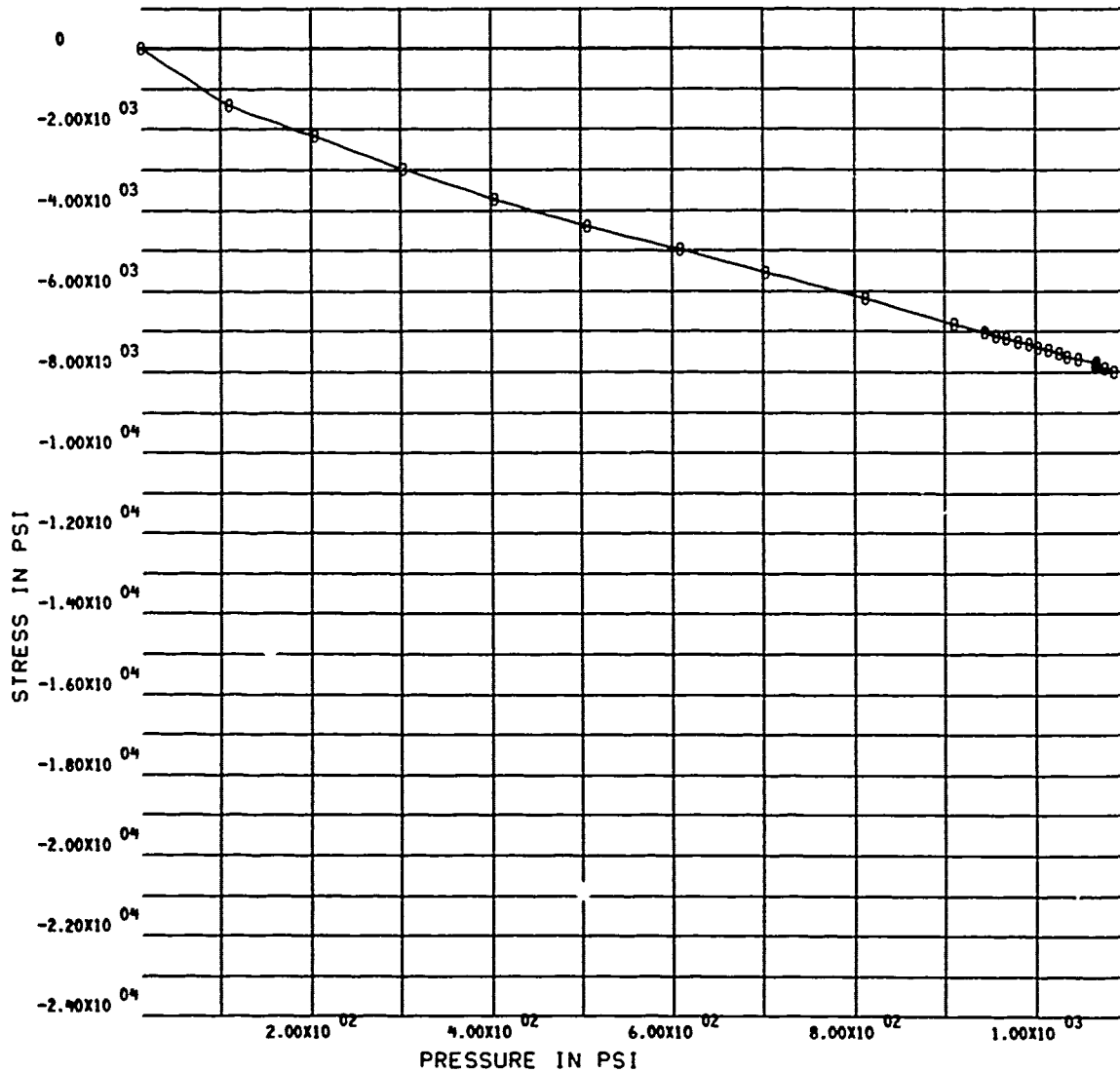


Figure A.6.L. Minimum Principal Stress on the Interior Surface of the Flange of a Shell of Constant Thickness ( $t/R_i = 0.046$ ) Under Short-Term Hydrostatic Loading. Orientation: hoop.

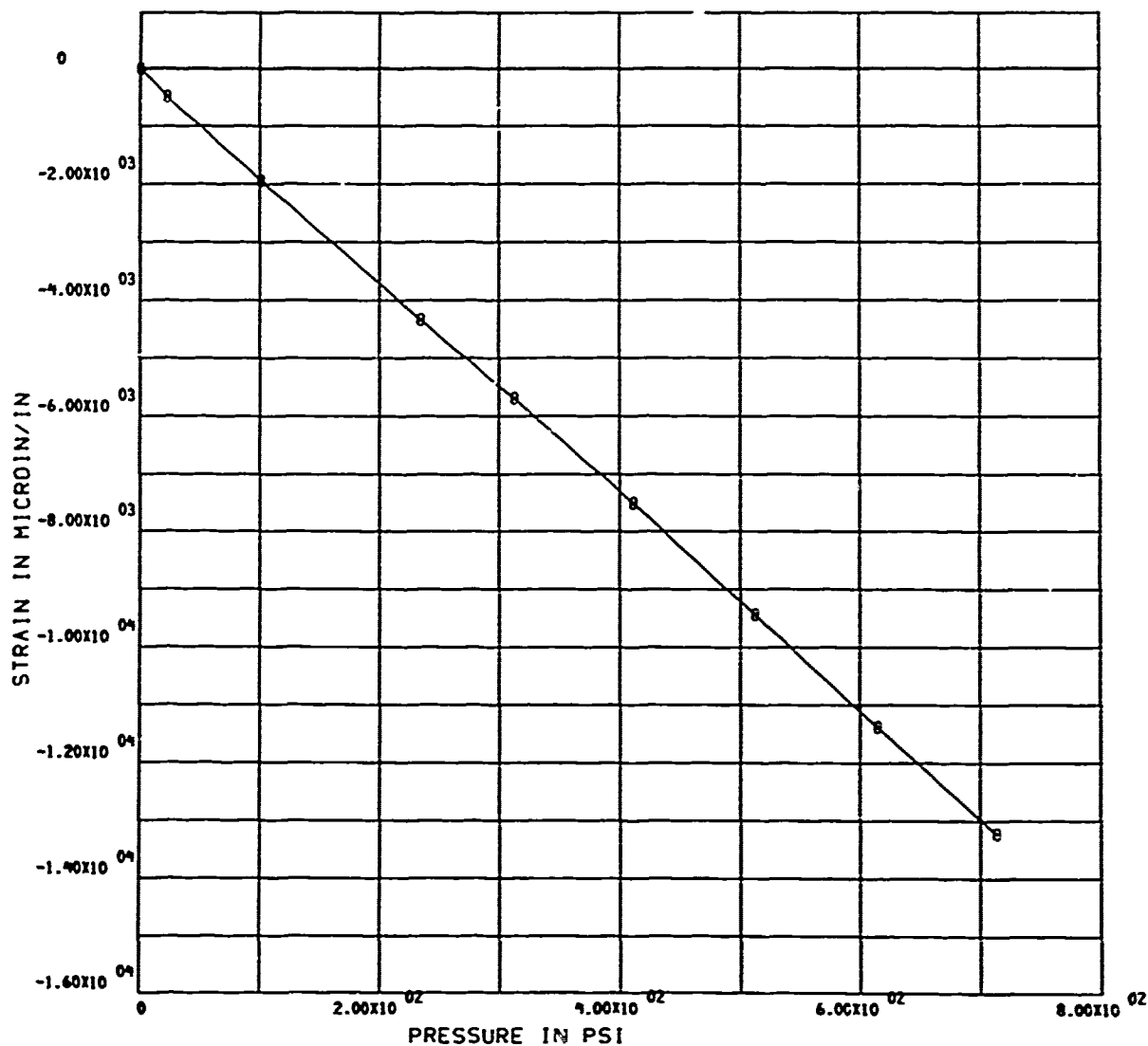


Figure A.7.A. Strain on the Interior Surface at the Apex of a Flanged Shell of Variable Thickness ( $t/R_i = 0.046$ ) Under Short-Term Hydrostatic Loading.

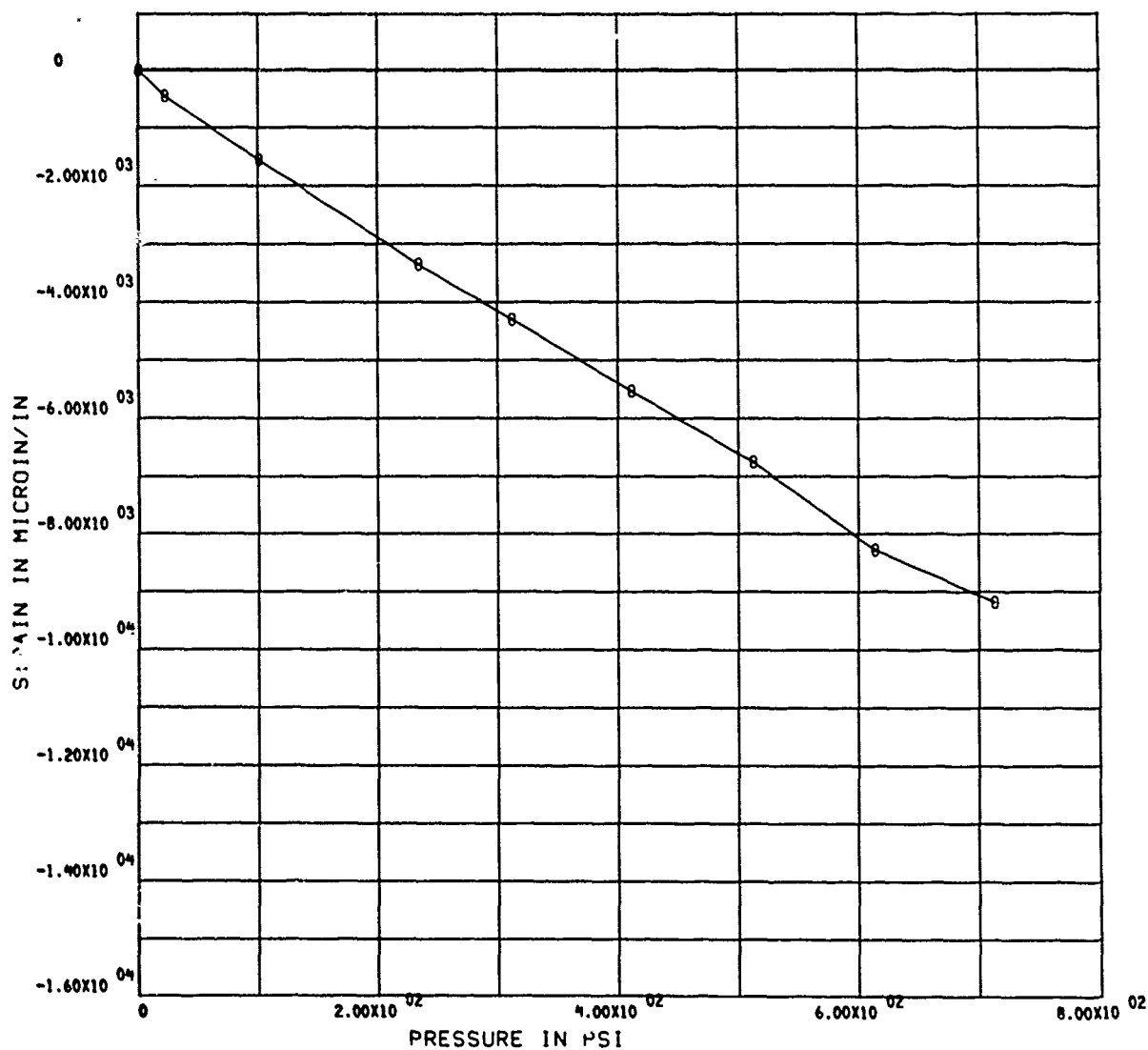


Figure A.7.B. Strain on the Interior Surface 20 Degrees Above the Flange of a Shell of Variable Thickness ( $t/R_i = 0.046$ ) Under Short-Term Hydrostatic Loading. Orientation: meridional.

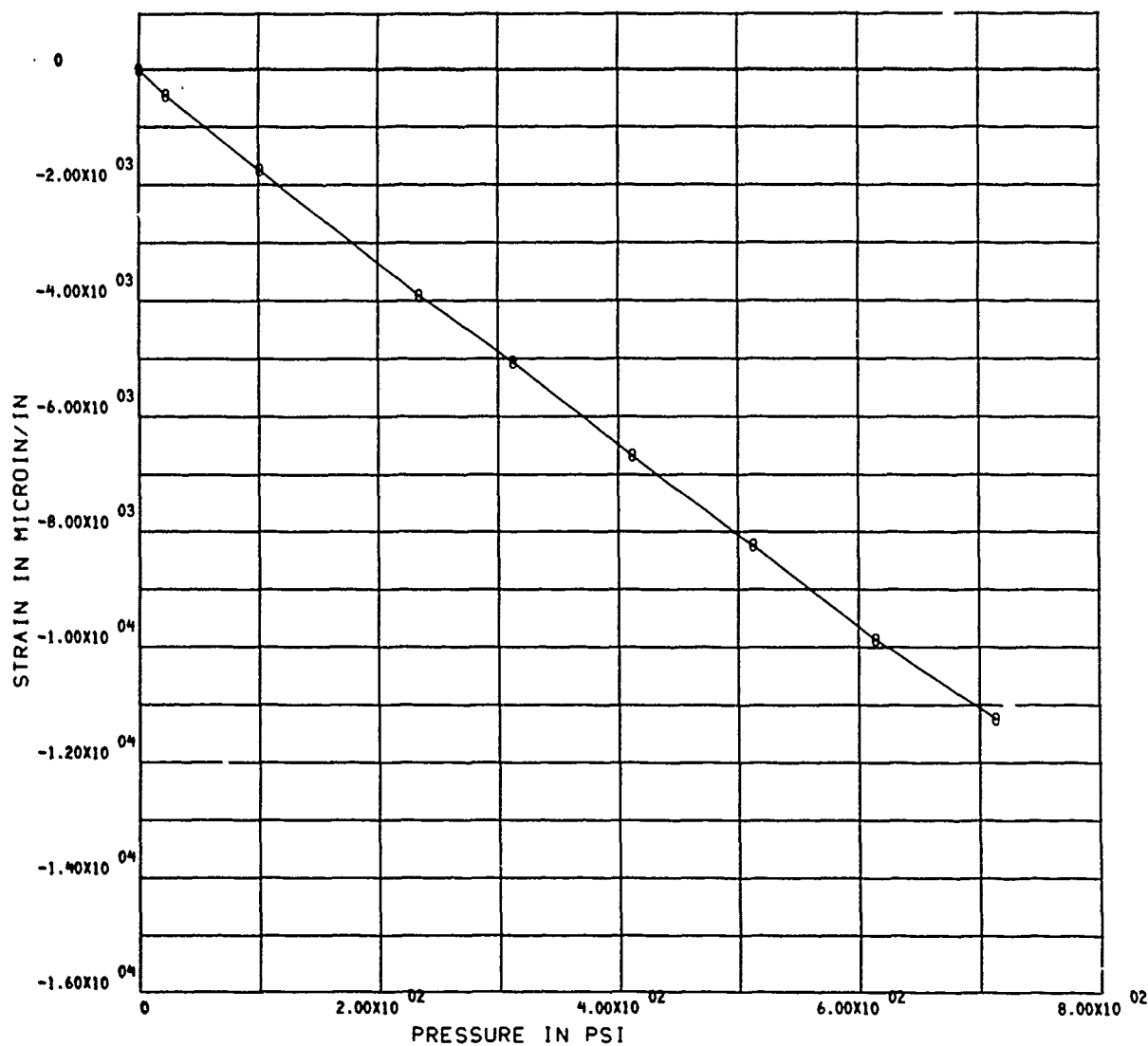


Figure A.7.C. Strain on the Interior Surface 20 Degrees Above the Flange of a Shell of Variable Thickness ( $t/R_i = 0.046$ ) Under Short-Term Hydrostatic Loading. Orientation: 45 degrees with meridian.

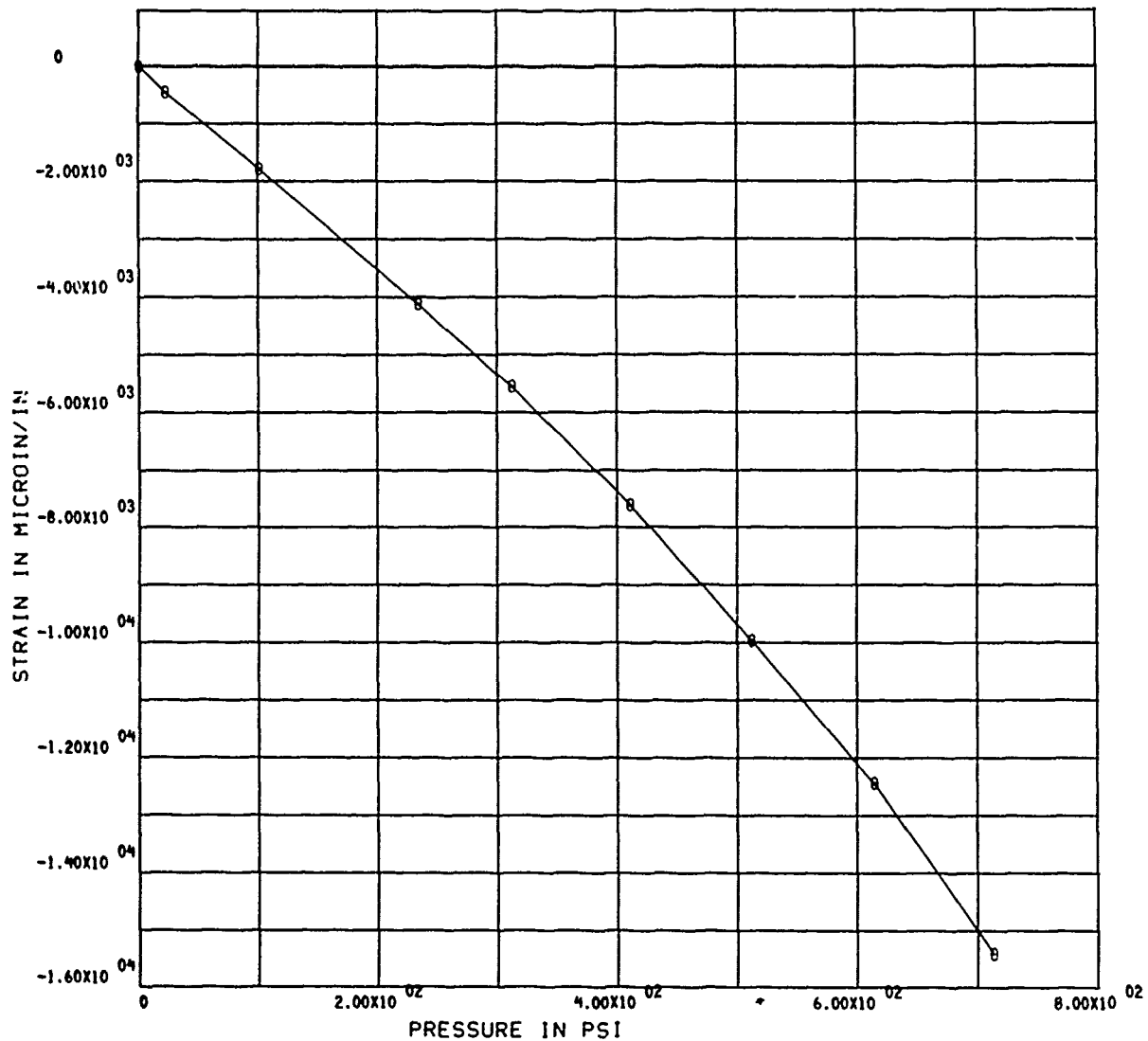


Figure A.7.D. Strain on the Interior Surface 20 Degrees Above the Flange of a Shell of Variable Thickness ( $t/R_i = 0.046$ ) Under Short-Term Hydrostatic Loading. Orientation: hoop.

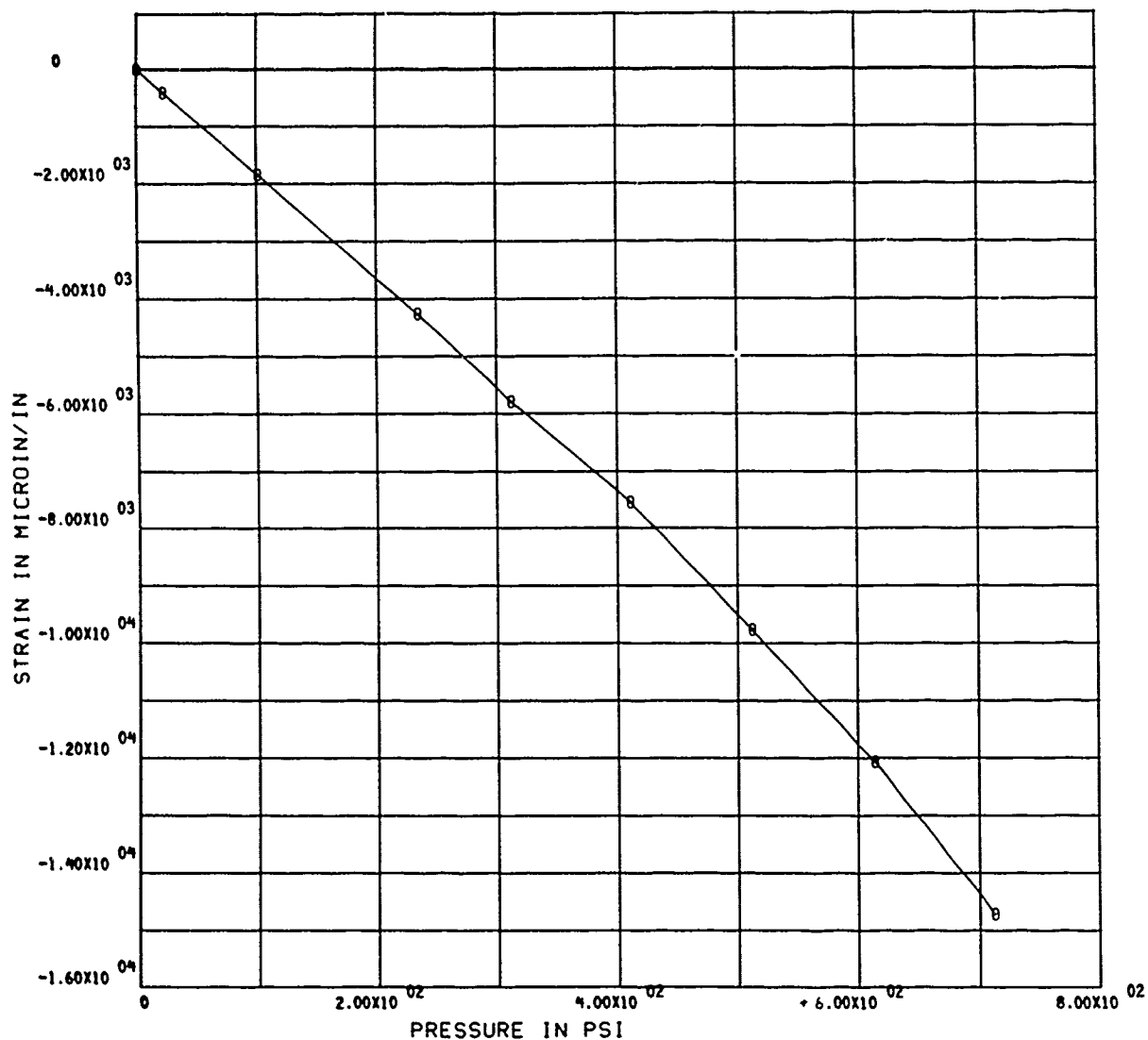


Figure A.7.E. Strain on the Interior Surface of the Flange of a Shell of Variable Thickness ( $t/R_i = 0.046$ ) Under Short-Term Hydrostatic Loading. Orientation: meridional.

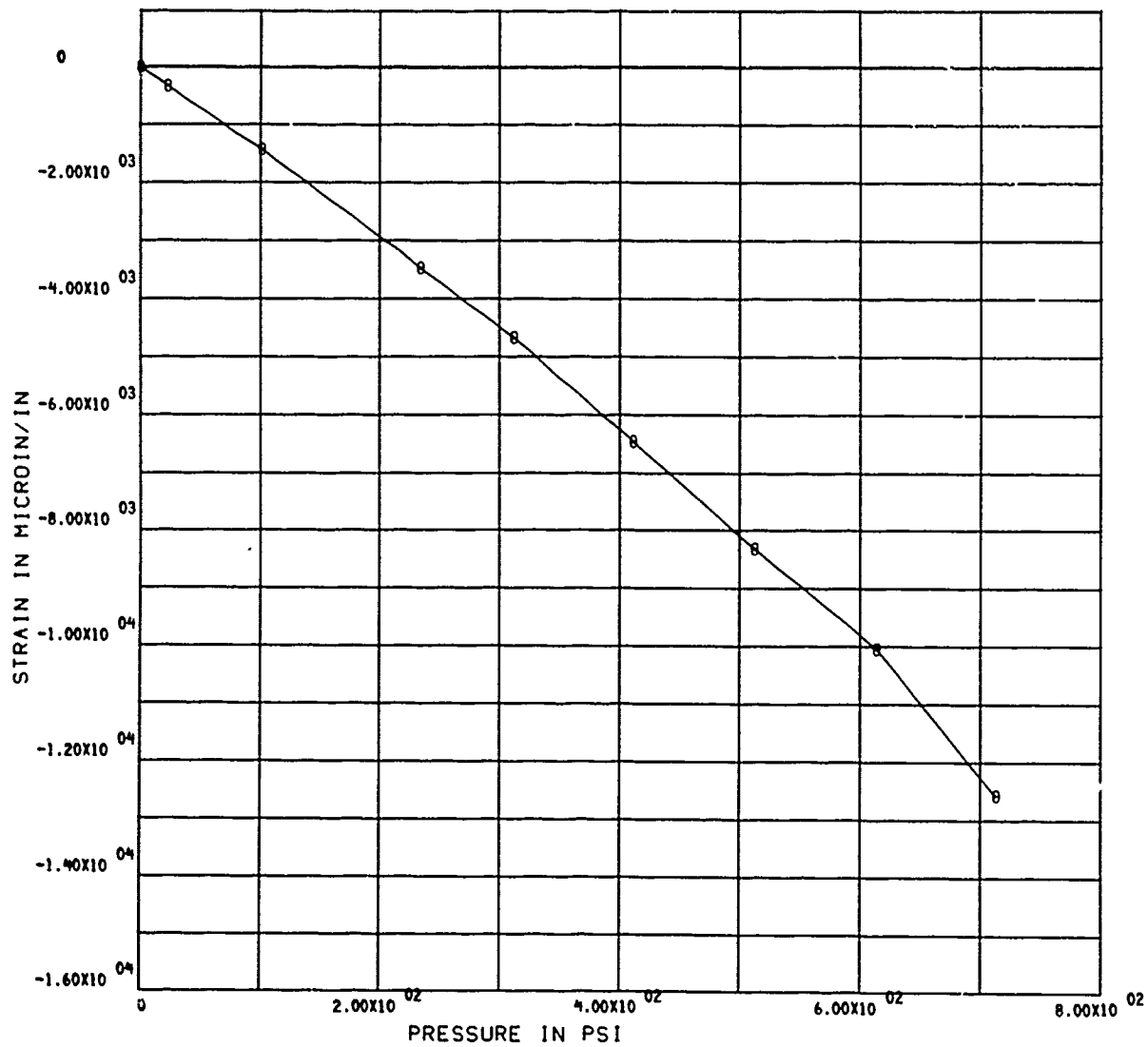


Figure A.7.F. Strain on the Interior Surface of the Flange of a Shell of Variable Thickness ( $t/R_i = 0.046$ ) Under Short-Term Hydrostatic Loading. Orientation: 45 degrees with meridional.



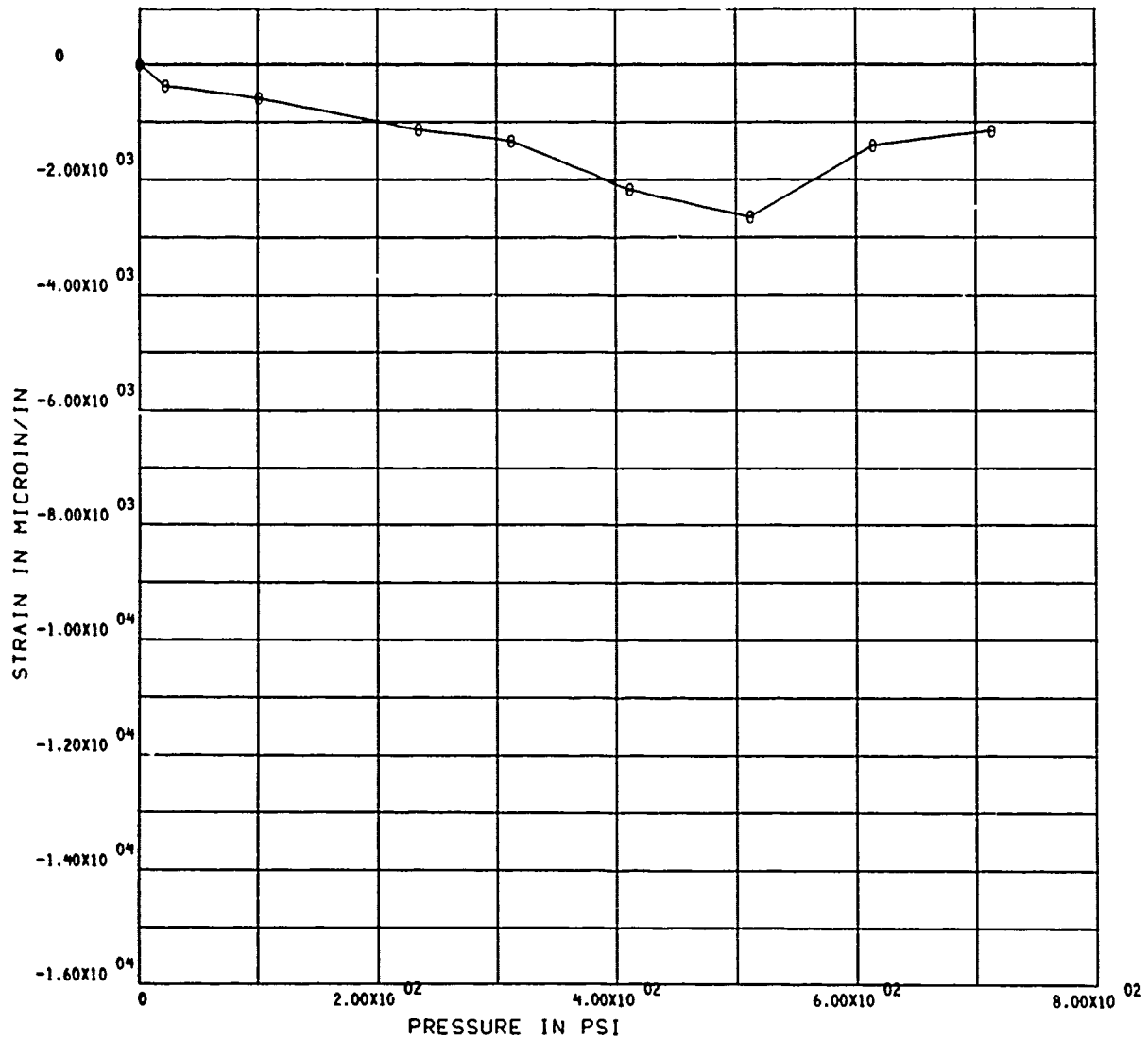


Figure A.7.G. Strain on the Interior Surface of the Flange of a Shell of Variable Thickness ( $t/R_i = 0.046$ ) Under Short-Term Hydrostatic Loading. Orientation: hoop.

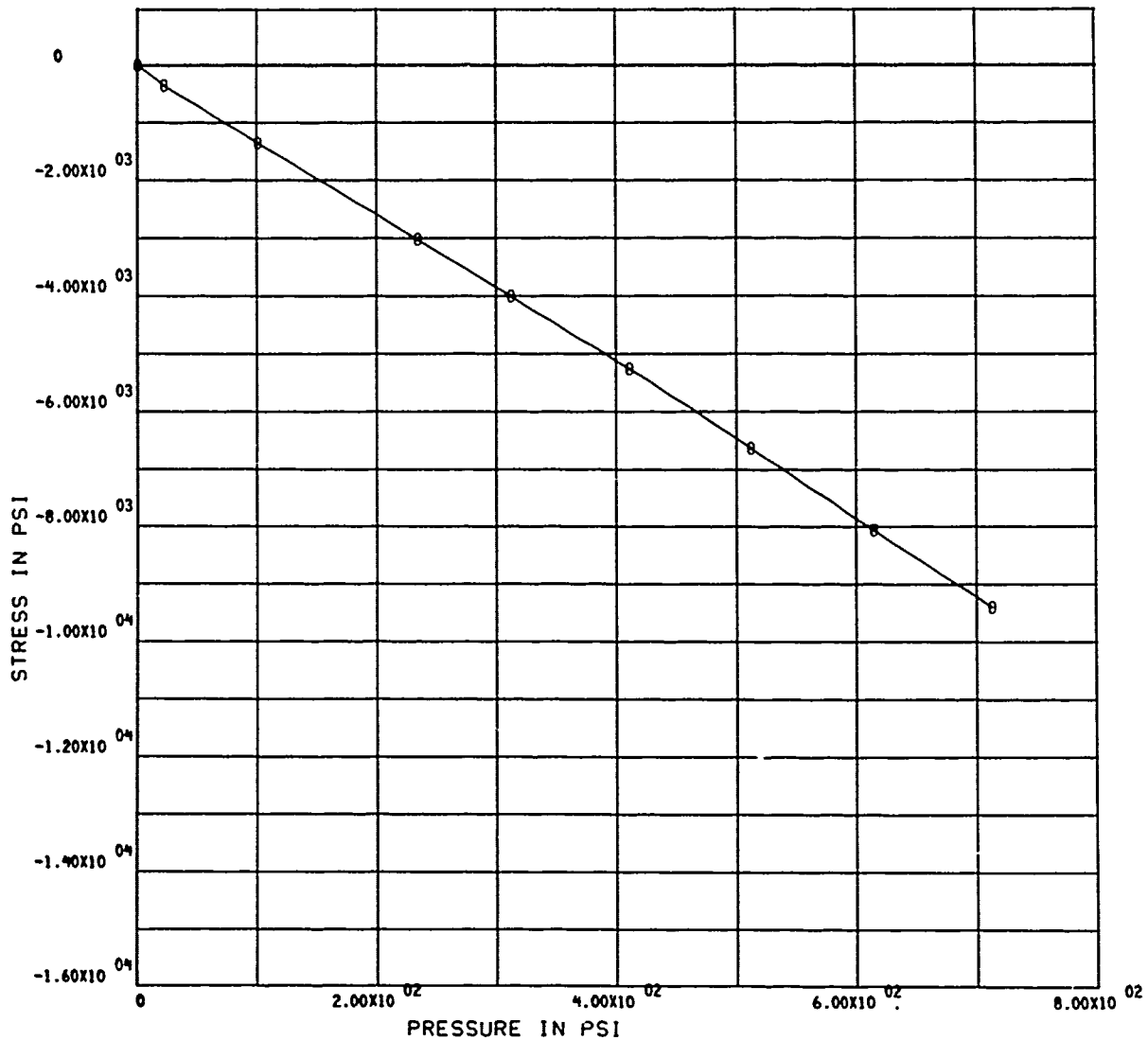


Figure A.7.H. Maximum Principal Stress on the Interior Surface at the Apex of a Flanged Shell of Variable Thickness ( $t/R_i = 0.046$ ) Under Short-Term Hydrostatic Loading.

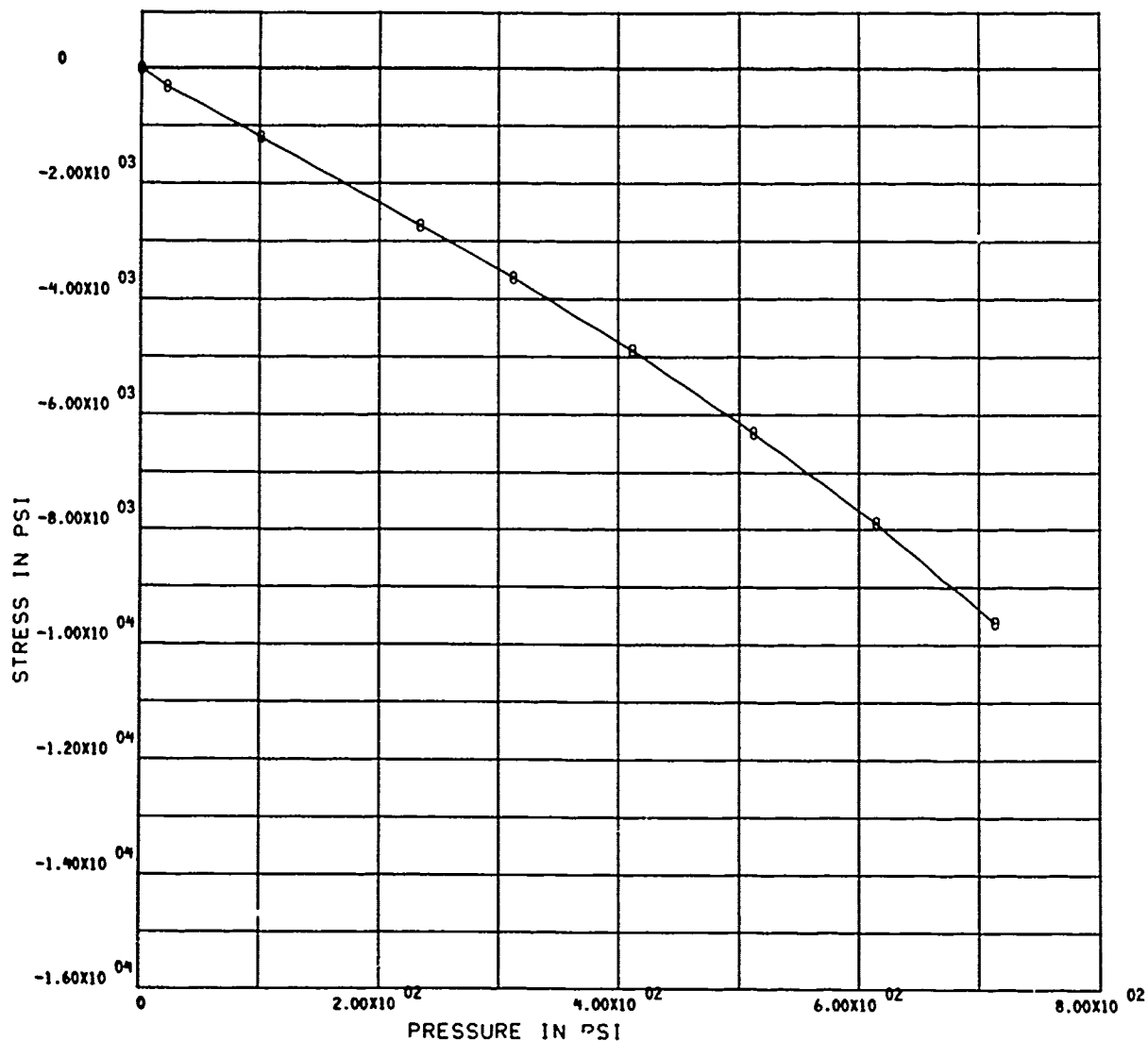


Figure A.7.1. Maximum Principal Stress on the Interior Surface 20 Degrees Above the Flange of a Shell of Variable Thickness ( $t/R_i = 0.046$ ) Under Short-Term Hydrostatic Loading. Orientation: hoop.

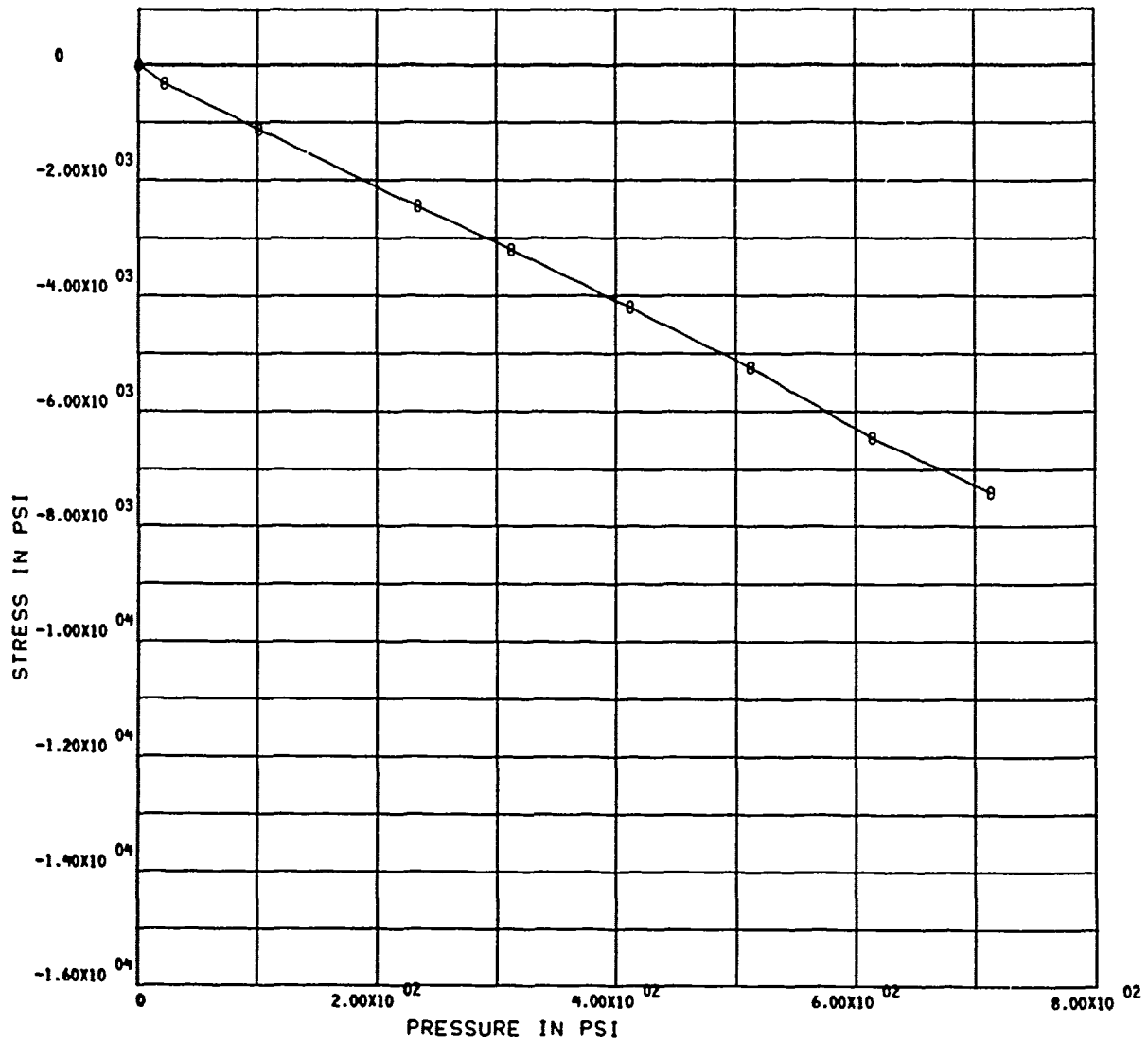


Figure A.7.J. Minimum Principal Stress 20 Degrees Above the Flange of a Shell of Variable Thickness ( $t/R_i = 0.046$ ) Under Short-Term Hydrostatic Loading. Orientation: meridional.

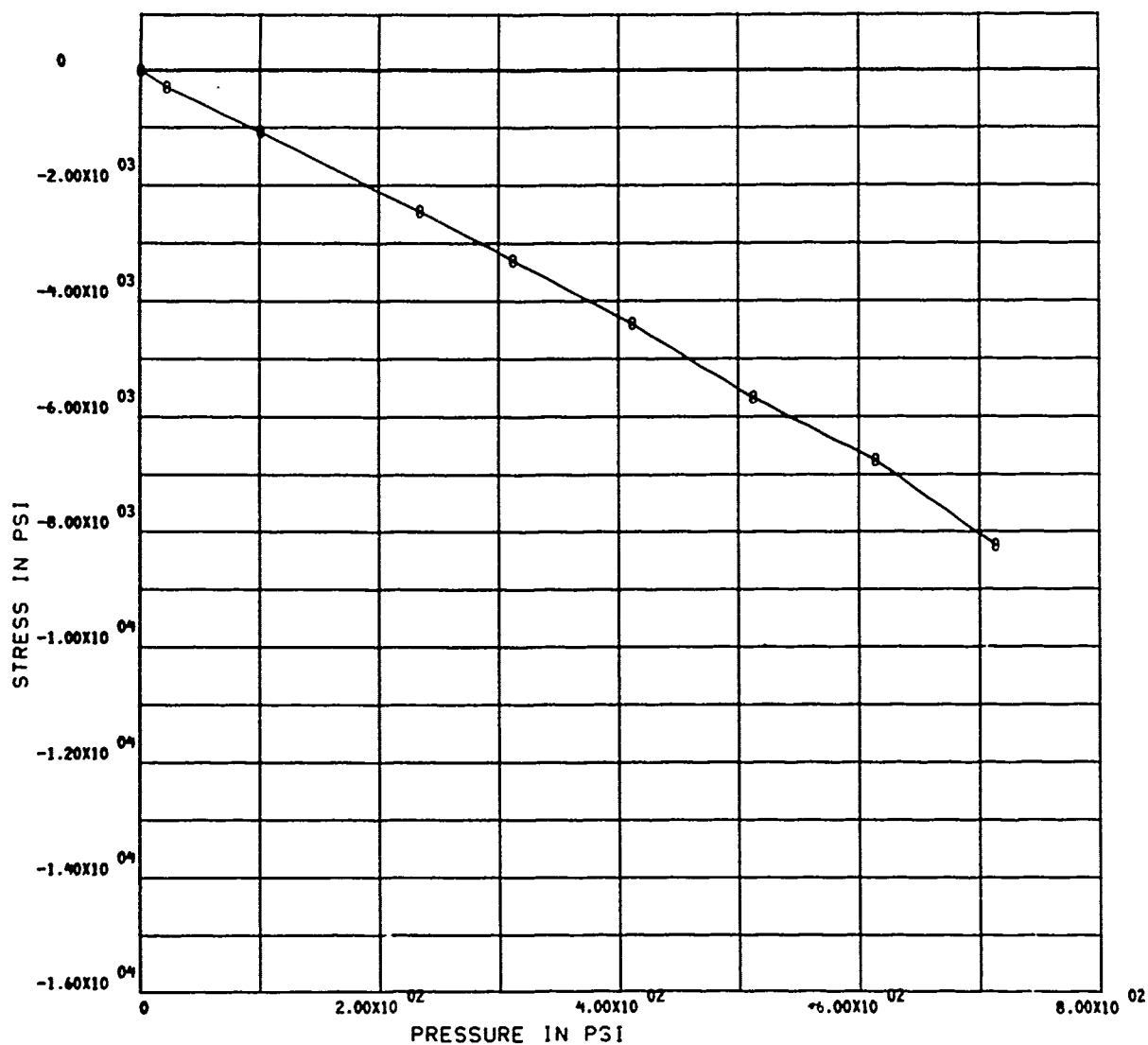


Figure A.7.K. Maximum Principal Stress on the Interior Surface of the Flange of a Shell of Variable Thickness ( $t/R_1 = 0.046$ ) Under Short-Term Hydrostatic Loading. Orientation: meridional.

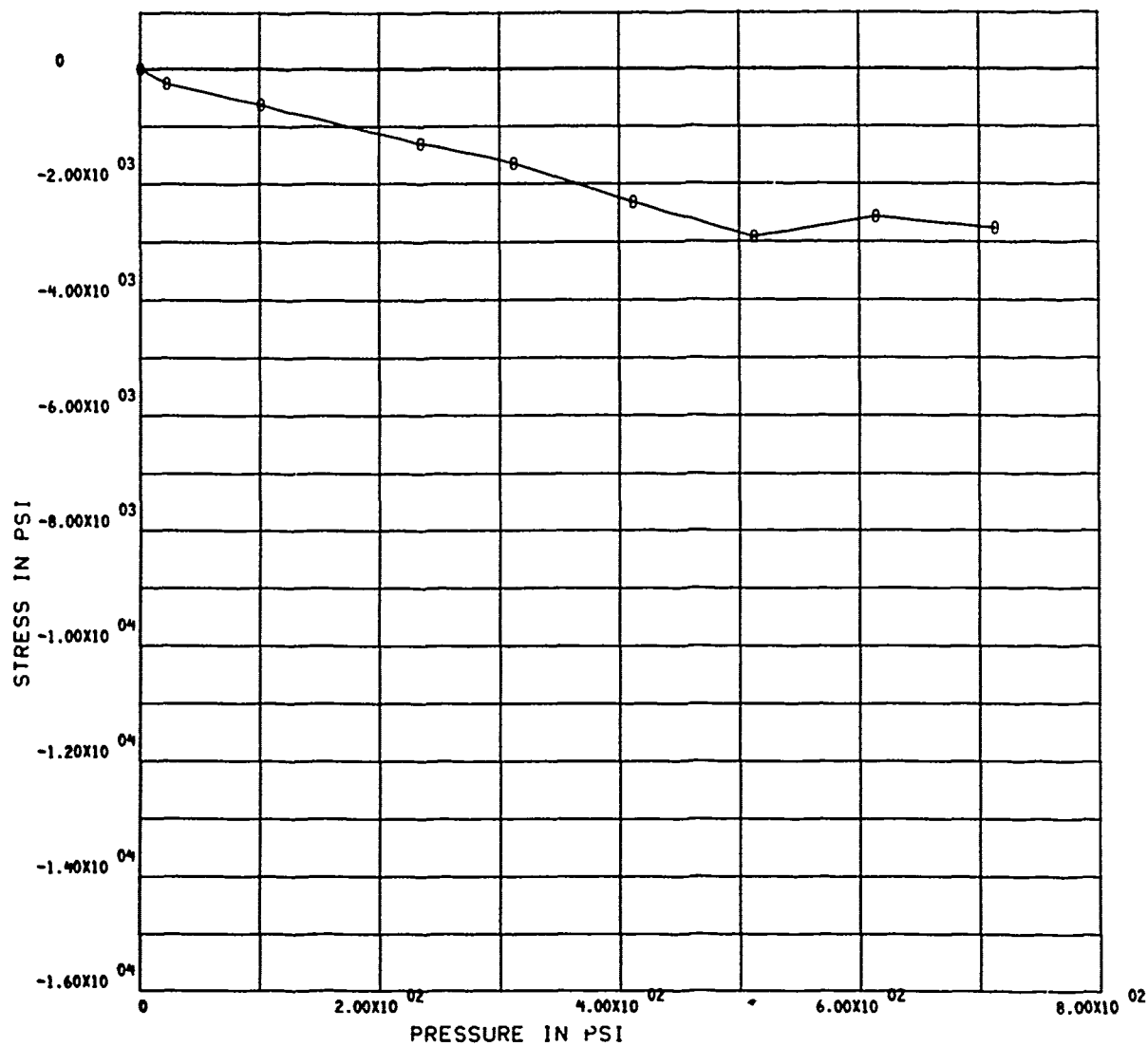


Figure A.7.L. Minimum Principal Stress on the Interior Surface of the Flange of a Shell of Variable Thickness ( $t/R_i = 0.046$ ) Under Short-Term Hydrostatic Loading. Orientation: hoop.

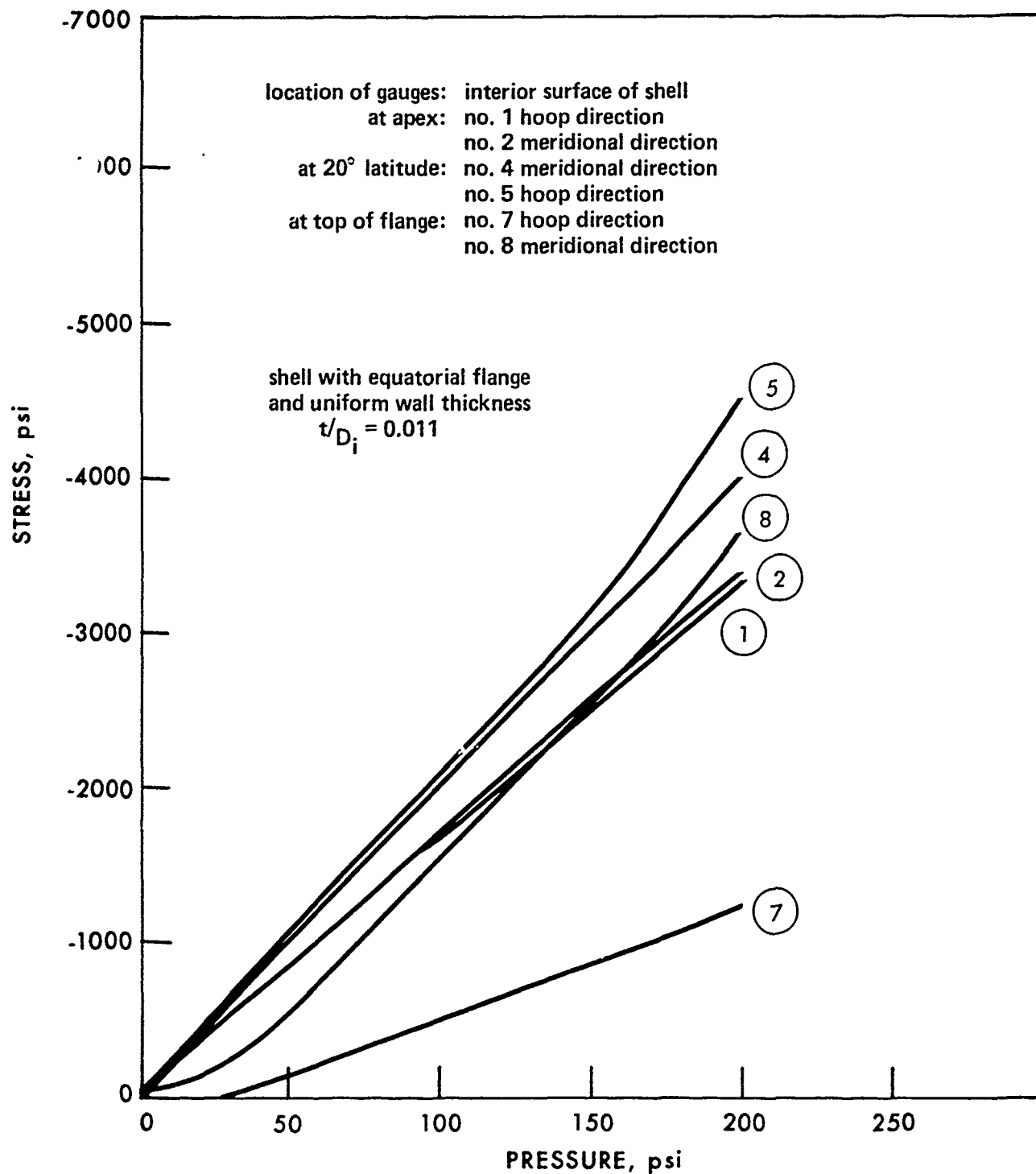


Figure A.8.A. Measured Stresses on the Interior Surface of a Flanged Shell of Constant Thickness ( $t/R_i = 0.022$ ).

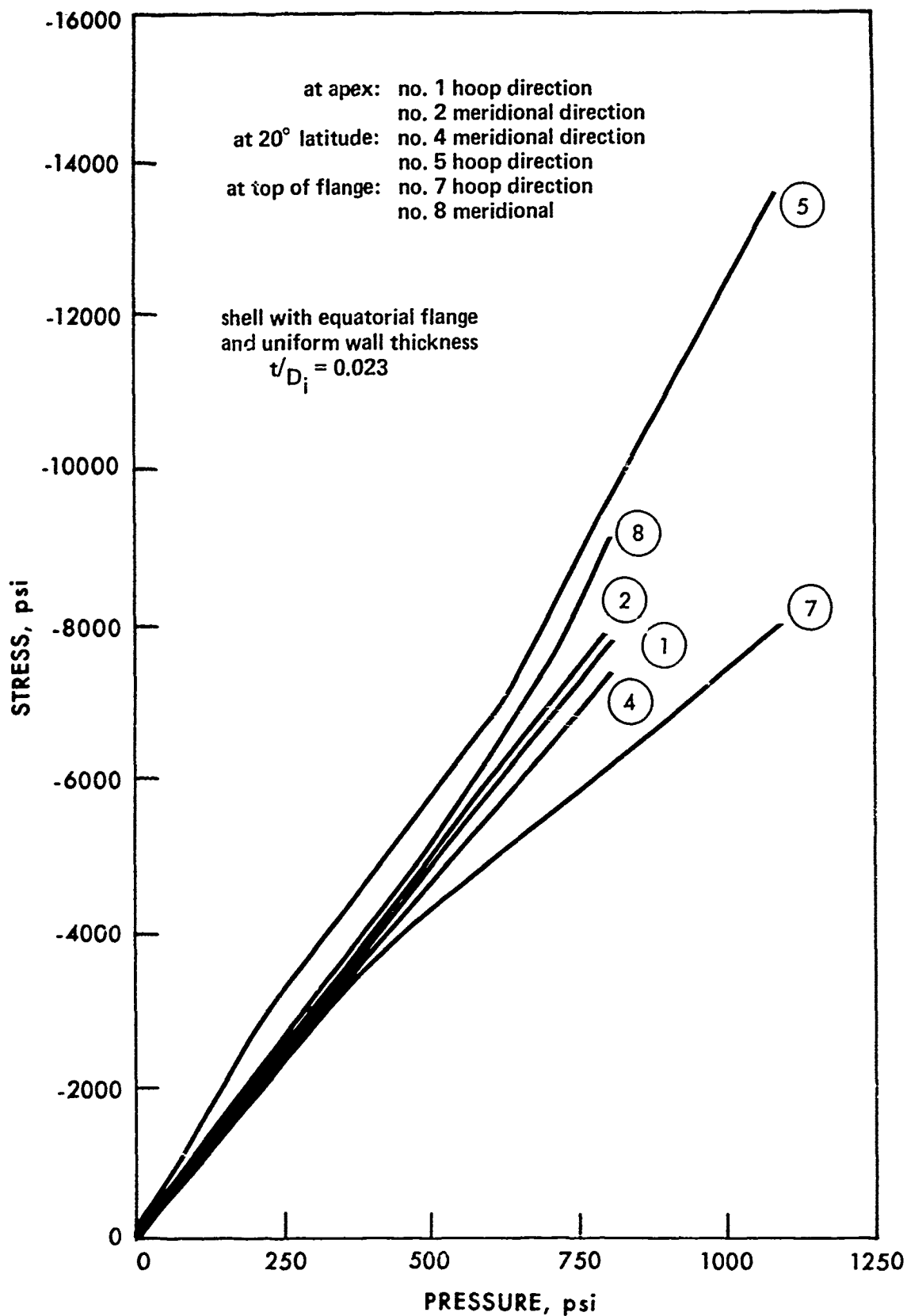


Figure A.8.B. Measured Stresses on the Interior Surface of a Flanged Shell of Constant Thickness ( $t/R_i = 0.046$ ).



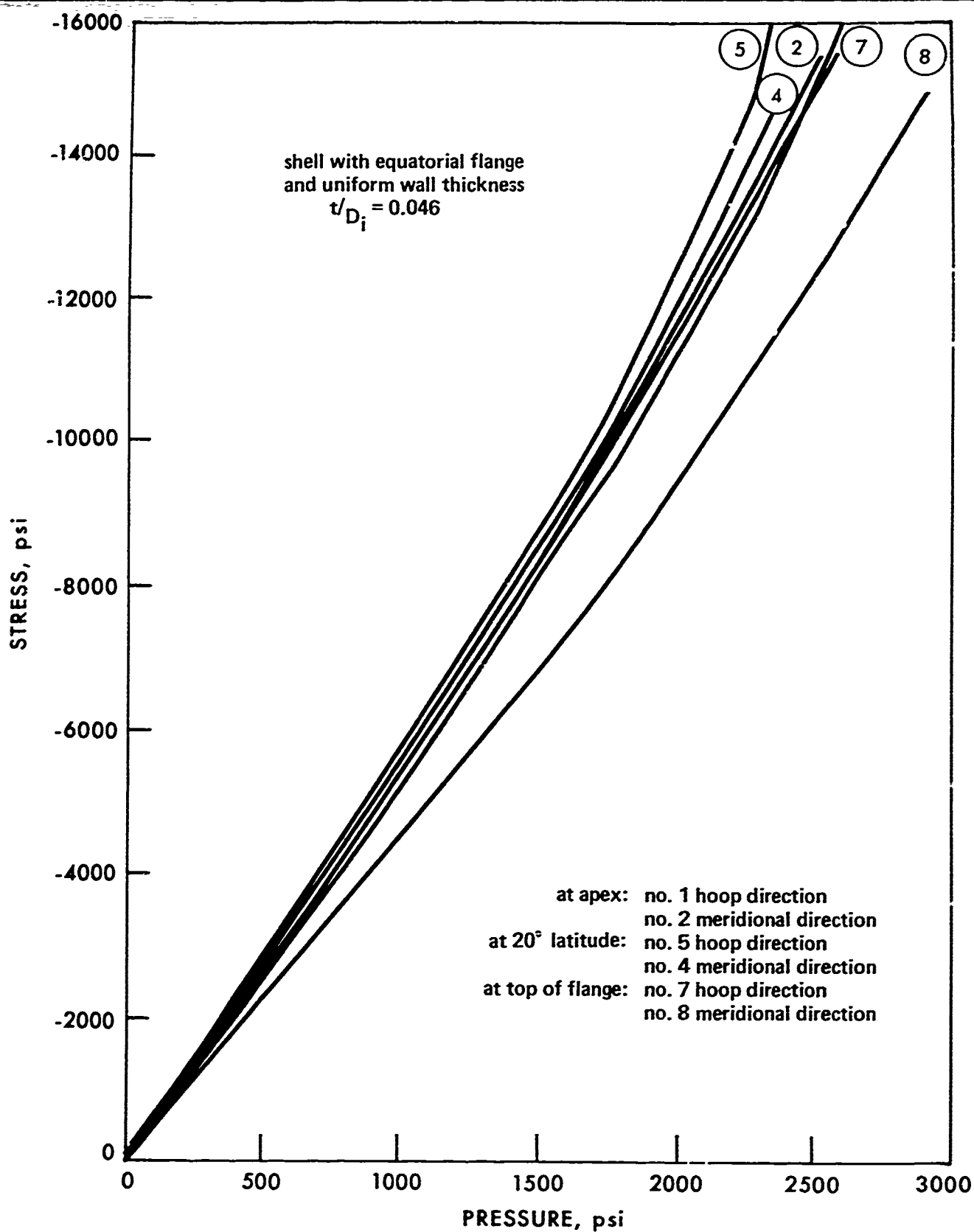


Figure A.8.C. Measured Stresses on the Interior Surface of a Flanged Shell of Constant Thickness ( $t/R_i = 0.093$ ).

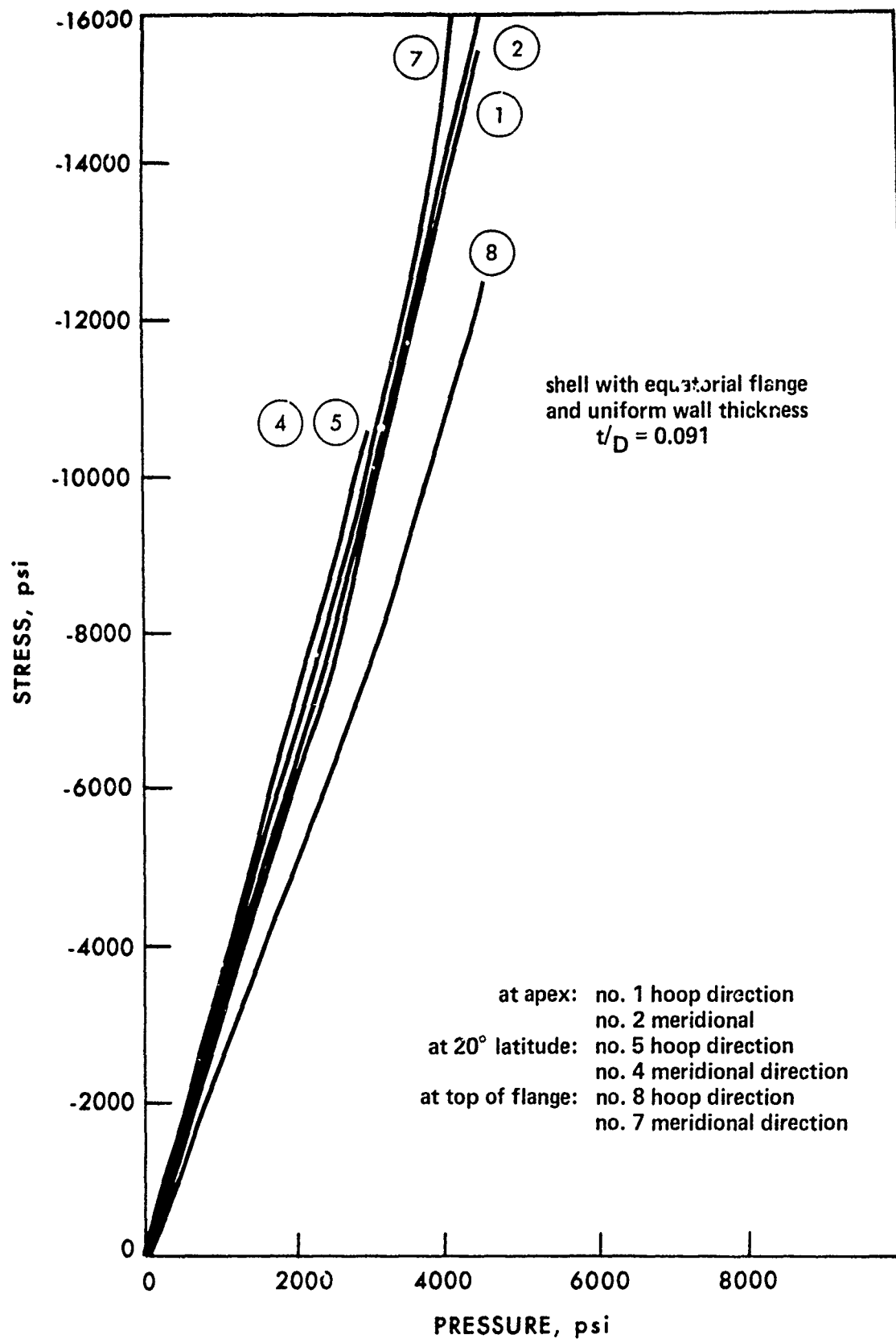


Figure A.8.D. Measured Stresses on the Interior Surface of a Flanged Shell  
of Constant Thickness ( $t/R_f = 0.182$ ).

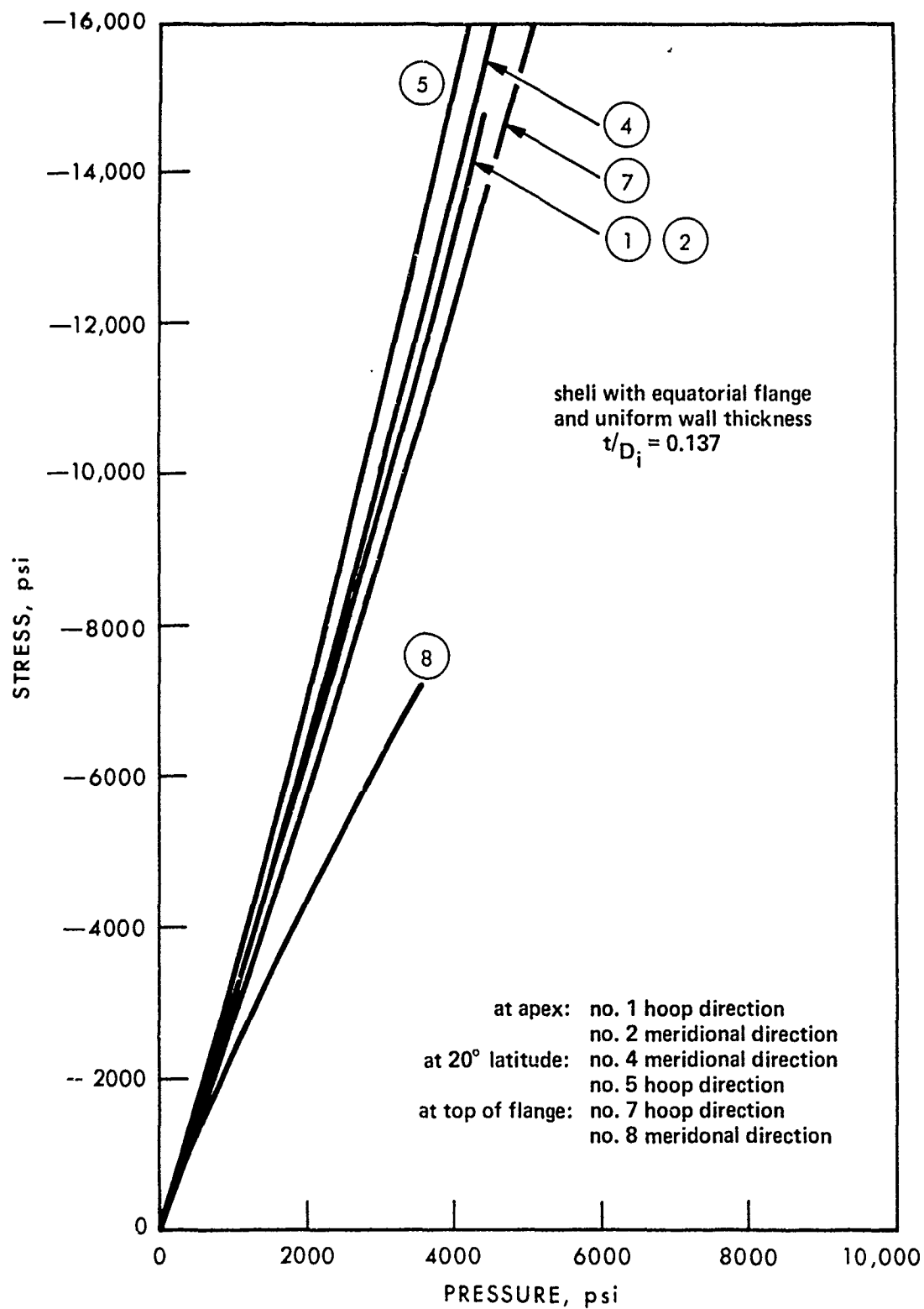


Figure A.8.E. Measured Stresses on the Interior Surface of a Flanged Shell of Constant Thickness ( $t/R_i = 0.237$ ).

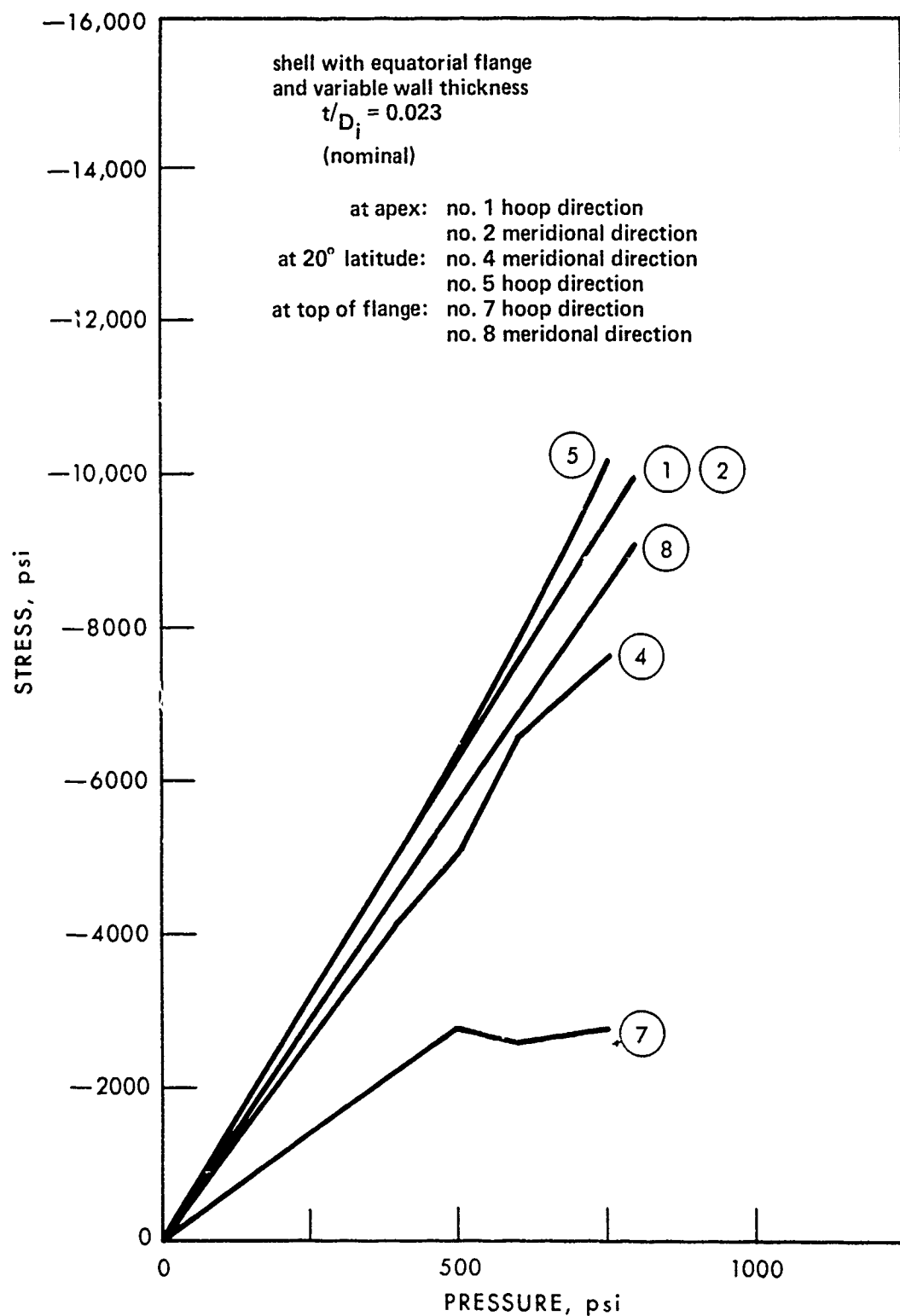


Figure A.9.A Measured Stresses on the Interior Surface of a Flanged Shell of Variable Thickness ( $t/R_1 = 0.046$ )

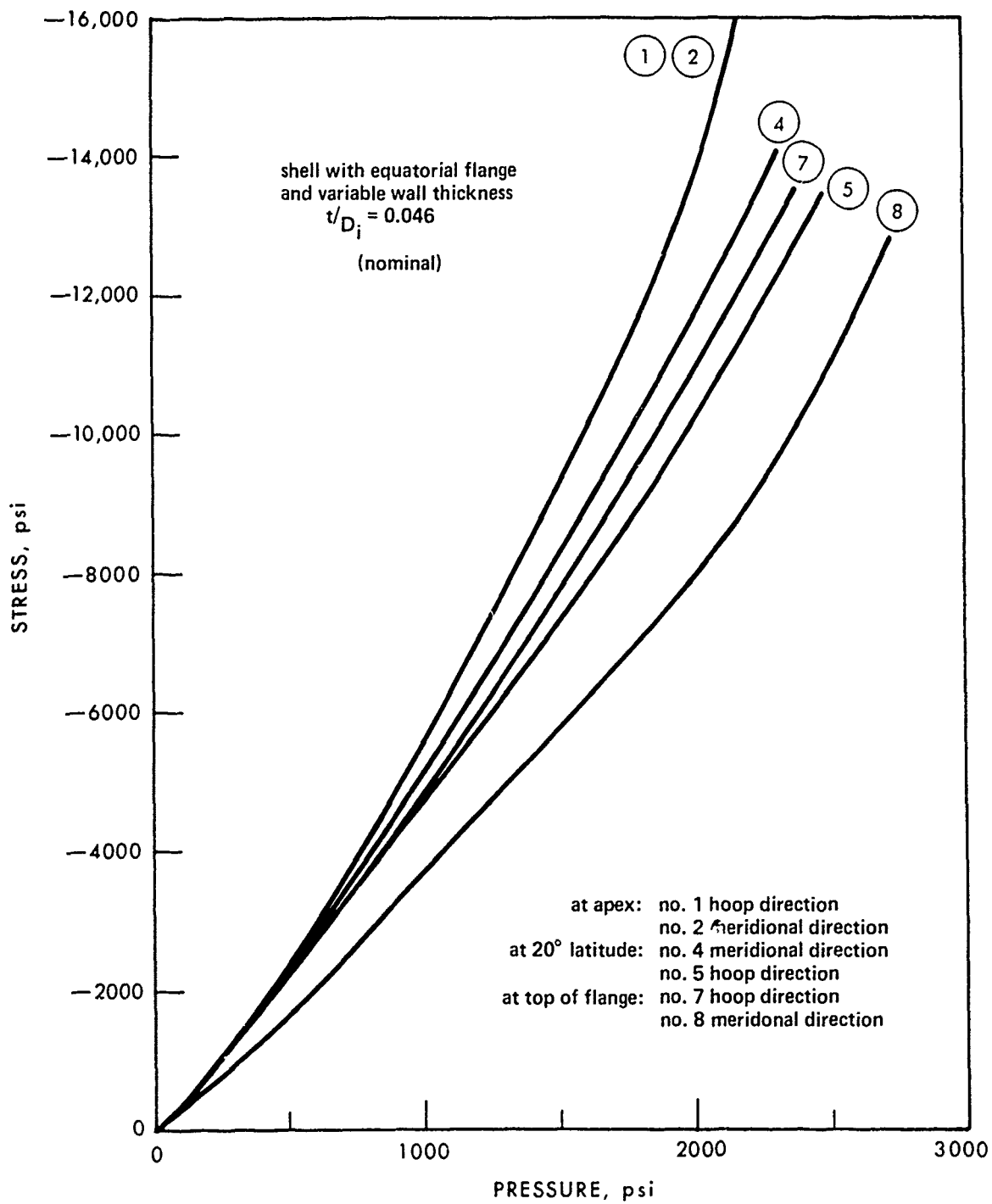


Figure A.9.B. Measured Stresses on the Interior Surface of a Flanged Shell of Variable Thickness ( $t/R_i = 0.093$ ).

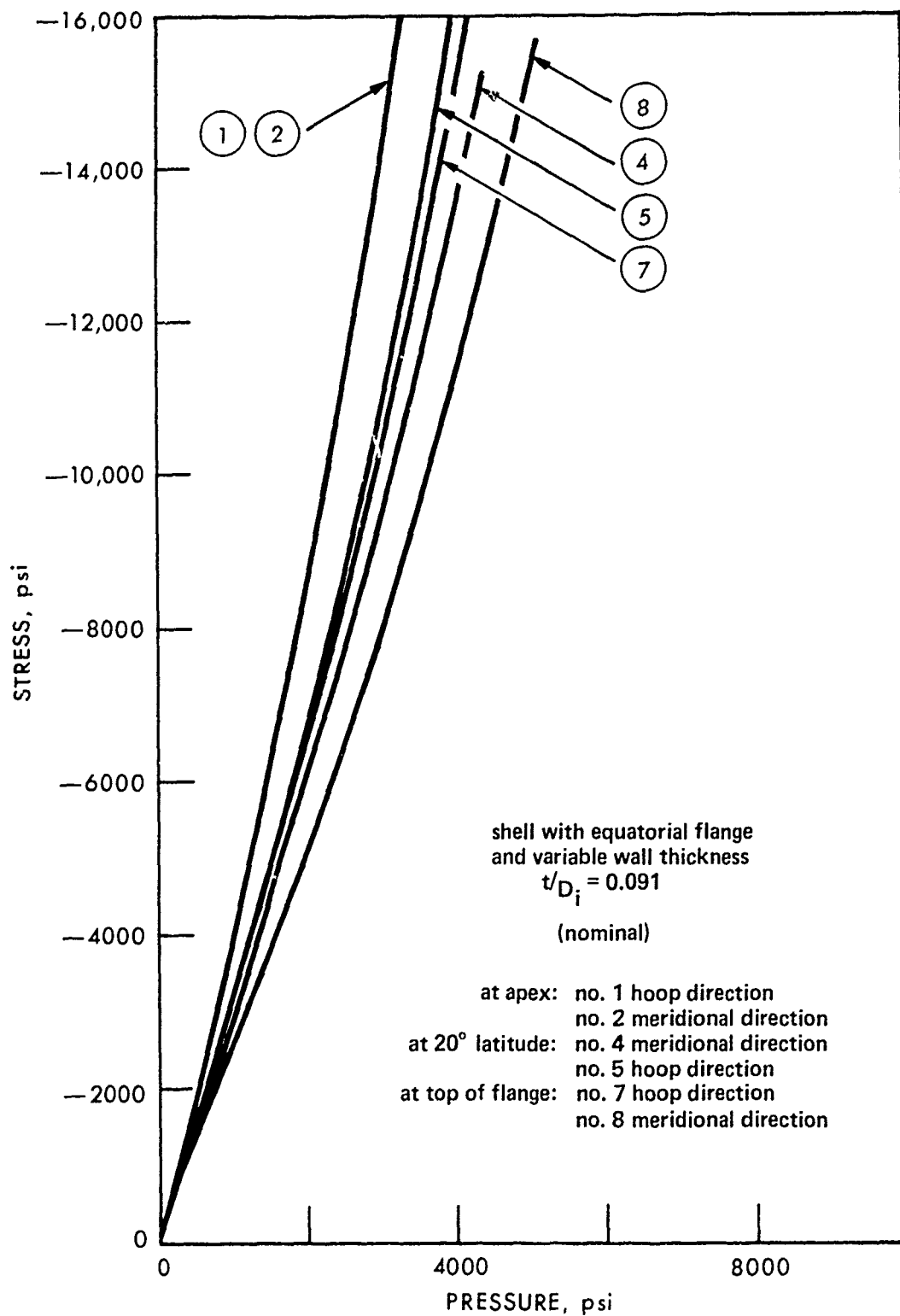


Figure A.9.C. Measured Stresses on the Interior Surface of a Flanged Shell of Variable Thickness ( $t/R_i = 0.182$ ).

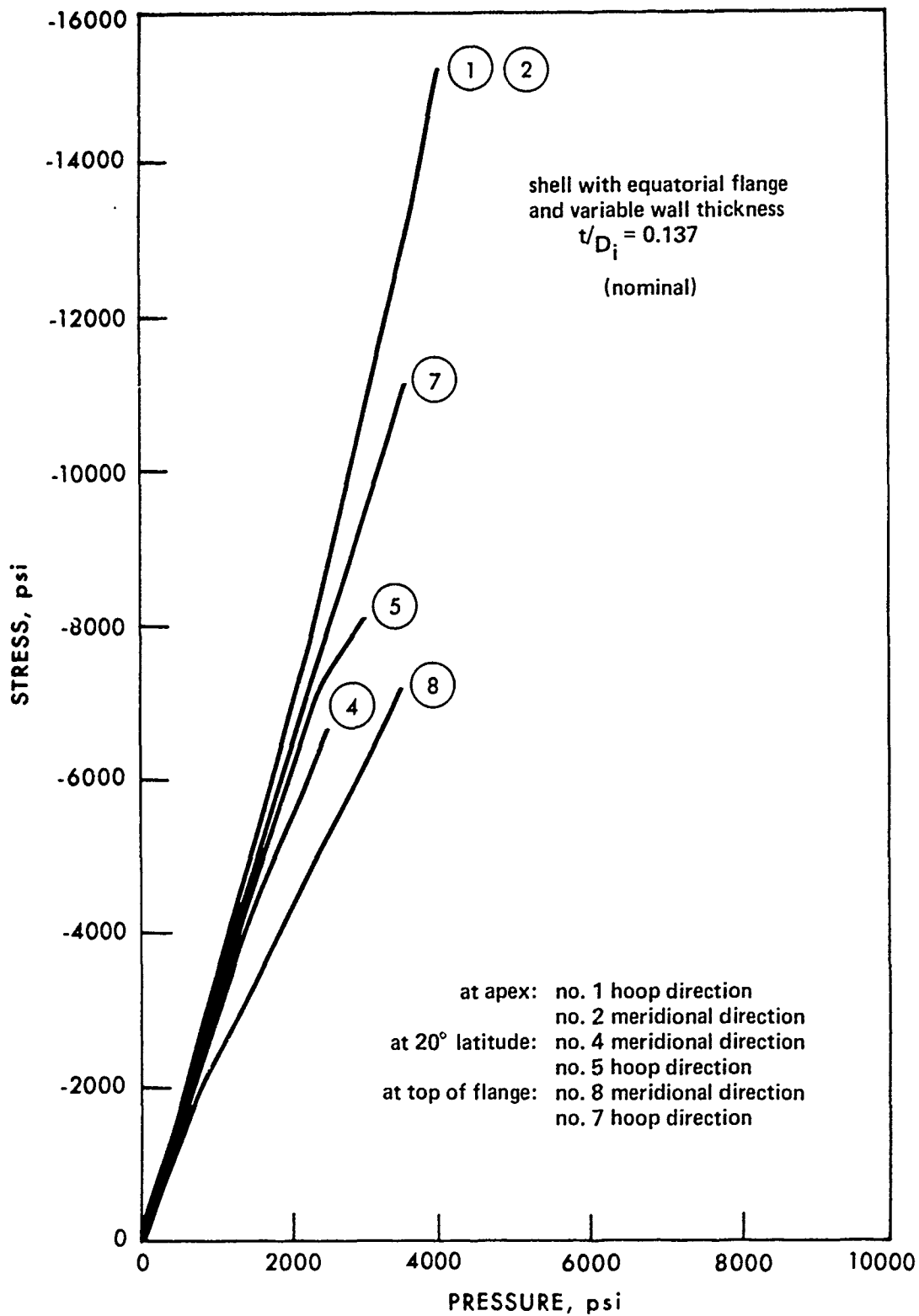


Figure A.9.D. Measured Stresses on the Interior Surface of a Flanged Shell of Variable Thickness ( $t/R_i = 0.273$ ).

UNCLASSIFIED

Security Classification

## DOCUMENT CONTROL DATA - R &amp; D

(Security classification of title, body of abstract and indexing annotation must be entered when the overall report is classified)

1. ORIGINATING ACTIVITY (Corporate author) Naval Undersea Center San Diego, Calif. 92132		2a. REPORT SECURITY CLASSIFICATION <b>UNCLASSIFIED</b>	
		2b. GROUP	
3. REPORT TITLE  FLANGED ACRYLIC PLASTIC HEMISPHERICAL SHELLS FOR UNDERSEA SYSTEMS			
4. DESCRIPTIVE NOTES (Type of report and inclusive dates) Research and development: January 1971-December 1972			
5. AUTHOR(S) (First name, middle initial, last name) Jerry D. Stachiw      Naval Undersea Center Jack R. Maison      Naval Civil Engineering Laboratory			
6. REPORT DATE September 1973		7a. TOTAL NO. OF PAGES 103	7b. NO. OF REFS 9
8a. CONTRACT OR GRANT NO Work was funded internally under NUC Independent Exploratory Development.		9a. ORIGINATOR'S REPORT NUMBER(S)  NUC TP 355	
b. PROJECT NO		9b. OTHER REPORT NO(S) (Any other numbers that may be assigned this report)	
c.			
d.			
10. DISTRIBUTION STATEMENT  Approved for public release; distribution unlimited.			
11. SUPPLEMENTARY NOTES		12. SPONSORING MILITARY ACTIVITY Naval Material Command Washington, D.C.	
13. ABSTRACT  The effects of an equatorial flange and a nonuniform wall thickness upon the critical pressure and stress distribution in acrylic plastic hemispheres has been investigated by experimental and analytical methods. Forty acrylic hemispheres were fabricated and tested to destruction under short-term hydrostatic pressure applied on the convex surface. Dome apex displacements were obtained from each specimen and strains were obtained from a selected few. A finite-element elastic analysis was performed on one window configuration for two different boundary conditions and the experimentally derived stresses were used to determine which assumed boundary condition was best for analysis.  It appears that in acrylic plastic hemispheres with $t/R \leq 0.200$ an integral equatorial flange has no deleterious effect on the critical pressure of the hemisphere. Reduced wall thickness at the apex, however, significantly reduces the critical pressure of flanged and flangeless hemispheres. Critical pressures of hemispheres with varying wall thickness correlate well with the mean wall thickness.  Axial displacements of the apex under hydrostatic loading were found to be approximately of the same magnitudes for both flanged and flangeless shells of constant thickness. The displacements of flanged shells with variable thickness were significantly higher than of flanged shells with constant thickness when the comparison was made at the same nominal $t/R_i$ ratio.			

UNCLASSIFIED

Security Classification



UNCLASSIFIED

Security Classification

14	KEY WORDS	LINK A		LINK B		LINK C	
		ROLE	WT	ROLE	WT	ROLE	WT
	acrylic plastic viewports pressure testing pressure vessel windows submersible windows hyperbaric chamber windows spherical shells implosion pressure undersea habitat windows						

UNCLASSIFIED

Security Classification

# Technical



# Note

**TN no. N-1468**

**title:** FLANGED ACRYLIC PLASTIC HEMISPHERICAL SHELLS FOR  
UNDERSEA SYSTEMS - Static and Cyclic Fatigue Life  
Under Hydrostatic Loading

**author:** J. D. Stachiw and R. Sletten

**date:** January 1977

**sponsor:** NAVAL FACILITIES ENGINEERING COMMAND

**program nos:** YF54.593.008.01.004



## CIVIL ENGINEERING LABORATORY

NAVAL CONSTRUCTION BATTALION CENTER  
Port Hueneme, California 93043

Approved for public release; distribution unlimited.

J. D. Stachiw is a technical consultant, Ocean Technology Department, Naval Undersea Research and Development Center, San Diego, California.

R. Sletten is a marine engineer, Division of Marine Technology, Det norske Veritas, Oslo, Norway, on temporary assignment at the Civil Engineering Laboratory, May 1974 to March 1975 and September to November 1975.

Unclassified

SECURITY CLASSIFICATION OF THIS PAGE (When Data Entered)

REPORT DOCUMENTATION PAGE		READ INSTRUCTIONS BEFORE COMPLETING FORM	
1. REPORT NUMBER TN-1468	2. GOVT ACCESSION NO. DN244039	3. RECIPIENT'S CATALOG NUMBER	
4. TITLE (and Subtitle) FLANGED ACRYLIC PLASTIC HEMISPHERICAL SHELLS FOR UNDERSEA SYSTEMS - Static and Cyclic Fatigue Life Under Hydrostatic Loading		5. TYPE OF REPORT & PERIOD COVERED Final; Jul 1973 - Jun 1975	
		6. PERFORMING ORG. REPORT NUMBER	
7. AUTHOR(s) J. D. Stachiw R. Sletten		8. CONTRACT OR GRANT NUMBER(s)	
		10. PROGRAM ELEMENT, PROJECT, TASK AREA & WORK UNIT NUMBERS 62755N; YF54.593.008.01.004	
9. PERFORMING ORGANIZATION NAME AND ADDRESS CIVIL ENGINEERING LABORATORY Naval Construction Battalion Center Port Hueneme, California 93043		12. REPORT DATE January 1977	
		13. NUMBER OF PAGES 104	
11. CONTROLLING OFFICE NAME AND ADDRESS Naval Facilities Engineering Command Alexandria, Virginia 22332		15. SECURITY CLASS (of this report) Unclassified	
		15a. DECLASSIFICATION DOWNGRADING SCHEDULE	
14. MONITORING AGENCY NAME & ADDRESS (if different from Controlling Office)			
16. DISTRIBUTION STATEMENT (of this Report)  Approved for public release; distribution unlimited.			
17. DISTRIBUTION STATEMENT (of the abstract entered in Block 20, if different from Report)			
18. SUPPLEMENTARY NOTES			
19. KEY WORDS (Continue on reverse side if necessary, and identify by block number)  Windows, deep ocean, acrylic plastic, spherical shell, hydrostatic pressure tests.			
20. ABSTRACT (Continue on reverse side if necessary and identify by block number)  Twenty-four acrylic plastic windows in the shape of hemispherical domes with equatorial flanges have been thermoformed from flat sheets and tested under short-term, long-term, and cyclic pressure loading at 65° to 75°F (18.5° to 24.1°C) ambient temperature. Two kinds of flanges were studied: Type I, a flat lip with a rounded heel and instep, and Type VI, a conical lip with a rounded heel. The 14,500-psi, short-term critical pressure for hemispherical windows with $t/R_1 = 0.364$ was found to be independent of the equatorial			

DD FORM 1 JAN 73 1473 EDITION OF 1 NOV 55 IS OBSOLETE

Unclassified

continued

SECURITY CLASSIFICATION OF THIS PAGE (When Data Entered)

Unclassified

SECURITY CLASSIFICATION OF THIS PAGE(When Data Entered)

20. Continued

flange configuration. Both the static and cyclic fatigue lives of the windows were also found to be independent of equatorial flange configuration. In either case, the maximum acceptable working pressure for 65° to 75°F temperature range was found to be 1,000 psi. Only by elimination of the O-ring groove in the bearing surface of the window flange and the use of a thin neoprene bearing gasket between the acrylic flange and the steel seat is it possible to extend the working pressure for 65° to 75°F (18.5° to 24.1°C) temperature range to 2,000 psi. Operating the flanged windows at pressures in excess of the safe working pressures shown above will generate fatigue cracks in the bearing surface of the flange in less than 1,000 pressure cycles, at 5,000-psi pressure the cyclic fatigue life decreases to less than 100 cycles.

Library card

Civil Engineering Laboratory  
FLANGED ACRYLIC PLASTIC HEMISPHERICAL SHELLS  
FOR UNDERSEA SYSTEMS - Static and Cyclic Fatigue Life  
Under Hydrostatic Loading (final), by J. D. Stachiw and R. Sletten  
TN-1468 104 pp illus January 1977 Unclassified

1. Acrylic windows 2. Deep ocean structures I. YF54.593.008.01.004

Twenty-four acrylic plastic windows in the shape of hemispherical domes with equatorial flanges have been thermoformed from flat sheets and tested under short-term, long-term, and cyclic pressure loading at 65° to 75°F (18.5° to 24.1°C) ambient temperature. Two kinds of flanges were studied. Type I, a flat lip with a rounded heel and instep, and Type VI, a conical lip with a rounded heel. The 14,500-psi, short-term critical pressure for hemispherical windows with  $t/R_1 = 0.364$  was found to be independent of the equatorial flange configuration. Both the static and cyclic fatigue lives of the windows were also found to be independent of equatorial flange configuration. In either case, the maximum acceptable working pressure for 65° to 75°F temperature range was found to be 1,000 psi. Only by elimination of the O-ring groove in the bearing surface of the window flange and the use of a thin neoprene bearing gasket between the acrylic flange and the steel seat is it possible to extend the working pressure for 65° to 75°F (18.5° to 24.1°C) temperature range to 2,000 psi. Exceeding the safe working pressures will generate fatigue cracks in the flange bearing surface <1,000 pressure cycles, at 5,000-psi, the cyclic fatigue life decreases to <100 cycles.

Unclassified

SECURITY CLASSIFICATION OF THIS PAGE(When Data Entered)

# CONTENTS

	Page
INTRODUCTION . . . . .	1
BACKGROUND . . . . .	1
STUDY PARAMETERS . . . . .	2
TEST SPECIMENS . . . . .	3
TEST SETUP . . . . .	3
Flanges . . . . .	3
Pressure Vessels . . . . .	3
Instrumentation . . . . .	4
Test Procedure . . . . .	4
TEST PROGRAM . . . . .	5
TEST OBSERVATIONS . . . . .	5
Short-Term Critical Pressure Tests . . . . .	5
Long-Term Tests . . . . .	10
Cyclic Pressure Tests . . . . .	12
Modifications of Seating Arrangement . . . . .	15
DISCUSSION OF FINDINGS . . . . .	17
Short-Term Critical Pressure Tests . . . . .	17
Long-Term Critical Pressure . . . . .	19
Cyclic Fatigue Life . . . . .	20
Deformations . . . . .	23
SUMMARY OF FINDINGS . . . . .	25
CONCLUSIONS . . . . .	26
RECOMMENDATIONS . . . . .	26
Design . . . . .	26
Fabrication . . . . .	26
REFERENCES . . . . .	27

## CONTENTS

	Page
APPENDIX — Detailed Data . . . . .	88
DEFINITION OF TECHNICAL TERMS . . . . .	100

## INTRODUCTION

Since its introduction into the hydrospace field by Professor Auguste Piccard, acrylic plastic has become the acknowledged standard material for windows in submersibles, diving bells, and hyperbaric chambers. Several shapes have been developed over the years for the acrylic windows.

The most common shape is the plane conical frustum. Its behavior under hydrostatic loading has been extensively researched and its design criteria well-established [1-5]. A somewhat less common shape is a plane circular disc [6,7]. Its application has been confined to pressures under 1,000 psi; as for greater pressures, the retaining flanges become too bulky.

The spherical shell sector, whose included spherical angle can vary from 30 to 180 degrees, has been used only recently for undersea systems. Considerable effort has been devoted to understanding the characteristics of this window because the spherical surfaces endow such windows with increased field of vision and resistance to hydrostatic pressure [8,9]. In parallel with the research into structural and optical properties of spherical shell sector windows, investigations have been conducted into the problems associated with economical fabrication of large diameter windows for the whole depth range [10,11,12].

Because spherical shell sector windows are not as easy to retain in their flanges as plane conical frustum or plane disc windows, consideration has been given to equipping the spherical shell sector windows with integral flanges [13,14]. Such flanges, however, generally introduce bending moments and stress concentrations into the otherwise uniformly stressed spherical window. To assess the effects of flanges on the stress distribution in spherical windows an experimental study was undertaken; the results of that study form the body of this report.

## BACKGROUND

Equatorial flanges on spherical shell sector windows are sometimes the byproduct of the fabrication process, while at other times they are the planned result of engineering design. The fabrication processes which produce equatorial flanges on acrylic hemispherical shells are thermoforming techniques utilizing either compressed air or mechanical plungers (Figure 1). In either case, an equatorial flange is produced whose thickness is equal to that of the acrylic sheet utilized in thermoforming.



After completion of the thermoforming process, the flanges can be removed by machining so that the end product is a flangeless hemisphere whose structural response has been studied both analytically and experimentally in the past. The removal of the flange by machining is, however, an expensive operation that increases the cost of the end product approximately 100%. The thermoforming fabrication techniques for acrylic hemispherical shells would be more economically competitive if an equatorial flange could be tolerated from the structural viewpoint.

Furthermore, an equatorial flange on the acrylic hemisphere can often be used in securing the window to its seat in the viewport. This is of particular importance if the window is exposed during a typical operational cycle not only to external but also to internal pressure. Also, the flange can serve as a convenient location for the pressure seal. Since exploratory studies conducted in the past [13 and 14] have shown that an equatorial flange does not decrease significantly the short-term strength of acrylic plastic hemispherical shells, it appeared worthwhile to investigate further the concept of flanged hemispherical windows.

The flanged hemispherical shell windows tested in the first exploratory study utilized flanges with a sharp right-angle heel [14]. The sharp heel was chosen at that time as it was shown by another study [13] that a well-rounded heel on the flange may generate excessive bending moments in the shell accompanied by a high positive flexural stress component on the interior and a high negative flexural stress component on the exterior surfaces in the immediate vicinity of the flange-shell interface. It was felt that further studies on flanged acrylic hemispherical shells should include a curvature at the heel and the instep of the flange to simulate better the appearance of typical flanged hemispheres produced by thermoforming processes.

## STUDY PARAMETERS

The objective of the study was to establish the safe operational pressure for typical flanged hemispherical shells of acrylic plastic utilized in pressure vessels for human occupancy.

The approach chosen was to fabricate and test representative flanged acrylic plastic hemispherical shells under short-term, long-term, and cyclic pressure loadings until signs of failure appeared.

The scope of the study was limited to a single thickness over inside diameter ( $t/D_i$ ) ratio and two flange configurations (Figures 2 and 3). The  $t/D_i$  ratio chosen was 0.182, equal to a  $t/R_i$  ratio of 0.364. This ratio was considered to be adequate for working pressures in the 1,000- to 2,000-psi range based on the short-term collapse data from a previous study on flangeless acrylic plastic hemispherical shells.

## TEST SPECIMENS

The flanged test specimens of acrylic plastic hemisphere were fabricated by thermoforming 3-inch-thick Plexiglas G stock. The thermoforming process consisted of forcing an appropriately shaped metallic plunger into the acrylic stock supported by a metal ring on four legs (Figures 4 and 5). The wall thickness of the extrusion was found to be more uniform than in hemispheres thermoformed by free blowing with compressed air [13]. The hemispherical extrusion was subsequently machined on the outside and inside to give the shell appropriate thickness, in and around the flange particularly.

Since the thermoforming process produced flanges that could be economically modified to another shape, if so desired, the test specimens were equipped with either a Type I or a Type VI flange (Figures 2 and 3). Twenty-four flanged windows were fabricated; 10 were equipped with Type I and 14 with Type VI flanges. Each window was identified by a capital letter.

The Plexiglass G material utilized in the thermoforming process met all the minimum physical requirements specified for man-rated windows by the Navy and the American Society of Mechanical Engineers [15].

## TEST SETUP

### Flanges

The flanged windows were tested on thick circular discs machined from low carbon steel (Figure 6). The steel test flanges were equipped with a central opening through which strain gage wires could be passed from inside the window. Holes around the circumference of the steel test flange were used for attaching the test flange to the vessel end closure adaptor plate and for securing the window to the flange. A smooth surface was provided on the steel test flange to minimize sliding friction between the contracting window and the test flange.

### Pressure Vessels

For the testing of flanged windows both the 18- and 9.5-inch-diameter pressure vessels were utilized. The window was secured with a retainer ring or rubber bands to a steel test flange which, in turn, was attached to a pressure vessel closure adaptor that screwed directly into the vessel end closure. Since the steel test flange, vessel closure adaptor, and vessel end closure were equipped with a central opening, electric strain gage wires and a mechanical dial indicator rod could pass from the window interior to the vessel exterior.

Some of the vessels were provided with insulated jackets containing heating and cooling coils. In these vessels the temperature could be maintained within narrow limits. In other vessels the temperature of

the pressurized water could be maintained only within a wide range as the uninsulated vessels would rapidly follow the diurnal temperature variations inside the uninsulated laboratory building. As a result, the ambient test temperature in these vessels during the pressure testing of windows over a period of 24 months varied from a low of 65°F to a high of 75°F.

#### Instrumentation

The instrumentation for the pressure vessel consisted of a Bourdon type pressure gage and a remote reading thermometer. The pressure gage could be read within 50-psi intervals and the thermometer within 1°F.

The instrumentation for the acrylic plastic window undergoing hydrostatic testing consisted of rectangular 1/8 inch long\* electrical resistance strain gage rosettes located on the interior face of the windows and a mechanical dial indicator measuring the radial displacement of the window's apex within 0.001 inch. The strain gages were attached to the acrylic at specific locations (Figure 7) with M-Bond 200 cement and subsequently waterproofed with Dow Corning 3140 room temperature vulcanizing silicone rubber coating.

The strains were recorded by a 100-channel B & F automatic data logger with magnetic tape data storage and digital paper tape printout. This recording unit was capable of recording at a rate of either 1 or 10 channels per second. As a rule, the 10-channel/second recording rate was utilized during pressurization and the 1-channel/second rate during sustained loading of window specimens.

#### Test Procedure

The bearing surface of the window flange was coated with silicone grease, a 1/8-inch-diameter O-ring was placed into the groove in the window flange, and the whole assembly was carefully placed on the steel test flange. Strain gage wires were fed through the opening in the steel test flange to the outside of the vessel end closure, and the dial indicator rod was centered on the window's low-pressure face.

To secure the window to the steel test flange, either steel retaining rings or elastic bands were employed. The steel rings were primarily utilized in the 18-inch-diameter pressure vessel (Figure 8) while the elastic bands were used to secure the windows to the steel test flange in the 9.5-inch diameter pressure vessel (Figure 9). In both cases, the radial restraint imposed on the window flange was minimal, only sufficient to compress the O-ring for proper sealing.

After the window was secured to the steel test flange, the interior of the pressure vessel was pressurized with tap water at a 650-psi/minute rate utilizing a positive displacement air-driven pump.

---

\*Micro-Measurements gages type EP-08-125RA-120.

## TEST PROGRAM

The experimental test program was designed to establish the maximum safe working pressures for the two types of flanged windows. On the basis of experimental data, the two types of windows could be compared to each other and to windows of the same geometry without a flange. The maximum safe working pressure was to be established by subjecting the windows of Type I and VI to a series of tests that would:

- (1) Determine short-term critical-pressure (STCP) by pressurizing windows at a standard rate of 650 psi/minute until failure occurred.
- (2) Determine long-term critical pressure by maintaining a constant sustained pressure loading until failure occurred.
- (3) Determine cyclic fatigue life by subjecting the windows to cyclic pressure loading until failure occurred. The pressure cycles employed in the test program consisted of (a) pressurizing the window at 650 psi/minute to a specified pressure, (b) holding that pressure for 7 hours, (c) depressurizing to zero pressure at a rate of 650 psi/minute, and finally (d) relaxing at zero pressure for at least 17 hours before the next cycle was started. This cycle is termed for the purposes of this report the "standard load cycle."

Since there were more tests planned than the available number of windows, some windows had to be used in more than one test. Two windows were modified after testing to establish the effect of structural modification to the flange. In one case the rounded heel of the flange on Type I window E was replaced with a square heel to become (E) while in the other case, the flange was removed completely, converting the Type I window I into a true hemisphere (I). All of the tests to which the windows were subjected have been summarized in Tables 1 through 5.

## TEST OBSERVATIONS

### Short-Term Critical Pressure Tests

Pressure. Five windows were subjected to continuous pressurization at the standard rate of 650 psi/minute until they failed (Table 1) (windows Y and Z had been tested previously). Window Y had endured long-term hydrostatic testing at 2,000-psi pressure without any visual damage. Window Z had been pressure-cycled twice to 8,000 psi with a rubber gasket and had suffered some crazing and a few slight cracks in the seating surface. The two Type I windows tested had an average short term critical pressure of 14,310 psi while the three Type VI windows had an average critical pressure of 14,700 psi.

Modes of Failure. All the windows that failed did so catastrophically after cracking sounds had been heard for a short time. Extensive fragmentation took place in all these cases.

Table 1. Short-Term Critical Pressure Tests

Window	Flange Type	Test Temperature (°F)	Location of Strain Gages (Figure 7)	Displacement	Short-Term Critical Pressure (psi)	Principal Results
A	I	<i>a</i>	—	yes	14,000	Catastrophic failure
B	I	<i>a</i>	—	—	14,620	Catastrophic failure
C	I	<i>a</i>	A, C, E	—	—	Test stopped at 12,500 psi and de-pressurized to zero
S	VI	<i>a</i>	A, C, E	—	14,530	Catastrophic failure
<i>Y<sup>b</sup></i>	VI	71	—	—	14,325	Catastrophic failure; bottom plug blowout of pressure vessel at the same time the window failed
<i>Z<sup>c</sup></i>	VI	70	—	—	15,225	Catastrophic failure

<sup>a</sup> Room temperature not specifically recorded.

<sup>b</sup> Window was previously tested at 2,000 psi (see Table 3).

<sup>c</sup> Window was previously tested at 8,000 psi with a gasket (see Table 4).

Table 2. Long-Term Critical Pressure Tests

Window	Flange Type	Average Test Pressure (psi)	Test Temperature (°F)	Location of Strain Gages (Figure 7)	Principal Results
D	I	9,670	<i>a</i>	A, C, E	Catastrophic failure after 22 hours
J	I	10,000	75	A, C, E, G, I	Catastrophic failure after 3 hours
H	I	7,675	45-75	A, C, E	Catastrophic failure after 153 hours
O	VI	9,700	<i>a</i>	A, C, E <sup>b</sup>	Catastrophic failure after 14 hours
P	VI	≈10,000	<i>a</i>	A, E <sup>b</sup>	Catastrophic failure after 6 hours
V	VI	≈11,800	<i>a</i>	A, C, E <sup>c</sup>	Catastrophic failure after 42 hours
T	VI	≈9,850	<i>a</i>	A, C, E <sup>c</sup>	Catastrophic failure after 100 hours
<i>R<sup>d</sup></i>	VI	≈12,000	71-73	—	Catastrophic failure after 0.5 hour

<sup>a</sup> Room temperature not specifically recorded.

<sup>b</sup> Gages functioned properly.

<sup>c</sup> Gages failed prematurely.

<sup>d</sup> Window was previously tested at 4,000 psi for 262 hours (see Table 3).

Table 3. Long Term Tests Without Implosion

Window	Flange Type	Average Test Pressure (psi)	Test Temperature (°F)	Location of Strain Gages (Figure 7)	Displacement	Duration of Loading (hours)	Principal Results
E	I	4,000	<i>a</i>	A, C, E	—	240	Some circumferential cracks in the bearing surface on the flange
I	I	2,000	75-76	A, B, C, D, E, F, G, H, I	—	269	No cracks or crazing detectable by visual inspection
Q	VI	7,000	<i>a</i>	A, C, E	—	139	Extensive crazing and large circumferential cracks in seat; one crack penetrating to outside
R	VI	4,000	<i>a</i>	A, C, E	—	262	Some crazing and shallow cracks in seat
U	VI	8,000	<i>a</i>	—	—	312	Window flange sheared off; numerous cracks and extensive crazing of seating surface; seat conical
Y	VI	2,000	71-73	A, B, C, D, E, F, G, H, I	—	119	No cracks or crazing detectable by visual inspection
Y	VI	2,000	72	A, B, C, D, E, F, G, H, I	—	7	No cracks or crazing detectable by visual inspection
W	VI	2,000	71-73	—	yes	95	No cracks or crazing detectable by visual inspection

<sup>a</sup> Room temperature not specifically recorded.

<sup>b</sup> Rubber gasket used instead of O-ring, window previously tested to 2,000 psi without gasket.

Deformation Under Short-Term Loading. At the standard rate of pressurization of 650 psi/minute, the compressive strain recorded by the strain gages increased in direct proportion to the pressure up to about 4,000 psi (Figure 10). Above this pressure the strain began to increase more rapidly, thus indicating the nonlinearity of stress versus strain.

The strain produced in the window in the linear range varied according to direction and location of the strain gages. At the apex, the strain was approximately the same in all directions with little change in magnitude from one point to another (Figures 11, 12, and 13). Moving away from the polar area, the circumferential strain increased by an average of 22% for the Type I windows and by an average of 14% for the Type VI windows (Figure 11), and at the same time, the meridional strains fell off sharply to small values (Figure 12).

Table 4. Cyclic Tests

Window	Flange Type	Test Pressure (psi)	Test Temperature (°F)	Location of Strain Gages (Figure 7)	Number of Pressure Cycles	Principal Results
I <sup>a</sup>	I	2,000	70-75	A, B, C, D, E, F, G, H, I	58	Cracking in window-bearing surface developed between cycle No. 33 and last cycle
J	I	10,000	75	A, C, E, G, I	1	Window failed catastrophically after about 3 hours of first pressure cycle
K	I	8,000	69-72	E	1	Window failed during first cycle by cracking along flange, causing leakage when pressure was released
M	I	6,000	66-73	A, C, E	22	Window developed cracks during second cycle; leaked after twenty-second cycle
BB	VI	8,000	68-72	E	2	Small cracks and crazing of bearing surface after first cycle; window leaked after second cycle
Z <sup>b</sup>	VI	8,000	70-72	A, C, E	2	Some crazing and three very shallow cracks in bearing surface after second cycle
AA	VI	6,000	66-73	—	22	Crack along O-ring groove after third cycle; cracks and crazing in bearing surface after fifth cycle
X	VI	5,000	68-73	E	40	Crazing of bearing surface developed between second and sixth cycles; cracks in bearing surface developed between twenty-second and twenty-seventh cycles

<sup>a</sup>This window was previously tested under sustained loading at 2,000 psi (see Table 3).

<sup>b</sup>A window was pressurized to failure under short-term loading (see Table 1).

The circumferential strain varied only moderately from test to test, the maximum deviation from the average of any test being only about 6% for the Type I windows and about 10% for the Type VI windows (Figure 11). For the strain in the meridional direction, there was a similar spread in the data for the polar area. Closer to the edge, however, the meridional strain varied markedly from test to test and at gage

Table 5. Cyclic Tests of Modified Windows

Window	Modification	Test	Test Temperature (°F)	Location of Strain Gages (Figure 7)	Principal Results
Ⓔ <sup>a</sup>	O-ring groove and rounded heel removed by machining. Disc glued on to restore original dimensions, but with a sharp heel on the flange	11 pressure cycles at 2,000 psi	68-72	A, C, E	Some change in strain distribution compared to windows with rounded heel: 10 cycles performed with neoprene bearing gasket and 1 cycle without
Ⓔ <sup>a</sup>	O-ring groove and rounded seat corner removed by machining. Disc glued on to restore original dimensions but with a sharp heel on the flange	1 cycle at 8,000 psi	70-74	A, C, E	Window bearing surface almost unharmed. Window cracked radially
Ⓘ <sup>b</sup>	Flange and cylindrical part removed by machining	7 cycles at 2,000 psi	68-72	A, C, E	The strains are more uniform all over the interior surface of the window
Ⓘ <sup>b</sup>	Flange and cylindrical part removed by machining	2 cycles at 8,000 psi	70-75	A, C, E	No cracks observed on the bearing surface or anywhere else on the window

<sup>a</sup> Window was tested for 240 hours at 4,000 psi prior to modification (see Table 3).

<sup>b</sup> Window was tested for 269 hours at 2,000 psi prior to modification (see Table 3).

A (Figure 12) the results were almost erratic, particularly for the Type VI windows. The cause of this large spread has not been investigated.

At hydrostatic pressures in excess of 4,000 psi, the nonuniform character of the strain over the window surface was exaggerated (Figure 14), and the strains were higher than predicted by linear extrapolation of the strains at low pressure. Thus, at 10,000-psi external pressure, the nonlinear part was between one-third and one-half of the linear strain, depending on location (Figure 15).

Displacement of Apex. In one case, the displacement of the windows at the apex towards the center of the sphere was measured. The specimen was a Type VI window (window W). After an initial phase where the window seated itself, the displacement was linear with pressure up to the test pressure of 2,000 psi. The displacement per unit change of pressure divided by the internal radius of the spherical part of the window was  $3.5 \times 10^{-6}/\text{psi}$  (Figure 16).



## Long-Term Tests

Tests Resulting in Implosion. Five Type VI windows and three Type I windows were pressurized at the standard rate of 650 psi/minute up to the test pressure. The test pressure was maintained constant until failure occurred.

The life of the windows loaded this way varied inversely with the test pressure. The relationship between the life and the test pressure was nonlinear with a very rapid fall off in life above approximately 8,000 psi (Figure 17). The spread in the data was very large compared to the spread in the magnitude of short-term critical pressures, indicating that long-term test parameters, like temperature, were not maintained within a sufficiently narrow range to preclude large spread in test data.

In all cases of failure under long-term loading, the failure was catastrophic, resulting in heavy fragmentation of the windows (Figures 18 through 26). Typically, the force of implosion blew a hole in the window dome producing grain size fragments of the blown-out material. The rest of the dome stayed relatively intact, although it was always fractured radially into several pieces (Figure 21). In addition to the radial fractures, a large number of in-plane fractures occurred. The number of in-plane fractures increased toward the interior surface of the window. The outer 1/4 inch or so of the wall was usually not laminated (Figure 24).

After implosion, the flanges were found to be separated from the main body of the windows. In Type I windows, the separation was all around the flange (Figures 18 and 19), while in the Type VI windows the separation was partial (Figures 20 and 21). The flange separated from the dome generally before implosion occurred, as demonstrated by window U whose long-term loading was terminated prior to implosion (Figures 22 and 23).

The window flange bearing surfaces fractured during the tests in the circumferential direction (Figure 25). The heel (inside edge) of the flange was permanently deformed, resulting in the formation of a sharp edge that contrasted sharply with the original well-rounded-heel geometry (Figure 25). The deformed fragments also showed that the thickness of the wall above the flange permanently increased by about 25% of the original thickness (window J). A similar increase was observed in the width of the flange measured between the inside edge of the heel and the O-ring groove. The height of the flange, however, was unchanged (Figure 25). These observations were further confirmed by a study of the fragments of window H (Figure 26).

Tests Terminated Prior to Implosion. Two Type I and five Type VI windows were subjected to long-term tests of varying length and at different pressures (Table 3).

At 2,000 psi, no visible damage was caused during the 269 hours of loading on window I at 75°F. The window strains relaxed completely after the test (Figure 27).

At 4,000 psi, some crazing and shallow cracks were observed in the seat of window R when inspected after 262 hours (Figure 28). Also, this window relaxed completely after the test. All strain gage readings were within 100  $\mu$ in./in. of the reading before the test after a relaxation time of about 100 hours. The bearing surface on the flange, however, had some permanent deformation, producing a slight conical shaped surface similar to that shown in Figure 22.

At 7,000 psi, window Q suffered extensive crazing and several large cracks at the seat during the 439-hour test (Figures 29 and 30). In this window, the strain in the polar area averaged 0.056/in./in. at the end of the creep period. But even so, after about 100 hours of relaxation, the strain in this area was within 0.001 in./in. of the reading before the test. Significant permanent deformation was observed in the bearing surface of the flange, transforming it from a plane to a conical surface.

At 8,000 psi, window U lasted 312 hours without imploding; the window was, however, severely damaged. The flange had separated and the bearing surface was deformed into a conical surface which had several large cracks in it (Figures 22 and 23).

In those tests where the pressure was kept constant for a long period of time, the strain on the interior surface did not become tensile at the end of the relaxation period.

Deformation Under Long-Term Loading. At 10,000 psi (70% of STCP) of external pressure, the strain increased very rapidly after pressurization was completed. The increase was largest in the window areas that already had the largest strains. Thus, the unevennesses of the window deformation already apparent after pressurization became more pronounced with time (Figure 31). As evident from the end result, the rate of deformation at 10,000 psi was so high that after a few hours the window became so plastically deformed that it could no longer sustain the load (window J).

At 8,000 psi (56% of STCP) and lower pressures, the strains still increased rapidly immediately after the end of pressurization. The strain rate slowed down sufficiently, however, after the first 2 to 3 hours to give the window extended life. At 7,000 psi (49% of STCP), window Q did not fail catastrophically during the 139 hours the pressure was maintained. At 8,000 psi, the unevenness of the window deformation became greater with time (Figure 32), just as for the window tested at 10,000 psi (Figure 31). At lower pressures, this tendency became less pronounced and at 2,000 psi was hardly noticeable (Figure 33).

At moderate strain levels, the deformation of the windows appeared to be quite symmetrical. This was evident from the measurements on windows I, Y, and J, which had strain gages on both sides (Figure 13, 31, and 33). In these cases, all three gages of the rectangular strain gage rosette at the apex indicated essentially the same strain values. As the strains increased in magnitude, however, the differences in the readings of the three gages at the apex often became greater.

This occurrence may be the result of the window starting to lose its sphericity. In the case of window J (tested at 10,000 psi) the distribution of circumferential strain appeared to be symmetrical at the end of pressurization. During the first hour under pressure, however, the strain increased much faster on one side than on the other indicating that the window was losing its spherical shape (Figure 31).

Taking into account the scatter in data, no significant difference was observed in the time-dependent deformation of the two types of windows (Figure 34). In both cases, the location on the window that had the highest strains at the end of pressurization also had the highest strain throughout the creep period. In both cases, the strain distribution became more uneven as time went on (Figures 32 and 35).

The strain in the window after any given duration of sustained load was found to be a nonlinear function of the load. Thus, after 1 hour at 4,000 psi, the strain at the apex of the window was approximately 2.1 times the strain after 1 hour at 2,000 psi. After 1 hour at 10,000 psi, the strain at the apex was 10 times the strain after 1 hour at 2,000 psi (Figure 36). This clearly demonstrates that acrylic material becomes more compliant as temperature or stress is increased. If the additional strain due to creep alone is plotted, the nonlinear behavior becomes even more apparent (Figure 37).

As noted before, long-term loading at pressures high enough to cause catastrophic failure, also caused permanent tensile radial strain in the dome. By measuring the thickness of fragments of the dome of the imploded windows, the average permanent radial strain was found to vary from about 25% (0.25 in./in.) above the flange to about 12.5% halfway between the flange and the apex (windows J and H) (Figure 38).

### Cyclic Pressure Tests

Fatigue Life. It was immediately realized after initiation of cyclic pressure testing that the fatigue life of the windows would be lower than expected.

At 10,000 psi, which is approximately 70% of STCP, the test specimen (window J) did not complete the first cycle. The window failed catastrophically after about 3 hours.

At 8,000 psi (56% STCP) the Type I (window K) cracked during the first cycle to the extent that when the pressure approached zero at the end of the cycle, water filled up the low pressure cavity. The Type VI window that was tested at 8,000 psi (window BB) developed similar cracks and leakage during its second cycle.

At 6,000 psi (42% of STCP) the Type I window (window M) cracked catastrophically during its twenty-second load cycle. The Type VI window (window AA) tested at the same pressure was still intact after 22 load cycles, but had deep cracks in the seat area.

At 5,000 psi (35% of STCP) crazing of the seat was apparent when the Type VI window (window X) was inspected after the sixth pressure cycle. Cracks developed in the seat between cycle 22 and 27, but no leaks occurred before the test was terminated after the fortieth cycle.

At 2,000 psi (14% of STCP) the Type I window (window I) did not show any change after 33 pressure cycles. When the window was inspected again after the fifty-eighth cycle, however, a deep crack was found in the flange starting from the O-ring groove.

Modes of Failure. In all cases, cracks initiating from the bearing surface on the flange were the cause of failure. In some cases (windows AA, Figures 39, 40, and 41; and I, Figure 42), the first sign of fatigue was a crack originating from the O-ring groove. The cracks had a characteristic half-moon shape when viewed from the side and appeared to be approximately parallel to the low-pressure face of the window as shown in Figure 43.

In all the other cases, the cracks originated at the bearing surface of the flange between the heel and the O-ring groove and were always preceded by crazing. The crazing, as well as the subsequent cracks, had the same orientation as the cracks originating from the O-ring groove (Figures 39 to 46). The cracks not originating in the O-ring groove had the characteristic mushroom shape instead (Figures 39, 40, 41, 47, and 48).

Cracking of the interior face occurred in two Type I windows (windows M and (E)). In window M, the failure occurred after 22 standard load cycles to 6,000 psi and consisted of three fractures running in the meridional direction originating on the bearing surface of the window. One of the cracks ran like a meridian across the apex from one side of the window to another, while two other cracks stopped at the apex (Figure 49). The cracks penetrated between 25 and 50% of the wall thickness. On the inside face of the window, the width of the cracks varied from close to zero at the apex to about 0.040 inch at the flange. The entire inside surface was markedly crazed after the test but less than on the bearing surface (Figure 50).

Window (E) failure occurred after one cycle at 8,000 psi. The window had previously been subjected to 11 standard load cycles at 2,000 psi and a long-term test at 4,000 psi for 259 hours. After the long-term test, but before the cyclic tests, the seat of the window was machined down to remove the rounded inside edge of the heel and the O-ring groove. An annular disc was bonded in its place to restore the original height of the flange. When the pressure was down to about 500 psi during depressurization from 8,000 psi at the standard rate, three or four loud cracks were heard and the window's interior filled with water.

Inspection of the window (E) revealed that spalling had taken place on the square edge of the heel, that crazing and a number of shallow half moon cracks had formed in the bearing surface of the flange, and that the interior face of the window had three large cracks as shown in Figures 51, 52, and 53.

Low-pressure leaks developed in four cases. In two of these (windows BB and K, both tested at 8,000 psi) the leak was due to the circumferential cracks propagating through the flange to the exterior face of the windows (Figure 54 and 55). In the third case (window M, tested at 6,000 psi), the usual circumferential cracks occurred after the second cycle, but the window did not develop a leak until it cracked on

the interior face after 22 load cycles as noted above (Figure 49). In the fourth case (window E tested at 8,000 psi), a leak occurred after the first cycle.

Deformation. Deformation of the windows was measured with electrical strain gages located on the low-pressure face (Figure 7). In three tests (windows I, M, and X), where such measurements were performed, it was found that tensile strains were building up on the internal face at the end of each relaxation period; i.e., the strain datum value prior to each load cycle was increasing in the positive sense. The tensile strains had a distribution over the face of the window similar to the distribution of maximum compressive strains at the end of each load cycle (Figures 56 and 57). In the case of window M, this buildup of tension on the inside surface caused the failure of the window - apparent from the radial cracks that developed during the twenty-second load cycle (Figure 49). After several days of relaxation, the cracks in window M were actually widening as time went on indicating that the interior face was contracting.

The rate of buildup of the tensile strains on the window's interior face increased dramatically with magnitude of pressure loading during a typical pressure cycle. During pressure cycling to 2,000 psi (window I) the increase in tensile strain during the relaxation period averaged about 45  $\mu\text{in./in./load cycles}$  performed (Figure 58). During pressure cycling to 5,000 psi (window X) the same level of tensile strain was reached in 3 cycles that it previously took 40 cycles to reach during the cycling to 2,000 psi. Also, at 5,000 psi, the increase in tensile strain per cycle was no longer linear and increasing rapidly (Figure 59). At 6,000 psi, the tensile strain built up even more rapidly (Figure 60). The data were somewhat scattered, but it was apparent that the buildup rate was more than twice that observed during the pressure cycling to 5,000 psi.

The specimen tested at 5,000 psi (window X) had only one strain gage rosette (at the apex) so that no information was obtained about the buildup of tensile strain at other locations. Window M, which was tested at 6,000 psi, however, had rosettes also at locations A and C in addition to one at the pole. This test confirmed the results from the test on window I at 2,000 psi, i.e., that the strain builds up even faster closer to the window flange than at the apex. The data from pressure cycling to 5,000 psi (window M) show appreciable scatter from cycle to cycle. It is not known why this occurred but a contributing cause may have been that in some cases the pressure vessel was closed off during the relaxation period instead of being connected to the constant header tank. If the vessel was closed off, the expansion of the window would cause some buildup of pressure in the vessel which would tend to counteract the relaxation. Unfortunately, no record was kept of the times that this was done.

For window I the cycling at 2,000 psi did not lead to changes in the maximum strain produced during each separate load cycle; i.e., the strain recorded at the end of the creep period minus the recording just prior to pressurization was very close to the same for all cycles (Figure 56 and 57).

The same behavior was observed also for window M cycled at 6,000 psi (Figure 60) and window X cycled at 5,000 psi. The total change of strain at the pole of window M was about 0.030 in./in. with a random variation of less than 2% up and down. The total change of strain at the pole of window X was about 0.024 in./in. and, again, the variation was less than  $\pm 2\%$ .

#### Modifications of Seating Arrangement

After most of the test program was completed but during the initial stages of the cyclic tests, it became apparent that the cyclic life of the Type I and Type VI windows would be substantially less than anticipated. Compared to conical frustum windows with the same STCP, the cyclic fatigue life of Type I and Type VI windows was significantly less. Cyclic fatigue primarily consisted of circumferential cracks in the bearing surface of the flange and secondarily of radial cracks in the low-pressure face of the window. To improve the fatigue life of the bearing surface on the flange, it was decided to try the following modifications:

- (1) Remove O-ring and use a thin neoprene bearing gasket to seal and absorb shear strain.
- (2) Remove O-ring groove and replace the rounded heel of the flange with a square heel.
- (3) Remove flange and cylindrical part of window.

Only a very limited number of tests were performed on each modification.

Effect of Neoprene Bearing Gasket. To reduce the shearing force on the acrylic plastic in contact with the steel surface, a soft neoprene gasket of 0.020-inch thickness was bonded to the bearing surface on the window flange. The gasket consisted of nylon cloth coated with neoprene. The O-ring used previously for sealing was removed from the groove in the window flange, and the gasket was placed over the whole bearing surface on the flange. Before assembly, silicone grease was applied to the steel bulkhead as in the earlier tests.

Two tests were carried out with this arrangement. The first was Type I window Z, subjected to two standard pressure cycles at 8,000 psi. The effect was very marked. The acrylic plastic bearing surface protected by the neoprene gasket was only slightly damaged. The damage consisted of minor crazing of the bearing surface, reflecting the pattern of the weave in the gasket plus three very shallow cracks (Figures 61 and 62). In contrast, the two windows tested at 8,000 psi without the gasket (windows K and BB) suffered through-the-thickness cracks after two cycles. The crazing and small cracks in the seat of window Z almost disappeared after the window had relaxed for 14 days after the test (Figure 63) in atmospheric environment.

On the other hand, the deformation of the window having the neoprene gasket was not significantly changed compared to the deformation of windows seated directly on steel. In the linear range (up to approxi-

mately 4,000 psi) the strains recorded were all within the range of earlier tests. (Compare Figure 64 to Figure 12.) This also applied to the strains recorded at pressures above 4,000 psi and during the creep periods. (Compare Figure 64 to Figure 34.)

The gasket was cut during the vessel cycling to 8,000 psi. Two cuts were found in the circumferential direction at the inside corner of the window seat. The cuts were about 3 inches long and located diametrically opposite each other (Figure 65).

The second window tested with the neoprene gasket was Type VI (window Y). This window had previously been tested for 119 hours at 2,000 psi (Table 3). A neoprene gasket was cut radially at four locations about halfway through to enable its being slipped over the window without having to disconnect the strain gage wires. This time the neoprene gasket was not bonded to the window flange, but was coated with silicone grease on both sides. The window was tested at 2,000 psi for 7 hours, and strains were recorded both during the pressurization and the creep period. As in window Z, the strains in the window were not significantly changed by the presence of the gasket (Figure 66).

Effect of Rounded Flange Heel. Window E was machined down about 1/4 inch to remove the rounded heel and the O-ring groove. An annular acrylic plastic disc was bonded in its place to restore the original height to the flange, as shown in Figure 67. Finally, the window was annealed at 170°F for 24 hours.

The modified window (E) was subjected to 10 standard pressure cycles at 2,000 psi while mounted on the neoprene gasket and one standard load cycle at 2,000 psi without the gasket sealing but with silicone grease. Finally, window (E) was tested at room temperature for 7 hours at 8,000 psi, again with no gasket. The intentions of the tests were to determine whether or not the modifications had changed (1) strain distribution on the interior face of the window, (2) buildup of tensile strain on the interior face of the window after relaxation, and (3) the tendency for the bearing surface to crack under high loading.

The change in strain distribution without a gasket as measured after 7 hours at 2,000 psi was quite marked near the heel of the window while the strain at the apex was changed very little (Figure 68). As expected, the distribution of meridional strain became more uniform.

The 10 cycles with a gasket seal produced a steady buildup of tensile strain in the interior face of the dome (Figure 69). The rate of buildup was similar to that measured earlier in Type I window I tested at 2,000 psi without gasket (Figure 58).

In the final test consisting of one standard cycle at 8,000 psi, no gasket was used. The window performed normally until the pressure reached about 500 psi during depressurization at the end of the load period. At that time several load cracks were heard. On inspection afterwards, it was seen that:

(1) the seat was in good condition with only moderate crazing and some small circumferential half-moon cracks less than 1/16 inch deep. No spalling had taken place on the sharp flange heel (Figure 70).

(2) The window had cracked radially in the meridional direction on the inside of the dome (Figure 51).

It may be concluded that a square inside seat edge improves the life of the window seat, while the effect on the tendency for the dome to crack is probably small or absent.

Effect of Flange Removal. Window I was machined down so that the entire flange was removed as shown in Figures 71 and 72.

The modified ① window was then cycled four times to 2,000 psi. The first and the fourth cycle consisted of 23 hours under pressure followed by at least 17 hours of relaxation. In the second and third cycles, the pressure was held for 7 hours. At the end of the 23-hour load period of the fourth loading, the pressure was raised to 8,000 psi and held at that level for 6-1/2 hours. After 17 hours of relaxation, window ① was finally pressurized once more to 8,000 psi for 7 hours. At 2,000 psi, the window deformed uniformly over most of the dome. At the edge, the meridional strain increased somewhat compared to the level at the apex. The circumferential strain at the edge was slightly lower than at the apex (Figure 73). This distribution is quite different from the distribution in typical Type I flanged window.

After the two cycles to 8,000 psi, window ① was removed from the vessel for inspection. The findings were: (1) the seat was still in good condition - no cracks and only very slight crazing (Figures 74 and 75), and (2) the plane seat was permanently deformed (Figure 76) to form a conical surface similar to that observed in flanged windows (Figure 22).

The test was too short to give firm data on any buildup of tensile strain on the interior face.

## DISCUSSION OF FINDINGS

### Short-Term Critical Pressure (STCP)

#### Findings.

(1) The average STCP of Type I windows at 70°F was 14,310 psi while the average STCP of Type VI windows at 70°F was 14,700 psi. The difference between the two values is statistically insignificant, and the average of all short-term window tests (that is, 14,500 psi) is considered to be the STCP for both types of windows.

(2) The failure of the windows on reaching the STCP was catastrophic. The window failed by plastic instability of an area on the window located between the flange and the apex. The implosion caused complete fragmentation of the window. The formation of the flat spots on the windows (typical of plastic instability failure) was reflected in the strain distribution on the interior face of the windows. Whereas the strain distribution was symmetric about the apex at lower hydrostatic loadings, the distribution became unsymmetric prior to catastrophic failure.



(3) The flange of the windows sheared from the dome before or during catastrophic failure at STCP.

Discussion. Short-term critical pressure tests of hemispherical windows were reported previously for flangeless (Reference 8) and flanged (Reference 14) configurations. Compared to the predicted STCP based on previously published data for flangeless hemispherical windows, the STCP of the present windows is about 5% lower. A reduction of the STCP of flanged windows when compared to flangeless windows in the higher  $t/R_i$  range has been previously reported (Reference 14). This indicates that, for  $t/R_i \geq 0.25$ , flanged windows may have a lower STCP than similar windows without a flange (Figure 77). Since the comparison is based on tests carried out at different times on windows of different manufacture, firm conclusions on this point cannot be drawn. The reason for the seemingly lower STCP of flanged windows as compared to flangeless windows is probably the increase in meridional edge bending moment caused by the rounded heel of the equatorial flange.

It has been shown previously that thick-wall spherical windows fail catastrophically by plastic instability of the dome (References 8 and 14). The windows with thinner walls fail by elastic buckling, and the transition between the two modes of failure is found to be at  $t/R_i$  ratios of approximately 0.09. The present tests confirm that at  $t/R_i = 0.364$ , the failure is caused by plastic instability of the dome.

It can also be shown theoretically that a thick-wall spherical window attains complete plasticity through its wall thickness before it fails. Using Lamé's equations for thick-wall hollow spheres subjected to external hydrostatic pressure, it is seen that as the external pressure increases, the material at the inner face of the sphere reaches its yield point first. If the pressure is raised further, yielding extends deeper and deeper into the wall until finally, yielding reaches the outer surface.

By making two simplifying assumptions, the external pressure at which the whole wall becomes plastic can be estimated. The assumptions are: (1) the distribution of radial stress is not affected by the yielding of the material (i.e., it can be calculated based on elastic theory); and (2) once the yield point is reached, the material will not support higher stresses, but continues to support the same stress independent of further increase in strain.

Using these assumptions, the Lamé's equation can be applied to predict conservatively the pressure  $P_c$  at which complete plasticity is reached during short term pressurization. The formula becomes:

$$\frac{P_c}{\sigma_y} = \frac{(1 + \alpha)(1 - \alpha^3)}{3\alpha^2}$$

where  $\alpha = 1/(1 + t/R_i)$

$\sigma_y$  = yield stress of material in uniaxial compression under short term loading

$t$  = wall thickness of sphere

$R_i$  = internal radius of sphere

The equation has been plotted for a yield stress of 18,000 psi, typical of Plexiglass G acrylic plastic used in the fabrication of flanged windows (Figure 77). It can be seen that the result is nearly a straight line falling below all the experimental points for  $t/R_i > 0.1$ .

For experimental points with  $t/R_i \leq 0.1$ , the complete plasticity curve lies above the experimental points indicating that elastic instability and not plasticity is the cause of failure in these cases. It can be stated therefore, that for hemispherical windows with a  $t/R_i > 0.15$  the  $P_c$  as calculated by the above equation (using the appropriate  $\sigma_y$  value for the ambient temperature) gives a conservative estimate of the STCP of these windows.

#### Long-Term Critical Pressure

##### Findings.

(1) No significant difference was found between the long-term life of the Type I and Type VI windows (Figure 17).

(2) Above 8,000 psi of external pressure loading (55% of STCP) the life of the windows decreased rapidly with increasing pressure, approaching only a few hours at 10,000 psi.

(3) The maximum external pressure loading at which the windows still retain the  $10^6$  minutes minimum static fatigue life required of man-rated windows (Reference 15) was extrapolated to be approximately 5,800 psi.

(4) The failure of the windows subjected to long-term loading was catastrophic in all cases with extensive fragmentation.

(5) Prior to failure, extensive plastic deformation had taken place in the windows increasing the wall thickness by about 25% immediately above the flange and decreasing the interior diameter at the flange by about 10% (windows R and J, Figures 25, 26, and 78).

Discussion. It is evident from the large spread in the results that at pressures above about 65% of the STCP, the windows become increasingly sensitive to variations in factors affecting their load-carrying capacity.

Tests were not conducted to investigate this point further. However, since a similar spread in results was not observed for the STCP, the spread in long-term critical pressures is probably tied to long-term variables in the tests. One such variable was sustained external pressure loading. Because of a relatively large ratio of window displacement to pressure vessel volume, there were problems in maintaining a constant test pressure during the high-pressure tests. Typically, the pressure would be restored each hour during the daytime but not at night. To compensate for this, an estimated average pressure was worked out for each test, but this procedure had obvious deficiencies.

Another long-term test variable was the ambient temperature, which changed somewhat from test to test. Although the difference was generally less than 5°F, the effect on the creep properties of the material was significant. Published data from other studies indicates that a 5°F variation in ambient temperature can change the fatigue life of an acrylic structure by a factor of at least 10 and possibly 15 (Reference 16).

The fact that the window walls increased in thickness by as much as 25% during the long-term critical pressure tests, further substantiates the postulate made before that the window wall is completely plasticized before failure takes place (Figure 26).

## Cyclic Fatigue Life

### Original Design Findings.

(1) Both types of windows exhibited signs of fatigue at hydrostatic pressures at less than 15% of their short-term critical pressure. The failures, defined here as leakage through cracks, occurred in less than 100 cycles of the standard load cycles at 30% of their short-term critical pressure.

(2) The first sign of fatigue was circumferential crazing marks on an annular bearing area between the O-ring groove and the heel of the flange (Figure 62), except for one case where a crack started from the O-ring groove before any crazing had developed.

(3) If cycling continued after appearance of crazing on the window seat, the crazing increased until eventually actual cracks were formed. The cracks always ran in the circumferential direction, sometimes in the O-ring groove but more often in the bearing surface between the heel of the flange and the O-ring. The cracks typically had a mushroom shape (Figures 39, 40, and 41).

(4) Under moderate cyclic loading of up to 5,000 psi external pressure, both crazing and cracks in the seat grew slowly once they had formed and did not render the window incapable of sealing in less than 30 load cycles. At cyclic loading of 6,000 psi, cracks grew noticeably faster with each cycle; but even so, the window sustained 20 cycles without leaking.

(5) At severe cyclic loading of 8,000 psi, the rate of crack propagation was greatly increased. Only two cycles were needed at this pressure for the cracks to propagate through the flange to the outside and hence cause a low-pressure leak (Figures 54 and 55).

(6) Cracks were found in the bearing surfaces of windows that imploded during the first standard cycle (Figure 25). The cracks must therefore have formed while the windows were under sustained pressure and not during relaxation periods.

(7) Cycling of the windows caused a step-wise buildup of tensile strain on the interior face of the spherical dome during relaxation after each load period. The magnitude of tensile strain recorded during relaxation periods between individual pressure cycles was found to be a nonlinear function of pressure and number of load cycles sustained. In both cases, the magnitude of tensile strain increased faster than the maximum pressure, or the number of load cycles. The tensile strain also built up faster in the areas where the compressive strains were the highest during the loading period (Figures 58, 59, and 60).

(8) In one case the buildup of tensile strain was the cause of severe cracking of the window's concave surface. The cracking occurred as the pressure was approaching zero during depressurization after 22 standard load cycles at 6,000 psi with the magnitude of tensile strain estimated at about 0.050 in./in. (Figures 49 and 50).

(9) Fatigue cracking did not cause catastrophic failure of any window during cyclic load testing. In the worst case, the windows leaked after the pressure had been relieved. (This seems reasonable because cracking at the seat is not a part of the STCP failure mode of the window.)

Original Design Discussion. In view of the above findings, the fatigue life of a window must be taken as either the number of cycles taken to produce the first crack or the number of cycles taken to produce a leak. The criteria chosen may depend on the application of the windows. For man-rated applications, the first criterion should be used; for example, the fatigue life of a window used in a man-rated chamber is the number of cycles sustained by the window when the first crack appears anywhere in the window (Figures 79 and 80).

Due to the scatter in the data and the limited number of cyclic tests performed, it is not possible to establish a firm fatigue life for the windows. The recommended course of action at the present time is to inspect the windows after each pressurization *in excess of 1,000 psi* and replace any window immediately that shows signs of fatigue.

Modified Design Findings. Improved fatigue life was obtained by each of the following modifications:

(1) Use of 0.020-inch-thick neoprene gasket between the window and the steel flange.

(2) Removal of the O-ring groove and replacing the rounded heel of the flange with a square heel.

(3) Removal of the flange to make the window a true hemispherical dome.

The limited number of tests available did not allow determination of quantitative improvement obtainable by each, or by a combination of these modifications.

Modified Design Discussion. The original Type I and Type VI design is not suitable for cyclic loading except at pressures below 1,000 psi at 75°F. If the original designs were to be used, Type VI would probably give the longest life.

If the flanges are to be retained, it is required that for cyclic loading above 1,000 psi both the O-ring groove and the rounded heel of the flange be removed and that a thin, soft, nylon-fiber-reinforced neoprene gasket be installed underneath the window's bearing surface to absorb the shear strain at the steel/window interface. To find what the improved cyclic fatigue life is if these modifications are incorporated into Type I and Type VI windows, a series of new tests would have to be carried out. These tests should be designed not only to check the effect on the bearing surface of the window, but also the buildup of strain on the interior surface of the window at the apex, as it is postulated that this will be the limiting factor of the cyclic fatigue life in the modified design. By incorporating the above-mentioned modifications an adequate fatigue life (1,000 cycles without leakage) is predicted for operational pressures to 2,000 psi.

Removal of the flange improves the cyclic fatigue life significantly both for the bearing surface and the interior face at the apex. Although the improvement in cyclic fatigue life has not been quantitatively established for flangeless windows it is conservatively estimated to be in excess of 2,500 psi at 75°F.

As stated above, the fatigue life of the windows is limited by cracking of the bearing surface on the flange and the interior face of the dome. Both conditions have been observed by earlier investigators [8,10].

The cracking of the bearing surface on the flange is undoubtedly tied to the differential motion taking place at the window/steel interface during the sustained pressure phase. The natural remedy for this problem is, therefore, to enable the window to slide with the least possible resistance. Hence, the neoprene gasket was tried. It is possible that even better results could be obtained using other materials, such as polycarbonate which has been successfully incorporated in the NEMO Mod 2,000 [17]. The polycarbonate insert not only is capable of absorbing the shear strain to a much larger degree than the acrylic, but should it crack, only the insert needs to be changed and not the whole window. Whatever material is used for the insert, it has to be either sufficiently stiff or sufficiently thin to prevent its being pushed into the window cavity by external hydrostatic pressure.

The problem of cracking on the interior face of the window due to buildup of tensile strain is more difficult to explain and to remedy. Probably, this phenomenon is a result of the loading conditions, the geometry of the window and the physical properties of acrylic plastic. If the dome had been made from steel, the stress (effective von Mises's) at the inner face would have been about 2.5 times higher than the stress at the outer face. If the dome was overpressurized, the steel at the inner face would yield. During depressurization, the plastically deformed interior face would therefore not be able to expand as much as required by the material at larger radii that had been deformed only elastically. Releasing the pressure, therefore, generates tensile stresses in the interior face of the dome.

In the acrylic plastic dome the mechanism, although similar, is complicated by the time, temperature, and stress-dependent properties of the material. Because of the viscoelastic property of acrylic elastic tensile stress may be generated on the inner face of the window during depressurization even though the hydrostatic loading was not of sufficient magnitude to deform the material on the inner face permanently. Thus, in the acrylic plastic, a sudden release of pressure is likely to cause higher tensile stresses on the inner face than a slow release, as the rate of relaxation for the inner face is slower than for the outer face that is subjected to a viscoelastic strain of lesser magnitude. Also, the duration of the sustained loading, the length of the relaxation, and ambient temperature influence the magnitude of tensile stresses during relaxation.

## Deformations

### Original Design Findings.

(1) The interior surface of the windows at the apex deformed elastically up to at least 0.020 in./in. of compressive strain. Relaxation from this strain level was about 99% complete in 10 hours after release of pressure.

(2) Polar strains (interior surface at the apex) of 0.0020 in./in. magnitude were attained at about 6,250 psi of external pressure during short-term loading (650 psi/minute rate). During long-term loading, this strain level was reached in less than 1 hour at 5,000 psi, while at 4,000 psi the same strain level was reached only after 262 hours. At sustained hydrostatic loading of 2,000 psi, this strain level would definitely not be reached in less than 10,000 hours.

(3) Permanent deformation of the material at the bearing surface of the window's flange occurred even when no permanent deformation took place elsewhere. In all cases of permanent deformation in the flange, the deformation was such as to change the bearing surface from a plane surface into a slightly conical surface having an imaginary apex inside the window cavity. The onset of permanent deformation of this type was observed in the window loaded at 2,000 psi of hydro-

static pressure for 269 hours at 75°F. The deformation was very slight, being hardly measurable. On the other hand, in a window subjected to hydrostatic loading of 8,000 psi for 312 hours, the bearing surface of the window was deformed approximately 4 degrees (Figure 22).

(4) In the elastic strain region, the internal window surface of the windows at the apex deformed uniformly with the same strains in all directions. Comparing the measured strain in this area with the theoretical value for the interior face of a thick-wall hollow sphere (Lame's equation with  $\mu = 0.4$  and  $E = 400,000$  psi), the measured value was found to be about 18% smaller than the theoretical (Figure 81). This indicates that the effect of restraint imposed by the flange is almost damped out in this area. The equatorial area of the window also deformed uniformly in the circumferential direction. In the meridional direction on the other hand, the strain changed substantially, reflecting the effect of flange restraint. Moving from the apex towards the edge, the meridional strains decreased; at the same time, the circumferential strains increased. This behavior is probably due to the outward bending movement at the edge caused by the rounded heel of the flange. The deformed shape of the window is postulated to be as shown in Figure 82.

(5) Under extreme loading, the deformation of the window inevitably would also become nonuniform at the apex and in the circumferential direction elsewhere. This was substantiated by the formation of flat spots; and, unless the pressure was reduced, the window failed catastrophically. If the pressure was maintained, the windows would implode when the compressive strain on the interior surface at the apex reached a magnitude of 0.080 to 0.10 in./in. The strains at the flat spot were often even higher, possibly more than double, as indicated by the data from one test (Figure 31).

#### Modified Design Findings.

(1) The introduction of a thin neoprene gasket between the window and the steel led to a slight increase of strain on the dome of the window (Figure 66).

(2) The replacement of the rounded heel with a square heel in window (E) led to a much more even distribution of meridional strains on the inside of the window. The meridional and the circumferential strains also became more equal, particularly near the heel of the flange (Figure 68).

(3) The total removal of the whole flange led to a remarkable change in the deformation of the window. Window (I), now a true hemisphere with no wall-thickness variation, deformed quite evenly from the apex to the equator (Figure 83). The ratio of the highest to the lowest compressive strain measured on the interior face of the window was now 1.3 (compared to 1.8 for the window with rectangular heel on the flange and 12 for the original geometry with well-rounded heel).

## SUMMARY OF FINDINGS

The maximum safe working pressure of a hemispherical window with equatorial flange is, as has been experimentally determined previously for other window shapes, a function of short-term critical pressure,<sup>a</sup> long-term critical pressure, and cyclic fatigue. For flanged hemispheres with a  $t/R_i = 0.364$ , the short-term critical pressure at 75°F has been found to be 14,500 psi; long term critical pressure,<sup>b</sup> 6,000 psi; and cyclic fatigue life,<sup>c</sup> 1,000 psi. No significant difference was found in the performance of windows with Type I or Type VI flanges.

The primary effects of cyclic fatigue is in the form of circumferential cracks that develop on the bearing surface of the flange at approximately 1,000-psi cyclic pressure loading level. If stress discontinuities in the form of O-ring grooves on the bearing surface are eliminated and the effect of shear loading on the bearing surface ameliorated by use of neoprene bearing gaskets, the effects of cyclic fatigue on the bearing surface can be eliminated at cyclic pressure loadings  $\leq 4,000$  psi.

Raising the cyclic fatigue life threshold on the bearing surface from 1,000 psi to 4,000 psi pressure does not, however, raise the overall cyclic fatigue life of the flanged window to 4,000 psi since now the secondary effects of cyclic fatigue on other areas of the window become the factor controlling the overall cyclic fatigue life.

The secondary effects of cyclic fatigue in the form of meridional cracks become apparent on the concave face of the window at pressure loadings  $\geq 2,000$  psi. These cracks are caused by tensile strains found on the concave face of the window during relaxation phases of pressure cycles. The magnitude of tensile strains in flanged windows are a function of  $t/R_i$  ratio and the magnitude of compressive creep during the loading phases of pressure cycles. Since the  $t/R_i$  ratio is a geometrical and the magnitude of creep a physical constant, little can be done to decrease their effect on the generation of tensile strains on the concave face of the window during relaxation phases of pressure cycles. Thus, the secondary effects of cycling fatigue in the form of meridional cracks on the concave face of the window become at 2,000-psi loading level the limiting factor on the fatigue life of the flanged hemispherical window.

---

<sup>a</sup> Short term critical pressure — pressure at which catastrophic failure of window occurs when pressurized at 650 psi/minute rate.

<sup>b</sup> Long term critical pressure — sustained pressure at which catastrophic failure of window occurs after uninterrupted sustained loading of  $10^6$ -minute duration.

<sup>c</sup> Cyclic fatigue life — cyclically applied pressure (7 hours sustained loading followed by 17 hours of relaxation at 0 psi) that will initiate cracks in the window after 1,000 pressure cycles.



The ratio of 1:0.414:0.138 (14,500 psi:6,000 psi:2,000 psi) between short-term critical pressure, long-term critical pressure and cyclic fatigue pressure established experimentally in this study for flanged hemispherical windows with  $t/R_i = 0.364$  seated on neoprene gaskets is also applicable conservatively to similar windows with  $t/R_i < 0.364$ . For flanged hemispherical windows with  $t/R_i > 0.364$  the above ratio probably applies also, but not on the conservative side.

## CONCLUSIONS

Flanges in acrylic plastic windows of hemispherical shape do not affect significantly their short-term critical pressure; however, they seriously decrease their static and cyclic fatigue life. When such windows with  $t/R_i = 0.364$  are mounted on thin neoprene bearing gaskets, they can be subjected safely in the 65-75°F temperature range to a maximum working pressure of 2,000 psi, which is approximately equal to one-seventh of the window's short-term critical pressure.

## RECOMMENDATIONS

To maximize the cyclic and static fatigue life of flanged hemispherical windows, the following precautions must be taken in their design, fabrication, and installation.

### Design

Since the cyclic fatigue life of a flanged window is primarily determined by the appearance of cracks on the bearing surface of the flange, special attention must be paid to the design of the flange. To decrease the magnitude of bending movements in the flange, the instep of the flange must have a generous radius while the heel must approach the shape of a square edge. No discontinuities like O-ring grooves can be tolerated on the bearing surface of the flange as they tend to act as crack initiators. The maximum working pressures at which acrylic hemispherical windows with Type I or Type VI flanges can probably be safely operated are shown in Table 6.

### Fabrication

Appearance of cracks in the bearing surface of the flange can be delayed significantly by following up the machining process with polishing. After polishing, the whole window must be annealed, preferably at 175°F for 22 hours.

Table 6. Maximum Recommended Working Pressures for Hemispherical Windows With Type I and Type VI Equatorial Flanges

Temperature Ranges (°F)	Maximum Working Pressures <sup>a</sup>
≤50	0.167 x short-term critical pressure
≤75	0.143 x short-term critical pressure
≤100	0.111 x short-term critical pressure
≤125	0.091 x short-term critical pressure
≤150	0.059 x short-term critical pressure

<sup>a</sup>Short-term critical pressure is established by pressurizing the window at 650 psi/minute rate and 75°F ambient environment until explosive implosion of the window takes place.

#### Installation

The surface of the steel seat in the pressure vessel must have at least a 63 rms, and preferably 32 rms finish. A thin neoprene-coated nylon gasket (Fairprene 5722A or equal) must be bonded with polyvinyl resin glue (Pliobond or equal) to the bearing surface of the window flange. The steel seat must be liberally coated with silicone grease (Dow Corning No. 4) prior to placement of the gasketed window. Although the bearing gasket serves adequately as a seal, an O-ring is placed around the circumference of the flange to act as a secondary seal (Figure 84). A retaining ring placed around the flange is dimensioned to compress simultaneously both the window flange and the O-ring seal. The bolts holding down the retaining ring must be of adequate size and tensile strength to retain the window against accidental internal pressurization of the hemispherical window to 0.05 times short-term critical pressure.

#### REFERENCES

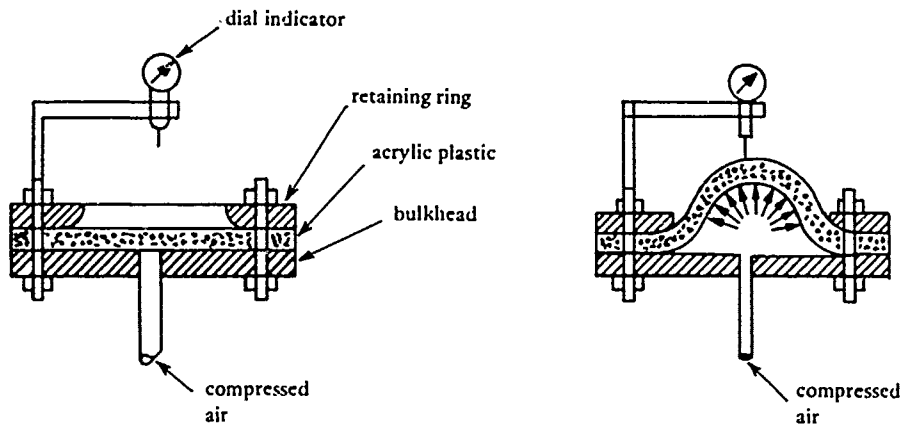
1. Naval Civil Engineering Laboratory. Technical Report R-512: Windows for external or internal hydrostatic pressure vessels; part I: Conical acrylic windows under short-term pressure application, by J. D. Stachiw and K. O. Gray. Port Hueneme, CA, 1967 (AD656882)
2. ———. Technical Report R-645: Windows for external or internal hydrostatic pressure vessels; part IV: Conical acrylic windows under long-term pressure applications at 20,000 psi, by J. D. Stachiw, Port Hueneme, CA, Oct 1969 (AD697272)

- 3.\_\_\_\_\_. Technical Report R-708: Windows for external or internal hydrostatic pressure vessels; part V: Conical acrylic windows under long-term pressure application of 10,000 psi, by J. D. Stachiw and W. A. Moody. Port Hueneme, CA, Jan 1970 (AD718812)
- 4.\_\_\_\_\_. Technical Report R-747: Windows for external or internal hydrostatic pressure vessels; part VI: Conical acrylic windows under long-term pressure application of 5,000 psi, by J. D. Stachiw and K. O. Gray. Port Hueneme, CA, Jun 1971 (AD736594)
- 5.\_\_\_\_\_. Technical Report R-773: Windows for external or internal hydrostatic pressure vessels; part VII: Effect of temperature and flange configurations on critical pressure of 90-degree conical acrylic windows under short-term loading by J. D. Stachiw and J. R. McKay. Port Hueneme, CA, Aug 1972.
- 6.\_\_\_\_\_. Technical Report R-527: Windows for external or internal hydrostatic pressure vessels; Part II: Flat acrylic windows under short-term pressure application, by J. D. Stachiw, G. M. Dunn, and K. O. Gray. Port Hueneme, CA, May 1967 (AD652343)
- 7.\_\_\_\_\_. Technical Note N-1127: Flat disc acrylic plastic windows for man-rated hyperbaric chambers at the USN Experimental Diving Unit, by J. D. Stachiw. Port Hueneme, CA, Nov 1970 (AD716751)
- 8.\_\_\_\_\_. Technical Report R-631: Windows for external or internal hydrostatic pressure vessels; part III: Critical pressure of acrylic spherical shell windows under short-term pressure application by J. D. Stachiw and F. W. Brier. Port Hueneme, CA, Jun 1969 (AD689789)
9. Naval Undersea Center. NUC TP 486: Acrylic plastic spherical shell windows under point impact loading, by J. D. Stachiw and O. Burnside. San Diego, CA, Jul 1975.
- 10.\_\_\_\_\_. NUC TP 410: Development of a precision casting process for acrylic plastic spherical shell windows applicable to high pressure service, by J. D. Stachiw. San Diego, CA, May 1974.
- 11.\_\_\_\_\_. NUC TP 383: Cast acrylic dome for undersea applications, by J. D. Stachiw. San Diego, CA, Jan 1974.
- 12.\_\_\_\_\_. NUC TP 493: Improved fabrication process for spherical acrylic plastic submersible hulls, by J. D. Stachiw. San Diego, CA, Dec 1975.
- 13.\_\_\_\_\_. NUC TP 315: Acrylic plastic hemispherical shells for NUC undersea elevator, by J. D. Stachiw. San Diego, CA, Jan 1974.
- 14.\_\_\_\_\_. NUC TP 355: Flanged acrylic plastic hemispherical shells for undersea systems, by J. D. Stachiw. San Diego, CA, Aug 1973 (AD 772213)

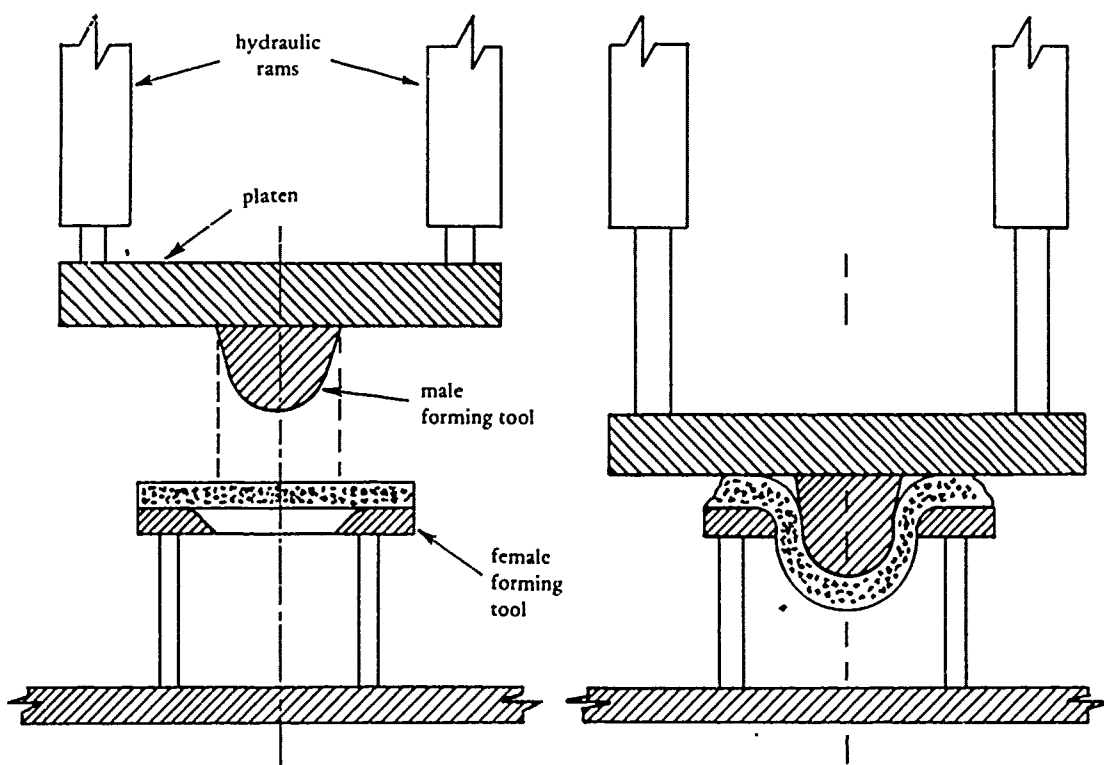
15.———. NUC TP 378: Recommended practices for the design, fabrication, prooftesting and inspection of windows in man-rated hyperbaric chambers, by J. D. Stachiw. San Diego, CA, Dec 1973 (AD773737).

16. J. J. Lohr, et al. "Accelerated Testing of the Mechanical and Thermal Integrity of Polymeric Materials, in Proceedings of 8th Structural Dynamics and Materials Conference, AIAA/ASME. Palm Springs, CA, Mar 1967.

17. Naval Undersea Center. NUC TP 451: NEMO Model 2000 acrylic plastic spherical hull for manned submersible operation, by J. D. Stachiw. San Diego, CA, Dec 1974.



Free Forming With Compressed Gas



Extrusion Forming With Dies

Figure 1. Typical techniques for thermoforming flanged hemispherical windows of acrylic plastic.

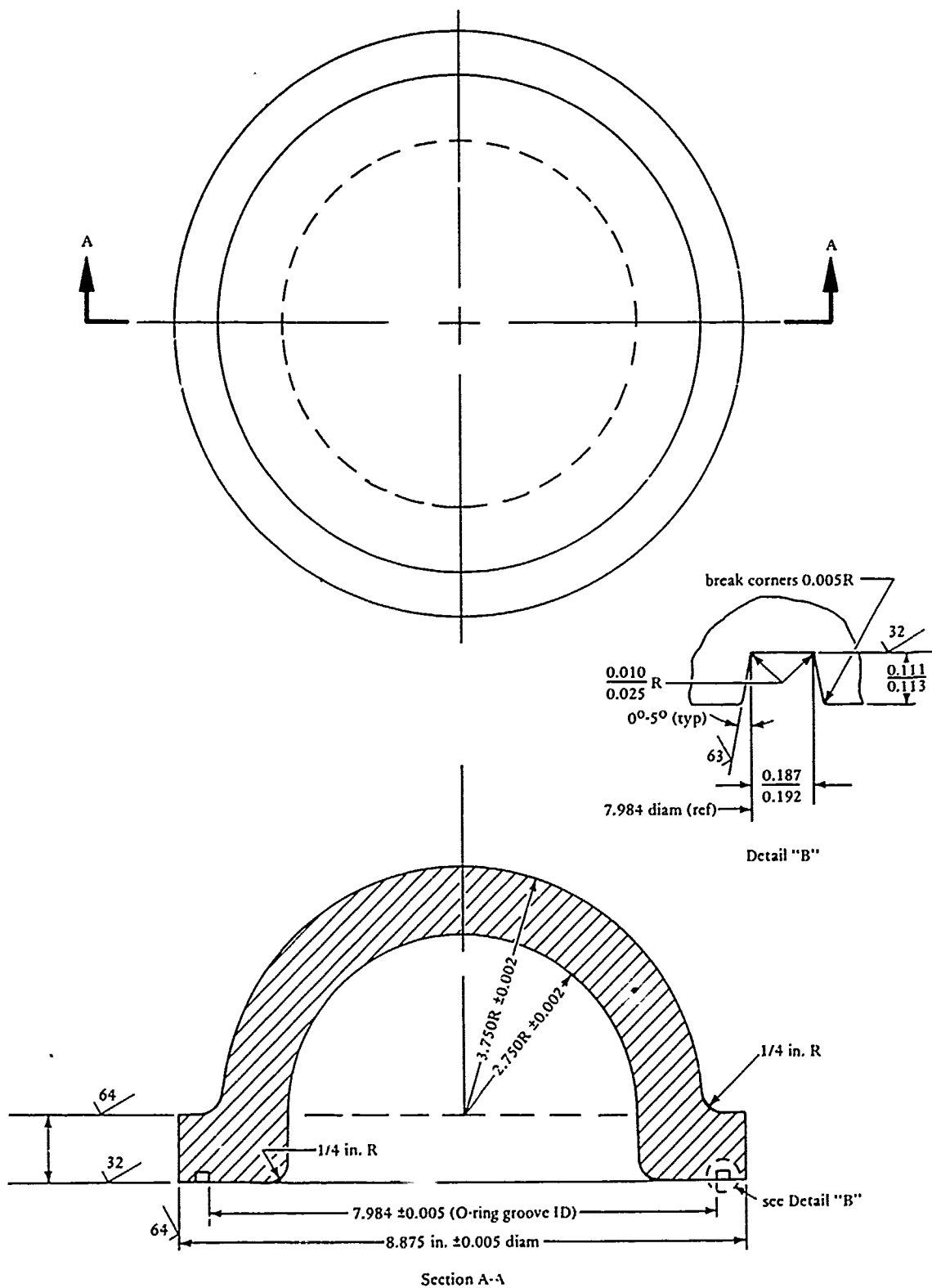


Figure 2. Type I flanged hemispheres used as test specimens in the experimental test program.

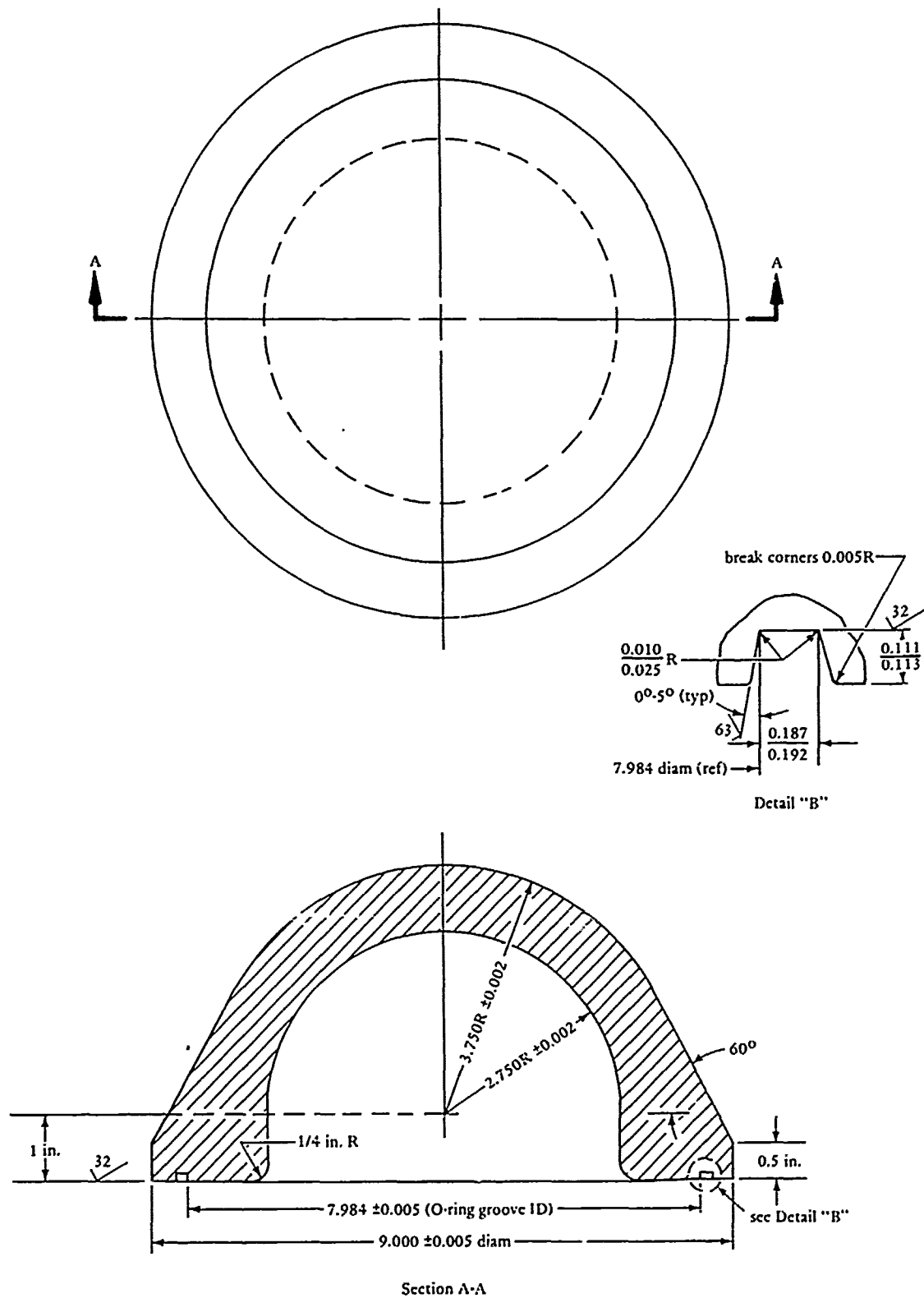
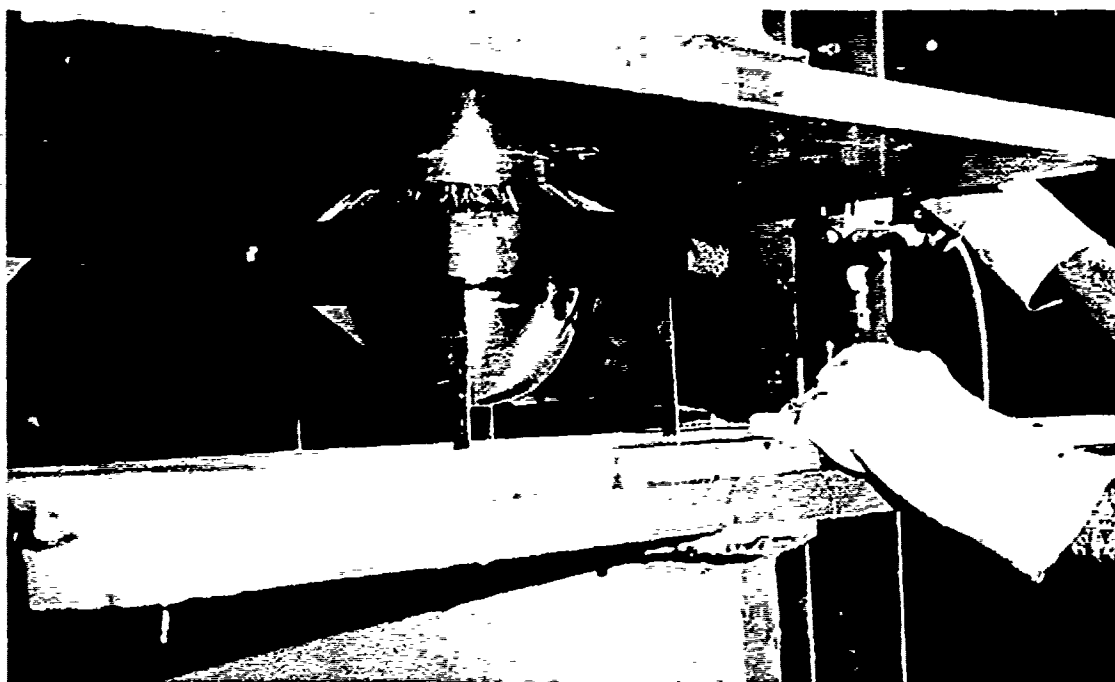


Figure 3. Type VI flanged hemispheres used as test specimens in the experimental test program.



(a) Placing the blank between dies.



(b) Forcing the material through the female die.

Figure 4. Thermoforming of flanged hemispheres for the experimental test program.





Figure 5. Typical cross section of thermoformed windows prior to machining.

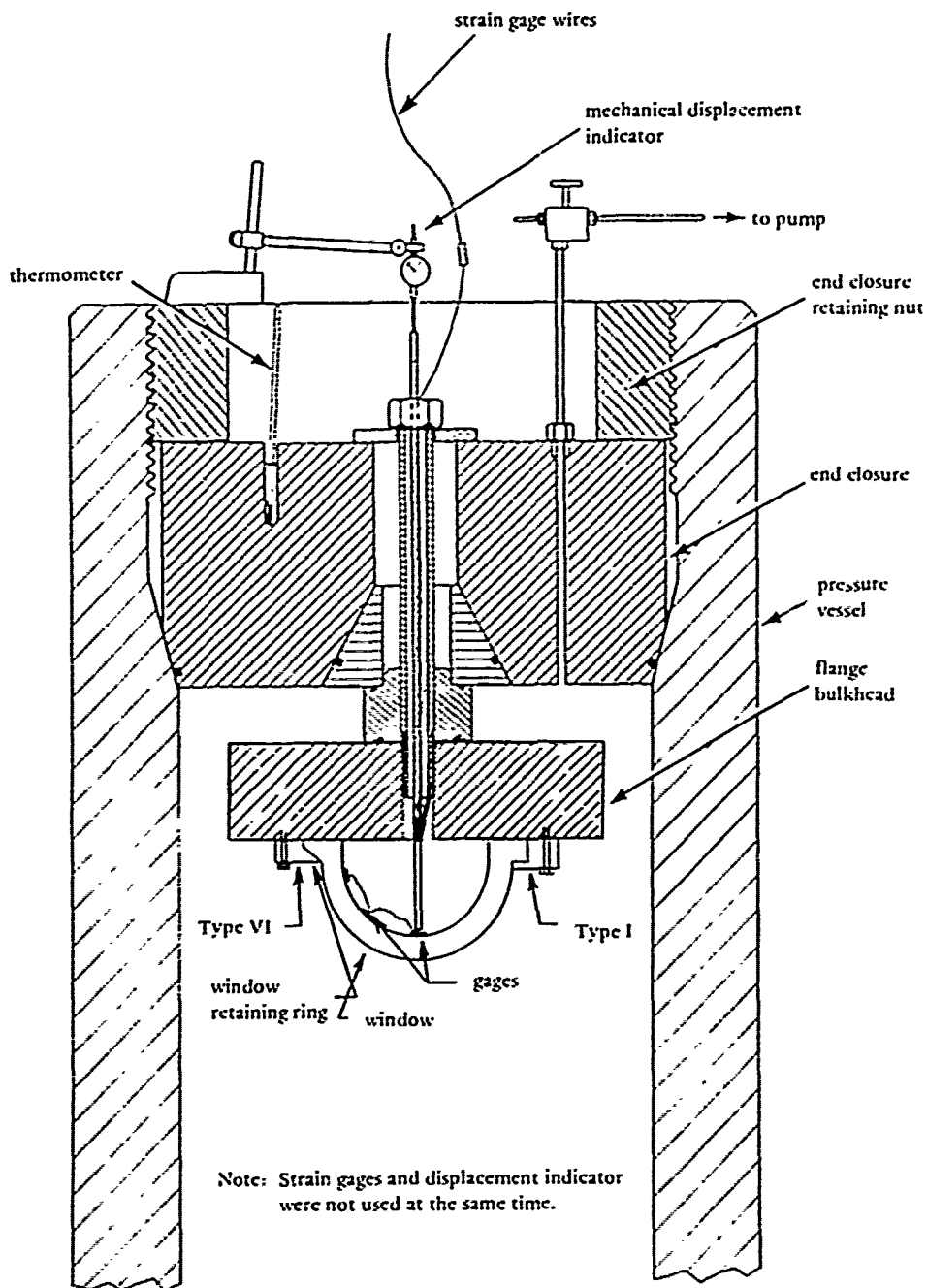


Figure 6. Test arrangement for Type I and Type VI windows in the 18-inch-diameter pressure vessel of CEL's Deep Ocean Simulation Facility.

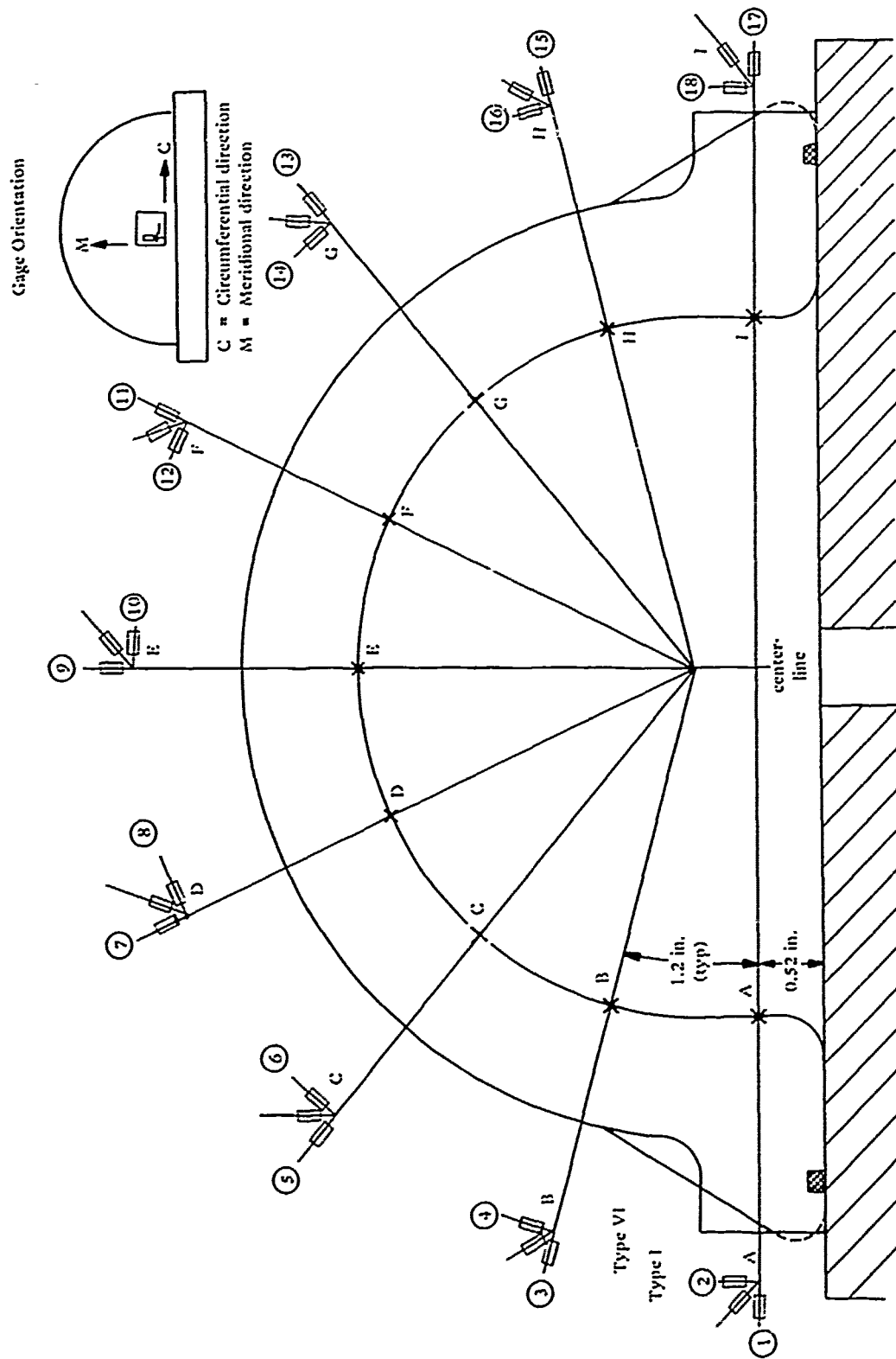


Figure 7. Location of electric resistance strain gages on the interior face of the flanged hemispheres.



Figure 8. Retaining ring for Type VI window testing in 18-inch-diameter pressure vessel; window V after 42 hours at 11,800-psi sustained hydrostatic loading.

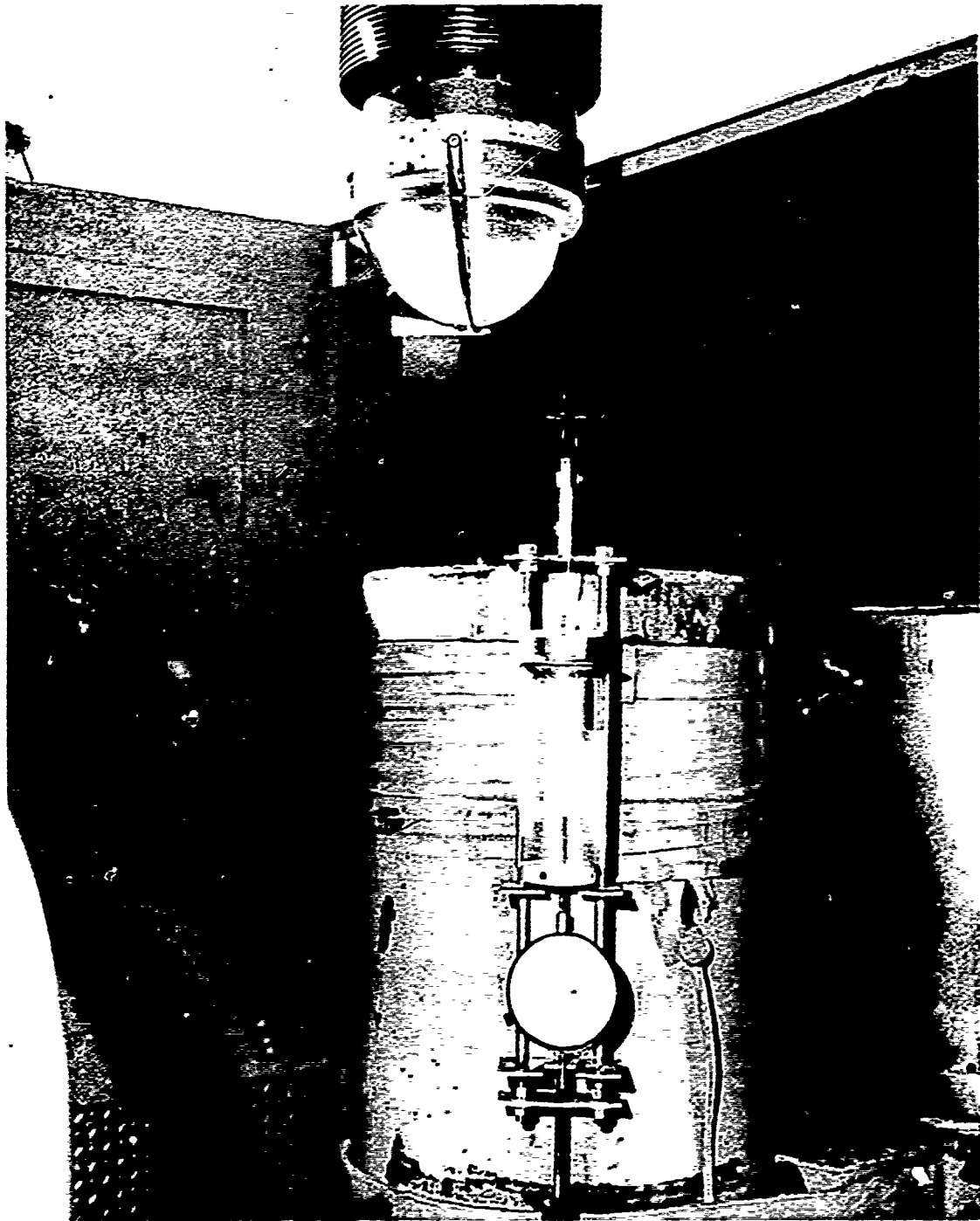


Figure 9. Retaining rubber bands for testing of windows in 9.5-inch-diameter pressure vessel.

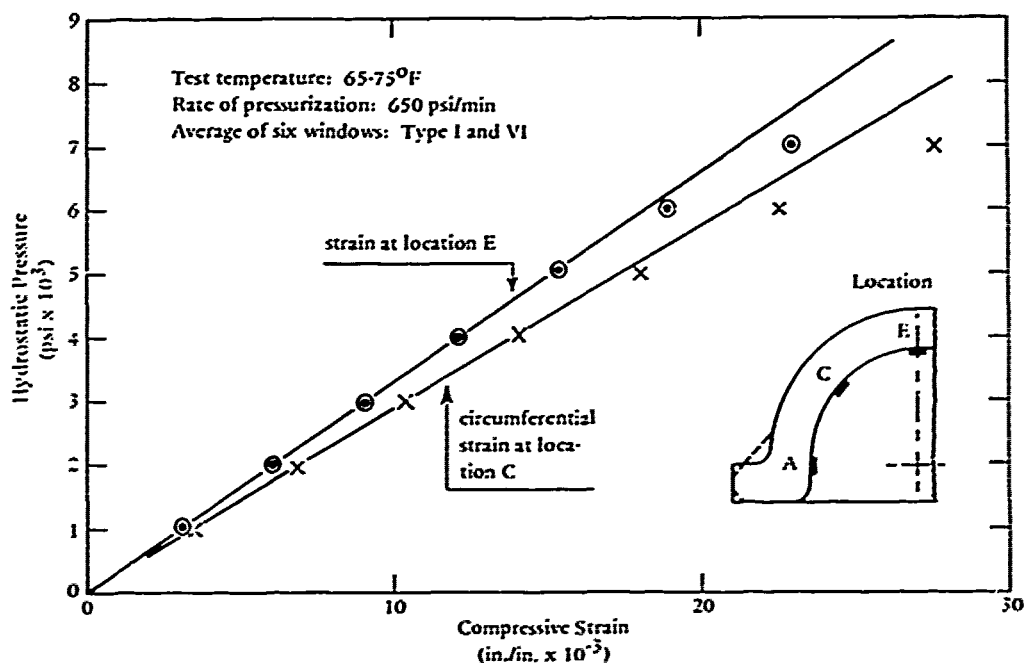


Figure 10. Linearity of strains in flanged windows during short-term pressurization in the 0 to 4,000 psi range.

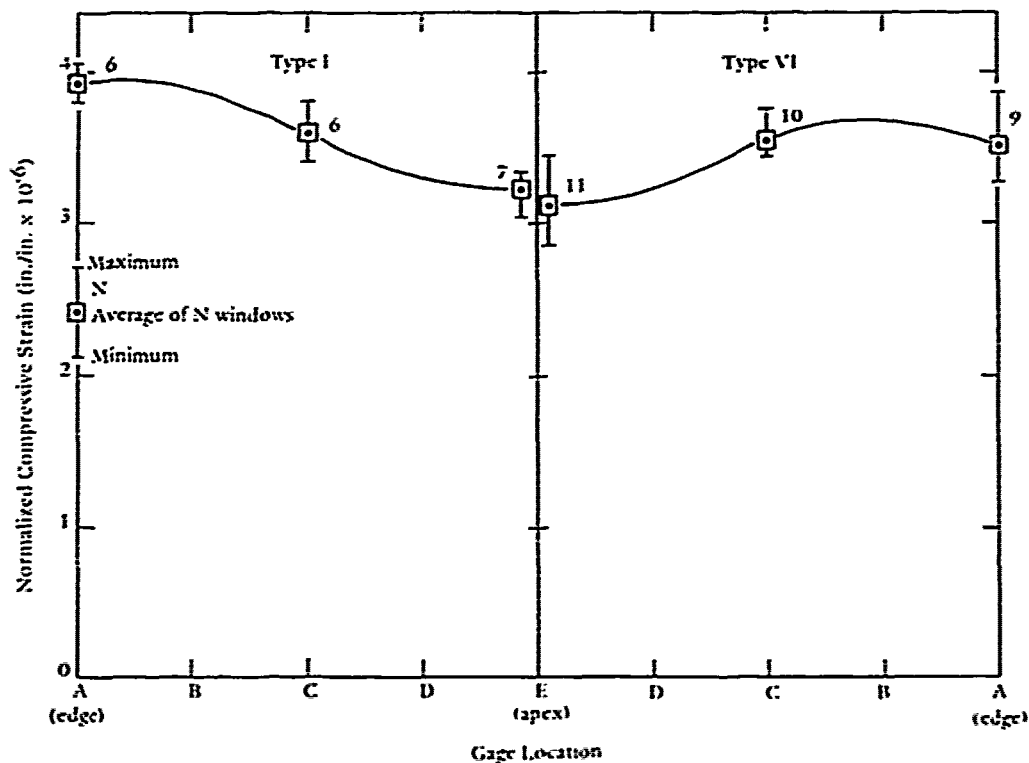


Figure 11. Distribution of circumferential strains on the interior face of Type I and Type VI windows during short-term pressurization in the 0 to 4,000 psi range; the strain plotted has been normalized to show magnitude of strain per unit of pressure in linear range.

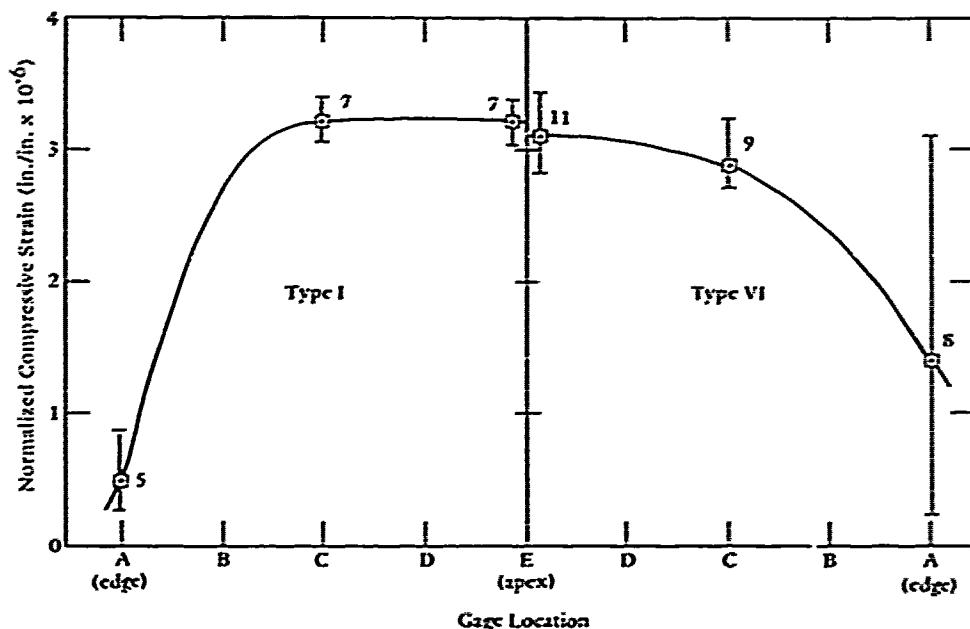


Figure 12. Distribution of meridional strains on the interior face of Type I and Type VI windows during short-term pressurization in the 0 to 4,000 psi range; the strain plotted has been normalized to show magnitude of strain per unit pressure in linear range.

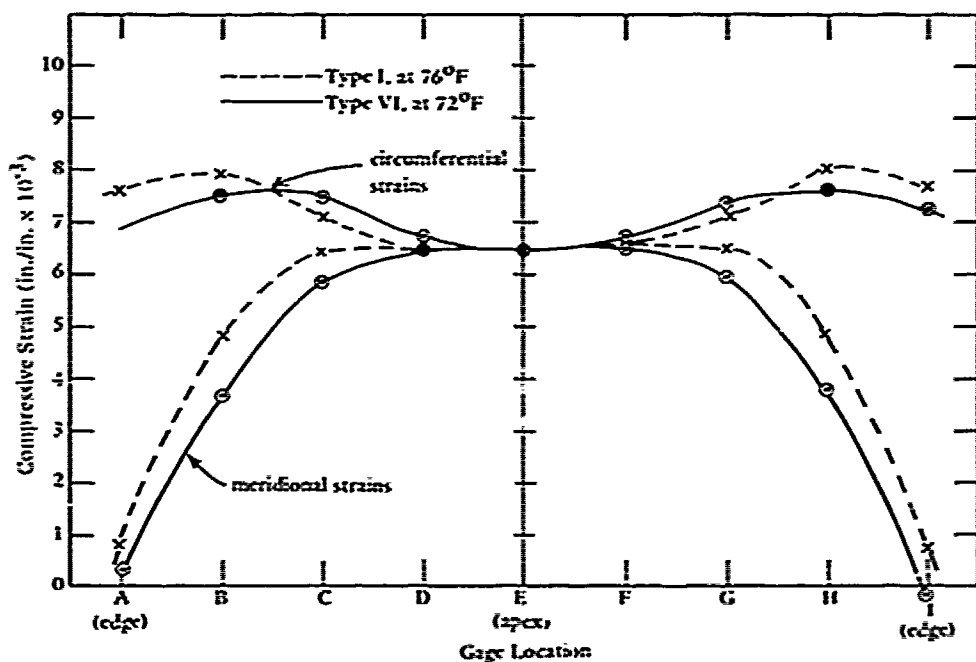


Figure 13. Distribution of strains on the interior face of Type I and Type VI windows at the conclusion of short-term pressurization to 2,000 psi.

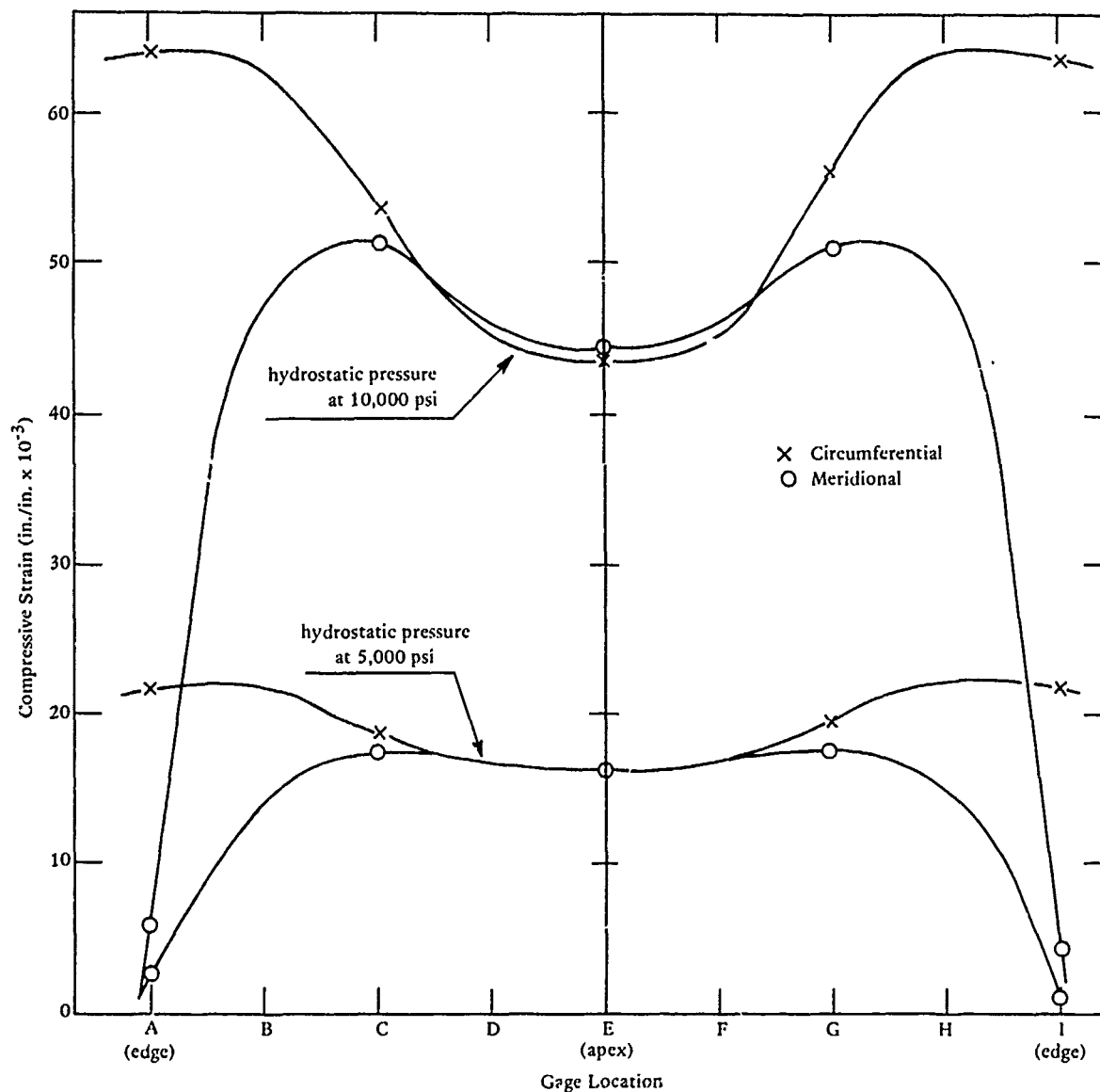


Figure 14. Distribution of strains on the interior face of Type I window J at 5,000 and 10,000 psi pressure levels during short-term pressurization; note the nonlinearity in strain increases at different locations.



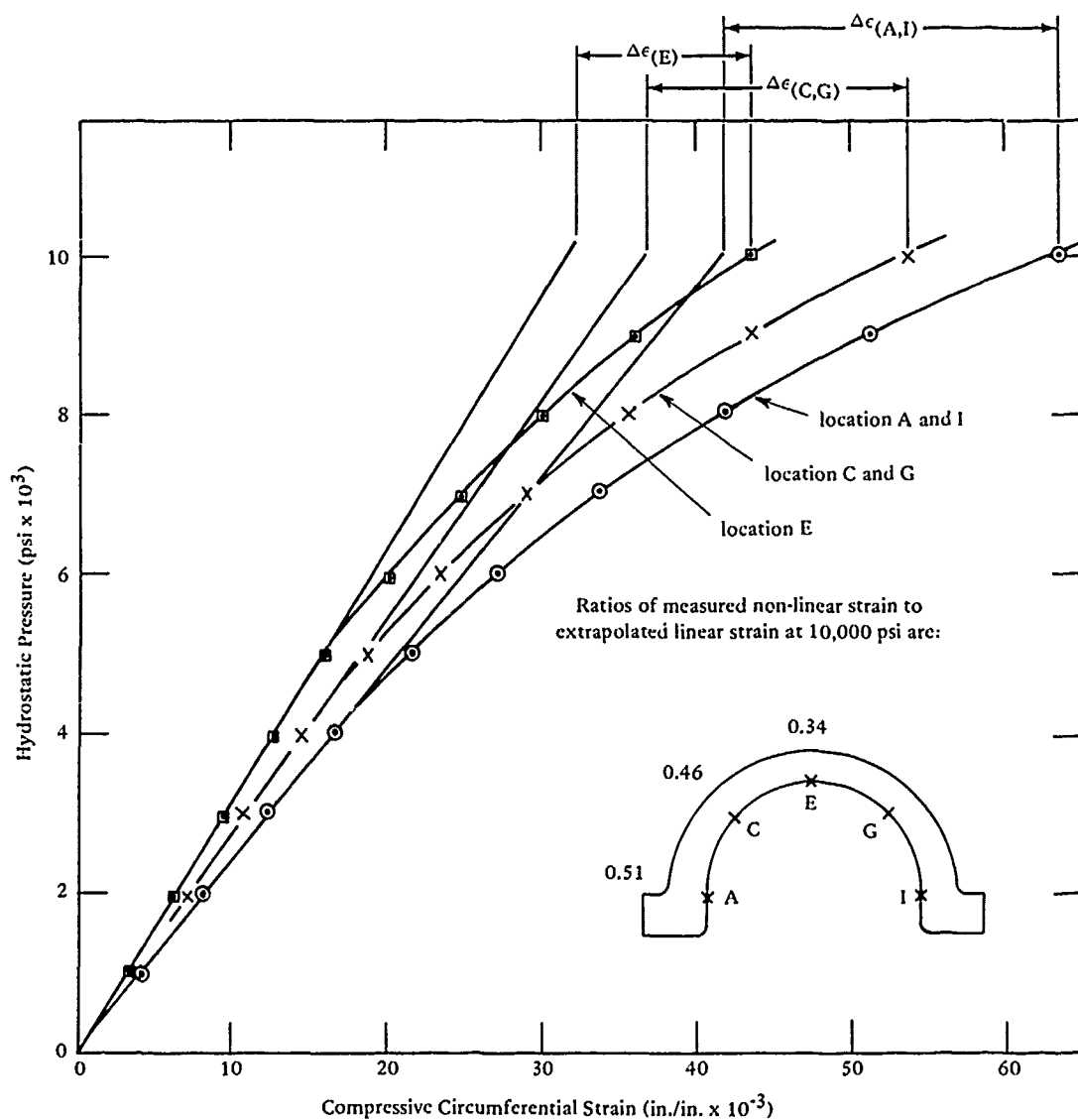


Figure 15. Magnitude of nonlinearity in strains measured on the interior face of Type I window J during short-term pressurization at 74°F to 10,000 psi.

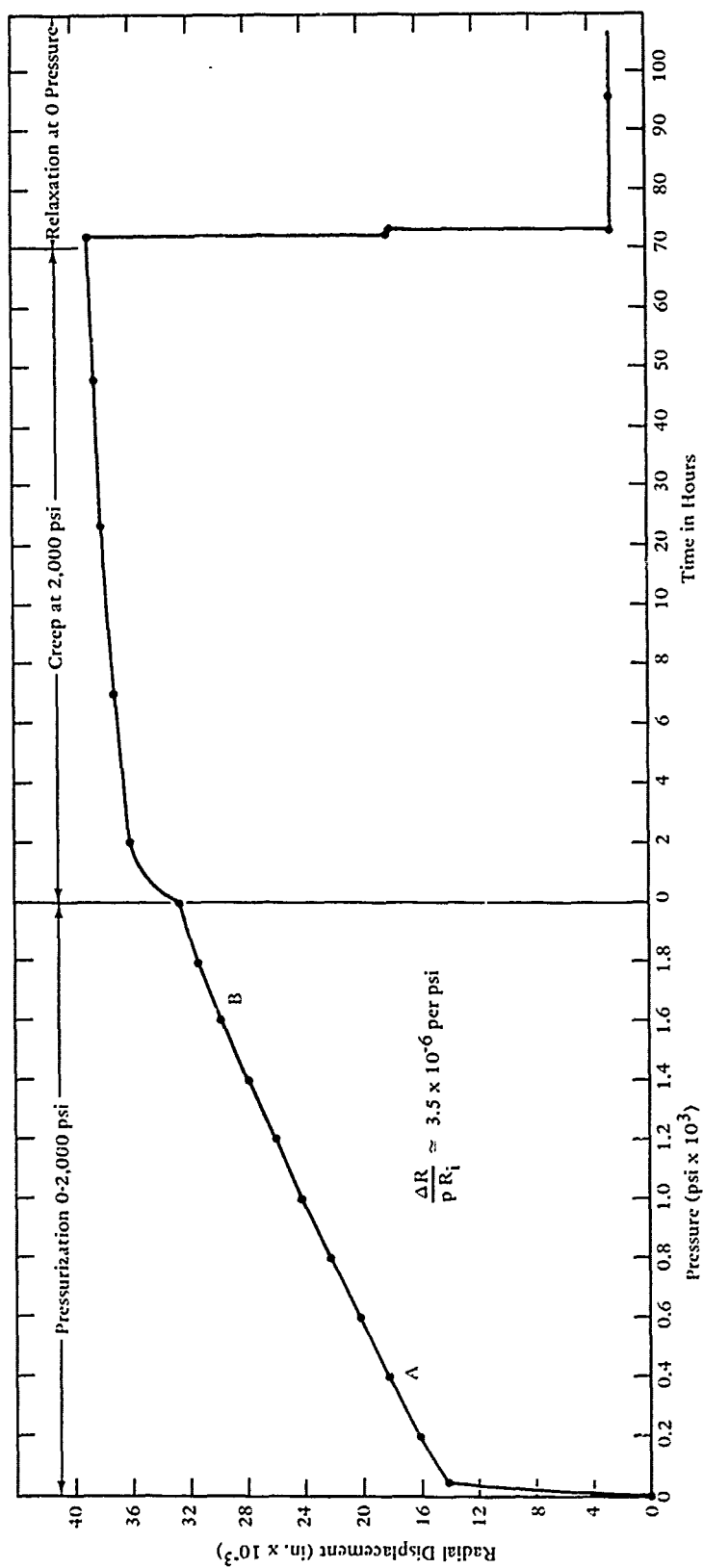


Figure 16. Radial displacement of apex on Type VI window W during short-term pressurization to and sustained pressure loading at 2,000 psi; 72°F.

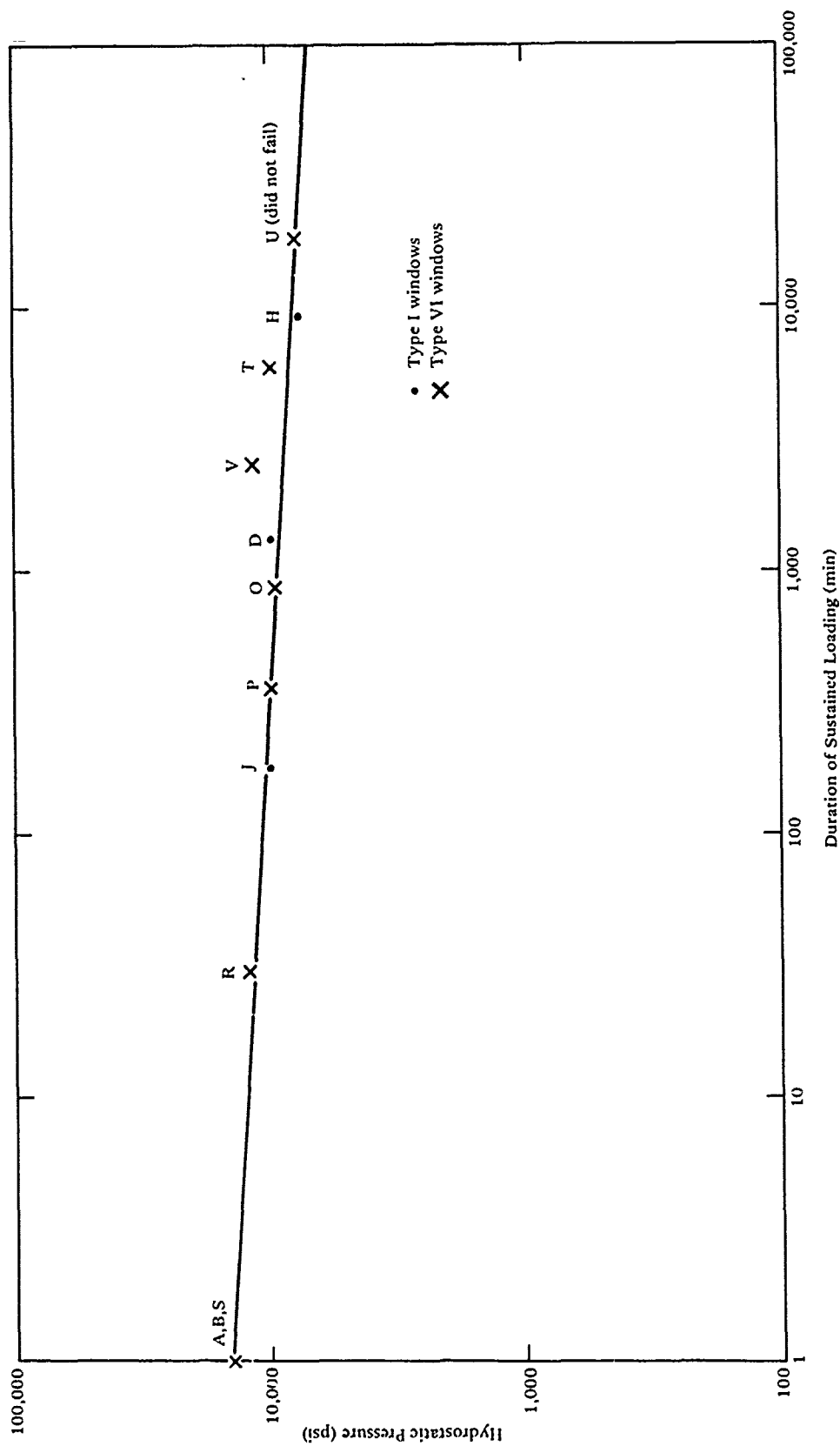


Figure 17. Long-term critical pressures of Type I and Type VI windows tested to catastrophic failure under sustained hydrostatic loading at 65-75°F ambient temperature.

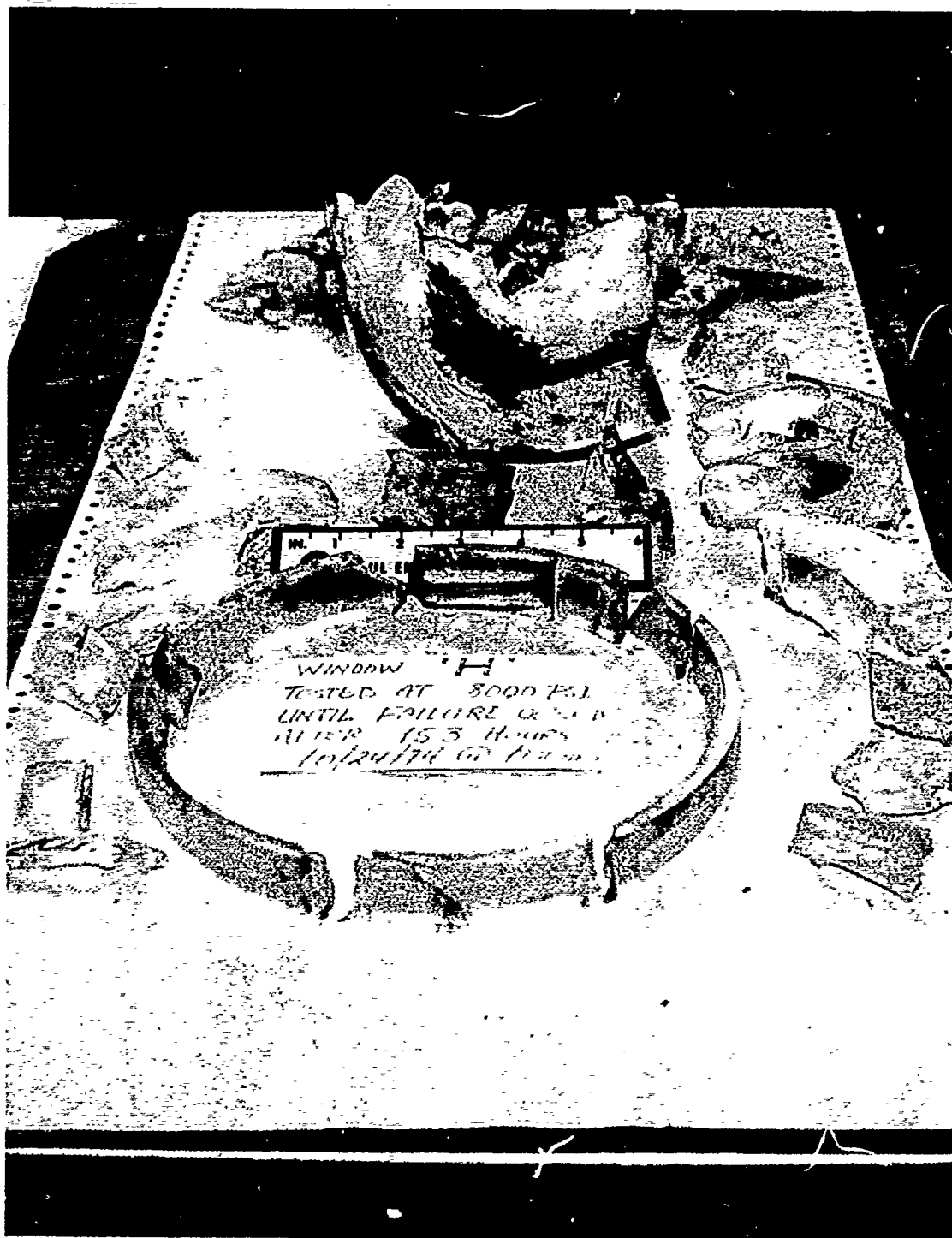


Figure 18. Window H, Type I after 153 hours of sustained pressure loading at 8,000 psi; note the separation of flange.

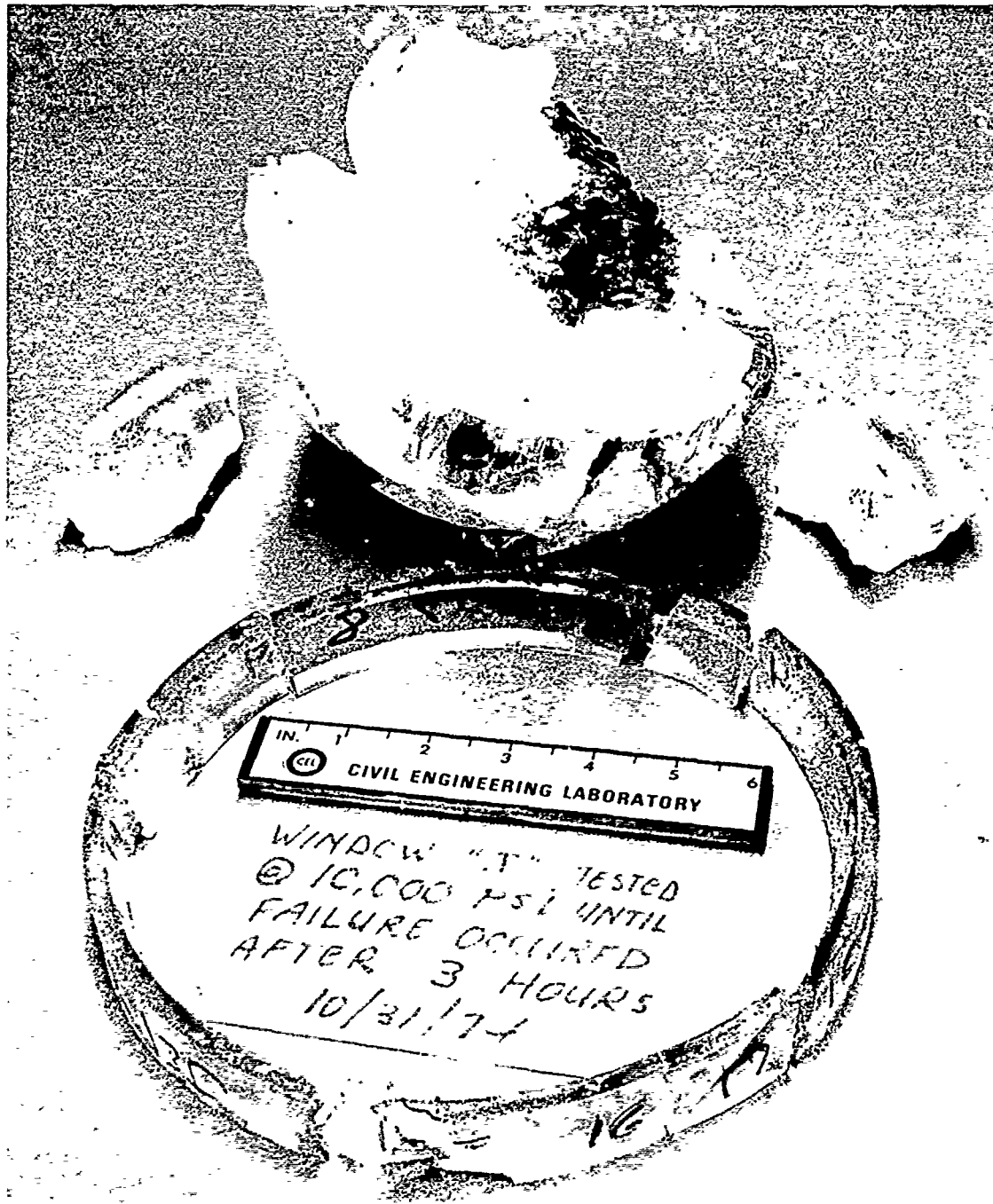


Figure 19. Window J, Type I after 3 hours of sustained pressure loading at 10,000 psi; note the undistorted flange fragments indicating that they broke off immediately after pressurization, before the window deformed plastically.



Figure 20. Window R, Type VI after 30 minutes of sustained pressure loading at 12,000 psi; note the extensive lamination and partial separation of flange.



Figure 21. Same window as Figure 20; note the partial separation of flange and large scale plastic deformation midway between the flange and apex that led to the plastic instability failure of the window.



Figure 22. Window U, Type VI after 312 hours of sustained pressure loading at 8,000 psi; note that (a) the flange has separated even though the window did not implode yet and (b) the bearing surface on the window has deformed plastically giving it the appearance of a very shallow cone.

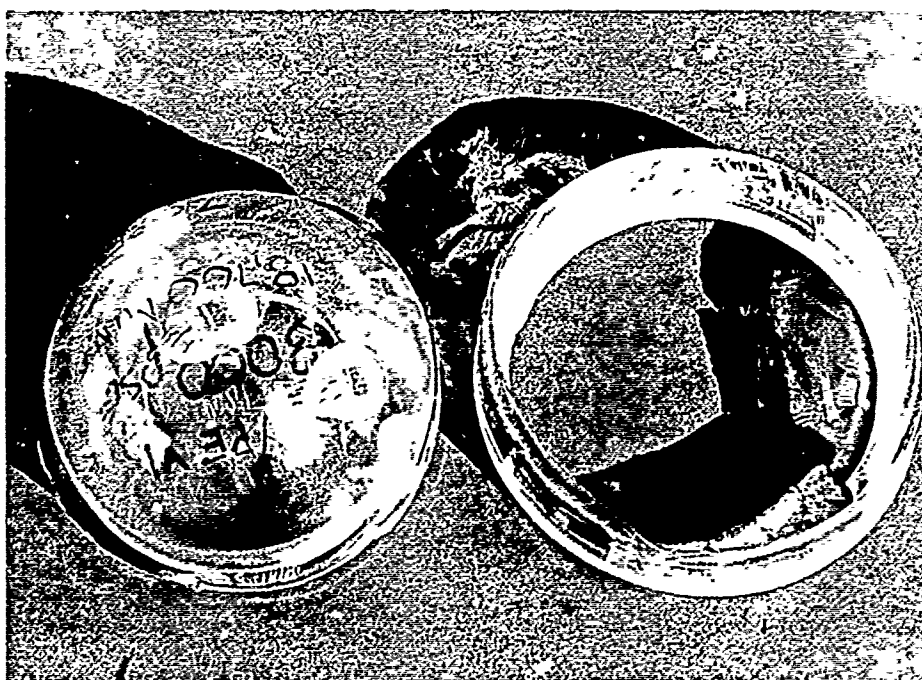


Figure 23. Same window as in Figure 22; note that the separated flange remains intact indicating that (a) the circumferential cracks initiate sooner and propagate faster than radial cracks and (b) the separation occurs before extensive plastic deformations occur.

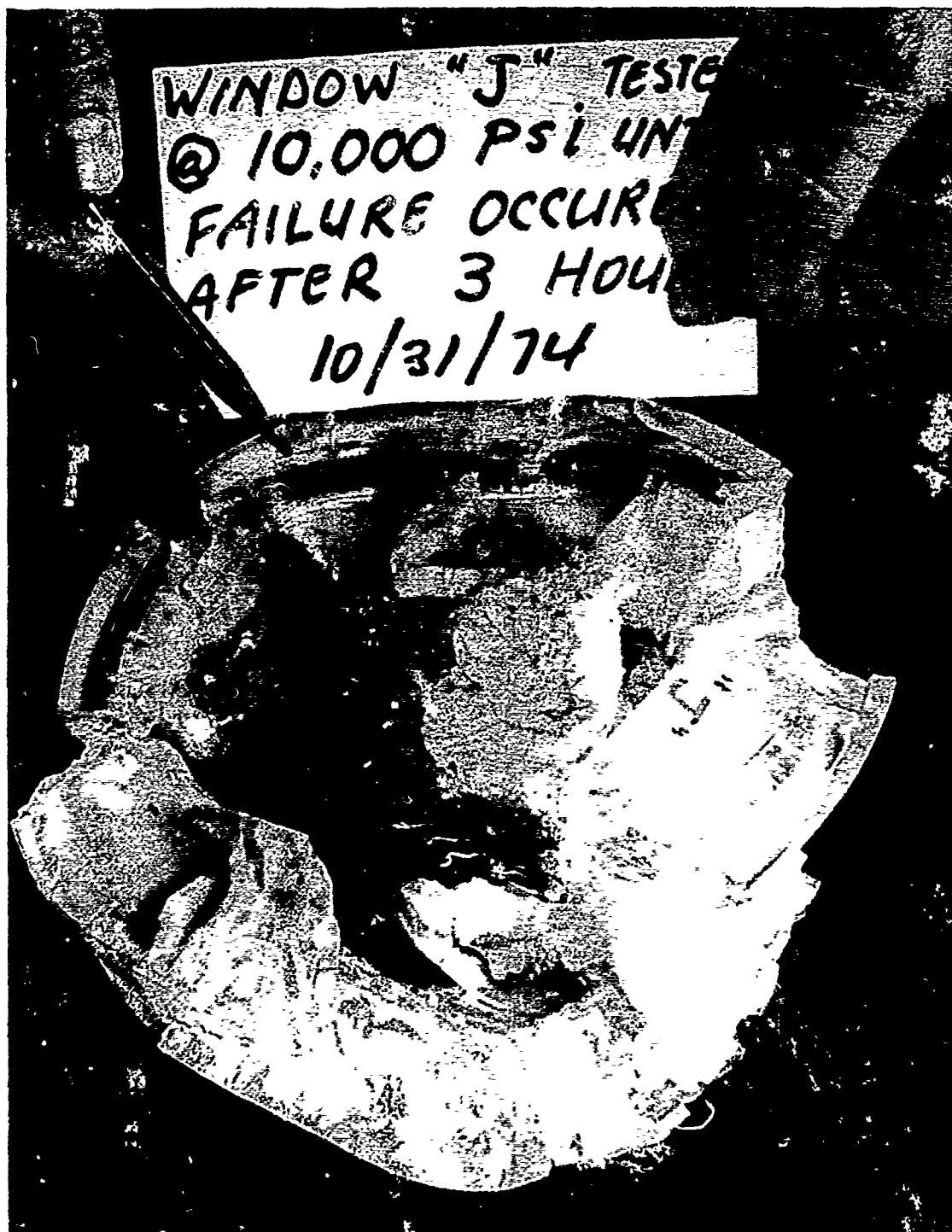


Figure 24. Window J, Type VI after 3 hours of sustained pressure loading at 10,000 psi; note the extensive lamination of the dome at the apex.



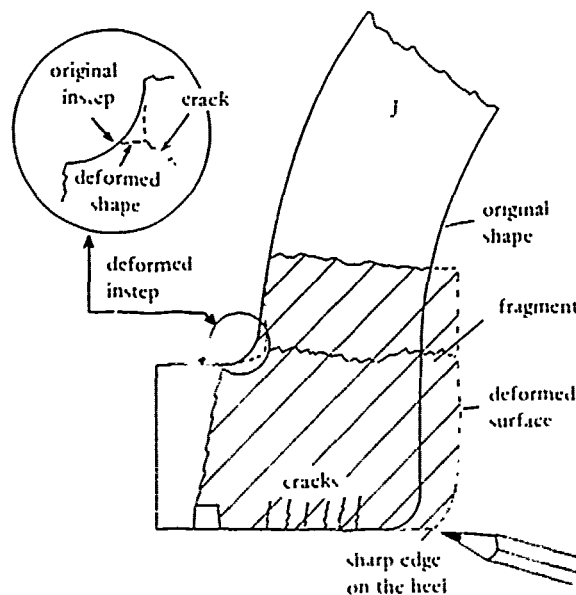
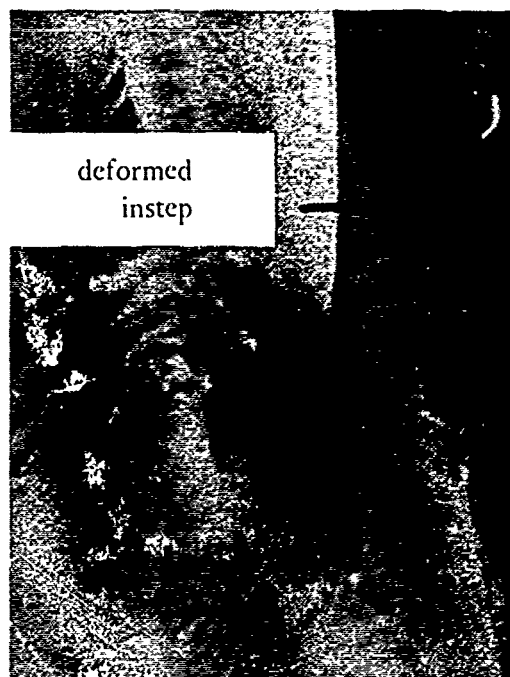
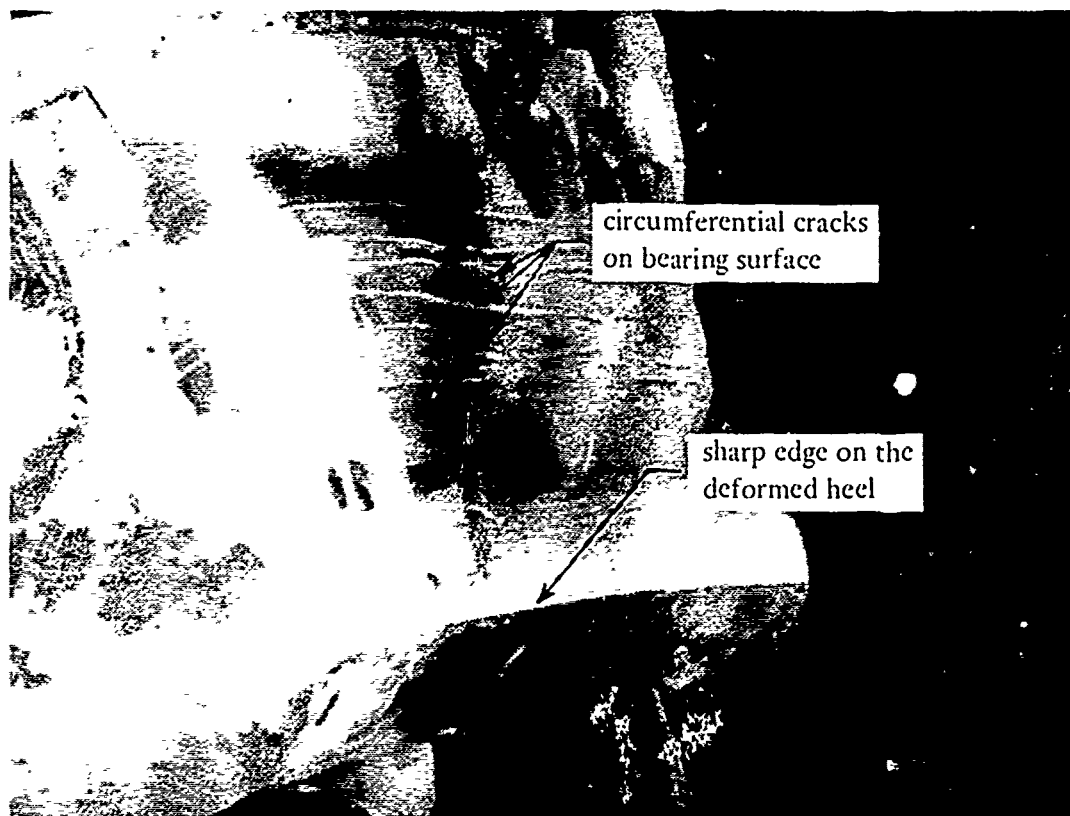


Figure 25. Same window as in Figure 24; note the presence of circumferential cracks in the bearing surface of the flange and the plastic transformation of the rounded heel into a sharp edge and the fillet on the instep into a sharp corner.



Figure 26. Window H, after 154 hours of sustained pressure loading at 8,000 psi; note the increase in wall thickness of the window near the flange due to plastic flow of acrylic under biaxial compression.

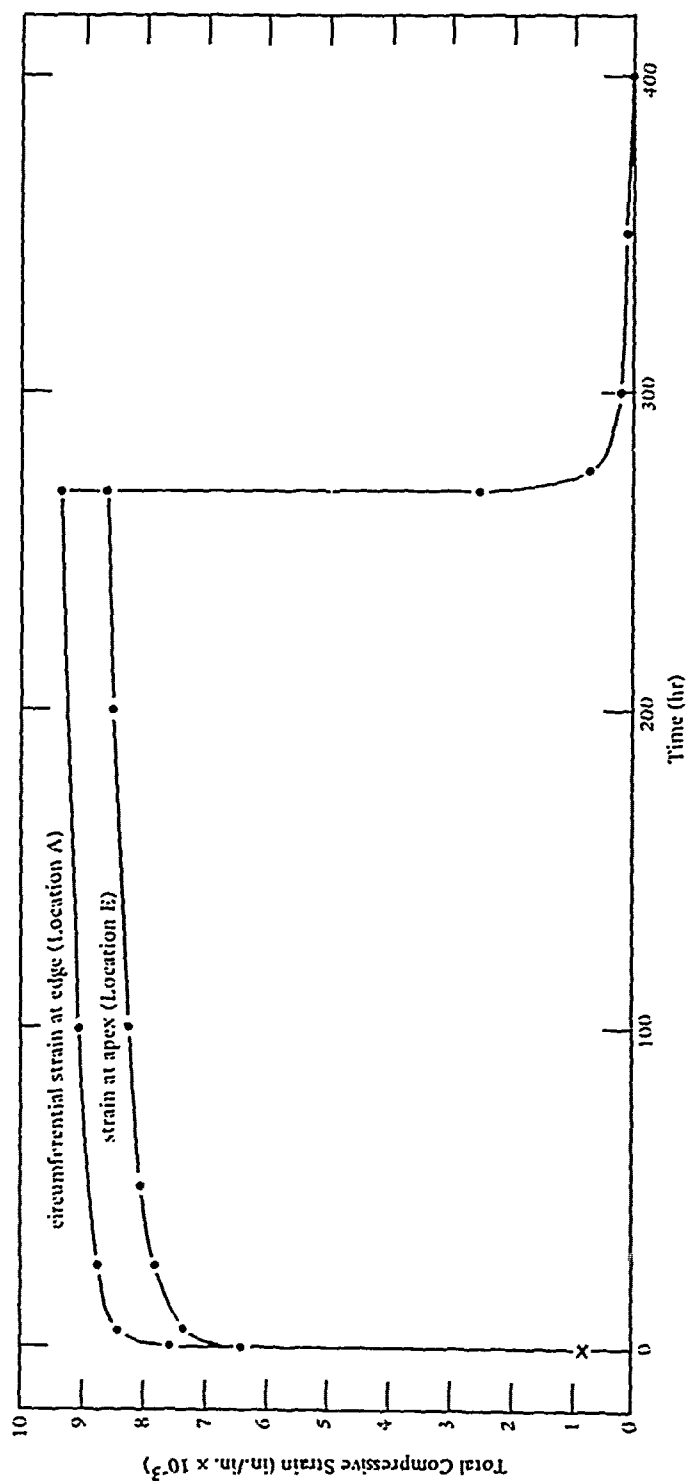


Figure 27. Typical total deformation and relaxation of Type I window I under sustained pressure loading of 2,000 psi.

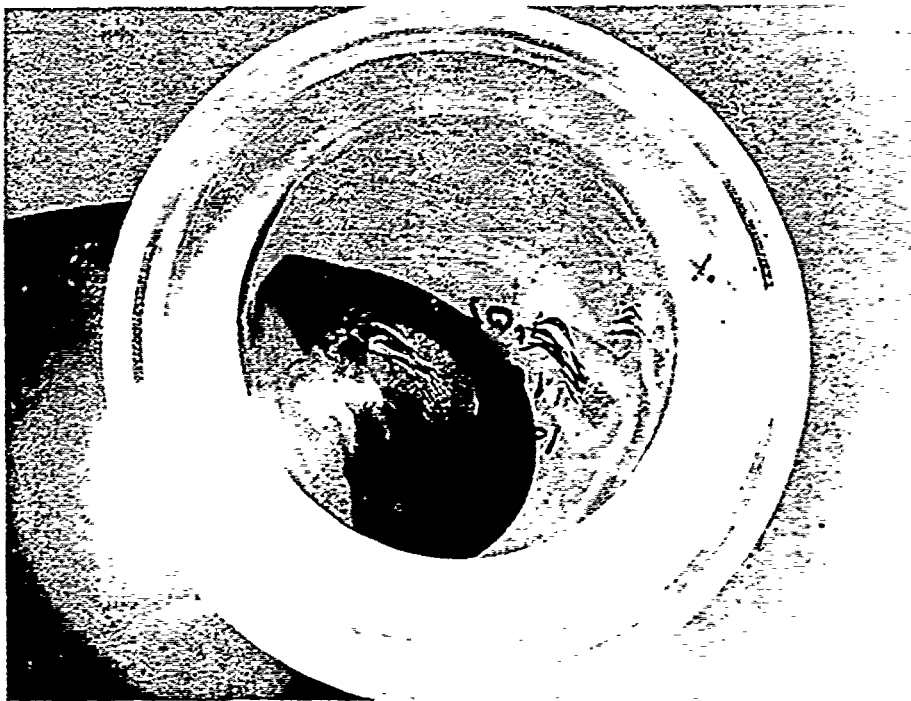


Figure 28. Extensive crazing and minor cracking on the bearing surface of Type VI window R after 262 hours of sustained pressure loading at 4,000 psi.

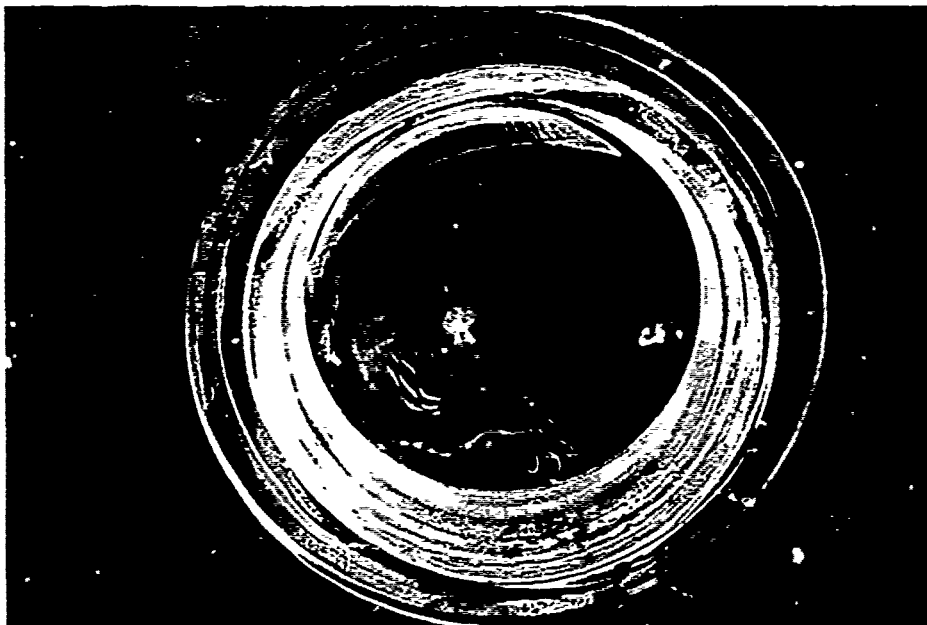


Figure 29. Extensive crazing and a major circumferential crack on the bearing surface of Type VI window Q after 139 hours of sustained pressure loading at 7,000 psi.

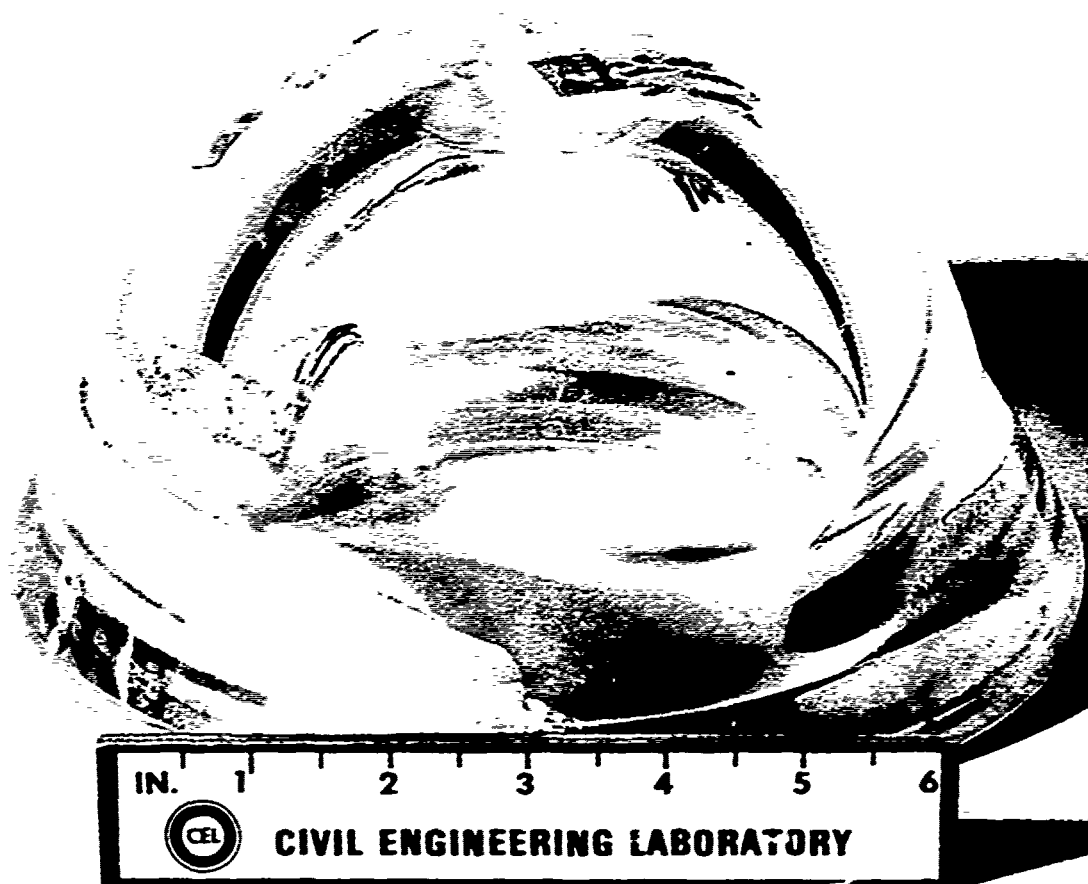


Figure 30. Same window as in Figure 29; note that the circumferential crack has completely penetrated the flange and the flange remains attached to the body of the window only at one place.

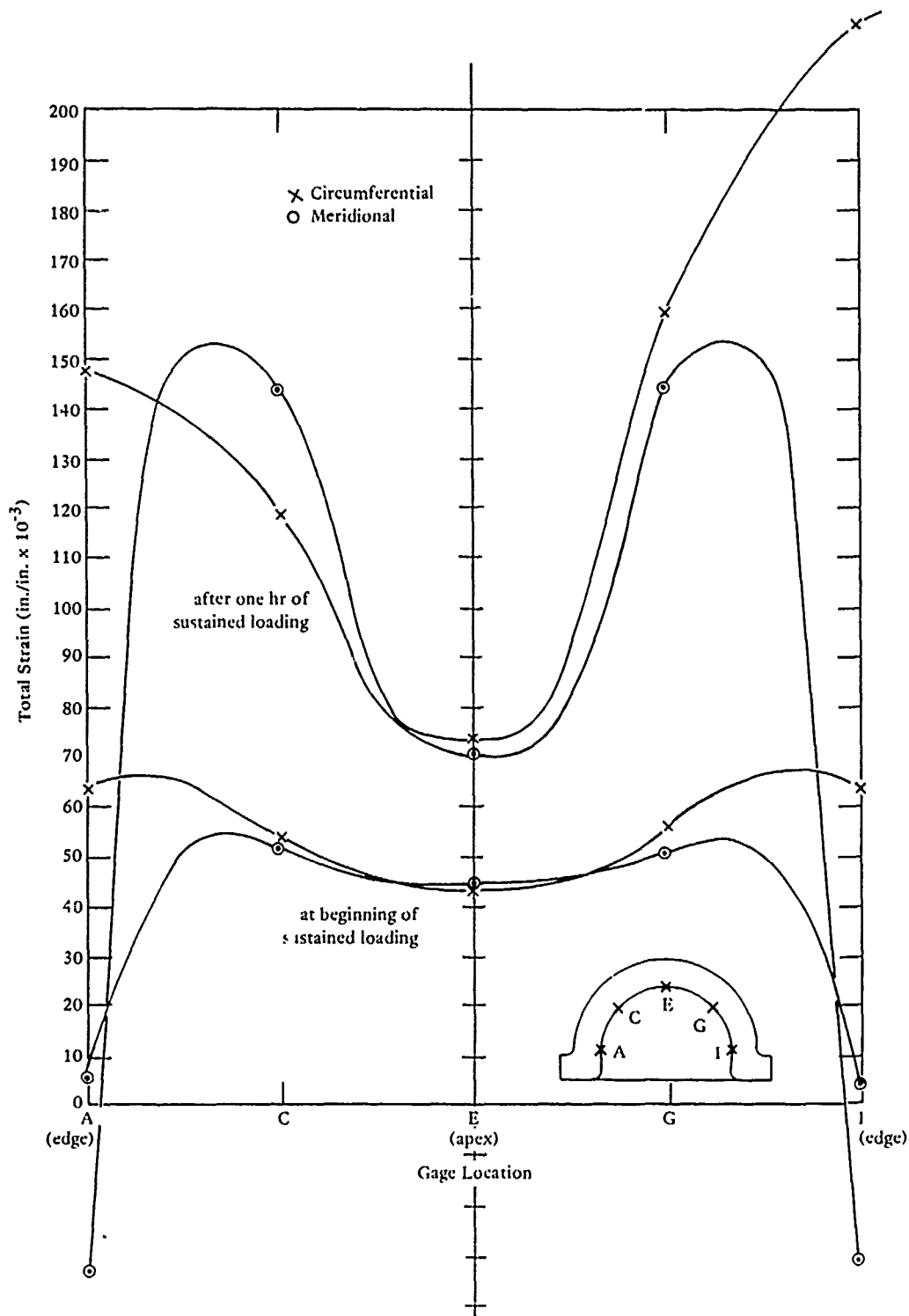


Figure 31. Change in magnitude and distribution of strains with duration of sustained pressure loading at 10,000 psi; window J, Type I; 75°F.

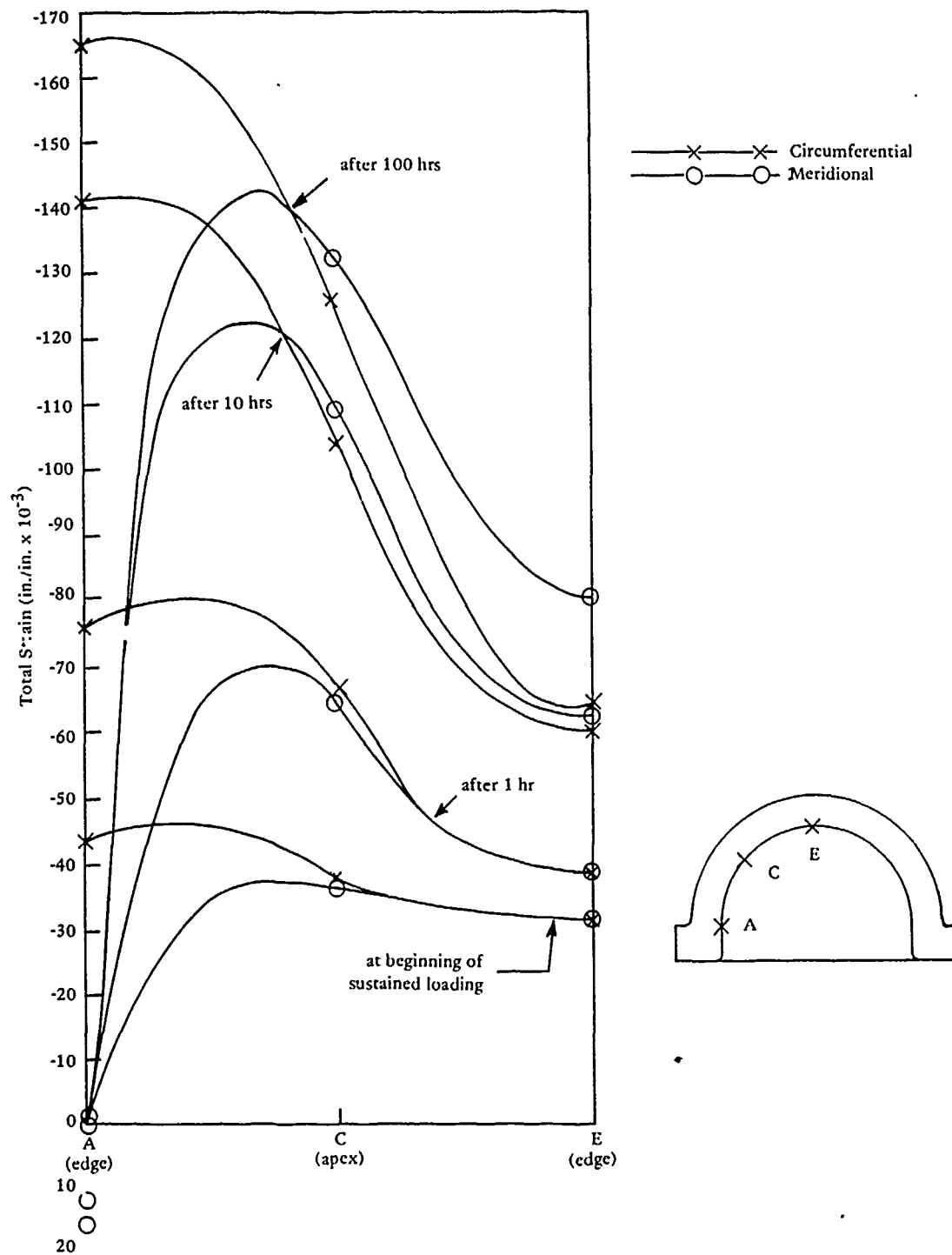


Figure 32. Change in magnitude and distribution of strains with duration of sustained pressure loading at 8,000 psi; window H, Type I; 75°F.

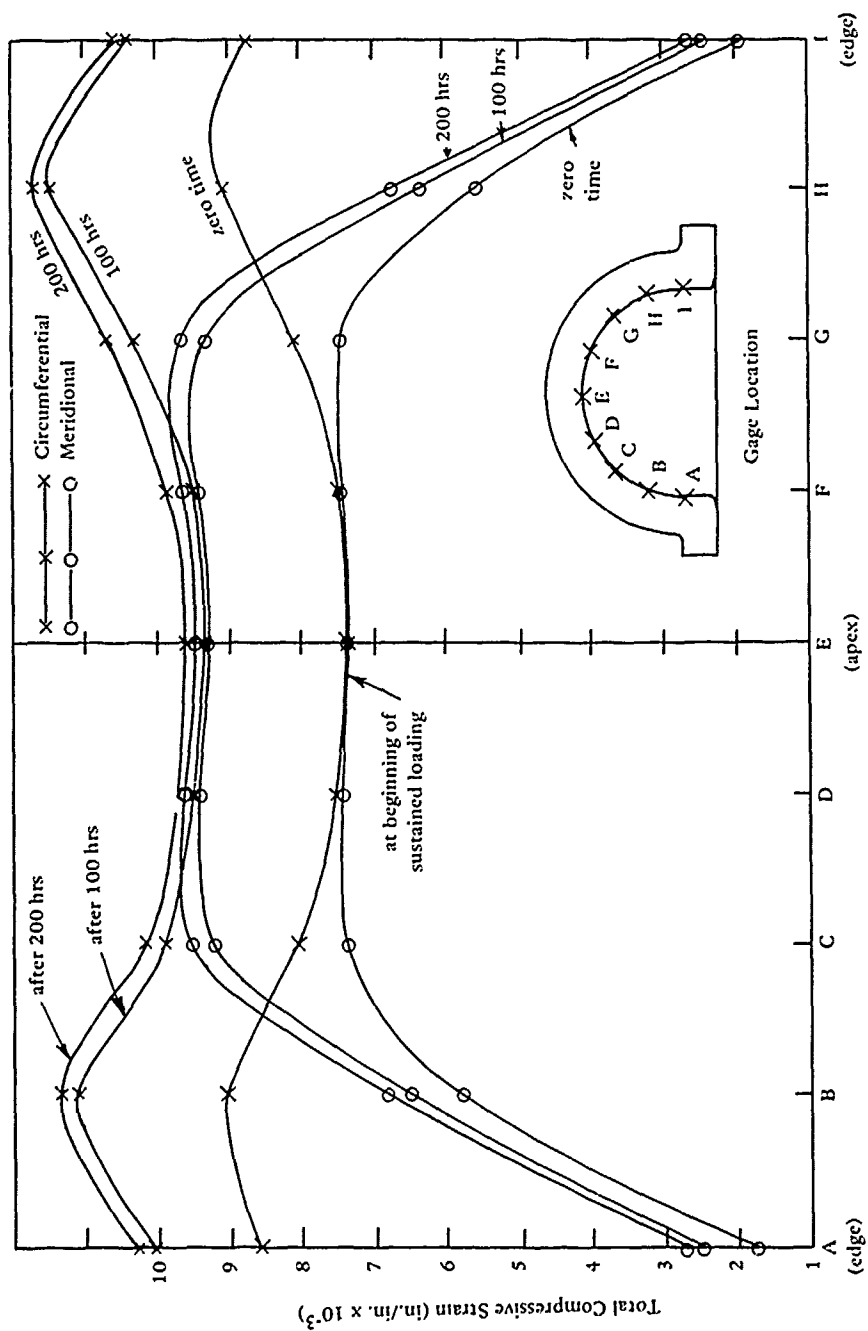
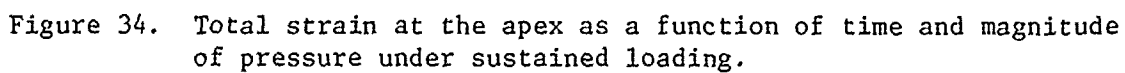


Figure 33. Change in magnitude and distribution of strains with duration of sustained pressure loading at 2,000 psi; window I, Type I; 76°F.





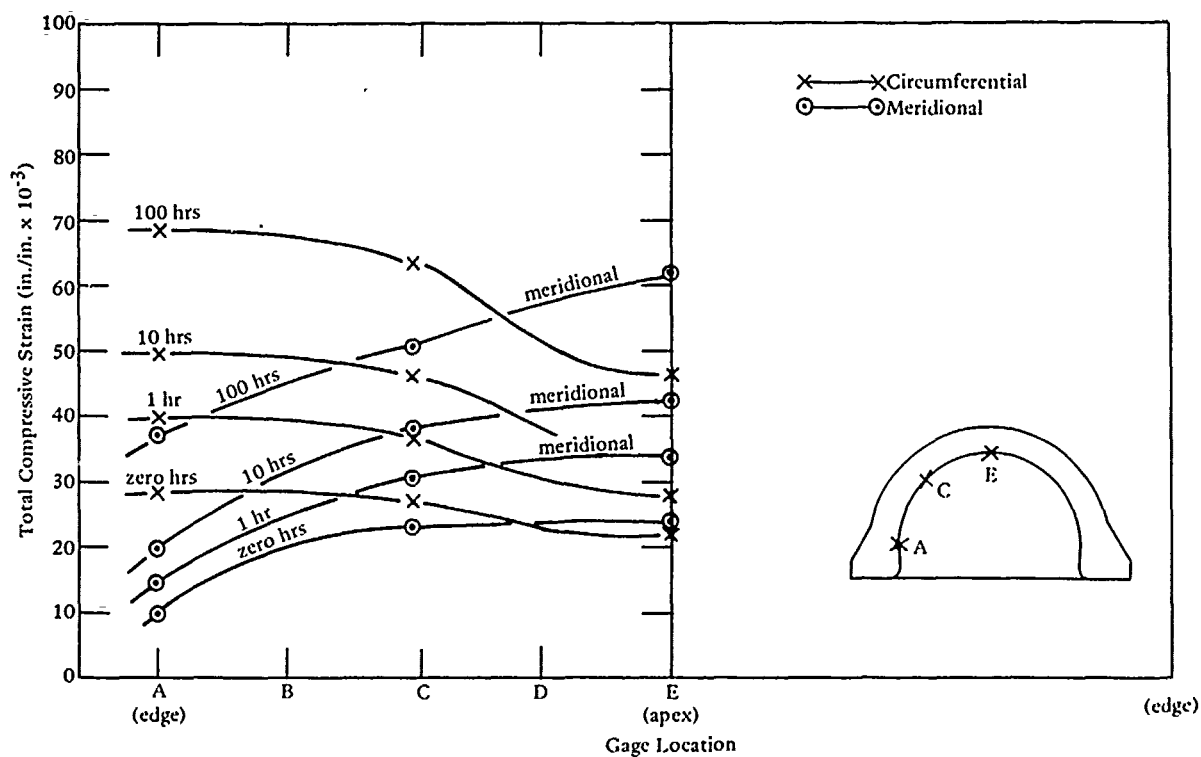


Figure 35. Total strain as a function of loading duration under 7,000 psi pressure; window Q, Type VI.

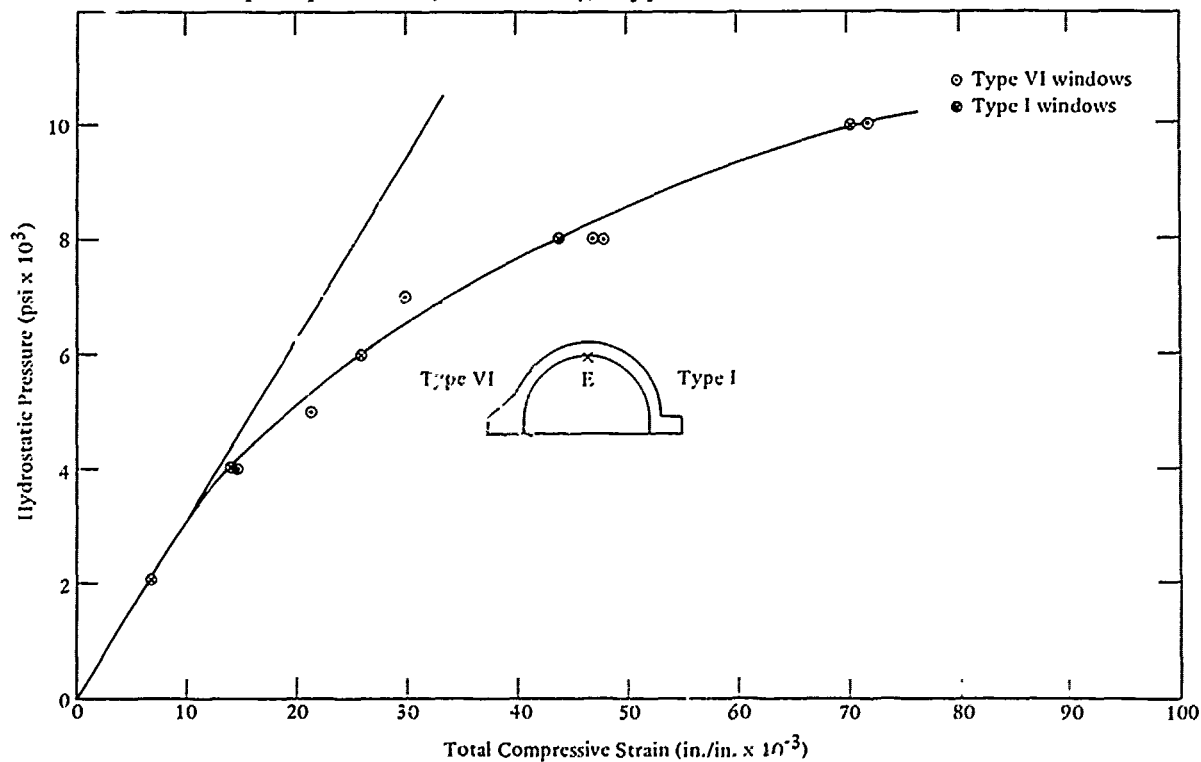


Figure 36. Typical nonlinearity in window deformation under short-term pressure loading.



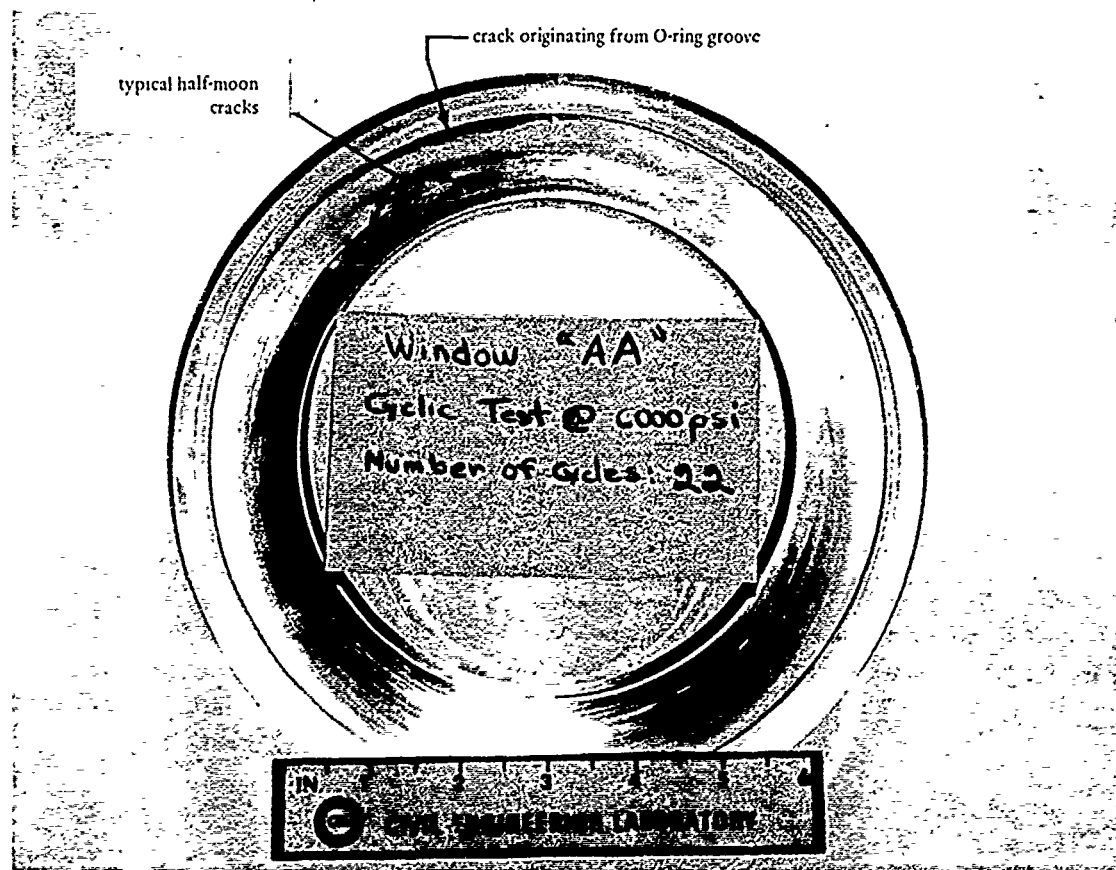


Figure 39. Typical cyclic fatigue cracks on the flange bearing surface; window AA, Type VI after 22 standard pressure cycles to 6,000 psi. Note that major crack originates at O-ring groove.



Figure 40. Same window as in Figure 39; note the shape of the typical cyclic fatigue crack in the bearing surface on the flange. Similar cracks were observed in bearing surfaces of acrylic windows subjected to cyclic pressure loading in other studies [2,8,10]. This peculiar shape is probably caused by expansion of grease or water trapped in the crack during relaxation phases of pressure cycling.

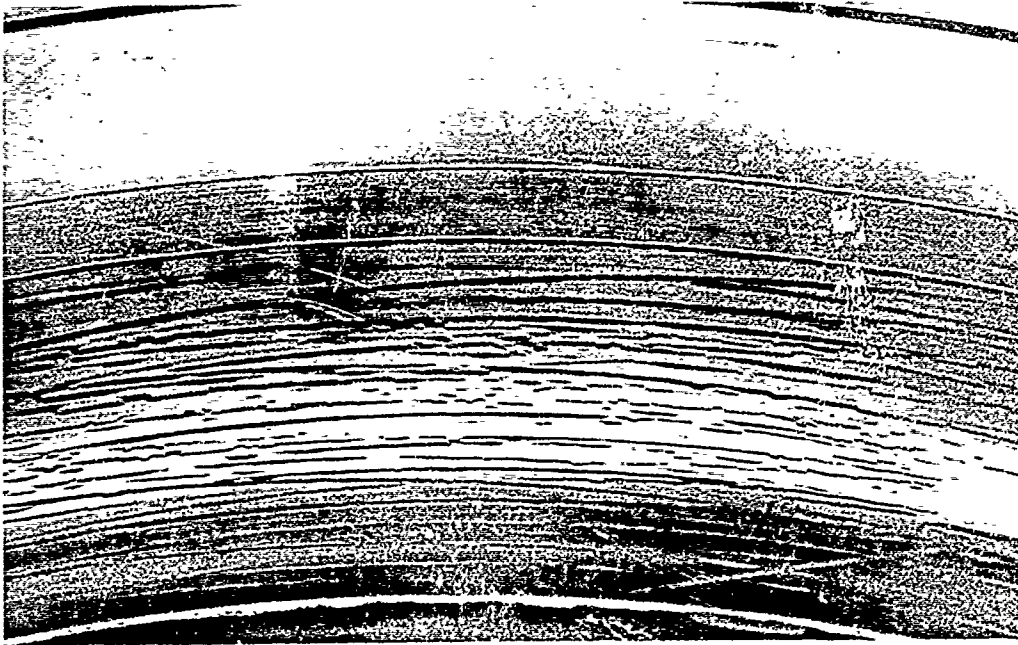


Figure 41. Same window as in Figure 39; note that the circumferential crazing on the bearing surface of the flange appears primarily near the heel of the flange and not the O-ring groove.

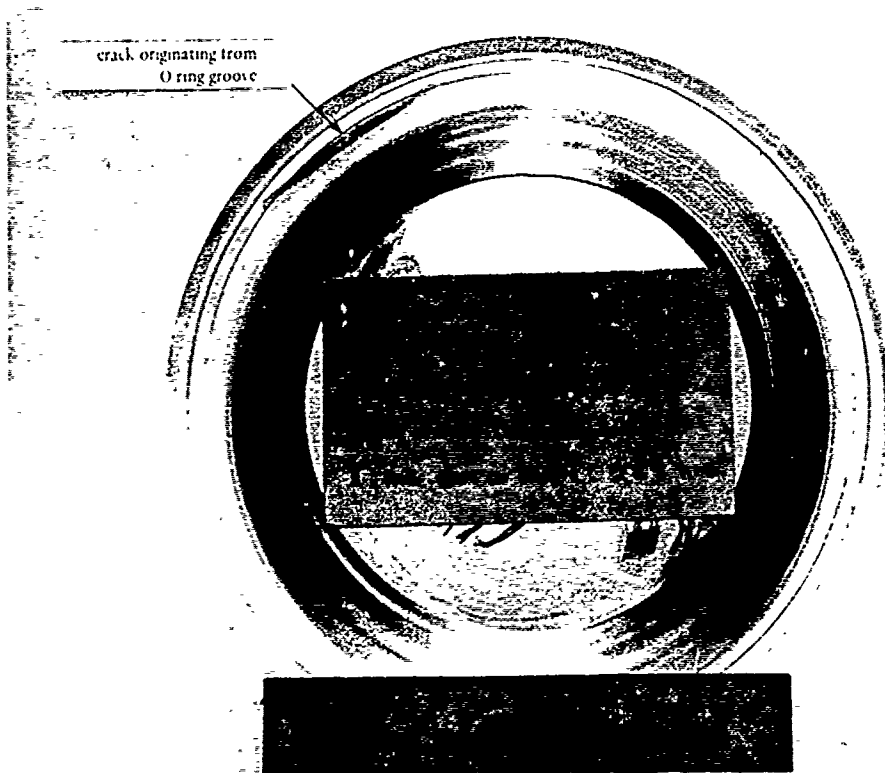


Figure 42. Typical cyclic fatigue cracks on the flange bearing surface; window I, Type I after 58 standard pressure cycles to 2,000 psi. Note that the crack originates at O-ring groove.

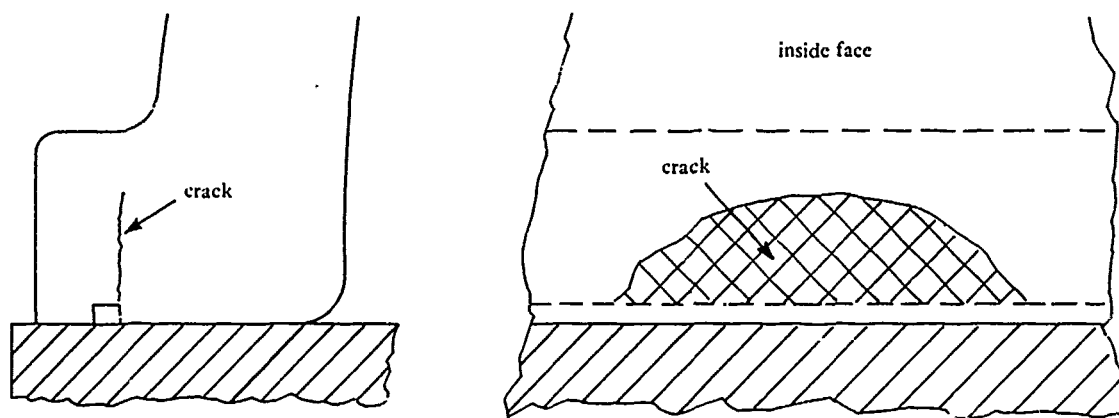


Figure 43. Cracks found in windows AA and I.

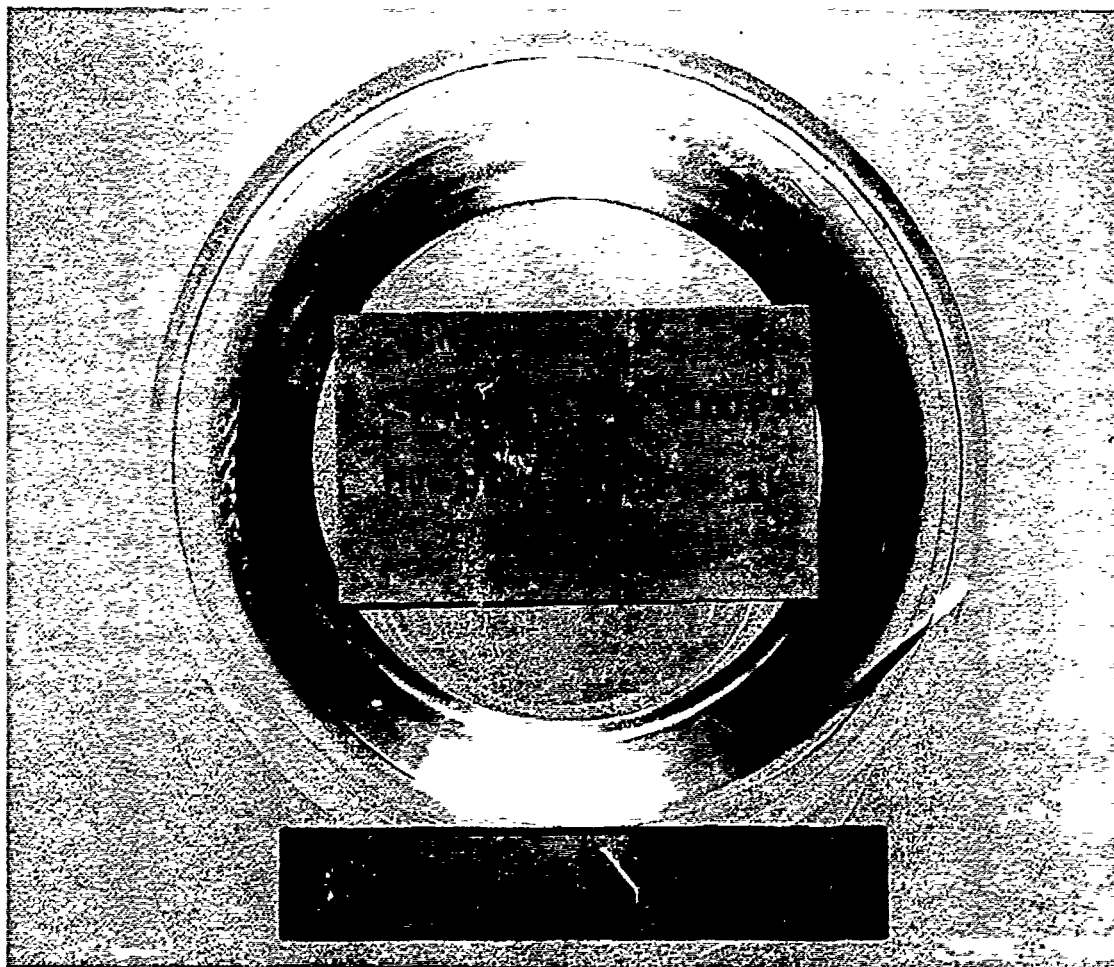


Figure 44. Typical cyclic fatigue cracks on the flange bearing surface; window K, Type I after one standard pressure cycle to 8,000 psi. Note major circumferential crack between the heel of the flange and the O-ring groove.

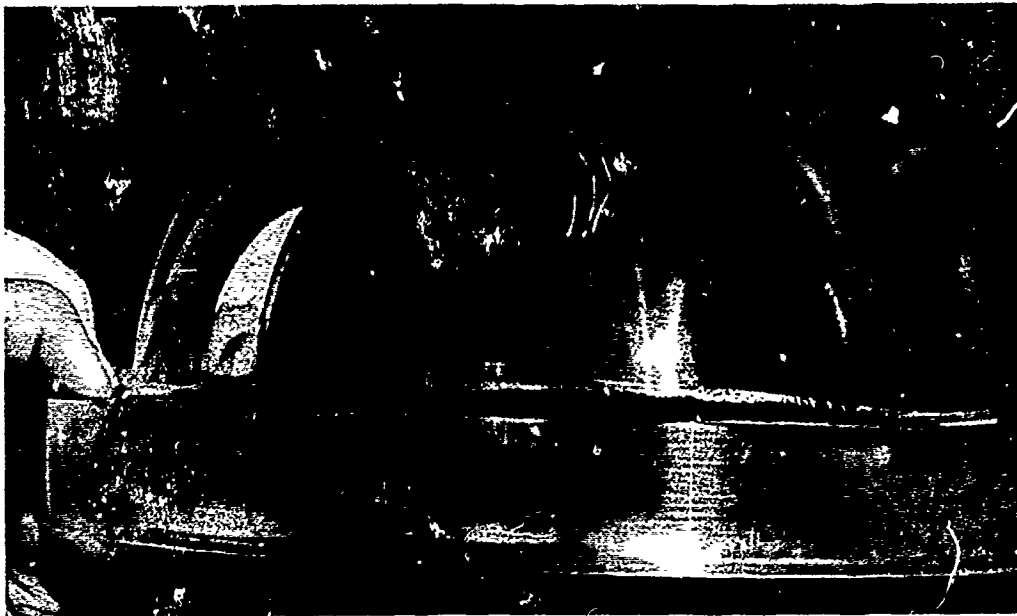


Figure 45. Same window as in Figure 44; note how the circumferential crack has penetrated the whole thickness of the flange.

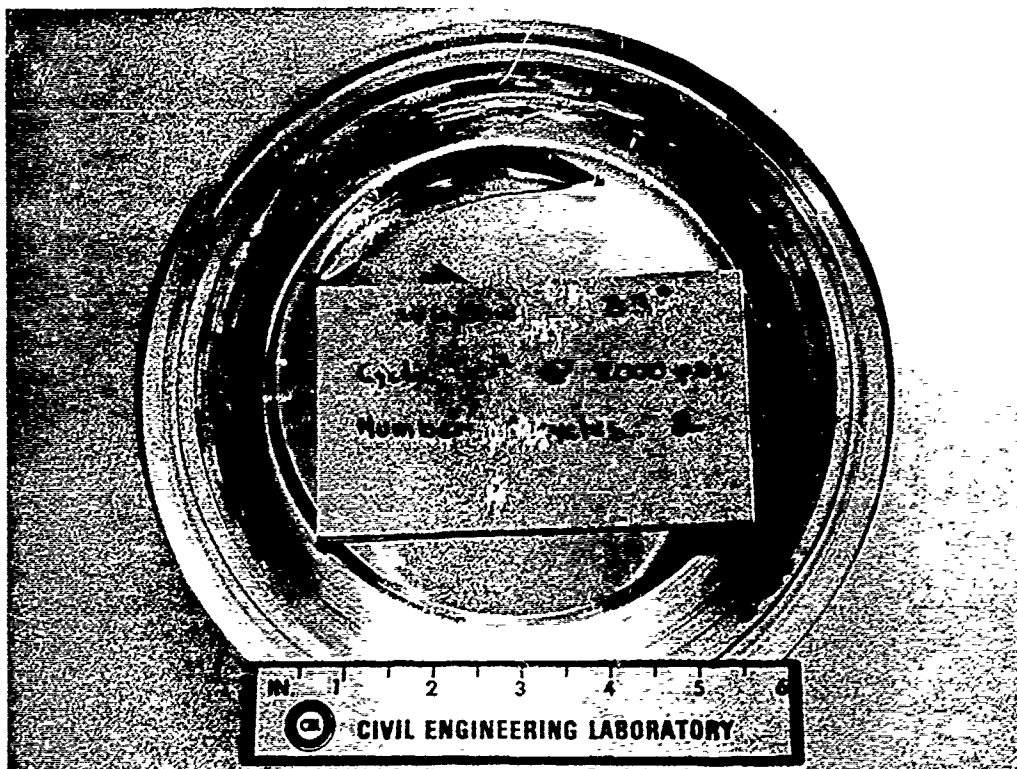


Figure 46. Typical cyclic fatigue cracks on the flange bearing surface; window BB, Type VI after two standard pressure cycles to 8,000 psi. Note many circumferential cracks between heel of the flange and O-ring groove.

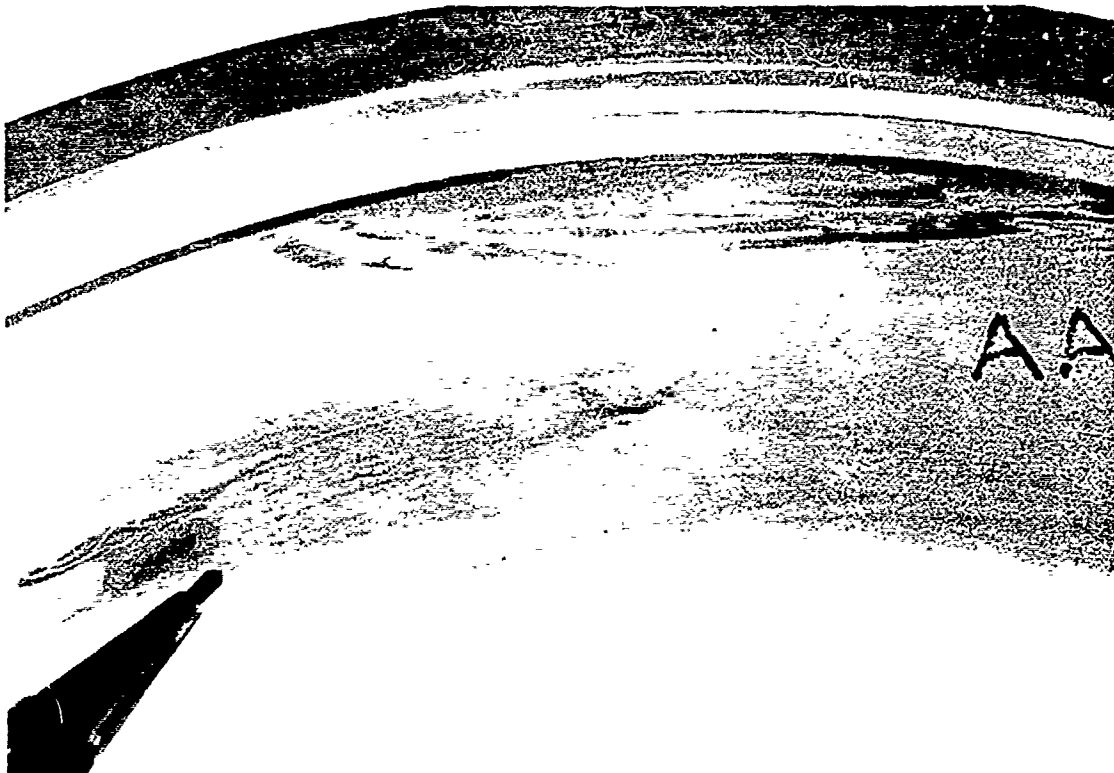


Figure 47. Same window as in Figures 39, 40, and 41; note that cyclic fatigue cracks on the flange bearing surface originating not at the O-ring groove have a characteristic mushroom shape.

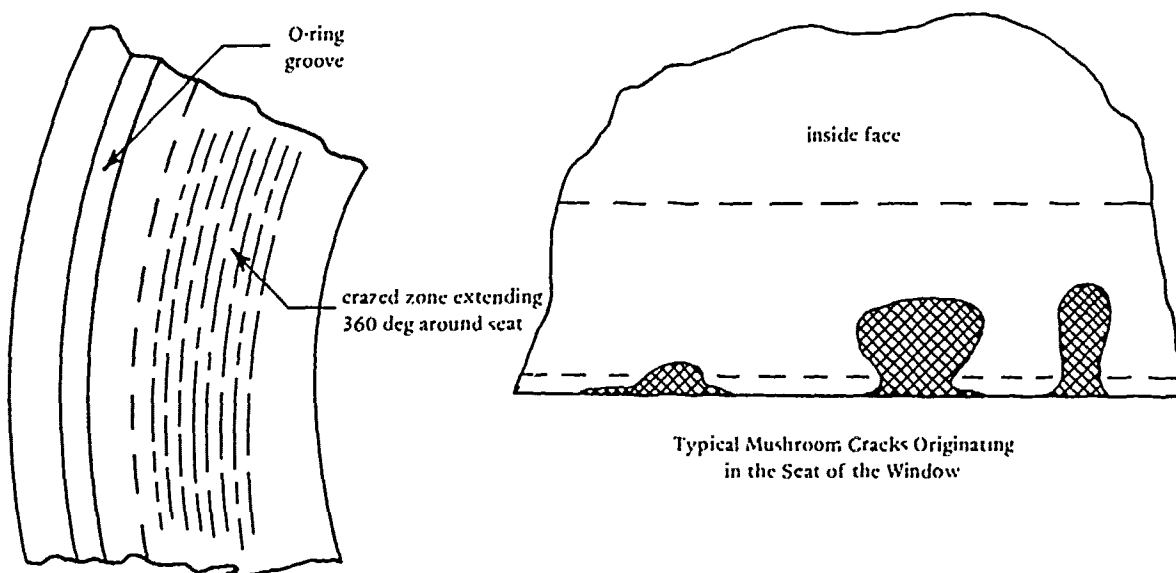


Figure 48. Two characteristic forms of window fracturing.





Figure 49. Typical cyclic fatigue meridional cracks on the interior face of window M, Type I window after 22 standard pressure cycles to 6,000 psi; note that the meridional cracks do not penetrate through the whole thickness of the window or flange.



Figure 50. Same window as in Figure 49; note the presence of extensive crazing and small circumferential cracks on the bearing surface of the flange that appeared prior to the meridional cracks.

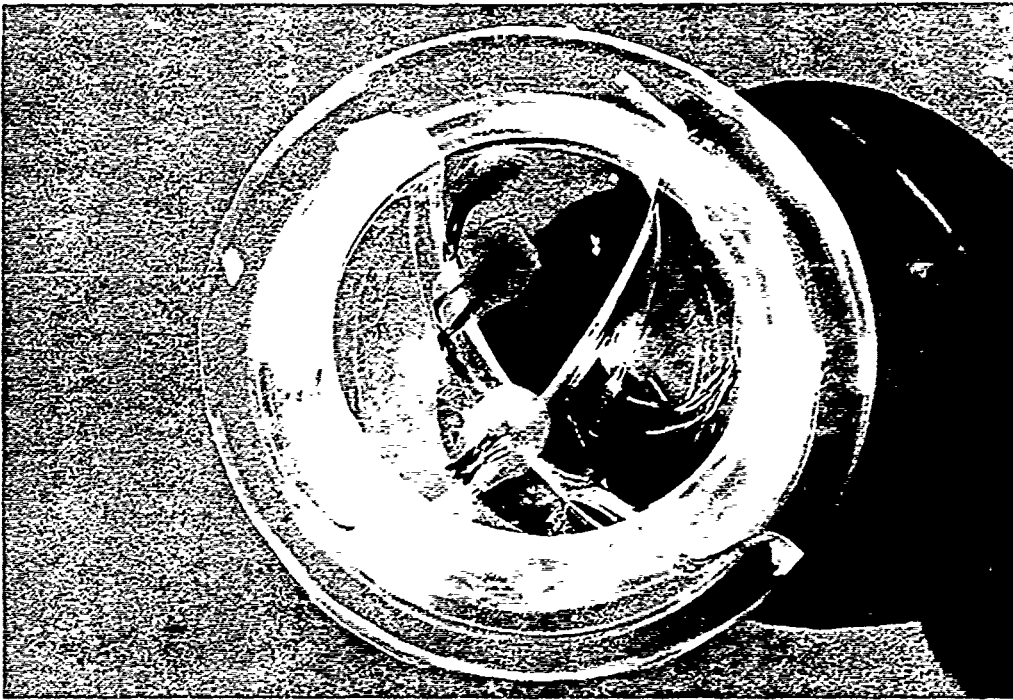


Figure 51. Typical cyclic fatigue meridional cracks on the interior face of window E, Type I (modified) after one standard pressure cycle to 8,000 psi; note that the cracks do not penetrate through the whole thickness of the window.



Figure 52. Same window as in Figure 51; note the wide crack between surfaces and that the width of the crack is widest on the interior face of the window indicating that the crack originated on the interior face and subsequently propagated outboard toward exterior face.

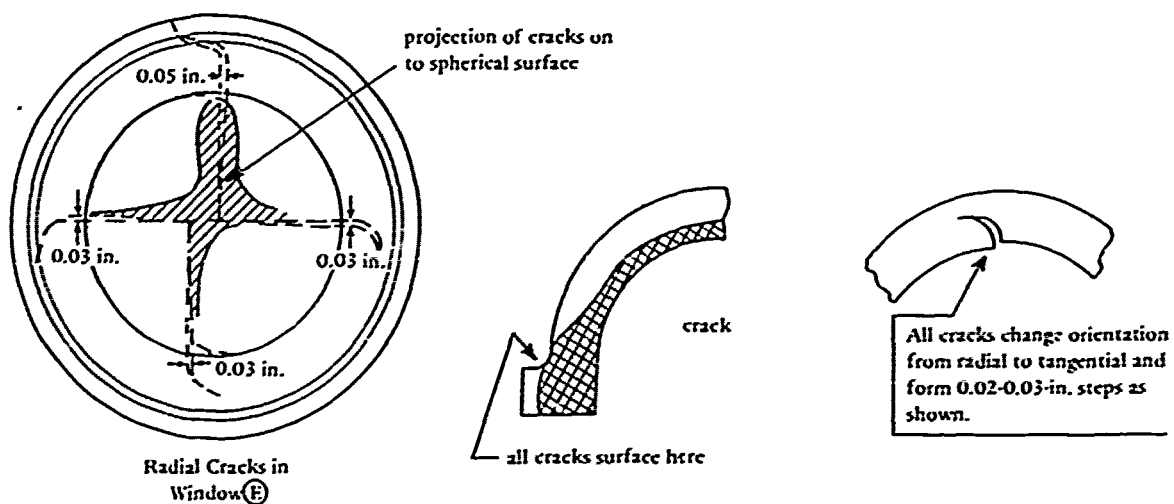


Figure 53. Cracking in Window E.

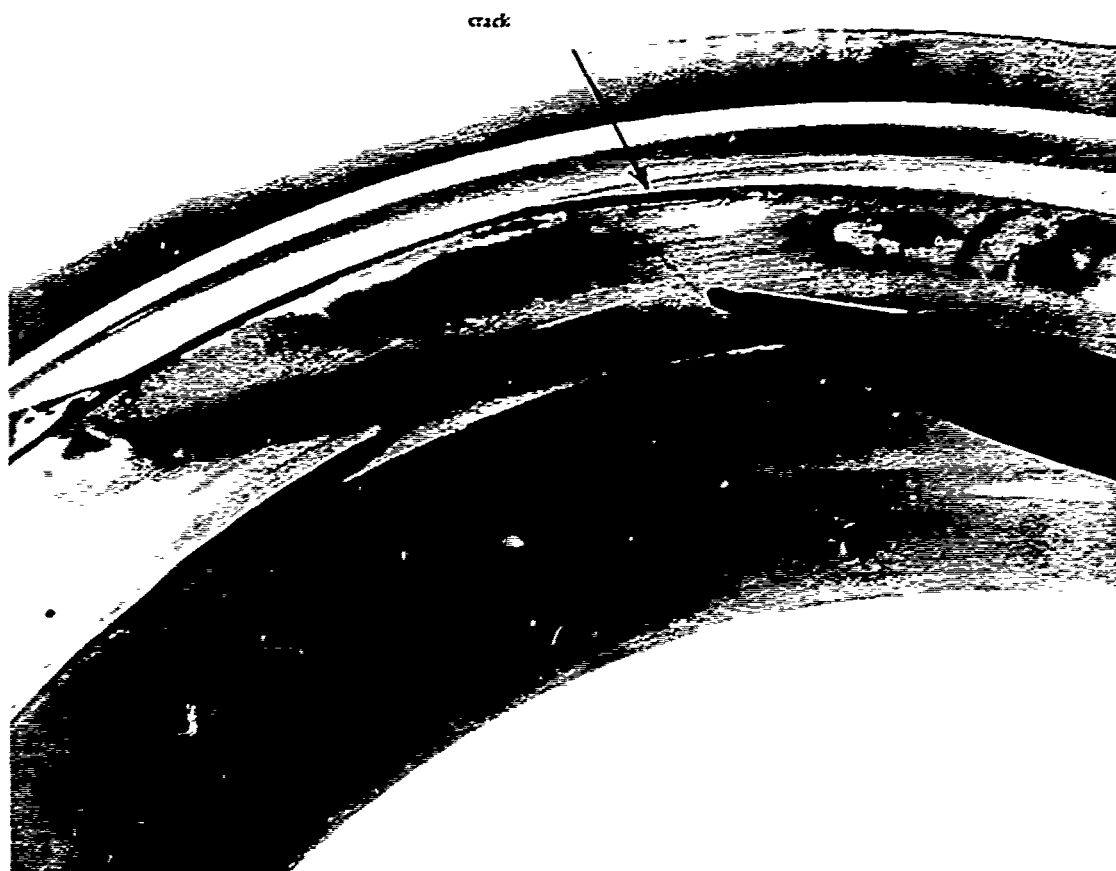


Figure 54. Typical cyclic fatigue circumferential cracks on the bearing surfaces of Type I flanges that cause the window to leak after a few pressure cycles; window K, Type I after one standard pressure cycle to 8,000 psi.

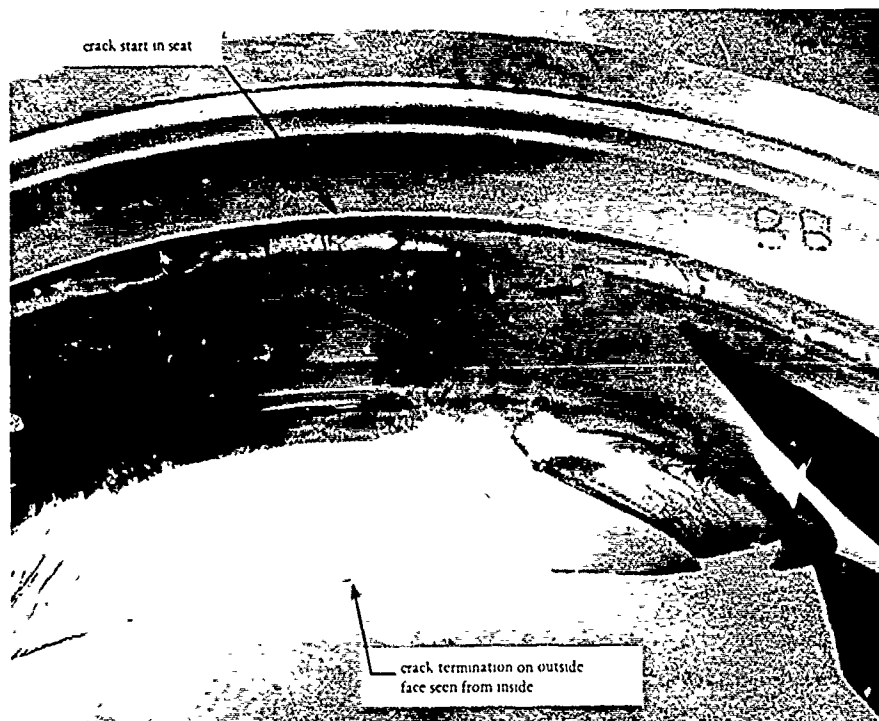


Figure 55. Typical cyclic fatigue circumferential cracks on the bearing surfaces of Type VI flanges that cause the window to leak after a few pressure cycles; window BB, Type VI after two standard pressure cycles to 8,000 psi.

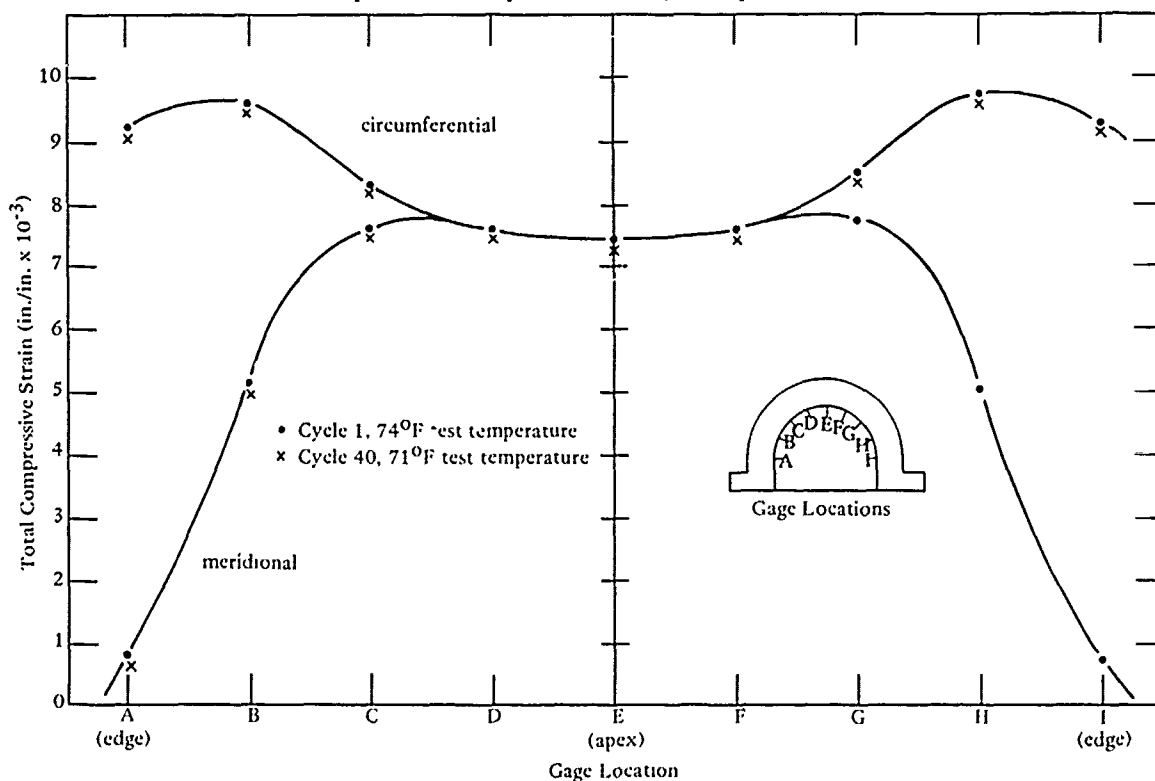


Figure 56. Distribution of compressive strains on the interior face of Type I windows at the end of 7-hour sustained pressure loading phase at 2,000 psi in a standard pressure cycle, window I.

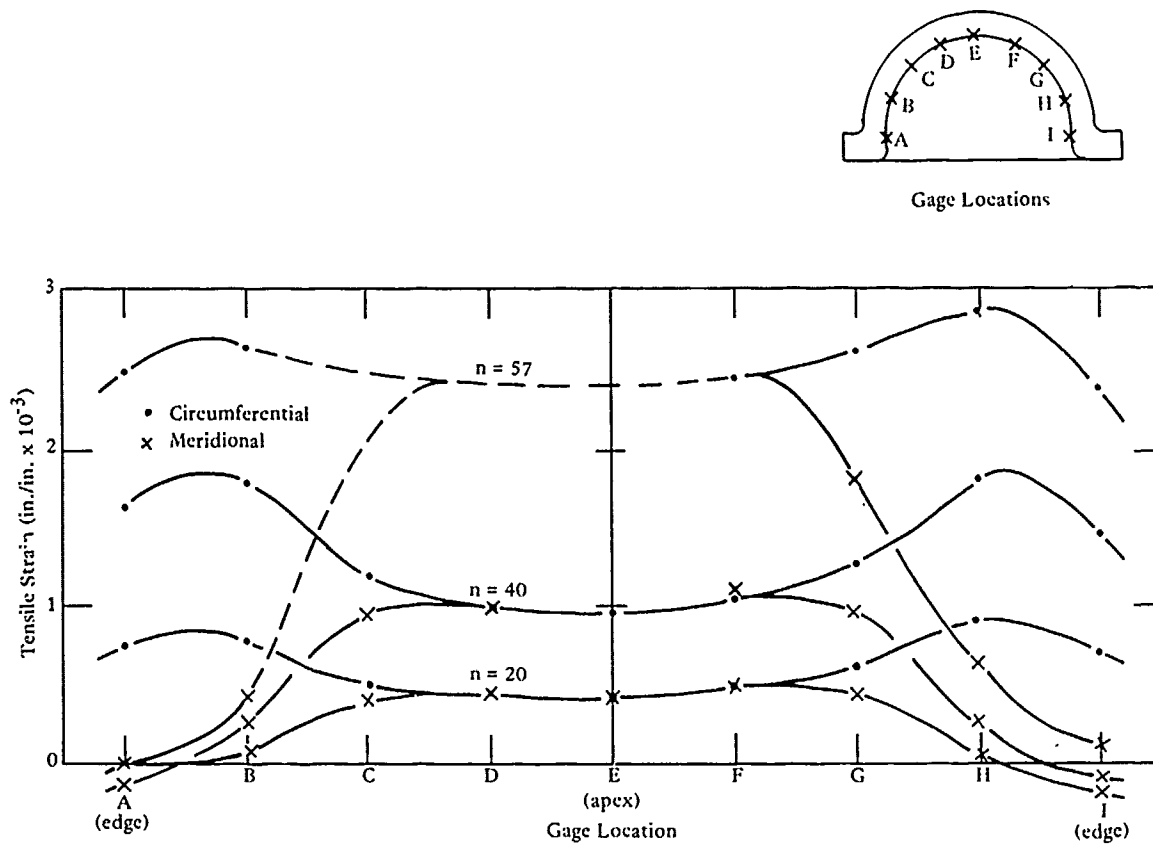


Figure 57. Distribution of residual tensile strains on the interior face of Type I window at the end of 17-hour-long relaxation phases at 0 psi in standard pressure cycles to 2,000 psi, window I. All residual strains are measured from the strain level prior to first pressure cycle; 70-75°F.

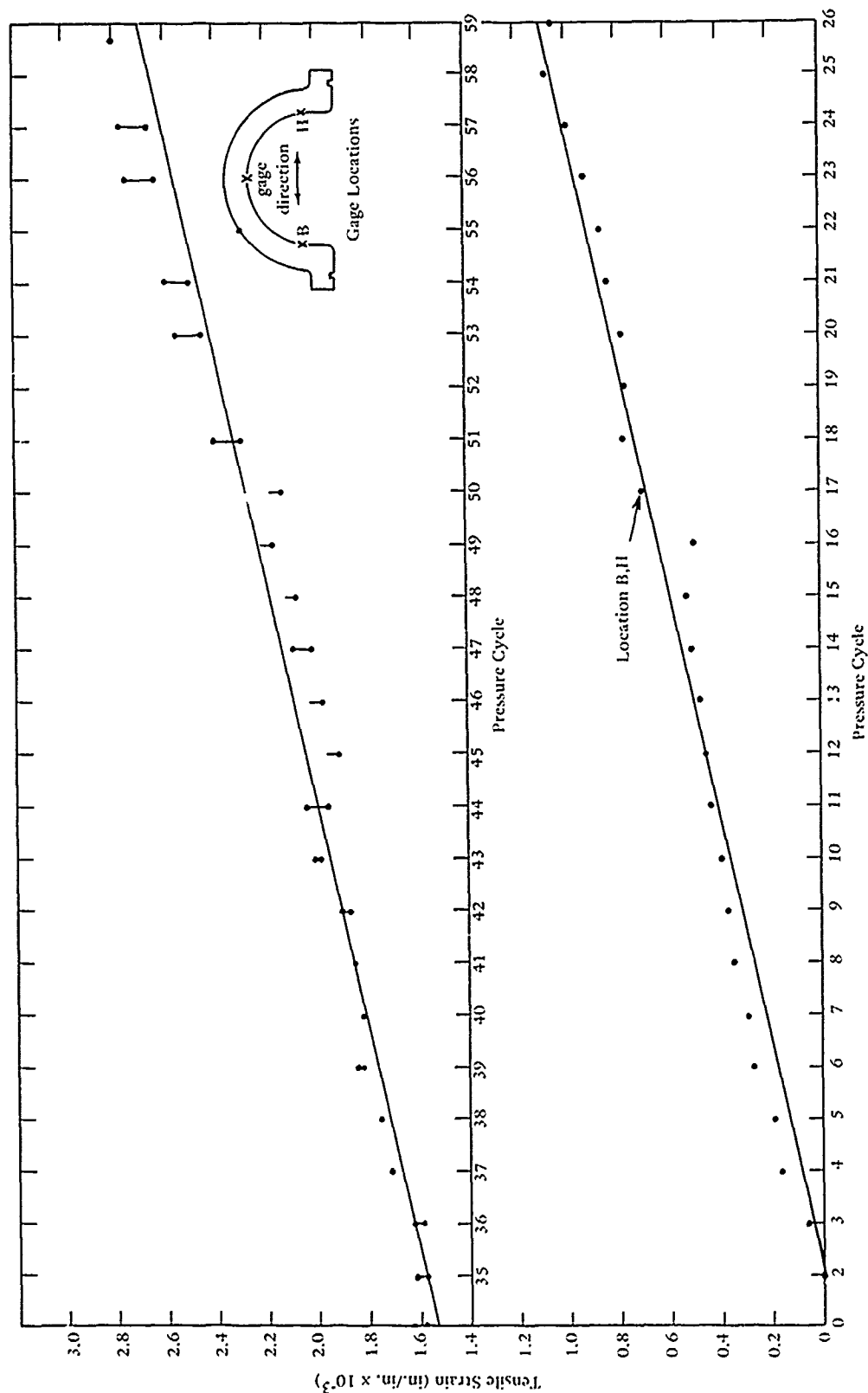


Figure 58. Rate of increase for residual tensile strains on the interior face of type I window at the end of 17-hour-long relaxation phases at 0 psi in standard pressure cycles to 2,000 psi, window I. All residual strains are measured from the strain datum prior to the first cycle.

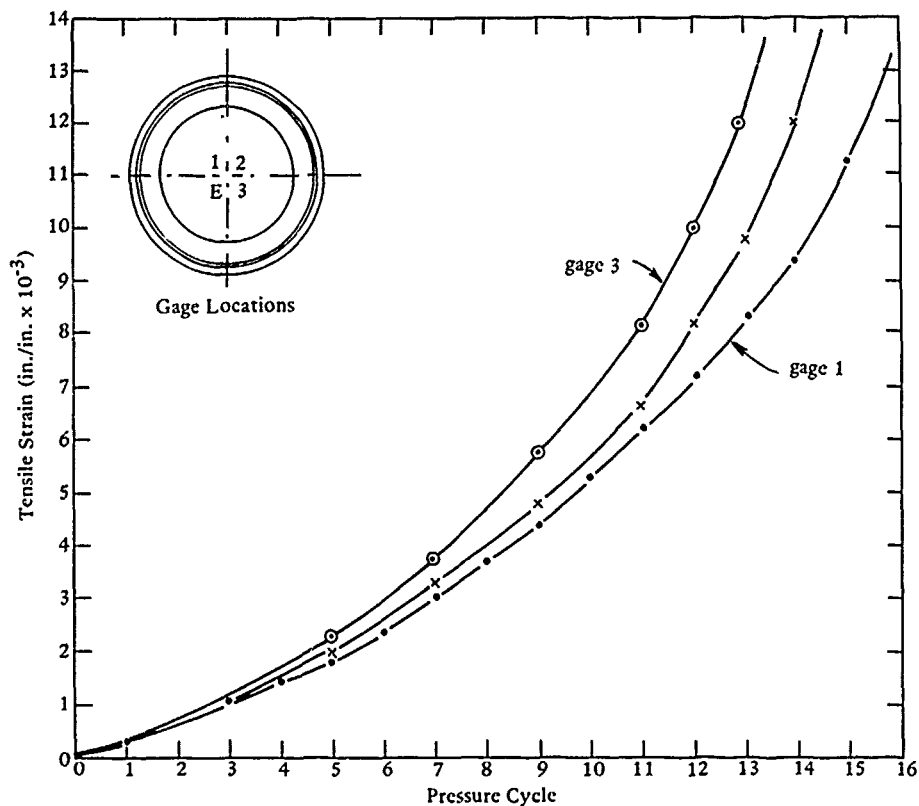


Figure 59. Rate of increase for residual tensile strains on interior face of Type VI window at the end of 17-hour-long relaxation phases at 0 psi in standard pressure cycles to 5,000 psi, window X. All residual strains are measured from the strain level prior to first pressure cycle; 68-73°F.

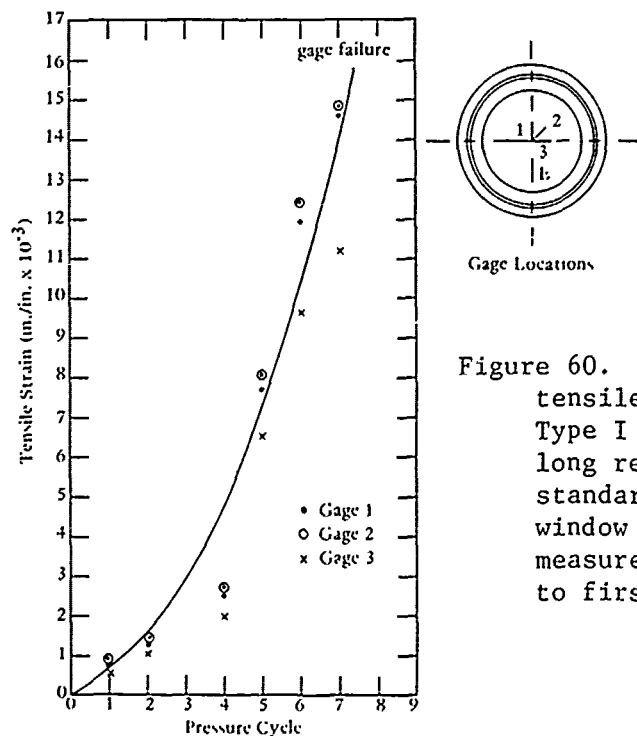


Figure 60. Rate of increase for residual tensile strains on interior face of Type I window at the end of 17-hour-long relaxation phases at 0 psi in standard pressure cycles to 6,000 psi, window M. All tensile strains are measured from the strain level prior to first pressure cycle.

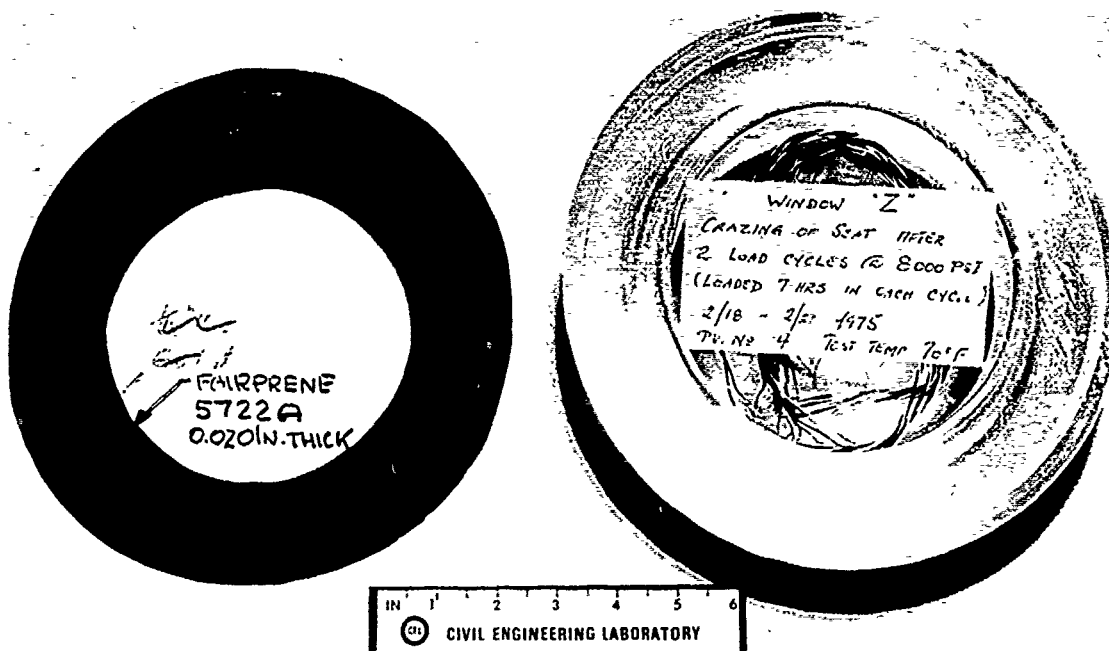


Figure 61. Window Z, Type VI after two standard pressure cycles to 8,000 psi on a neoprene-coated nylon cloth gasket; note the absence of major cracks, also compare to window BB, Type VI (Figures 46 and 55) that was tested under identical cyclic conditions but without a gasket.

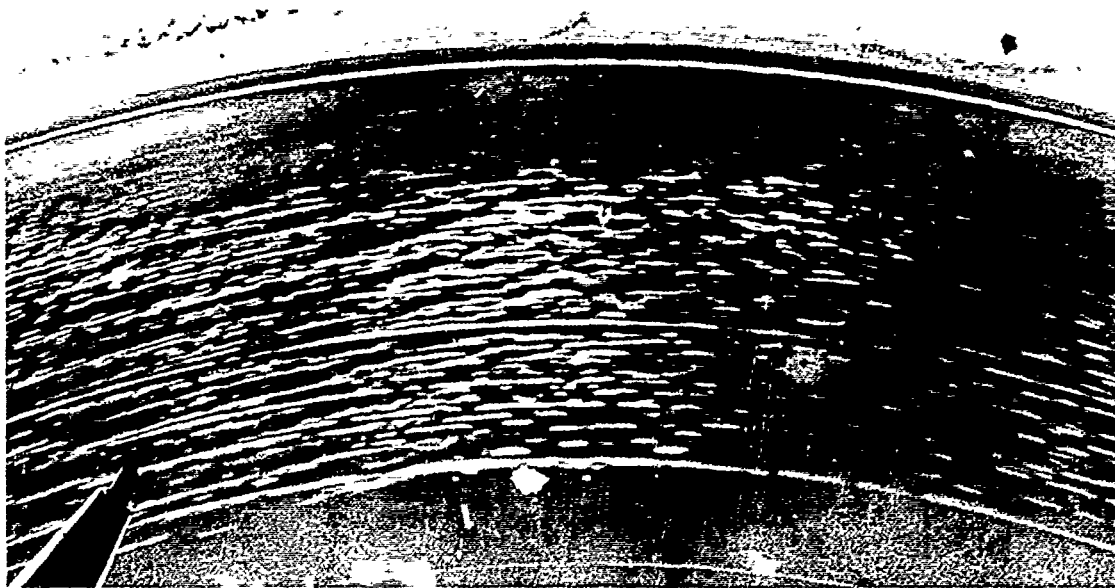


Figure 62. Same window as in Figure 61; note that only minor crazing is present on the bearing surface indicating the beneficial effect of the gasket.





Figure 63. Window Z, Type VI after two standard pressure cycles to 8,000 psi on a neoprene-coated nylon cloth gasket and 200 hours of relaxation at 0 pressure. Note the absence of crazing at the termination of second pressure cycle (Figure 62).

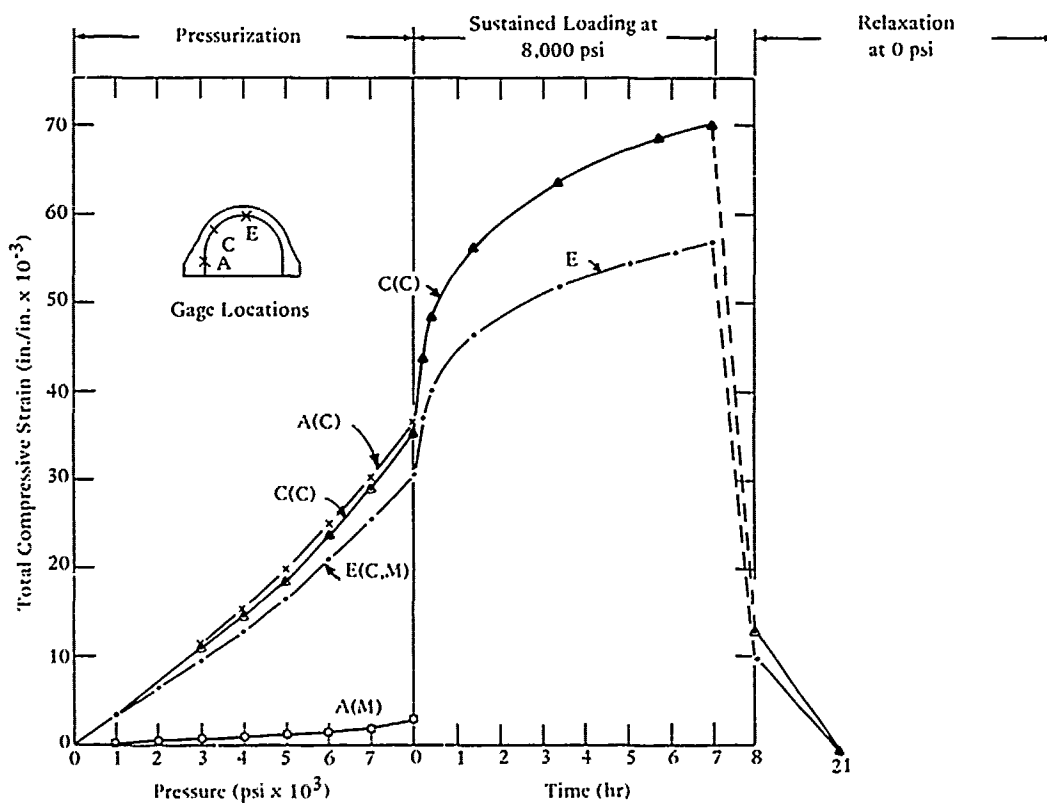


Figure 64. Distribution of strain in window Z, Type VI when pressure cycled to 8,000 psi on a neoprene-coated nylon cloth gasket.

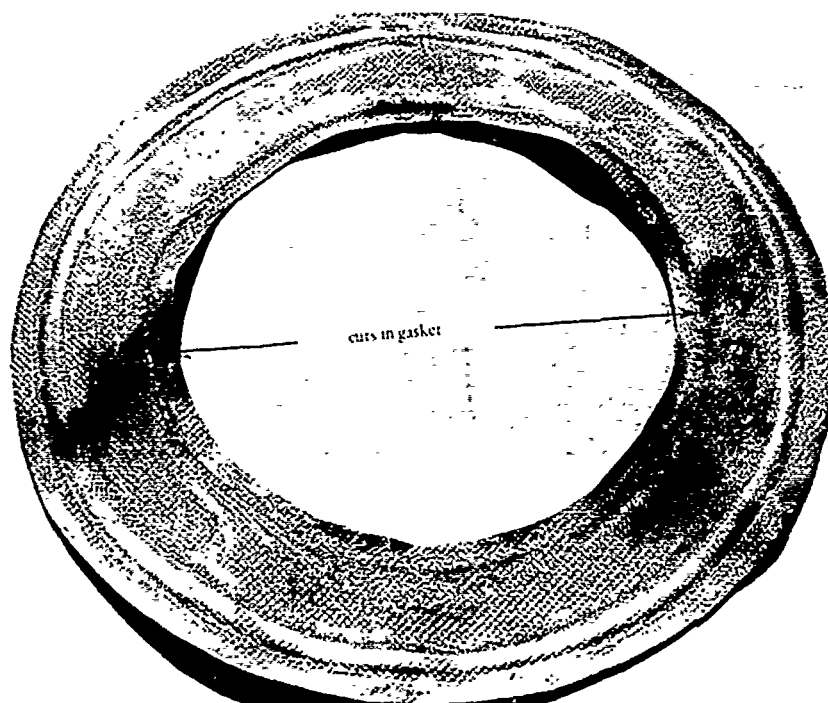


Figure 65. Cuts in neoprene-coated nylon cloth gasket by window Z, Type VI, subjected to two standard pressure cycles at 8,000 psi.

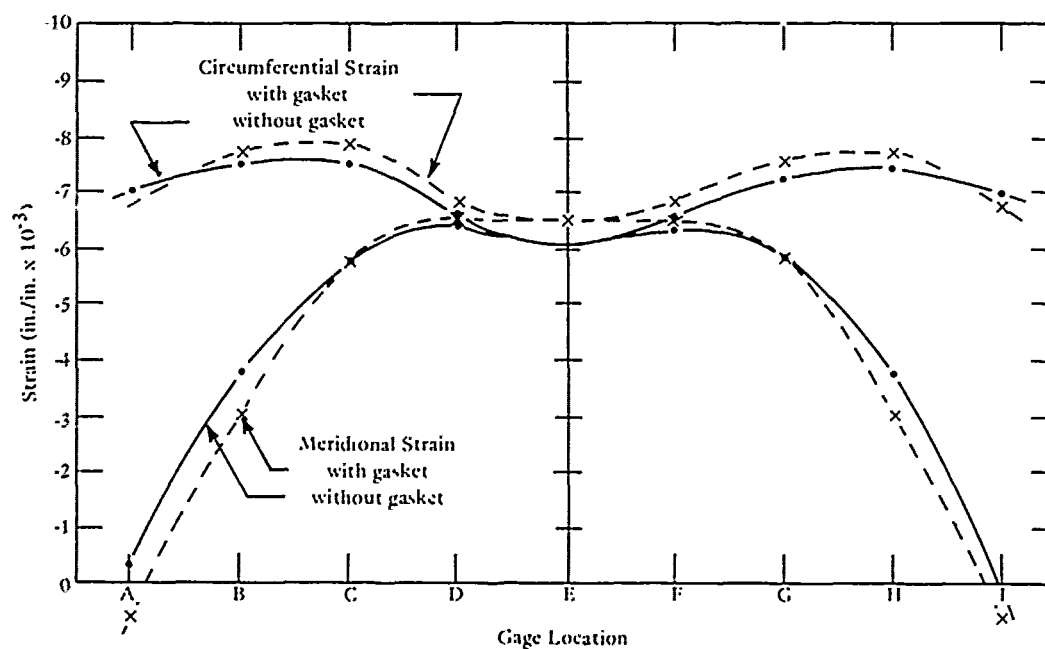


Figure 66. Comparison of short-term strain distributions for the same window Y, Type VI pressurized to 2,000 psi with and without a neoprene-coated nylon cloth bearing gasket.

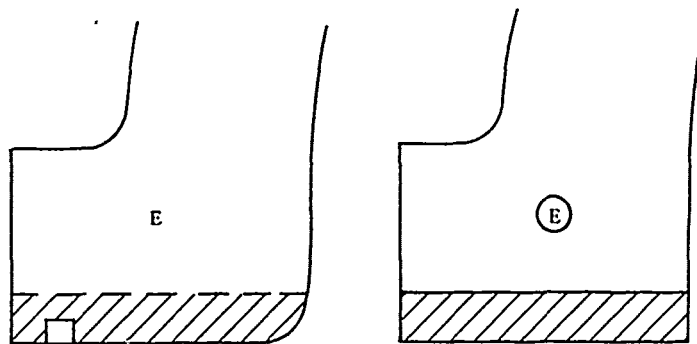


Figure 67. Shaded area machined off and replaced with a bonded-in-place acrylic disc.

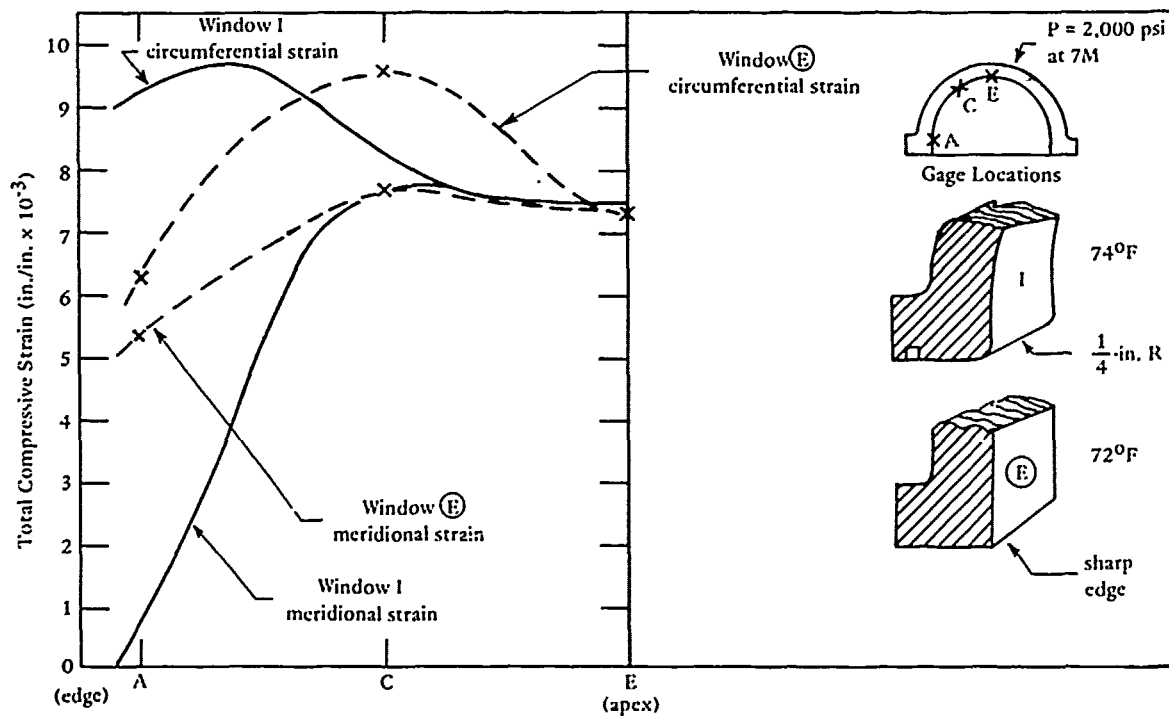


Figure 68. Comparison of strains in Type I windows with rounded and sharp heels after 7 hours of sustained pressurization to 2,000 psi; windows I and E, respectively.

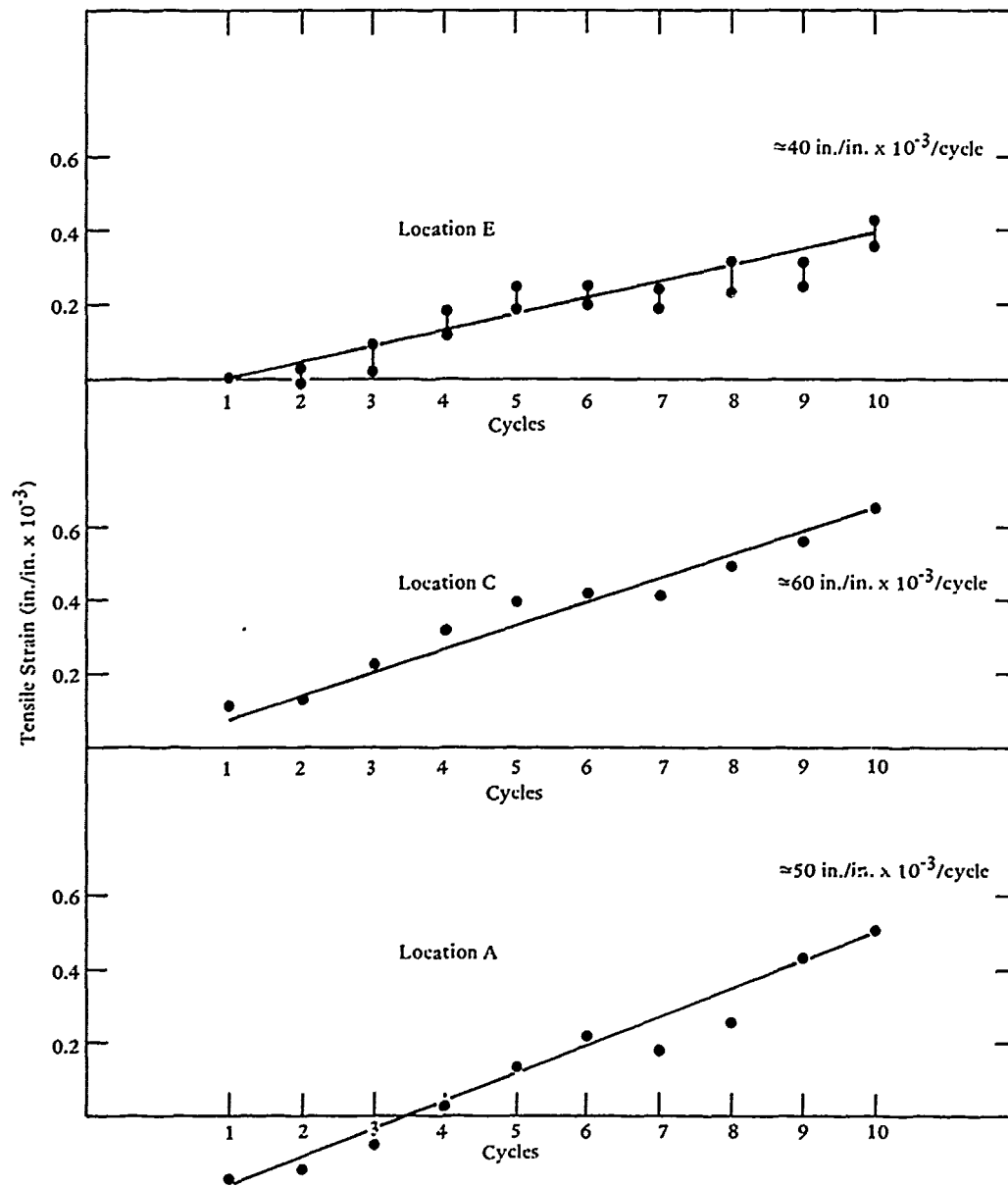
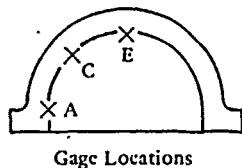


Figure 69. Rate of increase for residual tensile circumferential strains on the interior face of window (E), Type I with sharp heel at the end of 17-hour-long relaxation phases at 0 psi in standard pressure cycles to 2,000 psi.



Figure 70. Sharp edge on the heel of modified Type I, window (E) after one standard pressure cycle to 8,000 psi; note the absence of deformation.

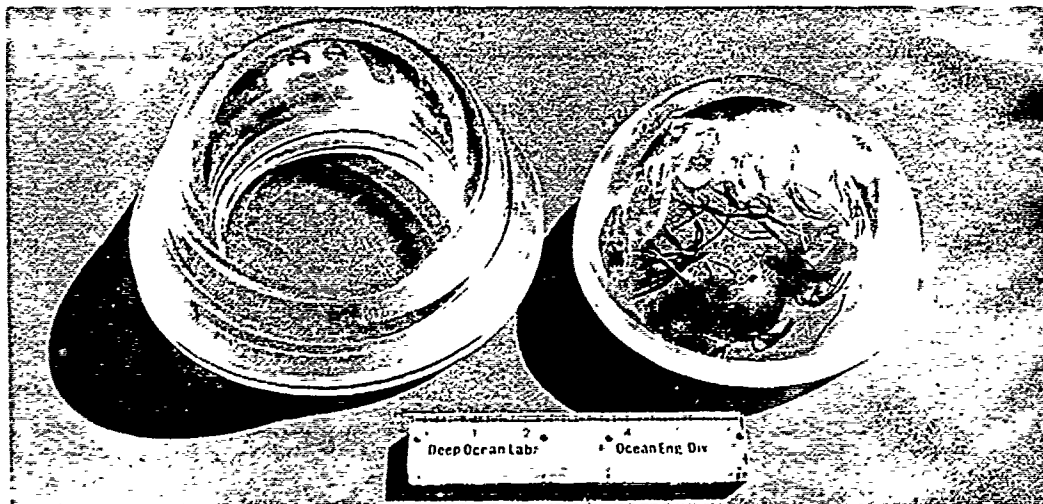


Figure 71. Type VI window prior to and after removal of flange by machining.

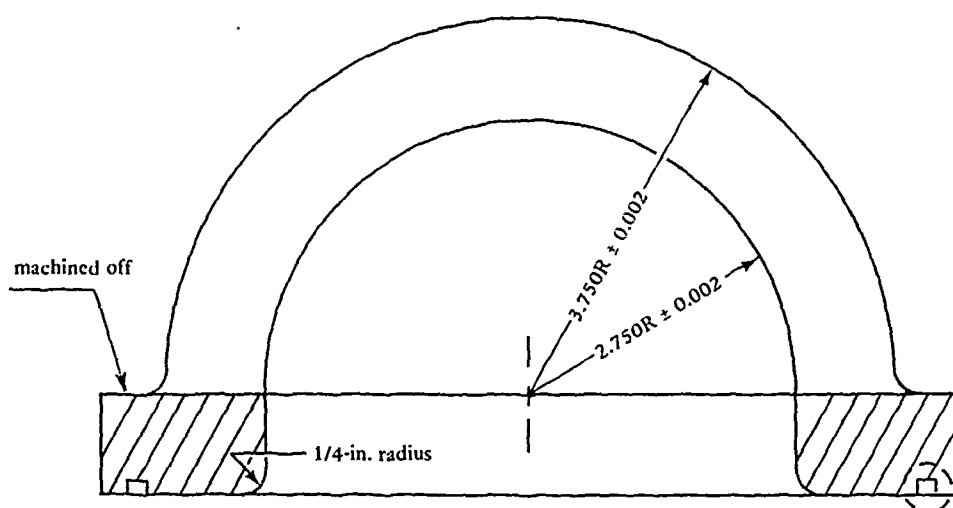


Figure 72. Machining of window I to remove flange.

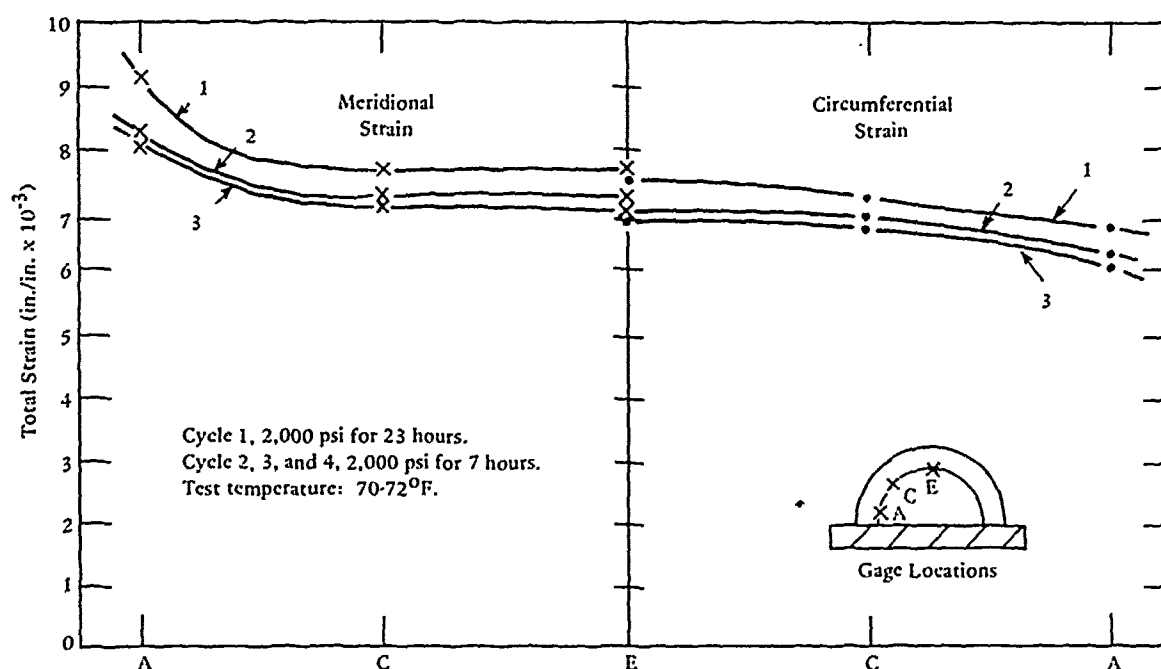


Figure 73. Distribution of strains on the interior face of flangeless hemispherical window I during sustained loading phases of pressure cycling to 2,000 psi; note that the strains on the interior face between the edge and apex are more uniform than in Type I and Type VI windows (Figures 56 and 66).



Figure 74. Flangeless window I after two standard pressure cycles to 8,000 psi without a bearing gasket.



Figure 75. Same window as in Figure 74; note absence of cracks and only very minor crazing on the bearing surface.

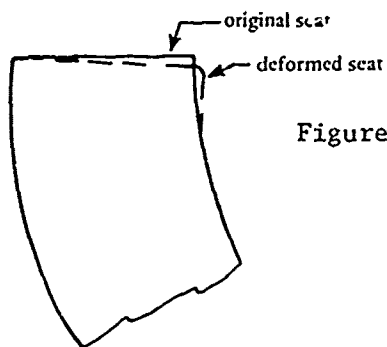


Figure 76. Seat deformation in window I after testing to 8,000 psi.

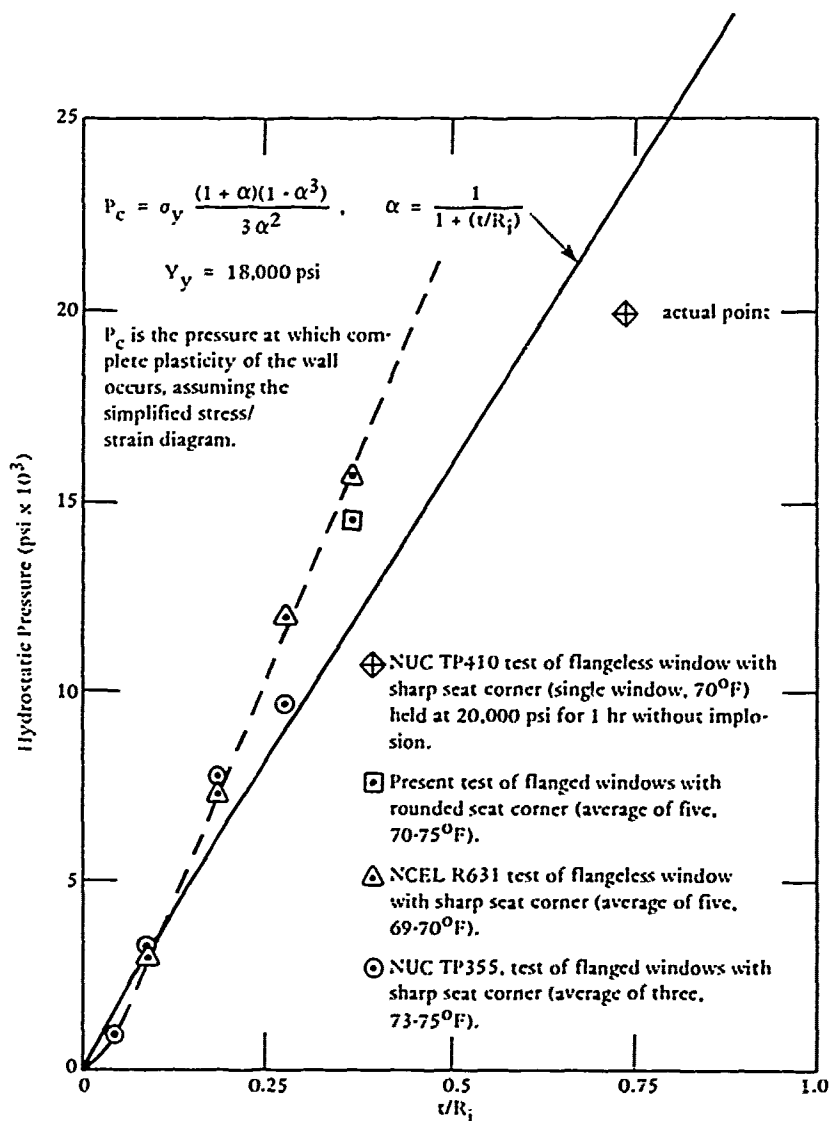


Figure 77. Comparison of actual and calculated critical pressures for hemispherical windows under short-term hydrostatic loading.



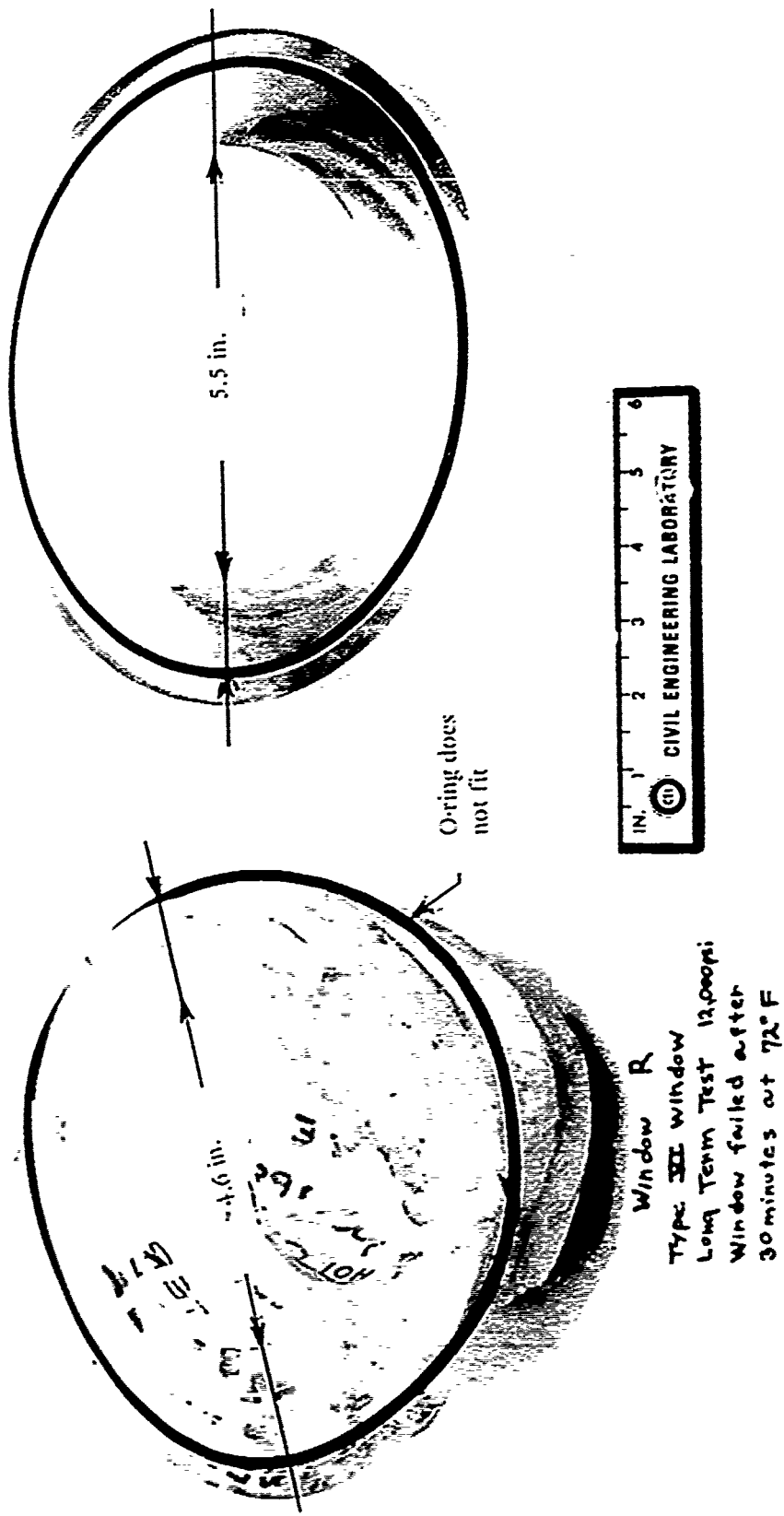


Figure 78. Plastic flow of acrylic plastic resulting in significant diameter deformation of windows prior to implosion under long-term pressure loading.

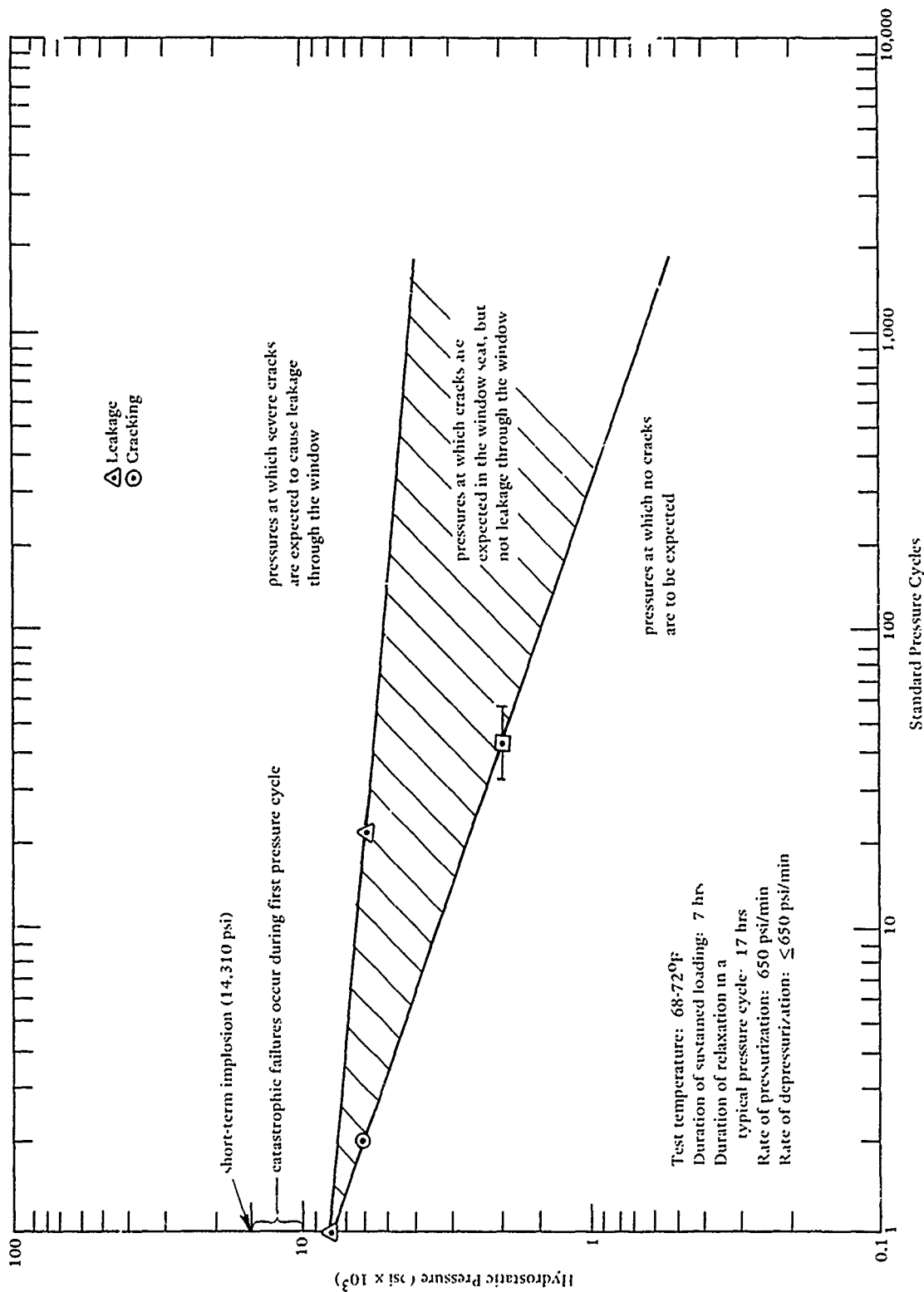


Figure 79. Cyclic fatigue life of hemispherical windows with Type C flanges without bearing gaskets when subjected to standard pressure cycles in room temperature range.

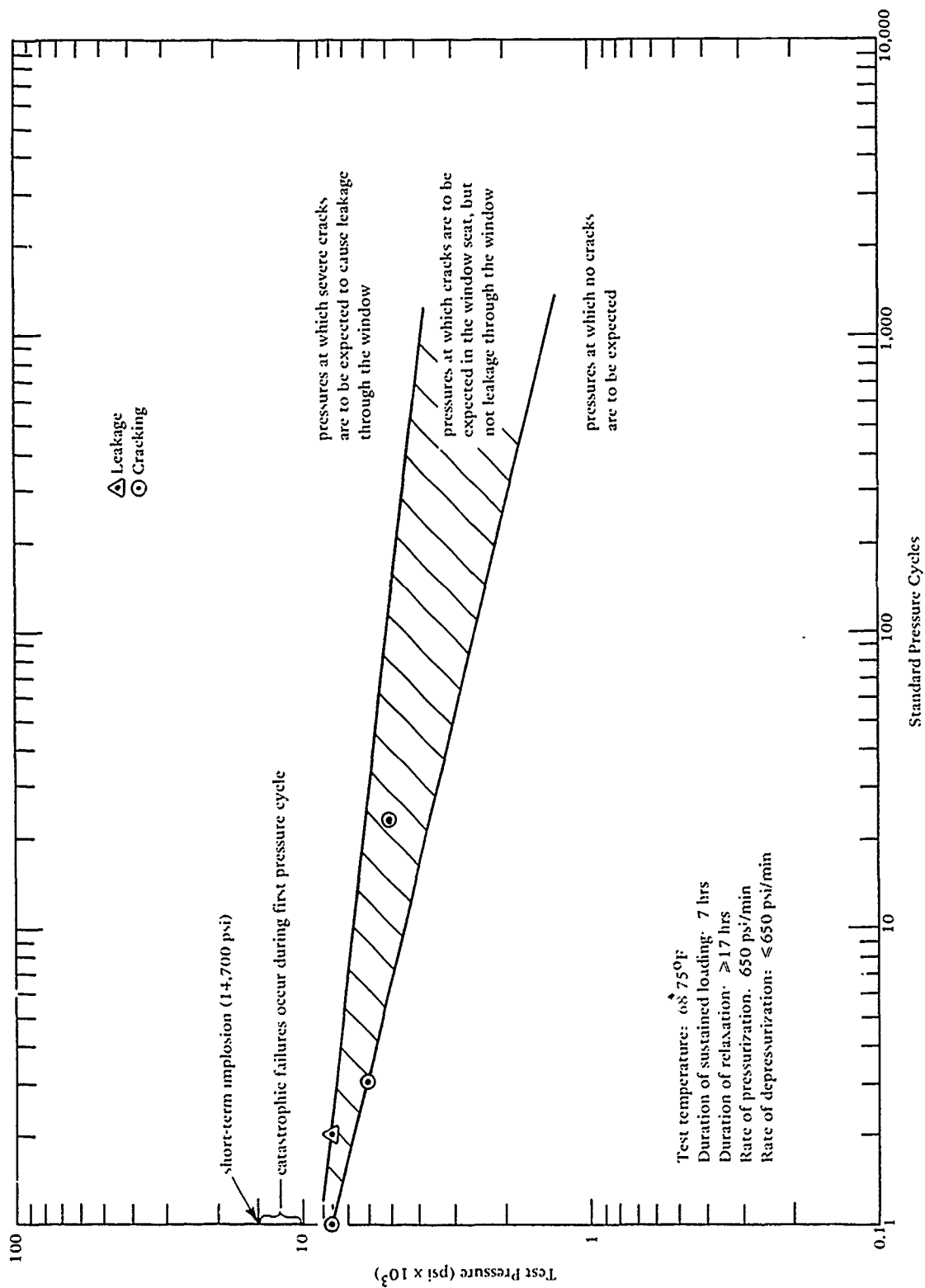


Figure 80. Cyclic fatigue life of hemispherical windows with Type VI flanges without bearing gasket when subjected to standard pressure cycles in room temperature range.

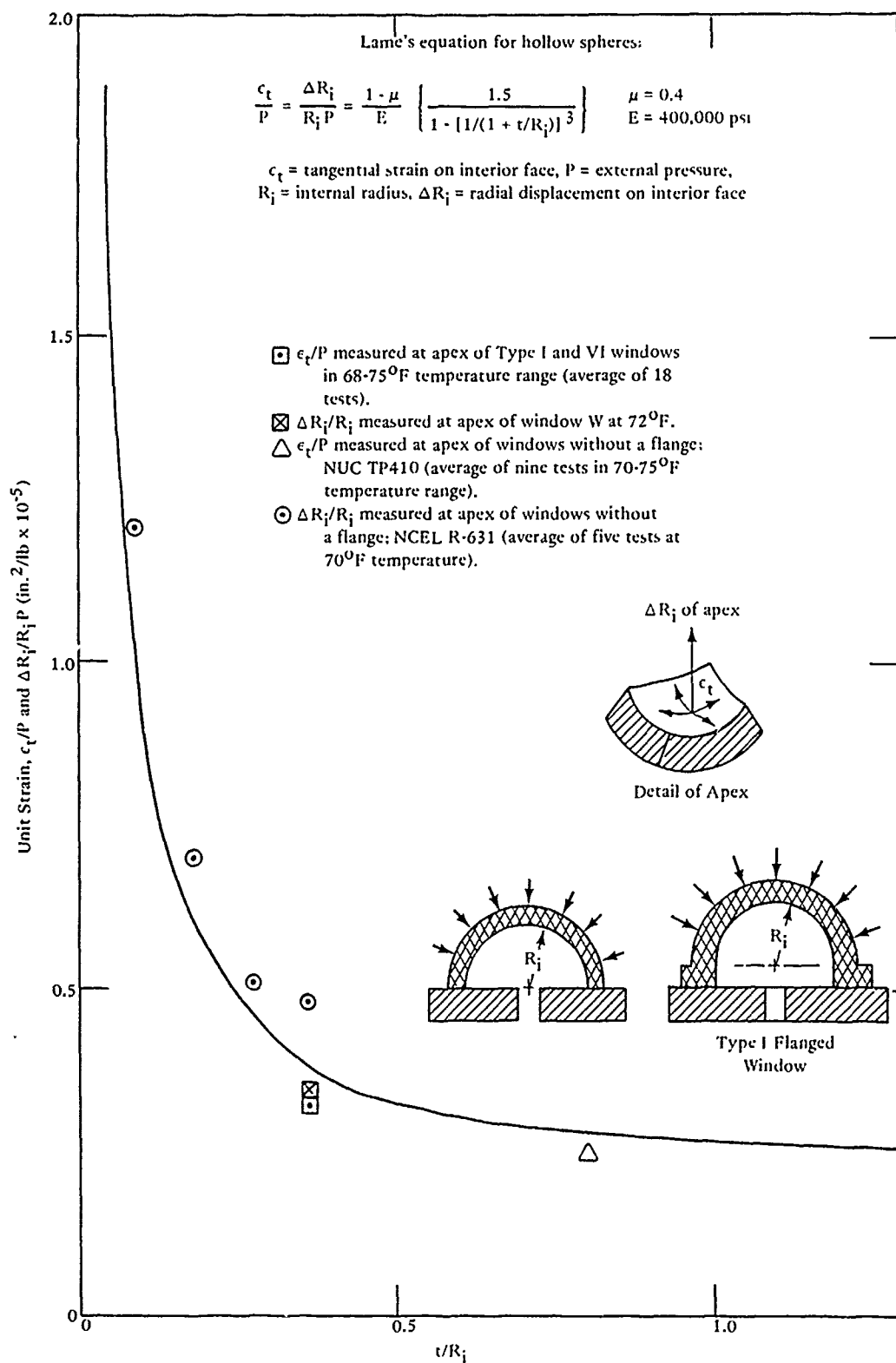


Figure 81. Comparison of measured and calculated strains in linear range of the apex of hemispherical windows with different  $t/R_i$  ratios when subjected to short-term external hydrostatic loading.

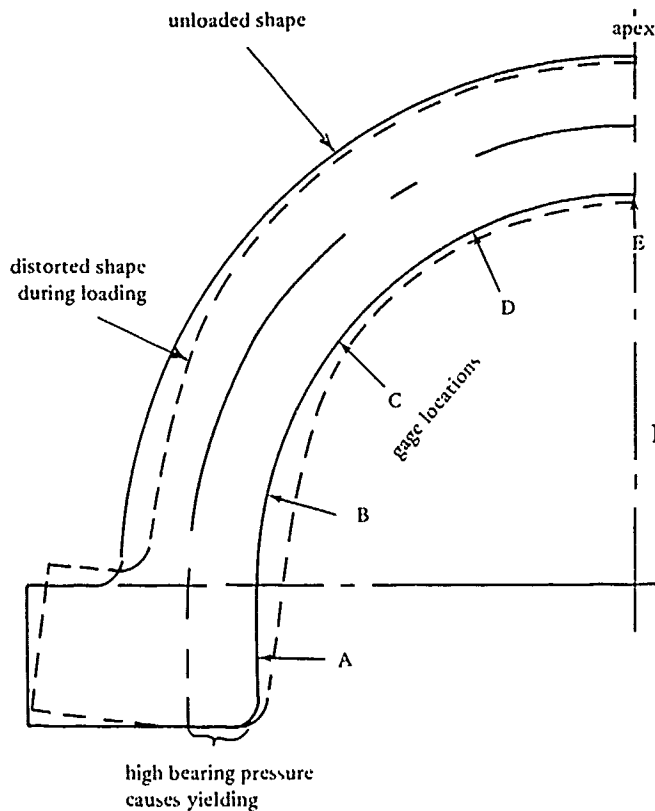


Figure 82. Reconstruction of type I window deformation in the elastic range when subjected to external short-term hydrostatic loading.

(C) = Circumferential strain  
(M) = Meridional strain

After 7 hrs at 2,000 psi  
at 72-74°F.

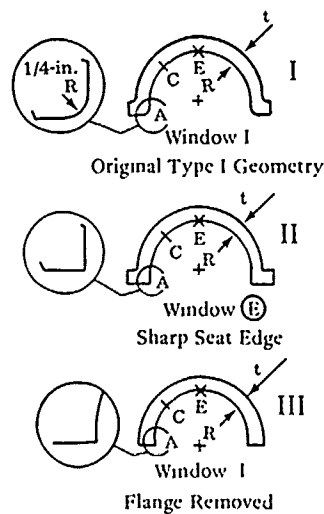
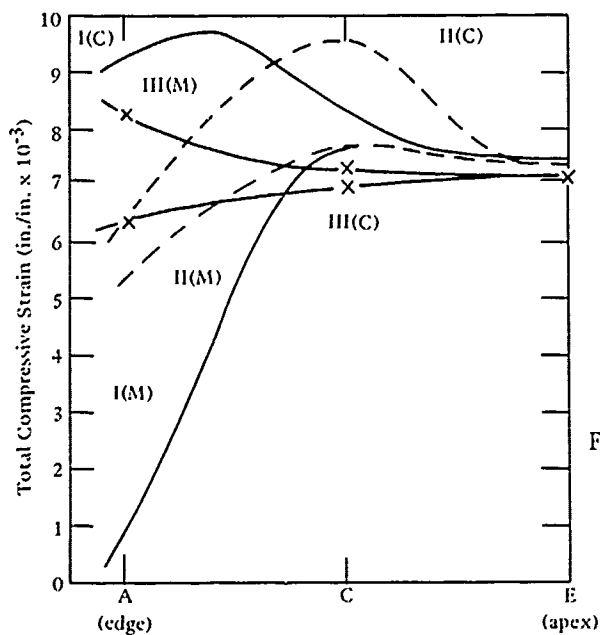


Figure 83. Comparison of measured strains for windows with different equatorial flange arrangements.

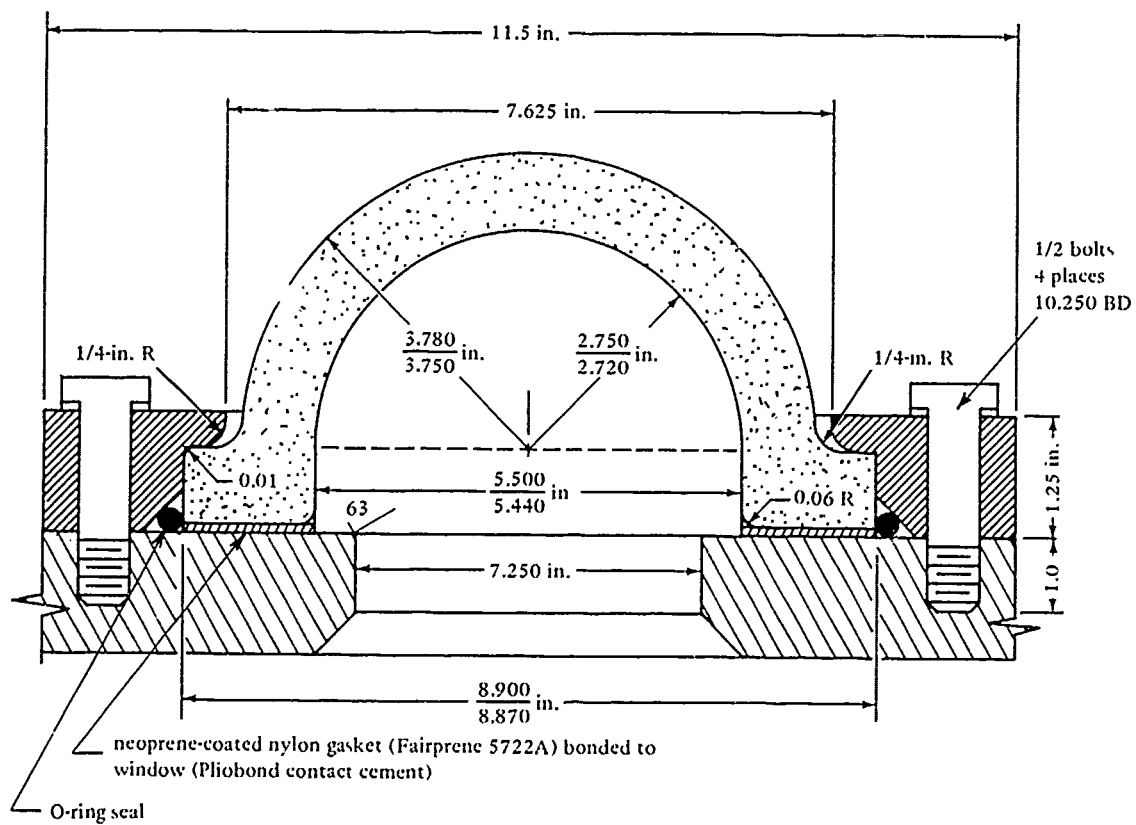


Figure 84. Recommended seat and seal design for modified Type I (Type II) windows.

## Appendix

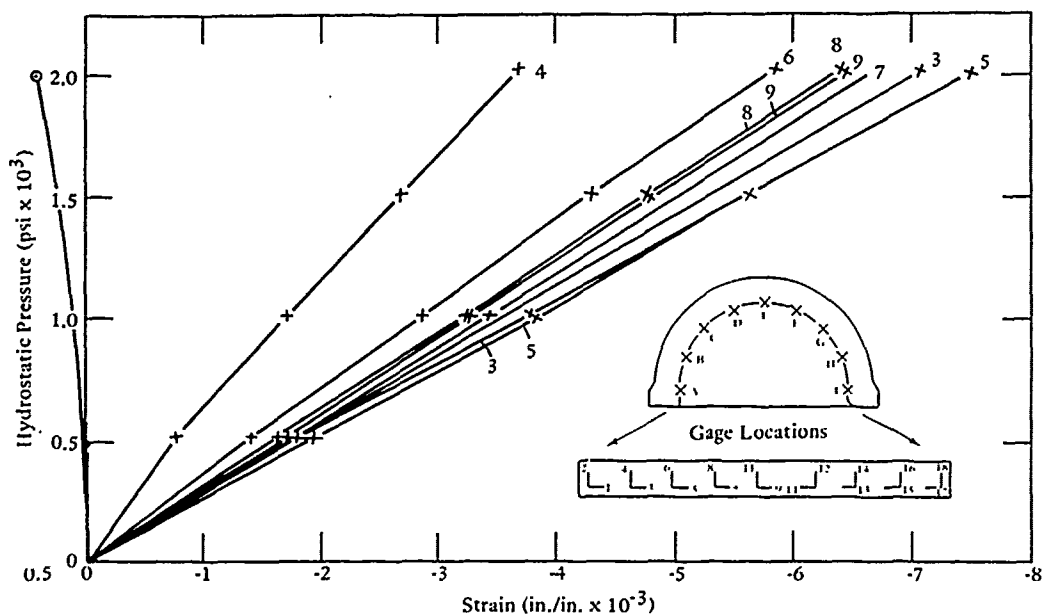
### DETAILED DATA

Although the body of the report presents summaries of strain distributions in Type I and Type VI windows under different kinds of hydrostatic loadings, there often is a need for detailed knowledge of strains at each strain gage location. To satisfy this requirement, detailed plots of strains are shown for representative windows of Type I and Type VI.

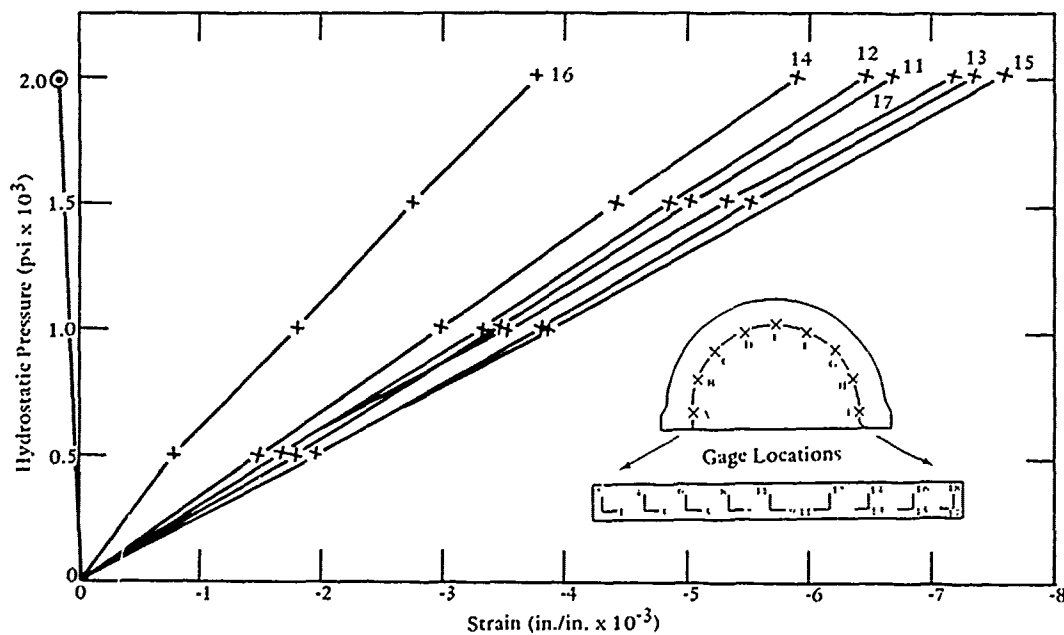
Figures 85 and 86 afford a direct comparison between strains on the same window subjected to short-term loading with and without a neoprene bearing gasket. Figures 87 and 88 allow a comparison, on the other hand, between strains on Type I and Type VI windows under short-term loading.

Figures 89 and 90 permit a comparison of creep strains on Type I and Type VI windows under the same sustained loading condition, that is, 10,000 psi. The effect of sustained loading magnitude on the rate of creep and subsequent relaxation in Type VI window can be observed by comparing Figures 91, 92, 93, and 94.

Figure 95 presents graphically the strain history of the concave surface at the apex for a Type VI window during sustained loading at 4,000 psi and subsequent relaxation.



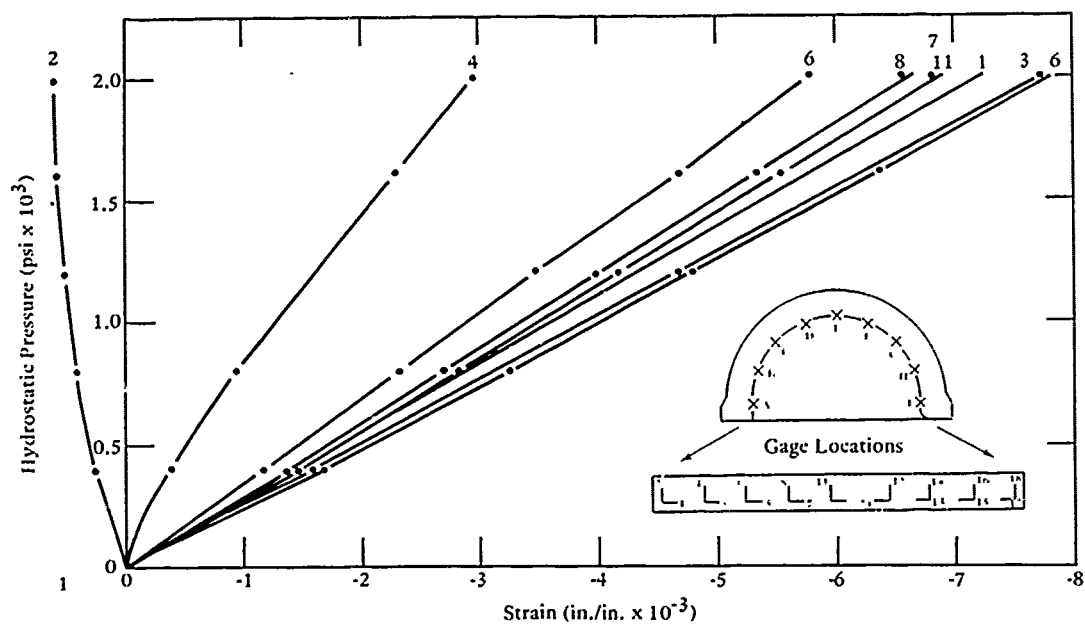
(a) For gages 1 through 9.



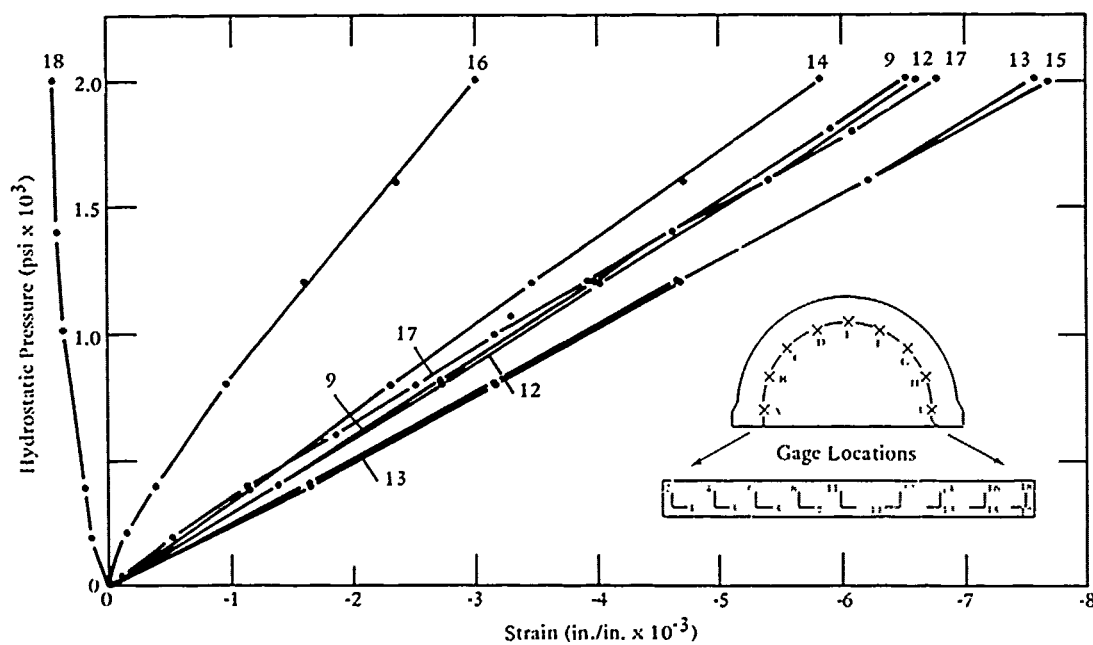
(b) For gages 11 through 18.

Figure 85. Window Y, Type VI under short-term loading without a neoprene bearing gasket.





(a) For gages 1 through 8 and gage 11.



(b) For gage 9 and gages 12 through 18.

Figure 86. Window Y, Type VI under short-term loading when resting on a 5722A Fairprene bearing gasket.

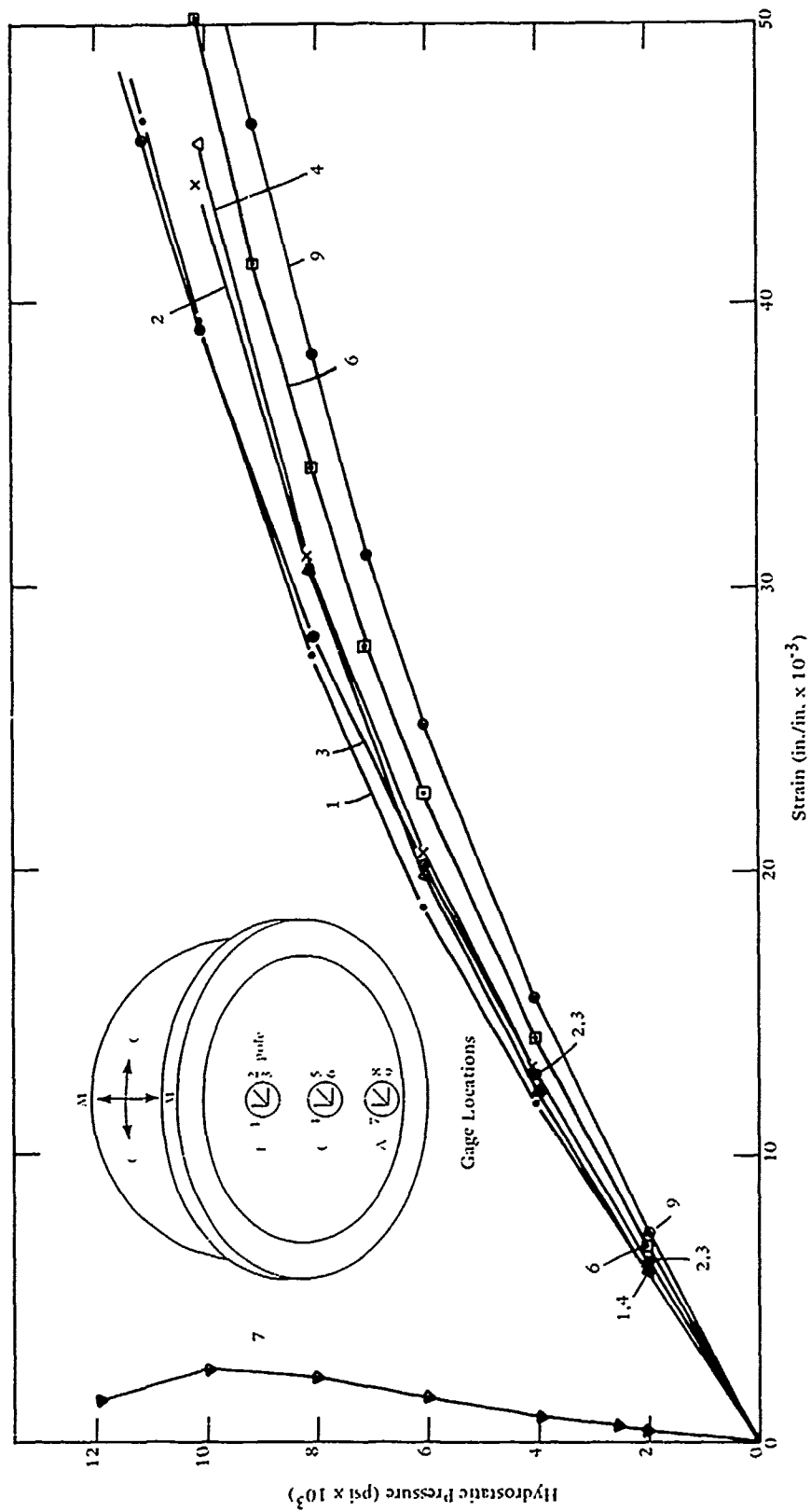


Figure 87. Window C, Type I under short-term loading.

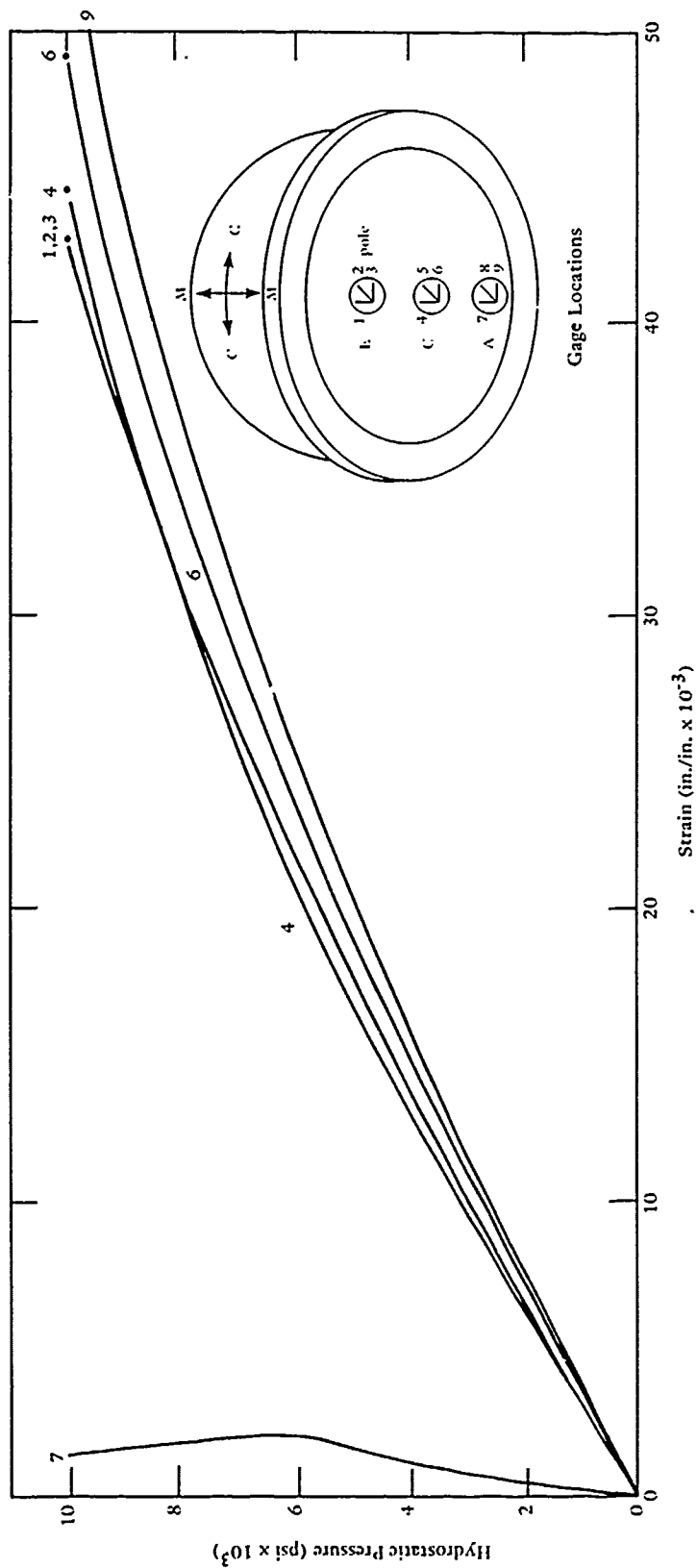


Figure 88. Window 0, Type VI under short-term loading.

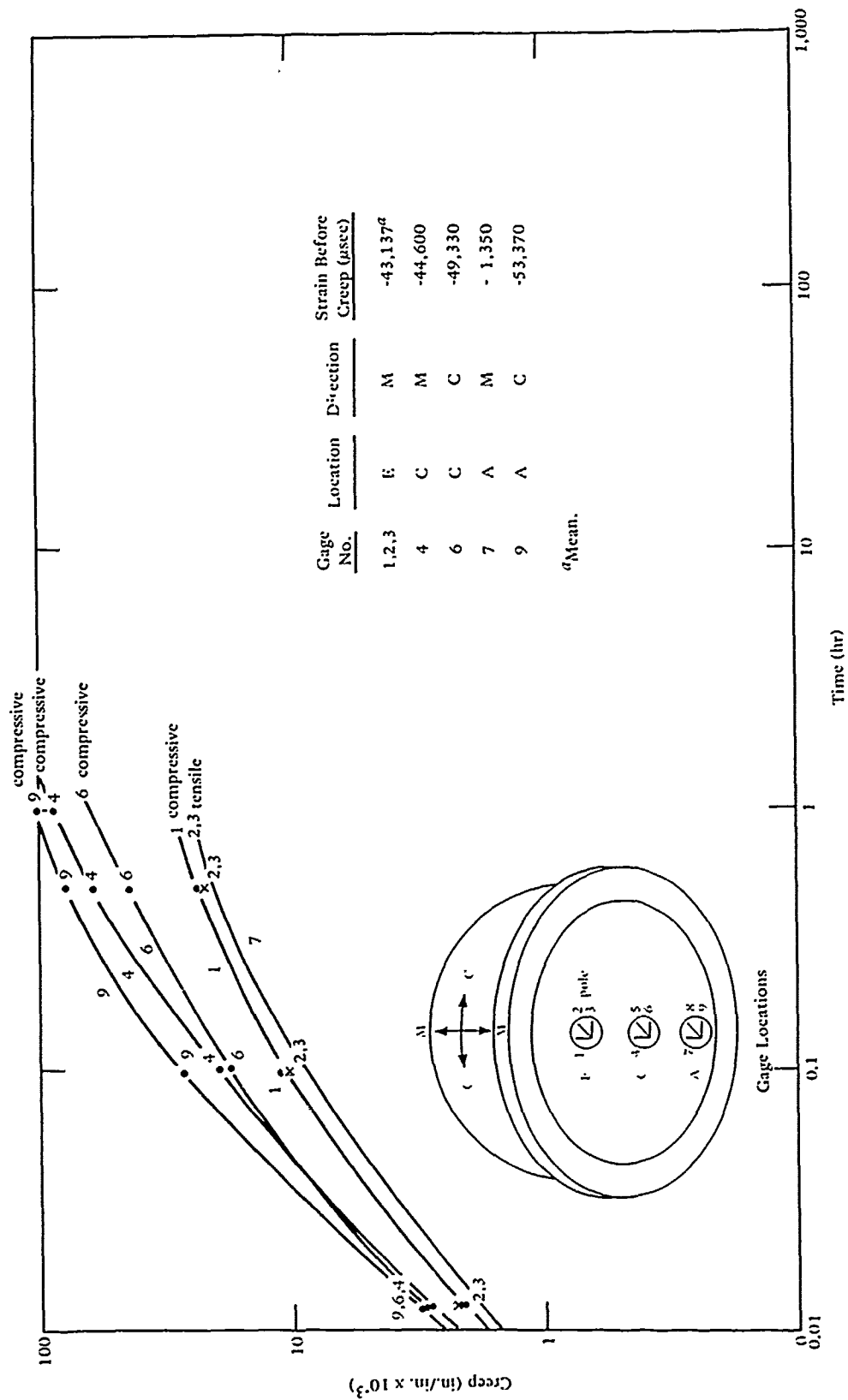


Figure 89. Window O, Type VI under sustained loading at 10,000 psi.

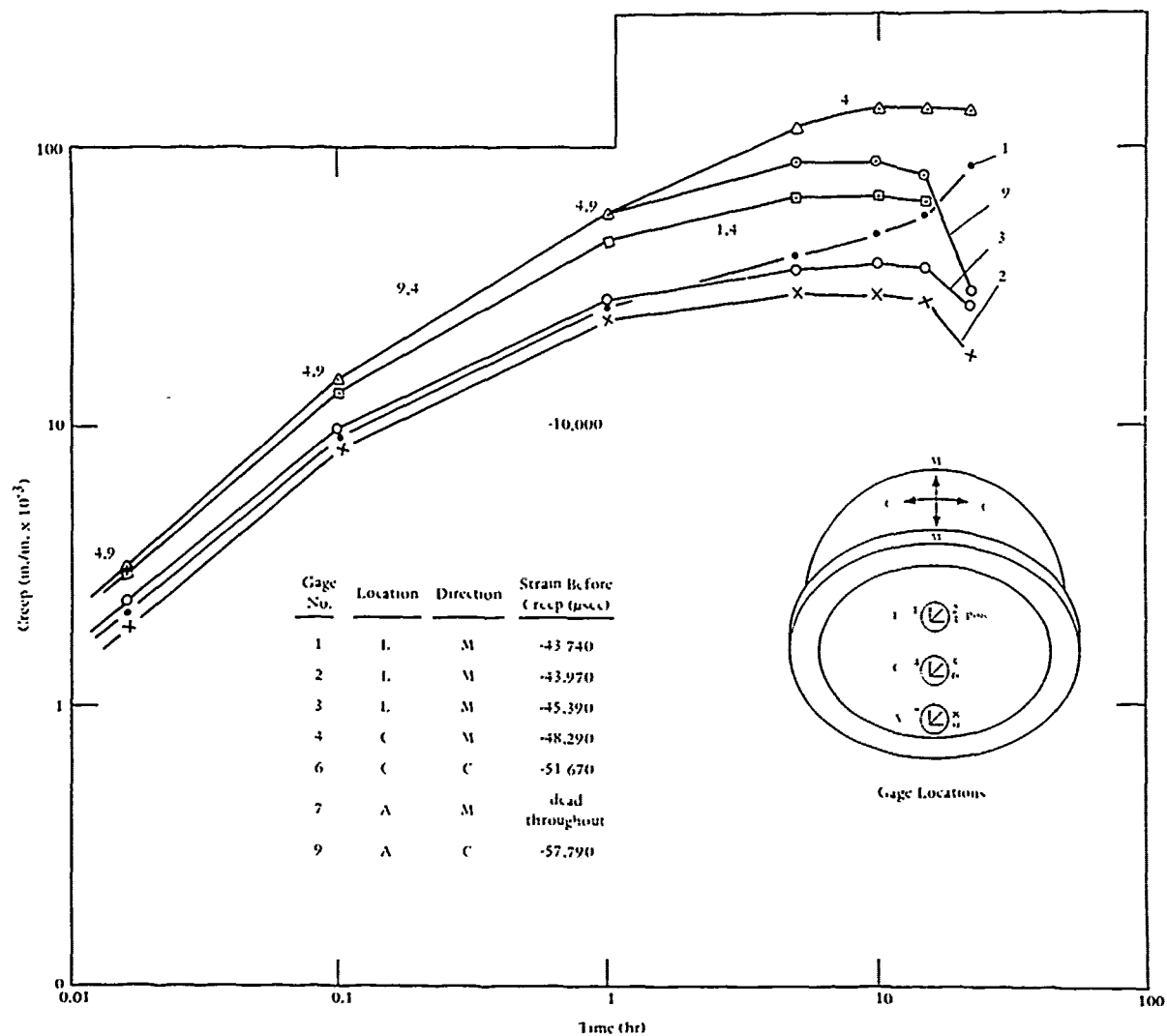


Figure 90. Window D, Type I under sustained loading at 10,000 psi.

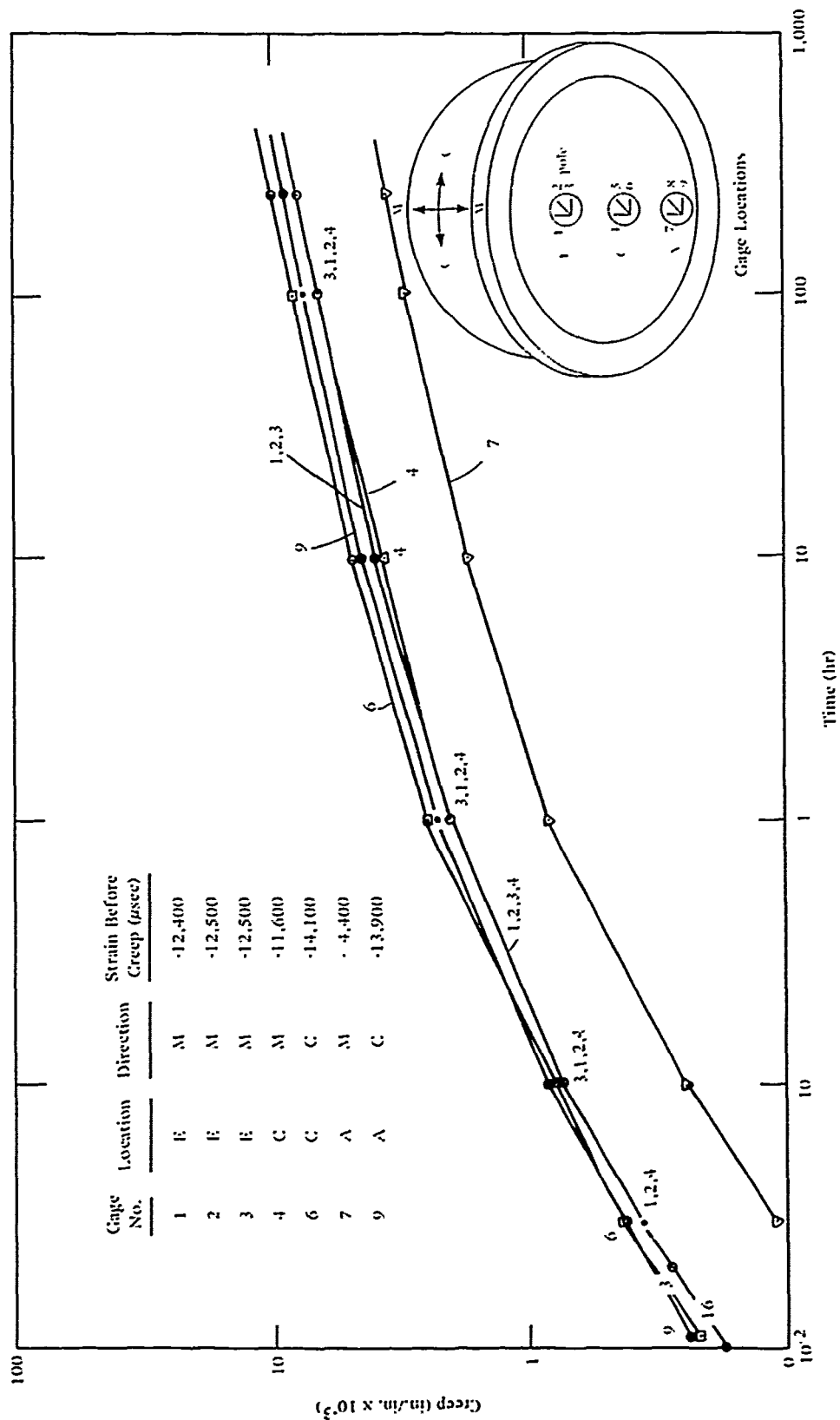


Figure 91. Window R, Type VI under sustained loading at 4,000 psi.

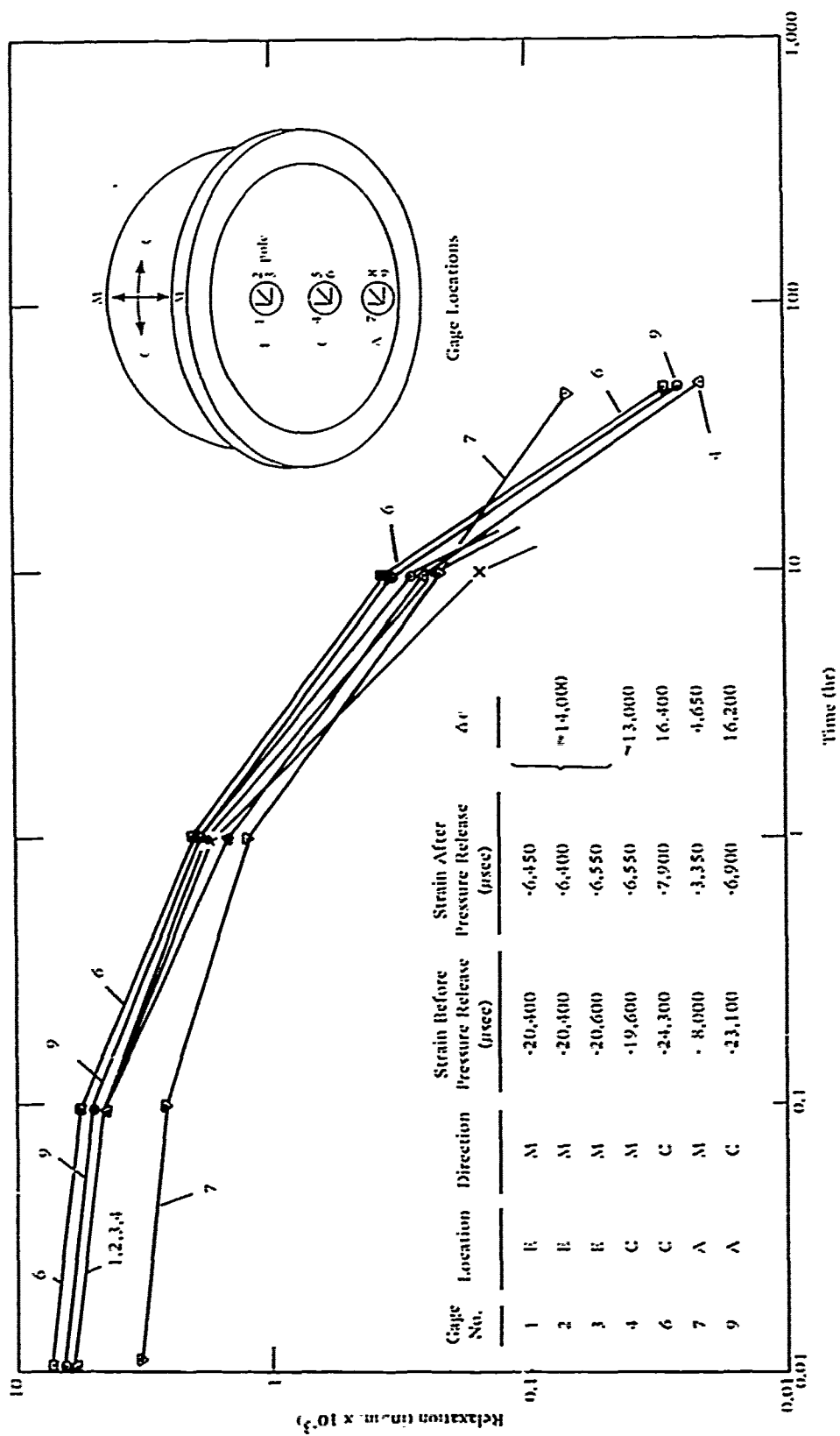


Figure 92. Window R, Type VI during relaxation from sustained loading at 4,000 psi.

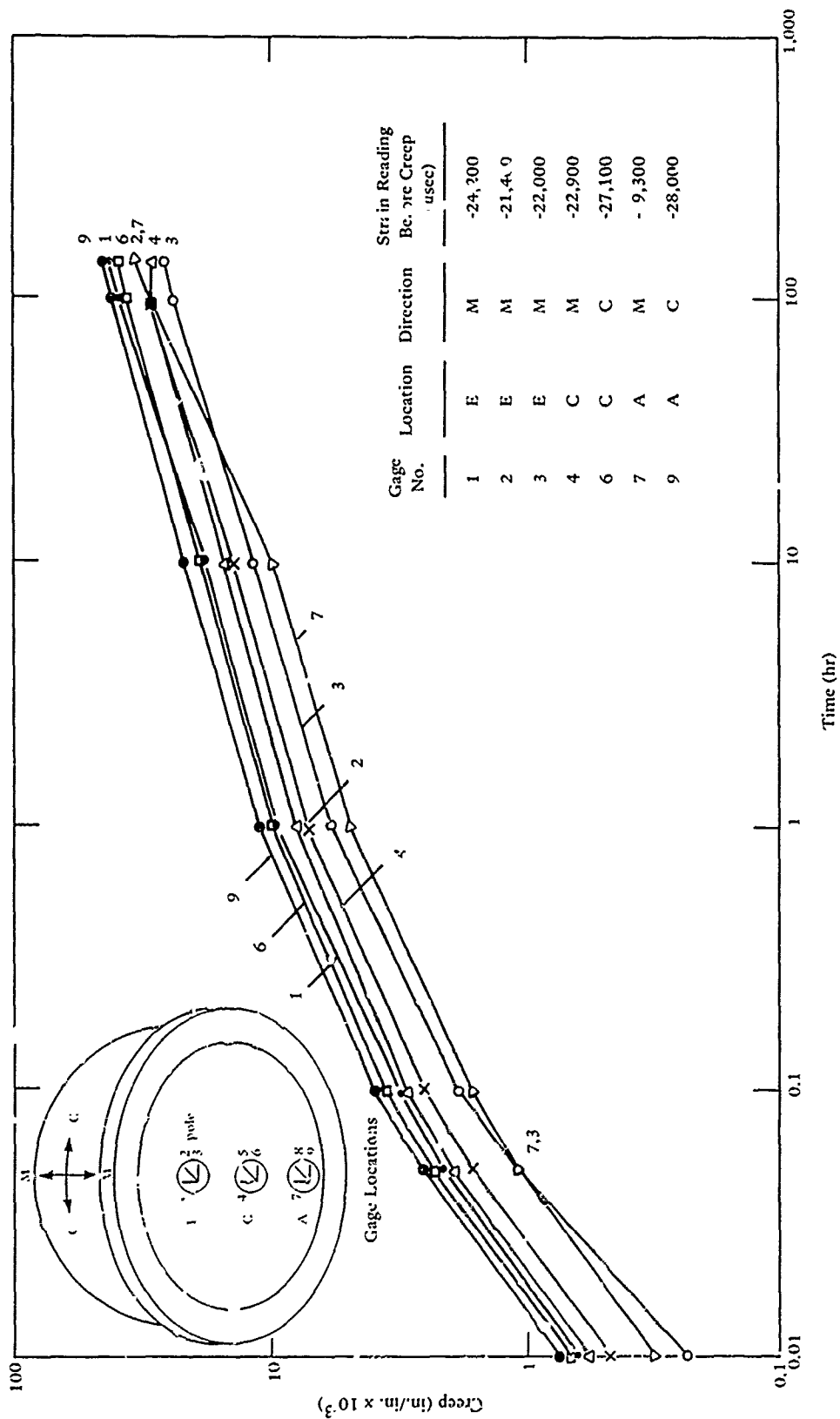


Figure 93. Window Q, Type VI during sustained loading at 7,000 psi.



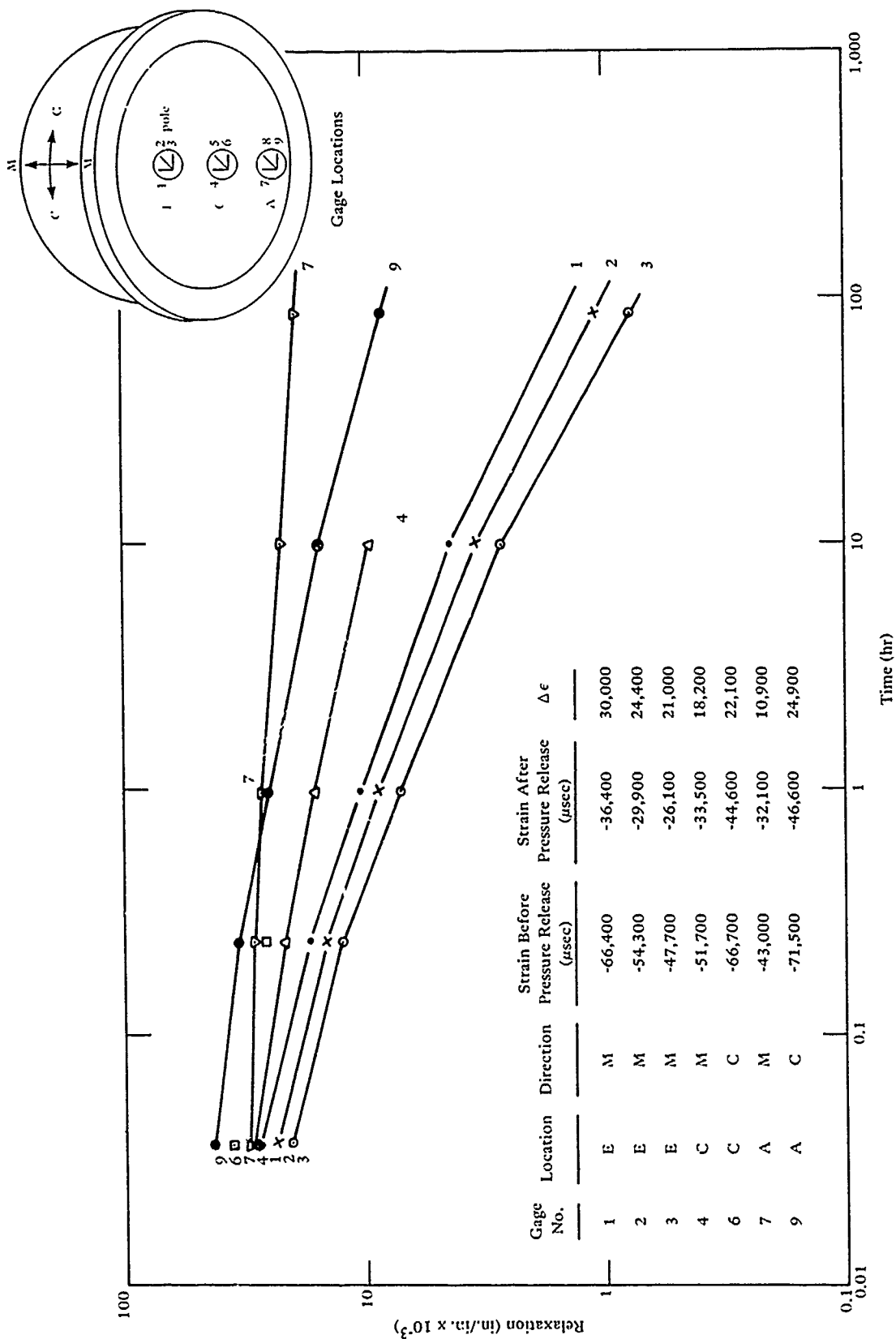


Figure 94. Window Q, Type VI during relaxation from sustained loading at 7,000 psi.

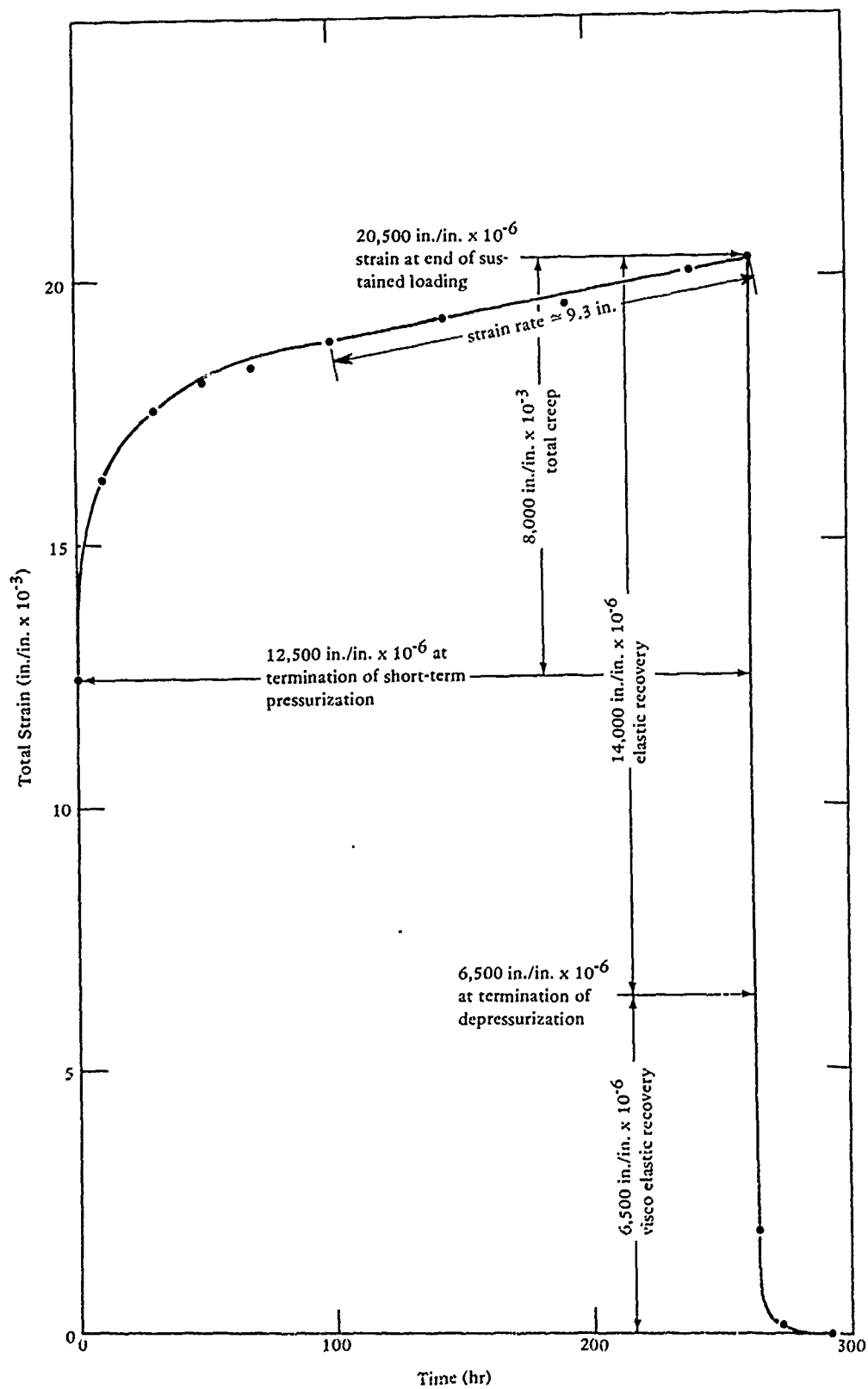


Figure 95. Window R, Type VI during a sustained pressure loading and the subsequent relaxation; strain on the interior face at the apex.

## Definition of Technical Terms

short-term loading	increasing the hydrostatic pressure at 650 psi/minute rate
short-term critical pressure (STCP)	pressure at which catastrophic failure of the window occurs when subjected to short-term hydrostatic loading at 75°F (24°C) ambient temperature
long-term or static loading	pressurizing the window to a specified pressure at 650 psi/minute rate and maintaining that pressure for specified number of hours
cyclic loading	pressurizing the window repeatedly to a specified pressure at 650 psi/minute rate, maintaining this pressure for a specified number of hours, depressurizing at 650 psi per minute to 0 psi and allowing the window to relax for a specified number of hours before repeating the procedure
strain	unit deformation, in./in. of original length
creep	time dependent deformation of material under sustained loading of constant magnitude; in./in. of original length
relaxation	time dependent restoration of material to its original dimensions under absence of external loading; in./in. of original length
hoop orientation of strains or stresses	direction parallel to the edge of spherical sector window
meridional orientation of strains or stresses	direction at right angle to the hoop direction; meridional lines pass through the apex
total strain	total deformation of material, includes both the short term and creep components of strain; in./in. of original length
short-term strain	deformation of material under short-term loading; in./in. of original length
radial displacement	displacement of the interior surface at the apex towards the center of curvature for the hemisphere
normalized strain	strain per unit increase of pressure under short-term loading; in./in./psi

## DISTRIBUTION LIST

AFB CESCH, Wright-Patterson, Stinfo Library, Offutt NE  
 ARMY BMDSC-RC (H. McClellan, Huntsville AL  
 ARMY BALLISTIC RSCH LABS AMXBR-XA-LB, Aberdeen Proving Ground MD  
 ARMY COASTAL ENGR RSCH CEN Fort Belvoir VA  
 ARMY CORPS OF ENGR Seattle Dist. Library, Seattle WA  
 ARMY CRREL A. Kovacs, Hanover NH  
 ARMY MATERIALS & MECHANICS RESEARCH CENTER Dr. Lenoe, Watertown MA  
 ASST SECRETARY OF THE NAVY Spec. Assist Energy (P. Waterman), Washington DC. Spec. Assist Submarines,  
 Washington DC  
 BUREAU OF RECLAMATION Code 1512 (C. Selander) Denver CO  
 MCB ENS S.D. Keisling, Quantico VA  
 CNO Code OPNAV 90H, OP987P4 (B. Petrie), Pentagon  
 COMFLEACT PWO, Okinawa Japan  
 COMSUBDEVGRUCNE Operations Offr, San Diego, CA  
 DEFENSE DOCUMENTATION CTR Alexandria, VA  
 DEFENSE INTELLIGENCE AGENCY Dir., Washington DC  
 DTNSRDC Code 1548 (T. Tsai), Bethesda MD, Code 1706, Bethesda MD  
 DTNSRDC Code 284 (A. Rufolo), Annapolis MD  
 ENERGY R&D ADMIN, INEL Tech. Lib. (Reports Section), Idaho Falls ID  
 NAD Code 011B-1, Hawthorne NV  
 NAS PWD Maint. Div., New Orleans, Belle Chasse LA, PWO  
 NAVAIRSYSCOM LT W. Hall, Washington DC  
 NAVAL FACILITY PWO, Centerville Bch, Ferndale CA  
 NAVARCLAB Library, Pt Barrow AK  
 NAVCOASTSYSLAB Code 710 (R. Elliott), Code 710.5 (J. Mittleman), Code 710.5 (J. Quirk), Library  
 NAVCOMMSTA PWO, Adak AK  
 NAVFACENGCOM Code 0433B, Code 0451, Code 04B5, Code 101, PC-22 (E. Spencer), PL-2  
 NAVFACENGCOM - CHES DIV, Code 403 (H. DeVoe), Code FPO-I (Ottson), Code FPO-1C2  
 NAVFACENGCOM - LANT DIV, RDT&ELO 09P2, Norfolk VA  
 NAVFACENGCOM - NORTH DIV, Code 1028, RDT&ELO, Philadelphia PA  
 NAVFACENGCOM - PAC DIV, Code 402, RDT&E, Pearl Harbor HI, Commanders  
 NAVFACENGCOM - SOUTH DIV, Code 90, RDT&ELO, Charleston SC  
 NAVFACENGCOM - WEST DIV, Codes 09PA, 09P/20  
 NAVHOSP LT R. Elsbernd, Puerto Rico  
 NAVOCEANO Code 1600, Code 3412 (J. DePalma), Washington DC  
 NAVPHIBASE Code S3T, Norfolk VA, OIC, UCT I  
 NAVSCOLCECOFF C35  
 NAVSHIPYD Code 400, Puget Sound, PWO  
 NAVSTA CO, PWD/Engr. Div, Puerto Rico, PWO, Puerto Rico  
 NAS OIC, CBU 417, Oak Harbor WA, PWD (ENS E.S. Agonoy), Chase Field, Beeville TX  
 NATL OCEAN AND ATMDS, ADMIN, Libraries Div.-D823, Silver Spring MD  
 NATL RESEARCH COUNCIL Naval Studies Board, Washington DC  
 NAVACT PWO, London UK  
 NAVCOMMSTA PWO  
 NAVCONSTRACEN CO (CDR C.L. Neugent), Port Hueneme, CA  
 NAVELEXSYSCOM Code PME-124-61, Washington DC  
 NAVEODFAC Code 605, Indian Head MD  
 NAVFACENGCOM CDR L K Donovan, Alexandria VA, Code 0453 (D. Potter)  
 NAVFACENGCOM - CHES DIV, Code 402 (R. Mczony), Code FPO-I (C. Bodey), Code FPO-ISP13 (T F Sullifan)  
 NAVFACENGCOM CONTRACTS Eng Div dir, Southwest Pac, PI, TRIDENT (CDR J.R. Jacobsen), Bremerton WA  
 98310  
 NAVMARCORESTRANCEN ORU 1118 (Cdr D.R. Lawson), Denver CO  
 NAVSEASYSYSCOM Code SEA OOC  
 NAVSEC Code 6034 (Library), Washington DC  
 NAVSHIPYD Code 202.4, Long Beach CA, Code 202.5 (Library) Puget Sound, Bremerton WA, Code Portsmouth NH,  
 PWD (LT N.B. Hall), Long Beach CA

NAVSUPPACT AROICC (LT R.G. Hocker), Naples Italy  
 NAVWPNSUPPCEN PWO  
 NAVXDIVINGU LT A.M. Parisi, Panama City FL  
 NCBC CEL (CDR N.W. Petersen), Port Hueneme, CA, Code 10  
 NCBU 411 OIC, Norfolk VA  
 NMCB One, LT F.P. Digeorge  
 NTC Code 54 (ENS P. G. Jackel), Orlando FL  
 NUC Code 4099 (E. Hamilton), San Diego CA, Code 65 (H. Talkington), Code 65402 (R. Jones), Code 6565 (Tech. Lib.), San Diego CA  
 NUSC Code EA123 (R.S. Munn), New London CT, Code S332, B-80 (J. Wilcox), Code TA131 (G. De la Cruz), New London CT  
 OCEANAV Mangmt Info Div., Arlington VA  
 OFFICE OF NAVAL RESEARCH CDR Harlett, Boston MA  
 ONR Code 484, Arlington VA, Dr. A. Laufer, Pasadena CA  
 PLASTICS TECH EVAL CTR PICATINNY ARSENAL A. Anzalone, Dover NJ  
 PMTC Pat. Counsel, Point Mugu CA  
 PWC ENS J.E. Surash, Pearl Harbor HI, ACE Office (LTJG St. Germain), Code 120C (A. Adams), ENS J.A. Squatrito, San Francisco Bay, Oakland CA  
 SUBASE NEW LONDON LTJG D. W. Peck Groton CT  
 USCG MMT-4, Washington DC  
 USCG ACADEMY LT N. Stramandi, New London CT  
 USCG R&D CENTER CO, D. Motherway, Groton CT, Tech. Dir.  
 USNA Ch. Mech. Engr. Dept, Sys. Engr Dept (Dr. Monney), Annapolis MD  
 CALIFORNIA INSTITUTE OF TECHNOLOGY PASADENA, CA (SCOTT)  
 CALIFORNIA STATE UNIVERSITY LONG BEACH, CA (CHELAPATI)  
 CITY OF CERRITOS Cerritos CA (J. Adams)  
 COLORADO STATE UNIV., FOOTHILL CAMPUS Engr Sci. Branch, Lib., Fort Collins CO  
 CORNELL UNIVERSITY Ithaca NY (Serials Dept, Engr Lib.)  
 DAMES & MOORE LIBRARY LOS ANGELES, CA  
 FLORIDA ATLANTIC UNIVERSITY BOCA RATON, FL (MC ALLISTER), Boca Raton FL (Ocean Engr Dept., C. Lin)  
 FLORIDA ATLANTIC UNIVERSITY Boca Raton FL (W. Tessin)  
 GEORGIA INSTITUTE OF TECHNOLOGY Atlanta GA (School of Civil Engr., Kahn), Atlanta GA (B. Mazanti)  
 INSTITUTE OF MARINE SCIENCES Morehead City NC (Director)  
 IOWA STATE UNIVERSITY Ames IA (CE Dept, Handy)  
 LEHIGH UNIVERSITY BETHLEHEM, PA (MARINE GEOTECHNICAL LAB., RICHARDS), Bethlehem PA (Fritz Engr. Lab No. 13, Beedle), Bethlehem PA (Linderman Lib. No. 30, Flecksteiner)  
 LIBRARY OF CONGRESS WASHINGTON, DC (SCIENCES & TECH DIV)  
 MAINE MARITIME ACADEMY CASTINE, ME (LIBRARY)  
 MASSACHUSETTS INST. OF TECHNOLOGY Cambridge MA (Rm 10-500, Tech. Reports, Engr. Lib.), Cambridge MA (Rm 14 E210, Tech. Report Lib.), Cambridge MA (Whitman)  
 MICHIGAN TECHNOLOGICAL UNIVERSITY HOUGHTON, MI (HAAS)  
 MIT Cambridge, MA (Harleman)  
 NATL ACADEMY OF ENG. ALEXANDRIA, VA (SEARLE, JR.)  
 OREGON STATE UNIVERSITY CORVALLIS, OR (CE DEPT, BELL), Corvallis OR (School of Oceanography), LT R.B. Steimer, NROTC Unit, Corvallis OR  
 PENNSYLVANIA STATE UNIVERSITY STATE COLLEGE, PA (SNYDER), UNIVERSITY PARK, PA (GOTOLSKI)  
 PURDUE UNIVERSITY LAFAYETTE, IN (ALTSCHAEFFL), LAFAYETTE, IN (CE LIB), Lafayette IN (Leonards)  
 RUTGERS UNIVERSITY New Brunswick NH (Civil & Environ Engr Dept., du Bouchet)  
 SAN DIEGO STATE UNIV. Dr. Krishnamoorthy, San Diego CA  
 SCRIPPS INSTITUTE OF OCEANOGRAPHY LA JOLLA, CA (ADAMS), San Diego, CA (Marina Phy. Lab. Spiess)  
 STANFORD UNIVERSITY STANFORD, CA (DOUGLAS)  
 TEXAS A&M UNIVERSITY COLLEGE STATION, TX (CE DEPT), College TX (CE Dept, Herbich)  
 BONNEVILLE POWER ADMIN Los Angeles CA (Hancock Lib. of Bio. & Ocean)  
 UNIVERSITY OF CALIFORNIA BERKELEY, CA (CE DEPT, MITCHELL), BERKELEY, CA (OFF BUS. AND FINANCE, SAUNDERS), DAVIS, CA (CE DEPT, TAYLOR), SAN DIEGO, CA, LA JOLLA, CA (SEROCKI)  
 UNIVERSITY OF DELAWARE Newark, DE (Dept of Civil Engineering, Chesson)  
 UNIVERSITY OF HAWAII HONOLULU, HI (SCIENCE AND TECH. DIV.)

UNIVERSITY OF ILLINOIS URBANA, IL (LIBRARY)  
 UNIVERSITY OF MASSACHUSETTS (Heronemus), Amherst MA CE Dept  
 UNIVERSITY OF MICHIGAN Ann Arbor MI (Richart)  
 UNIVERSITY OF NEBRASKA-LINCOLN LINCOLN, NE (SPLETTSTOESSER)  
 UNIVERSITY OF NEW HAMPSHIRE DURHAM, NH (LAVOIE)  
 UNIVERSITY OF PENNSYLVANIA PHILADELPHIA, PA (SCHOOL OF ENGR & APPLIED SCIENCE. ROLL)  
 UNIVERSITY OF RHODE ISLAND KINGSTON, RI (PAZIS)  
 UNIVERSITY OF TEXAS Inst. Marina Sci (Library), Port Aransas TX  
 UNIVERSITY OF WASHINGTON SEATTLE, WA (APPLIED PHYSICS LAB). SEATTLE, WA (OCEAN ENG  
 RSCH LAB. GRAY), SEATTLE, WA (PACIFIC MARINE ENVIRON. LAB., HALPERN)  
 US DEPT OF COMMERCE NOAA. Marine & Earth Sciences Lib., Rockville MD  
 UNIVERSITY OF CALIFORNIA Berkeley CA (E. Pearson), La Jolla CA (Acq. Dept, Lib. C-075A)  
 UNIVERSITY OF ILLINOIS Honolulu HI (Dr. Szilard)  
 UNIVERSITY OF RHODE ISLAND Narragansett RI (Pell Marine Sci. Lib.)  
 US GEOLOGICAL SURVEY Off. Marine Geology, Mailstop 915, Reston VA  
 AEROSPACE CORP. Acquisition Group, Los Angeles CA  
 ARCAIR CO. D. Young, Lancaster OH  
 ARVID GRANT OLYMPIA, WA  
 ATLANTIC RICHFIELD CO. DALLAS, TX (SMITH)  
 AUSTRALIA Dept. PW (A. Hicks), Melbourne  
 BECHTEL CORP. SAN FRANCISCO, CA (PHELPS)  
 BELGIUM NAECON, N.V., GEN.  
 BETHLEHEM STEEL CO. BETHLEHEM, PA (STEELE)  
 BROWN & ROOT Houston TX (D. Ward)  
 CANADA Can-Dive Services (English) North Vancouver. Lockheed Petrol. Srv. Ltd., New Westminster BC. Mem  
 Univ Newfoundland (Chari), St Johns, Surveyor, Nenninger & Chenevert Inc..  
 CHEVRON OIL FIELD RESEARCH CO. LA HABRA, CA (BROOKS)  
 COLUMBIA GULF TRANSMISSION CO. HOUSTON, TX (ENG. LIB.)  
 DILINGHAM PRECAST F. McHale, Honolulu HI  
 DRAVO CORP Pittsburgh PA (Giannino)  
 NORWAY DET NORSKE VERITAS (Library), Oslo  
 ESSO PRODUCTION RESEARCH CORP. HOUSTON, TX (RUNGE)  
 EVALUATION ASSOC. INC KING OF PRUSSIA, PA (FEDELE)  
 FRANCE P. Jensen, Boulogne, Pierre Launay, Boulogne-Billancourt, Roger LaCroix, Paris  
 GLOBAL MARINE DEVELOPMENT NEWPORT BEACH, CA (HOLLETT)  
 GOULD INC. Shady Side MD (Ches. Inst. Div., W. Paul)  
 GRUMMAN AEROSPACE CORP. Bethpage NY (Tech. Info. Ctr)  
 ITALY M. Caironi, Milan, Sergio Tattoni Milano  
 LAMONT-DOHERTY GEOLOGICAL OBSERV. Palisades NY (McCoy), Palisades NY (Selwyn)  
 LOCKHEED MISSILES & SPACE CO. INC. SUNNYVALE, CA (PHILLIPS)  
 MARATHON OIL CO Houston TX (C. Seay)  
 MARINE CONCRETE STRUCTURES INC. MEFAIRIE, LA (INGRAHAM)  
 NEWPORT NEWS SHIPBLDG & DRYDOCK CO. Newport News VA (Tech. Lib.)  
 NORWAY A. Torum, Trondheim, DET NORSKE VERITAS (Roren) Oslo, J. Creed, Ski, J.D. Holst, Oslo,  
 Norwegian Tech Univ (Brandtzaeg), Trondheim  
 OCEAN DATA SYSTEMS, INC. SAN DIEGO, CA (SNODGRASS)  
 OCEAN ENGINEERS SAUSALITO, CA (RYNECKI)  
 OCEAN RESOURCE ENG. INC. HOUSTON, TX (ANDERSON)  
 OFFSHORE DEVELOPMENT ENG. INC. BERKELEY, CA, Berkeley CA  
 PORTLAND CEMENT ASSOC. Skokie IL (Rsch & Dev Lab, Lib.)  
 PRESCON CORP TOWSON, MD (KELLER)  
 PUERTO RICO Puerto Rico (Rsch Lib.), Mayaguez P R  
 RAND CORP. Santa Monica CA (A. Laupa)  
 SANDIA LABORATORIES Library Div., Livermore CA  
 SCHUPACK ASSOC SO. NORWALK, CT (SCHUPACK)  
 SEATECH CORP. MIAMI, FL (PERONI)  
 SHELL DEVELOPMENT CO. Houston TX (E. Doyle)  
 SHELL OIL CO. HOUSTON, TX (MARSHALL), Houston TX (R. de Castongrene)  
 SWEDEN VBB (Library), Stockholm

TIDEWATER CONSTR. CO Norfolk VA (Fowler)  
TRW SYSTEMS CLEVELAND, OH (ENG. LIB.), REDONDO BEACH, CA (DAI)  
UNITED KINGDOM D. New, G. Maunsell & Partners, London, Shaw & Hatton (F. Hansen), London, Taylor,  
Woodrow Constr (014P), Southall, Middlesex, Taylor, Woodrow Constr (Stubbs), Southall, Middlesex, Univ. of  
Bristol (R. Morgan), Bristol  
UNITED TECHNOLOGIES Windsor Locks CT (Hamilton Std Div., Library)  
WESTINGHOUSE ELECTRIC CORP. Annapolis MD (Oceanic Div Lib, Bryan)  
WM CLAPP LABS - BATTELLE DUXBURY, MA (LIBRARY), DUXBURY, MA (RICHARDS)  
GREG PAGE EUGENE, OR